

Dissertation zur Erlangung des Doktorgrades
der Fakultät für Geowissenschaften
der Ludwig-Maximilians-Universität München



*Regional-Scale, Natural
Persistent Scatterer Interferometry,
Island of Crete (Greece), and Comparison to Vertical
Surface Deformation on the Millennial-, and Million-
Year Time-Scales.*

Stefanie Rieger

München
September 2015

Eingereicht am 16. September 2015

1. Gutachterin: Prof. Dr. Anke Friedrich

2. Gutachter: Prof. Dr. Michael Eineder

Tag der mündlichen Prüfung: 18. Dezember 2015

*Für meine Eltern
und meine Schwester*

TABLE OF CONTENTS

TABLE OF CONTENTS I

List of Tables V

List of Figures IX

List of Abbreviations XXII

ABSTRACT (SUMMARY)..... 1

ZUSAMMENFASSUNG 2

ACKNOWLEDGEMENTS 3

Danksagung 4

Chapter 1 5

INTRODUCTION 5

1.1 Tectonic Setting of Crete 8

1.2 Neotectonic Vertical Deformation 9

1.3 Archaeological and Historical Seismicity 10

1.4 Instrumental Seismicity 10

1.5 The PSI Method 11

References 12

Figures & Tables 20

Chapter 2 32

ACTIVE VERTICAL SURFACE-DEFORMATION PATTERN OF CRETE USING PERSISTENT SCATTERER INTERFEROMETRY (PSI) 32

2.1 Abstract 32

2.2 Introduction 32

2.3 Geological Setting 33

2.4 Tectonic Geodesy of Crete 34

2.5 Methods 34

2.5.1 Global Positioning System Processing 34

2.5.2 Persistent Scatterer Interferometry Processing 35

2.5.2.1 Persistent Scatterer Interferometry Error Propagation 35

2.5.2.2 Atmosphere Effect Compensation 35

2.5.2.3 Orbital Uncertainty Compensation 36

2.6 Results 37

2.6.1 Results of Global Positioning System Measurements 37

2.6.2 Results of Persistent Scatterer Interferometry Measurements 37

2.7 Analysis of Persistent Scatterer Interferometry Measurements	38
2.8 Discussion and Significance of Surface-Deformation Pattern	40
2.9 Conclusions	45
References	47
Figures & Tables	54
<i>Chapter 3</i>	87
<i>DETECTION OF ACTIVE MOTION ACROSS NORMAL FAULTS ON CRETE</i>	87
3.1 Abstract	87
3.2 Introduction	87
3.3 Geological Setting	88
3.4 Normal Faults across Crete	89
3.5 Methods	90
3.6 Results	91
3.7 Analysis of PSI Measurements across Normal Faults	91
3.8 Discussion and Significance of Surface Deformation across Normal Faults.....	93
3.9 Conclusions	95
References	96
Figures & Tables	101
<i>Chapter 4</i>	124
<i>MORPHOTECTONIC ANALYSIS AND IMPLICATIONS FOR THE INTERMEDIATE-TERM COASTAL UPLIFT PATTERN OF CRETE</i>	124
4.1	Abstract
.....	124
4.2 Introduction	124
4.3 Morphotectonic Setting	125
4.4 Present-Day Climate	125
4.5 Millennial-Scale Uplift History of Crete.....	126
4.6 Investigating Geomorphic Markers for Analysing the Surface Deformation Pattern and Uplift Rates	127
4.6.1 Longitudinal River Profiles	127
4.6.2 Marine Shorelines	128
4.7 Methods.....	130
4.7.1 Vertical Deformation based on River Longitudinal Profiles	130
4.7.2 Vertical Deformation based on Paleo-Shorelines	131

4.7.2.1 Pleistocene Paleo-Shorelines.....	131
4.7.2.2 Holocene Paleo-Shorelines	131
4.7.2.3 Pleistocene and Holocene Uplift Rates	131
4.8 Results	132
4.8.1. Concavity	132
4.8.2 Steepness Index	132
4.8.3 Knickpoints	132
4.8.4 Pleistocene Paleo-Shorelines.....	133
4.8.5 Holocene Paleo-Shorelines	133
4.9 Analysis	133
4.9.1 Vertical Deformation based on River Longitudinal Profiles	133
4.9.2 Vertical Deformation based on Paleo-Shoreline Analysis	135
4.9.2.1 Pleistocene Uplift Rates	135
4.9.2.2 Holocene Uplift Rates	136
4.9.2.3 Pleistocene and Holocene Paleo-Shorelines	136
4.9.2.3.1 Uplift-Rates only by Tectonics	136
4.9.2.3.2 Uplift-Rates only by Sea-Level Changes	137
4.9.2.1.3 Uplift-Rates based on Tectonic and Sea-Level corrected Analysis of Paleo-Shorelines	138
4.10 Discussion	138
4.11 Conclusions	140
References	141
Figures & Tables	148
<i>Chapter 5</i>	<i>185</i>
<i>SYNTHESIS OF NEOGENE GEOLOGICAL STRUCTURES AND SEDIMENTOLOGICAL DATA ACROSS CRETE AND IMPLICATIONS FOR THE LONG-TERM VERTICAL SURFACE-DEFORMATION PATTERN OF CRETE</i>	<i>185</i>
5.1 Abstract	185
5.2 Introduction	185
5.3 Neogene Structures and Sediments	185
5.4 Methods.....	187
5.5 Results	188
5.6 Discussion	188
5.7 Conclusions	189

References	190
Figures & Tables	194
<i>Chapter 6</i>	202
<i>PATTERN OF VERTICAL SURFACE DEFORMATION OF CRETE BASED ON A SYNTHESIS OF GEODETIC, GEOMORPHOLOGICAL, AND GEOLOGICAL DATA, AND IMPLICATIONS FOR CRUSTAL DEFORMATION MECHANISMS</i>	202
6.1 Abstract	202
6.1 Introduction	202
6.2 Synthesis of Vertical Deformation Rates across different Time-Scales	203
6.3 Results	204
6.4 Discussion	204
6.4 Conclusions	206
References	207
Figures & Tables	209
<i>II. APPENDIX</i>	215
Chapter 3	215
Chapter 4	229
Chapter 5	280
CURRICULUM VITAE	284

List of Tables

Table 1.1: Geomorphic and geologic markers.	30
Table 1.2: Historical earthquakes affecting Crete (Abraseys et al., 1994).....	30
Table 1.3: GCMT list of earthquakes in the vicinity of Crete.....	31
Table 2.1: Time span of GPS measurements on Crete.....	86
Table 2.2: The estimation precision lower bound for the four tracks of Crete.	86
Table 2.3: GPS measurements relative to stable Europe.	86
Table 2.4: Total number of all measured PSs per track, how many are uplifting, stable or subsiding.....	86
Table 2.5: Percentage of all measured PSs per track, how many are uplifting, stable or subsiding.	86
Table 3.1: PS measurements for the footwall and hanging wall across normal faults on Crete, and the calculated dip-slip component S	121
Table 3.2: Geological and geodetic data of slip along normal faults in Crete.	122
Table 3.3: Normal faults on Crete and their type of motion and lithology of footwall and hanging wall.	123
Table 4.1: Locations of published Pleistocene paleo-shorlines and the corresponding author....	172
Table 4.2: Locations of published Holocene paleo-shorlines and the corresponding author.....	172
Table 4.3: Marine isotopic stages (MIS), corresponding age and sea-level after Rohling et al. (2014).	172
Table 4.4: Locations of dated Pleistocene terraces, their corresponding MIS stage and the present elevation.	173
Table 4.5: Location and referring numbering of Pleistocene and Holocene shorelines at one locality.....	173
Table 4.6: Parameters for the 365 A.D. Mw 8.3 earthquake and the 1303 A.D. Mw7.9 earthquake.	173
Table 4.7: Terraces, their age, present elevation and calculated uplift rate. No sea-level.	174
Table 4.8: Mean uplift rates (R) for each author listed in Table 4.4.	175
Table 4.9: Displacement between terraces, the corresponding slip, M_0 and M_w	175
Table 4.10: Terraces, their age and calculated age, present elevation and sea-level change rate. No tectonics.....	176
Table 4.11: Constant uplift rate at Moni-Chryssoskalitissa terrace numbers, elevation heights, and uplift rates (Rohling et al., 2014).	177
Table 4.12: Mean uplift rates (R) for each author listed in Table 4.8.	180
Table 4.13: Not constant uplift rate at Moni-Chryssoskalitissa terrace numbers, elevation heights, and uplift rates (Rohling et al., 2014).....	180
Table 4.14: Mean uplift rates (R) for each author listed in Table 4.8.	183

Table 4.15: Average uplift rate, slip rate, recurrence time for the 21 st July 365 A.D. earthquake.	183
Table 4.16: Average uplift rate, slip rate, recurrence time for 21 st July 365 earthquake, and total slip for highest and oldest terrace. All values are sea-level corrected after Rohling et al. (2014).	183
Table 4.17: Influence on uplift rates based on the choice of the sea-level curve.....	184
Table 5.1: Age ranges of van Hinsbergen and Meulenkaamp (2006) correlated to ages [Ma].	201
Table 5.2: Calculated uplift rates for coastal regions.....	201
Table 6.1: Vertical surface-deformation above a subduction zone, Crete.	213
Table 6.2: Calculated uplift rates for coastal regions.....	213
Table 6.3: Vertical uplift-rates on the decadal-, and the millennial time-scale on Crete.....	213
Table 6.4: Above (+) or below (-) sea level. Please consider Figure 6.6 for time intervals.	214
Table 6.5: Vertical uplift-rates on the decadal-, millennial-, and long-term time-scale for NE Japan.....	214
Table II.1: Slip rates based on geological and geodetic data for the normal faults on Crete.....	215
Table II.2: Terraces, their age, present elevation and calculated uplift rate. No sea-level.	230
Table II.3: Average uplift rate, slip rate, and recurrence time.	231
Table II.4: Terraces, their age and calculated age, present elevation and sea-level change rate. No tectonics.....	233
Table II.5: Ierapetra (P1) terrace numbers, elevation heights, and uplift rates (Rohling et al., 2014).....	234
Table II.6: Average uplift rate, slip rate, and recurrence time.	235
Table II.7: Terraces, their age, present elevation and calculated uplift rate. No sea-level.	237
Table II.8: Average uplift rate, slip rate, and recurrence time.	238
Table II.9: Displacement between terraces, the corresponding slip, M_0 and M_w	238
Table II.10: Terraces, their age and calculated age, present elevation and sea-level change rate. No tectonics.....	241
Table II.11: Terrace numbers, elevation heights, and uplift rates. Sea-level corrected and tectonics (Rohling et al., 2014).	243
Table II.12: Average uplift rate, slip rate, and recurrence time.	243
Table II.13: Average uplift rate, slip rate, recurrence time for the 21 st July 365 A.D. earthquake, and total slip for highest and oldest terrace at Aradena Gorge.	244
Table II.14: Terraces, their age, present elevation and calculated uplift rate. No sea-level.	246
Table II.15: Average uplift rate, slip rate, and recurrence time.	247
Table II.16: Displacement between terraces, the corresponding slip, M_0 and M_w	247

Table II.17: Terraces, their age and calculated age, present elevation and sea-level change rate. No tectonics.....	250
Table II.18: Sougia terrace numbers, elevation heights, and uplift rates (Rohling et al., 2014)..	252
Table II.19: Average uplift rate, slip rate, and recurrence time.	252
Table II.20: Average uplift rate, slip rate, recurrence time for the 21 st July 365 A.D. earthquake, and total slip for highest and oldest terrace at Sougia.	253
Table II.21: Terraces, their age, present elevation and calculated uplift rate. No sea-level.	255
Table II.22: Average uplift rate, slip rate, and recurrence time.	255
Table II.23: Displacement between terraces, the corresponding slip, M_0 and M_w	256
Table II.24: Terraces, their age and calculated age, present elevation and sea-level change rate. No tectonics.....	257
Table II.25: Kalamia terrace numbers, elevation heights, and uplift rates (Rohling et al., 2014).	259
Table II.26: Average uplift rate, slip rate, and recurrence time.	259
Table II.27: Average uplift rate, slip rate, recurrence time for the 21 st July 365 A.D. earthquake, and total slip for highest and oldest terrace at Kalamia.	260
Table II.28: Terraces, their age, present elevation and calculated uplift rate. No sea-level.	262
Table II.29: Average uplift rate, slip rate, and recurrence time.	262
Table II.30: Displacement between terraces, the corresponding slip, M_0 and M_w	263
Table II.31: Terraces, their age and calculated age, present elevation and sea-level change rate. No tectonics.....	265
Table II.32: Cape Koutoulas terrace numbers, elevation heights, and uplift rates (Rohling et al., 2014).....	267
Table II.33: Average uplift rate, slip rate, and recurrence time.	267
Table II.34: Average uplift rate, slip rate, recurrence time for the 21 st July 365 A.D. earthquake, and total slip for highest and oldest terrace at Cape Koutoulas.	268
Table II.35: Terraces, their age, present elevation and calculated uplift rate. No sea-level.	270
Table II.36: Average uplift rate, slip rate, and recurrence time.	270
Table II.37: Displacement between terraces, the corresponding slip, M_0 and M_w	271
Table II.38: Terraces, their age and calculated age, present elevation and sea-level change rate. No tectonics.....	273
Table II.39: Phalasarna terrace numbers, elevation heights, and uplift rates (Rohling et al., 2014).	275
Table II.40: Average uplift rate, slip rate, and recurrence time.	275
Table II.41: Average uplift rate, slip rate, recurrence time for 21 st July 365 earthquake, and total slip for highest and oldest terrace. For tectonic only, sea-level only, and sea-level corrected. ...	276

Table II.42: Zakros terrace numbers, elevation heights, and uplift rates (Strobl et al., 2014; Rohling et al., 2014).....	279
Table II.43: Uplift rates from 16 Ma until 2.58 Ma derived from van Hinsbergen and Meulenkamp (2006).....	280

List of Figures

Figure 1.1: GPS velocity measurements based on Jet Propulsion Laboratory GPS time series stations.....	20
Figure 1.2: Distribution of Jet Propulsion Laboratory GPS time series stations. ETOPO1 global relief map after Amante et al. (2009).	21
Figure 1.3: Age of oceanic lithosphere after Mueller et al. (2008). ETOPO1 global relief map after Amante et al. (2009).....	22
Figure 1.4: Daily changes in longitude with respect to GPS station DRAO in Canada, modified after dragert et al. (2001).....	23
Figure 1.5: Schematic diagram of vertical displacement for geological, geomorphic and geodetic data with their corresponding units modified after Friedrich et al. (2003). A) The green box is for the geological displacement in [km/Ma]. B) The blue box displays the geomorphic displacement in [m/ka]. C) The red box illustrates geodetic data in [mm/yr].....	23
Figure 1.6: Vertical surface-deformation modified after Savage et al. (1991) and Hyndman and Wang (1993). A) The interseismic period lasting from years to thousand's of years. B) The coseismic moment lasting sec's to min's.	24
Figure 1.7: Distribution of $M_w > 7.0$ earthquakes combined from different earthquake catalogues since 1900. ETOPO1 global relief map after Amante et al. (2009).	25
Figure 1.8: Tectonic map of the Eastern Mediterranean after Chamot-Rooke et al. (2005). Background topography is derived from data of Smith and Sandwell (1997).....	26
Figure 1.9: Tectonic map and profile line. Tectonic map of the Eastern Mediterranean after Chamot-Rooke et al. (2005). Background topography is derived from data of Smith and Sandwell (1997). Profile is derived by data of microseismicity (Meier et al., 2004).	27
Figure 1.10: Values of coseismic uplift for W-Crete modified after Pirazzoli et al. (1996). Hill slope map generated from the Satellite Pour l'Observation de la Terre (SPOT) Digital Elevation Model (DEM). DEM derived from SPOT images with 20 m horizontal-resolution and vertical-resolution of 15 ± 5 m.	28
Figure 1.11: Distribution of instrumental recorded earthquakes near Crete between $7.0 < M_w > 7.4$ from 1900 until 1999 after Papazachos et al. (2000). GCMT recorded earthquakes near Crete between $6.0 < M_w > 6.8$ from 1976 until 2015. Topography and bathymetry from Google Earth ®.....	28
Figure 1.12: A) Persistent Scatterer distribution near the city of Chania, NW-Crete. B) Shows zoom into the urban area.	29
Figure 2.1: Tectonic map and profile lines. Tectonic map of the Eastern Mediterranean after Chamot-Rooke et al. (2005). Background topography is derived from data of Smith and Sandwell (1997).	54
Figure 2.2: Tectonic map and profile lines. Tectonic map of the Eastern Mediterranean after Chamot-Rooke et al. (2005). Background topography is derived from data of Smith and Sandwell (1997). GPS velocities after McCluskey et al. (2000).	55
Figure 2.3: Location of GPS stations and ERS frames on Crete.....	55

Figure 2.4: Sketch for illustration the absolute GPS calibration with TUC2 as reference station for Crete. All PS measurements are calibrated to the GPS plane fixed by the four GPS stations on Crete (TUC2, HERA, NEAP, and IERA, without RETH which is considered unreliable).....	56
Figure 2.5: PSs distribution close to the IERA GPS station.	57
Figure 2.6: Schematic diagram showing the composition of $vLOS_{PSI}$ into $v_{northPSI}$, $v_{eastPSI}$, and v_{upPSI}	58
Figure 2.7: Sketch for ERS-1/-2 satellite flight-tracks and look angle of 23° explaining the LOS.	59
Figure 2.8: Uncalibrated and GPS calibrated PS measurement.	60
Figure 2.9: Horizontal velocities based on GPS measurements with respect to Eurasia. Hill slope map generated from SPOT-DEM, with a horizontal-resolution of 20 m and vertical-resolution of 15 ± 5 m.....	60
Figure 2.10: GPS calibration uncertainties of the GPS plane.	61
Figure 2.11: PSI measurements in LOS.	62
Figure 2.12: Simplified map of PSI measurements in LOS.	63
Figure 2.13: Topography map of Crete based on SPOT-DEM.....	63
Figure 2.14: Fault map of Crete. Colored dots show 1992 to 2000 PSs velocities in LOS of 431,251 PSs in the GPS reference frame. Fault traces are modified after Caputo et al. (2010). Dashed lines are possible faults determined by geomorphic features in topography. GrF: Gramvousa Fault, RFZ: Rhodope Fault Zone, KeF: Kera Fault, RF: Rodope Fault, GF: Gionas Fault, SfF: Sfakia Fault, AF: Asomatos Fault, SpF: Spili Fault, AGF: Agia Galini Fault, EPFZ: Eastern Psiloritis Fault Zone, KrF: Kroussonas Fault, AVF: Agia Varvara Fault, KF: Kastelli Fault, IEZ: Ierapetra Fault Zone, HGF: Ha Gorge Fault, LF: Lastros Fault, ZF: Zou Fault.	63
Figure 2.15: Simplified map of PSI measurements with faults. Fault traces are modified after Caputo et al. (2010). Dashed lines are possible faults determined by geomorphic features in topography. For fault abbreviations see Figure 2.14.....	64
Figure 2.16: A) Simplified map of PSI measurements with faults. B) Topographic map with faults based on SPOT-DEM. GrF: Gramvousa Fault, KeF: Kera Fault, and RF: Rodope Fault. ..	65
Figure 2.17: Simplified map of PSI measurements with faults. B) Topographic map with faults based on SPOT-DEM. GrF: Gramvousa Fault, RFZ: Rhodope Fault Zone, KeF: Kera Fault, RF: Rodope Fault, GF: Gionas Fault, SfF: Sfakia Fault, AF: Asomatos Fault, and SpF: Spili Fault...	66
Figure 2.18: Simplified map of PSI measurements with faults. B) Topographic map with faults based on SPOT-DEM. SfF: Sfakia Fault, AF: Asomatos Fault, SpF: Spili Fault, AGF: Agia Galini Fault, EPFZ: Eastern Psiloritis Fault Zone, KrF: Kroussonas Fault, and AVF: Agia Varvara Fault.	67
Figure 2.19: A) Simplified map of PSI measurements with faults. B) Topographic map with faults based on SPOT-DEM. AGF: Agia Galini Fault, EPFZ: Eastern Psiloritis Fault Zone, KrF: Kroussonas Fault, AVF: Agia Varvara Fault, and KF: Kastelli Fault.	68
Figure 2.20: A) Simplified map of PSI measurements with faults. B) Topographic map with faults based on SPOT-DEM. IEZ: Ierapetra Fault Zone, HGF: Ha Gorge Fault, LF: Lastros Fault, and ZF: Zou Fault.....	69

Figure 2.21: Topographic map of Crete superimposed to the bathymetry map and location of upper-crustal faults in the overriding plate based on data by Google Earth.	70
2.22: Simplified map of PSI measurements with bathymetry map and location of upper-crustal faults in the overriding plate based on data by Google Earth.	71
Figure 2.23: Topographic map and profile of Gavdos. A) Topographic map of Gavdos with the location of the profile line A to B. Map from Google maps. B) Topographic profile line from A to B.	72
Figure 2.24: Bathymetry map of the Hellenic Trench, the location of Gavdos and the coseismic uplift contour line due to the 365 A.D. earthquake. Bathymetry map is from Google Earth. Topography map of Gavdos is from Google maps, and the hillshade of Crete is based on a SPOT-DEM.	73
Figure 2.25: Percentage of uplifting versus subsidence PSs for each track from W to E Crete. ...	74
Figure 2.26: A) 3D block diagram for vertical surface deformation caused by the incipient continent-continent collision, for the profile A-B. B) Map view. Tectonic map after Chamot-Rooke et al. (2005). Background topography is derived from data of Smith and Sandwell (1997). Geological profile modified after Meier et al. (2004). HSZ: Hellenic subduction zone, HT: Hellenic Trench, PT: Ptolemy Trench, PIT: Pliny Trench, and ST: Strabo Trench.	75
Figure 2.27: A) 3D block diagram for vertical surface deformation caused by subduction zone interface locking, for the profile A-B. B) Map view. Tectonic map after Chamot-Rooke et al. (2005). Background topography is derived from data of Smith and Sandwell (1997). Geological profile modified after Meier et al. (2004). HSZ: Hellenic subduction zone, HT: Hellenic Trench, PT: Ptolemy Trench, PIT: Pliny Trench, and ST: Strabo Trench.	76
Figure 2.28: A) 3D block diagram for vertical surface deformation caused by aseismic creep along the subduction zone interface, for the profile A-B. B) Map view. Tectonic map after Chamot-Rooke et al. (2005). Background topography is derived from data of Smith and Sandwell (1997). Geological profile modified after Meier et al. (2004). HSZ: Hellenic subduction zone, HT: Hellenic Trench, PT: Ptolemy Trench, PIT: Pliny Trench, and ST: Strabo Trench.	77
Figure 2.29: Tectonic map and profile lines. Tectonic map of the Eastern Mediterranean after Chamot-Rooke et al. (2005). Background topography is derived from data of Smith and Sandwell (1997). White lines represent the locations of the A-B and C-D profiles.	78
Figure 2.30 A) 3D block diagram for the vertical surface-deformation caused by major faults in the overriding plate, for the profile A-B. B) PSI results for the profile A-B. Tectonic map after Chamot-Rooke et al. (2005). Background topography is derived from data of Smith and Sandwell (1997). Geological profile modified after Meier et al. (2004). HSZ: Hellenic subduction zone, HT: Hellenic Trench, PT: Ptolemy Trench, PIT: Pliny Trench, and ST: Strabo Trench.	79
Figure 2.31: Map view for the vertical surface-deformation caused by major faults in the overriding plate. Tectonic map after Chamot-Rooke et al. (2005). Background topography is derived from data of Smith and Sandwell (1997).	80
Figure 2.32: A) 3D block diagram for the vertical surface-deformation caused by major faults in the overriding plate, for the profile C-D. B) PSI results for the profile A-B. Tectonic map after Chamot-Rooke et al. (2005). Background topography is derived from data of Smith and Sandwell (1997). Geological profile modified after Meier et al. (2004). HSZ: Hellenic subduction zone, HT: Hellenic Trench, PT: Ptolemy Trench, PIT: Pliny Trench, and ST: Strabo Trench.	81

- Figure 2.33: A) 3D block diagram for vertical surface deformation caused by underplating, for the profile A-B. B) Map view. Tectonic map after Chamot-Rooke et al. (2005). Background topography is derived from data of Smith and Sandwell (1997). Geological profile modified after Meier et al. (2004). HSZ: Hellenic subduction zone, HT: Hellenic Trench, PT: Ptolemy Trench, PIT: Pliny Trench, and ST: Strabo Trench. 82
- Figure 2.34: A) 3D block diagram for vertical surface deformation caused by return flow along the subduction channel, for the profile A-B. B) Map view. Tectonic map after Chamot-Rooke et al. (2005). Background topography is derived from data of Smith and Sandwell (1997). Geological profile modified after Meier et al. (2004). HSZ: Hellenic subduction zone, HT: Hellenic Trench, PT: Ptolemy Trench, PIT: Pliny Trench, and ST: Strabo Trench. 83
- Figure 2.35: A) 3D block diagram for vertical surface deformation caused by return flow, for the profile A-B. B) Map view. Tectonic map after Chamot-Rooke et al. (2005). Background topography is derived from data of Smith and Sandwell (1997). Geological profile modified after Meier et al. (2004). HSZ: Hellenic subduction zone, HT: Hellenic Trench, PT: Ptolemy Trench, PIT: Pliny Trench, and ST: Strabo Trench. 84
- Figure 2.36: All possible hypotheses explaining the uplift of Crete. 85
- Figure 3.1: Distribution of normal faults across Crete. Fault traces are modified after Caputo et al. (2010). Dashed lines are possible faults determined by geomorphic features in topography. GrF: Gramvousa Fault, RFZ: Rhodope Fault Zone, KeF: Kera Fault, RF: Rodope Fault, GF: Gionas Fault, SfF: Sfakia Fault, AF: Asomatos Fault, SpF: Spili Fault, AGF: Agia Galini Fault, EPFZ: Eastern Psiloritis Fault Zone, KrF: Kroussonas Fault, AVF: Agia Varvara Fault, KF: Kastelli Fault, IEZ: Ierapetra Fault Zone, HGF: Ha Gorge Fault, LF: Lastros Fault, ZF: Zou Fault. 101
- Figure 3.2: Geological map of Crete (after Papanikolaou and Vassilakis, 2010) superimposed on the Digital Elevation Model (DEM) derived from Satellite Pour l'Observation de la Terre (SPOT) images with a 20 m resolution. 101
- Figure 3.3: A) Topographic expression of the SfF and the location of the profile line A-B superimposed on the SPOT-DEM. B) Geological map of Crete (after Papanikolaou and Vassilakis, 2010) superimposed on the SPOT-DEM. C) Profile line across the SfF fault. D) PSI measurements. 102
- Figure 3.4: A) Topographic expression of the AF and the location of the profile line A-B superimposed on the SPOT-DEM. B) Geological map of Crete (after Papanikolaou and Vassilakis, 2010) superimposed on the SPOT-DEM. C) Profile line across the AF fault. 103
- Figure 3.5: A) Topographic expression of the SpF and the location of the profile line A-B superimposed on the SPOT-DEM. B) Geological map of Crete (after Papanikolaou and Vassilakis, 2010) superimposed on the SPOT-DEM. C) Profile line across the SpF fault. 104
- Figure 3.6: A) Topographic expression of the GrF and the location of the profile line A-B superimposed on the SPOT-DEM. B) Geological map of Crete (after Papanikolaou and Vassilakis, 2010) superimposed on the SPOT-DEM. C) Profile line across the GrF fault. 105
- Figure 3.7: A) Topographic expression of the GF and the location of the profile line A-B superimposed on the SPOT-DEM. B) Geological map of Crete (after Papanikolaou and Vassilakis, 2010) superimposed on the SPOT-DEM. C) Profile line across the GF fault. 106

Figure 3.8: A) Topographic expression of the RF and the location of the profile line A-B superimposed on the SPOT-DEM. B) Geological map of Crete (after Papanikolaou and Vassilakis, 2010) superimposed on the SPOT-DEM. C) Profile line across the RF fault.	107
Figure 3.9: A) Topographic expression of the KeF and the location of the profile line A-B superimposed on the SPOT-DEM. B) Geological map of Crete (after Papanikolaou and Vassilakis, 2010) superimposed on the SPOT-DEM. C) Profile line across the KeF fault.	108
Figure 3.10: A) Topographic expression of the KrF and the location of the profile line A-B superimposed on the SPOT-DEM. B) Geological map of Crete (after Papanikolaou and Vassilakis, 2010) superimposed on the SPOT-DEM. C) Profile line across the KrF fault.	109
Figure 3.11: A) Topographic expression of the AvF and the location of the profile line A-B superimposed on the SPOT-DEM. B) Geological map of Crete (after Papanikolaou and Vassilakis, 2010) superimposed on the SPOT-DEM. C) Profile line across the AvF fault.	110
Figure 3.12: A) Topographic expression of the KF and the location of the profile line A-B superimposed on the SPOT-DEM. B) Geological map of Crete (after Papanikolaou and Vassilakis, 2010) superimposed on the SPOT-DEM. C) Profile line across the KF fault. D) PSI measurements.	111
Figure 3.13: A) Topographic expression of the HGF and the location of the profile line A-B superimposed on the SPOT-DEM. B) Geological map of Crete (after Papanikolaou and Vassilakis, 2010) superimposed on the SPOT-DEM. C) Profile line across the HGF fault. D) PSI measurements.	112
Figure 3.14: A) Topographic expression of the LF and the location of the profile line A-B superimposed on the SPOT-DEM. B) Geological map of Crete (after Papanikolaou and Vassilakis, 2010) superimposed on the SPOT-DEM. C) Profile line across the LF fault.	113
Figure 3.15: A) Topographic expression of the ZF and the location of the profile line A-B superimposed on the SPOT-DEM. B) Geological map of Crete (after Papanikolaou and Vassilakis, 2010) superimposed on the SPOT-DEM. C) Profile line across the ZF fault.	114
Figure 3.16: Fault map of Crete. Colored dots show 1992 to 2000 PSs velocities in LOS of 431,251 PSs in the GPS reference frame. Dashed lines are possible faults determined by geomorphic features in topography. GrF: Gramvousa Fault, RFZ: Rhodope Fault Zone, KeF: Kera Fault, RF: Rodope Fault, GF: Gionas Fault, SfF: Sfakia Fault, AF: Asomatos Fault, SpF: Spili Fault, AGF: Agia Galini Fault, EPFZ: Eastern Psiloritis Fault Zone, KrF: Kroussonas Fault, AVF: Agia Varvara Fault, KF: Kastelli Fault, IEZ: Ierapetra Fault Zone, HGF: Ha Gorge Fault, LF: Lastros Fault, ZF: Zou Fault.	114
Figure 3.17: Fault map of Crete. Red rectangle show location of PSs measurements for analysis of deformation rates in LOS across the faults. Dashed lines are possible faults determined by geomorphic features in topography. For fault abbreviations please see Figure 3.16.	115
Figure 3.18: Schematic cross-section showing the relationship between differential velocity $\Delta v_{normal\ fault}$ in the LOS measured by PSI velocities of the footwall and the hanging wall. Illustration of the relationship between the dip-angle α and the dip slip component. Not drawn to scale. $t = 0$: is the start situation across the fault. $t = 1$: is the end situation of measurements, during which vertical motion occurred.	115
Figure 3.19: Percentage of PSs per lithological unit on Crete.	116

Figure 3.20: Fotos taken in the Plattenkalk and Phyllite-Quarzite unit on Crete during the field campaign in Mai 2012.....	116
Figure 3.21: A) normal motion means that the footwall is uplifting and the hanging wall. B) reverse motion means that the footwall is subsiding and the hanging wall is uplifting.....	117
Figure 3.22: V_{LOS} motion across normal faults respectively for the footwall (FW) and the hanging wall (HW) with the corresponding error bars.	118
Figure 3.23: V_{LOS} motion across normal faults with reverse motion respectively for the footwall (FW) and the hanging wall (HW) with the corresponding error bars.	119
Figure 3.24: Distribution of normal faults with either normal motion or reverse motion along them. GrF: Gramvousa Fault, RFZ: Rhodope Fault Zone, KeF: Kera Fault, RF: Rodope Fault, GF: Gionas Fault, SfF: Sfakia Fault, AF: Asomatos Fault, SpF: Spili Fault, AGF: Agia Galini Fault, EPFZ: Eastern Psiloritis Fault Zone, KrF: Kroussonas Fault, AVF: Agia Varvara Fault, KF: Kastelli Fault, IEZ: Ierapetra Fault Zone, HGF: Ha Gorge Fault, LF: Lastros Fault, ZF: Zou Fault.....	120
Figure 3.25: Distribution of normal faults with either normal motion or reverse motion superimposed on the bathymetry map of Google Earth.	120
Figure 4.1: Geomorphic map with contour lines with 1000 m interval, derived on a Satellite Pour l’Observation de la Terre – Digital Elevation Model (SPOT-DEM) with a horizontal spatial resolution of 20 m and vertical accuracy of 15 ± 5 m.	148
Figure 4.2: Average temperature in [$^{\circ}\text{C}$] and average rainfall in [mm] based on Hellenic National Metrological Service data averaged for time period of 1955 to 1997 for stations in Heraklion (blue), Chania (red), Rethymno (green), Sitia (purple), Ierapetra (light blue), and Tympaki (orange).	148
Figure 4.3: Locations of weather stations of the Hellenic National Metrological Service on Crete underlying the hill slope map generated from the SPOT-DEM.....	149
Figure 4.4: Location of Pleistocene paleo-shorelines. The hill slope map generated from the SPOT-DEM.....	149
Figure 4.5: Location of Holocene paleo-shorelines. The hill slope map generated from the SPOT-DEM.....	149
Figure 4.6: Schematic illustration of a wave-cut notch along an abrasion ramp modified after Burbank and Anderson (2015).	150
Figure 4.7: Map of concavity index Θ determined for Crete. Background is a shaded relief of Crete. The hill slope map generated from the SPOT-DEM.	150
Figure 4.8: Map of normalized steepness index k_{sn} for Crete. Background is a shaded relief of Crete. The hill slope map generated from the SPOT-DEM.	151
Figure 4.9: Map of normalized steepness index k_{sn} of small segments for Crete.	151
Figure 4.10: Map of knickpoint distribution and shaded relief of Crete. The hill slope map generated from the SPOT-DEM.....	151
Figure 4.11: River profiles with one knickpoint. Background shaded relief from SPOT-DEM.	152

Figure 4.12: River profiles with four knickpoints. Background shaded relief from SPOT-DEM.	153
Figure 4.13: Sea-level curve for the past 440 kyr by Rohling et al. (2014).	154
Figure 4.14: Pleistocene uplift rates in mm/yr. The hill slope map generated from the SPOT-DEM.	155
Figure 4.15: Holocene uplift rates in mm/yr. The hill slope map generated from the SPOT-DEM.	155
Figure 4.16: Location of Pleistocene and Holocene paleo-shorelines. The hill slope map generated from the SPOT-DEM.	155
Figure 4.17: Geological map with contour lines every 1000 m interval. Background map of lithology by Papanikolaou and Vassilakis (2010) superimposed on SPOT-DEM.	156
Figure 4.18: Map of concavity index Θ determined for Crete. Background is a map of lithology by Papanikolaou and Vassilakis (2010)	156
Figure 4.19: Concavity index versus geological units in percentage.	157
Figure 4.20: Map of concavity index Θ determined for Crete. Tectonic map showing faults on Crete and offshore underlying is the hill slope map generated from the SPOT-DEM. Dashed lines are possible faults determined by geomorphic features in topography. Fault traces are modified after Caputo et al. (2010). GrF: Gramvousa Fault, RFZ: Rhodope Fault Zone, KeF: Kera Fault, RF: Rodope Fault, GF: Gionas Fault, SfF: Sfakia Fault, AF: Asomatos Fault, SpF: Spili Fault, AGF: Agia Galini Fault, EPFZ: Eastern Psiloritis Fault Zone, KrF: Kroussonas Fault, AVF: Agia Varvara Fault, KF: Kastelli Fault, IEZ: Ierapetra Fault Zone, HGF: Ha Gorge Fault, LF: Lastros Fault, ZF: Zou Fault.	157
Figure 4.21: Map of normalized steepness index k_{sn} based on long profiles Background is lithological map by Papanikolaou and Vassilakis (2010).	158
Figure 4.22: Map of normalized steepness index k_{sn} based on small segments of the profiles. Background is the lithological map by Papanikolaou and Vassilakis (2010).	158
Figure 4.23: Percentage of k_{sn} values compared to the lithological units. A) k_{sn} value smaller than 30. B) k_{sn} value between 30 and 60. C) k_{sn} value between 60 and 90. D) k_{sn} value between 90 and 120. E) k_{sn} value higher than 120.	159
Figure 4.24: Map of normalized steepness index k_{sn} for Crete. Tectonic map showing faults on Crete and offshore underlying is the hill slope map generated from the SPOT-DEM. Dashed lines are possible faults determined by geomorphic features in topography. For fault abbreviations see Figure 4.20.	159
Figure 4.25: Map of normalized steepness index k_{sn} for Crete Background is a map of lithology by Papanikolaou and Vassilakis (2010). Tectonic map showing faults on Crete and offshore underlying is the hill slope map generated from the SPOT-DEM. Dashed lines are possible faults determined by geomorphic features in topography. For fault abbreviations see Figure 4.20.	160
Figure 4.26: Knickpoints superimposed on the geological map (Papanikolaou and Vassilakis, 2010). Background is shaded relief generated from the SPOT-DEM.	160
Figure 4.27: Percentage of knickpoints per lithological unit on Crete.	161

Figure 4.28: Map of knickpoints. Tectonic map showing faults on Crete and offshore underlying is the hill slope map generated from the SPOT-DEM. Dashed lines are possible faults determined by geomorphic features in topography. For fault abbreviations see Figure 4.20.	161
Figure 4.29: Distribution of knickpoints for small river segments.	162
Figure 4.30: Map of knickpoints correlated to their elevation. Tectonic map showing faults on Crete and offshore underlying is the hill slope map generated from the SPOT-DEM.	162
Figure 4.31: Knickpoint distribution for raster of 10 x 10 km across Crete. Color coded tiles represent number of knickpoints per 10 x 10 km tile.....	163
Figure 4.32: Number of knickpoint distribution from W to E based on Figure 4.31.....	163
Figure 4.33: Tentative terrace correlation of dated terraces.....	164
Figure 4.34: Tectonic map showing faults on Crete underlying is the hill slope map generated from the SPOT-DEM. Dashed lines are possible faults determined by geomorphic features in topography. For fault abbreviations see Figure 4.20.....	164
Figure 4.35: Coseismic uplift of the 365 A.D. earthquake. Uplift data based on Pirazzoli et al. (1996). Hill slope map generated from SPOT-DEM.	165
Figure 4.36: Elevation of Pleistocene and Holocene paloe-shorelines plotted against time at Moni Chryssoskalitissa, modified after Pirazzoli et al. (1996), and Wegmann (2008).....	166
Figure 4.37: Elevation of terraces and the height difference needed for the tectonic uplift at Moni Chryssoskaliissa, modified after Pirazzoli et al. (1996), and Wegmann (2008).	167
Figure 4.38: Inferred uplift diagram curve for tectonic uplift is determined by linear regression analysis at Moni Chryssoskalitissa.....	167
Figure 4.39: Regression of maximum displacement versus magnitude M_w modified after Wells and Coopersmith 1994. Maximum displacement 60 m ever measured for an earthquake is for the 2011 M_w 9.0 Tohoku-Oki (Japan) (Simons et al., 2011).	168
Figure 4.40: Elevation of terraces and the needed amount of sea-level fall at Moni Chryssoskalitissa, modified after Pirazzoli et al. (1996), and Wegmann (2008).....	168
Figure 4.41: Correlation of terraces at Moni Chryssoskalitissa with constant uplift to the sea-level curve of Rohling et al. (2014).	169
Figure 4.42: Correlation of terraces at Moni Chryssoskalitissa with not-constant uplift to the sea-level curve of Rohling et al. (2014).....	170
Figure 4.43: Inferred uplift diagram curve for sea-level correction is determined by linear regression analysis and the curve represents the polynomial fit.	171
Figure 4.44: Pleistocene vertical coastal uplift rates. NZ: New Zealand, V: Ventura, A: Arauco, HP: Huon Peninsula, W: Wairarapa, KJ: Kikai Jima, MV: Muroto, O: Osado, K: Kosado, HMB: Half Moon Bay, SC: Santa Cruz, RI: Royalty Islands, TA: Taaanaki, T: Timor, AT: Atauro, H: Haiti, B: Barbados, AH: Arroyo Hondo, CO: Cojo, Al: Algeria, IV: Isla Vista, SM: Santa Monica, PL: Point Loma, J: Jamaica, BA: Bahamas, Y: Yucatan, BE: Bermuda, Q: Queensland, and Cr: Crete. All data taken from Lajoie (1986), except Cr: Crete.	171
Figure 5.1: Geological map of Crete (after Papanikolaou and Vassilakis, 2010) superimposed on the Digital Elevation Model (DEM) derived from SPOT images with a 20 m resolution.....	194

Figure 5.2: Distribution of Neogene sediments on Crete (after Papanikolaou and Vassilakis, 2010) superimposed on the DEM.....	194
Figure 5.3: Depositional environment of the Middle Miocene of lacustrine-continental sediments modified after van Hinsbergen et al. (2006).	195
Figure 5.4: Depositional environment of late Serravallian modified after van Hinsbergen et al. (2006).	195
Figure 5.5: Depositional environment of early Tortonian modified after van Hinsbergen et al. (2006).	196
Figure 5.6: Depositional environment of Tortonian modified after van Hinsbergen et al. (2006).	196
Figure 5.7: Depositional environment of late Tortonian – early Messinian modified after van Hinsbergen et al. (2006).	197
Figure 5.8: Depositional environment the Messinian modified after van Hinsbergen et al. (2006).	197
Figure 5.9: Depositional environment in early Pliocene modified after van Hinsbergen et al. (2006).	198
Figure 5.10: Depositional environment in late Pliocene modified after van Hinsbergen et al. (2006).	198
Figure 5.11: Location of sections for analysis the paleo-bathymetry after van Hinsbergen and Meulenkamp (2006) superimposed on the DEM.	199
Figure 5.12: Schematic diagram of West, East, Central, North-Central and South-Central Crete above or below sea-level modified after van Hinsbergen and Meulenkamp (2006).....	200
Figure 5.13: Vertical deformation since Middle Miocene until Late Pleistocene. For time intervals labeled with letters please refer to Figure 5.12.....	201
Figure 6.1: Vertical surface-deformation after Savage et al. (1991) and Hyndman and Wang (1993). A) The interseismic period lasting from years to thousand's of years. B) The coseismic moment lasting sec's to min's	209
Figure 6.2: Recent coastal vertical deformation pattern.....	210
Figure 6.3: Holocene coastal vertical deformation pattern.	210
Figure 6.4: Pleistocene coastal vertical deformation pattern.	210
Figure 6.5: Schematic diagram of Crete above or below sea-level modified after van Hinsbergen and Meulenkamp (2006).	211
Figure 6.6: Vertical deformation since Middle Miocene until Late Pleistocene. For time intervals labeled with letters please refer to Figure 6.5.	212
Figure 6.7: Comparison of vertical deformation on the Pleistocene-, Holocene-, and recent time-scale.	212
Figure II.1: A) Shows the vertical displacement in mm/yr measured by PSI along the Asomatos fault. B) Shows the geodetic measurements versus the geologic slip-rate in ka/m derived from	

Caputo et al. (2010). The grey shade shows the error range of PSI measurements adjusted to the geological time.	216
Figure II.2: A) Shows the vertical displacement in mm/yr measured by PSI along the Kroussanos fault. B) Shows the geodetic measurements versus the geologic slip-rate in ka/m derived from Caputo et al. (2010). The grey shade shows the error range of PSI measurements adjusted to the geological time.	217
Figure II.3: a) Shows the vertical displacement in mm/yr measured by PSI along the Agia Varvara fault. B) Shows the geodetic measurements versus the geologic slip-rate in ka/m derived from Caputo et al. (2010). The grey shade shows the error range of PSI measurements adjusted to the geological time.	218
Figure II.4: A) Shows the vertical displacement in mm/yr measured by PSI along the Zou fault. B) Shows the geodetic measurements versus the geologic slip-rate in ka/m derived from Caputo et al. (2010). The grey shade shows the error range of PSI measurements adjusted to the geological time.	219
Figure II.5: A) Shows the vertical displacement in mm/yr measured by PSI along the Gionas fault. B) Shows the geodetic measurements versus the geologic slip-rate in ka/m derived from Caputo et al. (2010). The grey shade shows the error range of PSI measurements adjusted to the geological time.	220
Figure II.6: A) Shows the vertical displacement in mm/yr measured by PSI along the Kera fault. B) Shows the geodetic measurements versus the geologic slip-rate in ka/m derived from Caputo et al. (2010). The grey shade shows the error range of PSI measurements adjusted to the geological time.	221
Figure II.7: A) Shows the vertical displacement in mm/yr measured by PSI along the Lastros fault. B) Shows the geodetic measurements versus the geologic slip-rate in ka/m derived from Caputo et al. (2010). The grey shade shows the error range of PSI measurements adjusted to the geological time.	222
Figure II.8: A) Shows the vertical displacement in mm/yr measured by PSI along the Sfakia fault. B) Shows the geodetic measurements versus the geologic slip-rate in ka/m derived from Caputo et al. (2010). The grey shade shows the error range of PSI measurements adjusted to the geological time.	223
Figure II.9: A) Shows the vertical displacement in mm/yr measured by PSI along the Kastelli fault. B) Shows the geodetic measurements versus the geologic slip-rate in ka/m derived from Caputo et al. (2010). The grey shade shows the error range of PSI measurements adjusted to the geological time.	224
Figure II.10: A) Shows the vertical displacement in mm/yr measured by PSI along the Ha Gorge fault. B) Shows the geodetic measurements versus the geologic slip-rate in ka/m derived from Caputo et al. (2010). The grey shade shows the error range of PSI measurements adjusted to the geological time.	225
Figure II.11: A) Shows the vertical displacement in mm/yr measured by PSI along the Gramvousa fault. B) Shows the geodetic measurements versus the geologic slip-rate in ka/m derived from Caputo et al. (2010). The grey shade shows the error range of PSI measurements adjusted to the geological time.	226

Figure II.12: A) Shows the vertical displacement in mm/yr measured by PSI along the Rodopos fault. B) Shows the geodetic measurements versus the geologic slip-rate in ka/m derived from Caputo et al. (2010). The grey shade shows the error range of PSI measurements adjusted to the geological time.	227
Figure II.13: A) Shows the vertical displacement in mm/yr measured by PSI along the Spili fault. B) Shows the geodetic measurements versus the geologic slip-rate in ka/m derived from Caputo et al. (2010). The grey shade shows the error range of PSI measurements adjusted to the geological time.	228
Figure II.14: Elevation of Pleistocene and Holocene paloe-shorelines plotted against time, modified after Gaki-Papanastassiou et al. (2009) and Mourtzas (2012).	229
Figure II.15: Elevation of terraces and the height difference needed for the tectonic uplift, modified after Gaki-Papanastassiou et al. (2009) and Mourtzas (2012).	230
Figure II.16: Inferred uplift diagram curve for tectonic uplift is determined by linear regression analysis.	231
Figure II.17: Elevation of terraces and the needed amount of sea-level fall, modified after Gaki-Papanastassiou et al. (2009) and Mourtzas (2012).	232
Figure II.18: Correlation of terraces at Ierapetra with the sea-level curve of Rohling et al. (2014), modified after Gaki-Papanastassiou et al. (2009) and Mourtzas (2012).	234
Figure II.19: Inferred uplift diagram curve for sea-level correction is determined by linear regression analysis.	235
Figure II.20: Elevation of Pleistocene and Holocene paloe-shorelines plotted against time, modified after Wegmann (2008), Mourtzas (2012), and Pirazzoli et al. (1996). Elevation uncertainties for Pleistocene terraces are ± 1 m (Wegmann, 2008).	236
Figure II.21: Elevation of terraces and the height difference needed for the tectonic uplift, modified after Wegmann (2008), Mourtzas (2012), and Pirazzoli et al. (1996).	237
Figure II.22: Inferred uplift diagram curve for tectonic uplift is determined by linear regression analysis.	238
Figure II.23: Regression of maximum displacement versus magnitude M_w . Maximum displacement 60 m ever measured for an earthquake is for the 2011 M_w 9.0 Tohoku-Oki (Japan).	239
Figure II.24: Elevation of terraces and the needed amount of sea-level fall, modified after Wegmann (2008), Mourtzas (2012), and Pirazzoli et al. (1996).	240
Figure II.25: Correlation of terraces at Aradena Gorge with the sea-level curve of Rohling et al. (2014), modified after Wegmann (2008), Mourtzas (2012), and Pirazzoli et al. (1996).	242
Figure II.26: Inferred uplift diagram curve for tectonic uplift is determined by linear regression analysis.	244
Figure II.27: Elevation of Pleistocene and Holocene paloe-shorelines plotted against time, modified after Wegmann (2008), Pirazzoli et al. (1996), and Price et al. (2002). Elevation uncertainties for Pleistocene terraces are ± 1 m (Wegmann, 2008).	245
Figure II.28: Elevation of terraces and the height difference needed for the tectonic uplift, modified after Wegmann (2008), Pirazzoli et al. (1996), and Price et al. (2002).	246

Figure II.29: Inferred uplift diagram curve for tectonic uplift is determined by linear regression analysis.....	247
Figure II.30: Regression of maximum displacement versus magnitude Mw. Maximum displacement 60 m ever measured for an earthquake is for the 2011 Mw 9.0 Tohoku-Oki (Japan).	248
Figure II.31: Elevation of terraces and the needed amount of sea-level fall, modified after Wegmann (2008), Pirazzoli et al. (1996), and Price et al. (2002).....	249
Figure II.32: Correlation of terraces at Sougia with the sea-level curve of Rohling et al. (2014), modified after Wegmann (2008), Pirazzoli et al. (1996), and Price et al. (2002).....	251
Figure II.33: Inferred uplift diagram curve for sea-level correction is determined by linear regression analysis.....	253
Figure II.34: Elevation of Pleistocene and Holocene paloe-shorelines plotted against time, modified after Tibert et al. (2014), and Pirazzoli et al. (1996).....	254
Figure II.35: Inferred uplift diagram curve for tectonic uplift is determined by linear regression analysis.....	255
Figure II.36: Regression of maximum displacement versus magnitude Mw. Maximum displacement 60 m ever measured for an earthquake is for the 2011 Mw 9.0 Tohoku-Oki (Japan)	256
Figure II.37: Correlation of terraces at Kalamia with the sea-level curve of Rohling et al. (2014), modified after Pirazzoli et al. (1996); Tiberti et al. (2014); and Wegmann (2008).....	258
Figure II.38: Inferred uplift diagram curve for sea-level correction is determined by linear regression analysis.....	260
Figure II.39: Elevation of Pleistocene and Holocene paloe-shorelines plotted against time, modified after Wegmann (2008), and Pirazzoli et al. (1996).....	261
Figure II.40: Elevation of terraces and the height difference needed for the tectonic uplift, , modified after Wegmann (2008), and Pirazzoli et al. (1996).....	262
Figure II.41: Inferred uplift diagram curve for tectonic uplift is determined by linear regression analysis.....	263
Figure II.42: Regression of maximum displacement versus magnitude Mw. Maximum displacement 60 m ever measured for an earthquake is for the 2011 Mw 9.0 Tohoku-Oki (Japan)	264
Figure II.43: Elevation of terraces and the needed amount of sea-level fall, modified after Wegmann (2008), and Pirazzoli et al. (1996).	265
Figure II.44: Correlation of terraces at Cape Koutoulas with the sea-level curve of Rohling et al. (2014), modified after Wegmann (2008), and Pirazzoli et al. (1996).....	266
Figure II.45: Inferred uplift diagram curve for sea-level correction is determined by linear regression analysis.....	268
Figure II.46: Elevation of Pleistocene and Holocene paloe-shorelines plotted against time, modified after Wegmann (2008), and Pirazzoli et al. (1996).....	269

Figure II.47: Elevation of terraces and the height difference needed for the tectonic uplift, modified after Pirazzoli et al. (1996), Wegmann (2008), and Price et al. (2002).	270
Figure II.48: Inferred uplift diagram curve for tectonic uplift is determined by linear regression analysis.	271
Figure II.49: Regression of maximum displacement versus magnitude M_w . Maximum displacement 60 m ever measured for an earthquake is for the 2011 M_w 9.0 Tohoku-Oki (Japan).	272
Figure II.50: Elevation of terraces and the needed amount of sea-level fall, modified after Pirazzoli et al. (1996), Wegmann (2008), and Price et al. (2002).	273
Figure II.51: Correlation of terraces at Phalasarna with the sea-level curve of Rohling et al. (2014), modified after Pirazzoli et al. (1996), Wegmann (2008), and Price et al. (2002).	274
Figure II.52: Inferred uplift diagram curve for sea-level correction is determined by linear regression analysis.	276
Figure II.53: Regression of maximum displacement versus magnitude M_w . Maximum displacement 60 m ever measured for an earthquake is for the 2011 M_w 9.0 Tohoku-Oki (Japan).	277
Figure II.54: Correlation of terraces at Zakros with the sea-level curve of Rohling et al. (2014), modified after Strobl et al. (2014).	278

List of Abbreviations

A.D.	Anno Domini
AF	Asomatos Fault
AGF	Agia Galini Fault
AVF	Agia Varvara Fault
B.C.	Before Christ
DEM	Digital Elevation Model
DLR	German Aerospace Center
EBTP	Early Byzantine Tectonic Paroxysm
EPFZ	Eastern Psiloritis Fault Zone
EPN	EUREF Permanent Network
ERS	European Remote Sensing Satellite
ESA	European Space Agency
GF	Gionas Fault
GNSS	International Global Navigation Satellite System
GrF	Gramvousa Fault
GPS	Global Positioning System
HP/LT	high-pressure/low-temperature
HGF	Ha Gorge Fault
HSZ	Hellenic Subduction Zone
HT	Hellenic Trench
IEZ	Ierapetra Fault Zone
InSAR	Interferometry Synthetic Aperture Radar
ITRF	International Terrestrial Reference Frame
KeF	Kera Fault
KF	Kastelli Fault
KrF	Kroussonas Fault
LF	Lastros Fault
LOS	Line of Sight
m asl	Meters above sea-level
MIS	Marine Isotopic Stages
MKS	Mercalli-Cancani-Sieberg scale
NOA	National Observatory of Athens
NOANET	permanent GPS network of NOA
NWP	Numerical Weather Prediction Model
OIS	Oxygen Isotopic Stage
PIT	Pliny Trench
PSI	Persistent Scatterer Interferometry
PSs	Persistent Scatterers
PT	Ptolemy Trench
RCMT	European-Mediterranean Regional CentroidMoment Tensors
RF	Rodope Fault
RFZ	Rhodope Fault Zone
SCR	signal-to-cluter ratio
SfF	Sfakia Fault
SpF	Spili Fault
SPOT	Satellite Pour l'Observation de la Terre

ST	Strabo Trench
WAP	Wide Area Processing
WRF	Weather Research and Forecasting Model
ZF	Zou Fault

ABSTRACT (SUMMARY)

This thesis explores the suitability of Persistent-Scatterer Interferometry (PSI) for the first time on a regional scale to answer current research questions in active tectonics and earthquake geology. PSI is a widely-used satellite-geodetic technique, which traditionally has been applied to urban areas on the 5-km scale, profiting from densely-spaced anthropogenic scatterers. Here, I used radar interferometry data from the ERS satellites to monitor the surface deformation over the time period from 1992 to 2000.

The island of Crete represents an ideal study area, because it represents an over 250 km-wide, aerially exposed forearc high located above the Hellenic subduction zone. The purpose of this thesis is to determine the pattern of surface deformation on different spatial and temporal scales, ranging from currently active deformation to the past vertical deformation preserved in the landscape. I analyzed Persistent Scatterer Interferometry (PSI) data to detect the active vertical surface-deformation pattern across Crete. Results of the PSI analysis illustrate that the western Crete is strongly affected by uplift, central Crete is relatively stable, and eastern Crete is dominated by subsidence. This deformation pattern is consistent with activity on offshore upper-crustal faults. Furthermore, the PSI map pattern shows abundant small-scale strain gradients, particularly in central and eastern Crete, which coincide with the topographic expression of active normal faults, implying that the natural PSI technique applied here is suitable to detect regional-scale surface deformation on varying scales. The PSI signal across some of the normal faults indicates reverse-sense vertical motion, implying transient behaviour or aseismic creep along the upper-crustal faults on Crete.

For the detection of the vertical surface-deformation pattern on the millennial and the million-year time-scale, I synthesized and analysed river profiles, uplifted paleo-shorelines, and Neogene sedimentary rocks. All, the resultant Holocene and Pleistocene uplift rates, and the geomorphological analysis yield a heterogeneous pattern of vertical surface deformation across Crete, consistent with crustal-scale segmentation and the PSI analysis.

The results of this thesis indicate that the vertical surface-deformation pattern across Crete is heterogeneous on the decadal-, the millennial-, and the million-year time-scale. This may imply that the Hellenic subduction zone is not the main tectonic structure to produce the surface-deformation pattern observed on Crete, but instead upper-crustal faults are responsible for the present and past vertical deformation. These faults are also capable producing large and devastating earthquakes and will need to be considered in seismic hazard assessment and mitigation studies. Long-term constraints on the active deformation pattern provided by geological measurements are an important data source, in particular in the absence of effective kinematic and mechanical faulting models.

ZUSAMMENFASSUNG

Diese Dissertation beschäftigt sich mit der ersten Anwendung der Persistent-Scatterer Interferometrie (PSI) auf einem regionalen Maßstab, um damit aktuelle Fragen der modernen Geowissenschaften aus den Bereichen aktiver Tektonik und Erdbebengeologie zu beantworten.

Die PSI Methode ist eine geodätische Standardtechnik, die traditionell in urbanen Gebieten auf einem Maßstab von 5 km angewendet wird. Dabei werden dicht beieinanderliegende anthropogene Objekte als Reflektoren von Satellitensignalen genutzt.

In dieser Studie habe ich Radar-Interferometriedaten der European Remote Sensing Satelliten (ERS) genutzt, um auf der Insel Kreta die vertikale Deformation der Oberfläche von 1992 bis 2000 zu analysieren. Kreta stellt in diesem Zusammenhang eine ideale Testregion dar, denn die Insel repräsentiert einen mehr als 250 km langen, exponierten Inselbogen direkt oberhalb der Hellenischen Subduktionszone.

Der Zweck dieser Studie ist eine genaue Untersuchung der Oberfläche-Deformationsmuster auf verschiedenen räumlichen und zeitlichen Skalen. Die Analyse erfolgt mit der rezenten Deformation bis hin zu vergangenen vertikalen Bewegungen, die bis heute in der Morphologie sichtbar sind. Ich habe Persistent-Scatterer Interferometrie (PSI) Daten analysiert um damit die aktiven, vertikalen Deformationsmuster auf der Insel Kreta zu untersuchen. Die Ergebnisse meiner Studie zeigen, dass West-Kreta stark von Hebung beeinflusst ist, wobei hingegen Zentral-Kreta sich relativ stabil verhält und Ost-Kreta von einer deutlichen Absenkung dominiert wird.

Diese vertikalen Deformationen sind konsistent mit den aktiven Hauptstörungssystemen der oberen Kruste, die sich vor der Küste der Insel befinden. Weiterhin zeigen die untersuchten PSI Daten diverse kleinräumige Verformungen, dies insbesondere in Zentral- und Ost-Kreta. Die Ergebnisse korrelieren mit der für aktive Abschiebungen typischen Topographie. Dies impliziert, dass die Anwendung der neu entwickelten PSI Methode geeignet ist regionale Deformationen der Oberfläche präzise zu messen. Das über verschiedene morphologische Abschiebungen gemessene PSI Signal deutet allerdings auf einen umgekehrten Bewegungssinn der Störungen hin (Aufschiebung). Diese Beobachtung kann entweder auf ein temporäres Signal oder ein aseismisches Kriechen entlang der oberflächennahen Störungen auf Kreta hindeuten.

Für eine Messung von vertikalen Deformationsmustern der Oberfläche auf Zeitskalen von 10^3 bis 10^6 Jahren wurden außerdem Flussprofile, Paläoküstenlinien und Neogene Sedimente untersucht. Die resultierenden holozänen und pleistozänen Hebungsraten, sowie die geologische Analyse ergeben zusammen ein heterogenes Muster der vertikalen Deformation auf Kreta, insbesondere entlang der Küste. Dieses Ergebnis stimmt mit der Segmentierung der PSI Analyse auf dem Krustenmaßstab überein.

Die Ergebnisse meiner Studie zeigen, dass die vertikale Deformation der Oberfläche von Kreta auf allen untersuchten Zeitskalen (Dekade, Millennium, Millionen Jahre) heterogen ist. Dies bedeutet, dass die Hellenische Subduktionszone nicht die dominierende tektonische Struktur ist, welche für die vertikalen Deformationen verantwortlich ist. An Stelle dessen scheinen verschiedene Störungssysteme in der Kruste, bzw. der oberen Kruste die Deformation zu steuern. Diese Störungen sind dabei auch in der Lage verheerende Erdbeben zu erzeugen und müssen daher in Studien zum Erdbebenrisiko und zur Schadensprävention einbezogen werden. Die langzeitlichen Rahmenbedingungen der aktiven Deformation, die aus geologischen Messungen abgeleitet werden, sind dabei eine wichtige Datenquelle, insbesondere in Fällen in denen sich kinematisch-mechanische Modelle aufgrund der Komplexität des Störungssystems nur schwer erstellen lassen.

ACKNOWLEDGEMENTS

First of all, I want to thank my thesis advisor Prof. Anke Friedrich for her support, motivation and inspiration over the last years. Thanks for your expertise, constructive criticism and your confidence to enable me to write this thesis.

This study was carried out together with the Remote Sensing Technology Institute (IMF) at the German Aerospace Center (DLR). I thank Prof. Richard Bamler and Prof. Michael Eineder for the opportunity to work together with the DLR. Special thanks is to Nico Adam and his SAR research group at the DLR. Thanks to Werner Liebhardt, Stefan Gernhardt, Alessandro Parizzi, and Fernando Rodriguez-Gonzalez who supported my data processing Further I would like to thank Silke Kerkhoff, Wolfgang Balzer, Thomas Fritz, Steffen Suchandt and Andreas Niedermaier.

Special thanks also to my LMU Geology Amir Abolghasem for helping to process the GPS data. Special thanks to Simon Kübler, Markus Hoffmann, Christine Plattner for their support not only concerning scientific questions but also for their friendship and patience during this years.

Danksagung

An dieser Stelle möchte ich mich bei allen bedanken die zum Gelingen meiner Dissertation beigetragen haben.

Allen voran gilt mein besonderer Dank Prof. Anke Friedrich für die Ermöglichung dieser Dissertation. Ihr unglaubliche Fähigkeit Zusammenhänge komplexer Fragestellungen mit einer unglaublichen Logik von groß nach klein zu beschreiben, werden mich immer beeindrucken. Ihr Fachwissen und im Speziellen ihre Begeisterung wissenschaftlichen Problemen gegenüber waren, sind und werden mir immer ein Vorbild sein.

Diese Arbeit entstand durch eine Zusammenarbeit mit dem Institut der Methotik der Fernerkundung des Deutschen Zentrums für Luft- und Raumfahrt. Dank gilt daher der Leitung der Abteilung Prof. Richard Bamler und Prof. Michael Eineder. Besonderer Dank geht an Nico Adam, Leiter der SAR-Gruppe, sowie Werner Liebhardt, Alessandro Parizzi, und Fernando Rodriguez-Gonzalez. Dank geht auch an Stefan Gernhardt der die SUN immer wieder zum leuchten gebracht hat und nicht müde war mein „Mieses Karma“ zu verspotten. Weiterer Dank geht an Silke Kerkhoff, Wolfgang Balzer, Thomas Fritz, Steffen Suchandt und Andreas Niedermaier für ihre Freundschaft und Hilfsbereitschaft zu allen möglichen Fragen.

Des weiteren gebührt ein besonderer Dank meinem Kollegen Amir Abolghasem für die Unterstützung bei der GPS Prozessierung. Weiterer großer Danke geht an meine Kollegen und Freunde Simon Kübler, Markus Hoffmann, Christine Plattner und Alessandro Verdecchia aus der Geologie für ihre Unterstützung bei fachlichen aber auch persönlichen Fragen im Zusammenhang mit der Dissertation.

Ganz besonders bedanken möchte ich mich bei meinen Eltern und meiner Schwester für ihren immerwährenden Rückhalt ohne den mein Studium und diese Dissertation nicht möglich gewesen wären.

Weiter möchte ich mich bei meinem persönlichen Umfeld und Freunden bedanken die immer ein offenes Ohr für mich hatten und jede Menge Zuspruch gegeben haben. Dank geht an Claudia Zagonel, die immer ein offenes Ohr für meine „mi mi mi“ Stimmung hatte. Dank geht an Heidi Rappl, Christiane Weiß, Gaby Mühl und Michael Hari (*Apple is ja so toll*) für Ihre Unterstützung gerade zum Ende hin.

Mein letzter Dank gilt Johann Wagner.

Chapter 1

INTRODUCTION

The quantification of vertical surface-deformation patterns on different time-scales is essential to understand active tectonic processes. Tectonic processes lead to horizontal and vertical deformation. Global horizontal tectonic motion is well known based on Global Positioning System (GPS) measurements and NUVEL-1A, which is the global geological plate motion model (DeMets et al., 1990; DeMets et al., 1994). Deformation rates were determined by comparison of synthetic magnetic anomalies with magnetic profiles across mid-oceanic spreading ridges over a uniform time-interval of 3.16 Myr (DeMets et al., 1990).

GPS measurements provide information about the three-dimensional displacement of crustal deformation (Segall and Davis, 1997). Although, the accuracy of GPS horizontal measurements is on the order of < 1 mm, the precision of the vertical component is worse by a factor of two to three due to the satellite constellation and tropospheric delay errors (Segall and Davis, 1997; Bürgmann and Thatcher, 2013). GPS time-series data are used mainly for analyzing horizontal motion (Figure 1.1), but due to sparse global GPS coverage do not allow precise quantification of the vertical motion, except in Japan and the United States of America (Figure 1.2). Traditionally, to measure vertical deformation tide gauge data and terrestrial leveling data provide reliable information, but these measurements are labor-intensive and costly (Bürgmann and Thatcher, 2013). Also, all of these techniques provide point-measurements, but do not yield information on the dense spatial vertical-deformation pattern.

To quantify the contemporary spatial vertical-deformation pattern, radar interferometry is the most promising geodetic tool. Interferometry Synthetic Aperture Radar (InSAR) deformation estimates are obtained along the line-of-sight (LOS) of the satellite, and therefore are more sensitive to vertical motions than to horizontal motion (e.g. Massonnet and Feigl, 1998; Bürgmann, 2000). For detecting vertical surface-deformation using conventional InSAR a short-acquisition time is required to maintain interferometry phase stability, due to temporal decorrelations and atmospheric inhomogeneities (Zebker and Villasenor, 1992; Hanssen, 2001). Therefore, InSAR studies have to be temporally closely related to earthquakes and long-acquisition time are not feasible. To overcome the limitation of the short-acquisition time, the Persistent Scatterer Interferometry (PSI) method was developed (Ferretti et al., 2001). Persistent Scatterers (PSs) are phase stable point targets with a consistent and strong reflectivity observed over several years (Ferretti et al., 2001). The changes of these phase-stable points are analysed in a series of Synthetic Aperture Radar (SAR) images acquired at different times over several years (Ferretti et al., 2001). While originally developed for urban areas (Ferretti et al., 2001), recent algorithmic developments allow the processing of non-urban and even mountainous areas (Adam et al., 2011). Many challenges are solved, e.g. the rare availability of PSs and the spatially varying PS density as well as a low PS quality with respect to their phase stability. This approach provides measurements of the vertical surface deformation pattern, with mm-accuracy and a wide spatial coverage of hundreds of kilometres.

Therefore, space-geodetic measurements provide invaluable data of contemporary surface deformation. These data provide information about active tectonic processes, such as the accumulation and release of strain along active faults. However, space-geodetic measurements are available only for two to three decades, and detected signals may represent transient processes leading to misinterpretation, e.g. of ongoing tectonic processes. To quantify whether the detected signals represents transients or permanent deformation, the contemporary vertical surface-deformation pattern is best compared with geomorphic and geological data. Long-term tectonic

processes are preserved and can be recognized in the landscape. Geomorphic and geologic markers provide information on tectonic processes on a millennial- to Myr-timescale.

The vertical surface-deformation pattern on different time-scales is of special interest above subduction zones. The recent 2004 M_w 9.1 Sumatra-Andaman earthquake (Lay et al., 2005) and the 2011 M_w 9.0 Tohoku-Oki earthquake (Simons et al., 2011) show that the potential of these subduction zones to generate M_w 9 earthquakes was failed to anticipate based on instrumental data (Matsuzawa et al., 2012; Goldfinger et al., 2013). Both regions were thought not to be capable to generate earthquakes exceeding M_w 8.4 (Matsuzawa et al., 2012; Goldfinger et al., 2013). For instance, the NE Japan subduction zone was considered to be weakly coupled based on the high background seismicity, the existence of small repeating earthquakes, GPS measurements and the age of the subducting plate (~ 180 Ma) (Figure 1.3) (Matsuzawa et al., 2012). However, short-term records are not sufficient to determine the potential of a subduction zone to be capable of large earthquakes, because the recurrence interval between such large earthquakes is too long. A rough estimation of the recurrence time of these two large earthquakes is determined by the assumption of plate motion convergence of 0.02 to 10 m/yr along subduction zones (McCaffrey, 2007), and the slip estimated of these earthquakes. The slip calculated for the 2004 M_w 9.1 Sumatra-Andaman earthquake is on the order of 20 m (Lay et al., 2005), and the slip of the 2011 M_w 9.0 Tohoku-Oki earthquake is on the order of 60 m (Simons et al., 2011). The recurrence time along the Sumatra-Andaman subduction zone is 200 to 1000 yrs, and for NE Japan is 600 to 3000 yrs. Therefore, instrumental records and even historical data are not sufficient to estimate the earthquake potential. Along the Sumatran subduction zone data concerning the growth pattern of corals showed evidence of a cluster of megathrust events between 1390 and 1455 A.D. (Meltzner et al., 2010). These events were associated with vertical displacement nearly large as or larger than the vertical displacement induced by the 2004 M_w 9.1 Sumatra-Andaman earthquake (Meltzner et al., 2010).

Further, along the Cascadian subduction zone no great earthquake of $M_w > 8$ is documented by instrumental seismic records or by historical reports for the last 200 yrs (Atwater et al., 1991; Satake et al., 1996). Geodetic continuous GPS measurements show episodic reversal of motion along GPS sites interpreted as silent slip events superimposed on the crustal shortening of the Cascadian Subduction zone (Figure 1.4) (Dragert et al., 2001; Miller et al., 2002). From 1992 to 2002 about eight slow slip events were geodetically recorded without detectable seismic shaking (Miller et al., 2002). Geological data, such as radiocarbon dating of tree stumps along the Cascadian coastline, and the height of tsunami deposits along the Japan coastline, indicate the occurrence of an M_w 9 earthquake on the 26th of January 1700 (Atwater et al., 1991; Satake et al., 1996). The historical earthquake shows the capability of the Cascadian subduction zone, whereas instrumental data suggest no potential for great earthquakes along this plate boundary.

These three examples of subduction zones indicate the necessity to analyze the vertical surface-deformation on decadal-, the millennial-, and the long-term times scale to understand deformation mechanisms above subduction zones. The analysis of the topography provides information of the millennial-, and long-term vertical surface deformation pattern and vertical deformation rates. The analyses of geomorphic and geological markers (Table 1.1) provide estimates on the millennial -, and long-term vertical surface deformation history.

What is currently missing are high precision and dense measurements of the contemporary vertical surface-deformation pattern on different time-scales. The comparison of short and long term, as well as the spatial distribution of vertical deformation, provides information on the past tectonic setting (Figure 1.5). The short-term signal may only represent a transient motion, which does not represent the actual tectonic motion of a region. Furthermore, the comparison gives insight to processes concerning the earthquake cycle along a subduction

zone, which describes the vertical displacement (Savage et al., 1983; Hyndman and Wang, 1993). During the interseismic period, when the upper plate interface is locked, strain is accumulated and stored elastically along the locked plate interface (Figure 1.6 A). Beneath the locking depth, and in the far field, the deeper fault is continuously creeping aseismically at long-term slip-rates. The locking along the plate interface leads to elastic bending and in turn to transient vertical surface displacement of both, the footwall and the hanging wall. The interseismic period can last from years to thousands of years. During the coseismic event, which last seconds to minutes, slip occurs along the former locked plate interface and the stress is reduced. The slip along the fault leads to a reversal of the vertical displacement pattern - formerly areas of subsidence experience coseismic uplift and vice versa (Figure 1.6 B). When locking along the plate interface occurs again, the earthquake cycle repeats.

Subduction zones are the tectonically and seismically most active regions on Earth (Figure 1.7). Studying subduction zone processes can be best achieved by the comparison of geodetic-, geomorphic-, and geological data.

This thesis provides the first PSI study for the detection of vertical surface-deformation on a large regional scale. The island of Crete, located in the Eastern Mediterranean, is an ideal test side, due to its E-W extension and coverage of several satellite tracks. I detected and analyzed the vertical deformation to identify which tectonic structures are responsible for the vertical surface-deformation pattern. This thesis aims to provide the first PSI study of Crete, in comparison to geomorphic and geologic data concerning the vertical surface-deformation pattern.

My main research questions pursued in this thesis are:

- (1) Can PSI be used on a regional scale, and what does the detected PSI vertical surface-deformation pattern tells us about the active subsurface tectonic processes?
- (2) How can I distinguish the respective source (geological feature) producing the vertical surface-deformation?
- (3) Is the emerging short-term deformation pattern transient or steady in comparison to longer-term deformation of the island?

I address these questions chapters below:

The main novelty of this thesis is the detection of the vertical surface-deformation pattern for the island of Crete during the interseismic period. The detected geodetic signal was analyzed to identify the possible tectonic structures responsible for the vertical surface-deformation. The contemporary deformation pattern was compared with the longer-term deformation pattern.

In Chapter 2, I analyze PSI measurements based on European Remote Sensing Satellite (ERS)-1 and ERS-2 satellite images from 1992 until 2000. I present the first PSI study of the island of Crete. Results of this study show a strong geodetic signal of vertical surface-deformation on Crete. Furthermore, I interpret the PSI pattern regarding the geological setting. I compare the vertical surface-deformation pattern to published hypothesis explaining the vertical uplift of Crete. The contemporary pattern is in accordance to tectonic processes along main upper crustal faults in the overriding plate.

Results of the PSI study as well as additional geomorphic and geological data of active upper-crustal normal faults on Crete are analyzed in Chapter 3. The vertical surface-deformation of the footwall and the hanging wall is measured respectively. The detected vertical geodetic signal along 13 normal faults does not always coincide with the expected vertical motion along normal faults. I compared the geodetic signal with geomorphic and geological data to determine the possible reason for the fault behaviour.

Chapter 4 provides a detailed study on geomorphic markers such as paleo-shorelines and river profiles, for estimating the vertical surface-deformation on the m/ka scale. I calculate uplift rates for paleo-shorelines for the Holocene and Pleistocene along the western, southern and

eastern coastline. Furthermore, analysis of river profiles and the distribution of knickpoints provide information on the spatial distribution of rock uplift from digital elevation models.

Chapter 5 focuses on the depositional depth of Neogene sediments in the grabens on Crete. I calculated the vertical surface-deformation on the km/Ma scale, when comparing the depositional depth of the sediments and the height distribution of the outcrop today.

Finally, in Chapter 6, I compare the vertical surface-deformation pattern of Crete, derived in the earlier chapters on the decadal-, millennial-, and long-term time scales.

In the next chapter I will give an overview of the tectonic setting, for better understanding of the tectonic evolution in the Eastern Mediterranean and Crete. Further, I will describe the historical and instrumental seismicity in this region.

1.1 Tectonic Setting of Crete

The island of Crete is located in the Eastern Mediterranean (Figure 1.8), which is characterized by the interaction of the Eurasian - African plate boundary system, and the Anatolian and Aegean microplates (McKenzie, 1972; Faccenna et al., 2014). In the vicinity of Crete the plate boundary is defined by the Hellenic subduction zones, where the African oceanic lithosphere is subducting towards the N beneath the continental Aegean microplate (McKenzie, 1972; Wortel and Spakman, 2000). The complex tectonic setting (Figure 1.8) is characterized by an early continent-continent collision between the Eurasian and African/Arabian plates (Royden, 1993).

Since the Eocene, the Hellenic subduction zone migrates towards the S, representing rollback of the subducting African oceanic lithosphere associated with backarc extension of the Aegean microplate, gravitational collapse, and the westward extrusion of the Anatolian microplate (Dewey and Sengör, 1979; Faccoulas et al., 1994; Le Pichon et al., 1995; Royden, 1993).

The Aegean region is distinguished by stacked nappes due to the northward subduction of the African plate beneath the Eurasian plate (Jacobshagen, 1986) and the collision of the European continental margin and the Apulian microcontinent (Creutzburg and Seidel, 1975).

Since Early Miocene, the rapid trench retreat of the African oceanic lithosphere towards the S led to N-S extension of the Aegean microplate (Le Pichon and Angelier, 1979). In the Late Oligocene and the Early Miocene the active thrust front was located in Crete forming the metamorphic core-complex by nappe stacking (Jolivet et al., 1996).

In the late Cenozoic (between 24 – 15 Ma) extensional stretching in N-S direction resulted in exhumation of metamorphic complexes along E-W striking detachment faults on Crete (Angelier, 1978; Jolivet et al., 1996; Thomson et al., 1998; van Hinsbergen et al., 2005). The low-angle detachment faults dip 10° – 30° towards the N under the Cretan Sea and towards the S under the Libyan Sea (Papanikolaou and Vassilakis, 2008), respectively.

The extension further led to the formation of the characteristic horst and graben structure, separated along deep faults, on Crete (Hall et al., 1984; Meulenkamp et al., 1988).

The contemporary active margin, defined by the Hellenic subduction zone, is located about 200 km S of Crete in the Libyan sea and was activated about 15 Ma (Thomson et al., 1998). The Mediterranean Ridge (Figure 1.8), a morphological high, subparallel to the Hellenic subduction zone, is the surface expression of an accretionary complex (Jolivet and Faccenna, 2000).

The continuously subducting African lithospheric-slab is detectable by global seismic tomography below the Aegean microplate and penetrates into the lower mantle (Wortel and Spakman, 2000) to a depth of ~1750 km (Hafkenscheid et al., 2006). Below Crete the subducting lithosphere dips with an angle of ~ 15° (Figure 1.9) (Meier et al., 2004), towards the N the dipping of the slab increases to 45° at a depth from 100 to 180 km (Papazachos et al., 2000).

Offshore S of Crete is characterized by the Hellenic Trench (Figure 1.9), representing morphologic depressions in the overriding Aegean microplate. The NE-dipping morphological trench system is segmented, and is the expression of a major reverse fault, located 25 km along the southwestern edge of Crete (Figure 1.9). It represents a major reverse fault in the overriding plate (Shaw et al., 2008). The Ptolemy, Pliny, and Strabo trenches (Figure 1.8) are arranged en echelon and represent transtensional strike-slip faults with sinistral sense (Le Pichon and Angelier, 1979; Le Pichon et al., 1995; Becker et al., 2010) and are located in the S and E of the island (Figure 1.8).

The island represents a first-order horst structure, and is further characterized by secondary horst and grabens, where horsts are of pre-Neogene age and the grabens are filled with Neogene and recent sediments (Hall et al., 1984; van Hinsbergen and Meulenkamp, 2006). The horst and graben structure is the result of extensional stress conditions, and its change in late Pliocene (Angelier, 1979; Armijo et al., 1992). The first N-S extensional stress regime created E-W striking normal faults on the island, the second E-W extensional stress regime led to formation of N-S normal faults (Angelier, 1979; Armijo et al., 1992). Due to its proximity to the Hellenic subduction zone, Crete represents one of the few places where the forearc high is exposed subaerially (Figure 1.8). A forearc high is an elevated region above the sea-level located between the subduction zone and the associated volcanic arc.

1.2 Neotectonic Vertical Deformation

Tectonic geomorphic markers, such as river channels and marine terraces, are utilized to extract information concerning rates and surface deformation patterns from topography. River profile analysis provides information about the variation of rock uplift across the landscape (Hack, 1973; Whipple and Tucker, 1999; Kirby et al., 2003). On Crete Roberts et al. (2013) investigated river profiles by inverse modeling to estimate the vertical uplift-rate history for the last 4 Ma. The study of marine terraces along the Huon Peninsula in New Guinea, showed that marine terraces record former sea-level changes tectonic uplift and tilting of coastal regions (Bloome et al., 1974; Chappell, 1974). On Crete several studies on Pleistocene and Holocene terraces were carried out to investigate the vertical surface deformation along the western, southern and eastern coastline (e.g. Pirazzoli et al., 1996; Wegmann, 2008; Shaw et al., 2008). Studies of Pleistocene paleo-shorelines were corrected not for one single eustatic sea-level curve, but for individual eustatic sea-level curves derived from different regions in the world.

Analyses of geological data, such as sedimentary records of Neogene sediments, provide estimates of the vertical deformation. The vertical deformation history can be quantified by using paleodepth estimates derived from foraminifera in sedimentary rocks (e.g. Bandy, 1953; Zoback et al., 1992). On Crete various studies concerning the vertical evolution of the Neogene sedimentary basins were carried out (e.g. Meulenkamp et al., 1994; Hinsbergen et al., 2005; Hinsbergen et al., 2006; Zachariasse et al., 2011).

1.3 Archaeological and Historical Seismicity

Archaeological, historical and instrumental seismic data are available for Crete. Since the Bronze Age, the island was inhabited by the Minoan civilization, representing the first high culture in Europe (Monaco and Tororici, 2004). Based on archaeological investigation on destroyed Minoan settlements on Crete, two large earthquakes with an intensity of IX-X on the macroseismic intensity Mercalli-Cancani-Sieberg scale (MCS) have been identified as cause of the destruction around 1700 B.C and 1450 before Christ (B.C.) (Monaco and Tororici, 2004). The Eastern Mediterranean region has one of the longest records of historical earthquakes in the world, starting 550 B.C. (Ambraseys et al., 1994; Papazachos et al., 2000). The island of Crete was affected by several destructive earthquakes, also triggering tsunamis, in the past. The two most important earthquakes are specified below. Further earthquakes affecting Crete are listed in Table 1.1.

On July 21st in 365 Anno Domini (A.D.) a strong earthquake occurred on the southwestern coast of Crete and triggered a tsunami affecting the whole Mediterranean region (Ambraseys et al., 1994; Stiros, 2001; Shaw et al., 2008; Guidoboni et al., 2009). The earthquake induced coseismic uplift of the southwestern coastline up to 9 m (Figure 1.9) (Spratt, 1865; Pirazzoli et al. 1996). The magnitude is estimated to be M_w is 8.3 - 8.5 (Shaw et al., 2008). This earthquake was one of a number of events in the Eastern Mediterranean during the time period from the middle of the fourth to the middle of the sixth century (Pirazzoli et al., 1996). This clustering of earthquakes is called the Early Byzantine Tectonic Paroxysm (EBTP), and is based on dated sublittoral fossils along the coasts of Greece, Turkey, Syria, Lebanon, Israel, and Cyprus (Pirazzoli et al., 1996). It is still under debate if the 365 A.D. earthquake was an unique event or a cluster of accretion of earthquakes occurring between 355 and 450 A.D. (Guidoboni et al., 2009; Stiros, 2001), due to uncertainties in dating of radiocarbon ages of up to $\sim \pm 140$ yrs (Shaw et al., 2008), or ± 80 yrs (Pirazzoli et al., 1996). The error range of the radiocarbon ages makes it impossible to distinguished clearly if the uplift was caused by one single earthquake, a series of rapid small events, or slow aseismic creep (Shaw et al., 2008). Stiros (2001) suggests, based on historical and archaeological data, that the 365 A.D. earthquake was an exceptional event during a time the seismic activity across the Eastern Mediterranean region was abnormally high.

On October 8th in 1303 A.D. an earthquake with a maximum intensity of XI on the macroseismic intensity MCS occurred close to the southeastern coast of Crete (Ambraseys et al., 1994; Guidoboni and Comastri, 1997). The earthquake triggered a tsunami in the Mediterranean region (Ambraseys et al., 1994; Guidoboni and Comastri, 1997). Tsunami modeling suggests a magnitude ~ 8 for this earthquake (Yolsal et al., 2012).

1.4 Instrumental Seismicity

The instrumental seismicity catalogue from 1900 until 1999 (Papazachos et al., 2000) shows three $M_w > 7$ earthquakes in the vicinity of Crete (Figure 1.11). The first of the three events occurred N of Crete with M_w 7 in 1935, the second occurred NNE of the island M_w 7.1 in 1948, and the third M_w 7 was located S of Crete in 1952. The errors in the magnitudes are in the interval ± 0.25 (Papazachos et al., 2000)

The Global Centroid-Moment-Tensor (GCMT) catalogue lists no earthquakes $M_w > 6.8$ between 1976 and 2015 February near Crete (Dziewonski et al., 1981; Ekström et al., 2012). Earthquakes with $6.0 < M_w < 6.8$ are displayed in Figure 1.11 with their corresponding focal mechanisms and listed in Table 1.2. Onshore Crete no earthquake is located between 0 to 20 km

depth. Offshore the island nine events are displayed for this depth range. One single event is located close to the western coastline of Crete indicating dip-slip motion striking in NW-SE direction. 100 km NW of Crete two earthquakes occurred in 2008, indicating dip-slip and strike slip mechanism (Figure 1.11). NE of Crete one event is located indicating normal faulting. The E-W extension along normal faults is concentrated in the western and the eastern part of the arc (Taymaz et al., 1990; Bohnhoff et al., 2005; Shaw et al., 2010). Analysis of focal mechanisms between a magnitude range of 0 and 6.5 shows that Central Crete has a heterogeneous distribution and no preferred orientation (Bohnhoff et al., 2005). Whereas, E-Crete is characterized by strike-slip focal mechanism with components of reverse and normal faulting along left-lateral faults (Bohnhoff et al., 2005). Between 0 and 20 km depth most events occur S of Crete (Figure 1.11). One single event is located ~ 100 km SSW of Crete indicating strike-slip motion. S of central Crete a cluster of four events (1979, 2009, 2013, 2013) is located indicating dip slip motion with tendency towards reverse motion. One single event is displayed for the depth range of 21 to 33 km ~ 200 km SSW of Crete close to the Libyan coastline, beneath the Mediterranean Ridge (Figure 1.11). This event most likely occurred in the basement and probably in the uppermost mantle of the subducting African plate (Taymaz et al., 1990).

Below 34 km depth seven earthquakes are displayed in Figure 1.11. Below south central Crete one event occurred in 1994 indicating oblique reverse. Three events NW and N of Crete indicate reverse motion, NE of Crete one event has also reverse motion, and two events have oblique strike-slip motion.

1.5 The PSI Method

As mentioned above PSI was developed in urban areas (Ferretti et al., 2001), where the PSs density is very high (~ 100 PSs per km²) (Figure 1.12) to correct for effects of the atmosphere and to achieve deformation measurements with mm-accuracy. In non-urban and mountainous regions the density of PSs is sparse (Figure 1.12) and therefore PSI investigations in rural regions were not possible. Recent algorithmic developments allow the processing of non-urban, on a regional scale, and even mountainous areas (Adam et al., 2011).

This approach provides measurements of the vertical surface deformation pattern, with mm-accuracy and a wide spatial coverage of hundreds of kilometres, for the first time.

References

- Abe K., Noguchi S. (1983): Determination of magnitude for large shallow earthquakes 1898-1917. *Physics of the Earth and Planetary Interiors*. Vol. 32. Iss. 1. Pages: 45–59. DOI: 10.1016/0031-9201(83)90077-8.
- Adam N.; Rodriguez Gonzalez F.; Parizzi A. and W. Liebhart W. (2011): Wide area persistent scatterer interferometry. In *Proc. IGARSS 2011*. Pages: 1481-1484. Vancouver, Canada.
- Amante C., Eakins B.W. (2009): ETOPO1 1 Arc-Minute Global Relief Model: Procedures, Data Sources and Analysis. NOAA Technical Memorandum NESDIS NGDC-24. National Geophysical Data Center, NOAA. DOI: 10.7289/V5C8276M.
- Ambraseys, N., Melville, C., Adams R. (1994): *Seismicity of Egypt, Arabia and the Red Sea*. Cambridge University Press.
- Angelier J. (1978): Tectonic evolution of the Hellenic arc since the Late Miocene. *Tectonophysics*. Vol. 49. Pages: 23-36. DOI: 10.1016/0040-1951(78)90096-3.
- Angelier J. (1979): Neotectonique de l'arc Eggen. These d'etat. University de Paris VI, 405 pp.
- Atwater B.F., Stuiver M., Yamaguchi D.K. (1991): Radiocarbon test of earthquake magnitude at the Cascadia subduction zone. *Nature*. Vol. 353. Pages: 156-158. DOI: 10.1038/353156a0.
- Bandy O.L. 1953: Ecology and paleoecology of some California foraminifera. Part I. The frequency distribution of recent foraminifera off California. *Journal of Paleontology*. Vol. 27. No. 2. Pages: 200-203.
- Becker D., Meier T., Bohnhoff M., Harjes H.P. (2010): Seismicity at the convergent plate boundary offshore Crete, Greece, observed by an amphibian network. *Journal of Seismology*. Vol. 14: Pages: 369-392. DOI: 10.1007/s10950-009-9170-2.
- Bloome A.L., Broecker W.S., Chappell J.M.A., Matthews R.K., Mesolello K.J. (1974): Quaternary Sea Level Fluctuations on a Tectonic Coast: New 230th/234u Dates from the Huon Peninsula, New Guinea. *Quaternary Research*. Vol. 4. Iss. 2. Pages: 185-205. DOI: 10.1016/0033-5894(74)90007-6.
- Bohnhoff M., Harjes H.-P., Meier T. (2005): Deformation and stress regimes in the Hellenic subduction zone from focal Mechanisms. *Journal of Seismology*. Vol. 9. Pages: 341-366. DOI: 10.1007/s10950-005-8720-5.
- Bürgmann R., Rosen P.A., Fielding E.J. (2000): Synthetic Aperture Radar Interferometry to Measure Earth's Surface Topography and Its Deformation. *Annual Review of Earth and Planetary Sciences*. Vol. 28. Pages: 169-209. DOI: 10.1146/annurev.earth.28.1.169
- Bürgmann R., Thatcher W. (2013): Space geodesy: A revolution in crustal deformation measurements of tectonic processes. *GSA Special Papers 2013*. Vol. 500. Pages: 397-430. DOI: 10.1130/2013.2500(12).
- Chamot-Rooke N., Rangin C., Le Pichon X. (2005): DOTMED – Deep Offshore Tectonics of the Mediterranean: A synthesis of deep marine data in Eastern Mediterranean, The Ionian basin and margins, the Calacria wedge and the Mediterranean ridge. *Société Géologique de France*. Paris. Pages: 64.

- Chappel J. and Polach H.A. (1974): Holocene sea-level change and coral-reef growth at Huon Peninsula, Papua New Guinea. *Geological Society of America Bulletin*. Vol. 87. Iss. 2. Pages: 235-240. DOI: 10.1130/0016-7606(1976)87<235:HSCACG>2.0.CO;2
- Chlieh M., deChabalier J.B., Ruegg J.C., Armijo R., Dmowska R., Campos J., Feigl K.L. (2004): Crustal deformation and fault slip during the seismic cycle in the North Chile subduction zone, from GPS and InSAR observations. *Geophysical Journal International*. Vol. 158. Pages: 695-711. DOI: 10.1111/j.1365-246X.2004.02326.x.
- Creutzburg N., and Seidel E. (1975): Zum Stand der Geologie des Präneogens auf Kreta. *Neues Jahrbuch für Geologie und Paläontologie. Abhandlungen*. 141. Pages: 259-285.
- DeMets C., Gordon R.G., Argus D.F., Stein S. (1990): Current plate motions. *Geophysical Journal International*. Vol. 101. Pages: 425-478. DOI: 10.1111/j.1365-246X.1990.tb06579.x.
- DeMets C., Gordon R.G., Argus D.F., Stein S. (1994): Effect of recent revisions to the geomagnetic reversal time scale on estimates of current plate motions. *Geophysical Research Letters*. Vol. 21. Pages: 2191-2194. DOI: 10.1029/94GL02118.
- DeMets C., Dixon T.H. (1999): New kinematic models for Pacific-North America motion from 3 Ma to present, I: Evidence for steady motion and biases in the NUVEL-1a model. *Geophysical Research Letters*. Vol. 26. Pages: 1921-1924. DOI: 10.1029/1999GL900405.
- Dewey, J.F. and Sengor, A.M.C., 1979. Aegean and surrounding regions: complex multiplate and continuum tectonics in a convergent zone. *Geol. Soc. Amer. Bull.* Vol. 90. No. 1. Pages: 84-92. DOI: 10.1130/0016-7606(1979)90<84:AASRCM>2.0.CO;2.
- Dragert H., Wang K., James T.S. (2001): A silent slip event on the deeper Cascadia subduction interface. *Science*. Vol. 292. No. 5521. Pages: 1525-1528. DOI: 10.1126/science.1060152.
- Dziewonski A. M., Chou T.A., Woodhouse J. H.(1981): Determination of earthquake source parameters from waveform data for studies of global and regional seismicity. *Journal of Geophysical Research*. Vol. 86. Pages: 2825-2852. DOI: 10.1029/JB086iB04p02825.
- Ekström G., Nettles M., Dziewonski A. M. (2012): The global CMT project 2004-2010: Centroid-moment tensors for 13,017 earthquakes. *Physics of the Earth and Planetary Interiors* Vol. 200-201. Pages: 1-9. DOI: 10.1016/j.pepi.2012.04.002.
- Faccenna C., Becker T.W., Auer L., Billi A., Boschi L., Brun J.P., Capitanio F.A., Funicello F., Horvath F., Jolivet L., Piromallo C., Royden L., Rossetti F., Serpelloni E. (2014): Mantle dynamics in the Mediterranean. *Reviews of Geophysics*. Vol. 52. Iss. 3. Pages: 283-332. DOI: 10.1002/2013RG000444.
- Fassoulas C., Kiliadis A., Mountrakis D. (1994): Postnappe stacking extension and exhumation of high-pressure/low-temperature rocks in the island of Crete, Greece. *Tectonics*. Vol. 13. Iss. 1. Pages: 127-138. DOI: 10.1029/93TC01955.
- Ferretti A., Prati C. and Rocca F. (2001): Permanent Scatterers in SAR Interferometry. *IEEE Transactions on Geoscience and Remote Sensing*. Vol. 38. Pages: 2202-2212. DOI: 10.1109/36.898661.
- Friedrich A.M., Wernicke B.P., Niemi N.A., Bennett R.A., Davis J.L. (2003): Comparison of geodetic and geological data from the Wasatch region, Utah, and implications for the spectral character of Earth deformation at periods of 10 to 10 million years. *Journal of Geophysical Research*. Vol. 108. No. 2199. DOI: 10.1029/2001JB000682.

- Jacobshagen, V., ed. (1986): *Geologie von Griechenland*: Berlin. Stuttgart. Gebrüder Borntraeger. Pages: 363.
- Jolivet L., Goffé B., Monié P., Truffert-Luxey C., Patriat M., Bonneau M. (1996): Miocene detachment in Crete and exhumation P-T-t paths of high-pressure metamorphic rocks. *Tectonics*. Vol. 15. No. 6. Pages: 1129-1153. DOI: 10.1029/96TC01417.
- Jolivet L., Faccenna C. (2000): Mediterranean extension and the Africa-Eurasia collision. *Tectonics*. Vol. 19. No. 6. Pages: 1095-1106. DOI: 10.1029/2000TC900018.
- Goldfinger C., Ikeda Y., Yeats R.S., Ren J. (2013): Superquakes and supercycles. *Seismological Research Letters*. Vol. 84. No. 1. DOI: 10.1785/0220110135.
- Guidoboni E., Comastri A. (1997): The large earthquake of 8 August 1303 in Crete: seismic scenario and tsunami in the Mediterranean area. *Journal of Seismology*. Vol. 1. Pages: 55-72. DOI: 10.1023/A:1009737632542.
- Guidoboni E., Ebel J.E. (2009): *Earthquakes and tsunamis in the past: A guide to techniques in historical seismology*. Cambridge University Press. Pages: 590.
- Gutenberg B., Richter C.F. (1949): *Seismicity of the Earth and associated phenomena*. Princeton University Press. Princeton, New Jersey. Pages: 295.
- Hack J.T. (1973): Stream-profile analysis and stream-gradient index. *US. Geol. Survey Jour. Research*. Vol. 1. No. 4. Pages: 421-429.
- Hafkenschied E., Wortel M.J.R., and Spakman W. (2006): Subduction history of the Tethyan region derived from seismic tomography and tectonic reconstructions. *Journal of Geophysical Research*. Vol. 111. B08401. DOI: 10.1029/2005JB003791.
- Hall R., Audley-Charles M. G., Carter D.J. (1984): The significance of Crete for the evolution of the Eastern Mediterranean. *Geological Society. London. Special Publications*. Vol. 17. Pages: 499-516. DOI: 10.1144/GSL.SP.1984.017.01.37.
- Hanssen R.F. (2001): *Radar Interferometry: Data Interpretation and error analysis*. Kluwer Academic. Dordrecht.
- Hollenstein C., Müller M.D., Geiger A., Kahle H.G. (2008): Crustal motion and deformation in Greece from a decade of GPS measurements, 1993-2003. *Tectonophysics*. Vol. 449. Page: 17-40. DOI: 10.1016/j.tecto.2007.12.006.
- Hyndman R.D., Wang K. (1993): Thermal constraints on the zone of major thrust earthquake failure: The Cascadia Subduction Zone. *Journal of Geophysical Research*. Vol. 98. Iss. B2. Pages: 2039-2060. DOI: 10.1029/92JB02279.
- Kirby E., Whipple K.X., Tang W., Chen Z. (2003): Distribution of active rock uplift along the eastern margin of the Tibetan Plateau: Inferences from bedrock channel longitudinal profiles. *Journal of Geophysical Research-Solid Earth*. Vol. 108. Iss. B4. DOI: 10.1029/2001JB000861.
- Kopf A., Mascle J., and Klaeschen D. (2003): The Mediterranean Ridge: A mass balance across the fastest growing accretionary complex on Earth. *Journal of Geophysical Research*. Vol. 108. No. B8. DOI: 10.1029/2001JB000473.
- Landgraf A., Zielke O., Arrowsmith J.R., Ballato P., Strecker M.R., Schildgen T.F., Friedrich A.M., Tabatabaei S.H. (2013): Differentiating simple and composite tectonic landscapes using numerical fault slip modeling with an example from the south central Alborz Mountains, Iran.

- Journal of Geophysical Research. Earth Surface. Vol. 118. Pages: 1792-1805. DOI: 10.1002/jgrf.20109.
- Lay T., Kanamori H., Ammon C.J., Nettles M., Ward S.N., Aster R.C., Beck S.L., Bilek S.L., Brudzinski M.R., Butler R., DeShon H.R., Ekström G., Satake K., Sipkin S. (2005): The great Sumatra-Andaman earthquake of 26 December 2004. *Science*. Vol. 308. No. 1127. DOI: 10.1126/science.1112250.
- Le Pichon X., Angelier J. (1979): The Hellenic Arc and Trench System: A Key to the Neotectonic Evolution of the Eastern Mediterranean Area. *Tectonophysics*. Vol. 60. Pages: 1-42. DOI: 10.1016/0040-1951(79)90131-8.
- Le Pichon X., Chamot-Rooke N., Lallemand S., Noomen R., Veis G. (1995): Geodetic determination of the kinematics of central Greece with respect to Europe: Implications for Eastern Mediterranean tectonics. *Journal of Geophysical Research*. Vol. 100. Iss. B7. Pages: 12675-12690. DOI: 10.1029/95JB00317.
- Massonnet D., Feigl K.L. (1998): Radar interferometry and its application to changes in the Earth's surface. *Reviews of Geophysics*. Vol. 36. Pages: 441-500. DOI: 10.1029/97RG03139.
- Matsuzawa T., Iio Y. (2012): The reasons why we failed to anticipate M9 earthquakes in northeast Japan. Japan Association for Earthquake Engineering. Proceedings of the International Symposium on Engineering Lessons Learned from the 2011 Great East Japan Earthquake. March 1-4, 2012. Tokyo, Japan.
- McCaffrey R. (2007): The next great earthquake. *Science*. Vol. 315. No. 5819. Pages: 1675-1676. DOI: 10.1126/science.1140173.
- McClusky S., Balassanian S., Barka A., Demir C., Ergintav S., Georgiev I., Gurkan O., Hamburger M., Hurst K., Kahle H., Kastens K., Kekelidze G., King R., Kotzev V., Lenk O., Mahmoud S., Mishin A., Nadariya M., Ouzounis A., Paradissis D., Peter Y., Prilepin M., Reilinger R., Sanli I., Seeger H., Tealeb A., Toksöz M. N., Veis G. (2000): Global Positioning System constraints on plate kinematics and dynamics in the Eastern Mediterranean and Caucasus. *Journal of Geophysical Research*. Vol. 105. No. B3. Pages: 5695-5719. DOI: 10.1029/1999JB900351.
- McKenzie D. (1972): Active Tectonics of the Mediterranean Region. *Geophysical Journal of the Royal Astronomical Society*. Vol. 30. Iss. 2. Pages: 109-185. DOI: 10.1111/j.1365-246X.1972.tb02351.x.
- Meier T., Rische M., Endrun B., Vafidis A., and Harjes H.-P. (2004): Seismicity of the Hellenic subduction zone in the area of western and central Crete observed by temporary local seismic networks. *Tectonophysics*. Vol. 383. Pages: 149-169. DOI: 10.1016/j.tecto.2004.02.004.
- Melnick D., Bookhagen B., Echtler H., and Strecker M., (2006): Coastal deformation and great subduction earthquakes, Isla Santa María, Chile (37°S). *Geological Society of America Bulletin*: V. 118. Pages: 1463-1480. DOI: 10.1130/B25865.1.
- Meltzner A.J., Sieh K., Chaing H.W., Shen C.C., Suwargadi B.W., Natawidjaja D.H., Philibosian B.E., Briggs R.W., Galetzka J. (2010): Coral evidence for earthquake recurrence and an A.D. 1390-1455 cluster at the south end of the 2004 Aceh-Andaman rupture. *Journal of Geophysical Research*. Vol. 115. DOI: 10.1029/2010JB007499.

- Meulenkamp J.E., Wortel M.J.R., Wamel van W.A. Spakman W., Hoogerduyn Strating E. (1988): On the Hellenic subduction zone and the geodynamic evolution of Crete since the late Middle Miocene. *Tectonophysics*. Vol. 146. Pages: 203-215. DOI: 10.1016/0040-1951(88)90091-1.
- Miller M.M., Melbourne T., Johnson D.J., Summer W.Q. (2002): Periodic slow earthquakes from the Cascadia subduction zone. *Science*. Vol. 295. No. 5564. Pages: 2423. DOI: 10.1126/science.1071193.
- Monaco C., Tortorici L. (2004): Faulting and effects of earthquakes on Minoan archaeological sites in Crete (Greece). *Tectonophysics*. Vol. 382. Pages: 103-116. DOI: 10.1016/j.tecto.2003.12.006.
- Obara K. (2002): Nonvolcanic deep tremor associated with subduction in southwest Japan. *Science*. Vol. 296. No. 5573. Pages: 1679-1681. DOI: 10.1126/science.1070378.
- Pacheco J.F., Sykes L.R. (1992): Seismic moment catalog of large shallow earthquakes, 1900 to 1989. *Bulletin of the Seismological Society of America*. VOL. 82. No. 3. Pages: 1306-1349.
- Papanikolaou D., Vassilakis E. (2010): Middle Miocene E-W Tectonic Horst Structure of Crete through Extensional Detachment Faults. *Tectonophysics*. Vol. 488. Iss. 1-4, 5. Pages: 233-247. DOI: 10.1088/1755-1307/2/1/012003.
- Papazachos, B.C., Dimitriu P.P. (1991): Tsumamis in and near Greece and their relation to the earthquake focal mechanisms. *Natural Hazards*. Vol. 4. Pages: 161-170. DOI: 10.1007/BF00162785.
- Papazachos, B.C., Comninakis, P.E., Karakaisis, G.F., Karakostas, B.G., Papaioannou, Ch.A., Papazachos, C.B., Scordilis E.M. (2000): A catalogue of earthquakes in Greece and surrounding area for the period 550BC-1999. *Publ. Geophys. Lab., Univ. of Thessaloniki*. 1. Pages: 333.
- Papazachos, B.C., Comninakis, P.E., Scordilis, E.M., Karakaisis, G.F. and C.B. Papazachos (2009): A catalogue of earthquakes in the Mediterranean and surrounding area for the period 1901 - Sep2009, *Publ. Geophys. Laboratory, University of Thessaloniki*.
- Pirazzoli P.A., Laborel J., Stiros S.C. (1996): Earthquake clustering in the Eastern Mediterranean during historical times. *Journal of Geophysical Research - Solid Earth*. Vol. 101. Iss. B3. Pages: 6083-6097. DOI: 10.1029/95JB00914.
- Pondrelli S., Salimbeni S., Morelli A., Ekström G., Postpischl L., Vannucci G. and Boschi E. (2011): European-Mediterranean Regional Centroid Moment Tensor Catalog: solutions for 2005-2008. *Physics of the Earth and Planetary Interiors*. Vol. 185. Issue 3-4. Pages: 74-81.
- Reid H.F. (1910): The mechanics of the earthquake. Vol. II of Lawson, A.C., chairman. The California earthquake of April 18, 1906: Report of the State Earthquake Investigation Commission: Carnegie Institution of Washington Publication 87. Pages: 192.
- Reilinger R., McClusky S., Vernant P., Lawrence S., Ergintav S., Cakmak R., Ozener H., Kadiror F., Guliev I., Stepanyan R., Nadariya M., Hahubia G., Mahmoud S., Sakr K., ArRajehi A., Paradissis D., Al-Aydrus A., Prilepin M., Guseva T., Evren E., Dmitrova T., Filikov S.V., Gomez F., Al-Ghazzi R., Karam G. (2006): GPS constraints on continental deformation in the Africa-Arabia-Eurasia continental collision zone and implications for the dynamics of plate interactions. *Journal of Geophysical Research - Solid Earth*. Vol. 111. Iss. B5. DOI: 10.1029/2005JB0045051.

- Ricou L.E., Burg J.P., Godfriaux I., Ivanov Z. (1998): Rhodope and Vardar: the metamorphic and the olistostromic paired belts related to the Cretaceous subduction under Europe. *Geodynamic Acta*. Vol. 11. Pages: 285-309.
- Roberts G.G., White N.J., Shaw B. (2013): An uplift history of Crete, Greece, from inverse modeling of longitudinal river profiles. *Geomorphology*. Vol. 198. Pages: 177-188. DOI: 10.1016/j.geomorph.2013.05.026.
- Royden L.H. (1993): The Tectonic Expression Slab Pull At Continental Convergent Boundaries. *Tectonics*. Vol. 12. No. 2. Pages: 303-325. DOI: 10.1029/92TC02248.
- Ryder I., Rietbrock A., Kelson K., Bürgmann R., Floyd M., Socquet A., Vigny C., Carizzo D. (2012): Large extensional aftershocks in the continental forearc triggered by the 2010 Maule earthquake, Chile. *Geophysical Journal International*. Vol. 188. Pages: 879-890. DOI: 10.1111/j.1365-246X.2011.05321.x.
- Satake K., Shimazaki K., Tsuji Y., Ueda K. (1996): Time and size of a giant earthquake in Cascadia inferred from Japanese tsunami records of January 1700. *Nature*. Vol. 379. Pages: 246 - 249. DOI: 10.1038/379246a0.
- Savage J.C. (1983): A dislocation model of strain accumulation and release at a subduction zone. *Journal of Geophysical Research*. Vol. 88. Pages: 4984-4996. DOI: 10.1029/JB088iB06p04984.
- Scholz C. (1990): *The Mechanics of Earthquakes and Faulting*. Cambridge Univ. Press. New York. Pages: 461.
- Segall P., Davis J.L. (1997): GPS applications for geodynamics and earthquake studies. *Annual Review of Earth and Planetary Sciences*. Vol. 25. Page: 301-36. DOI: 10.1146/annurev.earth.25.1.301. DOI: 10.1146/annurev.earth.25.1.301.
- Shaw B., Ambraseys N.N., England P.C., Floyd M.A., Gorman G.J., Higham T.F.G., Jackson J. A., Nocquet J.-M., Pain C. C., Piggott M. D. (2008): Eastern Mediterranean tectonics and tsunami hazard inferred from the A.D. 365 earthquake. *Nature Geoscience*. Vol. 1. DOI: 10.1038/ngeo151.
- Shaw B., Jackson J. (2010): Earthquake mechanisms and active tectonics of the Hellenic subduction zone. *Geophysical Journal International*. Vol. 181. Pages: 966-984. DOI: 10.1111/j.1365-246X.2010.04551.x.
- Shimazaki K., Nakata T. (1980): Time-predictable recurrence model for large earthquakes. *Geophysical Research Letters* Vol. 7. No. 4. Pages: 279-282. DOI: 10.1029/GL007i004p00279.
- Shirzaei M., Bürgmann R., Oncken O., Walter T.T., Victor P., Ewiak O. (2012): Response of forearc crustal faults to the megathrust earthquake cycle: InSAR evidence from Mejillones Peninsula, Northern Chile. *Earth and Planetary Science Letters*. Vol: 333-334. Pages: 157-164. DOI: 10.1016/j.epsl.2012.04.001.
- Sibson R.H. (1985): A note on fault reactivation. *Journal of Structural Geology*. Vol. Pages: 751-754. DOI: 10.1016/0191-8141(85)90150-6.
- Simons M., Minson S.E., Sladen A., Ortega F., Jiang J., Owen S.E., Meng L., Ampuero J-P., Wei S., Chu R., Helmberger D.V., Kanamori H., Hetland E., Moore A.W., Webb F.H. (2011): The 2011 magnitude 9.0 Tohoku-Oki earthquake: Mosaicking the megathrust from seconds to centuries. *Science*. Vol. 332. No. 6036. Pages: 1421-1425. DOI: 10.1126/science.1206731.

- Smith W.H.F. and Sandwell D.T. (1997): Global seafloor topography from satellite altimetry and ship depth soundings. *Science*. Vol. 277. No. 5224. Pages: 1957-1962. DOI: 10.1126/science.277.5334.1956.
- Spratt T.A.B. (1865): *Travels and Researches in Crete*. Vol. I. London. John van Voorst. Pages: 327.
- Stiros S.C. (2001): The AD 365 Crete earthquake and possible seismic clustering during the fourth to sixth centuries AD in the Eastern Mediterranean: a review of historical and archaeological data. *Journal of Structural Geology*. Vol. 23. Iss. 2-3. Pages: 545-562. DOI: 10.1016/S0191-8141(00)00118-8.
- Taymaz T., Jackson J., Westaway R. (1990): Earthquake mechanisms in the Hellenic Trench near Crete. *Geophysical Journal International*. Vol. 102. Iss. 3. Pages: 695-731. DOI: 10.1111/j.1365-246X.1990.tb04590.x.
- Thomson S.N., Stockhert B., Brix M.R. (1998): Thermochronology of the high-pressure metamorphic rocks of Crete, Greece: Implications for the speed of tectonic processes. *Geology*. Vol. 26. Iss. 9. Pages: 259-262. DOI: 10.1130/0091-7613(1998)026<0259:TOTHPM>2.3.CO;2.
- Tsapanos T.M. (2001): Earthquake hazard parameters estimated in Crete Island and the adjacent area. *Pure and applied Geophysics*. Vol. 158. Pages: 1691-1718. DOI: 10.1007/s00024-003-2358-4.
- Van Hinsbergen D.J.J., Hafkenscheid E., Spakman W., Meulenkaamp J.E., Wortel R. (2005): Nappe stacking resulting from subduction of oceanic and continental lithosphere below Greece. *Geology*. Vol. 33. Pages: 325-328. DOI: 10.1130/G20878.1.
- Van Hinsbergen D.J.J., Meulenkaamp J.E. (2006): Neogene supradetachment basin development on Crete (Greece) during exhumation of the South Aegean core complex. *Basin Research* 18. Pages: 103-124. DOI: 10.1111/j.1365-2117.2005.00282.x.
- Wegmann K.W. (2008): *Tectonic Geomorphology above Mediterranean Subduction Zones. Northeastern Apennines of Italy and Crete, Greece*. Lehigh University (Ph.D. thesis).
- Wesson R.L., Melnick D., Cisternas M., Moreno M., Ely L.L. (2015): Vertical deformation through a complete seismic cycle at Isla Santa Maria, Chile. *Nature Geoscience*. Vol. 8. Pages: 547-551. DOI: 10.1038/ngeo2468.
- Whipple K.X. and Tucker G.E. (1999): Dynamics of the stream-power river incision model: Implications for height limits of mountain ranges, landscape response timescales, and research needs. *Journal of Geophysical Research*. Vol. 104. No. B8. Pages: 17.661. DOI: 10.1029/1999JB900120.
- Wortel M.J.R., and Spakman W. (2000): Subduction and Slab Detachment in the Mediterranean-Carpathian Region. *Science*. Vol. 290. No. 2498. Pages: 1910-1917. DOI: 10.1126/science.290.5498.1910.
- Yeats R.S., Sieh K., Allen C.R. (1997): *The geology of earthquakes*. Oxford University Press. Pages: 576.
- Yolsal-Cevikbilen S., Taymaz T. (2012): Earthquake source parameters along the Hellenic subduction zone and numerical simulations of historical tsunamis in the Eastern Mediterranean. *Tectonophysics*. Vol. 536-537. Pages: 61-100. DOI:10.1016/j.tecto.2012.02.019.

Zachariasen J., Sieh K., Taylor F.W., Hantoro W.S. (2000): Modern vertical deformation above the Sumatran subduction zone: paleogeodetic insights from coral microatolls. *Bulletin of the Seismological Society of America*. Vol. 90. Pages: 897-913. DOI: 10.1785/0119980016.

Zachariasse W.J., van Hinsbergen D.J.J., Fortuin, A. (2011): Formation and fragmentation of a late Miocene supradetachment basin in central Crete: implications for exhumation mechanisms of high-pressure rocks in the Aegean forearc. *Basin Research*. Vol. 23. Pages: 678-701. DOI: 10.1111/j.1365-2117.2011.00507.x.

Zebker H.A., Villasenor J. (1992): Decorrelation in Interferometric Radar Echoes. *IEEE Transactions on Geoscience and Remote Sensing*. Vol. 30. No. 5. Pages: 950-959. DOI: 10.1109/36.175330.

Zoback M.D., Stephenson R.A., Cloetingh S., Larsen B.T., Van Hoorn B., Robinson A., Horvath F., Puigdefabregas C., Ben-Avraham Z. (1993): Stresses in the lithosphere and sedimentary basin formation. *Tectonophysics*. Vol. 226. Pages: 1-13. DOI: 10.1016/0040-1951(93)90107-U.

Figures & Tables

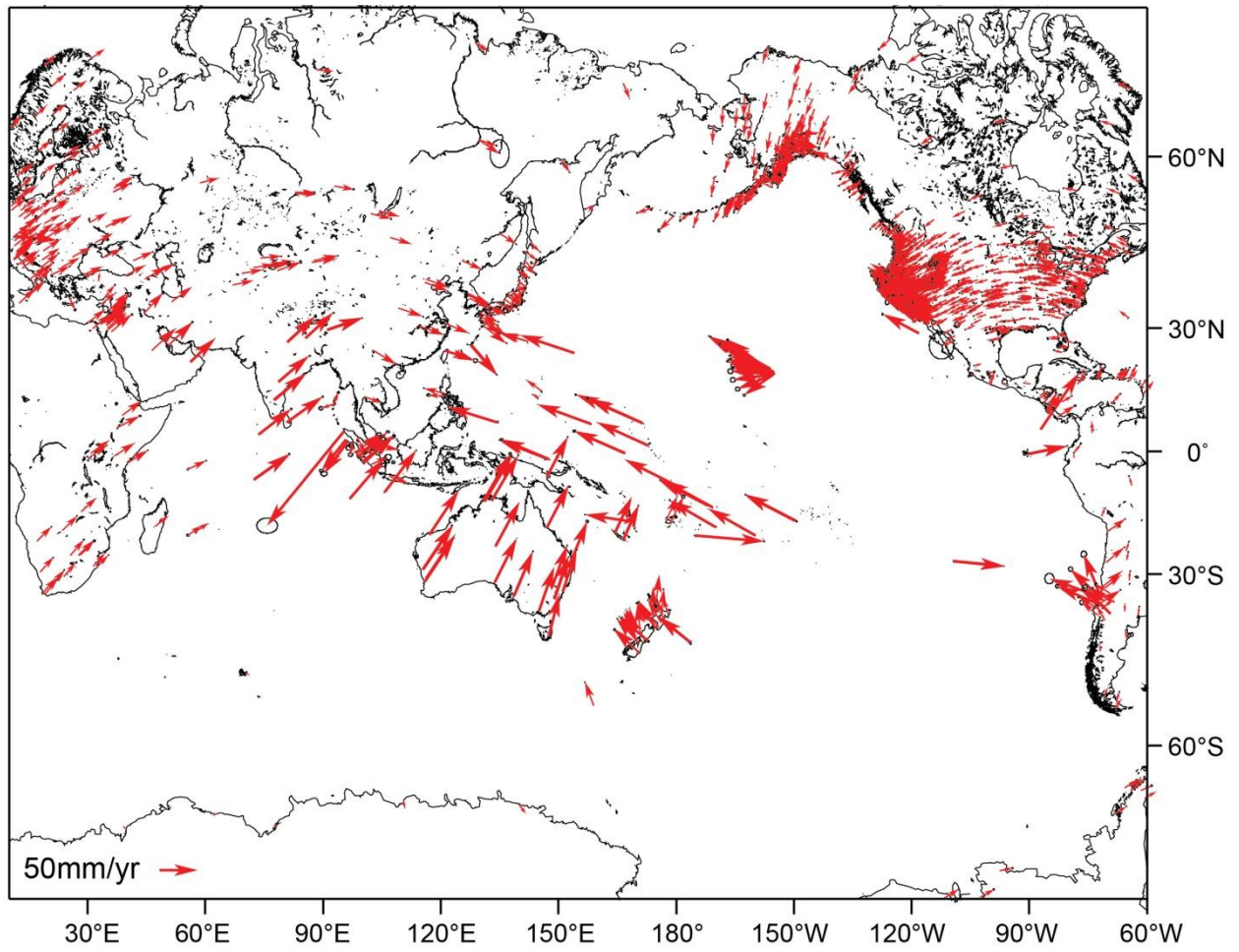


Figure 1.1: GPS velocity measurements based on Jet Propulsion Laboratory GPS time series stations.

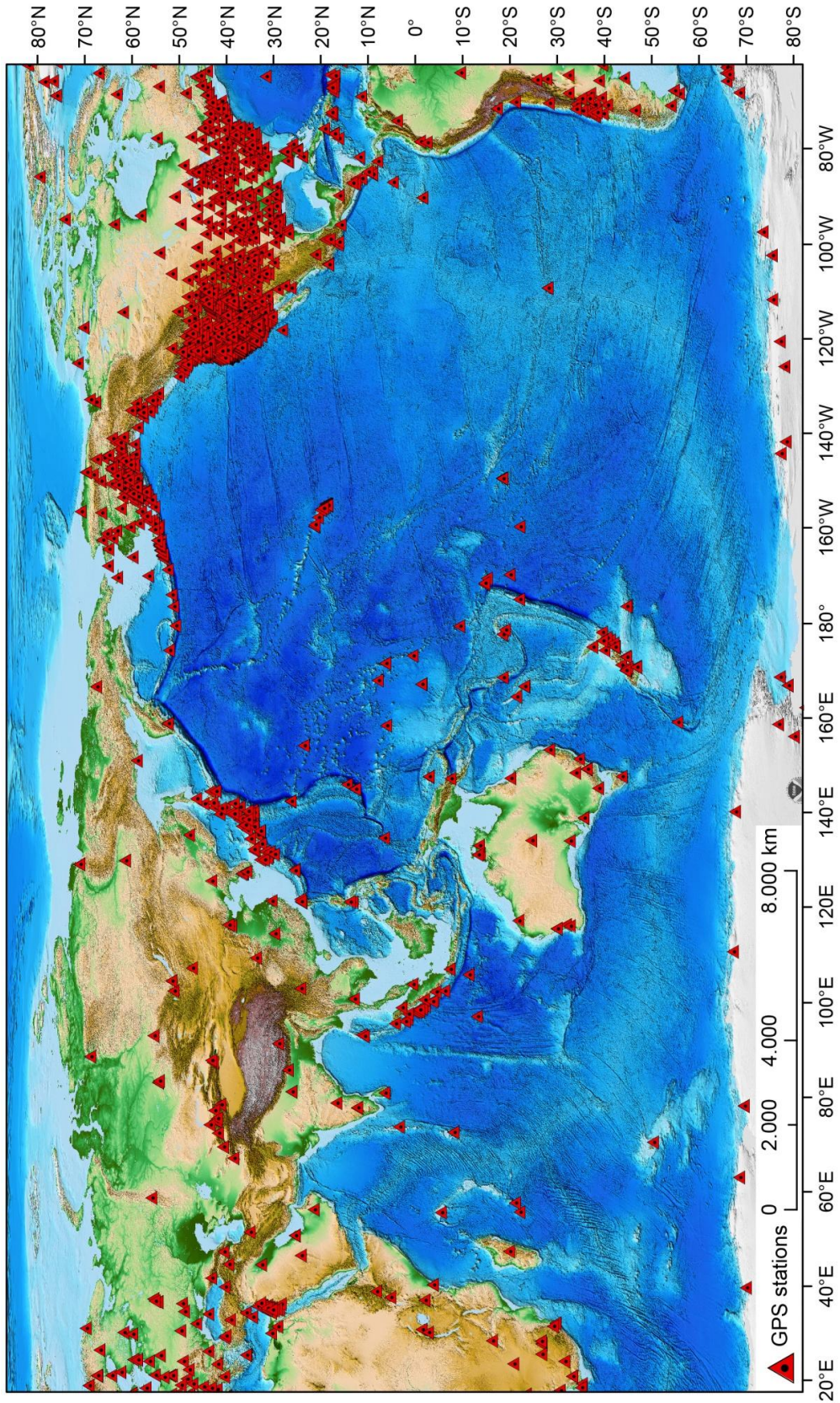


Figure 1.2: Distribution of Jet Propulsion Laboratory GPS time series stations. ETOPO1 global relief map after Amante et al. (2009).

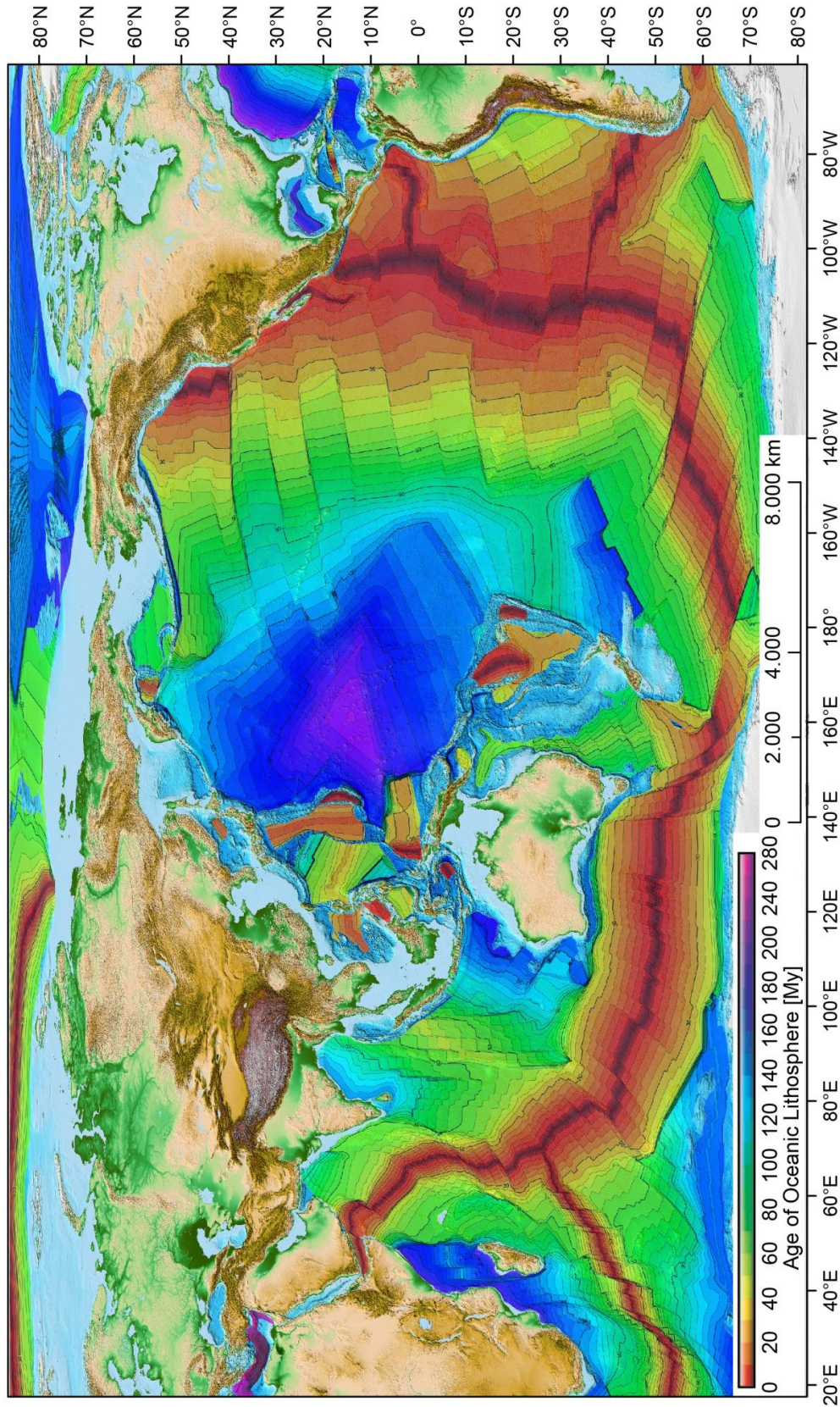


Figure 1.3: Age of oceanic lithosphere after Mueller et al. (2008). ETOPO1 global relief map after Amante et al. (2009).

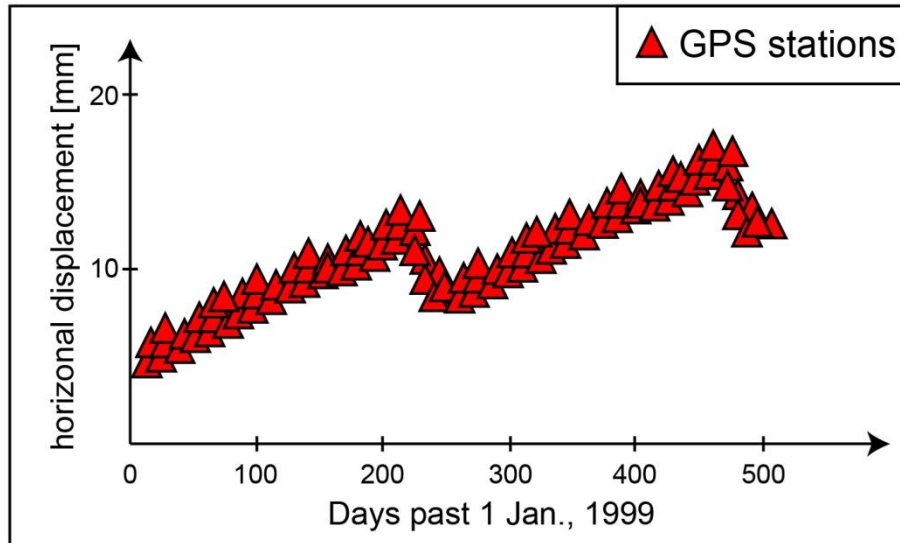


Figure 1.4: Daily changes in longitude with respect to GPS station DRAO in Canada, modified after dragert et al. (2001).

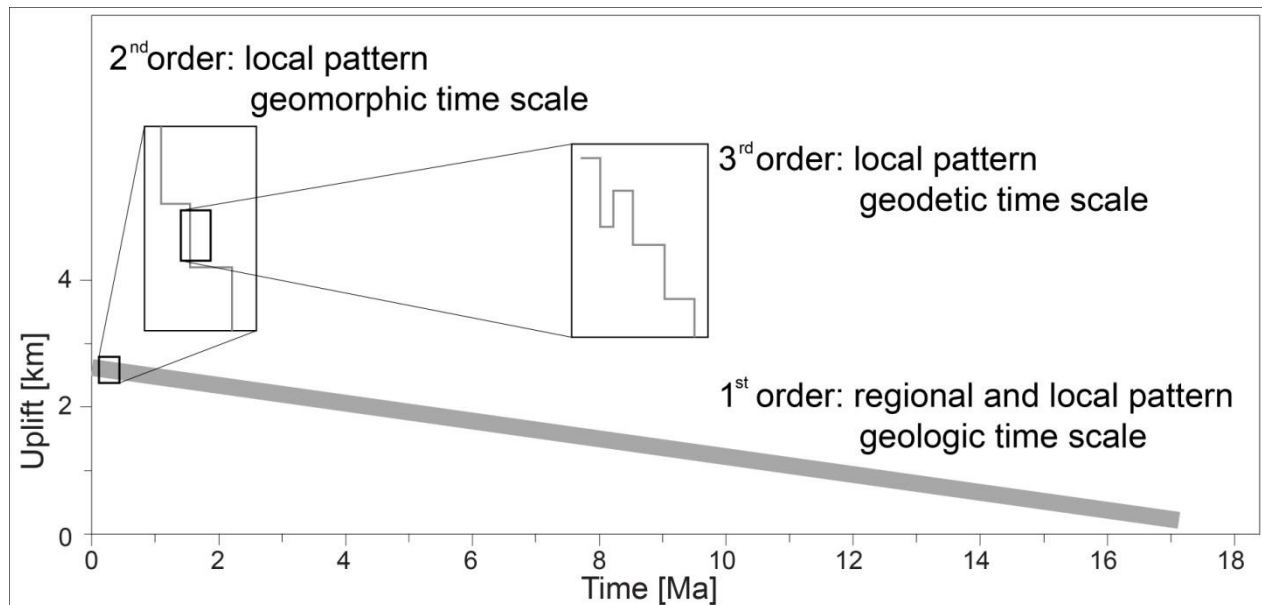


Figure 1.5: Schematic diagram of vertical displacement for geological, geomorphic and geodetic data with their corresponding units modified after Friedrich et al. (2003). A) The green box is for the geological displacement in [km/Ma]. B) The blue box displays the geomorphic displacement in [m/ka]. C) The red box illustrates geodetic data in [mm/yr].

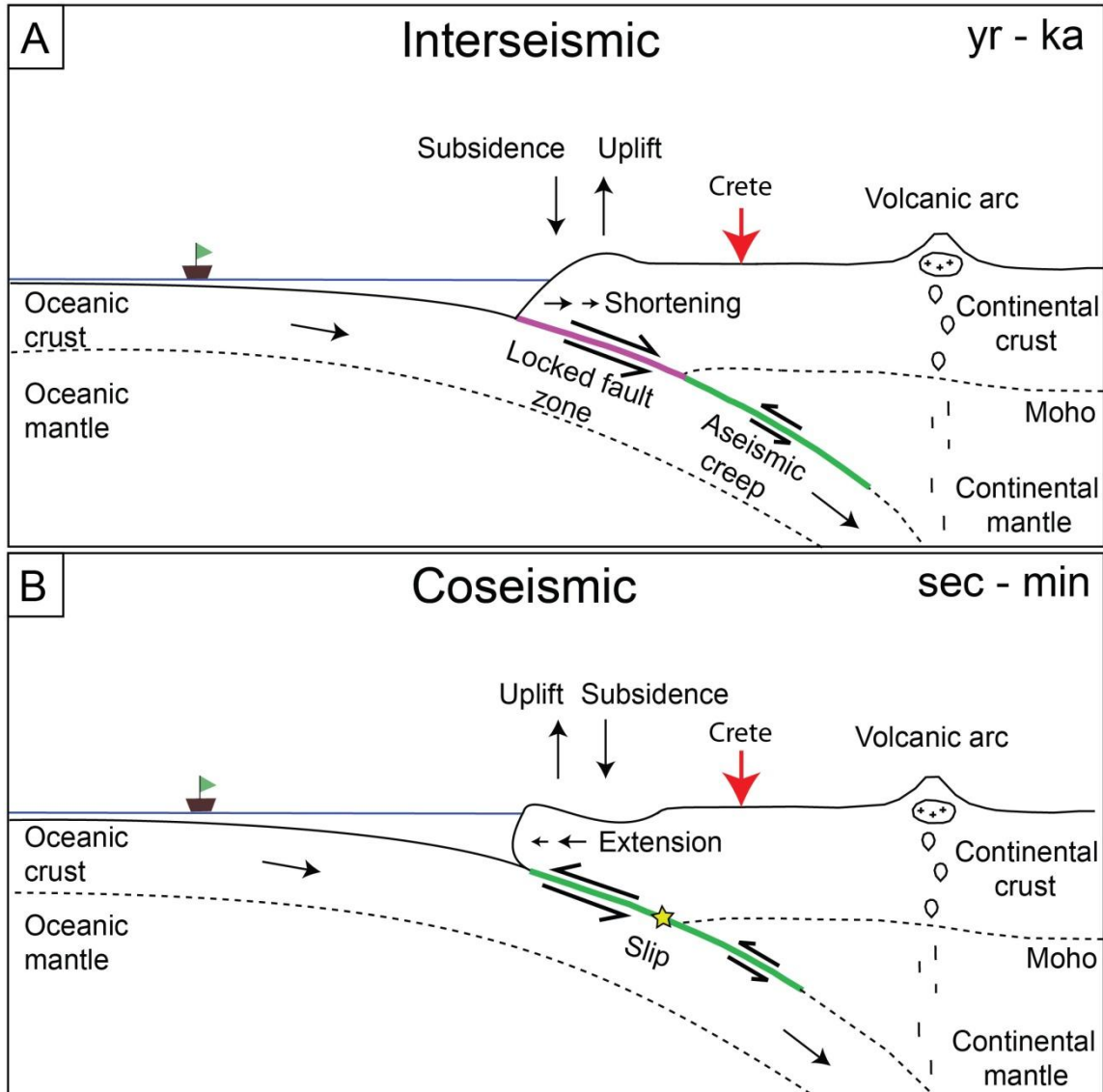


Figure 1.6: Vertical surface-deformation modified after Savage et al. (1991) and Hyndman and Wang (1993). A) The interseismic period lasting from years to thousand's of years. B) The coseismic moment lasting sec's to min's.

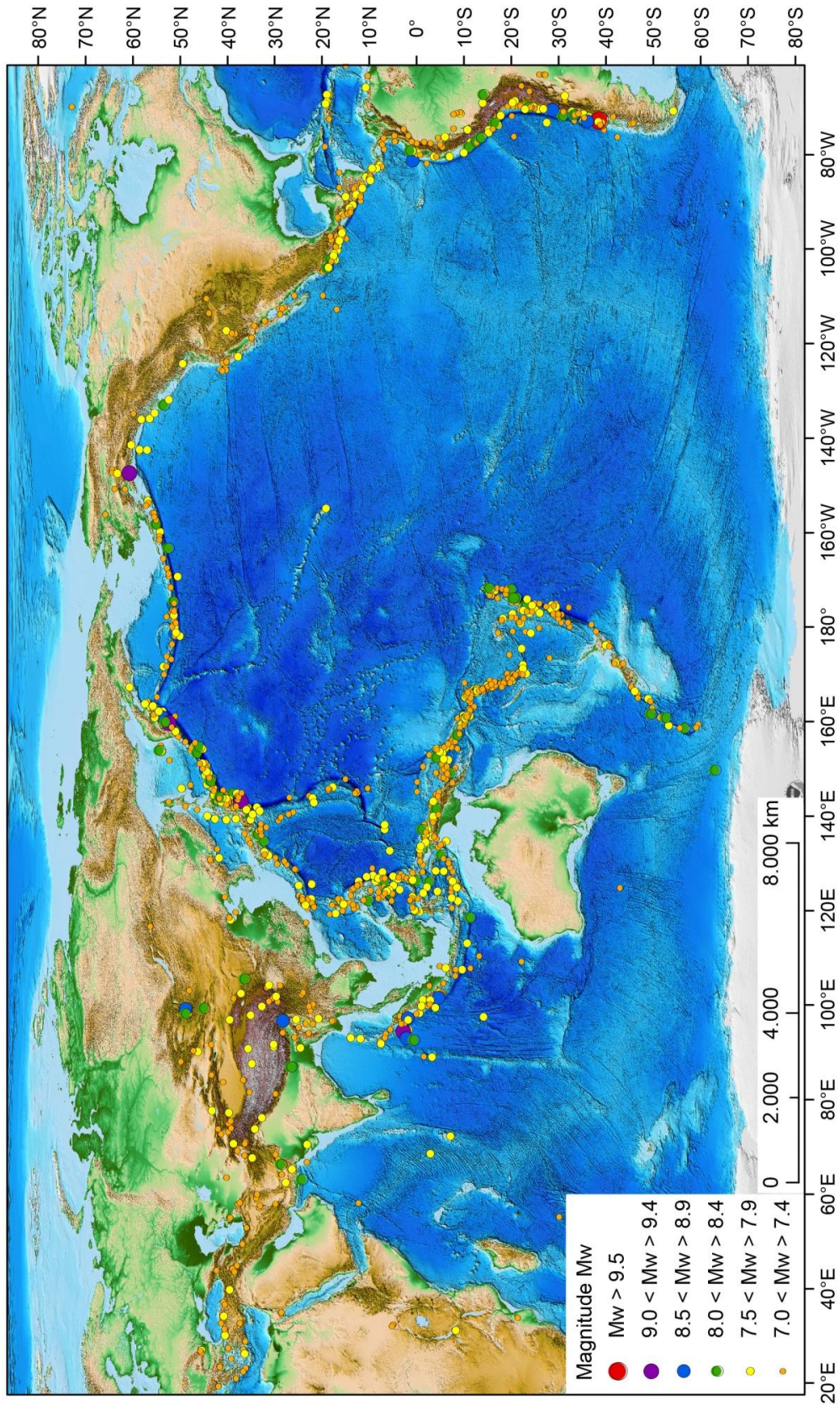


Figure 1.7: Distribution of $M_w > 7.0$ earthquakes combined from different earthquake catalogues since 1900. ETOPO1 global relief map after Amante et al. (2009).

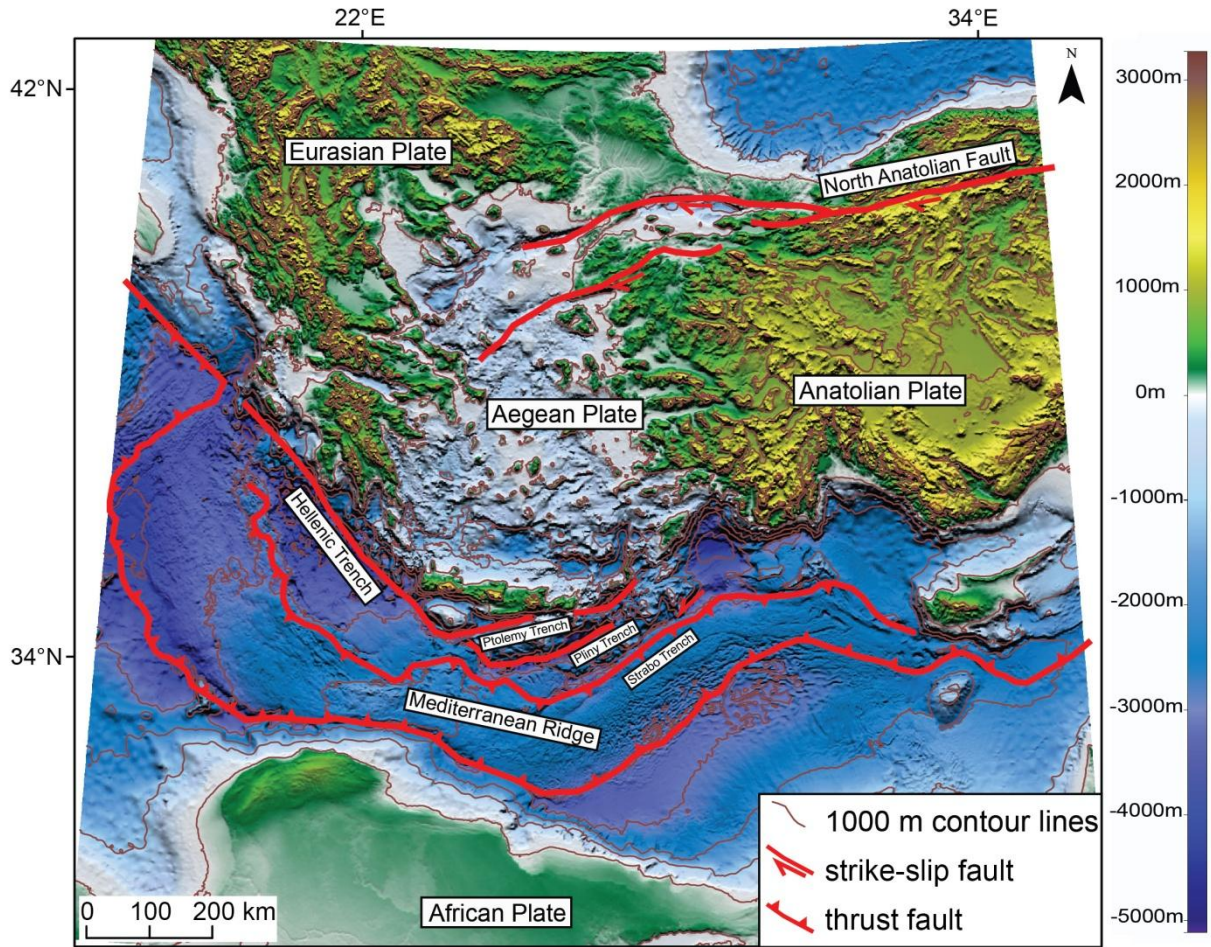


Figure 1.8: Tectonic map of the Eastern Mediterranean after Chamot-Rooke et al. (2005). Background topography is derived from data of Smith and Sandwell (1997).

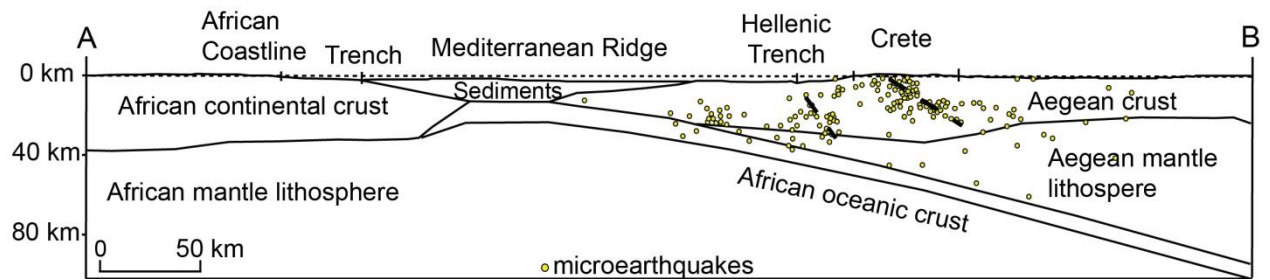
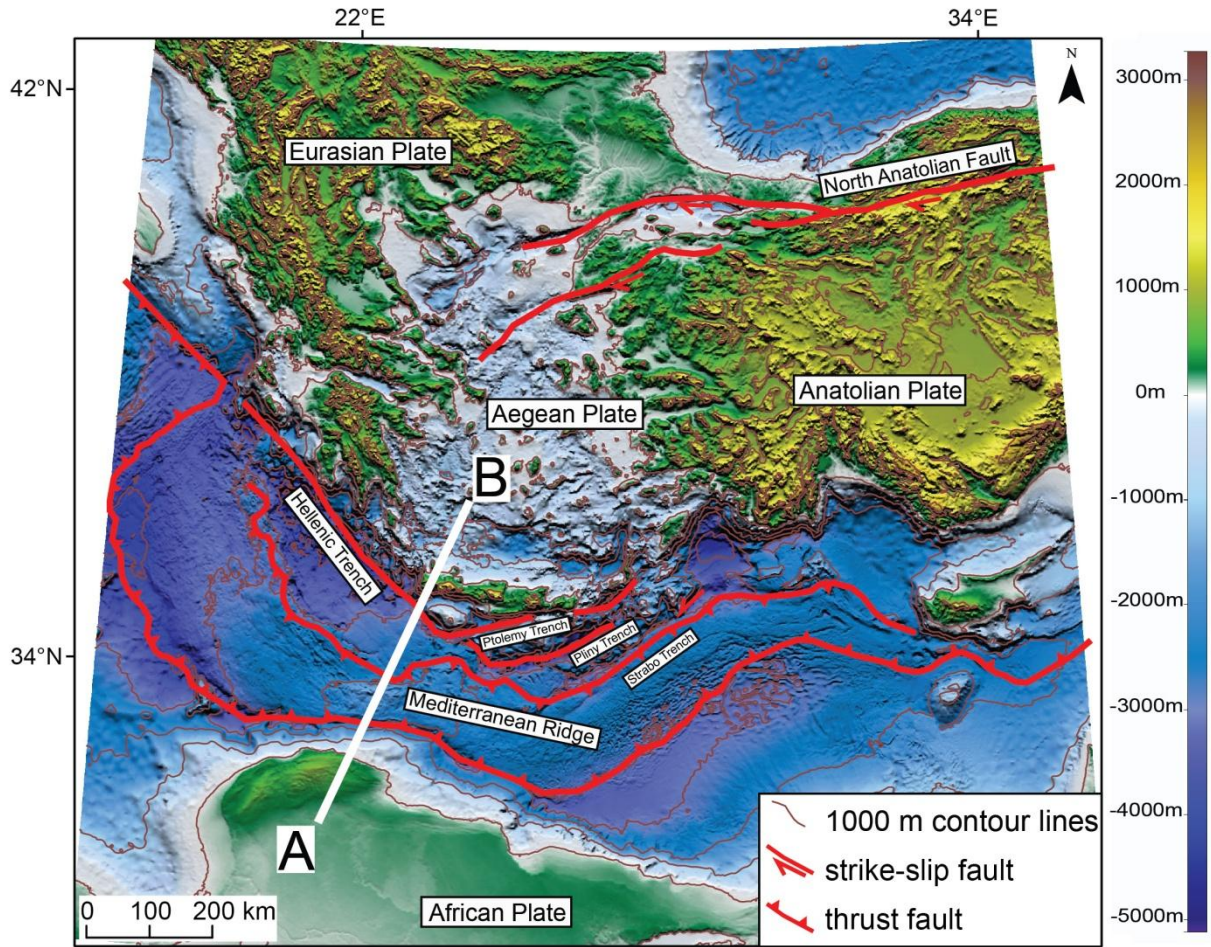


Figure 1.9: Tectonic map and profile line. Tectonic map of the Eastern Mediterranean after Chamot-Rooke et al. (2005). Background topography is derived from data of Smith and Sandwell (1997). Profile is derived by data of microseismicity (Meier et al., 2004).

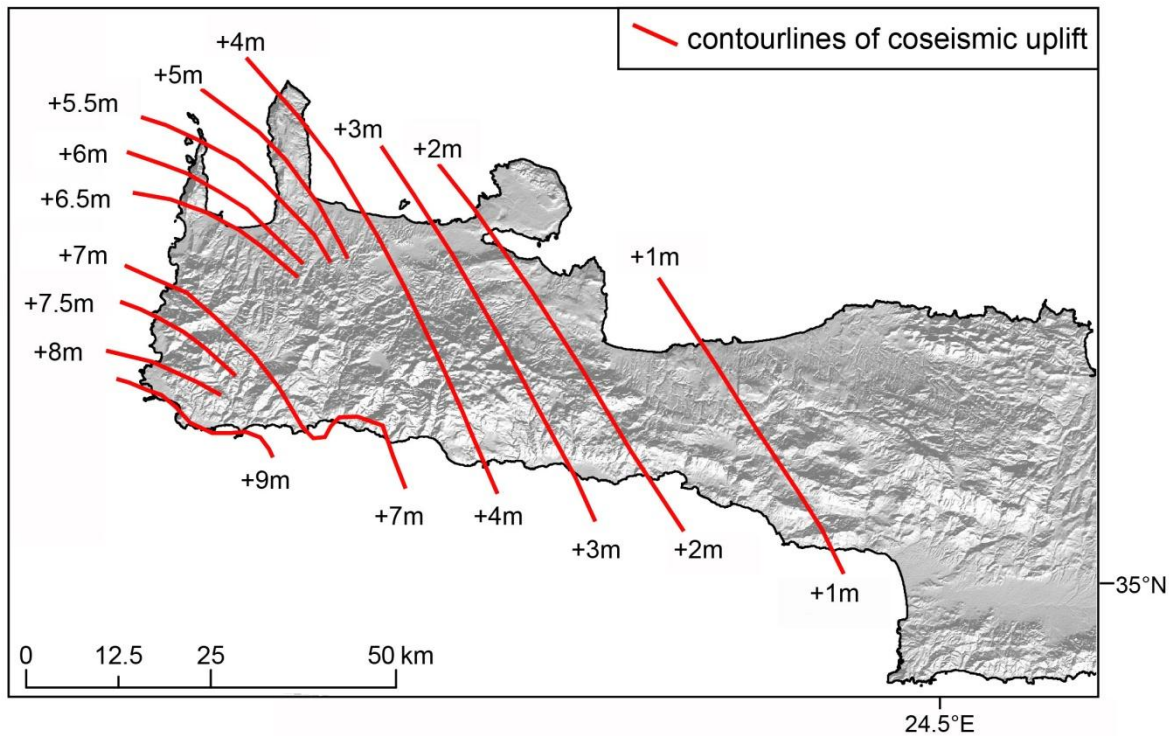


Figure 1.10: Values of coseismic uplift for W-Crete modified after Pirazzoli et al. (1996). Hill slope map generated from the Satellite Pour l'Observation de la Terre (SPOT) Digital Elevation Model (DEM). DEM derived from SPOT images with 20 m horizontal-resolution and vertical-resolution of 15 ± 5 m.

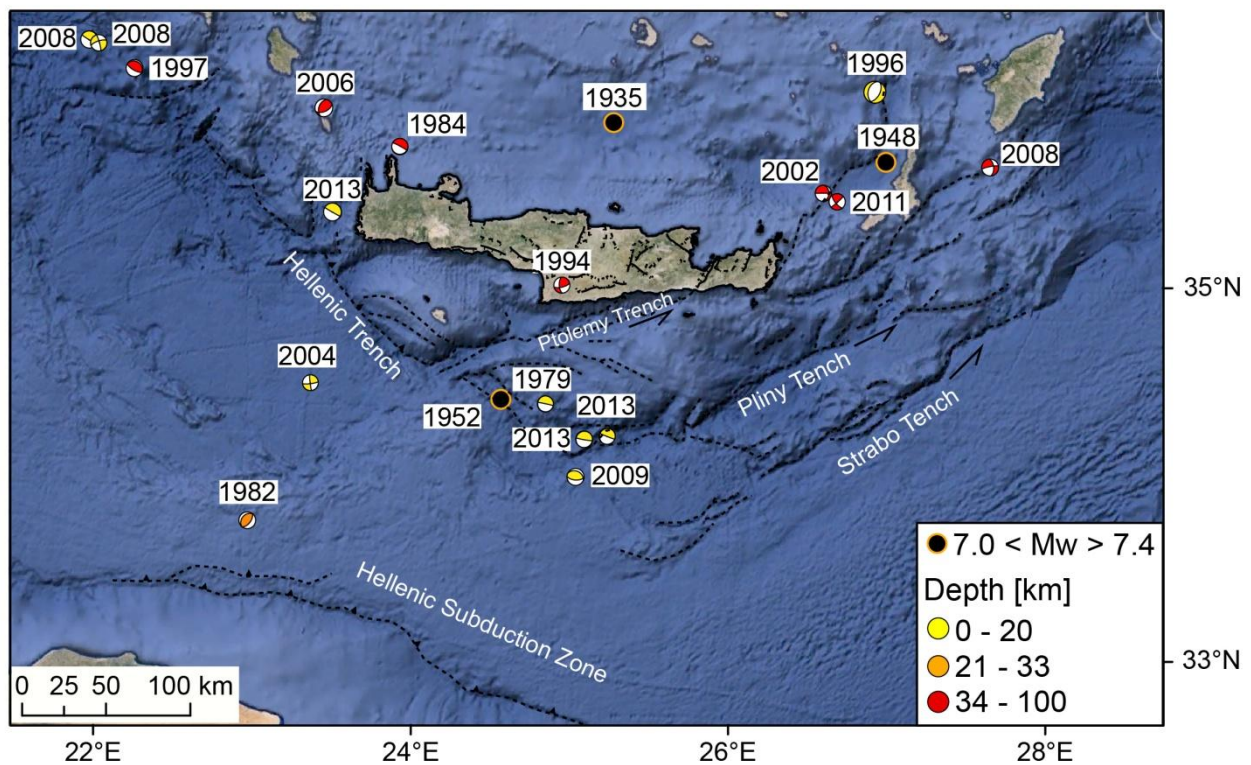


Figure 1.11: Distribution of instrumental recorded earthquakes near Crete between $7.0 < M_w < 7.4$ from 1900 until 1999 after Papazachos et al. (2000). GCMT recorded earthquakes near Crete between $6.0 < M_w < 6.8$ from 1976 until 2015. Topography and bathymetry from Google Earth®.

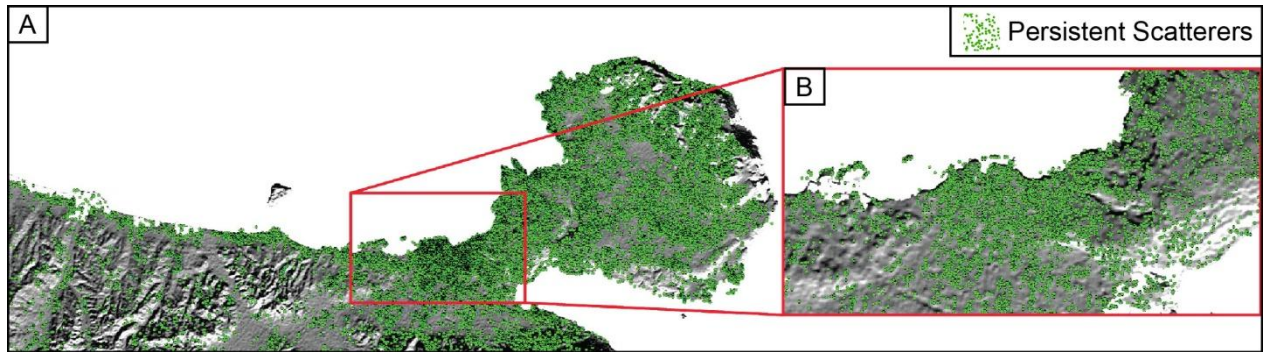


Figure 1.12: A) Persistent Scatterer distribution near the city of Chania, NW-Crete. B) Shows zoom into the urban area.

Table 1.1: Geomorphic and geologic markers.

Method	Time interval	Data	What is measured
geomorphic	millennial 10 ³ to 10 ⁶ years	river profiles paleo-shorelines coral growth	Vertical surface deformation pattern and rates
geologic	long-term 10 ⁶ to 10 ⁷ years	depositional depth of sediments	Vertical surface deformation pattern and rates

Table 1.2: Historical earthquakes affecting Crete (Abraseys et al., 1994).

Date [A.D.]	Main area affected	Damage
53.	Whole Crete and Rhodes	Extensive damage. a mountain was cleft by this event and exposing the interiors of many tombs.
62 – 64.	Crete	The earthquake caused the sea to recede about 1.3 km along the southern coastline. Travelers arriving in Chania reported of an uplifted island between Crete and Thera.
July 1 st 1494	Heraklion	Other places on the island were less affected.
May 29 th 1508	East Crete	Damage also in the southwestern extremity of Asia Minor. Was felt in Cairo.
1612	Heraklion	Damage mainly in Heraklion.
1613	Crete	Damaged buildings throughout Crete, and was felt in Cairo.
February 1629	Crete	Damaged buildings across Crete.
1662	Heraklion	Many buildings collapsed in Heraklion.
November 20 th 1664	West Crete	Damage heavily in Chania and was also felt in Egypt.
January 1 st 1681	Crete	Chania and Rethymno were seriously damaged. Heraklion was damaged by one third.
December 6 th 1779	East Crete	Easternmost part of Crete almost totally destroyed. Damaged buildings throughout the island.
July 3 rd 1805	West Crete	Western Crete was extensively damaged.
February 16 th 1810	Heraklion	One third to three quarters of Heraklion were destroyed and damage was throughout the island. The earthquake was felt in the whole Eastern Mediterranean.
October 12 th 1856	East Crete	Seriously damage on Crete, particularly the eastern part of the island. Was felt throughout the whole Eastern Mediterranean, but no tsunami was triggered.

Table 1.3: GCMT list of earthquakes in the vicinity of Crete.

Date	Lat	Long	Depth [km]	M _w
1979	34.38	24.80	15	6.1
1982	33.70	22.90	23	6.3
1984	35.74	23.80	34	6.2
1994	35.02	24.89	81	6.0
1996	36.07	26.92	15	6.2
1997	36.10	22.04	44	6.4
2002	35.53	26.59	90	6.1
2004	34.45	23.27	12	6.0
2006	35.93	23.29	64	6.7
2008	36.29	21.67	15	6.5
2008	36.24	21.73	18	6.2
2008	36.24	21.79	20	6.8
2008	36.98	22.87	92	6.2
2009	34.00	25.50	12	6.4
2011	35.49	26.67	76	6.1
2013	34.20	25.06	12	6.3
2013	35.37	23.37	15	6.8
2013	34.22	25.19	20	6.1

Chapter 2

ACTIVE VERTICAL SURFACE-DEFORMATION PATTERN OF CRETE USING PERSISTENT SCATTERER INTERFEROMETRY (PSI)

2.1 Abstract

Detection of the vertical deformation pattern of the Earth's surface permits to understand subsurface active tectonic-processes. Geodetic measurements provide invaluable information on the accumulation and release of strain along seismically active plate boundaries and upper-crustal faults. Until now, knowledge of present-day deformation patterns along plate boundaries are mainly based on Global Positioning System (GPS) horizontal measurements. Here, I present the first Persistent Scatterer Interferometry (PSI) study on a regional scale to determine the vertical surface-deformation pattern across Crete, with mm-accuracy for a time-span of eight years. The detected PSI signal shows two main regions with strong vertical surface-deformation. The highest uplift of 5 mm/yr is detected southwestern Crete, which coincides with the region affected by the 365 A.D. earthquake. I interpret the vertical surface motion as the result of aseismic creep along the Hellenic Trench. The highest subsidence (-5 mm/yr) is detected in eastern Crete, which constitutes the prolongation of the offshore depression of the Ptolemy Trench. My analysis of the vertical surface-deformation pattern suggest that processes along major faults in the overriding plate control the vertical surface-deformation rather than processes along the Hellenic subduction zone.

2.2 Introduction

The quantification of the vertical surface-deformation pattern is essential to identify, analyse and interpret active subsurface tectonic processes, especially along subduction zones. The island of Crete represents a forearc high exposed subaerially above the Hellenic subduction zone in the Eastern Mediterranean (Figure 2.1). Subduction zones are complex plate boundaries where different faults systems are superimposed. Earthquakes cannot only be generated along the main plate interface of the subduction zone but also along upper crustal faults. Space geodetic measurements provide invaluable information to understand subsurface active tectonic-processes along these different fault systems.

I detect the vertical surface-deformation pattern using the geodetic approach Persistent Scatterer Interferometry (PSI), which is a powerful tool for the spatiotemporal detection of the Earth's surface-deformation by combining multiple SAR (Synthetic Aperture Radar) images acquired over time. PSI enables to measure vertical surface-deformation pattern where conventional InSAR (Interferometric SAR) fails. InSAR measurements are based on the phase shift between different acquisitions of Synthetic Aperture Radar (SAR) images to determine the displacement of the Earth's surface (e.g. Massonnet and Feigl, 1998; Bürgmann, 2000). Several InSAR studies illustrate the coseismic displacement along the Chilean subduction zone (e.g. Chlieh et al., 2004; Ryder et al., 2012; Shirzaei et al., 2012). However, conventional InSAR studies are restricted to short acquisition time-intervals to maintain interferometric phase-stability, due to temporal decorrelations, and atmospheric inhomogeneities (Zebker and Villasenor, 1992; Hanssen, 2001). With conventional InSAR algorithms, long acquisition time-intervals of the vertical surface-deformation pattern are impossible. To resolve these InSAR limitations, the PSI method has been developed (Ferretti et al., 2001). PSI uses the persistent

scatterers (PSs) which are characterized by a high signal-to-clutter-ratio (SCR) and a long-time stable backscattering behaviour (Ferretti et al., 2001). This is the reason, the amplitude information in SAR images is used to identify these phase-stable point scatterers. The temporal analysis of the differential phases is thus restricted to the PSs and can be analysed in a series of SAR images. While originally developed for urban areas and rocky terrains (Ferretti et al., 1999; Ferretti et al., 2001), recent algorithmic developments allow the processing of non-urban and even mountainous areas (Adam et al., 2011). In urban and rocky areas, the PS density is sufficient (~ 100 PSs per km^2) to correct for effects of the atmosphere and to achieve deformation measurements with mm-accuracy. This is accomplished by the relative estimation of PSs located close to each other (Adam et al., 2004). In non-urban regions, the PS density decreases significantly due to the lack of man-made structures and rocks, which makes phase unwrapping difficult, and isolated measurement cluster result (Adam et al., 2011). Therefore, the spatial error propagation needs to be minimized in non-urban and mountainous regions (Adam et al., 2011). Mountainous regions are difficult to process with interferometry, due to geometric distortion, such as foreshortening, layover, and radar shadow. In the course of the TerraFirma project, the PSI-GENESIS system was enhanced for wide areas processing (WAP) at the German Aerospace Center (DLR) (Adam et al., 2011). It copes with spatial error propagation caused by rare availability of PSs, the spatially varying PS density, the reduced PS phase stability and allows monitoring the vertical surface-deformation pattern on wide areas of 100×100 km including mountainous regions (Adam et al., 2011).

In this chapter, I present the first PSI analysis concerning the vertical surface-deformation pattern on Crete. The PSI analysis provides data of the vertical surface-deformation pattern for a time range of eight years across the whole island. The PSI spatially-dense measurements are calibrated with point-wise continuous GPS observations, to convert the relative PSI measurements of each separate track into absolute measurements. Therefore the PSI measurements are transformed in the GPS reference frame. After the calibration, PSI measurements of individual tracks are comparable with each other and thus facilitate the geological interpretation of the geodetic data over wide areas. The detection of vertical surface-deformation pattern permits the investigation of active tectonic-processes connected with the subduction zone and related structures in the overriding plate.

I examine whether the geodetic pattern correlates with upper crustal faults distributed across Crete and if the PS distribution depends on the distribution of lithologies on Crete. I further evaluate the detected PSI surface-deformation in context with published theories on the uplift of Crete in general. The detected vertical surface-deformation pattern permits the investigation of active tectonic-processes connected with the subduction zone and related structures in the overriding plate.

2.3 Geological Setting

Offshore Crete is characterized by the Hellenic Trench system (Figure 2.1), dominated by morphologic deep-sea depressions in the overriding Aegean microplate, that are filled with sediments (Bohnhoff et al., 2001). The word ‘trench’ is misleading, because these structures are upper crustal faults, and do not represent the main subduction trench, as labeled on other subduction zones worldwide. The Hellenic Trench system consists of the Hellenic Trench, a major NE-dipping reverse fault located 25 km SW of Crete (Bohnhoff et al., 2001; Shaw et al., 2008). The Ptolemy, Pliny, and Strabo trenches are arranged en echelon and represent

transensional strike-slip faults with sinistral sense (Le Pichon and Angelier, 1979; Le Pichon et al., 1995; Becker et al., 2010) located in the S and E of the island (Figure 2.1).

The island is characterized by its horst and graben structures bounded by active normal faults. Horsts are of pre-Neogene age, represented by metamorphosed and unmetamorphosed nappes (Jolivet et al., 1996; Thomson et al., 1998), whereas the grabens are filled with Neogene and recent sediments (Hall et al., 1984; van Hinsbergen and Meulenkamp, 2006). The horst and graben structures, and the resulting formation of the complex mosaic of fault blocks, is the result of an extensional stress regime, and the change of it in the late Pliocene (Angelier, 1979; Meulenkamp et al., 1988; Armijo et al., 1992). The first extensional stress regime had a N-S orientation creating E-W normal faults on the island. This changed to an E-W extensional stress regime leading to N-S normal faults (Angelier, 1979; Armijo et al., 1992).

2.4 Tectonic Geodesy of Crete

The first geodetic study for the Eastern Mediterranean was based on GPS data from 1988 to 1997 (Figure 2.2), showing convergent motion of 36 ± 2 mm/yr between the Aegean microplate and the African plate relative to stable Eurasia (McClusky et al., 2000). The Aegean microplate is moving south-westward relative to Eurasia with 30 ± 2 mm/yr, and the African plate is moving towards the north with 6 ± 2 mm/yr relative to stable Europe (McClusky et al., 2000).

Two vertical and two horizontal velocities are available for Crete based on GPS measurements from 1993 to 2003 (Hollenstein et al., 2008). TUC1 moves with 30.73 ± 0.28 mm/yr and has a vertical component of -2.8 ± 0.4 mm/yr, and ANYA moves with 32.84 ± 1.63 mm/yr towards the SW and has a vertical component of -4.7 ± 3.7 mm/yr (Hollenstein et al., 2008). Horizontal velocities are measured with respect to stable Europe (Hollenstein et al., 2008).

One vertical GPS measurement exists for TUC2 with 0.85 ± 0.18 mm/yr, and one additional GPS vertical measurement exists on the island of Gavdos, located S of Crete, with 1.42 ± 0.21 mm/yr (Serpelloni et al., 2013).

Recent GPS analysis conclude that the convergence of the Hellenic subduction zone is mostly aseismic, suggesting low coupling along the main plate interface on the order of 0.1 to 0.2 (Reilinger et al., 2010; Vernant et al., 2014). Further, the Hellenic Trench is also assumed to have low coupling of less than 0.2 based on GPS estimates (Vernant et al., 2014).

2.5 Methods

In the first step I processed horizontal and vertical GPS measurements across Crete. In the second step I processed PSI estimates across the island. In the last step I compared my GPS and PSI measurements.

2.5.1 Global Positioning System Processing

Precise GPS records for Crete were downloaded from the EUREF Permanent Network (EPN) (Bruyninx, 2004) and the National Observatory of Athens permanent GPS network (NOANET) (Ganas et al., 2013). GPS station locations are shown in Figure 2.3. The time spans of the continuous measurements range between 2 to 9 years, from 2004 until 2013 (Table 2.1). I

processed all data using the GPS software package GAMIT/GLOBK 10.40 (Herring et al., 2010). For processing, the International Terrestrial Reference Frame (ITRF) 2008 (Altamimi et al., 2011) was used. For precise orbits of satellites, I used the International Global Navigation Satellite System (GNSS) Service (IGS) (Dow et al., 2009). In the first step I processed the daily position estimates of all GPS sites using GAMIT (Herring et al., 2010). In the second step, I generated time series, and estimated position and velocities based on the daily solution using GLOBK (Herring et al., 2010), from observations ranging from September 2004 until August 2013. I defined ‘Stable Europe’ as reference frame based on 10 selected EPN stations (ANKR, BUCU, GRAZ, ISTA, MAT1, ORID, POTS, SOFI, WTZR, ZIMM).

2.5.2 Persistent Scatterer Interferometry Processing

The PSI measurements are based on data from European Space Agency (ESA) European Remote Sensing Satellites (ERS-1/2). The time span for the acquisition ranges from June 1992 to January 2000. Crete is covered by four descending and four ascending tracks of the ERS-1/2 satellites (Figure 2.3). I have processed four descending tracks (from W to E: No. 193, No. 422, No. 150, and No. 379) independently using the wide area package of the PSI-GENESIS system (Adam et al., 2011). I tried to process the ascending tracks covering Crete, but due to the limited number of available satellite images, PSI processing was not possible.

2.5.2.1 Persistent Scatterer Interferometry Error Propagation

PSI error propagation is required because of increased phase noise, uncompensated atmosphere and non-linear motion of the PSs. In urban and rocky regions, misdetected PSs and estimation outliers can easily be detected and compensated by neighbouring PSs. A typical measurement precision depends on the number of scenes (N) and the practical lower bound of the estimation precision (σ_{PSI}) [mm/yr] is found to be (Adam et al., 2009):

$$\sigma_{PSI}(N) = \frac{1.3}{\sqrt{N}} \quad (2.1)$$

This equation (2.1) is valid for an ideal scatterer only. An ideal scatterer has a coherence equal to one, i.e. a signal-to-clutter-ratio (SCR) of infinity, and linear deformation, which can be approximated in a test area with a high amount of PSs and moderate deformation (Adam et al., 2009).

The expected estimation-precision (σ_{defo}) [mm/yr] for the four tracks on Crete needs to be estimated from the atmosphere standard-deviation (σ_{APS}), the number of interferograms (N), and the covered time range (ΔT) (Adam et al., 2009):

$$\sigma_{defo} = \frac{\sigma_{APS} * \sqrt{12}}{\sqrt{N} * \Delta T} \quad (2.2)$$

The atmosphere standard-deviation is: $\sigma_{APS} \sim 1$ rad (Rocca, 2004), the number of interferograms (N) is listed in Table 2.2, and the covered time ΔT range from 1992 until 2000. As a consequence the expected estimation-precision (σ_{defo}) ranges between 0.7 and 0.9 mm/yr (Table 2.2) for the four tracks on Crete (Figure 2.3).

2.5.2.2 Atmosphere Effect Compensation

Atmosphere stratification in mountainous regions introduces an additional signal component, which needs to be considered. This temporal noise can even make the interpretation

of PSI impossible (Adam et al., 2011). Therefore, the WAP algorithm includes the mitigation of tropospheric effects by the inclusion of a numerical weather prediction model, the Weather Research and Forecasting Model (WRF) (Done et al., 2004). The WRF is used to estimate the temperature, the partial water vapor pressure and the total pressure (Adam et al., 2011). These parameters are then converted into an atmospheric refractivity to mitigate the influences of atmospheric effects (Adam et al., 2011).

2.5.2.3 Orbital Uncertainty Compensation

In order to compensate uncertainties caused by the orbital errors, the data are calibrated using GPS measurements. Orbital errors result from small shifts in the orbital trajectories (Massonnet and Feigl, 1998). For the ERS satellites the orbital uncertainties are estimated to be less than 1.5 mm/yr 100 km⁻¹ (Fattahi and Amelung, 2014). Further, in this processing step, the relative PSI measurement is converted into an absolute GPS reference frame. PSI measurements of individual tracks are comparable to each other and thus facilitate the geological interpretation of the geodetic data across wide areas. The principle of the GPS calibration is visualized in Figure 2.4. In the test site, PSs are given by chance at locations not coincident with the GPS locations (Figure 2.5). Because of orbit uncertainties, and the relative measurement, the tilt of the PS measurements the PSI plane is unknown (Figure 2.4).

Practically, the PSI velocity measurement v_{LOS}^{PSI} is composed of three different components plus the unknown offset v_{rel} , which is eliminated in the course of the GPS calibration (Figure 2.4).

$$v_{LOS}^{PSI} = v_{north}^{PSI} + v_{east}^{PSI} + v_{up}^{PSI} + v_{rel} \quad (2.3)$$

The goal of the GPS calibration is to make the PSI deformation compatible with the GPS measurements. Based on the SAR observation principle, the three components of the GPS motion vector is projected into the LOS (Figure 2.6). The respective factors a, b, and c, are derived from the observation geometry, with a = -0.075, b = 0.3311, and c = 0.9405 (Figure 2.6)

$$v_{LOS}^{GPS} = a * v_{north}^{GPS} + b * v_{east}^{GPS} + c * v_{up}^{GPS} \quad (2.4)$$

First, the absolute GPS velocity needs to be interpolated for all PS locations, which is achieved by interpolated GPS-planes. With four GPS stations, the absolute deformation can be modeled by planes in each deformation component (v_{north} , v_{east} , v_{up}) (Figure 2.4 & Figure 2.6).

Radar satellites, such as ERS, have a near-polar orbit and they are side-looking. Due to the nearly N flight-direction (208° - descending tracks) (Figure 2.6 & Figure 2.7), the horizontal motion in the N to S direction v_{north}^{PSI} (azimuth) is projected imperceptibly onto the v_{LOS}^{PSI} , and can be neglected (a = -0.075).

In order to relate the PSI measurements into the reference frame of the GPS measurements, the relevant GPS measurements are projected into the PSI LOS direction. With the assumptions above, equation 2.3 transforms into

$$v_{LOS}^{PSI} = b * v_{east}^{GPS} + c * v_{up}^{GPS} + v_{rel} \quad (2.5)$$

which is solved for the calibration offset v_{rel} (Figure 2.4):

$$v_{rel} = v_{LOS}^{PSI} - b * v_{east}^{GPS} - c * v_{up}^{GPS} \quad (2.6)$$

In the next processing step, the respective v_{rel} is subtracted from each v_{LOS}^{PSI} .

The error propagation of the absolute GPS calibration is:

$$\sigma_{LOS} = \sqrt{a^2 * \sigma_{north}^2 + b^2 * \sigma_{east}^2 + c^2 * \sigma_{up}^2} \quad (2.7)$$

with the north component $a = -0.075$, the east component $b = 0.331$, and vertical component $c = 0.940$ for ERS descending tracks (Figure 2.6).

Finally, the GPS signal is used for the compensation of the expected east motion component, which transforms into the LOS with $b = 0.331$ (Figure 2.6), in order to achieve only the vertical deformation. Figure 2.8 shows the uncalibrated PS measurements versus the GPS calibrated PS measurements.

2.6 Results

The GPS and PSI measurements are acquired at different times. The PSI measurements range from 1992 until 2000, while the GPS measurements represent the deformation starting 2004 until 2013 (Table 2.1). I can combine GPS and PSI observations, because the surface-deformation of Crete can be assumed to be constant. During 1992 until 2013 no large earthquakes $M_w > 5$ is recorded on Crete. Earthquake data are based on the Global Centroid Moment Tensor Catalogue (Table 1.2).

2.6.1 Results of Global Positioning System Measurements

GPS results of the five EUREF/NOA sites on Crete (TUC2, RETH, HERA, NEAP, and IERA) are listed in Table 2.3. The horizontal velocities of the GPS stations are shown in Figure 2.10, and their corresponding vertical component are listed in Table 2.1. All five GPS measurements show a relative horizontal motion towards SW with respect to stable Europe. The time span of GPS measurements ranges from 1.6 to 8.9 yrs (Table 2.1). IERA moves with 31.31 ± 0.88 mm/yr, RETH has a velocity of 4.27 ± 8.69 mm/yr; HERA has a velocity of 30.24 ± 0.92 mm/yr, NEAP moves with 36.07 ± 0.83 , and TUC 2 moves with 27.66 ± 0.14 mm/yr (Table 2.3).

GPS measurements by Hollenstein et al. (2008) are not included, because the GPS station ANYA was occupied for 1.1 years as campaign station and not operated as continuous GPS station. The error at this station is > 3 mm/yr (Hollenstein et al., 2008). GPS measurements by Serpelloni et al. (2013) were also not included in this study, because TUC2 is uplifting, whereas TUC1 is subsiding in the study of Hollenstein et al. (2008), and I also measure subsidence for TUC2 (Table 2.3).

2.6.2 Results of Persistent Scatterer Interferometry Measurements

The PSI relative estimates are calibrated using GPS observations of the EUREF/NOA sites measurements with respect to Eurasia (Figure 2.9 & Table 2.1). For the calibration only four GPS sites are used (TUC2, HERA, NEAP, and IERA), because RETH was excluded due to the large error propagation at this station. The absolute calibration was performed using the GPS station TUC2 as reference station for Crete, therefore all PS deformation rates are relative to TUC2. The ill-posed distribution of GPS stations on Crete (Figure 2.2) lead to GPS calibration uncertainties of the GPS reference-plane of up to 9 mm/yr along the southern coastline (Figure 2.10). The GPS reference-plane uncertainty does not influence the PSI deformation precisions, because PSs are only projected onto the reference-plane.

The detected geodetic signal ranges from 5 mm/yr of subsidence to 5 mm/yr of uplift across Crete (Figure 2.11). The PSs are not distributed homogeneously across the island. The

lowest number of PSs is found in the Heraklion and Messara basins, and along the southern coast of the Dikti mountains, and S of the Spili fault (Figure 2.14). Small patches where no PSs measurements are heterogeneously distributed across the island. Other regions have a denser distribution of PS measurements.

Based on the PSI measurements I created a simplified map, to illustrate the measured PSI vertical surface-deformation (Figure 2.12). I can subdivide the island into individual zones of uplift and subsidence depending on the color pattern (Figure 2.11 & Figure 2.12). The western part of Crete is dominated by uplift on the order of up to 5 mm/yr, whereas the eastern part is dominated by subsidence ranging between 0 to -5mm/yr (Figure 2.11).

The simplified map (Figure 2.12) visualizes the strong uplift of the SW corner of Crete, and the decrease of the signal towards the northern coastline of Crete. The uplift signal along the southern coastline reaches as far as the western part of the Asteroussia Mountains in Central Crete. Along northern coastline of W-Crete no significant vertical deformation is obvious until the Psiloritis Mountains.

Central Crete is characterized by the uplift along the northern coastline. The southern coastline shows uplift, whereas the middle part of Central Crete is relative stable with zero deformation.

Eastern Crete is dominated by two bifurcating regions of strong subsidence.

The Heraklion and Massara basins have the least amount of PSs measurements. Along the northern coastline of the Heraklion basin I have a high PSs density, due to the urban area.

2.7 Analysis of Persistent Scatterer Interferometry Measurements

I compare my PSI measurements with the topography derived from the Satellite Pour l'Observation de la Terre - Digital Elevation Model (SPOT-DEM) (horizontal-resolution of 20 m, vertical-resolution of 15 ± 5 m) of Crete (Figure 2.13). If Crete represents a simple landscape, meaning that it is the result of a single set of tectonic processes, then I would expect a perfect correlation between the PSI measurements and the highest topography. But I can clearly see that this is not the case for Crete. The region of strongest uplift does not coincide with the highest elevations on Crete, and regions of low relief do not automatically coincide with PSI measurements of subsidence. Because of the discrepancy between the PSI measurements and topography, I can interpret the vertical surface-deformation measured by PSI to be representing the signal of a complex landscape, where past boundary conditions are inherited.

Further, I compare my PS measurements with the distribution of faults I have mapped on the SPOT-DEM of Crete (Figure 2.14 & Figure 2.15).

The SW corner is dominated by strong vertical uplift, along this area I mapped two possible normal faults based on the morphologic expression (Figure 2.16). But the location of the possible normal faults and the change in color from red to yellow does not coincide. Therefore, no clear pattern is visible indicating that these two possible normal faults are linked to the strong geodetic signal. Further, the two faults are interpreted to be normal faults, with the footwall towards the N and E, respectively, and the hanging wall towards the S and W, respectively. From the analysis of the geomorphology and topography these faults cannot be explained as reverse faults. Therefore, the signal is not based on these two normal faults.

The central part of W-Crete shows a decrease of vertical uplift based on the PSs measurements, in this region I cannot find clear pattern of faults in the geomorphology.

The northern part and the coastline of W-Crete towards the E (Figure 2.17) shows no real variations in its vertical signal. The overall vertical motion in this area is more or less equal to zero.

Several normal faults are located in this area. Along the RF fault the PSI measurements do not coincide with the vertical motion of a normal fault. Further towards the E, a possible normal fault striking in E-W direction is mapped based on the geomorphology. But here the PSs measurements are reverse as along the RF fault.

The other mapped normal faults show no clear pattern depending on these faults.

The southern coastline of W-Crete is dominated by uplift located close to the Sfakia (SfF), Asomatos (AF), and the Spili fault (SpF) (Figure 2.18). Along the SpF the western and eastern branch of the fault coincide quite well with PSs measurements, but the PSs measurements indicate a reverse fault. But the geomorphologic analysis indicates a normal fault. The same applies for the AF and the SpF. Branches of these faults also match quite well the PSs measurements, but based on PSs measurements these faults should be reverse faults, and the geomorphological mapping indicates normal faults.

East of the faults PSs measurements indicate an area of subsidence, which coincides well with the AGF fault and the location of the small graben N of the Messara Basin. In this area the sense of the PSs measurements with the topography coincide quite well.

Along the southern coastline of Central Crete the Asteroussia Mountains PSs measurements show vertical uplift along the western part and decrease of this uplift towards the eastern part. The geomorphological investigation of this area does not show any significant faults in this area.

North of the Psiloritis Mountains the area is dominated by subsidence on the order of 3 mm/yr, this area of subsidence coincides with the hanging wall of a possible reverse fault. PSs measurements in this region coincide quite well with the location of this possible reverse fault. But based on the geomorphology there is no clear sign for a normal fault explaining the PSI signal. The findings of my geomorphological study and the PSI results indicate the hanging wall of the reverse fault to be subsiding with respect to the footwall. This may indicate a transient signal on the fault.

The central part of Crete is relatively stable, and along the basins I do not detect many PSs due to agricultural usage in this area and decorrelation of the agricultural areas (Figure 2.19).

The northern part of the Heraklion basin shows uplift and a dense pattern of PSs. The high amount of PSs can be explained by urbanization. Based on the geomorphology I cannot detect any possible clear fault in this region explaining the uplift. The PSs measurements along the NW part of the Heraklion basin coincides perfectly well with the little fault branch mapped on the topographic map, the Eastern Psiloritis Fault Zone (EPEZ). E of Heraklion basin PSs measurements indicate further uplift along the northern coastline. From mapping of the geomorphology in this region I cannot see clear indications of reverse faults.

The eastern part of the island is dominated by subsidence along two linear bifurcating structures ranging from ENE- WSW, and EEN-SSW.

Along the Dikit Mountains I also do not find many PSs. The northern part of the Dikit Mountains is characterized by strong subsidence ranging in ENE-SWS direction, and towards this region is parallel by a further lineation of subsidence. Between these two lineation of subsidence I mapped a small possible normal fault, but the sense of motion does not coincide with the motion of a normal fault. Along the northern coastline a possible normal fault corresponds well with the PSs measurements, but again the sense of the motion is opposite to a normal fault.

Along the IFZ and the western boarder of the Omo Mountains the PSs measurements coincide well with the mapped fault, but the sense is opposite (Figure 2.20). Towards the E the

island is dominated by the second linear structure of subsidence in EEN-SSW direction. This PSs measurement lineation of subsidence is not obvious in the topography. Along the ZF normal fault I find a coincidence of the PSs measurements and a small branch of the mapped normal fault, but the sense is reverse. The normal fault located along the eastern coastline corresponds well with PSs measurements and the topography, but the sense is opposite.

I further mapped the topography of the ocean floor based on bathymetry data from Google Earth®. I mapped the main escarpments located W, S, and E, the Hellenic Trench system (Figure 2.21). The Hellenic Trench is mapped as major reverse fault in the overriding plate (Shaw et al., 2008). Whereas, the Ptolemy, the Pliny, and the Strabo trenches mark transtensional features in the overriding plate (Le Pichon and Angelier, 1979; Le Pichon et al., 1995). The most striking feature based on the bathymetry mapping and the PSI measurements is the prolongation of the Ptolemy Trench offshore and onshore (Figure 2.22).

The island of Gavdos is located S of western Crete nearly half way between the Hellenic Trench and Crete (Figure 2.23). I analyse the topography profile of Gavdos to additional distinguish if W-Crete is behaving as a rigid block. The profile line was generated by contour lines taken from Google maps. The profile of the island shows that the SSW coastline was affected by strong uplift, and the NNW part of the island has gentle slopes decreasing towards the coast. This tilt of the island can be induced from a possible normal fault located towards the SSW of the island, which is striking parallel as the uplifted coastline of Gavdos (Figure 2.24).

I processed in all four tracks on Crete a total of 421315 PSs. I analyse the number of uplifting PSs ($v_{vertical} > 0$), the number of PSs with zero deformation ($v_{vertical} = 0$), and the amount of subsiding PSs ($v_{vertical} < 0$) (Table 2.4 & Table 2.5)

I further visualize the PSI results to show uplift and subsidence (Figure 2.25). The western part of Crete is clearly dominated by PSs indicating uplift, whereas the eastern part shows the opposite. Here the highest number of PSs shows subsidence. The western Central part of Crete shows uplift, and in the eastern Central part the proportion of uplift and subsidence is balanced.

2.8 Discussion and Significance of Surface-Deformation Pattern

PSI measurements on Crete show a strong geodetic signal over a time period of eight years. PSI analysis reveals a heterogeneous vertical surface-deformation pattern on Crete over between 1992 and 2000. From this, I can infer that Crete is not moving vertically as a coherent block, but is more likely divided into several independent tectonic blocks. This suggests a combination of different tectonic processes responsible for vertical surface-deformation. Crete is a forearc high located close to the Hellenic subduction zone, where several generations of fault systems are superimposed. Possible tectonic structures responsible for the differential vertical surface-deformation pattern are: (1) the Hellenic subduction zone as first order fault system (Figure 2.1), (2) major faults in the overriding plate as second order fault system, and (3) crustal faults on Crete as third order fault system. This suggests that the island represents a fault-controlled landscape in a tectonically active region.

The inhomogeneous PSI surface deformation-pattern does not coincide with the topography of the island (Figure 2.12 & Figure 2.13). Neither, the strongest geodetic vertical uplift takes place in areas of highest elevations, nor does the strongest subsidence occur in the topographically lowest areas. Vertical surface-deformation is often linked with fault motions, but

the detected PS measurements do not always coincide with the location of the normal faults distributed on Crete (Figure 2.14 & Figure 2.15).

My PSI measurements show two main regions on the island indicating strong activity of vertical motion (Figure 2.11 & Figure 2.12). The strongest signal of vertical uplift is located along the SW coastline. Here, two suspected normal faults are located, but the uplift pattern cannot be linked to motion of these faults as it does not coincide clearly with the fault strike. The spatial distribution of vertical uplift suggests that rather a superior structure, e.g. the Hellenic Trench located close to this area (~ 25 km SW of Crete), or the Hellenic subduction zone (~ 200 km S of Crete) is responsible for the observed surface deformation.

PSI measurements show the strongest vertical uplift in the region, which experienced coseismic uplift of 9 m induced by the 365 A.D. earthquake (Pirazzoli et al., 1996). Previous studies (Shaw et al., 2008) concluded that a M_w 8.3- 8.5 earthquake along the Hellenic Trench could have caused this uplift coseismically. Data of radiocarbon ages of corals, bryozoa, and lithophaga in western Crete were modeled to fit the uplift data by a dislocation elastic half-space model (Shaw et al., 2008). Due to uncertainties of the radiocarbon ages of up to $\sim \pm 140$ yr, it cannot clearly be distinguished if the uplift was caused by slow aseismic creep along the Hellenic Trench during this time span, a series of rapid small events, or due to one single earthquake causing the historically tsunami of 365 A.D. (Shaw et al., 2008). To obtain 9 m of uplift in 140 yr, the calculated linear uplift rate would be 64.3 mm/yr, which seems to be unusually high. However, comparable strong uplift rates have been observed along the Isla Mocha, an island 30 km off the coast of south-central Chile and 90 km away from the subduction zone (Nelson et al., 1992). The island shows strong uplift of up to 73.3 mm/yr, measured by the mean-tide-level change of 1.76 ± 0.15 m between 1965 to 1989 (Nelson et al., 1992). The uplift is interpreted to be the result of aseismic creep along a thrust fault in the overriding plate (Nelson et al., 1992). But it seems more likely that the detected signal of aseismic creep along the Isla Mocha is a postseismic signal following the 1960 M_w 9.5 Valparadiso Chile earthquake (Kanamori, 1977; Barrientos et al., 1990). Maybe my detected signal of vertical motion along the SW corner of Crete represents a postseismic motion caused by the 365 A.D. earthquake. Postseismic motion is caused by viscous relaxation of the lower crust and upper mantle, which is a transient time-dependent surface deformation (Nur et al., 1974; Scholz, 1990). Pollitz (1997) modeled relaxation effects lasting up to 1000 yrs in the upper mantle for an earthquake along a 200 km long thrust fault. Postseismic deformation is characterized by its decay time, which implies strongest motion directly after the earthquake and declines with time (Scholz, 1990). Assuming a postseismic uplift rate of 5 mm/yr (PSI measurements) for 1635 years would result in an uplift of at least 8.18 m for the SW corner of Crete. As the postseismic signal is expected to decay with time after the 365 A.D. earthquake, the total postseismic uplift would most likely be higher than the calculated 8.18 m and such a strong signal should be visible in the morphology along the SW coastline. Further, the longest geodetic measurements for postseismic deformation are 36 ± 16 yrs detected in northern California following the 1906 M_w 7.9 San Francisco earthquake (Kanamori, 1977; Kenner and Segall, 2000). Therefore, postseismic relaxation explaining the strong vertical surface-deformation of up to 5 mm/yr seems to be an unrealistic scenario. The strong uplift of W-Crete is interpreted as the result of incipient continent-continent collision (Figure 2.28), between the Aegean microplate and the African continental plate (Masclé et al., 1999; Ten Veen and Kleinspehn, 2003; Bohnhoff et al., 2005). The kinematic stress regime is proposed to be active since 3.4 Ma (Ten Veen and Kleinspehn, 2003). If I assume that the PSI signal is the result of this incipient collision together with a constant uplift rate, the calculated uplift of 17 km for W-Crete for the last 3.4 Ma seems to be unrealistic. The maximum elevation reached in W-Crete is the Lefka-Ori Mountains with ~2450 m (Figure 2.13). Vertical uplift caused by the incipient

continent-collision should affect western Crete in a more homogenous surface pattern (Figure 2.26), and not only the small corner of SW Crete. To further verify this hypothesis, further seismic data are needed to assess the location of the transition between the African oceanic crust and the African continental crust.

The strong uplift of the SW corner of Crete could be interpreted as result of locking along a plate interface, either along the subduction interface (Figure 2.27) or a fault in the overriding plate, during the interseismic period, which induces vertical uplift. However, the coseismic and interseismic vertical surface-motion would be expected to show the opposite direction than the one observed, regardless of locking along the Hellenic subduction or along the Hellenic Trench. I would expect subsidence in this region, but my PSI measurements show uplift. Thus the vertical surface-deformation has the same sense for the coseismic event, as for the interseismic period. Recent GPS measurements concerning the interseismic and coseismic vertical surface-deformation along NE Japan coast showed that the M_w 9.0 Tohoku-Oki earthquake (Simons et al., 2011) induced subsidence along the coast of former interseismic subsidence (Suwa et al., 2005). GPS measurements show subsidence of 5 mm/yr from 1997-2001 (Suwa et al., 2005) in the region of Sendai, monthly tide gauge data (1951-1981) show subsidence between 5 to 10 mm/yr, and N of Sendai even 10 mm/yr of subsidence (Kato, 1983). The Tohoku-Oki earthquake leads to maximum subsidence of the coast by ~ 1 m (Ikeda, 2012; Kamiyama et al., 2012). Only along few subduction zones it is possible to compare geodetic data and longer-term data, because for most subduction zones these measurements are not available. More vertical geodetic-data are needed to understand if the conceptual model of vertical motion during the earthquake cycle is reliable.

A possible explanation for the vertical uplift is aseismic creep. Aseismic creep is a common feature along many subduction zones, e.g. along the Kyushu segment of the Nankai subduction zone, along the Manila Trench, along the Hikurangi subduction zone, along the Costa Rican subduction zone, the Peru margin, and the Sumatra-Java subduction zone (Wang et al., 2014). Shallow slow slip is expected to occur at many, if not most subduction zones (Saffer & Wallace, 2015). Earlier studies (Jackson and McKenzie, 1988; Reilinger et al., 2010; Vernant et al., 2014) have concluded that the convergence of the Hellenic subduction zone is mostly aseismically and no strain is accumulated, based on the absence of historical large earthquakes after 365 A.D. (Jackson and McKenzie, 1988) and GPS measurements (Reilinger et al., 2010; Vernant et al., 2014). GPS measurements suggest low coupling along the plate interface of the order of 0.1 to 0.2 (Reilinger et al., 2010; Vernant et al., 2014). I presume that aseismic creep along the subduction interface of the Hellenic subduction zone is not responsible for the detected vertical surface-deformation on Crete. If aseismic creep takes place along the subduction interface I would not detect any – or only very little - vertical surface deformation on Crete (Figure 2.28). This does not coincide with my PSI measurements. The localization of the strongest uplift only in the SW corner and southwestern coastline of Crete rather suggests aseismic creep along a smaller second order structure, such the Hellenic Trench. The vertical uplift signal in SW-Crete coincides with the location and the prolongation of the Hellenic Trench to depth (Figure 2.29 & Figure 2.30). I constructed a profile (Figure 2.30) based on the dip value of 30° for the Hellenic Trench from Shaw et al. (2008), and seismic data of Bohnhoff et al. (2001) and Meier et al. (2004). The profile shows that the signal on Crete corresponds with the location and prolongation of the Hellenic Trench with depth (Figure 2.30 A & B). Towards the northern coastline in W-Crete the vertical uplift changes to zero vertical uplift. I therefore conclude that my detected signal along the SW-coastline is best explained with aseismic creep along the Hellenic Trench (Figure 2.30). As mentioned above, locking is not an explanation because in this case the sense of the detected signal should be opposite to the coseismic signal,

but I detect uplift. The accordance of motion caused by aseismic creep along the major crustal faults in the overriding plate (Figure 2.30) and the detected vertical surface-deformation pattern (Figure 2.30) is striking.

PSI uplift rates of 5 mm/yr can be interpreted as aseismic creep along the Hellenic Trench. GPS estimates suggest low seismic coupling along the Hellenic Trench on the order of 0.2 (Vernant et al., 2014).

Assuming a constant uplift rate of 5 mm/yr it would take 1800 years to result in 9 m uplift. However, a constant uplift rate of 5 mm/yr seems unrealistic, because historical and recent documents should report such a strong and constant signal. My PSI measurements represent vertical surface-deformation for eight years; therefore I cannot distinguish whether my measured signal represents a transient signal or a signal on the longer time-scale.

For generating 5 mm/yr of vertical uplift a convergence of 8.7 mm/yr along the Hellenic Trench is needed – assuming a dip of $\sim 30^\circ$ of the Hellenic Trench (Shaw et al., 2008). My GPS measurements on TUC2 (Table 2.3) show a horizontal velocity of 27.7 ± 0.35 mm/yr towards the SW. These estimates suggest that the convergence for TUC2 is divided into ~ 9 mm/yr (8.7 mm/yr) along the Hellenic Trench, and 19 mm/yr along the Hellenic subduction zone.

Figure 2.32 shows the hypothetical vertical surface-deformation pattern caused by motion along the major fault system in the overriding plate.

The eastern part of Crete is dominated by two elongations of strong subsidence in NEN-SWS, and EEN-WWS direction. If I compare my findings with bathymetry data along the southern coastline of Crete, the elongations project into the Ptolemy Trench located parallel the southern coastline of Crete (Figure 2.32). The Ptolemy trench is interpreted to be a left-lateral transtensional strike-slip fault (Le Pichon and Angelier, 1979; Le Pichon et al., 1995; Becker et al., 2010). Based on focal mechanisms Bohnhoff et al. (2005) interpret the stress regime for E-Crete as left-lateral transpressional, and as continuation of the Ptolemy trench. PSI measurements do not resolve horizontal motion, but the subsidence pattern I observe onshore coincides with the expected projection of the Ptolemy trench. The NEN-SWS elongation coincides very well with the topography, whereas the second elongation (EEN-WWS) is not obvious in the topography. The elongation is obvious in my PSI findings (Figure 2.29 & Figure 2.32). My findings coincide perfectly with the faults of ten Veen and Kleinspehn (2003). They conclude that these 070° sinistral faults are the prolongation of the Ptolemy trench (which they call Eastern South Cretan Trough) (ten Veen and Kleinspehn, 2003). They conclude that these 070° faults represent the principle shear zone of the neotectonic forearc since ~ 3.4 Ma (ten Veen and Kleinspehn, 2003). The extensional dip-slip component is caused by tectonic escape caused by the incipient continent-continent collision proposed for W-Crete (ten Veen and Kleinspehn, 2003).

Vertical surface-deformation in central Crete is relatively homogenous, except a clear pattern of tilt towards the N. Uplift along the southern coastline is on the range of 1 to 3 mm/yr, whereas subsidence along the northern coastline is on the order of 3 mm/yr.

Former studies explained the vertical uplift of Crete by underthrusting of sediments (Le Pichon and Angelier, 1982; Angelier et al., 1982; Taymaz et al., 1990; Roberts et al., 2013; Gallen et al., 2014; Strobl et al., 2014). During the process of underplating sediments or crustal slices of the subducting plate are accreted to the bottom of an accretionary wedge (Platt, 1986). The accretion of sediments off the subducting plate occurs in front of the backstop of the overriding plate and the subducting plate along the plate interface (Platt, 1986). The backstop of the Hellenic subduction zone (Chamot-Rooke et al., 2005) and the plate interface of the Hellenic subduction zone are located S of Crete (Figure 2.33) (Meier et al., 2004; Becker et al., 2010). I conclude that underplating occurs beneath the Mediterranean Ridge and is not the responsible tectonic process for the uplift of Crete.

Meier et al. (2007) explained the vertical uplift of Crete caused by the existence of a subduction channel. The subduction-channel model assumes that subducted sediments behave as viscous material in the subduction channel, situated between the subducting and the overriding plate (Cloos et al., 1988 a,b). The subducted material can turn back and flow upward along the upper side of the subduction channel (Cloos et al., 1988 a,b). The return flow material spreads out below the forearc and may build up the lower Aegean lithosphere (Meier et al., 2007). If I assume the accretion of upflow material to cause the vertical surface-deformation, then the location of the accreted material should be located on Crete were I find metamorphic rocks. Figure 3.34 shows schematically the location of the return flow. This pattern does not coincide with my detected PSI signal, further this theory cannot explain the coexistence of uplift and subsidence on Crete. The same reasoning is valid for the Asthenospheric return flow postulated by Becker et al. (2010) as cause for the vertical uplift on Crete. Asthenospheric return flow should induce uplift of the island as coherent single block (Figure 2.35), which does not coincide with the PSI measurements.

Our detected vertical motions are most likely caused by structures in the overriding plate (Figure 2.29 & Figure 2.30 & Figure 2.32).

The strongest signal of vertical uplift is located in the SW corner, adjacent to the Hellenic Trench (Figure 2.30). The strongest signal of vertical subsidence is located along two bifurcation lineation on E-Crete, which coincides very well with the prolongation of the Ptolemy Trench (Figure 2.32).

The motion along the overriding faults can be caused by the postulated incipient continent-continent collision, additional seismic studies are needed to verify this hypothesis.

Figure 2.37 shows the detected PSI surface-deformation pattern in comparison to all above mentioned hypothesis explaining the uplift of Crete existing in the literature. The main similarity is given by motion along the major fault system in the overriding plate, this image is of great consistence with the detected PSI measurements. Images showing the expected vertical motion caused by the incipient continent collision and locking along the Hellenic subduction zone further can explain the uplift in south central Crete. As mentioned above I cannot distinguish if the movements on the faults in the overriding plate are caused by the incipient continent collision. I suggest that the signal caused by locking along the plate interface of the Hellenic subduction zone is not very realistic, which is also supported by GPS measurements. Crustal faults in the overriding plate can only in some small parts on Crete explain the vertical motion (Figure 2.36), but not the overall pattern of uplift in the SW and subsidence in the eastern part. Underthrusting, aseismic creep along the plate interface of the subduction zone, return flow along a subduction channel or of the Asthenosphere are not possible explanation explaining my detected PSI measurements (Figure 2.36).

Limitations and uncertainties of my PSI analysis are caused by error propagation in PSI and GPS calibration. For PSI I described the main error sources of the technique in chapter 3.4.2. The error propagation in the deformation estimates of the PSs is ranging in my four tracks between 0.7 and 0.9 mm/yr (Table 2.2). The error estimation of the deformation is depending on the number of interferograms available for a region. I had to deal in two tracks with only 23 interferograms available for Crete. In general, further interferometry was not possible due to platform instabilities of the ERS-2 satellite since 2000. GPS-calibration allows relating PSs of all four tracks to each other with an accuracy of about 1 mm/yr; before GPS calibration it was only possible to relate PS measurements in the same track.

Atmospheric InSAR errors are caused by the refractivity of the InSAR signal with the troposphere (Hansen, 2001). Tropospheric effects influencing the signal are the hydrostatic, the wet and the liquid components (Hansen, 2001). The hydrostatic effect is related to the

dependency of the refractive index of the air pressure, thus the altitudes of the PSs (Hansen, 2001). The wet component depends on the water vapour pressure, and the liquid effect is caused by clouds and water droplets (Hansen, 2001). These atmospheric errors are mitigated by using a numerical weather prediction model which simulates and predicts the atmosphere for every SAR image.

Orbital errors further influence the PSI measurements. These effects are compensated by GPS measurements derived from the NOANET. The vertical component of my GPS measurements has an uncertainty of ~ 0.2 to 2.6 mm/yr (Table 2.3). The distribution of GPS stations on Crete are sparse, and are located nearly along a line from NW to SE, and no GPS stations are located along the southern coastline (Figure 2.1). The uncertainty of the GPS reference plane reaches values of 9 mm/yr along the southern coastline. The calibration uncertainty of the GPS plane would be less if I would have GPS stations along the southern coastline. But the high uncertainties do not influence the deformation estimation of my PS measurements.

In this study I was able to measure and analyse the vertical surface-deformation pattern of the whole island of Crete for the first time. The vertical surface-deformation pattern enables us to detect and analyse ongoing subsurface tectonic-processes. I was able to show that faults in the overriding plate are most likely the main cause for the vertical surface-deformation on Crete. These faults are capable to produce large earthquakes, such as the 365 A.D. earthquake along the Hellenic Trench. Previous GPS measurements in this region could not show any indication for activity along the faults in the overriding plate, due to only point-wise measurements. GPS measurements show aseismic slip along the plate interface of the Hellenic subduction zone.

Therefore, the detection of vertical surface-deformation along subduction zones are invaluable information of subsurface tectonic processes not only active along the first order fault zone, the subduction interface, but also along second and third order faults systems in the overriding plate. Vertical measurements are essential information for this differentiation of ongoing tectonic processes, which may lead to future strong earthquakes. PSI measurements of the vertical surface-deformation pattern of a forearc high are a promising way to support GPS strain accumulation studies along subduction zones.

2.9 Conclusions

I carried out analysis of PSI measurements on the island of Crete, a forearc high located close to the Hellenic subduction zone. Results show strong geodetic signals of vertical surface-motion in the LOS of up to ± 5 mm/yr heterogeneously distributed over the whole island. This implies that vertical surface-deformation on Crete is not induced by a single tectonic process, but rather by the complex interaction of superimposed fault systems including the subduction interface, major faults in the overriding plate, and minor crustal faults located on Crete. I was able to show that faults in the overriding plate are most likely the main cause for the vertical surface-deformation on Crete. The strongest signal of vertical uplift is located along the SW corner, whereas the strongest signal of vertical subsidence is situated along two bifurcation lineation on the eastern part of the island. The area of strong uplift corresponds to the region most affected by the coseismic uplift of the 365 A.D. earthquake. This may indicate that the Hellenic Trench is creeping aseismically, due to the fact, that locking along this major reverse fault in the overriding crust would led to subsidence of this formerly uplifted region. The subsidence in the eastern part of Crete coincides perfectly with the prolongation of the Ptolemy trench, a

transensional structure in the overriding plate. The central part of Crete is characterized by subsidence in the N and uplift in the S. The geodetic signal detected on Crete indicates ongoing subsurface tectonic-processes caused most likely along faults in the overriding plate. Geodetic measurements of the vertical surface-deformation pattern are invaluable for understanding subsurface processes, especially along subduction zones where several active tectonic processes are superimposed. PSI measurements are the only geodetic approach which permits the detection of the vertical surface-pattern over a wide area and long-time range. It is not anymore restricted to single point measurements, such as tide-gauge or GPS measurements, or conventional InSAR measurements temporal close to an earthquake. The vertical surface-deformation enhances my understanding of the dynamics and interaction along subduction zones, not only along the main plate interface, but also along faults in the overriding plate. Vertical measurements are essential information for this differentiation of ongoing tectonic processes, which may lead to future strong earthquakes. PSI measurements of the vertical surface-deformation pattern of a forearc high are a promising way to support GPS strain accumulation studies along subduction zones.

References

- Adam N., Kampes B., Eineder M., Worawattanamateekul J., Kircher M. (2004): The development of a scientific permanent scatterer system. ISPRS Hannover Workshop, Inst. for Photogramm and Geoinf. Hannover. Germany.
- Adam N., Parizzi A., Eineder M., Crosetto M. (2009): Practical persistent scatterer processing validation in the course of the TerraFirma project. *Journal of Applied Geophysics*. Vol. 69. Pages: 59-65. DOI: 10.1016/j.jappgeo.2009.07.002.
- Adam N.; Rodriguez Gonzalez F.; Parizzi A. and W. Liebhart W. (2011): Wide area persistent scatterer interferometry. In Proc. IGARSS 2011. Pages: 1481-1484. Vancouver, Canada.
- Angelier J. (1979): Neotectonique de l'arc Eggen. These d'etat. University de Paris VI, 405 pp.
- Angelier J., Lyberis N., Le Pichon X., Barrier E., Huchon P. (1982): The tectonic development of the Hellenic arc and the Sea of Crete: A synthesis. *Tectonophysics*. No. 86. Pages: 159-196. DOI: 10.1016/0040-1951(82)90066-X.
- Armijo, R., Lyon-Caen, H. Papanastassiou, D. (1992): East-west extension and Holocene normal fault scarps in the Hellenic arc. *Geology*. Vol. 20. Pages: 491-494. DOI: 10.1130/0091-7613(1992)020<0491:EWEAHN>2.3.CO;2.
- Altamimi Z., Collilieux X., Métivier L. (2011): ITRF2008: an improved solution of the International Terrestrial Reference Frame: *Journal of Geodesy*. Vol. 85. Number 8. Page 457-473. DOI: 10.1007/s00190-011-0444-4, 2011.
- Barrientos S.E., Ward S.N. (1990): The 1960 Chile earthquake: inversion for slip distribution from surface deformation. *Geophysical Journal International*. Vol. 103. Iss. 3. Pages: 589-598. DOI: 10.1111/j.1365-245X.1990.tb05673.x.
- Becker D., Meier T., Bohnhoff M., Harjes H.P. (2010): Seismicity at the convergent plate boundary offshore Crete, Greece, observed by an amphibian network. *Journal of Seismology*. Vol. 14: Pages: 369-392. DOI: 10.1007/s10950-009-9170-2.
- Bohnhoff M., Makris J., Papanikolaou D., and Stavrakakis G. (2001): Crustal investigation of the Hellenic subduction zone using wide aperture seismic data. *Tectonophysics*. Vol. 343. Pages: 239-262. DOI: 10.1016/S0040-1951(01)00264-5.
- Bohnhoff M., Harjes H.-P., Meier T. (2005): Deformation and stress regimes in the Hellenic subduction zone from focal Mechanisms. *Journal of Seismology*. Vol. 9. Pages: 341-366. DOI: 10.1007/s10950-005-8720-5.
- Bruyninx C. (2004): The EUREF Permanent Network: a multi-disciplinary network serving surveyors as well as scientists. *GeoInformatics*. Vol. 7. Pages: 32-35.
- Bürgmann R., Rosen P.A., Fielding E.J. (2000): Synthetic Aperture Radar Interferometry to Measure Earth's Surface Topography and Its Deformation. *Annual Review of Earth and Planetary Sciences*. Vol. 28. Pages: 169-209. DOI: 10.1146/annurev.earth.28.1.169.
- Bürgmann R., Thatcher W. (2013): Space geodesy: A revolution in crustal deformation measurements of tectonic processes. *GSA Special Papers 2013*. Vol. 500. Pages: 397-430. DOI: 10.1130/2013.2500(12).

- Caputo R., Catalano S., Monaco C., Romagnoli G., Tortorici G., Tortorici L. (2010): Active faulting on the island of Crete (Greece). *Geophysical Journal International*. Vol. 183. Iss. 1. Pages: 111–126. DOI: 10.1111/j.1365-246X.2010.04749.x.
- Chamot-Rooke N., Rangin C., Le Pichon X. (2005): DOTMED – Deep Offshore Tectonics of the Mediterranean: A synthesis of deep marine data in Eastern Mediterranean, The Ionian basin and margins, the Calacria wedge and the Mediterranean ridge. Société Géologique de France. Paris. Pages: 64.
- Chlieh M., deChabalier J.B., Ruegg J.C., Armijo R., Dmowska R., Campos J., Feigl K.L. (2004): Crustal deformation and fault slip during the seismic cycle in the North Chile subduction zone, from GPS and InSAR observations. *Geophysical Journal International*. Vol. 158. Pages: 695-711. DOI: 10.1111/j.1365-246X.2004.02326.x.
- Cloos M., Shreve R.L. (1988): Subduction-channel model of prism accretion, melange formation, sediment subduction, and subduction erosion at convergent plate margins. 1. Background and Description. *Pure and Applied Geophysics*. Vol. 128. Iss. 3-4. Pages: 455-500. DOI: 10.1007/BF00874548.
- Cloos M., Shreve R.L. (1988): Subduction-channel model of prism accretion, melange formation, sediment subduction, and subduction erosion at convergent plate margins. 2. Implications and Discussion. *Pure and Applied Geophysics*. Vol. 128. Iss. 3-4. Pages: 501-545. DOI: 10.1007/BF00874549.
- Collettini C., Niemeijer A., Viti C., Marone C. (2009): Fault zone fabric and fault weakness. *Nature*. Vol. 462. Pages: 907-910. DOI: 10.1038/nature08585.
- Done J., Davis C.A., Weisman M. (2004): The next generation of NWP: explicit forecasts of convection using the weather research and forecasting (WRF) model. *Atmospheric Science Letters*. Vol. 5. Pages: 110-117. DOI: 10.1002/asl.72.
- Dow J.M., Neilan R. E., and Rizos C (2009): The International GNSS Service in a changing landscape of Global Navigation Satellite Systems. *Journal of Geodesy*. Vol. 83. Pages: 191–198. DOI: 10.1007/s00190-008-0300-3.
- Dragert H., Wang K., James T.S. (2001): A silent slip event on the deeper Cascadia subduction interface. *Science*. Vol. 292. No. 5521. Pages: 1525-1528. DOI: 10.1126/science.1060152.
- Endrun B., Meier T., Bischoff M., and Harjes H.-P. (2004): Lithospheric structure in the area of Crete constrained by receiver functions and dispersion analysis of Rayleigh phase velocities. *Geophysical Journal International*. Vol. 158. Pages 592-608. DOI: 10.1111/j.1365-246X.2004.02332.x.
- Faccenna C., Becker T.W., Auer L., Billi A., Boschi L., Brun J.P., Capitanio F.A., Funiciello F., Horvath F., Jolivet L., Piromallo C., Royden L., Rossetti F., Serpelloni E. (2014): Mantle dynamics in the Mediterranean. *Reviews of Geophysics*. Vol. 52. Iss. 3. Pages: 283-332. DOI: 10.1002/2013RG000444.
- Fassoulas C., Kiliass A., Mountrakis D. (1994): Postnappe stacking extension and exhumation of high-pressure/low-temperature rocks in the island of Crete, Greece. *Tectonics*. Vol. 13. Iss. 1. Pages: 127-138. DOI: 10.1029/93TC01955.
- Fattahi H., Amelung F. (2014): InSAR uncertainty due to orbital errors. *Geophysical Journal International*. Vol. 199. Pages: 549-560. DOI: 10.1093/gji/ggu276.

- Ferretti A.; Prati C. and Rocca F. (1999): ESA empedocle project: Monitoring mount Etna by space techniques-POLIMI SAR group-final report. ESAStudy Contract Report. Contract N. 13 155/98/I-DC. Ispra. Italy.
- Ferretti A.; Prati C. and Rocca F. (2001): Permanent Scatterers in SAR Interferometry. *IEEE Transactions on Geoscience and Remote Sensing*. Vol. 38. Pages: 2202-2212. DOI: 10.1109/36.898661.
- Gallen S.F., Wegmann K.W., Bohnenstiehl D.R., Pazzaglia F.J., Brandon M.T., Fassoulas C. (2014): Active simultaneous uplift and margin-normal extension in a forearc high, Crete, Greece. *Earth and Planetary Science Letters*. Vol. 398. Pages: 11-24. DOI: 10.1016/j.epsl.2014.04.038.
- Ganas, A., Marinou A., Anastasiou D., Paradissis D., Papazissi K., Tzavaras P., Drakatos G. (2013): GPS-derived estimates of crustal deformation in the central and north Ionian Sea, Greece: 3-yr results from NOANET continuous network data. *Journal of Geodynamics*. Vol. 67. Pages: 62-71. DOI: 10.1016/j.jog.2012.05.010.
- Hall R., Audley-Charles M. G., Carter D.J. (1984): The significance of Crete for the evolution of the Eastern Mediterranean. Geological Society. London. Special Publications. V. 17. Pages: 499-516. DOI: 10.1144/GSL.SP.1984.017.01.37.
- Hanssen R.F. (2001): *Radar Interferometry: Data Interpretation and error analysis*. Kluwer Academic. Dordrecht.
- Herring T.A., King S. McClusky C. (2010): *Introduction to GAMIT/GLOBK*. Release 10.4. Massachusetts Institute of Technology. Cambridge.
- Hollenstein C., Müller M.D., Geiger A., Kahle H.G. (2008): Crustal motion and deformation in Greece from a decade of GPS measurements, 1993-2003. *Tectonophysics*. Vol. 449. Page: 17-40. DOI: 10.1016/j.tecto.2007.12.006.
- Hyndman R.D., Wang K. (1993): Thermal constraints on the zone of major thrust earthquake failure: The Cascadia Subduction Zone. *Journal of Geophysical Research*. Vol. 98. Iss. B2. Pages: 2039-2060. DOI: 10.1029/92JB02279.
- Ikeda Y. (2012): Long-term strain buildup in the northeast Japan arc-trench system and its implications for the gigantic subduction earthquake of March 11, 2011. *Proceedings of the International Symposium on Engineering Lessons Learned from the 2011 Great East Japan Earthquake, March 1-4, 2012*. Tokyo. Japan.
- Jacobshagen, V., ed. (1986): *Geologie von Griechenland*: Berlin. Stuttgart. Gebrüder Borntraeger. Pages: 363.
- Jackson J., McKenzie D. (1988): The relationship between plate motions and seismic tremors, and the rates of active deformation in the Mediterranean and Middle East. *Geophysical Journal*. Vol. 93. Pages: 45-73. DOI: 10.1111/j.1365-246X.1988.tb01387.x.
- Jolivet L., Goffé B., Monié P., Truffert-Luxey C., Patriat M., Bonneau M. (1996): Miocene detachment in Crete and exhumation P-T-t paths of high-pressure metamorphic rocks. *Tectonics*. Vol. 15. No. 6. Pages: 1129-1153. DOI: 10.1029/96TC01417.
- Kamiyama M., Sugito M., Kuse M. (2012): Precursor of crustal movements before the 2011 great east Japan earthquake. *Proceedings of the International Symposium on Engineering Lessons Learned from the 2011 Great East Japan Earthquake, March 1-4, 2012*. Tokyo. Japan.

- Kanamori H. (1977): The energy release in great earthquakes. *Journal of Geophysical Research*. Vol. 82. No. 20. Pages: 2981-2987. DOI: 10.1029/JB082i020p02981.
- Kato T. (1983): Secular and earthquake-related vertical crustal movements in Japan as deduced from tidal records (1951-1981). *Tectonophysics*. Vol. 97. Pages: 183-200. DOI: 10.1016/0040-1951(83)90147-6.
- Kenner S.J., Segall P. (2000): Postseismic deformation following the 1906 San Francisco earthquake. *Journal of Geophysical Research*. Vol. 105. Pages: 13195-13209. DOI: 10.1029/2000JB900076.
- Kopf A., Mascle J., and Klaeschen D. (2003): The Mediterranean Ridge: A mass balance across the fastest growing accretionary complex on Earth. *Journal of Geophysical Research*. Vol. 108. No. B8. DOI: 10.1029/2001JB000473.
- Le Pichon X., Angelier J. (1979): The Hellenic Arc and trench system: a key to the neotectonic evolution of the Eastern Mediterranean area. *Tectonophysics*. Vol. 60. Iss. 1-2. Pages: 1-42. DOI: 10.1016/0040-1951(79)90131-8.
- Le Pichon X., Angelier J. (1981): The Aegean Sea. *Philosophical Transactions of the Royal Society of London*. Vol. 300. No. 1454. Pages: 357-372. DOI: 10.1098/rsta.1981.0069.
- Le Pichon X., Chamot-Rooke N., Lallemand S., Noomen R., Veis G. (1995): Geodetic determination of the kinematics of central Greece with respect to Europe: Implications for Eastern Mediterranean tectonics. *Journal of Geophysical Research*. Vol. 100. Iss. B7. Pages: 12675-12690. DOI: 10.1029/95JB00317.
- Lin J., Stein R.S. (2004): Stress triggering in thrust and subduction earthquakes and stress interaction between the southern San Andreas and nearby thrust and strike-slip faults. *Journal of Geophysical Research*. Vol. 109. DOI: 10.1029/2003JB002607.
- Mascle J., Huguen C., Benkhelil J., Chamot-Rooke E., Chaumillon E., Foucher J.P., Griboulard R., Kopf A., Lamarche G., Volkonskaia A., Woodside J., Zitter T. (1999): Images may show start of European-African plate collision. *EOS. Transactions American Geophysical Union*. Vol. 80. Iss. 37. Pages: 421-428. DOI: 10.1029/99EO00308.
- Massonnet D., Feigl K.L. (1998): Radar interferometry and its application to changes in the Earth's surface. *Reviews of Geophysics*. Vol. 36. Pages: 441-500. DOI: 10.1029/97RG03139.
- McCaffrey R., Qamar A.I., King R.W., Wells R., Khazaradze G., Williams C.A., Stevens C.W., Vollick J.J., Zwick P.C. (2007): Fault locking, block rotation and crustal deformation in the Pacific Northwest. *Geophysical Journal International*. Vol. 169. Pages: 1315-1340. DOI: 10.1111/j.1365-246X.2007.03371.x.
- McClusky S., Balassanian S., Barka A., Demir C., Ergintav S., Georgiev I., Gurkan O., Hamburger M., Hurst K., Kahle H., Kastens K., Kekelidze G., King R., Kotzev V., Lenk O., Mahmoud S., Mishin A., Nadariya M., Ouzounis A., Paradissis D., Peter Y., Prilepin M., Reilinger R., Sanli I., Seeger H., Tealeb A., Toksöz M. N., Veis G. (2000): Global Positioning System constraints on plate kinematics and dynamics in the Eastern Mediterranean and Caucasus. *Journal of Geophysical Research*. Vol. 105. No. B3. Pages: 5695-5719. DOI: 10.1029/1999JB900351.

- McKenzie D. (1972): Active Tectonics of the Mediterranean Region. *Geophysical Journal of the Royal Astronomical Society*. Vol. 30. Iss. 2. Pages: 109-185. DOI: 10.1111/j.1365-246X.1972.tb02351.x.
- Meier T., Rische M., Endrun B., Vafidis A., and Harjes H.-P. (2004): Seismicity of the Hellenic subduction zone in the area of western and central Crete observed by temporary local seismic networks. *Tectonophysics*. Vol. 383. Pages: 149-169. DOI: 10.1016/j.tecto.2004.02.004.
- Meier T., Becker D., Endrun B., Rische M., Bohnhoff M., Stöckhert B., Harjes H.P. (2007): A model for the Hellenic subduction zone in the area of Crete based on seismological investigations. *Geological Society, London, Special Publications*. Vol. 291. Pages: 183-199. DOI: 10.1144/SP291.9.
- Meulenkamp J.E., Wortel M.J.R., Wamel van W.A. Spakman W., Hoogerduyn Strating E. (1988): On the Hellenic subduction zone and the geodynamic evolution of Crete since the late Middle Miocene. *Tectonophysics*. Vol. 146. Pages: 203-215. DOI: 10.1016/0040-1951(88)90091-1.
- Miller M.M., Melbourne T., Johnson D.J., Summer W.Q. (2002): Periodic slow earthquakes from the Cascadia subduction zone. *Science*. Vol. 295. No. 5564. Pages: 2423. DOI: 10.1126/science.1071193.
- Nelson A.R., Manley W.F. (1992): Holocene coseismic and aseismic uplift of the Isla Mocha, south-central Chile. *Quaternary International*. Vol. 15/16. Pages: 61-76. DOI: 10.1016/1040-6181(92)90036-2.
- Nur A., Mavko G. (1974): Postseismic Viscoelastic Rebound. *Science*. Vol. 183. No. 4121. Pages: 204-206. DOI: 10.1126/science.183.4121.204.
- Obara K. (2002): Nonvolcanic deep tremor associated with subduction in southwest Japan. *Science*. Vol. 296. No. 5573. Pages: 1679-1681. DOI: 10.1126/science.1070378.
- Papanikolaou D., Vassilakis E. (2010): Middle Miocene E-W Tectonic Horst Structure of Crete through Extensional Detachment Faults. *Tectonophysics*. Vol. 488. Iss. 1-4, 5. Pages 233-247. DOI: 10.1088/1755-1307/2/1/012003.
- Papazachos, B.C., Comninakis, P.E., Karakaisis, G.F., Karakostas, B.G., Papaioannou, Ch.A., Papazachos, C.B., Scordilis E.M. (2000): A catalogue of earthquakes in Greece and surrounding area for the period 550BC-1999. *Publ. Geophys. Lab., Univ. of Thessaloniki*. 1. Pages: 333.
- Papazachos, B.C., Comninakis, P.E., Scordilis, E.M., Karakaisis, G.F. and C.B. Papazachos (2009): A catalogue of earthquakes in the Mediterranean and surrounding area for the period 1901 - Sep2009, *Publ. Geophys. Laboratory, University of Thessaloniki*.
- Pirazzoli P.A., Laborel J., Stiros S.C. (1996): Earthquake clustering in the Eastern Mediterranean during historical times. *Journal of Geophysical Research - Solid Earth*. Vol. 101. Iss. B3. Pages: 6083-6097. DOI: 10.1029/95JB00914.
- Platt J.P. (1986): Dynamics of orogenic wedges and the uplift of high-pressure metamorphic rocks. *The Geological Society of America Bulletin*. Vol. 97. No. 9. Pages: 1037-1053. DOI: 10.1130/0016-7606(1986)97<1037:DOOWAT>2.0CO;2.
- Pollitz F.F. (1997): Gravitational viscoelastic postseismic relaxation on a layered spherical Earth. *Journal of Geophysical Research*. Vol. 102. No. B8. Pages: 17921-17941. DOI: 10.1029/97JB01277.

- Pondrelli S., Salimbeni S., Morelli A., Ekström G., Postpischl L., Vannucci G. and Boschi E. (2011): European-Mediterranean Regional Centroid Moment Tensor Catalog: solutions for 2005-2008. *Physics of the Earth and Planetary Interiors*. Vol. 185. Iss. 3-4. Pages 74-81.
- Reilinger R., McClusky S., Vernant P., Lawrence S., Ergintav S., Cakmak R., Ozener H., Kadiror F., Guliev I., Stepanyan R., Nadariya M., Hahubia G., Mahmoud S., Sakr K., ArRajehi A., Paradissis D., Al-Aydrus A., Prilepin M., Guseva T., Evren E., Dmitrotsa T., Filikov S.V., Gomez F., Al-Ghazzi R., Karam G. (2006): GPS constraints on continental deformation in the Africa-Arabia-Eurasia continental collision zone and implications for the dynamics of plate interactions. *Journal of Geophysical Research - Solid Earth*. Vol. 111. Iss. B5. DOI: 10.1029/2005JB0045051.
- Reilinger R., McClusky S., Paradissis D., Ergintav S., Vernant P. (2010): Geodetic constraints on the tectonic evolution of the Aegean region and strain accumulation along the Hellenic subduction zone. *Tectonophysics*. Vol. 488. Pages: 22-30. DOI: 10.1016/j.tecto.2009.05.027.
- Roberts G.G., White N.J., Shaw B. (2013): An uplift history of Crete, Greece, from inverse modeling of longitudinal river profiles. *Geomorphology*. Vol. 198. Pages: 177-188. DOI: 10.1016/j.geomorph.2013.05.026.
- Rocca F. (2004): Diameters of the orbital tubes in long-term interferometric SAR surveys. *IEEE Geoscience Remote Sensing Letters*. Vol. 1 (13). Pages: 224-227. DOI: 10.1109/LGRS.2004.830125.
- Royden L.H. (1993): The Tectonic Expression Slab Pull At Continental Convergent Boundaries. *Tectonics*. Vol. 12. No. 2. Pages: 303-325. DOI: 10.1029/92TC02248.
- Ryder I., Rietbrock A., Kelson K., Bürgmann R., Floyd M., Socquet A., Vigny C., Carizzo D. (2012): Large extensional aftershocks in the continental forearc triggered by the 2010 Maule earthquake, Chile. *Geophysical Journal International*. Vol. 188. Pages: 879-890. DOI: 10.1111/j.1365-246X.2011.05321.x.
- Saffer D., Wallace L.M. (2015): The frictional, hydrologic, metamorphic and thermal habitat of shallow slow earthquakes. *Nature Geoscience*. Vol. 8. Pages: 594-600. DOI: 10.1038/NGEO2490.
- Savage J.C. (1983): A dislocation model of strain accumulation and release at a subduction zone. *Journal of Geophysical Research*. Vol. 88. Pages: 4984-4996. DOI: 10.1029/JB088iB06p04984.
- Savage J.C., Lisowski M. (1991): Strain measurements and the Potential for a Great Subduction Earthquake Off the Coast of Washington. *Science*. Vol. 252. No. 5002. Pages: 101-103. DOI: 10.1126/science.252.5002.101.
- Scholz C. (1990): *The Mechanics of Earthquakes and Faulting*. Cambridge Univ. Press. New York. Pages: 461.
- Segall P., Davis J.L. (1997): GPS applications for geodynamics and earthquake studies. *Annual Review of Earth and Planetary Sciences*. Vol. 25. Page: 301-36. DOI: 10.1146/annurev.earth.25.1.301. DOI: 10.1146/annurev.earth.25.1.301.
- Serpelloni E., Faccenna C., Spada G., Dong D., Williams S.D.P. (2013): Vertical GPS ground motion rates in the Euro-Mediterranean region: New evidence of velocity gradients at different spatial scales along the Nubia-Eurasia plate boundary. *Journal of Geophysical Research*. Vol. 118. Pages: 6003-6024. DOI: 10.1002/2013/JB010102.

- Shaw B., Ambraseys N.N., England P.C., Floyd M.A., Gorman G.J., Higham T.F.G., Jackson J. A., Nocquet J.-M., Pain C. C., Piggott M. D. (2008): Eastern Mediterranean tectonics and tsunami hazard inferred from the A.D. 365 earthquake. *Nature Geoscience*. Vol. 1. DOI: 10.1038/ngeo151.
- Shirzaei M., Bürgmann R., Oncken O., Walter T.T., Victor P., Ewiak O. (2012): Response of forearc crustal faults to the megathrust earthquake cycle: InSAR evidence from Mejillones Peninsula, Northern Chile. *Earth and Planetary Science Letters*. Vol: 333-334. Pages: 157-164. DOI: 10.1016/j.epsl.2012.04.001.
- Sibson R.H. (1985): A note on fault reactivation. *Journal of Structural Geology*. Vol. Pages: 751-754. DOI: 10.1016/0191-8141(85)90150-6.
- Simons M., Minson S.E., Sladen A., Ortega F., Jiang J., Owen S.E., Meng L., Ampuero J-P., Wei S., Chu R., Helmberger D.V., Kanamori H., Hetland E., Moore A.W., Webb F.H. (2011): The 2011 magnitude 9.0 Tohoku-Oki earthquake: Mosaicking the megathrust from seconds to centuries. *Science*. Vol. 332. No. 6036. Pages: 1421-1425. DOI: 10.1126/science.1206731.
- Strobl M., Hetzel R., Fassoulas C., Kubik P.W. (2014): A long-term rock uplift rate for eastern Crete and geodynamic implications for the Hellenic subduction zone. *Journal of Geodynamics*. Vol. 78. Pages: 21-31. DOI: 10.1016/j.jog.2014.04.002.
- Suwa Y., Miura S., Hasegawa A., Sato T., Tachibana K. (2006): Interplate coupling beneath NE Japan inferred from three-dimensional displacement field. *Journal of Geophysical Research*. Vol. 111. DOI: 10.1029/2004JB003203.
- Taymaz T., Jackson J., Westaway R. (1990): Earthquake mechanisms in the Hellenic Trench near Crete. *Geophysical Journal International*. Vol. 102. Iss. 3. Pages: 695-731. DOI: 10.1111/j.1365-246X.1990.tb04590.x.
- Ten Veen J.H. and Kleinspehn K.L. (2003): Incipient continental collision and plate-boundary curvature: Late Pliocene-Holocene transtensional Hellenic forearc, Crete, Greece. *Journal of the Geological Society*. Vol. 160. Pages: 161-181 DOI: 10.1144/0016-764902-067.
- Terrafirma project's home page: <http://www.terrafirma.eu.com/index.htm> (funded by ESA)
- Thomson S.N., Stockhert B., Brix M.R. (1998): Thermochronology of the high-pressure metamorphic rocks of Crete, Greece: Implications for the speed of tectonic processes. *Geology*. Vol. 26. Iss. 9. Pages: 259-262. DOI: 10.1130/0091-7613(1998)026<0259:TOTHPM>2.3.CO;2.
- Van Hinsbergen D.J.J., Meulenkamp J.E. (2006): Neogene supradetachment basin development on Crete (Greece) during exhumation of the South Aegean core complex. *Basin Research* 18. Pages: 103-124. DOI: 10.1111/j.1365-2117.2005.00282.x.
- Vernant P., Reilinger R., McClusky S. (2014): Geodetic evidence for low coupling on the Hellenic subduction plate interface. *Earth and Planetary Science Letters*. Vol. 385. Pages: 122-129. DOI: 10.1016/j.epsl.2013.10.018.
- Wang K., Bilek S.L. (2014): Invited review paper: Fault creep caused by subduction of rough seafloor relief. *Tectonophysics*. Vol. 610. Pages: 1-24. DOI: 10.1016/j.tecto.2013.11.024.
- Zebker H.A., Villasenor J. (1992): Decorrelation in Interferometric Radar Echoes. *IEEE Transactions on Geoscience and Remote Sensing*. Vol. 30. No. 5. Pages: 950-959. DOI: 10.1109/36.175330.

Figures & Tables

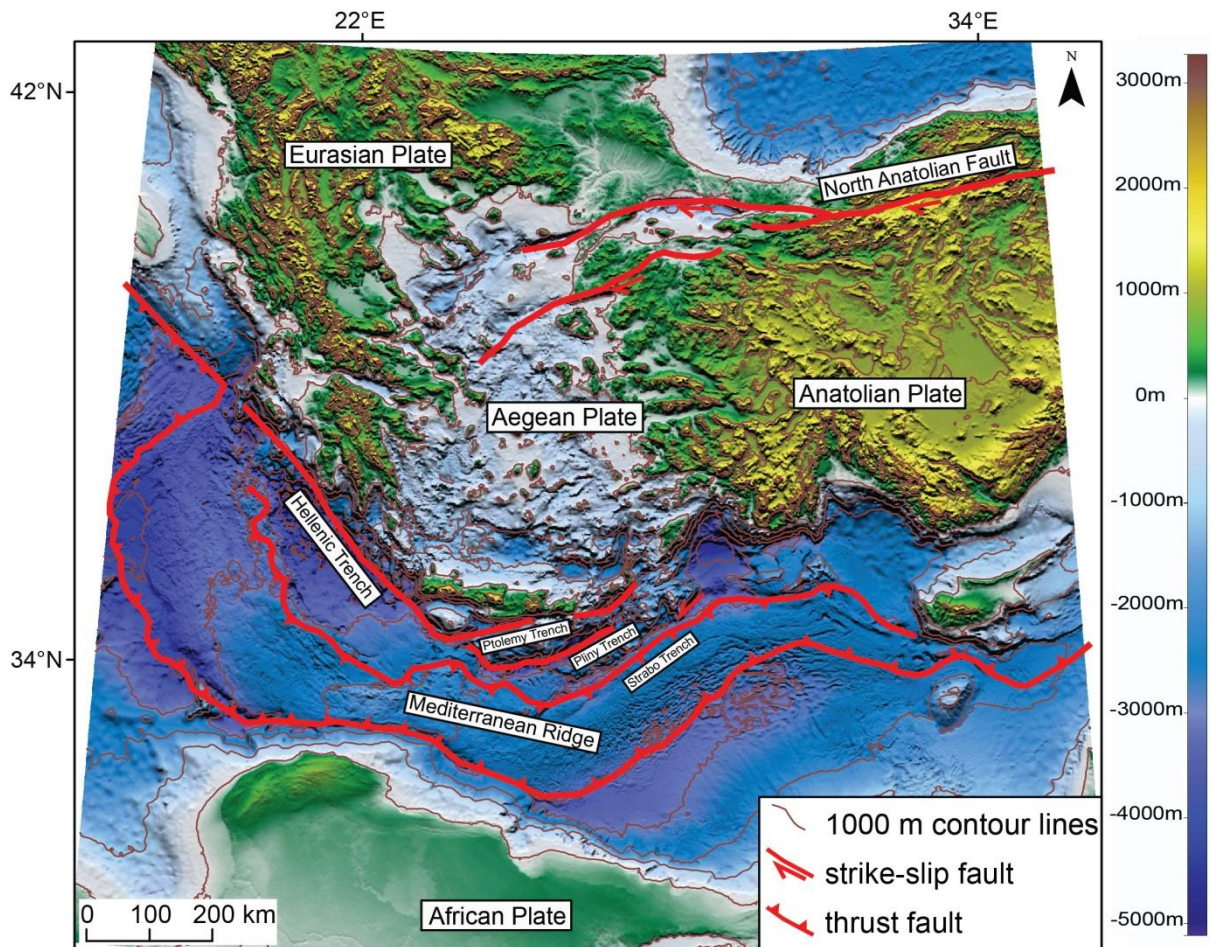


Figure 2.1: Tectonic map and profile lines. Tectonic map of the Eastern Mediterranean after Chamot-Rooke et al. (2005). Background topography is derived from data of Smith and Sandwell (1997).

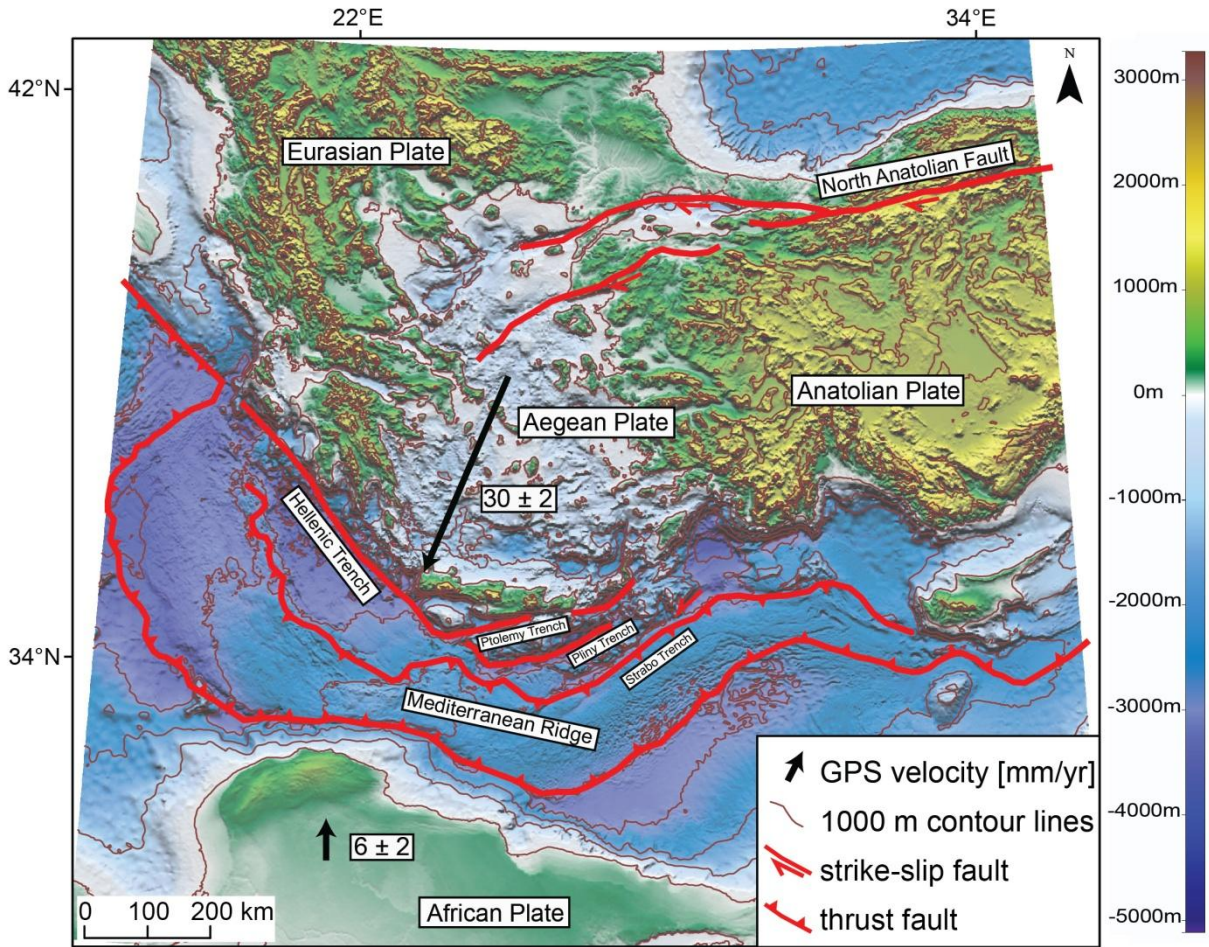


Figure 2.2: Tectonic map and profile lines. Tectonic map of the Eastern Mediterranean after Chamot-Rooke et al. (2005). Background topography is derived from data of Smith and Sandwell (1997). GPS velocities after McCluskey et al. (2000).

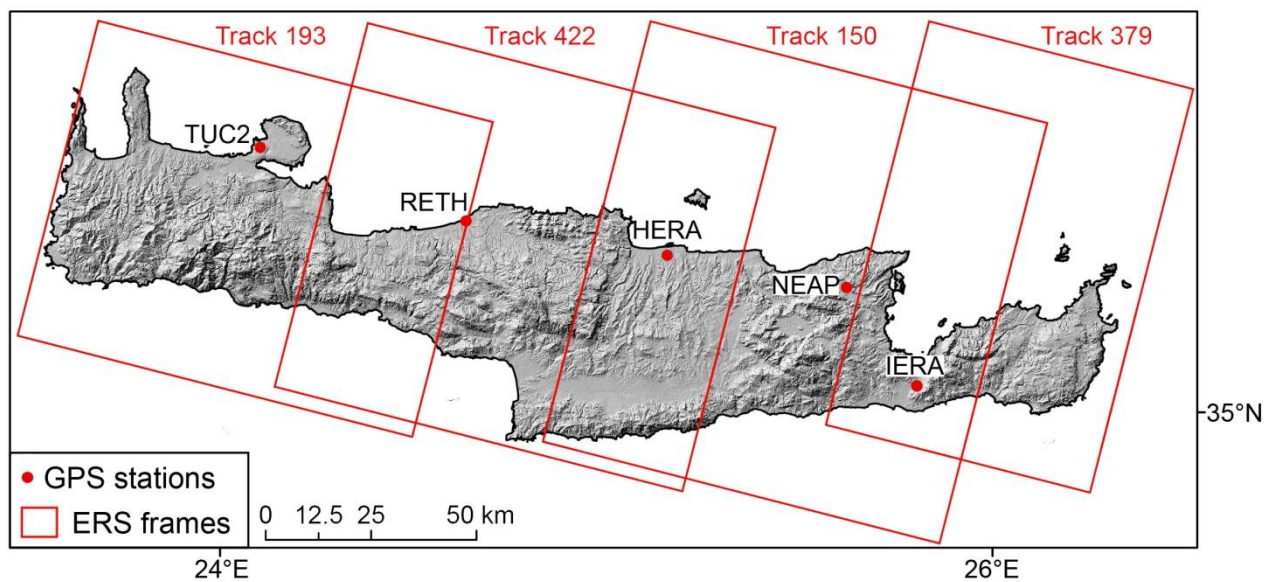


Figure 2.3: Location of GPS stations and ERS frames on Crete.

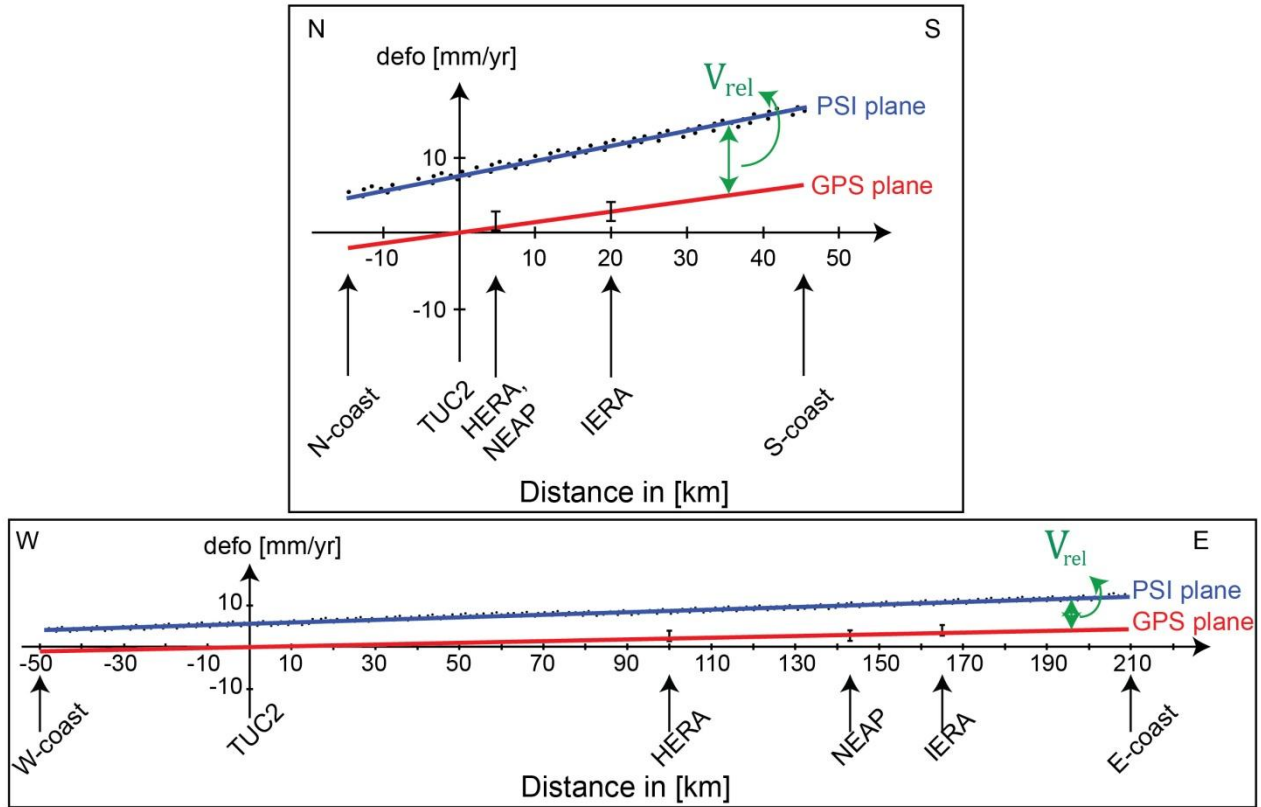


Figure 2.4: Sketch for illustration the absolute GPS calibration with TUC2 as reference station for Crete. All PS measurements are calibrated to the GPS plane fixed by the four GPS stations on Crete (TUC2, HERA, NEAP, and IERA, without RETH which is considered unreliable).

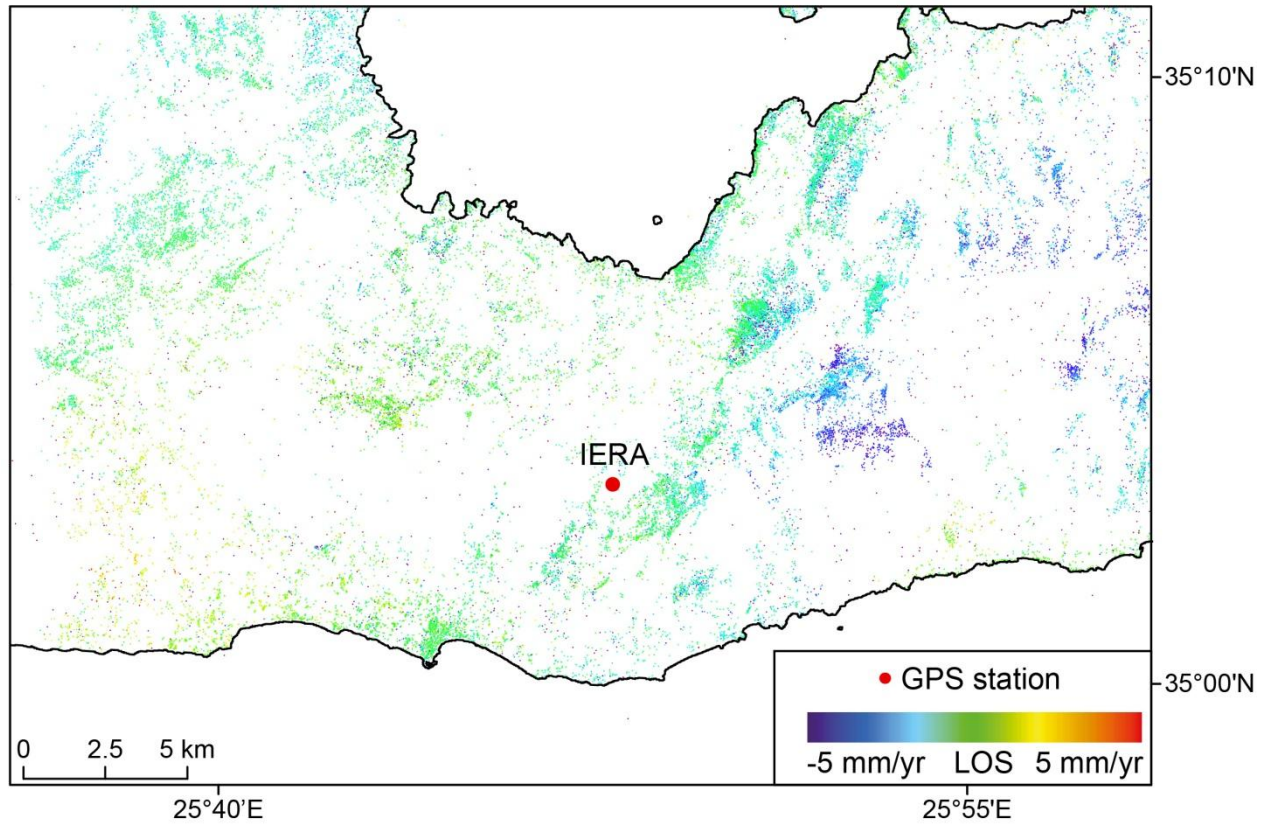


Figure 2.5: PSs distribution close to the IERA GPS station.

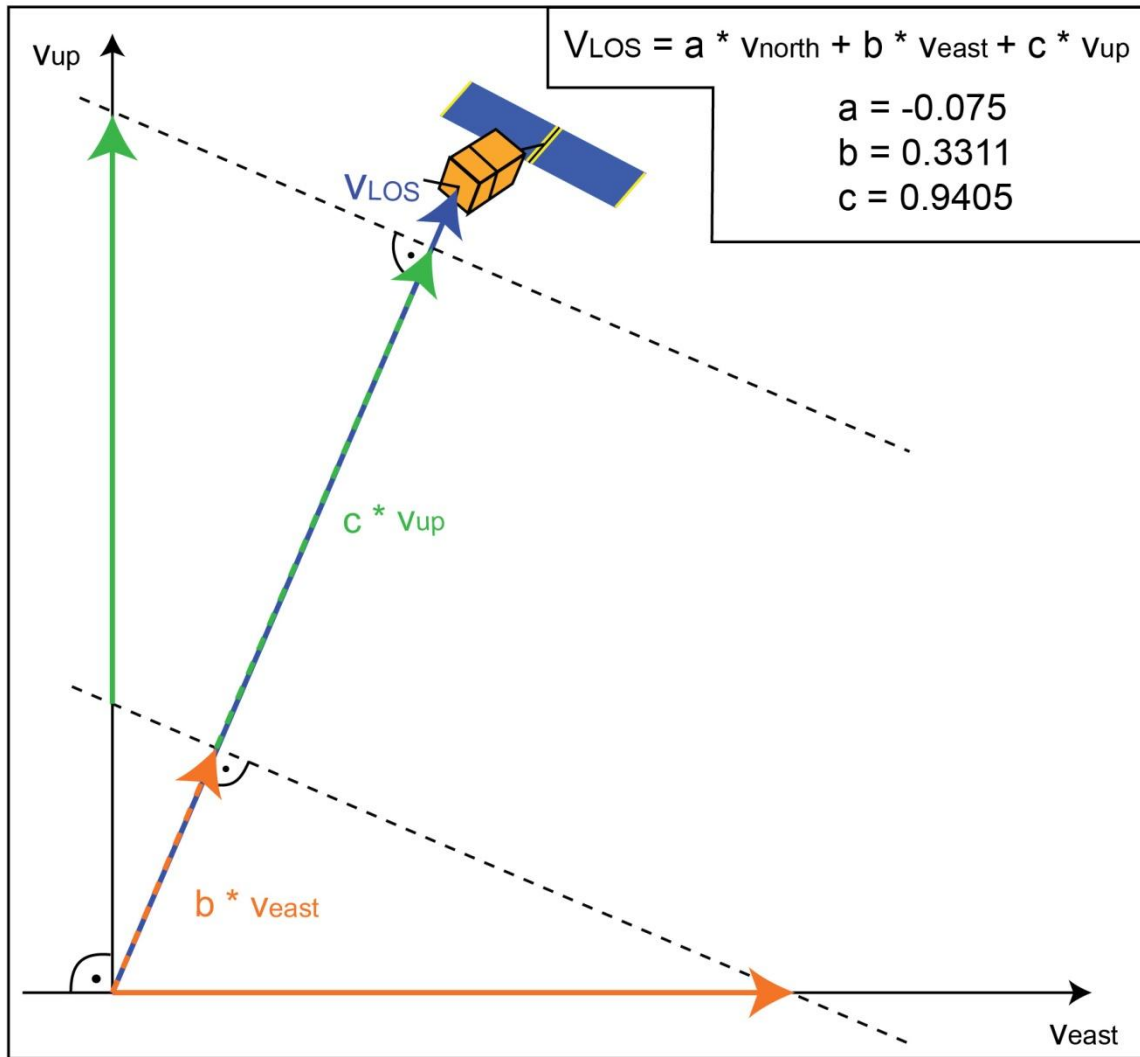


Figure 2.6: Schematic diagram showing the composition of v_{LOS}^{PSI} into v_{north}^{PSI} , v_{east}^{PSI} , and v_{up}^{PSI} .

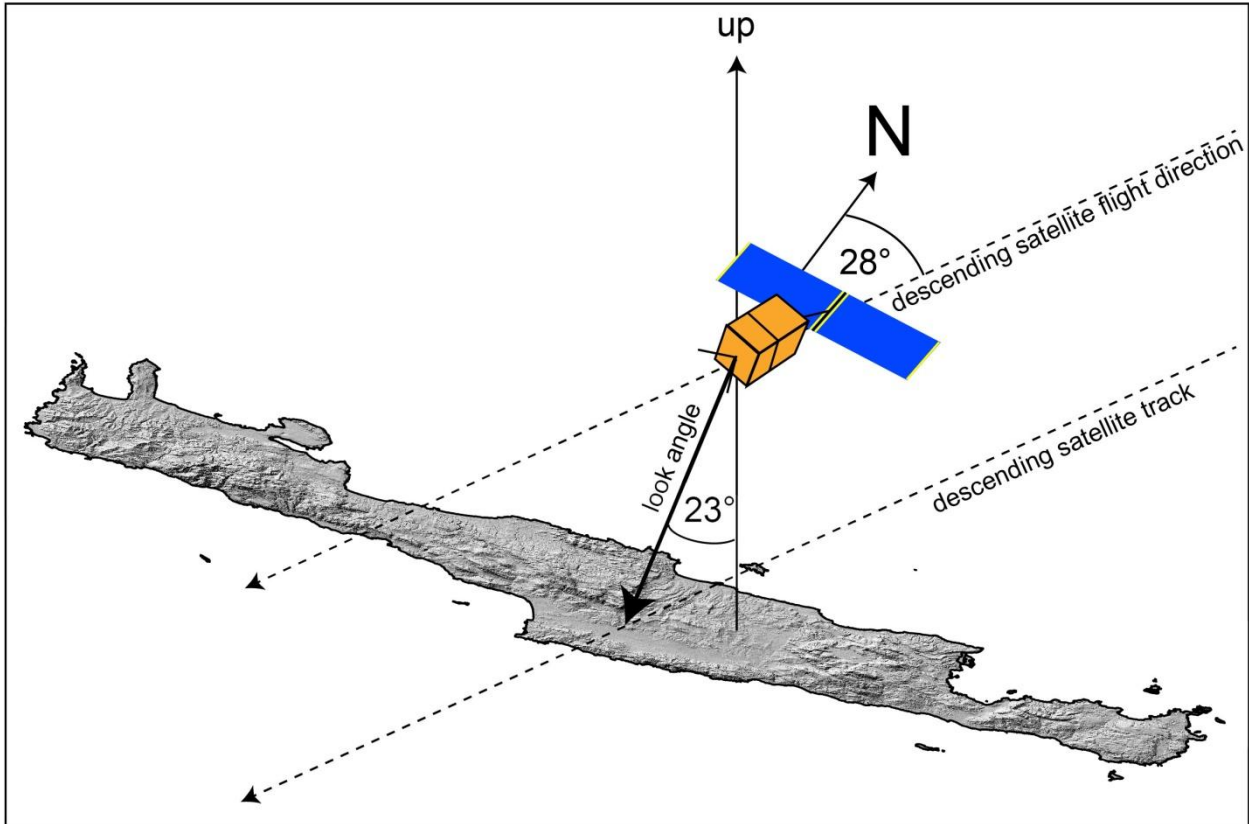


Figure 2.7: Sketch for ERS-1/-2 satellite flight-tracks and look angle of 23° explaining the LOS.

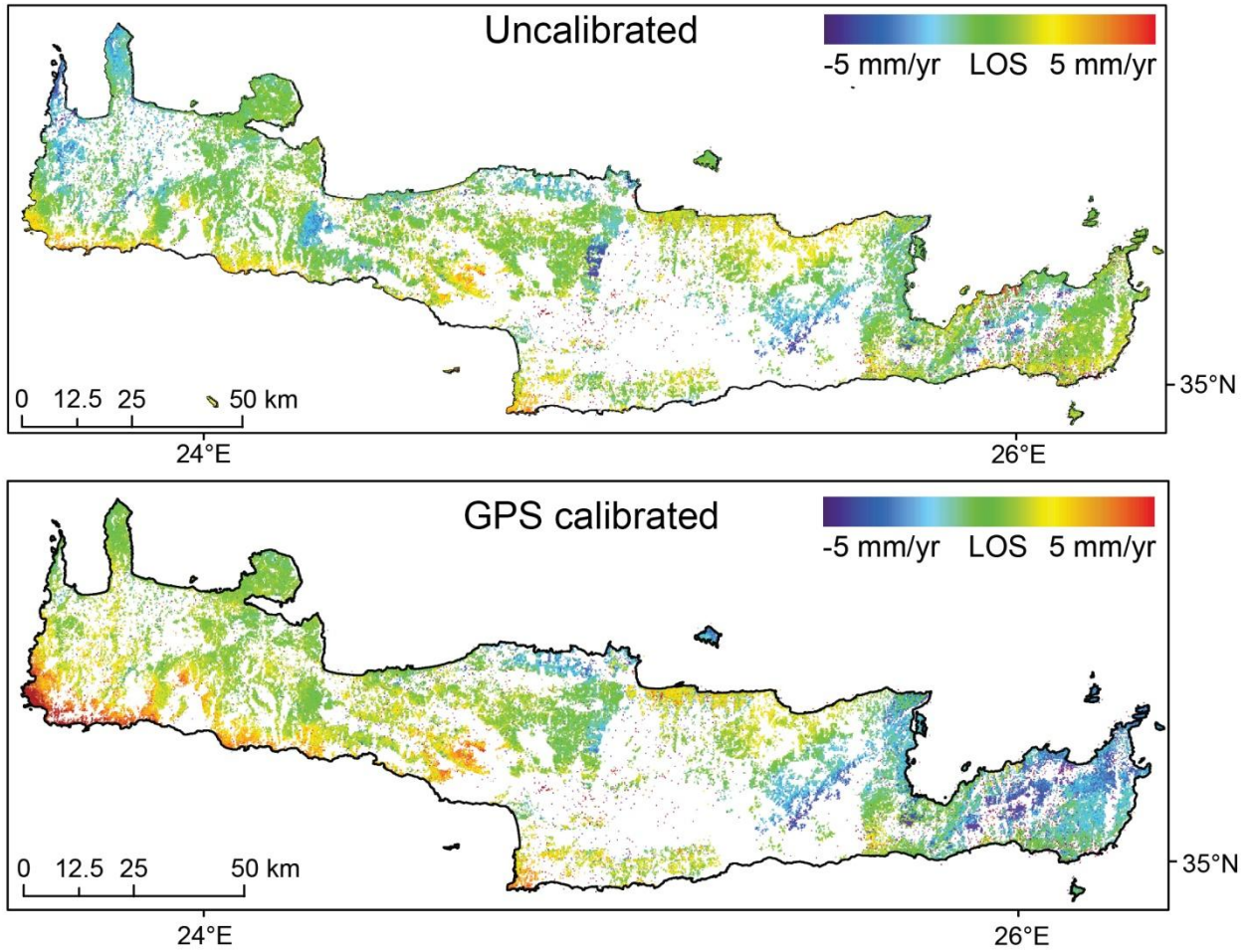


Figure 2.8: Uncalibrated and GPS calibrated PS measurement.

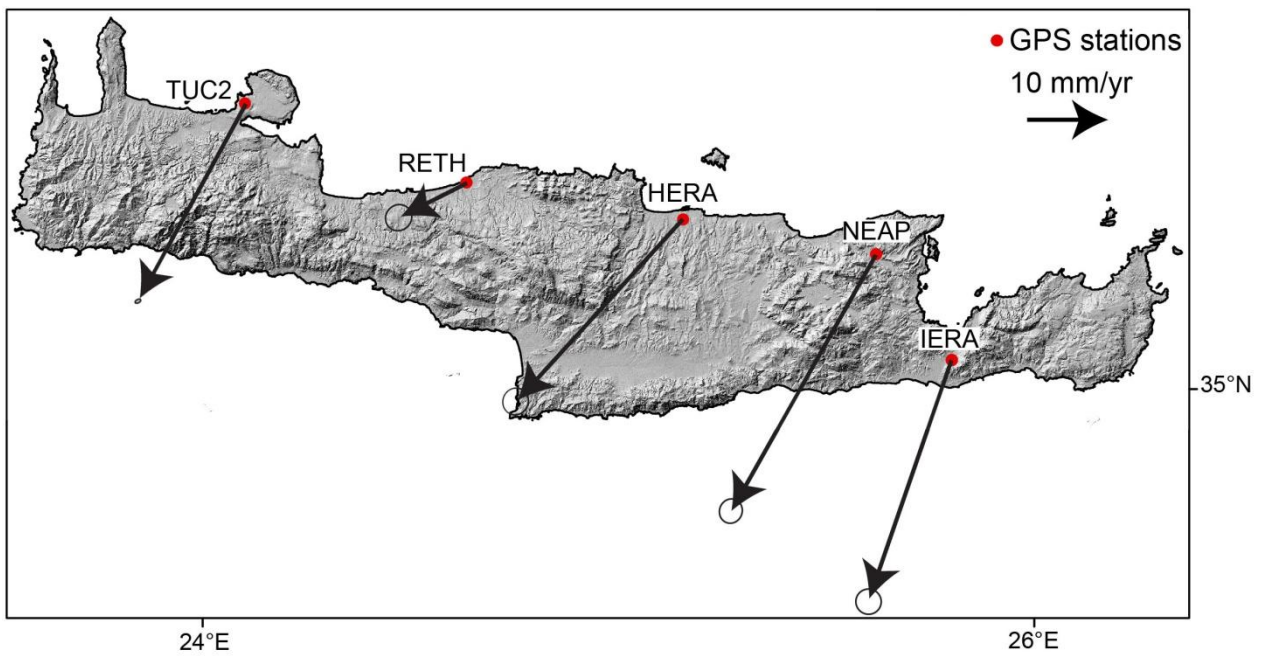


Figure 2.9: Horizontal velocities based on GPS measurements with respect to Eurasia. Hill slope map generated from SPOT-DEM, with a horizontal-resolution of 20 m and vertical-resolution of 15 ± 5 m.

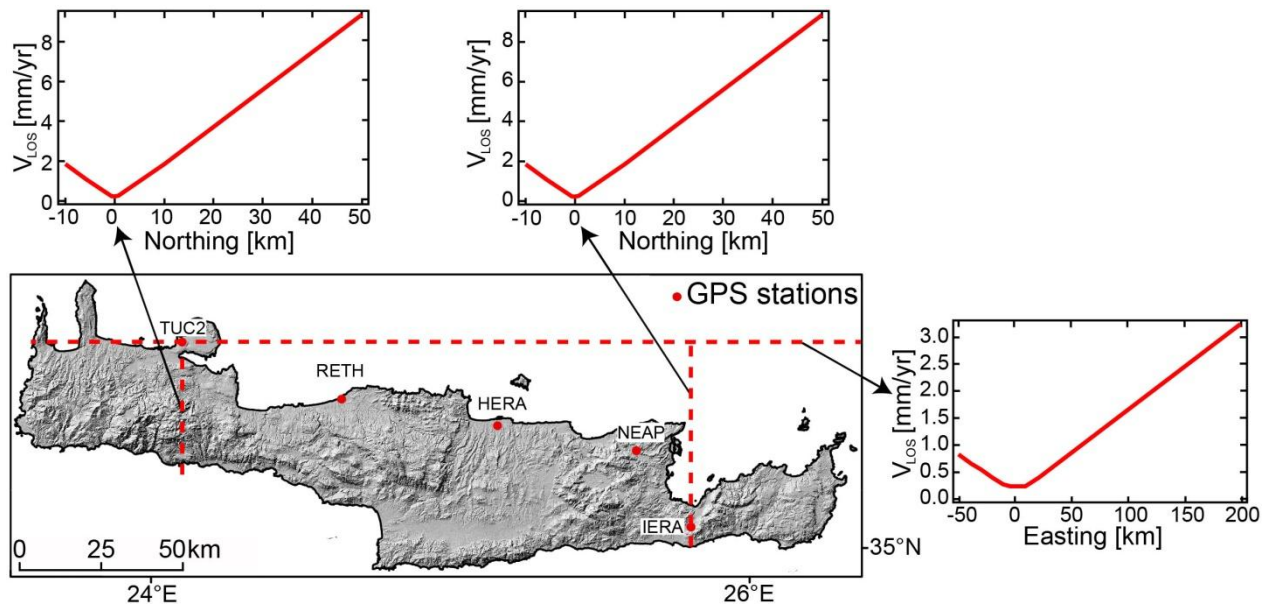


Figure 2.10: GPS calibration uncertainties of the GPS plane.

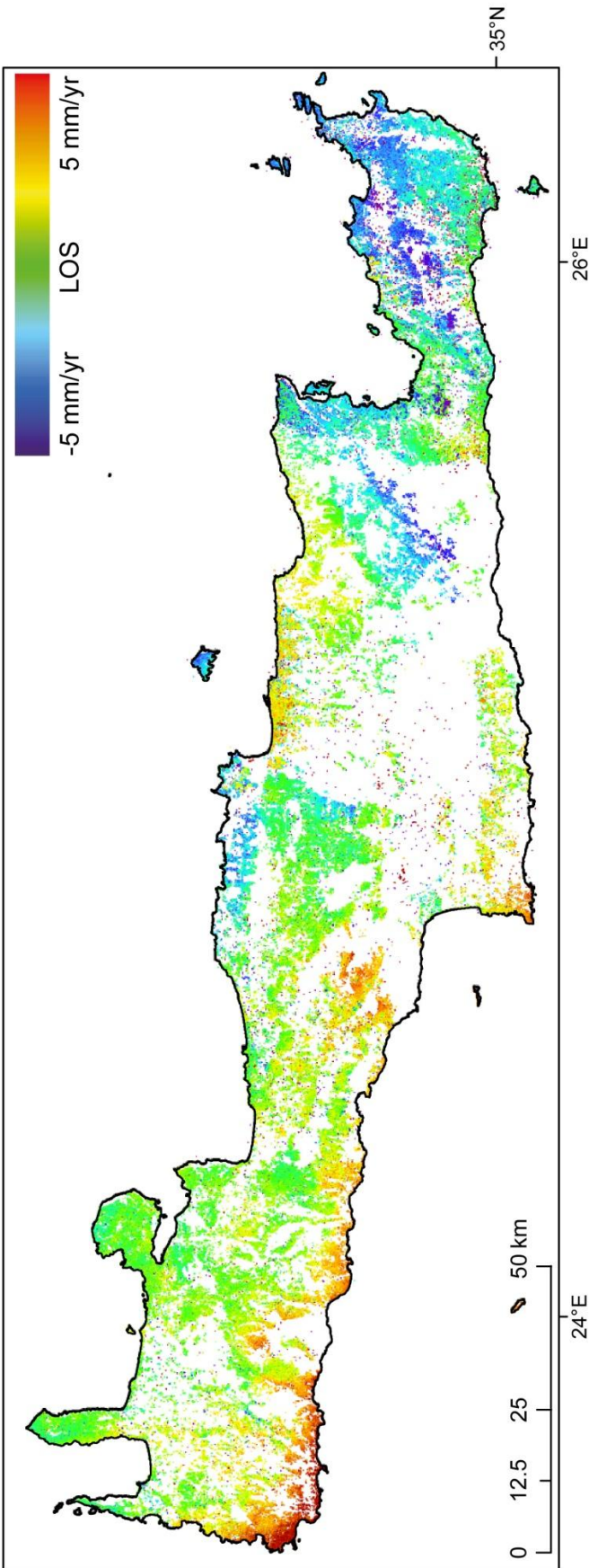


Figure 2.11: PSI measurements in LOS.

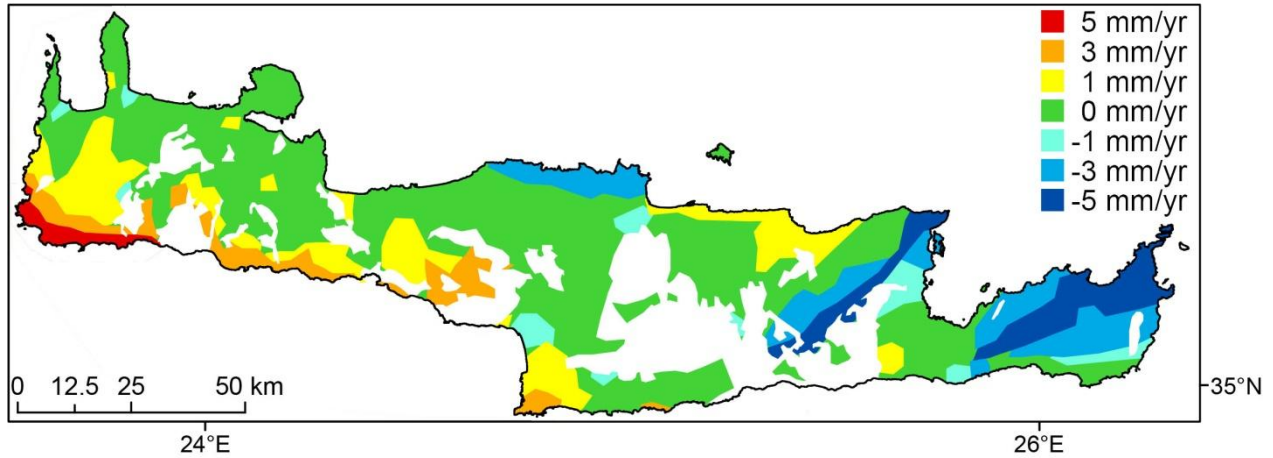


Figure 2.12: Simplified map of PSI measurements in LOS.

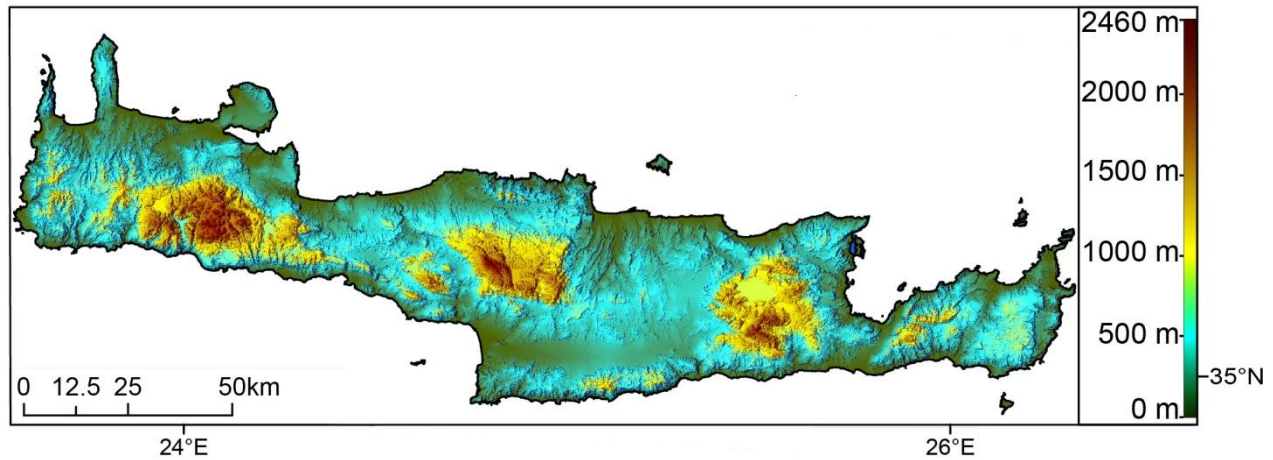


Figure 2.13: Topography map of Crete based on SPOT-DEM

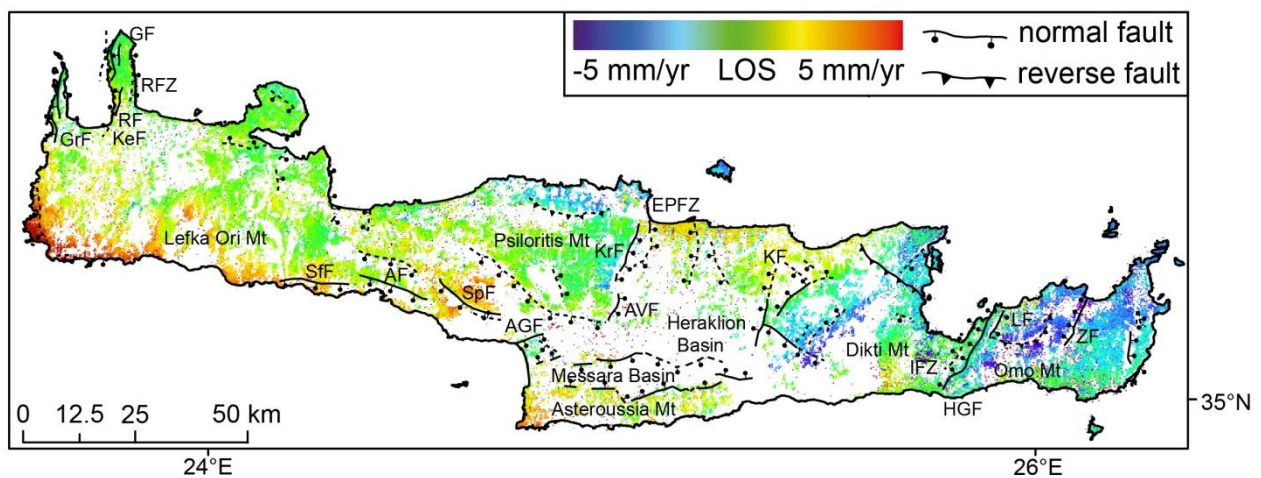


Figure 2.14: Fault map of Crete. Colored dots show 1992 to 2000 PSs velocities in LOS of 431.251 PSs in the GPS reference frame. Fault traces are modified after Caputo et al. (2010). Dashed lines are possible faults determined by geomorphic features in topography. GrF: Gramvousa Fault, RFZ: Rhodope Fault Zone, KeF: Kera Fault, RF: Rodope Fault, GF: Gionas Fault, SfF: Sfakia Fault, AF: Asomatos Fault, SpF: Spili Fault, AGF: Agia Galini Fault, EPFZ: Eastern Psiloritis Fault Zone, KrF: Kroussonas Fault, AVF:

Agia Varvara Fault, KF: Kastelli Fault, IEZ: Ierapetra Fault Zone, HGF: Ha Gorge Fault, LF: Lastros Fault, ZF: Zou Fault.

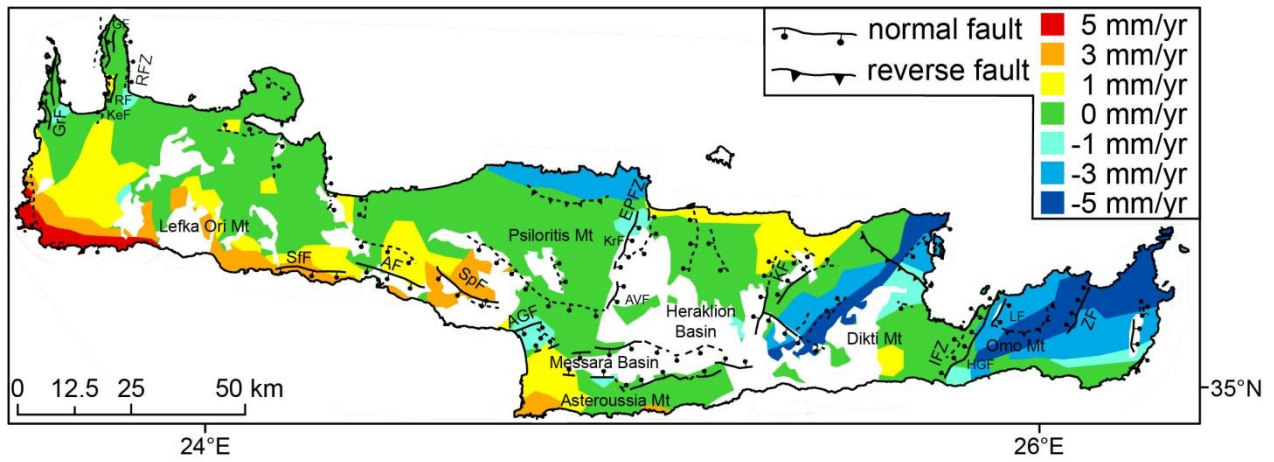


Figure 2.15: Simplified map of PSI measurements with faults. Fault traces are modified after Caputo et al. (2010). Dashed lines are possible faults determined by geomorphic features in topography. For fault abbreviations see Figure 2.14.

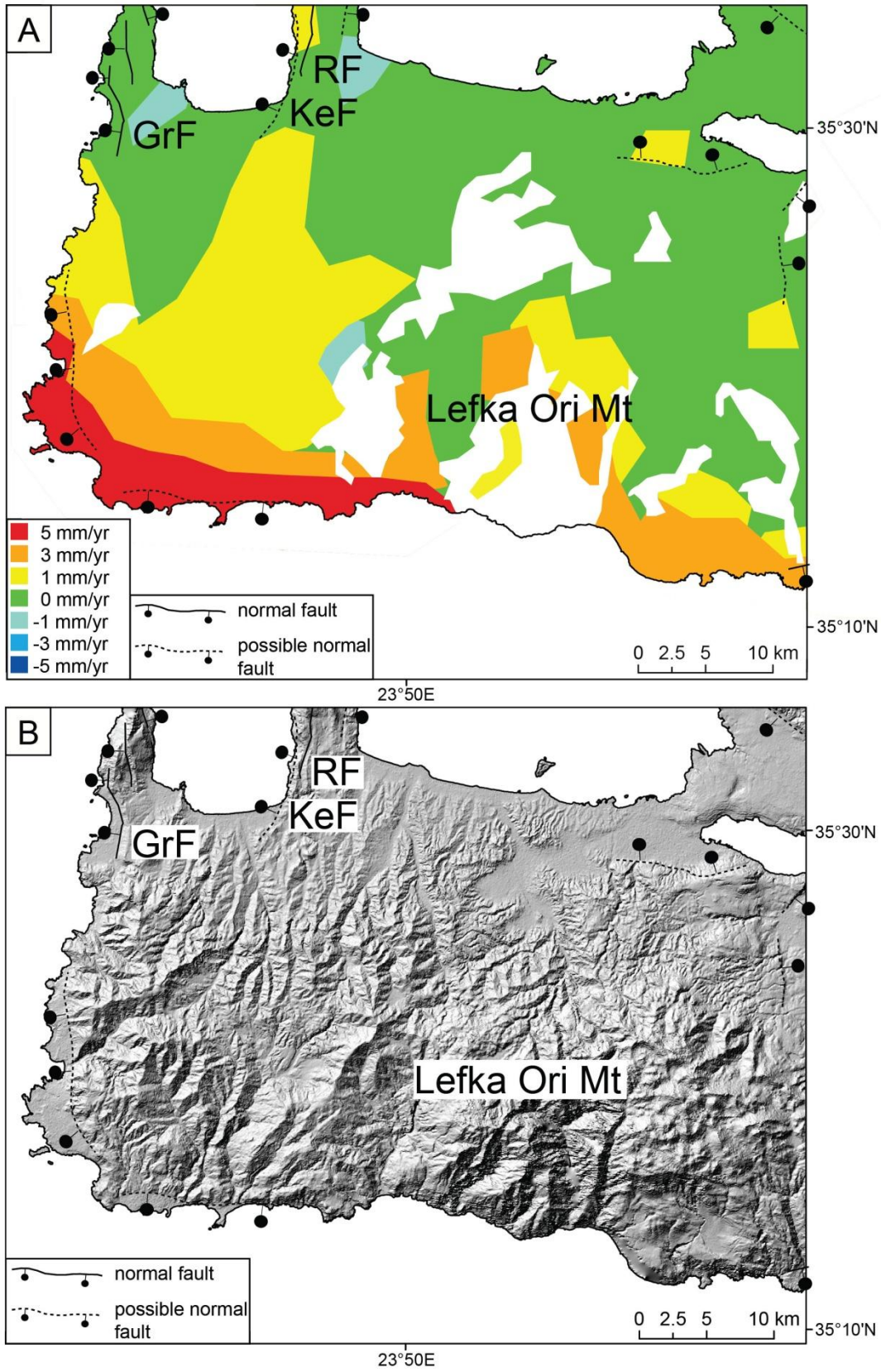


Figure 2.16: A) Simplified map of PSI measurements with faults. B) Topographic map with faults based on SPOT-DEM. GrF: Gramvousa Fault, KeF: Kera Fault, and RF: Rodope Fault.

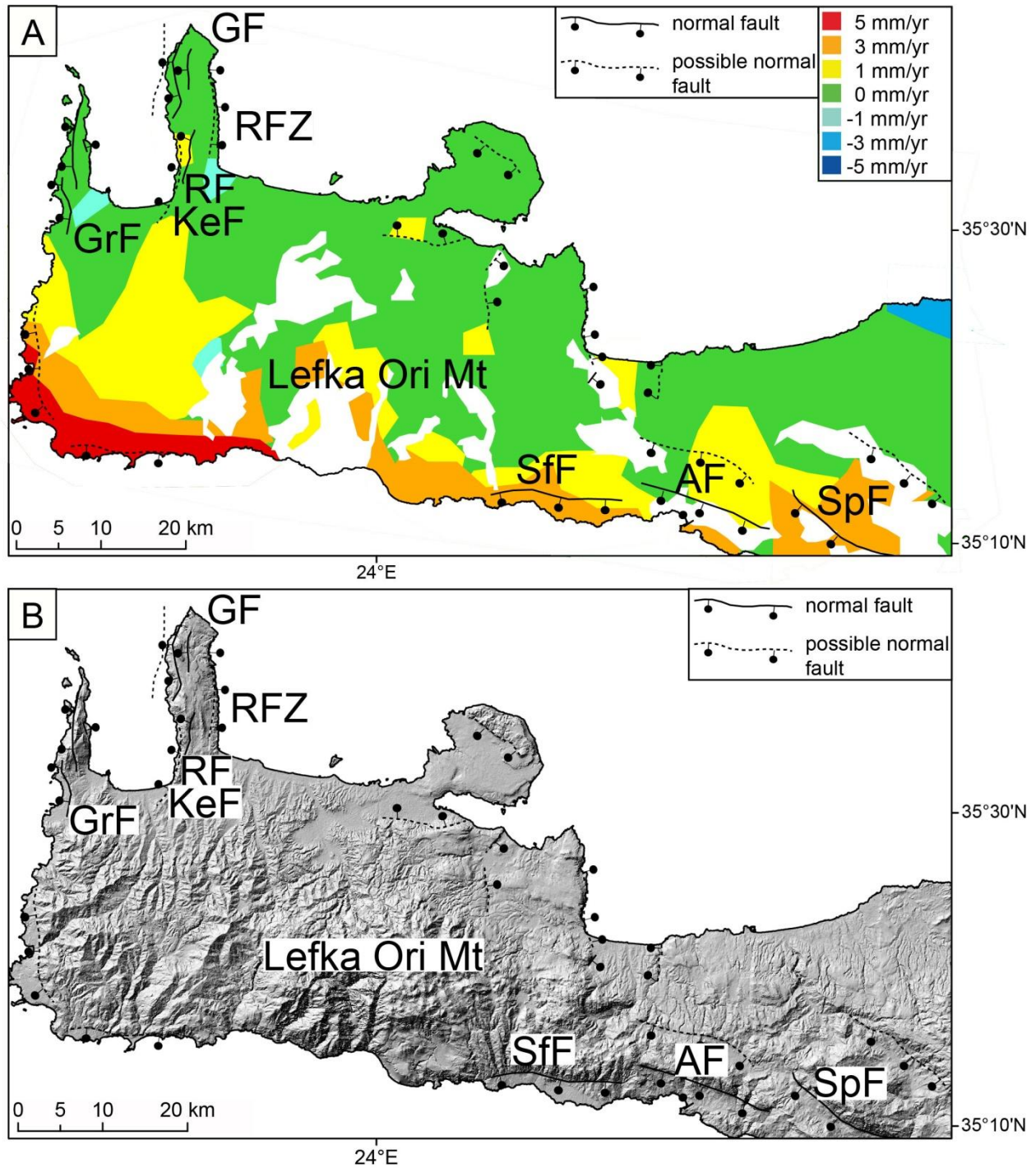


Figure 2.17: Simplified map of PSI measurements with faults. B) Topographic map with faults based on SPOT-DEM. GrF: Gramvousa Fault, RFZ: Rhodope Fault Zone, KeF: Kera Fault, RF: Rodope Fault, GF: Gionas Fault, SfF: Sfakia Fault, AF: Asomatos Fault, and SpF: Spili Fault.

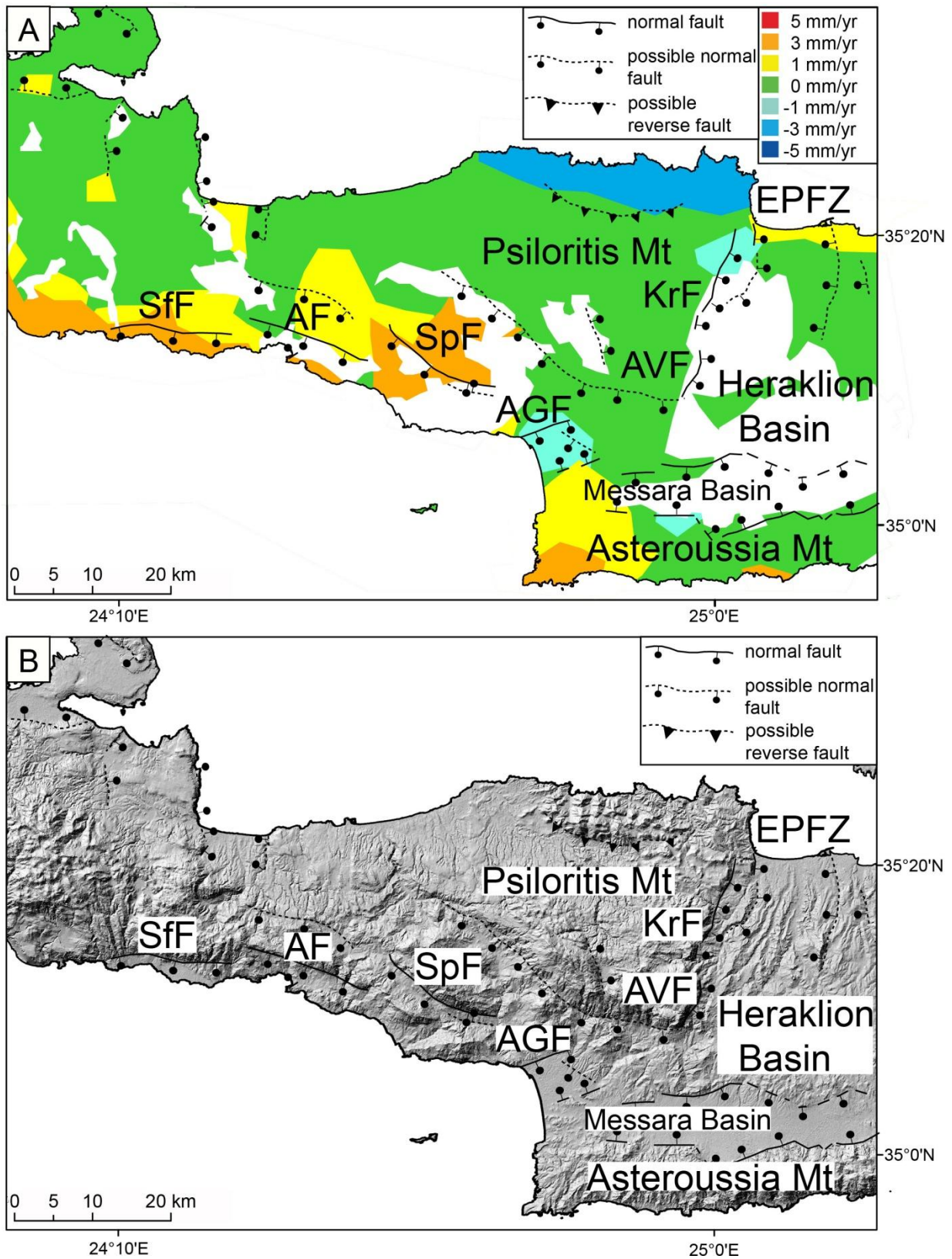


Figure 2.18: Simplified map of PSI measurements with faults. B) Topographic map with faults based on SPOT-DEM. SfF: Sfakia Fault, AF: Asomatos Fault, SpF: Spili Fault, AGF: Agia Galini Fault, EPFZ: Eastern Psiloritis Fault Zone, KrF: Kroussonas Fault, and AVF: Agia Varvara Fault.

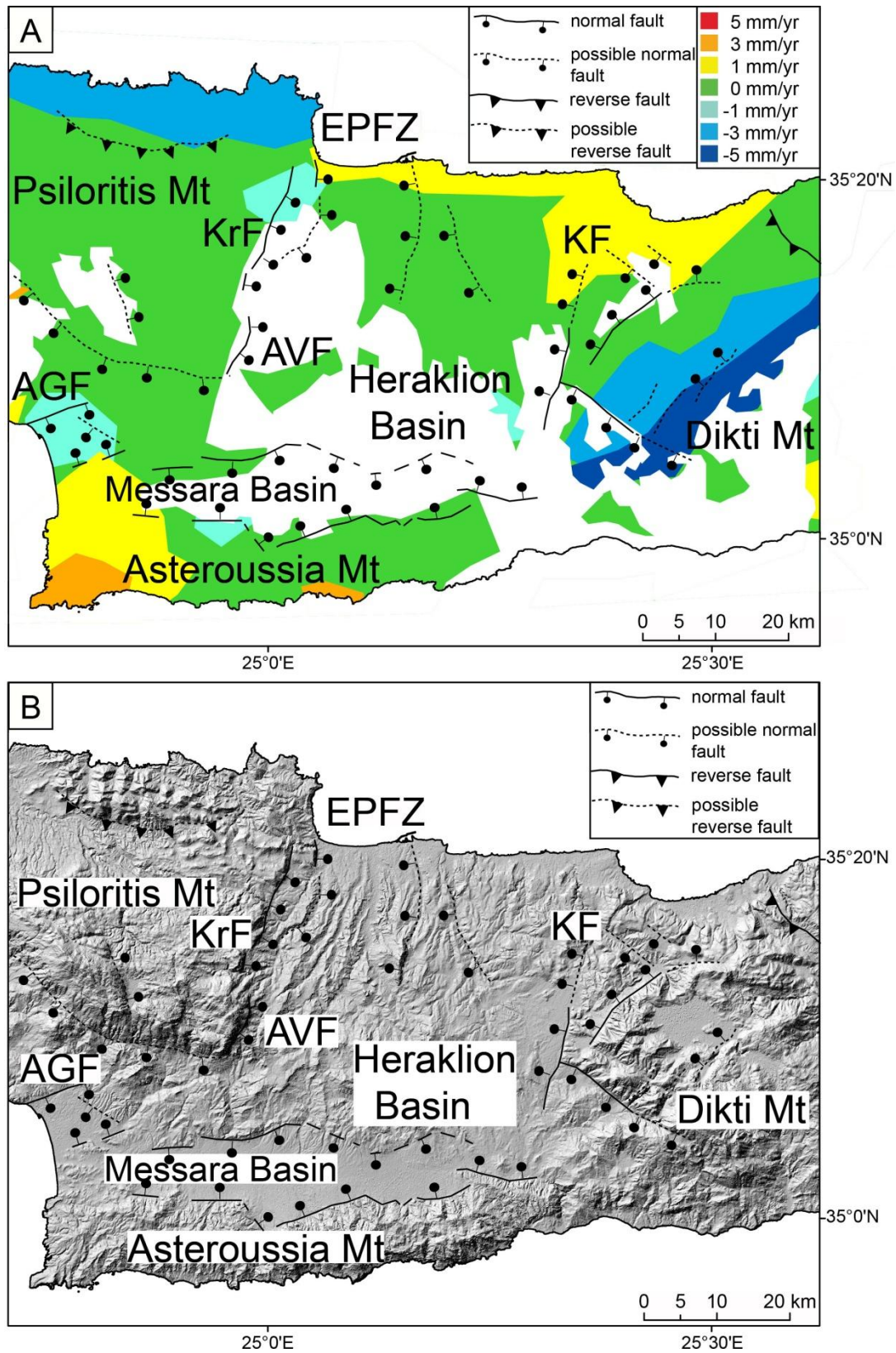


Figure 2.19: A) Simplified map of PSI measurements with faults. B) Topographic map with faults based on SPOT-DEM. AGF: Agia Galini Fault, EPFZ: Eastern Psiloritis Fault Zone, KrF: Kroussonas Fault, AVF: Agia Varvara Fault, and KF: Kastelli Fault.

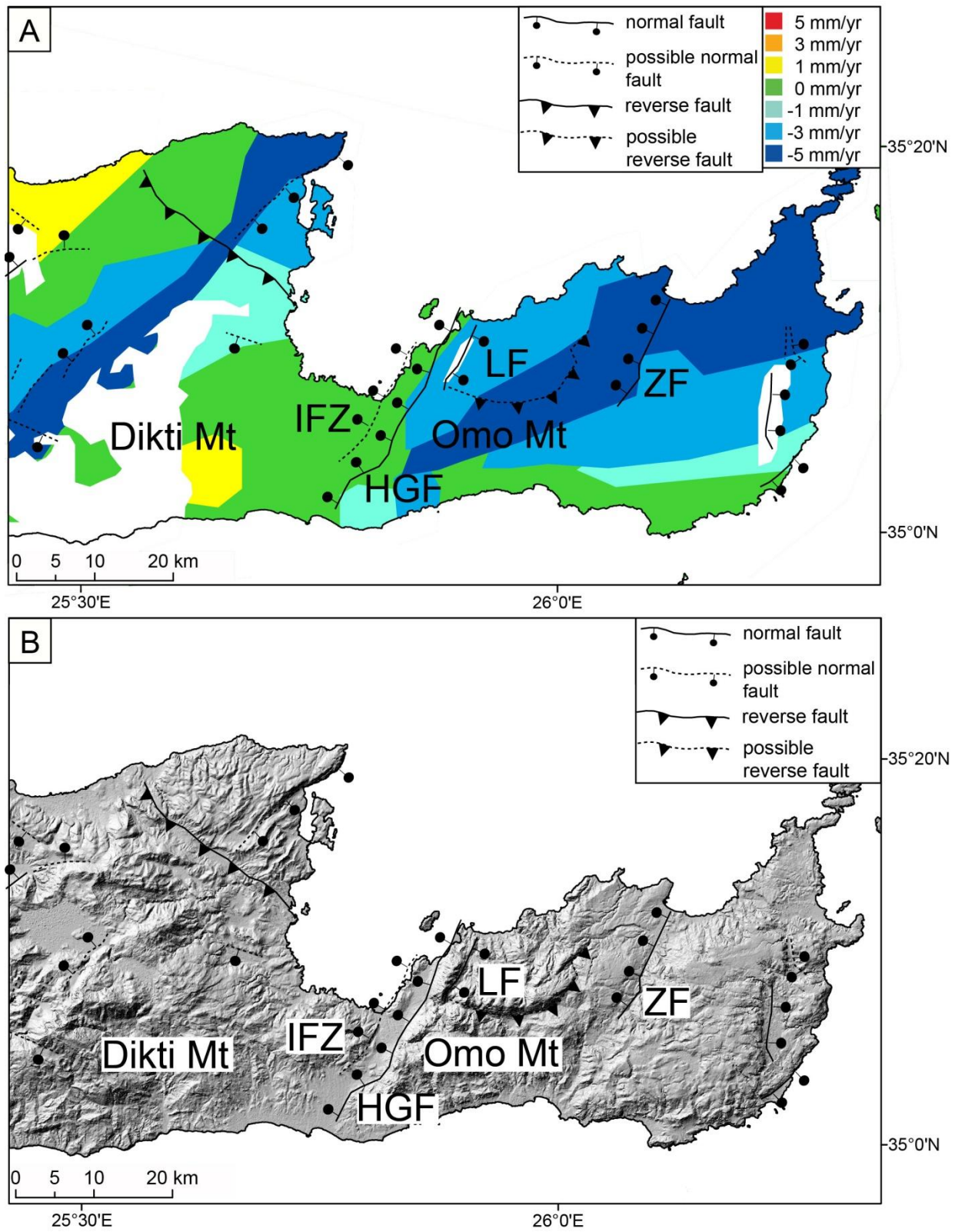


Figure 2.20: A) Simplified map of PSI measurements with faults. B) Topographic map with faults based on SPOT-DEM. IEZ: Ierapetra Fault Zone, HGF: Ha Gorge Fault, LF: Lastros Fault, and ZF: Zou Fault.

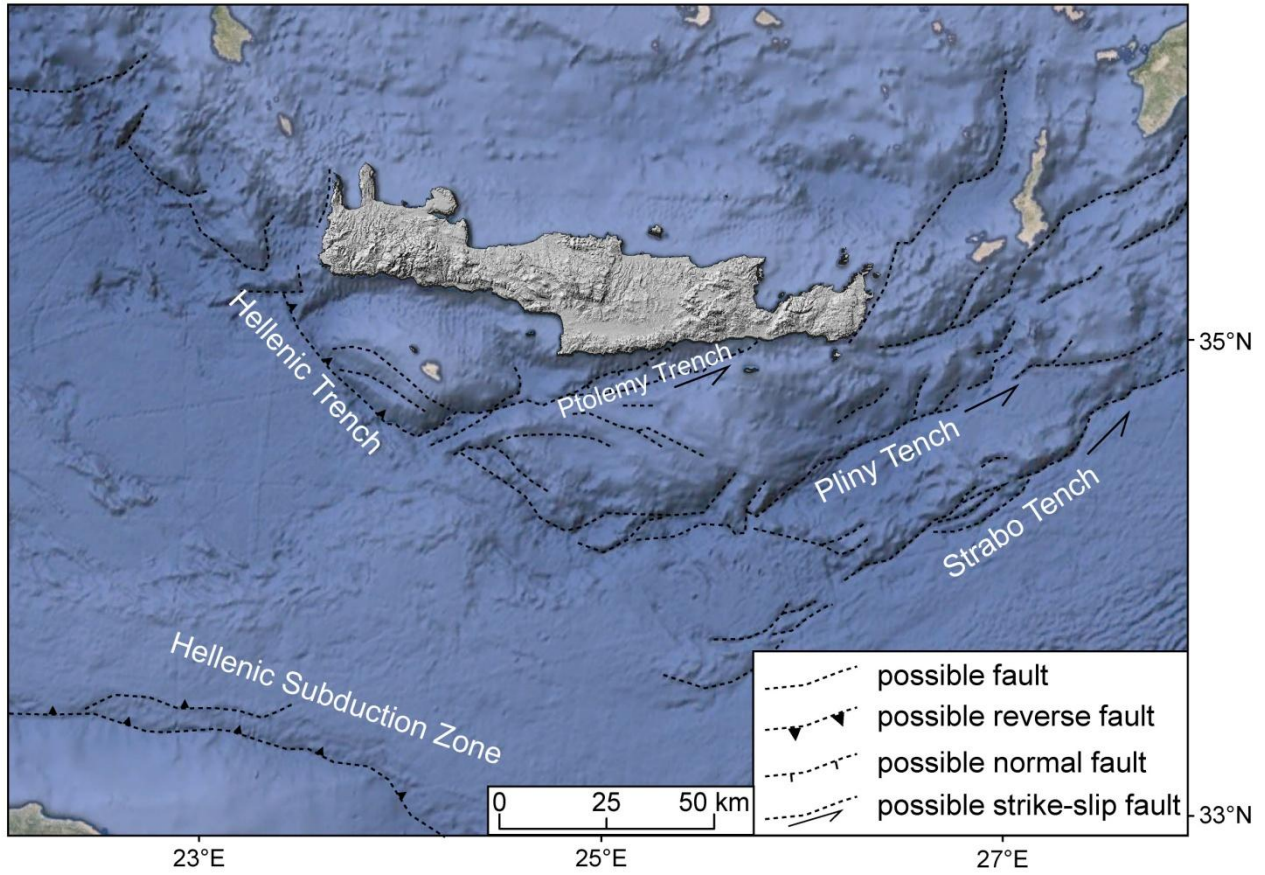
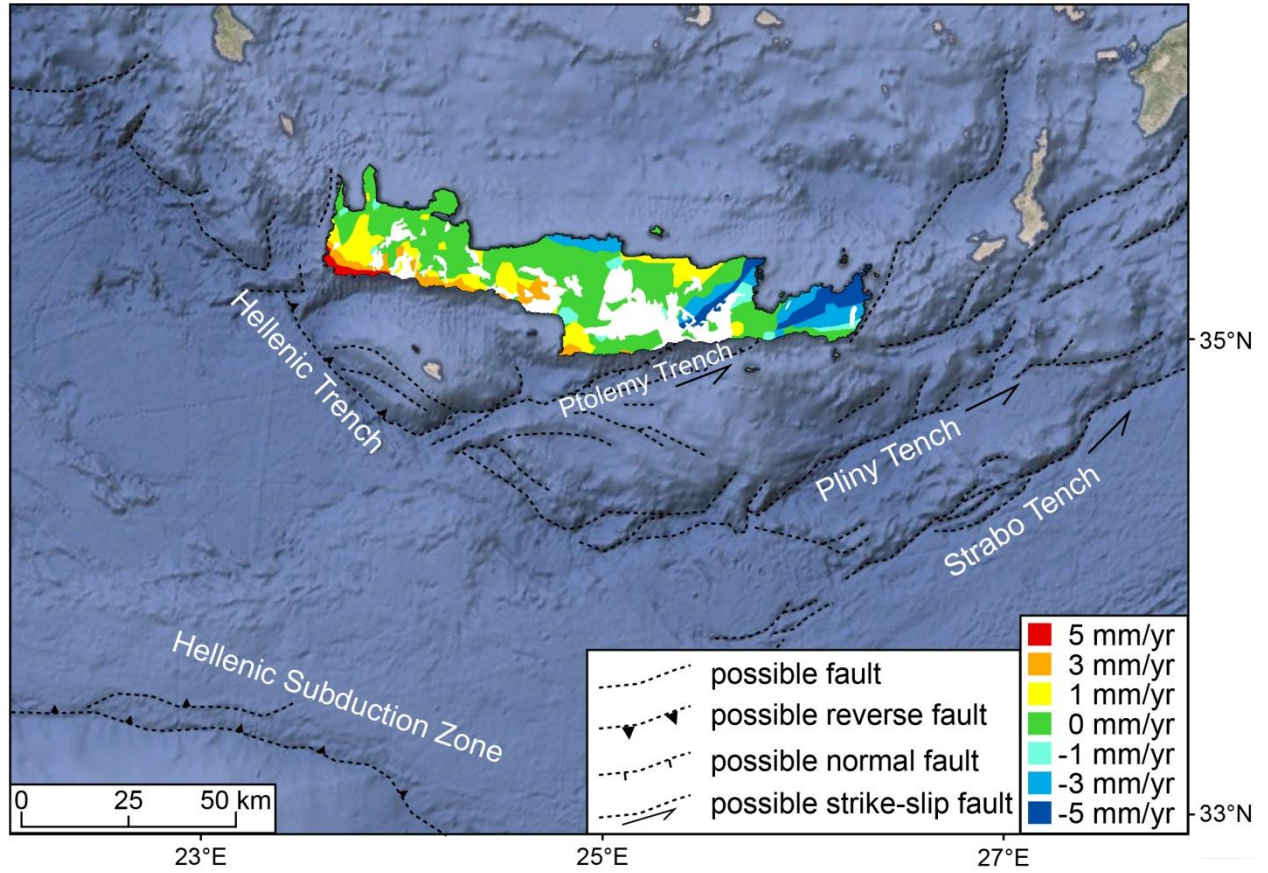


Figure 2.21: Topographic map of Crete superimposed to the bathymetry map and location of upper-crustal faults in the overriding plate based on data by Google Earth.



2.22: Simplified map of PSI measurements with bathymetry map and location of upper-crustal faults in the overriding plate based on data by Google Earth.

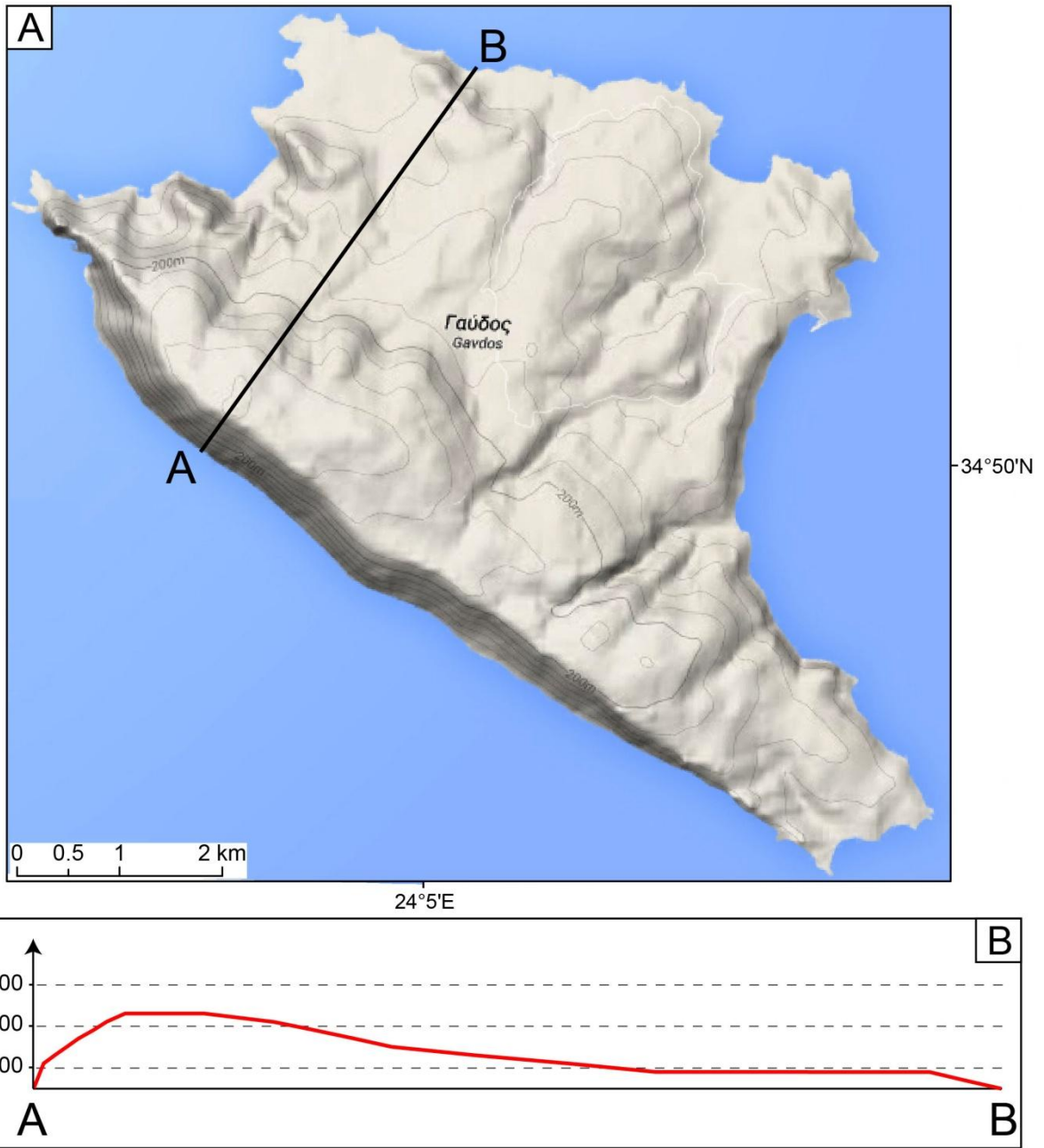


Figure 2.23: Topographic map and profile of Gavdos. A) Topographic map of Gavdos with the location of the profile line A to B. Map from Google maps. B) Topographic profile line from A to B.

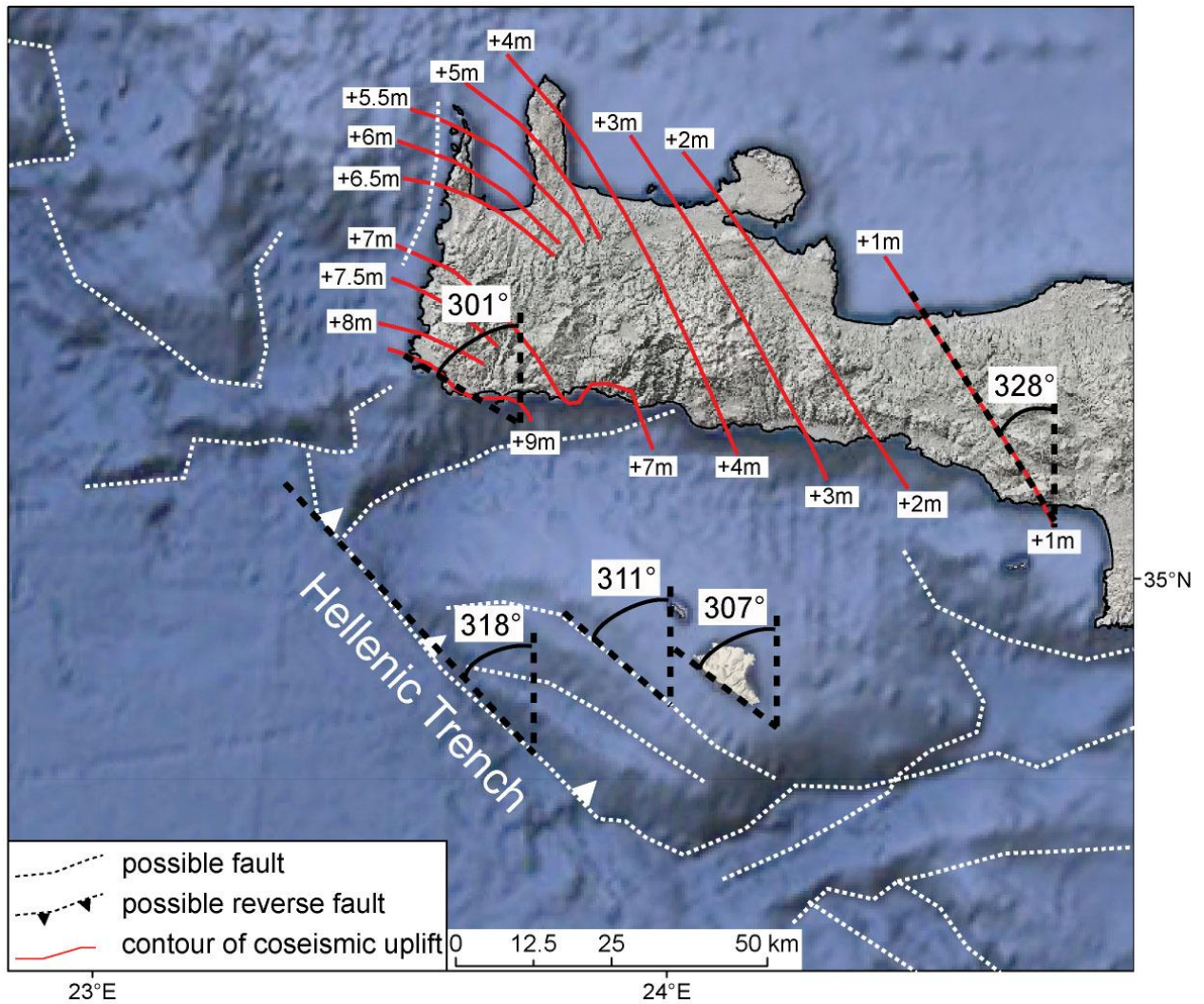


Figure 2.24: Bathymetry map of the Hellenic Trench, the location of Gavdos and the coseismic uplift contour line due to the 365 A.D. earthquake. Bathymetry map is from Google Earth. Topography map of Gavdos is from Google maps, and the hillshade of Crete is based on a SPOT-DEM.

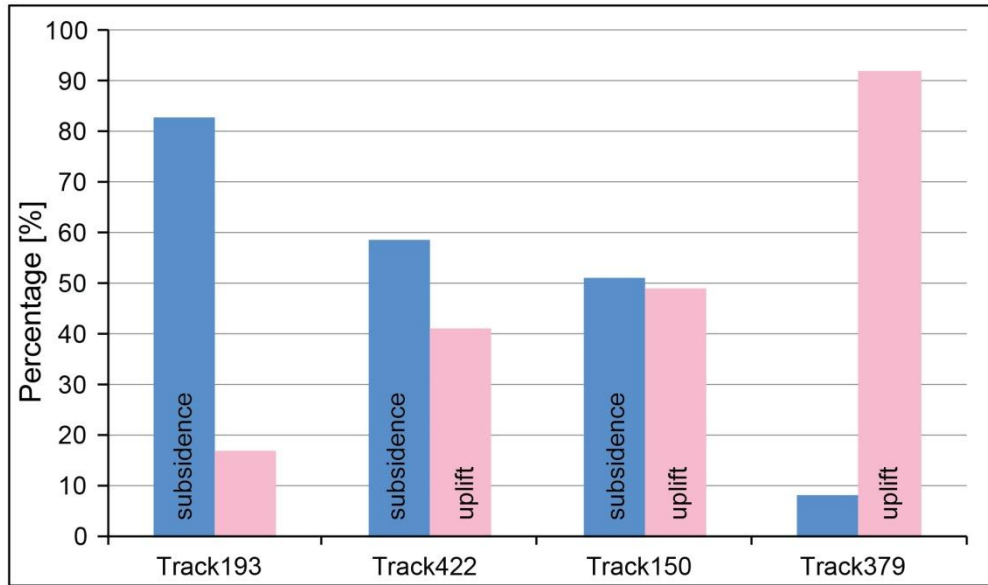


Figure 2.25: Percentage of uplifting versus subsidence PSs for each track from W to E Crete.

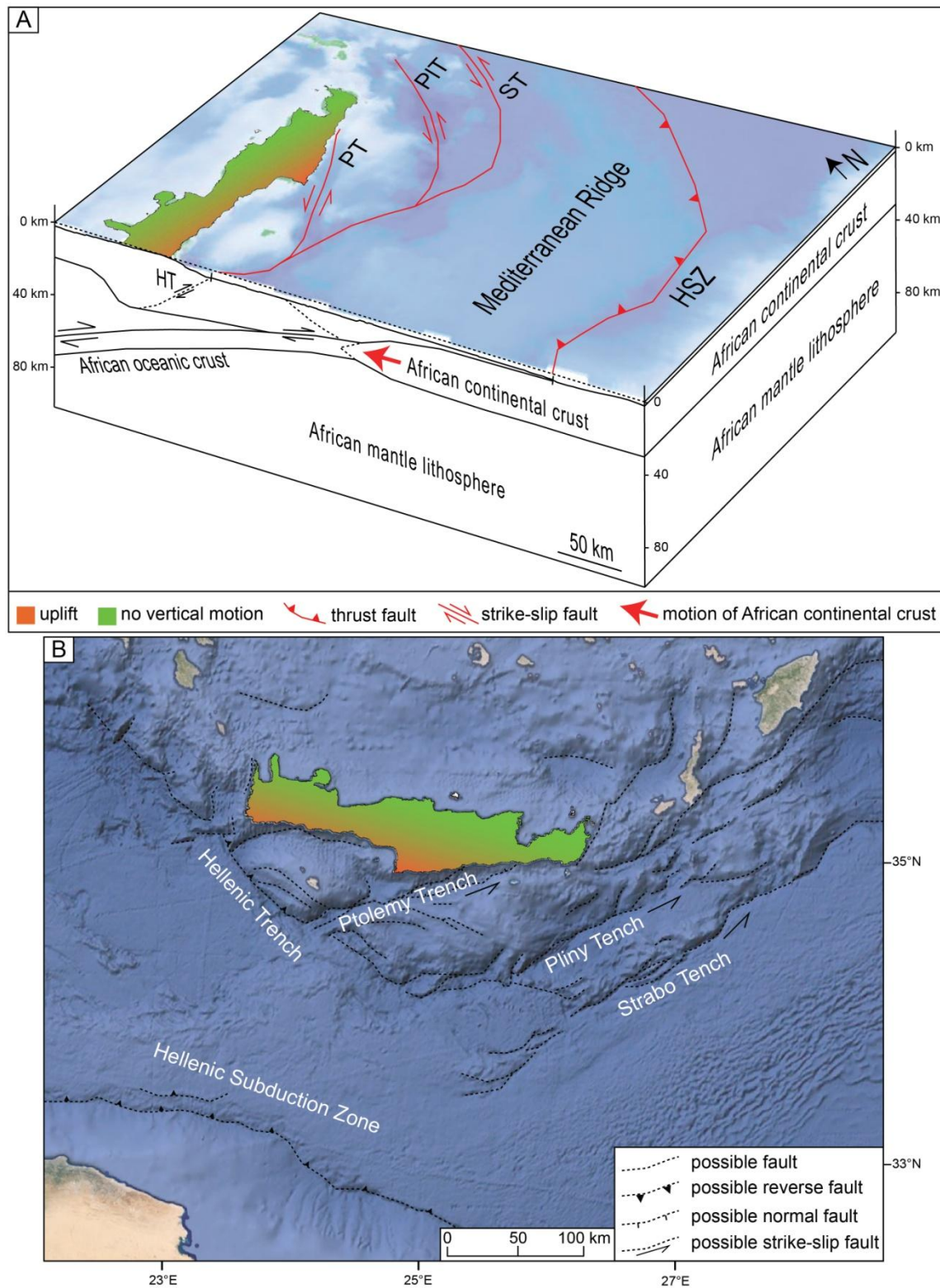


Figure 2.26: A) 3D block diagram for vertical surface deformation caused by the incipient continent-continent collision, for the profile A-B. B) Map view. Tectonic map after Chamot-Rooke et al. (2005). Background topography is derived from data of Smith and Sandwell (1997). Geological profile modified after Meier et al. (2004). HSZ: Hellenic subduction zone, HT: Hellenic Trench, PT: Ptolemy Trench, PIT: Pliny Trench, and ST: Strabo Trench.

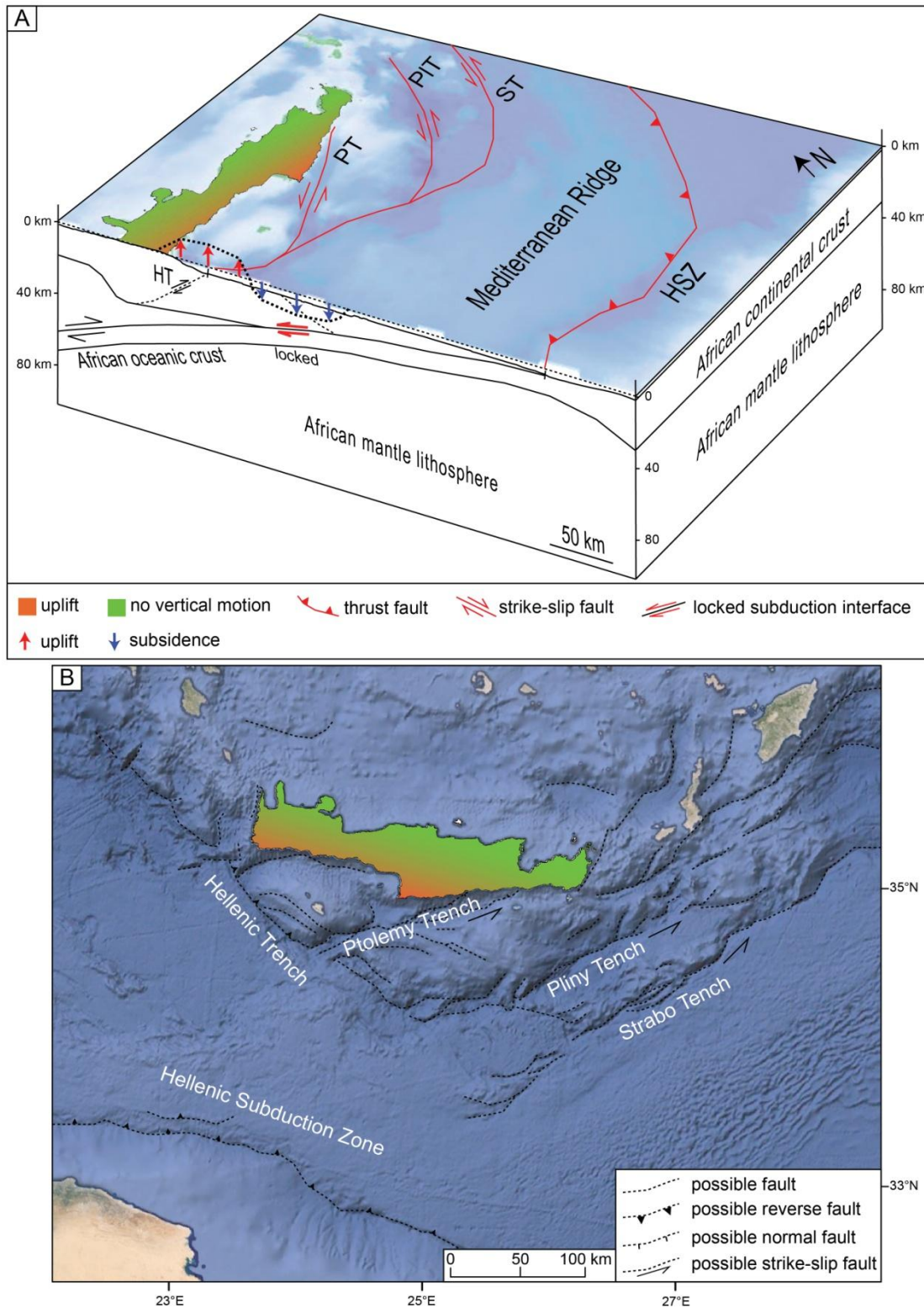


Figure 2.27: A) 3D block diagram for vertical surface deformation caused by subduction zone interface locking, for the profile A-B. B) Map view. Tectonic map after Chamot-Rooke et al. (2005). Background topography is derived from data of Smith and Sandwell (1997). Geological profile modified after Meier et al. (2004). HSZ: Hellenic subduction zone, HT: Hellenic Trench, PT: Ptolemy Trench, PIT: Pliny Trench, and ST: Strabo Trench.

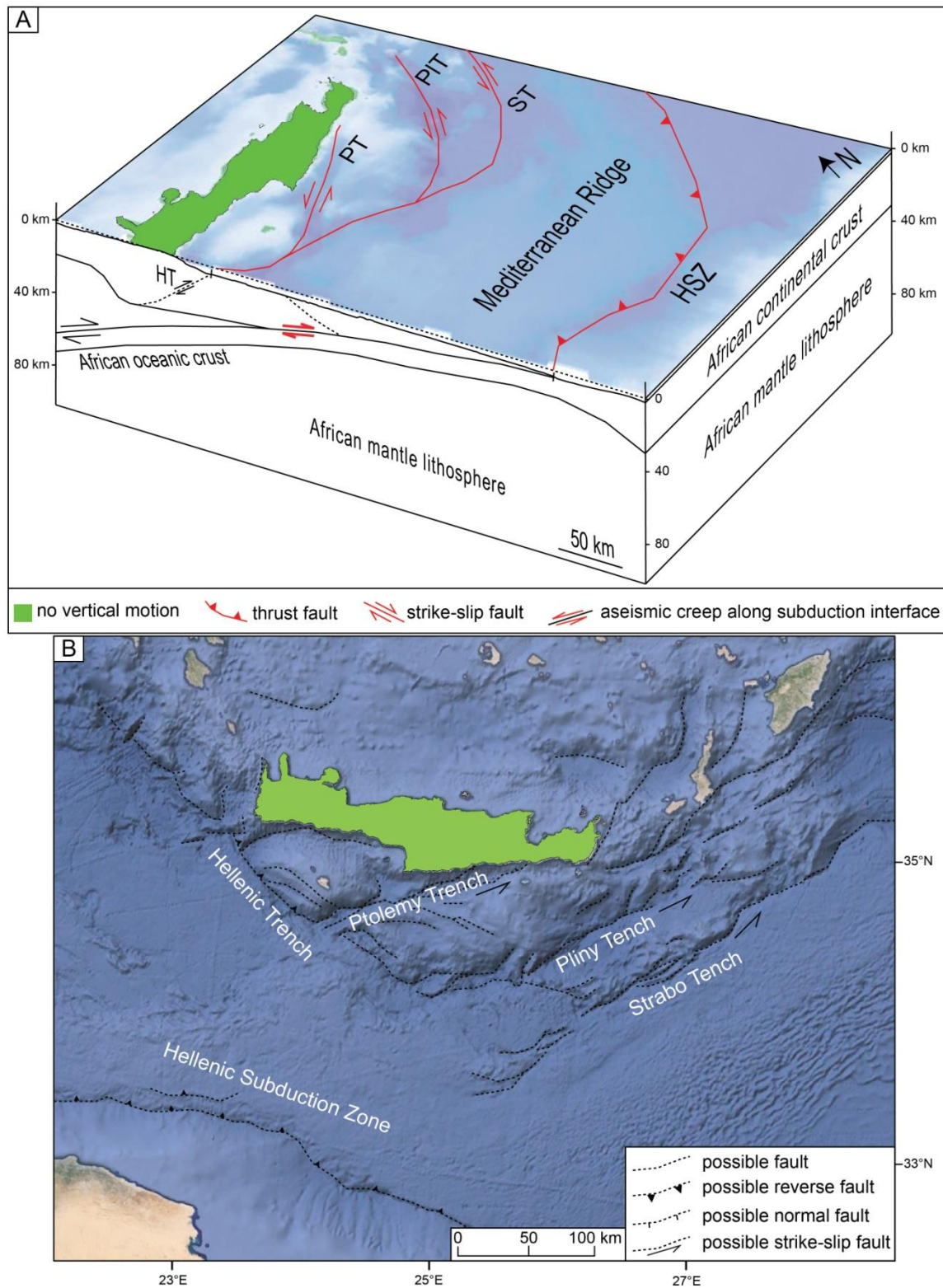


Figure 2.28: A) 3D block diagram for vertical surface deformation caused by aseismic creep along the subduction zone interface, for the profile A-B. B) Map view. Tectonic map after Chamot-Rooke et al. (2005). Background topography is derived from data of Smith and Sandwell (1997). Geological profile modified after Meier et al. (2004). HSZ: Hellenic subduction zone, HT: Hellenic Trench, PT: Ptolemy Trench, PIT: Pliny Trench, and ST: Strabo Trench.

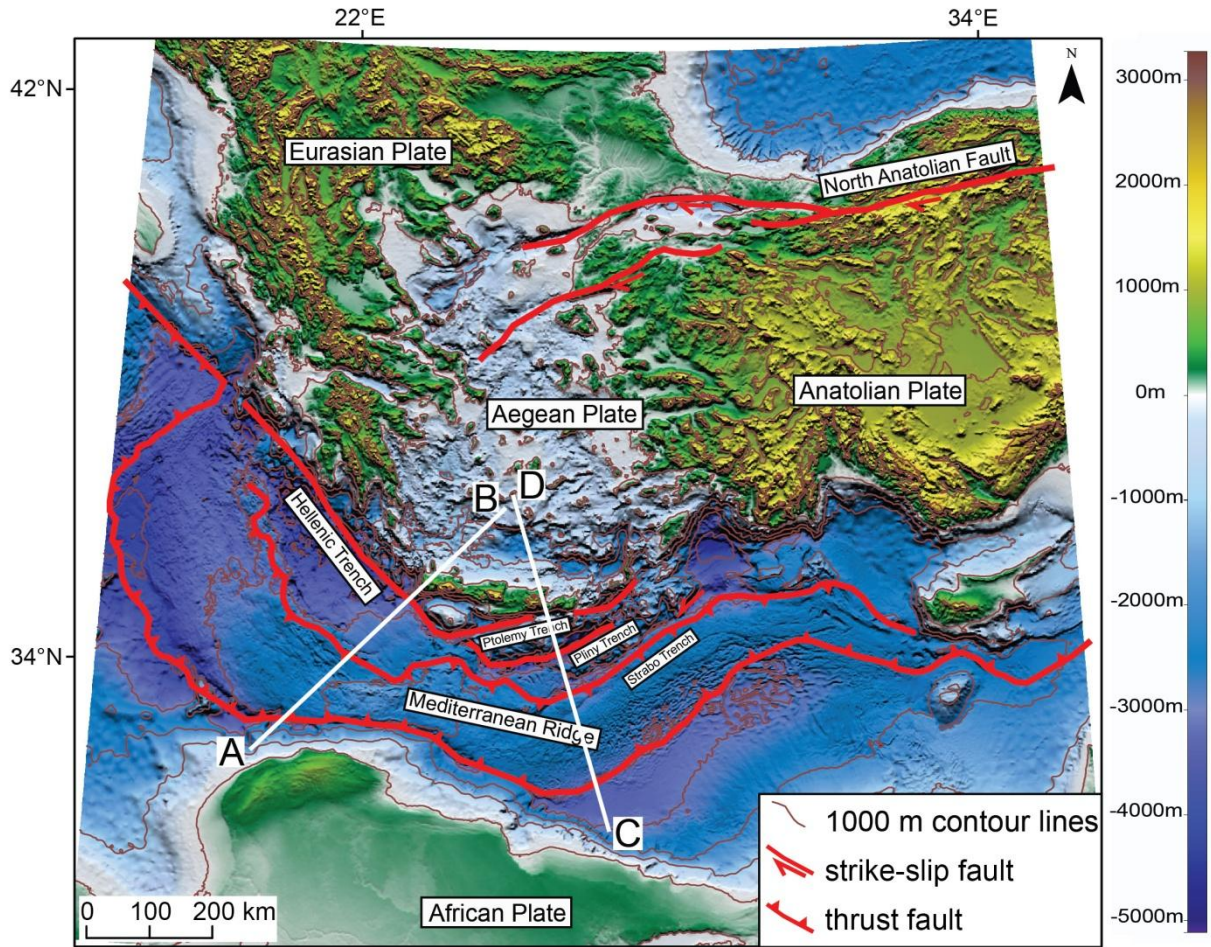


Figure 2.29: Tectonic map and profile lines. Tectonic map of the Eastern Mediterranean after Chamot-Rooke et al. (2005). Background topography is derived from data of Smith and Sandwell (1997). White lines represent the locations of the A-B and C-D profiles.

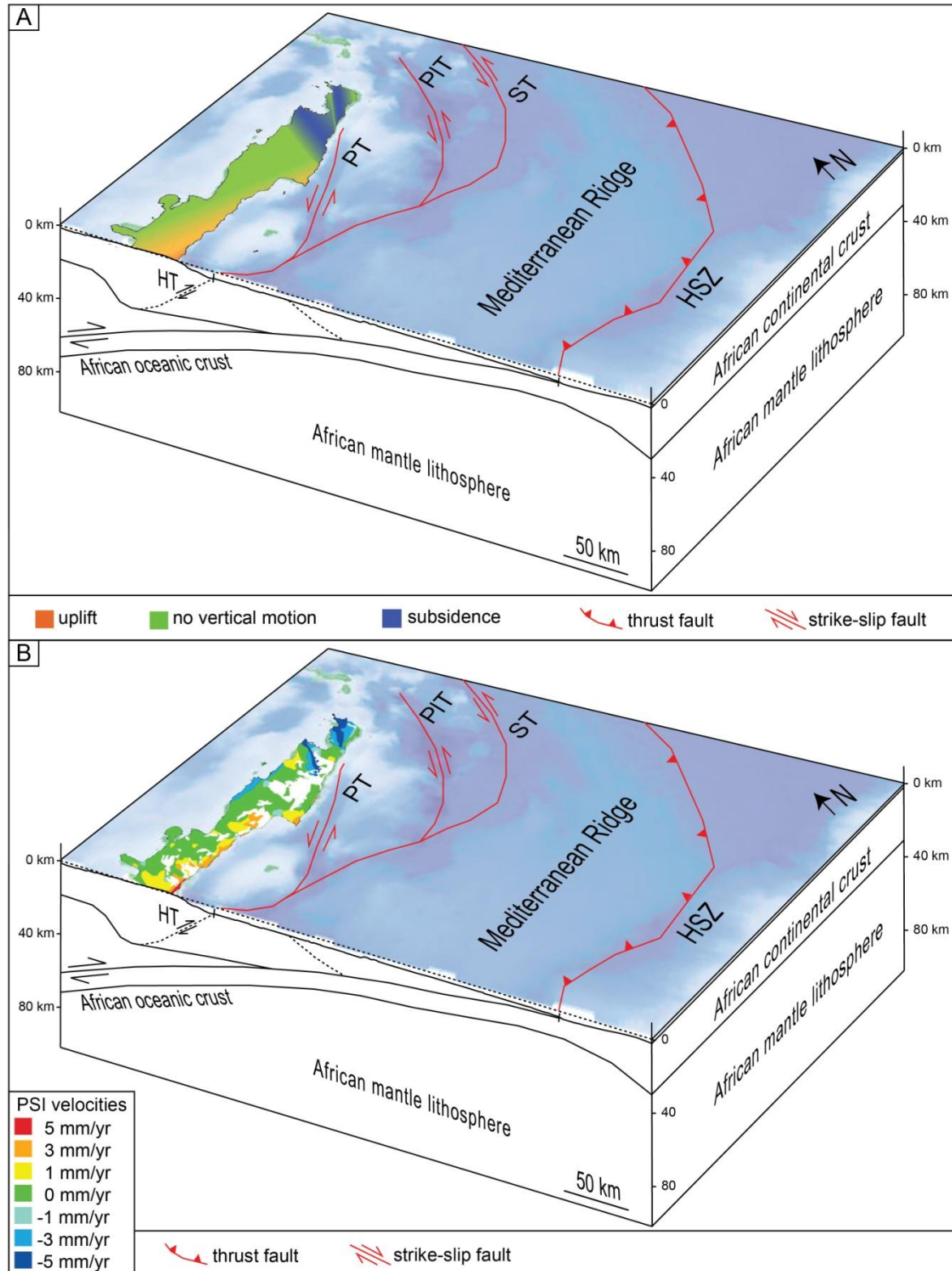


Figure 2.30 A) 3D block diagram for the vertical surface-deformation caused by major faults in the overriding plate, for the profile A-B. B) PSI results for the profile A-B. Tectonic map after Chamot-Rooke et al. (2005). Background topography is derived from data of Smith and Sandwell (1997). Geological profile modified after Meier et al. (2004). HSZ: Hellenic subduction zone, HT: Hellenic Trench, PT: Ptolemy Trench, PIT: Pliny Trench, and ST: Strabo Trench.

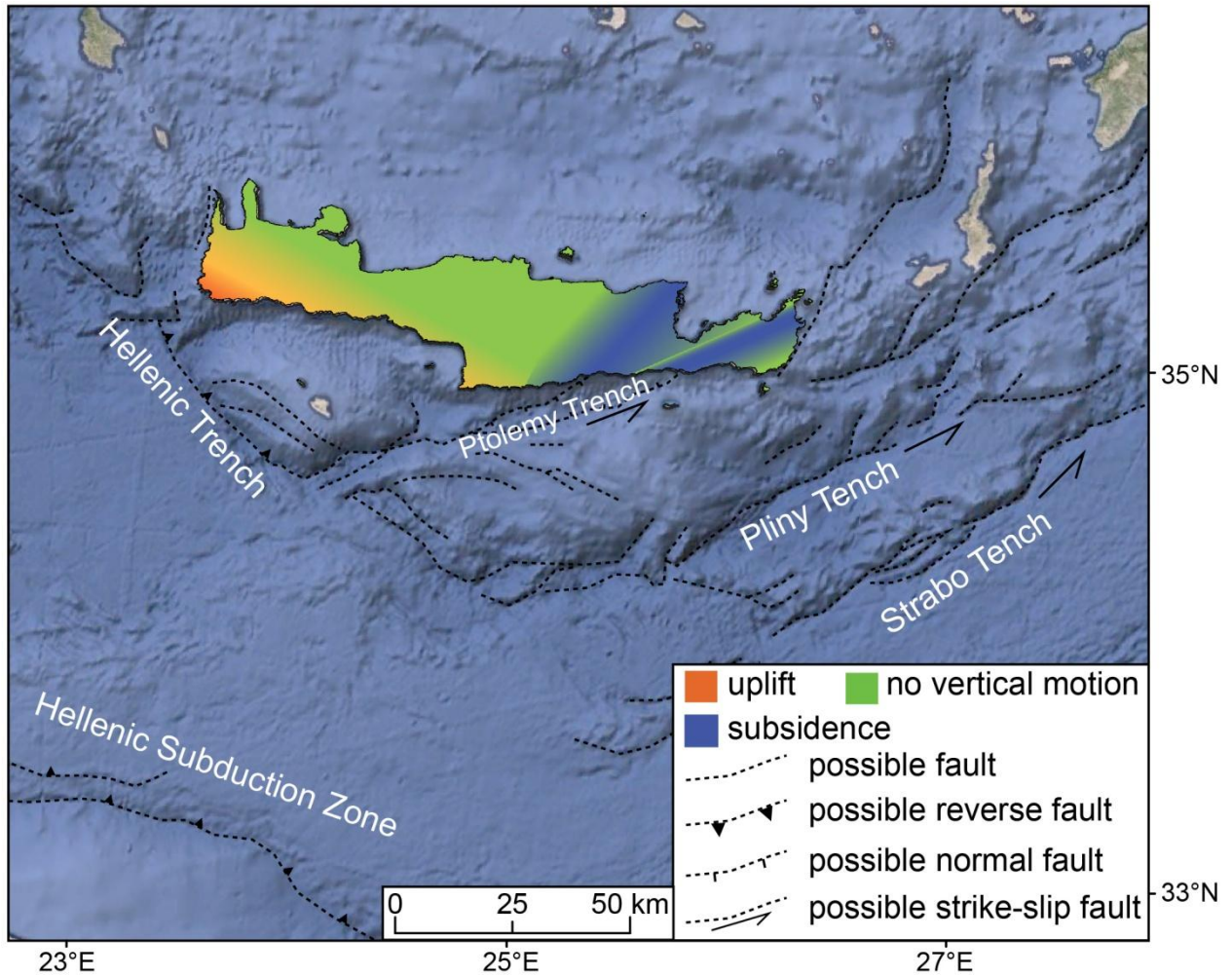


Figure 2.31: Map view for the vertical surface-deformation caused by major faults in the overriding plate. Tectonic map after Chamot-Rooke et al. (2005). Background topography is derived from data of Smith and Sandwell (1997).

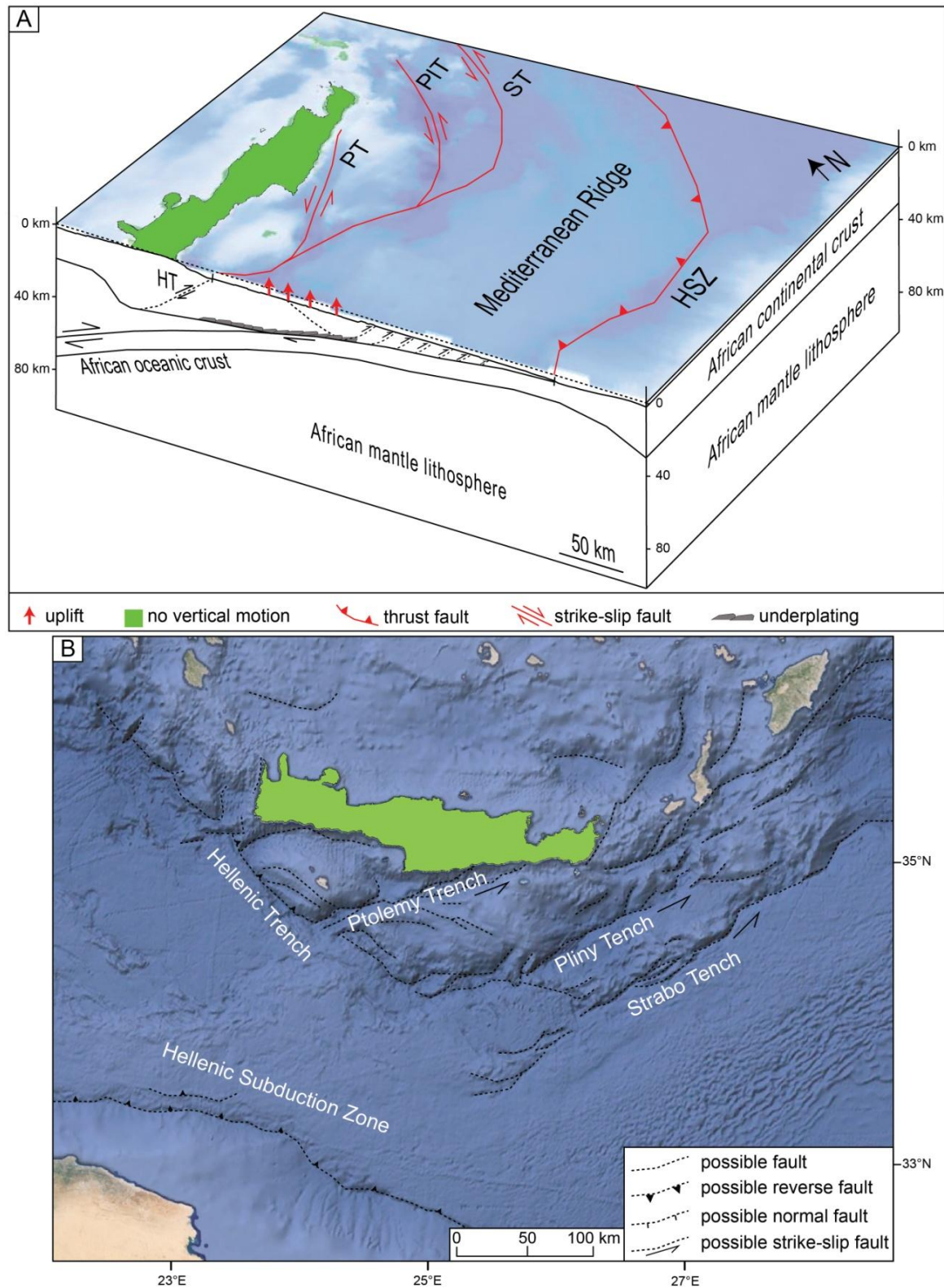


Figure 2.33: A) 3D block diagram for vertical surface deformation caused by underplating, for the profile A-B. B) Map view. Tectonic map after Chamot-Rooke et al. (2005). Background topography is derived from data of Smith and Sandwell (1997). Geological profile modified after Meier et al. (2004). HSZ: Hellenic subduction zone, HT: Hellenic Trench, PT: Ptolemy Trench, PIT: Pliny Trench, and ST: Strabo Trench.

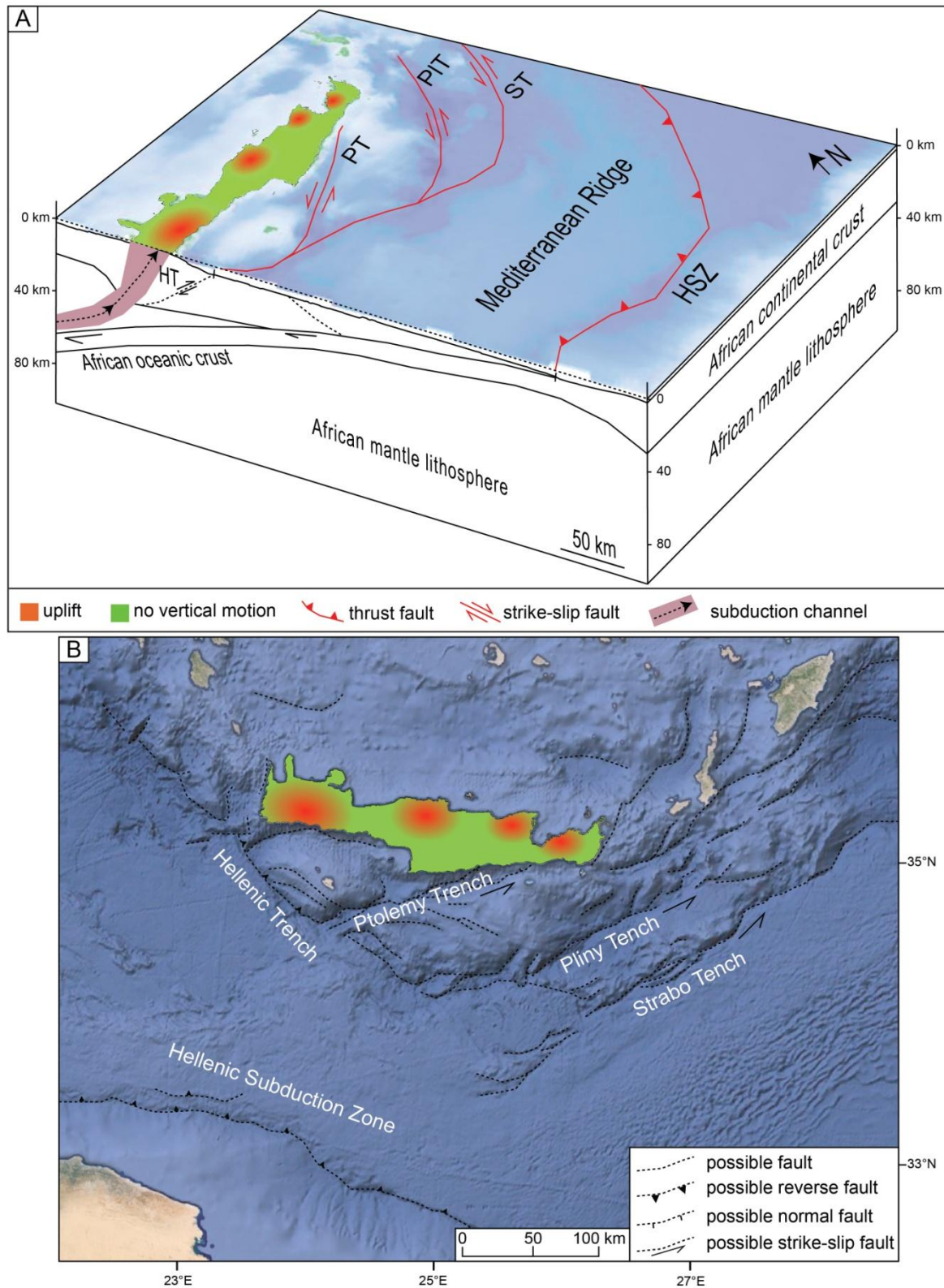


Figure 2.34: A) 3D block diagram for vertical surface deformation caused by return flow along the subduction channel, for the profile A-B. B) Map view. Tectonic map after Chamot-Rooke et al. (2005). Background topography is derived from data of Smith and Sandwell (1997). Geological profile modified after Meier et al. (2004). HSZ: Hellenic subduction zone, HT: Hellenic Trench, PT: Ptolemy Trench, PIT: Pliny Trench, and ST: Strabo Trench.

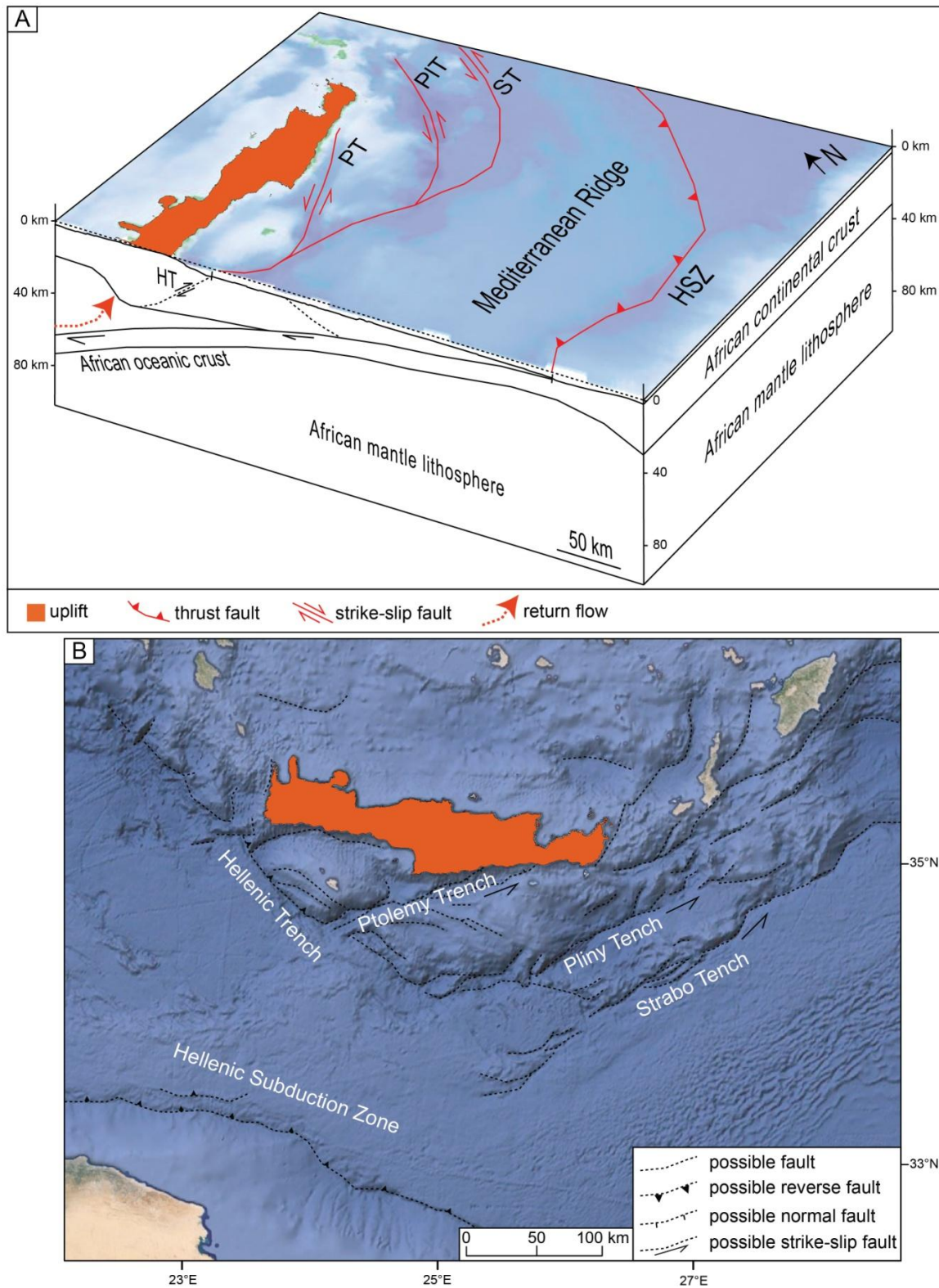


Figure 2.35: A) 3D block diagram for vertical surface deformation caused by return flow, for the profile A-B. B) Map view. Tectonic map after Chamot-Rooke et al. (2005). Background topography is derived from data of Smith and Sandwell (1997). Geological profile modified after Meier et al. (2004). HSZ: Hellenic subduction zone, HT: Hellenic Trench, PT: Ptolemy Trench, PIT: Pliny Trench, and ST: Strabo Trench.

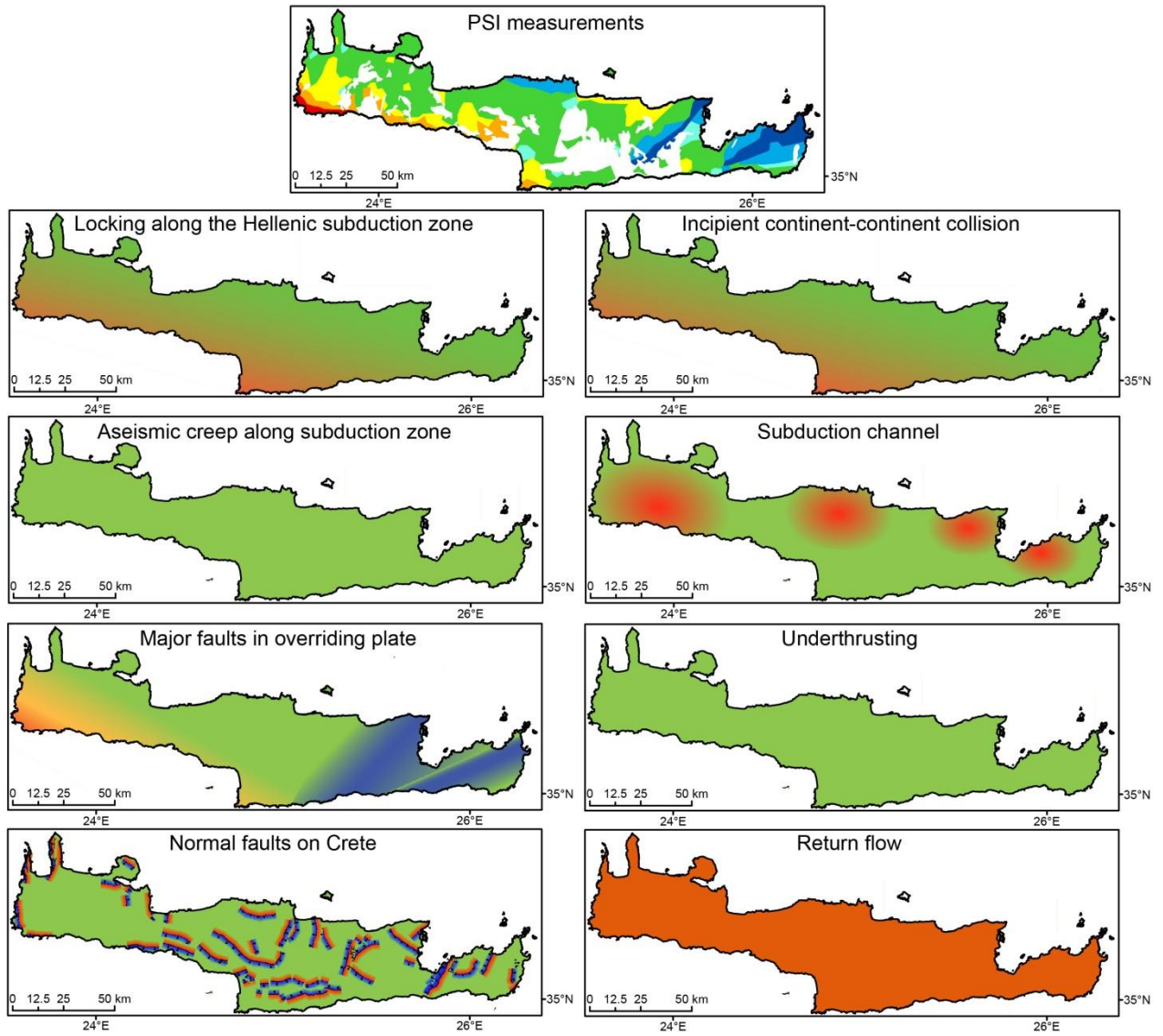


Figure 2.36: All possible hypotheses explaining the uplift of Crete.

Table 2.1: Time span of GPS measurements on Crete.

GPS station	Total time span	First observation [day of year]	Last observation [day of year]
IERA	1145 d = ~3.1 yr	2010 / 180	2013 / 229
HERA	1075 d = ~2.9	2010 / 250	2013 / 229
NEAP	731 d = ~2.0 yr	2008 / 345	2010 / 303
RETH	617 d = ~1.6 yr	2011 / 343	2013 / 229
TUC2	3247 d = ~8.9 yr	2004 / 270	2013 / 229

Table 2.2: The estimation precision lower bound for the four tracks of Crete.

	Track 193	Track 422	Track 150	Track 379
Number of images	39	24	24	31
Number of interferograms (N)	38	23	23	30
estimation precision (σ_{defo}) [mm/yr]	0.70	0.90	0.90	0.79

Table 2.3: GPS measurements relative to stable Europe.

GPS Station	Long [°]	Lat [°]	v_{north} [mm/yr]	v_{east} [mm/yr]	v_{up} [mm/yr]
IERA	25.79723	35.05307	-29.77 ± 0.62	-9.71 ± 0.63	0.56 ± 2.56
RETH	24.61308	35.38776	-8.14 ± 6.15	-4.27 ± 6.15	-0.22 ± 6.15
HERA	25.14150	35.32413	-22.62 ± 0.65	-20.07 ± 0.65	6.27 ± 2.57
NEAP	25.61037	35.26135	-31.68 ± 0.59	-17.25 ± 0.58	9.25 ± 2.41
TUC2	24.07056	35.53319	-24.64 ± 0.07	-12.56 ± 0.12	-0.99 ± 0.23

Table 2.4: Total number of all measured PSs per track, how many are uplifting, stable or subsiding.

Track	PSs total	$v_{vertical} > 0$	$v_{vertical} = 0$	$v_{vertical} < 0$
193	159870	132592	39	27239
422	118435	69473	24	48937
150	47476	24280	10	23186
379	95534	7734	13	87787
All Tracks	421315	234079	86	187149

Table 2.5: Percentage of all measured PSs per track, how many are uplifting, stable or subsiding.

Track	$v_{up} > 0$	$v_{up} = 0$	$v_{up} < 0$
193	82.94 %	0.02 %	17.04 %
422	58.66 %	0.02 %	41.32 %
150	51.14 %	0.02 %	48.84 %
379	8.10 %	0.01 %	91.89 %
All Tracks	55.56 %	0.02 %	44.42 %

Chapter 3

DETECTION OF ACTIVE MOTION ACROSS NORMAL FAULTS ON CRETE

3.1 Abstract

I explore the applicability of the Persistent Scatterer technique beyond urban areas, on a regional spatial-scale and decadal temporal-scale. I detected the vertical motion of > 400.000 PSs across the island, but the distribution of PS locations is heterogeneous. PSI results are most robust on bedrock carbonate exposures, while vegetated regions yield no correlation, and soil-dominated locales appear to yield partial returns. Because bedrock exposures are ubiquitous across the island, PSI results are robust over large coherent regions. Therefore, the PSI pattern across the island may be used to study local-scale signals at mm-level accuracy. I identified abundant localized zones of high surface strain, particularly in the central and eastern portion of the island to derive the vertical surface motion across normal faults during the interseismic period. I detected displacement between 0.05 to 2.2 mm/yr across these normal faults. Further, I observed reverse motion along three normal faults, implying that the hanging wall is apparently uplifting with respect to the footwall. I cannot distinguish whether this transient signal is caused by aseismic creep or by swelling of clay minerals. Additional data across these hanging walls, concerning the clay mineral content in the soil, would help to distinguish the possible reason for the transient signal.

3.2 Introduction

Quantification of vertical motion of the Earth's surface is crucial to characterized ongoing tectonic processes along upper-crustal faults. Geodetic observations, such as PSI measurements, permit the dense detection of vertical surface-deformation on large scales, such as the surface-deformation pattern across Crete (as described in the previous Chapter), and also the detection on small scales, such as across upper crustal faults.

The detection of vertical surface-motion is of special significance on Crete, due to its proximity to the Hellenic subduction zone. It represents one of the few places where the forearc high is exposed subaerially. Along a forearc high tectonic processes from different faults are superimposed. These superimposed processes are a composition of tectonic processes along the main subduction zone interface, major faults in the overriding plate, and small scale upper-crustal faults.

Crete is characterized by a horst and graben structure separated by normal faults. The horsts are of pre-Neogene age and the grabens are filled with Neogene and syn-tectonic, marine and continental sediments (Figure 3.1) (Hall et al., 1984; van Hinsbergen and Meulenkamp, 2006).

Normal faults can be separated into two groups based on their orientation. The first group of normal faults strikes in WNW-ESE direction, and is located mainly along the southern coast and in Central Crete (Figure 3.1). These faults are: the Sfakia fault (SfF), the Asomatos fault (AF), and the Spili fault (SpF). The second group of normal faults is uniformly distributed over the whole island (Figure 3.1), and strikes in NNE-SSW direction.

Paleoseismic studies along some of the normal faults, indicate $M_w > 6$ earthquakes along the Spili and Kera fault (Mouslopoulou et al., 2001; Mouslopoulou et al., 2014). Also Caputo et

al. (2010), estimates magnitudes between 6.0 and 6.7 to be responsible for the throw measured along the fault scarp.

Geodetic measurements on normal faults are mostly carried out using GPS horizontal measurements, e.g. for the Basin and Range (Niemi et al., 2004). The accuracy of GPS horizontal measurements is on the order of < 1 mm and is two to three times less precise for the vertical component (Segall and Davis, 1997; Bürgmann et al., 2000). Therefore, GPS measurements of the vertical component along normal faults are not very reliable. Some InSAR investigations were done along normal faults, but temporal close to an earthquake due to decorrelation of the InSAR phase signal (Zebker and Villasenor, 1992; Hanssen, 2001; Elliott et al., 2010).

Analyses of the vertical surface-deformation along normal faults using PSI during the interseismic period are not carried out until now.

In this chapter I present the first PSI study of vertical surface-deformation along normal faults on Crete. I analyse the vertical surface-deformation of the footwall and the hanging wall on 13 normal faults on Crete to measure the motion during the interseismic period across these faults. I further analyzed the PSs density distribution with the lithological units. Finally, I compared the geodetic deformation to the average long-term slip rate for the last 13 ka before present (B.P.), based on data by Caputo et al. (2010).

3.3 Geological Setting

Crete represents one of the few places where the forearc high is exposed subaerially close to a subduction zone. The island consists of several nappes, which can be divided in the lower and upper unit according to their tectono-metamorphic history, and Neogene sediments (Figure 3.1).

The lower unit experienced Early Miocene high-pressure/ low-temperature (HP/LT) metamorphism, with peak conditions of 10 ± 2 kbar and $400 \pm 50^\circ$ C (Thomson et al., 1998), whereas the upper unit is unmetamorphosed, both units are separated by a low-angle detachment (Fassoulas et al., 1994; Jolivet et al., 1996).

The footwall consists of the carbonate rocks of the Plattenkalk unit. This unit is overlain by the clastic, partly carbonate Phyllite-Quartzite nappe (Thomson et al., 1998; Papanikolaou and Vassilakis, 2010) (Figure 3.2).

The Plattenkalk unit represents a Permian to Oligocene sedimentary cover of the former southern margin of the colliding Apulian microcontinent (Figure 3.2) (Hall et al., 1984; Thomson et al., 1998). Triassic stromatolitic dolomites form the base of this unit, indicate inter-tidal sedimentation on continental crust (Hall et al., 1984).

The Phyllite-Quartzite nappe consists of Late Carboniferous to Middle Triassic sedimentary rocks, which represent the Apulian microcontinent (Figure 3.2) (Thomson et al., 1998). The Phyllite-Quartzite unit consists of continental to shallow marine siliciclastics, partly carbonates and evaporitic sedimentary rocks (Hall et al., 1984; Thomson et al., 1998). These rocks were intensively deformed under HP/LT conditions (Stöckhert et al., 1999).

The hanging wall represents the unmetamorphosed units consisting from bottom to top of the Tripolitza unit, Pindos unit and the Uppermost unit (Thomson et al., 1998).

The Tripolitza unit consists of proximal shallow-water platform carbonates of Upper Triassic to Middle Eocene (Figure 3.2) (Hall et al., 1984; Jolivet et al., 1996) overlain by Tertiary flysch (Jacoshagen, 1986; Thomson et al., 1998). This unit represents the northern continental margin of the Apulian microcontinent (Thomson et al., 1998). The Tripolitza unit is the

unmetamorphosed continuation of the Phyllite-Quartzite unit (Thomson et al., 1998; Van Hinsbergen et al., 2005).

The Pindos unit occurs above the Tripolitza unit and consists of a succession of pelagic limestone and radiolarite of late Triassic to Palaeocene age (Figure 3.2) (Hall et al., 1984). This unit of sedimentary basin rocks represents the former more distal part of the continental margin (Hall et al., 1984; Thomson et al., 1998).

The Uppermost unit represents a mélangé formed by oceanic pillow basalt, gabbro, deep-water carbonate and chert, serpentinite, clastic sedimentary rocks and metamorphic rocks (Figure 3.2) (Thomson et al., 1998).

Neogene sediments are composed of syn-tectonic, marine, and continental sediments (Figure 3.2) (van Hinsbergen and Meulenkamp, 2006; Papanikolaou and Vassilakis, 2010).

The distribution of the lithologic units across Crete shows that western Crete the dominant lithologic unit is Plattenkalk, followed by Phyllite-Quartzite, and the Tripolis unit (Figure 3.2). In central Crete the lithologic units are heterogeneously distributed. The basins are filled with sediments. The eastern part of Crete is more dominated by Plattenkalk and the Tripolis unit.

3.4 Normal Faults across Crete

The first group of faults is located along the S coastline of Crete. SE of the Lefka Ori mountains the Sfakia fault (SfF) (Figure 3.1) (Pirazzoli, 1982, Caputo et al., 2010) separates the coastal plain from the Lefka Ori mountains in the north. The footwall consists of Plattenkalk and Phyllite-Quartzite, and the hanging wall of Phyllite-Quartzite and marine sediments (Figure 3.3).

Adjacent to SfF is the Asomatos normal fault (AF) (Caputo et al., 2010) trending in WNW-ESE direction facing towards the SWS (Figure 3.1). The footwall consists of Tripolis, and the hanging wall consists of Phyllite-Quartzite, and Tripolis (Figure 3.4).

The Spili fault (SpF) is located east of the AF (Angelier, 1979, Caputo et al., 2010) (Figure 3.1). The footwall and hanging wall of SpF both consist of Pindos and marine sediments. The motion along SpF is reverse (Figure 3.5).

Along the NW coastline the Gramvousa peninsula is dominated by the Gramvousa normal fault (Grf) (Armijo et al., 1992; Caputo et al., 2010) (Figure 3.1). The footwall consists of marine sediments, and the hanging wall consists of marine, Holocene-Pleistocene sediments (Figure 3.6).

The Rodopos peninsula E of the Gramvousa peninsula is dominated by the Rodopos Fault Zone (RFZ), consisting of the Gionas normal fault (GF) (Figure 3.1), in the north of the peninsula, the Rodopos normal fault (RF), and the Kera normal fault (KeF) in the southern part of the peninsula (Armijo et al., 1992; Caputo et al., 2010). The footwall and the hanging wall of GF consists Tripolis (Figure 3.7). The footwall of RF consists of Tripolis and marine sediments, and the hanging wall of Tripolis (Figure 3.8). The footwall and the hanging wall of KeF consists Phyllite-Quartzite and Tripolis (Figure 3.9).

The Heraklion basin is terminated from the Psiloritis Mountains by the Eastern Psiloritis Fault Zone (EPFZ) in the W (Figure 3.1) (Fassoulas, 2001; Caputo et al., 2010). The fault zone compromises the Kroussonas normal fault (KrF) in the middle, and the Agia Varvara normal fault (AvF) in the S. The footwall of KrF consists of Tripolis, and the hanging wall of marine sediments (Figure 3.10). The footwall and the hanging wall of the AvF consist of Tripolis (Figure 3.11).

Towards the east the Heraklion basin is bordered by the Kastelli fault (KF) and separates the basin from the Dikti Mountains in the east (Figure 3.1) (Caputo et al., 2010). The footwall of

KF consists of Plattenkalk, and the hanging wall of Plattenkalk and Holocene-Pleistocene sediments (Figure 3.12).

The Dikti Mountains are separated of the Omo Mountains in the E by the Ierapetra Fault Zone (IFZ) (Figure 3.1) (Armijo et al., 1992; Le Pichon et al., 2002, Caputo et al., 2010). The IFZ consists of several faults (Caputo et al., 2010) most prominent are the Ha Gorge normal fault (HGF) and the Lastros normal fault (LF). The footwall of HGF consists of Plattenkalk and Holocene-Pleistocene sediments, and the hanging wall consists of Holocene sediments (Figure 3.13). The footwall of LF (Figure 3.14) consists of Plattenkalk and marine sediments, the hanging wall consists of Plattenkalk, Tripolis, and marine sediments.

East of IFZ is the Zou normal fault (ZF) located (Figure 3.1) (Armijo et al., 1992; Le Pichon et al., 2002; Caputo et al., 2010). The footwall of ZF (Figure 3.15) consists of Tripolis, marine, and Holocene-Pleistocene sediments, the hanging wall consists of marine and Holocene-Pleistocene sediments.

3.5 Methods

I analysed the PSs deformation measurements in the line-of-sight (LOS) (Figure 3.17) across faults, respectively for the footwall and hanging wall. I measured PSs velocities across from the faults, perpendicular to the strike of the fault (Figure 3.18).

I assume that the identified PSs measurements follow a Gaussian distribution:

$$n(x) = \frac{1}{\sigma * \sqrt{2\pi}} * e^{-\frac{(x-\bar{x})^2}{2\sigma^2}} \quad (3.1)$$

I first calculated the arithmetic mean \bar{x} and the standard deviation σ of the deformation in v_{LOS}

$$\bar{x} = \frac{1}{n} \sum_{i=1}^n x_i \quad (3.2)$$

and

$$\sigma = \sqrt{\frac{\sum(x-\bar{x})^2}{n}} \quad (3.3)$$

I calculated the interval of $[\bar{x} \pm 2\sigma]$, PSs measurements with higher values than this interval are deleted. For further eliminations of outliers I fit planes through the values. The plane is defined by three points:

$$def_1(lat_1, long_1) = \overline{def} + \overline{lat_1} * slope + \overline{long_1} * slope \quad (3.4)$$

For this I calculated the arithmetic means for the coordinates latitude $\overline{lat_1}$, and longitude $\overline{long_1}$, and deformation \overline{def} .

I then calculated def_2 :

$$def_2 = def - def_1(lat_1, long_1) \quad (3.5)$$

concerning the plane.

I further calculated the standard deviation $[\pm 2\sigma]$ of def_2 . All values larger than $[\pm 2\sigma]$ are deleted. A new plane is defined by

$$def_3(lat_1, long_1) = \overline{def_2} + \overline{lat_1} * slope + \overline{long_1} * slope \quad (3.6)$$

I then calculated

$$def_4 = def - def_3(lat_1, long_1) \quad (3.7)$$

The standard deviation $[\pm\sigma]$ of def_4 is the value for my error of the PSs measurements concerning the deformation in v_{LOS} . PS measurements of the footwall and the hanging wall are listed in Table 3.1.

I calculated the differential velocity Δv_{LOS} between the footwall and the hanging wall for 13 normal faults on Crete (Figure 3.4)

$$\Delta v_{normal\ fault} = |v_{footwall} - v_{hangingwall}| \quad (3.8)$$

The dip-slip component S (Figure 3.4) along the fault is calculated by:

$$S = \frac{\Delta v_{normal\ fault}}{\sin \alpha} \quad (3.9)$$

The dip-slip component S is given in LOS, which can be transformed to true vertical (Table 3.2) by multiplying with $c = 0.94$, which is the multiplication factor for the vertical v_{LOS} component (see chapter: 2.5.2.3 Orbital Uncertainty Compensation & Figure 2.4)

$$S_{geodetic}^{vertical} = S_{geodetic}^{LOS} * 0.94 \quad (3.10)$$

3.6 Results

The detected geodetic signal ranges from 5 mm/yr of subsidence to 5 mm/yr of uplift across Crete (Figure 3.17). The PSs are not distributed homogeneously across the island. The lowest number of PSs is found in the Heraklion and Messara basins, and along the southern coast of the Dikti mountains, and south of the Spili fault. A number of small regions where no PSs measurements are heterogeneously distributed across the island. Other regions have a denser distribution of PS measurements. The western part of Crete is dominated by uplift on the order of up to 5 mm/yr, whereas the eastern part is dominated by subsidence ranging between 0 to -5mm/yr. The strongest uplift occurs along the SW corner of Crete, and decreases towards the northern coastline. The uplift signal along the southern coastline reaches as far as the western part of the Asteroussia Mountains in Central Crete. Along northern coastline of W-Crete no significant vertical deformation is obvious until the Psiloritis Mountains. Central Crete is characterized by the uplift along the northern coastline. The southern coastline shows uplift, whereas the middle part of Central Crete is relative stable with zero deformation. Eastern Crete is dominated by two bifurcating regions of strong subsidence. The Heraklion and Massara basins have the least amount of PSs measurements, except in urban regions. Along the northern coastline of the Heraklion basin the PS point density is high, due to the urban area.

I calculated the mean deformation in LOS for the footwall and the hanging wall across 13 normal faults (Figure 3.18), respectively (Table 3.1), as well as the differential velocity between the footwall and the hanging wall, and the dip-slip component across these faults (Table 3.1).

3.7 Analysis of PSI Measurements across Normal Faults

First I analyzed the distribution of PSs and lithological units on Crete (Figure 3.19). The highest percentage of PSs is found in the Plattenkalk unit (37.2%), followed by the Tripolis unit (28.5%), sediments (23.2%), Pindos unit (5.3%), Phyllite-Quartzite unit (5.0%), and the least amount of PSs is found in the Uppermost unit (0.8%).

Vegetation and agricultural usage leads to strong temporal decorrelation effects and therefore to small numbers of detected PSs.

PSs density is highest in the Plattenkalk and the Tripolis unit, because these units consist of limestone, which is characterized by its higher resistivity to erosion (Blume et al., 2010). The vegetation cover is sparse resulting in numerous natural PSs, like rocks and large boulders and bedrock outcrops (Figure 3.20).

The sediment unit is characterized by a high number of PSs, but also with a very heterogeneously distribution of the PSs especially in the basins (Figure 3.16). The high numbers of PSs in sedimentary units can be explained due to the fact that most cities (Ierapetra, Heraklion, Rethymno, and Chania) are located in grabens. Urban regions have the highest density of PSs, caused by man-made structures.

The low number of PSs distributed in the Phyllite-Quartzite units is caused by weathering of Phyllites leading to soils with high content of clay minerals (Blume et al., 2010). Therefore, the Phyllite-Quartzite units consist of intensively weathered slope-building rocks with usually few PSs. This unit is widely used for agricultural purposes, such as olive plantations (Figure 3.20).

The analysis of PSI measurements across 13 normal faults shows normal motion across seven normal faults, and reverse motion across six normal faults, between 1992 and 2000 (Table 3.1 & Figure 3.21). Normal motion implies that the footwall is uplifting and the hanging wall is subsiding relatively to each other (Figure 3.21). Whereas, reverse motion implies that the footwall is subsiding and the hanging wall is uplifting relatively to each other (Figure 3.21).

Normal faults with normal motion are: AF (Asomatos Fault), KrF (Kroussonas Fault), AvF (Agia Varvara Fault), and ZF (Zou Fault). Along these normal faults the error bars do not overlap (Figure 3.22), whereas along the GF (Gionas Fault), KeF (Kera Fault), and the LF (Lastros Fault) I detected normal motion with error bars overlapping. Across the SfF (Sfakia Fault) (Figure 3.3 D), KF (Kastelli Fault) (Figure 3.10 D), and the HGF (Ha Gorge Fault) (Figure 3.12 D) I detected reverse motion with error bars not overlapping, whereas across GrF (Gramvousa Fault), RF (Rodopos Fault), and the SpF (Spili Fault) the error bar is overlapping strongly, which makes the reverse motion sense uncertain (Figure 3.23).

The distribution of faults with certain and uncertain normal motion, and certain and uncertain reverse motion (Figure 3.24) are heterogeneously distributed across the island (Figure 3.24). The Gionas (GF) and the Kera (KeF) faults have normal motion, while the Rhodopos (RF) fault shows reverse motion. The RF is located in between the GF and the KeF. The Sfakia (SfF) and the Spili (SpF) faults have reverse motion, and between the two faults, along the Asomatos (AF) I found normal motion. The motion at the EPFZ is normal for both PSI measured faults, the Kroussonas (KrF) and Agia Varvara (AvF) faults. The Ha Gorge (HGF) and the Lastros (LF) are located close to each other, the HGF has reverse motion and the LF has normal motion. The Gramvousa (GrF), the Kastelli (KF), and the Zou (ZF) faults are located remote to other faults.

The hanging walls of the above mentioned faults with certain reverse motion consist of sediments. The hanging wall of the SfF consists of Phyllite-Quartzite, and marine sediments (Table 3.3). The hanging wall of the KF fault consists of Plattenkalk and continental sediments, and the hanging wall of the HGF consists of continental sediments. The hanging wall of mentioned faults with uncertain reverse motion consists of sediments, but also of carbonat rocks at the RF (Table 3.3). But the error bar across this fault is too high to distinguish for a real signal of reverse motion across this fault (Figure 3.23).

Further, I compared the geodetic slip rates based on PSs LOS measurements with geological average slip-rates proposed by Caputo et al. (2010) (Table 3.2) for the last 13 ka. In this study the average slip-rate and recurrence times of earthquakes are derived by morphological and structural mapping based on satellite, and aerial images, topographical maps and field observations (Caputo et al., 2006). Therefore, historical fault scarps are used because earthquake ruptures are preserved as net cumulative effect along these faults (Caputo et al., 2006). During climate conditions which favor stable-slope conditions, fault scarp-erosion and slope-gradient restoration are slower than tectonic activity (Caputo et al., 2006). Whereas, during glacial conditions fault scarp-erosion and slope gradient restoration are faster than tectonic activity (Caputo et al., 2006). Slope-stable conditions began at 15 ka B.P. in the Eastern Mediterranean

(Bar-Matthews et al., 1997), and climate stable conditions as those of today established since about 10 ka B.P. (Gvirtzman and Wieder, 2001). The preferred age of 13 ka B.P. is based on similarities of fault-scarps with the Sparta fault in Greece (Benedetti et al., 2002) and the Magnolia fault in Italy (Palumbo et al., 2004), which have been dated using ^{36}Cl . The results show an exposition of the fault at least since 13 ka B.P. (Caputo et al., 2006). The maximum throw was measured with a possible error of $\pm 30\%$ (Caputo et al., 2006). These values, together with the measured dip along the fault plane, are used to estimate the slip rate for the last 13 ka B.P., and the mean recurrence interval for earthquakes with $M < 6$ (Caputo et al., 2010).

The KrF has the best fit between the average long-term slip rate and the geodetic slip-rate (Appendix, Figure II.1), followed by the Gionas fault (Appendix, Figure II.2). The GrF (Appendix, Figure II.3), HGF (Appendix, Figure II.4), and the SfF (Appendix, Figure II.5) also show a good fit between the geological slip-rates and the geodetic slip rates, but along these faults the motion is reverse during the geodetic observation. Remaining faults can be found in the Appendix, Figure II.5 to Figure II.13.

3.8 Discussion and Significance of Surface Deformation across Normal Faults

The PSI measurements along 13 upper-crustal normal faults across Crete, show that I was able to measure the vertical surface-motion for the footwall and the hanging wall, respectively (Table 3.1). With these PSI measurements I calculated the differential velocity of the footwall and the hanging wall and the geodetic slip rate across these normal faults (Table 3.2).

The reverse motion along the six normal faults are most likely transient signals, because the topography across these normal faults clearly shows normal motion on longer time-scales.

From the distribution of the faults with certain and uncertain normal and certain and uncertain reverse motion (Figure 3.24) I cannot distinguish a clear pattern.

Perhaps the detection of reverse motion is correlated to the orientation of the fault plane towards the ERS satellite flight direction of an azimuth of 28° . However, this seems unrealistic, because the SfF is striking in E-W direction, dipping towards the S (Figure 3.21). The KF is striking N-S dipping towards the W, and the HGF is striking NE-SW and dipping towards the NE. I cannot see any correlation between the striking of the faults and the detection of reverse motion.

Maybe the transient motion across these normal faults is caused by tectonic processes. In general, transient motion across faults can be caused by afterslip, poroelastic rebound, or postseismic relaxation due to earlier earthquakes, or aseismic creep. Afterslip, poroelastic rebound, and postseismic relaxation as reasons for the reverse motion are unlikely, because no recent strong $M_w 6$ earthquakes occurred on these upper-crustal normal faults (see Chapter 1 - Introduction).

Reverse motion may be caused by aseismic creep along the interface of these normal faults. For reverse motion of aseismic creep, meaning that the hanging wall is uplifting relative to the footwall, the extensional stress regime must have changed towards a compressional stress regime. Reversal in the stress regime may be caused by changes along the Hellenic subduction interface. Studies along the Chile subduction zone showed a change of motion due to processes along the subduction zone affecting the crustal faults in the overriding plate (Shirzaei et al., 2012). An InSAR study of the 2010 Maule $M_w 8.8$ earthquake along the coast of central Chile showed that the aftershocks on crustal faults in the overriding plate were extensional in an area of regional interseismic compression (Ryder et al., 2012). An InSAR study of the 2007 $M_w 7.7$

Tocopilla earthquake on the northern Chile subduction zone also showed aseismic creep and change in the sense of slip along crustal faults in the overriding plate (Shirzaei et al., 2012). The reversal of motion along these two faults is interpreted to be caused by the changing stress conditions induced by a megathrust earthquake (Shirzaei et al., 2012). The 2011 Mw 9.0 Tohoku-Oki earthquake (Simons et al., 2011) in NE Japan triggered a swarm-like sequence of earthquakes in the northern part of the Ibaraki Prefecture (Kato et al., 2011). The focal mechanism of these events shows normal faulting implying horizontal extension following the earthquake (Kato et al., 2011). Before the earthquake focal mechanism indicated reverse-faulting, this indicates that the stress field changed from E-W horizontal compression to E-W extension (Kato et al., 2011). There are more examples of reversal of fault creep along strike slip faults, such as Hayward fault following the 1989 Mw 6.9 Loma Prieta earthquake (Lienkaemper et al., 1997). Along the San Andreas Fault a reversal was detected after the 1983 M_w 6.7 Coalinga earthquake (Toda and Stein, 2002).

The reversal of the stress regime is not caused by processes along the Hellenic subduction zone, because no large earthquake is recorded and the distribution of faults with reverse and normal motion is heterogeneously distributed (Figure 3.24). The heterogeneous pattern may suggest that the reversal of the stress regime is not affecting the whole island, otherwise all normal faults should have reverse motion. I may conclude that the change of the stress regime is not caused by the subduction zone, as first order fault system. This is also confirmed by earlier studies (Jackson and McKenzie, 1988; Reilinger et al., 2010), which concluded that the convergence of the Hellenic subduction zone is mostly aseismically, no strain is accumulated and therefore no compressional stress regime is active due to the subduction interface. These interpretations are based on the absence of historical large earthquakes after the 365 A.D. event (Jackson and McKenzie, 1988) and GPS measurements (Reilinger et al., 2010). The compression is maybe caused by the interaction of upper-crustal faults in the overriding plate and the normal faults on Crete. In the previous chapter I suggested that the overall detected vertical surface-deformation pattern is caused mainly by aseismic creep along the Hellenic Trench and transtensional motion due to the Ptolemy Trench. But the distribution of normal faults with reverse and normal motion shows no connection to the upper-crustal faults. For example, the HGF fault shows reverse motion, but the stress regime in this area is dominated by transtension in elongation to the Ptolemy trench (Figure 3.25). Therefore, the vertical surface-deformation along the upper-crustal normal faults cannot be explained by the Hellenic Trench system.

Maybe the reverse motion along the normal faults with reverse motion is caused by swelling of clay minerals, especially smectite, in sediments. This could be a possible explanation for the reverse motion across the normal faults, because the hanging wall along these faults consists of sediments (Table 3.3), except along the RF, where the error bar overlaps too much for any reliable differentiation of the motion. Weathering of Phyllite leads to clay minerals. Clay minerals are prone for swelling due to water, which leads to volume changes of the soil (Blume et al., 2010). Volume changes in soils are only in vertical direction, which leads to height difference of the soil (Blume et al., 2010). Therefore, the swelling of clay minerals could be a possible explanation for the detected reverse motion along normal faults on Crete. Seasonal effects cannot be distinguished, because the the acquisition of ERS satellite images is all-season.

Limitations of my PSI measurements along normal faults are due to the small amount of PSs measurements on some faults. This is caused by the PSI approach itself due to decorrelation effects of landuse and vegetation. Further, the PSs measurements have a big error in their measurements.

I compared the PSs measurements of geodetic slip rates with the average geologic slip rates of Caputo et al. (2010). Slip rates on both time scales coincide well for eight faults,

independently of the sense of motion (normal or reverse), and only five faults are not consistent with the error range of Caputo et al. (2010). The discrepancy in different style and sense of motion for some faults could not result from random or systematic errors, because only for six faults the geodetic and geological measurements do not coincide, but for seven faults the geodetic and geological measurements coincide.

I therefore investigate the vertical surface-deformation pattern across Crete over the millennial and the longer time-scale. In chapter 4, I analyze geomorphic markers, such as river profiles and paleo-shorelines to estimate the vertical surface-deformation on the m/ka-scale. In chapter 5, I investigate the distribution of Neogene sediments across Crete for quantifying the vertical rate on the km/Ma-scale.

3.9 Conclusions

I have carried out the first PSI analysis of the vertical surface motion on a regional scale. PSI analysis may be successfully carried out beyond urban areas, as long as bedrock exposures are ubiquitous on a regional scale. The highest density of PSs occurs on bedrock, in particular on resistant carbonate rocks. The lowest density of PSs correlates with agricultural regions. I suspect that a combination of vegetation growth and changing soil moisture content above the Phyllite-Quartzite unit is responsible for the decorrelations. The Phyllite-Quartzite unit is prone to chemical weathering, hence soil formation with high clay mineral content. These regions are densely vegetated and used for agriculture, and PSs are restricted to man-made structures. Hence, the loss of high PSs density is caused by decorrelation effects due to vegetation growth.

The PSI pattern across the 250-km-long and 50-km-wide island is not uniform, but dominated by small-scale (> 1 km) signals. Apart from the regional-scale signal in SW Crete, which was discussed in the previous chapter, I observed c. 13 narrow (900 – 3000 m) zones of high strain. These zones best correlate with locations of active faults on Crete. I therefore attribute this differential motion of 0.05 to 2.2 mm/yr to reflect the surface expression of actively deforming faults. In most cases, the sense of deformation coincides with the sense of displacement along these faults on geological time scales, as established in earlier studies. In three cases, however, the observed signal is opposite in sign, implying transient deformation across the normal faults. Further studies will be necessary to investigate whether the detected signal is caused by tectonic or hydrologic effects.

Finally, I conclude that the PSI technique is a very promising tool to quantify decadal-scale surface deformation of processes involving the geosphere.

References

- Ambraseys, N., Melville, C., Adams R. (1994): Seismicity of Egypt, Arabia and the Red Sea. Cambridge University Press. Pages: 204.
- Angelier J. (1978): Tectonic evolution of the Hellenic arc since the Late Miocene. *Tectonophysics*. Vol. 49. Pages: 23-36. DOI: 10.1016/0040-1951(78)90096-3.
- Angelier J. (1979): Neotectonique de l'arc Eggen. These d'etat. University de Paris VI, 405 pp.
- Armijo, R., Lyon-Caen, H. Papanastassiou, D. (1992): East-west extension and Holocene normal fault scarps in the Hellenic arc. *Geology*. Vol. 20. Pages: 491-494. DOI: 10.1130/0091-7613(1992)020<0491:EWEAHN>2.3.CO;2.
- Bar-Matthews M., Ayalon A., Kaufman A. (1997): Late Quaternary Paleoclimate in the Eastern Mediterranean Regions from stable isotope analysis of Speleothems at Soreq Cave, Israel. *Quaternary Research*. Vol. 47. Pages: 155-168. DOI: 10.1006/gres.1997.1883.
- Benedetti L., Finkel R., Papanastassiou D., King G., Armijo R., Ryderson F., Farber D., Flerit F. (2002): Post-glacial slip history of the Sparta fault (Greece) determined by ³⁶Cl cosmogenic dating: Evidence for non-periodic earthquakes. *Geophysical Research Letters*. Vol. 29. No. 8. DOI: 10.1029/2001GL014510.
- Blume H.-P., Brummer G.W., Horn R., Kandeler E., Kogel-Knabner I., Kretschmar R., Stahr K., Wilke B.-M. (2010): Scheffer/Schachtschabel: Lehrbuch der Bodenkunde. Spektrum Akademischer Verlag Heidelberg. 16. Auflage. 578 pages.
- Bürgmann R., Rosen P.A., Fielding E.J. (2000): Synthetic Aperture Radar Interferometry to Measure Earth's Surface Topography and Its Deformation. *Annual Review of Earth and Planetary Sciences*. Vol. 28. Pages: 169-209. DOI: 10.1146/annurev.earth.28.1.169.
- Caputo R., Catalano S., Monaco C., Romagnoli G., Tortorici G., Tortorici L. (2010): Active faulting on the island of Crete (Greece). *Geophysical Journal International*. Vol. 183. Iss. 1. Pages: 111–126. DOI: 10.1111/j.1365-246X.2010.04749.x.
- Dziewonski A. M., Chou T.A., Woodhouse J. H. (1981): Determination of earthquake source parameters from waveform data for studies of global and regional seismicity. *Journal of Geophysical Research*. Vol. 86. Pages: 2825-2852. DOI: 10.1029/JB086iB04p02825.
- Ekström G., Nettles M., Dziewonski A. M. (2012): The global CMT project 2004-2010: Centroid-moment tensors for 13,017 earthquakes. *Physics of the Earth and Planetary Interiors*. Vol. 200-201. Pages: 1-9. DOI: 10.1016/j.pepi.2012.04.002.
- Elliott J.R., Walters R.J., England P.C., Jackson J.A., Li Z., Parsons B. (2010): Extension on the Tibetan plateau: recent normal faulting measured by InSAR and body wave seismology. *Geophysical Journal International*. Vol. 183. Iss. 2. Pages: 503-535. DOI: 10.1111/j.1365-246X.2010.04754.x.
- Fassoulas C., Kiliadis A., Mountrakis D. (1994): Postnappe stacking extension and exhumation of high-pressure/low-temperature rocks in the island of Crete, Greece. *Tectonics*. Vol. 13. Iss. 1. Pages: 127-138. DOI: 10.1029/93TC01955.
- Fassoulas C. (2001): The tectonic development of a Neogene basin at the leading edge of the active European margin: the Heraklion basin, Crete, Greece. *Journal of Geodynamics*. Vol. 31. Pages: 49-70. DOI: 10.1016/S0264-3707(00)00017-X.

- Guidoboni E., Comastri A. (1997): The large earthquake of 8 August 1303 in Crete: seismic scenario and tsunami in the Mediterranean area. *Journal of Seismology*. Vol. 1. Pages: 55-72. DOI: 10.1023/A:1009737632542.
- Gvirtzman G., Wieder M. (2001): Climate of the last 53000 years in the Eastern Mediterranean, based on soil-sequence Stratigraphy in the coastal plain of Israel. *Quaternary Science Reviews*. Vol. 20. Pages: 1827-1849. DOI: 10.1016/S0277-3791(01)00008-7.
- Hall R., Audley-Charles M. G., Carter D.J. (1984): The significance of Crete for the evolution of the Eastern Mediterranean. Geological Society. London. Special Publications. Vol. 17. Pages: 499-516. DOI: 10.1144/GSL.SP.1984.017.01.37.
- Jacobshagen, V., ed. (1986): *Geologie von Griechenland*: Berlin. Stuttgart. Gebrüder Borntraeger. 363 pages.
- Jackson J., McKenzie D. (1988): The relationship between plate motions and seismic tremors, and the rates of active deformation in the Mediterranean and Middle East. *Geophysical Journal*. Vol. 93. Pages: 45-73. DOI: 10.1111/j.1365-246X.1988.tb01387.x.
- Jolivet L., Goffé B., Monié P., Truffert-Luxey C., Patriat M., Bonneau M. (1996): Miocene detachment in Crete and exhumation P-T-t paths of high-pressure metamorphic rocks. *Tectonics*. Vol. 15. No. 6. Pages: 1129-1153. DOI: 10.1029/96TC01417.
- Kato A., Sakai S., Obara K. (2011): A normal-faulting seismic sequence triggered by the 2011 off the Pacific coast of Tohoku earthquake: Wholesale stress regime changes in the upper plate. *Earth Planets Space*. Vol. 63. Pages: 745-748. DOI: 10.5047/eps.2011.06.014.
- Landgraf A., Zielke O., Arrowsmith J.R., Ballato P., Strecker M.R., Schildgen T.F., Friedrich A.M., Tabatabaei S.H. (2013): Differentiating simple and composite tectonic landscapes using numerical fault slip modeling with an example from the south central Alborz Mountains, Iran. *Journal of Geophysical Research. Earth Surface*. Vol. 118. Pages: 1792-1805. DOI: 10.1002/jgrf.20109.
- Le Pichon X., Angelier J. (1979): The Hellenic Arc and trench system: a key to the neotectonic evolution of the Eastern Mediterranean area. *Tectonophysics*. Vol. 60. Iss. 1-2. Pages: 1-42. DOI: 10.1016/0040-1951(79)90131-8.
- Le Pichon X., Lallemand S.J., Chamot-Rooke N., Lemeur D., Pascal G. (2002): The Mediterranean Ridge backstop and the Hellenic nappes. *Marine Geology*. Vol. 186. Pages: 111-125. DOI: 10.1016/S0025-3227(02)00175-5.
- Lienkaemper J.J., Galehouse J.S., Simson R.W. (1997): Creep response of the Hayward fault to stress changes caused by the Loma Prieta earthquake. *Science*. Vol. 279. No. 5321. Pages: 2014-2016. DOI: 10.1126/science.276.5321.2014.
- McKenzie D. (1972): Active Tectonics of the Mediterranean Region. *Geophysical Journal of the Royal Astronomical Society*. Vol. 30. Iss. 2. Pages: 109-185. DOI: 10.1111/j.1365-246X.1972.tb02351.x.
- Meier T., Rische M., Endrun B., Vafidis A., and Harjes H.-P. (2004): Seismicity of the Hellenic subduction zone in the area of western and central Crete observed by temporary local seismic networks. *Tectonophysics*. Vol. 383. Pages: 149-169. DOI: 10.1016/j.tecto.2004.02.004.
- Meulenkamp J.E., Wortel M.J.R., Wamel van W.A. Spakman W., Hoogerduyn Strating E. (1988): On the Hellenic subduction zone and the geodynamic evolution of Crete since the late

- Middle Miocene. *Tectonophysics*. Vol. 146. Pages: 203-215. DOI: 10.1016/0040-1951(88)90091-1.
- Meulenkamp J.E., Zwaan van der G.J., Wamel van W.A. (1994): On Late Miocene to recent vertical motions in the Cretan segment of the Hellenic arc. *Tectonophysics*. Vol. 234. Pages: 53-72. DOI: 10.1016/0040-1951(94)90204-6.
- Mouslopoulou V., Andreou C., Atakan K., Fountoulis I. (2001): Paleoseismological investigations along the Kera fault zone, western Crete: Implications for seismic hazard assessment. *Bulletin of the Geological Society of Greece*. Vol. XXIV/4. Pages: 1531-1537.
- Mouslopoulou V., Moraetis D., Benedetti L., Guillou V., Bellier O., Hristopoulos D. (2014): Normal faulting in the forearc of the Hellenic subduction margin: Paleoearthquake history and kinematics of the Spili fault, Crete, Greece. *Journal of Structural Geology*. Vol. 66. Pages: 298-308. DOI: 10.1016/j.jsg.2014.05.017.
- Niemi N.A., Wernicke B.P., Friedrich A.M., Simons M., Bennett R.A., Davis J.L. (2004): BARGEN continuous GPS data across the eastern Basin and Range province, and implications for fault system dynamics. *Geophysical Journal International*. Vol. 159. Pages: 841-862. DOI: 10.1111/j.1365-246X.2004.02454.x.
- Palumbo L., Benedetti L., Bourles D., Cinque A., Finkel R. (2004): Slip history of the Magnola fault (Apennines, Central Italy) from ^{36}Cl surface exposure dating: evidence for strong earthquakes over the Holocene. *Earth and Planetary Science Letters*. Vol. 225. Pages: 163-176. DOI: 10.1016/j.epsl.2004.06.012.
- Papanikolaou D., Vassilakis E. (2010): Middle Miocene E-W Tectonic Horst Structure of Crete through Extensional Detachment Faults. *Tectonophysics*. Vol. 488, Iss. 1-4, 5. Pages: 233-247. DOI: 10.1088/1755-1307/2/1/012003.
- Papazachos, B.C., Dimitriu P.P. (1991): Tsumamis in and near Greece and their relation to the earthquake focal mechanisms. *Natural Hazards*. Vol. 4. Pages: 161-170. DOI: 10.1007/BF00162785.
- Papazachos, B.C., Comninakis, P.E., Karakaisis, G.F., Karakostas, B.G., Papaioannou, Ch.A., Papazachos, C.B., Scordilis E.M. (2000): A catalogue of earthquakes in Greece and surrounding area for the period 550BC-1999. *Publ. Geophys. Lab., Univ. of Thessaloniki*. 1. 333pp.
- Papazachos, B.C., Comninakis, P.E., Scordilis, E.M., Karakaisis, G.F. and C.B. Papazachos (2009): A catalogue of earthquakes in the Mediterranean and surrounding area for the period 1901 - Sep2009, *Publ. Geophys. Laboratory, University of Thessaloniki*.
- Pirazzoli P.A., Thommert J., Thommert Y., Laborel J., Montaggioni L.F. (1982): Crustal block movements from Holocene shorelines: Crete and Antikythira (Greece). *Tectonophysics*. Vol. 82. Pages: 27-43. DOI: 10.1016/0040-1951(82)90060-9.
- Pirazzoli P.A., Laborel J., Stiros S.C. (1996): Earthquake clustering in the Eastern Mediterranean during historical times. *Journal of Geophysical Research - Solid Earth*. Vol. 101. Iss. B3. Pages: 6083-6097. DOI: 10.1029/95JB00914.
- Pondrelli S., Salimbeni S., Morelli A., Ekström G., Postpischl L., Vannucci G. and Boschi E. (2011): European-Mediterranean Regional Centroid Moment Tensor Catalog: solutions for 2005-2008. *Physics of the Earth and Planetary Interiors*. Vol. 185. Issue 3-4. Pages 74-81. DOI: 10.1016/j.pepi.2011.01.007.

- Segall P., Davis J.L. (1997): GPS applications for geodynamics and earthquake studies. *Annual Review of Earth and Planetary Sciences*. Vol. 25. Page: 301-36. DOI: 10.1146/annurev.earth.25.1.301. DOI: 10.1146/annurev.earth.25.1.301.
- Reilinger R., McClusky S., Paradissis D., Ergintav S., Vernant P. (2010): Geodetic constraints on the tectonic evolution of the Aegean region and strain accumulation along the Hellenic subduction zone. *Tectonophysics*. Vol. 488. Pages: 22-30. DOI: 10.1016/j.tecto.2009.05.027.
- Ricou L.E., Burg J.P., Godfriaux I., Ivanova Z. (1998): Rhodope and Vardar: The metamorphic and the olistostromic paired belts related to the Cretaceous subduction under Europe: *Geodynamic Acta*. Vol. 11. Pages: 285-309. DOI: 10.1016/S0985-3111(99)80018-7.
- Ryder I., Rietbrock A., Kelson K., Bürgmann R., Floyd M., Socquet A., Vigny C., Carizzo D. (2012): Large extensional aftershocks in the continental forearc triggered by the 2010 Maule earthquake, Chile. *Geophysical Journal International*. Vol. 188. Pages: 879-890. DOI: 10.1111/j.1365-246X.2011.05321.x.
- Shirzaei M., Bürgmann R., Oncken O., Walter T.T., Victor P., Ewiak O. (2012): Response of forearc crustal faults to the megathrust earthquake cycle: InSAR evidence from Mejillones Peninsula, Northern Chile. *Earth and Planetary Science Letters*. Vol: 333-334. Pages: 157-164. DOI: 10.1016/j.epsl.2012.04.001.
- Stöckhert B., Wachmann M., Küster M., Bimmermann S. (1999): Low effective viscosity during high pressure metamorphism due to dissolution precipitation creep: the record of HP-LT metamorphic carbonates and siliclastic rocks from Crete. *Tectonophysics*. Vol. 303. Pages:299-319. DOI: 10.1016/S0040-1951(98)00262-5.
- Shaw B., Ambraseys N.N., England P.C., Floyd M.A., Gorman G.J., Higham T.F.G., Jackson J. A., Nocquet J.-M., Pain C. C., Piggott M. D. (2008): Eastern Mediterranean tectonics and tsunami hazard inferred from the A.D. 365 earthquake. *Nature Geoscience*. Vol. 1. DOI: 10.1038/ngeo151.
- Thomson S.N., Stockhert B., Brix M.R. (1998): Thermochronology of the high-pressure metamorphic rocks of Crete, Greece: Implications for the speed of tectonic processes. *Geology*. Vol. 26. Iss. 9. Pages: 259-262. DOI: 10.1130/0091-7613(1998)026<0259:TOTHPM>2.3.CO;2.
- Toda S., Stein R.S. (2002): Response of the San Andreas fault to the 1983 Coalinga-Nuñez earthquakes: An application of interaction-based probabilities for Parkfield. *Journal of Geophysical Research*. Vol. 107. Iss. B6. Pages: ESE 6-1-ESE 6-16. DOI: 10.1029/2001JB000172.
- Tsapanos T.M. (2001): Earthquake hazard parameters estimated in Crete Island and the adjacent area. *Pure and applied Geophysics*. Vol. 158. Pages: 1691-1718. DOI: 10.1007/s00024-003-2358-4.
- Van Hinsbergen D.J.J., Hafkenscheid E., Spakman W., Meulenkaamp J.E., Wortel R. (2005): Nappe stacking resulting from subduction of oceanic and continental lithosphere below Greece. *Geology*. Vol. 33. Pages: 325-328. DOI: 10.1130/G20878.1.
- Van Hinsbergen D.J.J., Meulenkaamp J.E. (2006): Neogene supradetachment basin development on Crete (Greece) during exhumation of the South Aegean core complex. *Basin Research* 18. Pages: 103-124. DOI: 10.1111/j.1365-2117.2005.00282.x.

Zachariasse W.J., van Hinsbergen D.J.J., Fortuin, A. (2011): Formation and fragmentation of a late Miocene supradetachment basin in central Crete: implications for exhumation mechanisms of high-pressure rocks in the Aegean forearc. *Basin Research*. Vol. 23. Pages: 678-701. DOI: 10.1111/j.1365-2117.2011.00507.x.

Figures & Tables

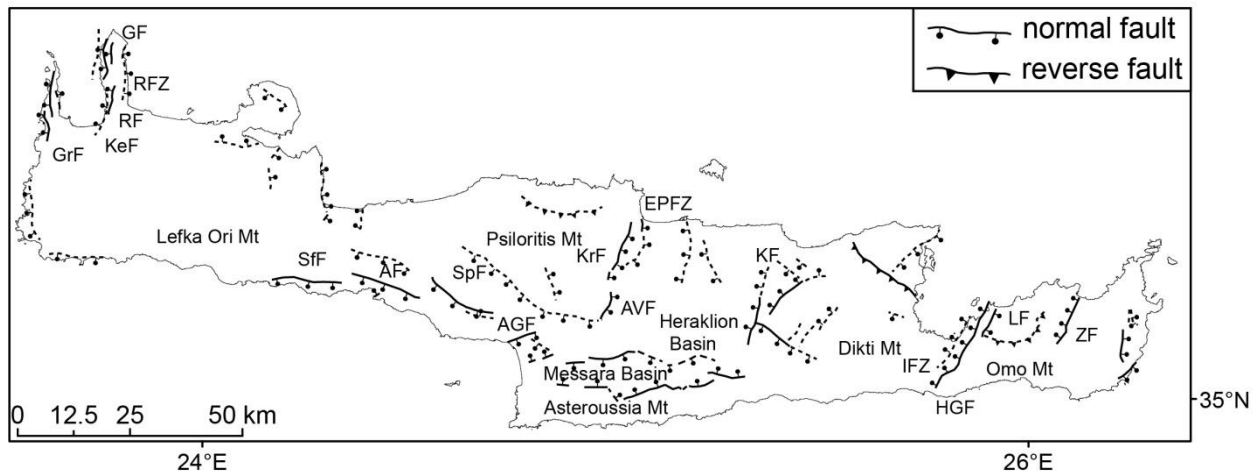


Figure 3.1: Distribution of normal faults across Crete. Fault traces are modified after Caputo et al. (2010). Dashed lines are possible faults determined by geomorphic features in topography. GrF: Gramvousa Fault, RFZ: Rhodope Fault Zone, KeF: Kera Fault, RF: Rodope Fault, GF: Gionas Fault, SfF: Sfakia Fault, AF: Asomatos Fault, SpF: Spili Fault, AGF: Agia Galini Fault, EPFZ: Eastern Psiloritis Fault Zone, KrF: Kroussonas Fault, AVF: Agia Varvara Fault, KF: Kastelli Fault, IEZ: Ierapetra Fault Zone, HGF: Ha Gorge Fault, LF: Lastros Fault, ZF: Zou Fault.

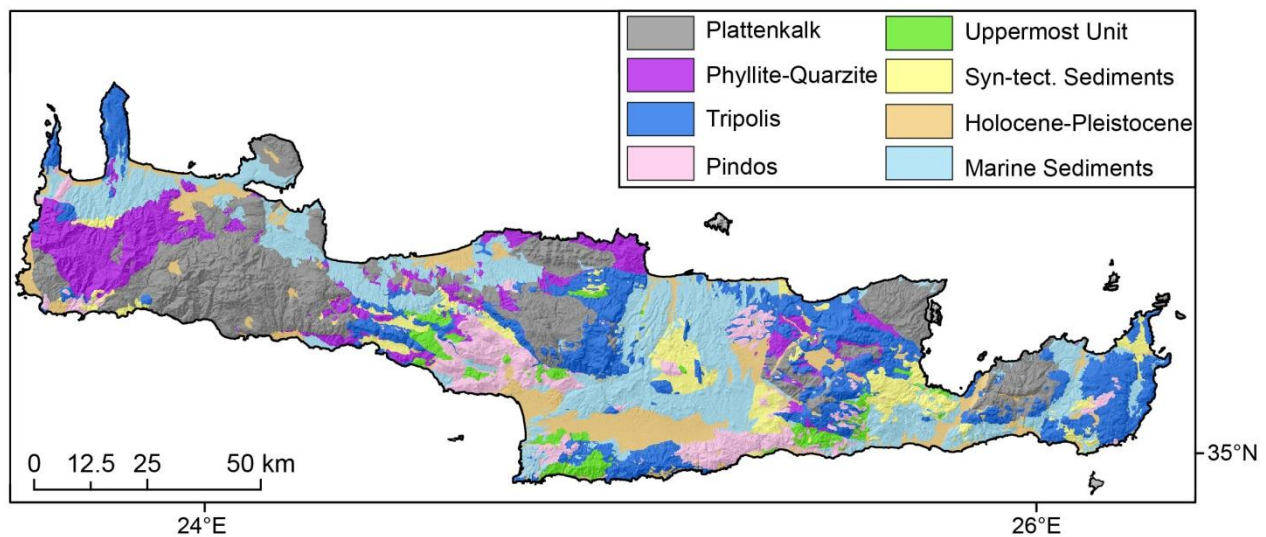


Figure 3.2: Geological map of Crete (after Papanikolaou and Vassilakis, 2010) superimposed on the Digital Elevation Model (DEM) derived from Satellite Pour l'Observation de la Terre (SPOT) images with a 20 m resolution.

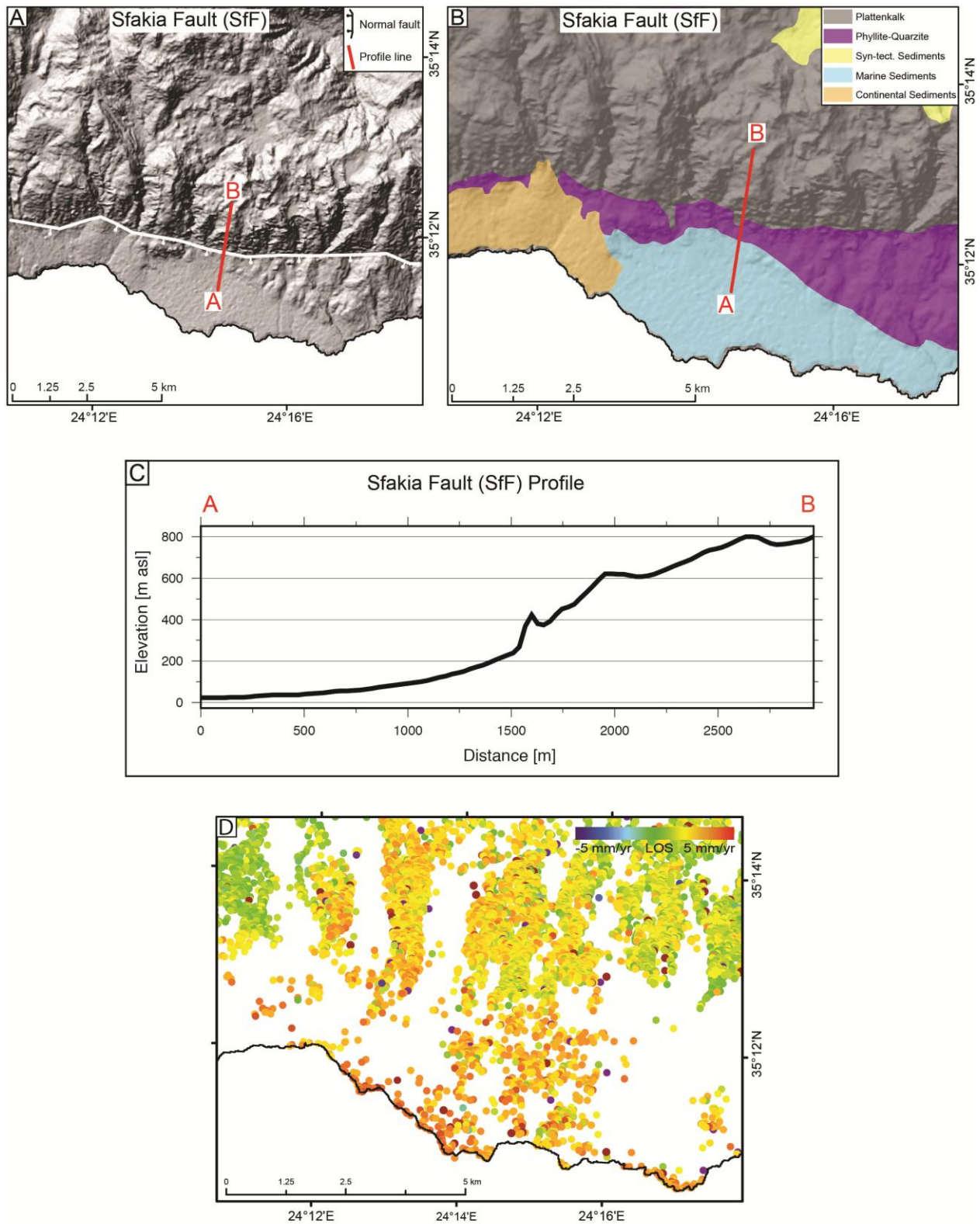


Figure 3.3: A) Topographic expression of the SfF and the location of the profile line A-B superimposed on the SPOT-DEM. B) Geological map of Crete (after Papanikolaou and Vassilakis, 2010) superimposed on the SPOT-DEM. C) Profile line across the SfF fault. D) PSI measurements.

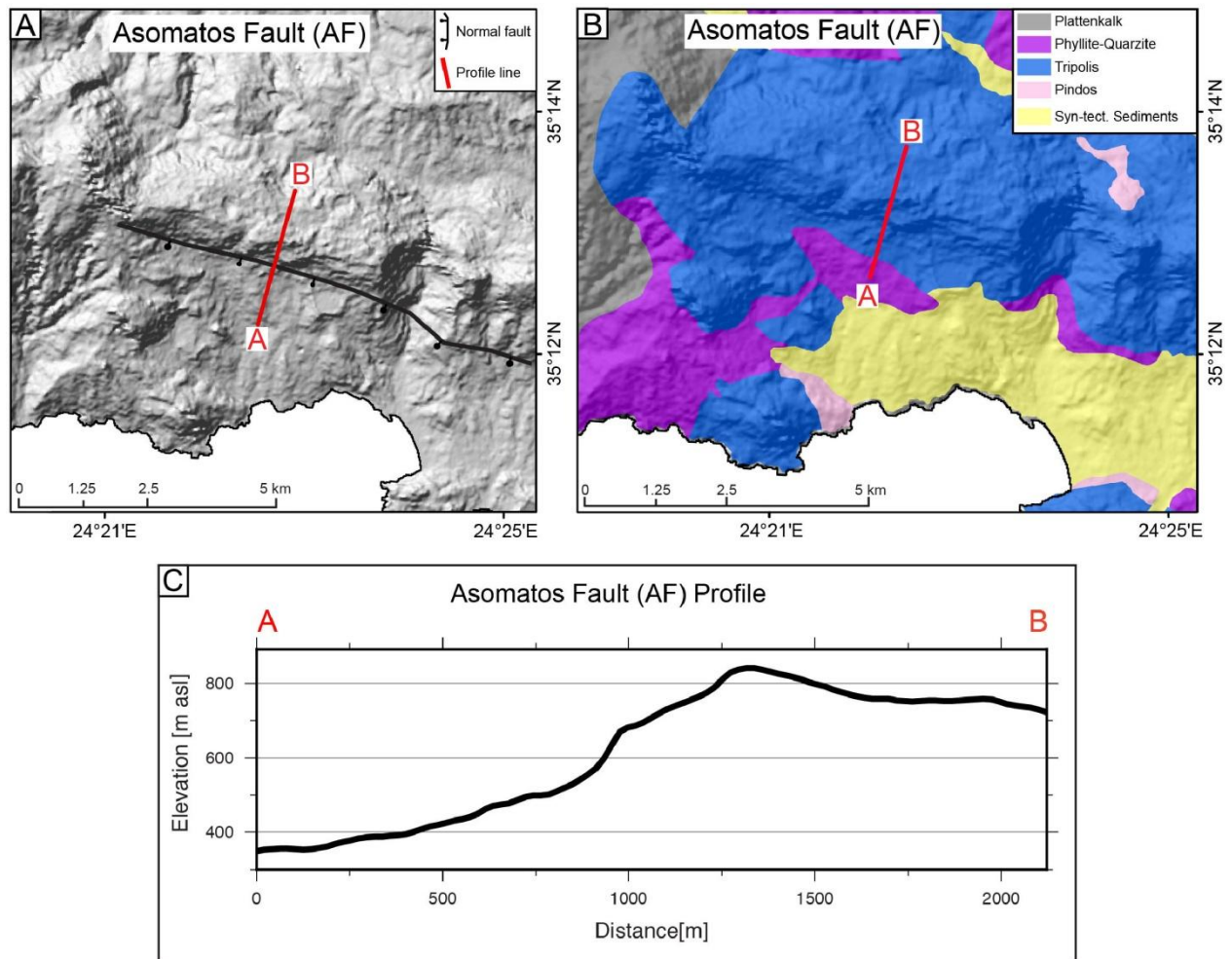


Figure 3.4: A) Topographic expression of the AF and the location of the profile line A-B superimposed on the SPOT-DEM. B) Geological map of Crete (after Papanikolaou and Vassilakis, 2010) superimposed on the SPOT-DEM. C) Profile line across the AF fault.

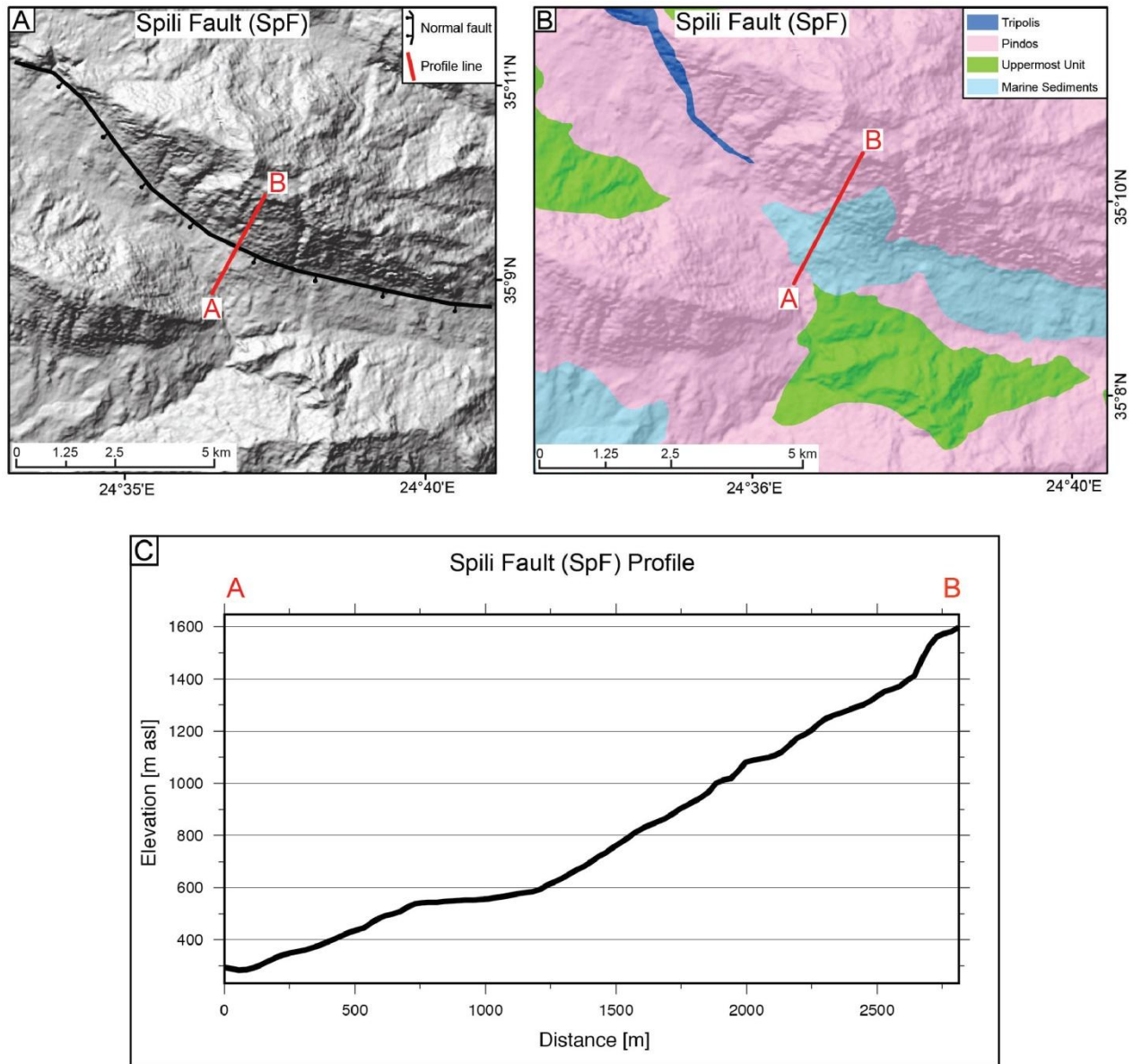


Figure 3.5: A) Topographic expression of the SpF and the location of the profile line A-B superimposed on the SPOT-DEM. B) Geological map of Crete (after Papanikolaou and Vassilakis, 2010) superimposed on the SPOT-DEM. C) Profile line across the SpF fault.

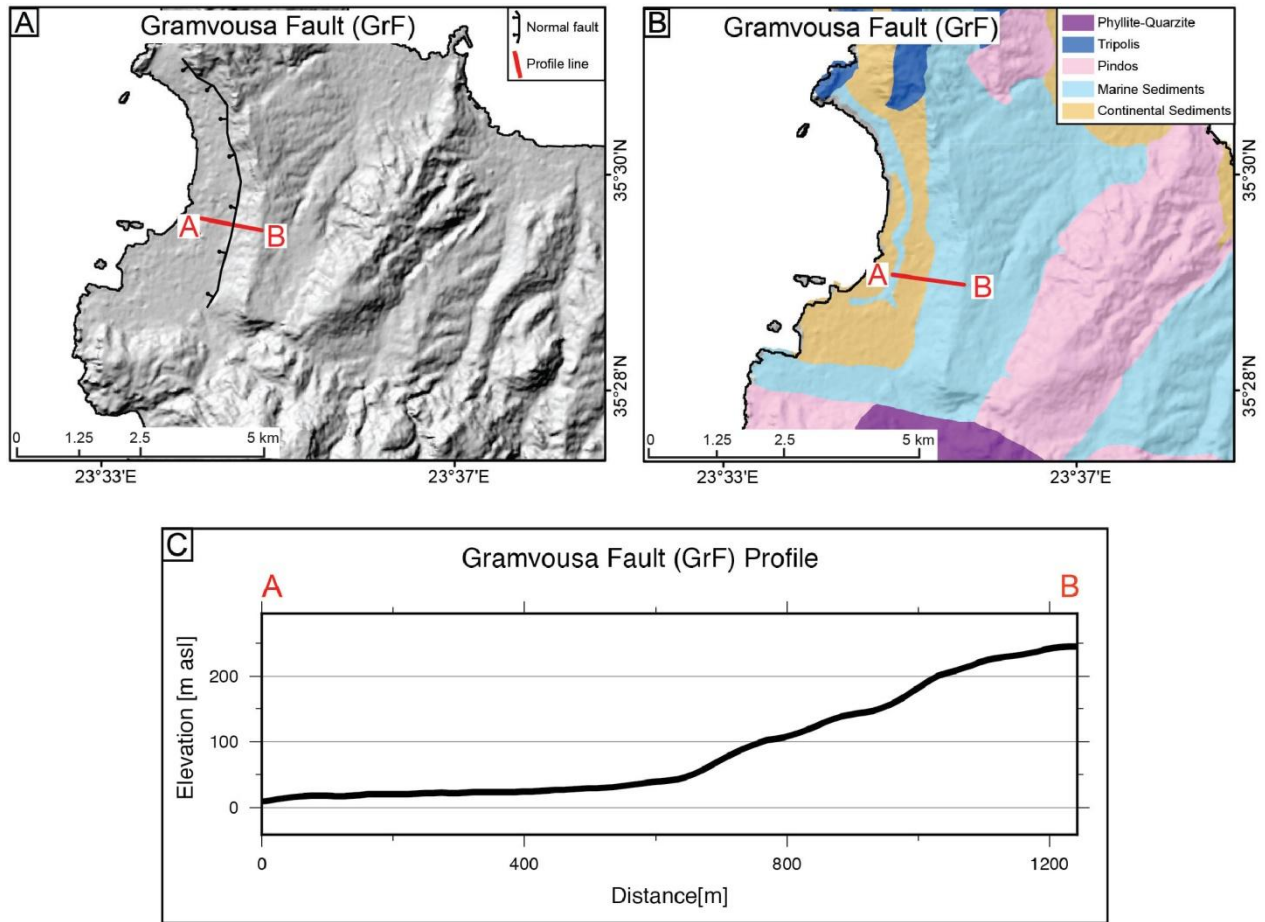


Figure 3.6: A) Topographic expression of the GrF and the location of the profile line A-B superimposed on the SPOT-DEM. B) Geological map of Crete (after Papanikolaou and Vassilakis, 2010) superimposed on the SPOT-DEM. C) Profile line across the GrF fault.

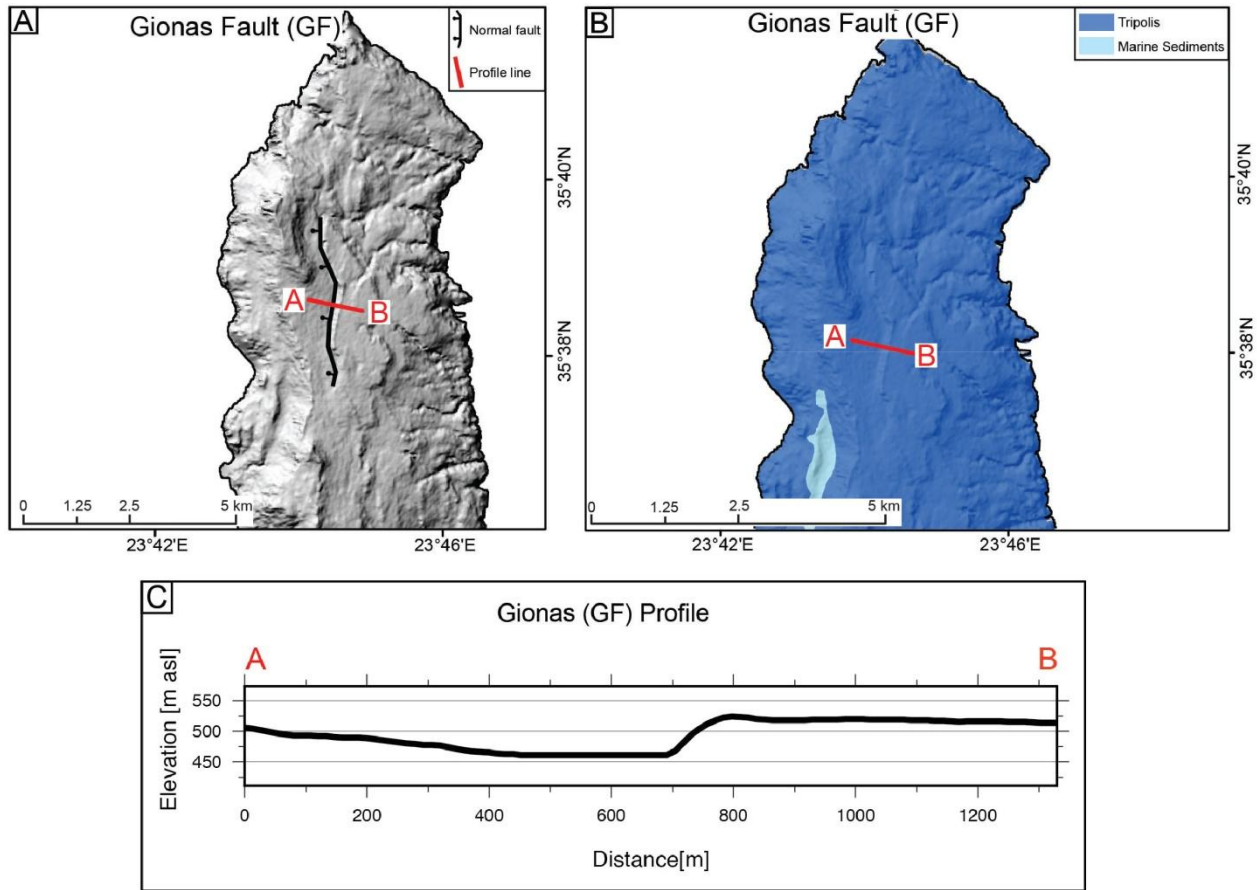


Figure 3.7: A) Topographic expression of the GF and the location of the profile line A-B superimposed on the SPOT-DEM. B) Geological map of Crete (after Papanikolaou and Vassilakis, 2010) superimposed on the SPOT-DEM. C) Profile line across the GF fault.

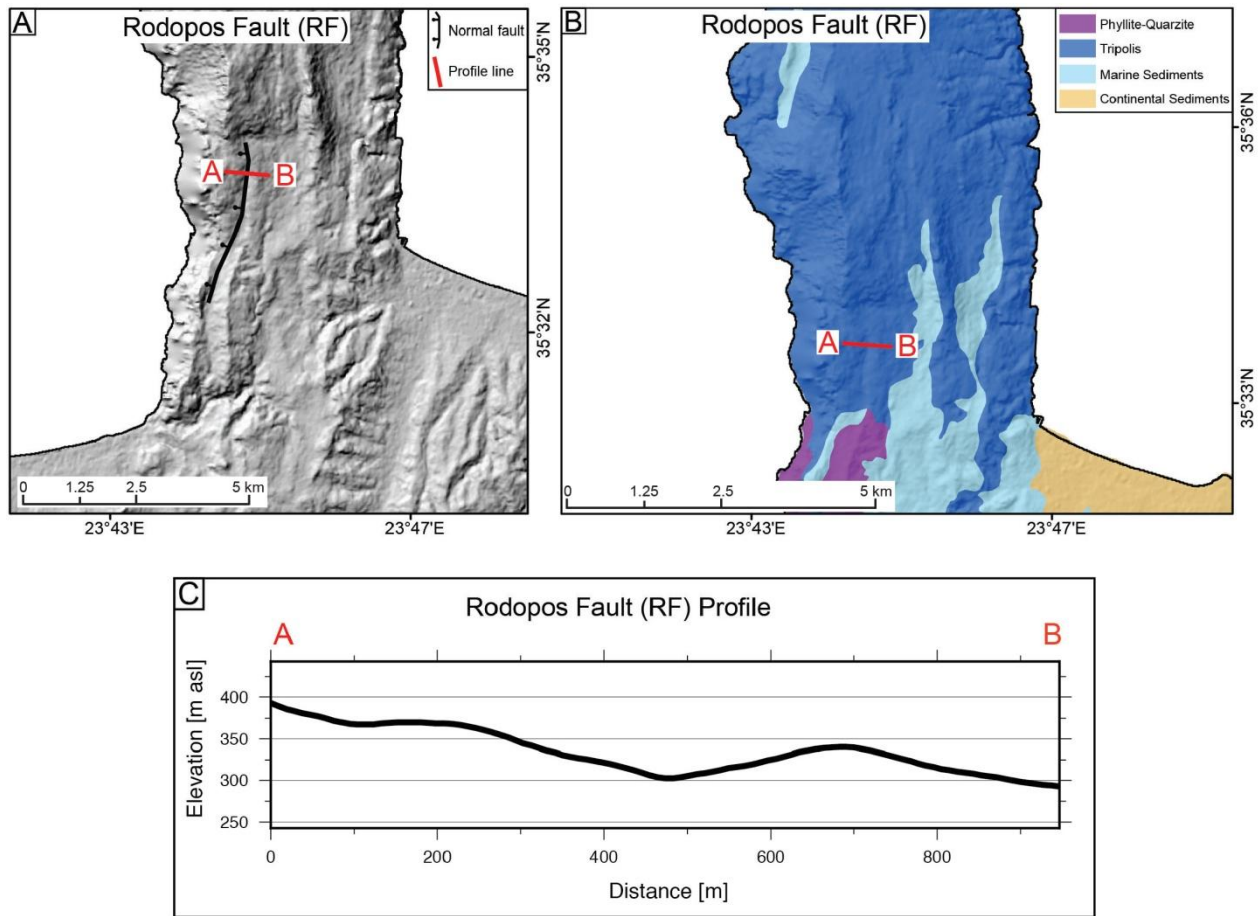


Figure 3.8: A) Topographic expression of the RF and the location of the profile line A-B superimposed on the SPOT-DEM. B) Geological map of Crete (after Papanikolaou and Vassilakis, 2010) superimposed on the SPOT-DEM. C) Profile line across the RF fault.

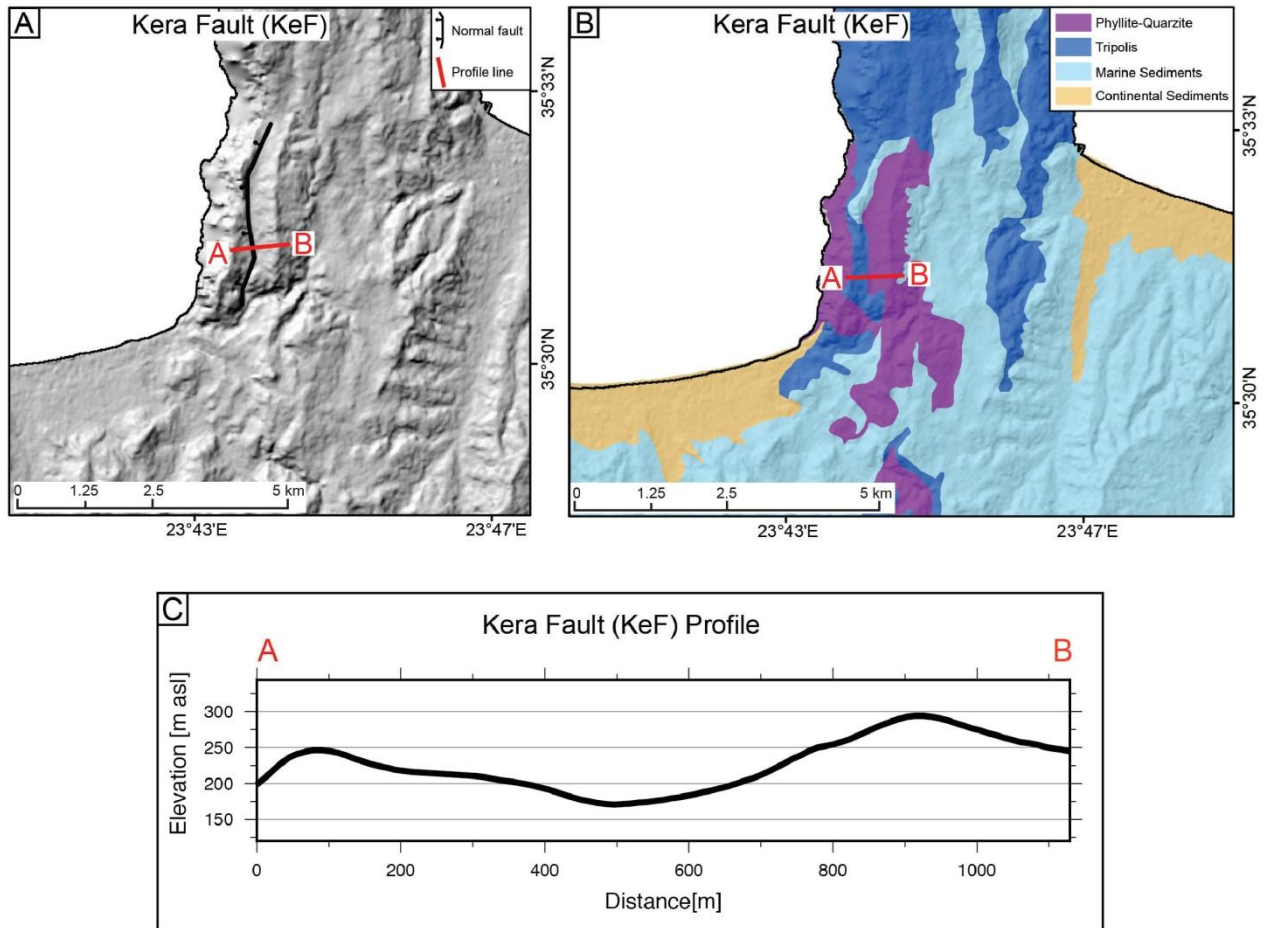


Figure 3.9: A) Topographic expression of the KeF and the location of the profile line A-B superimposed on the SPOT-DEM. B) Geological map of Crete (after Papanikolaou and Vassilakis, 2010) superimposed on the SPOT-DEM. C) Profile line across the KeF fault.

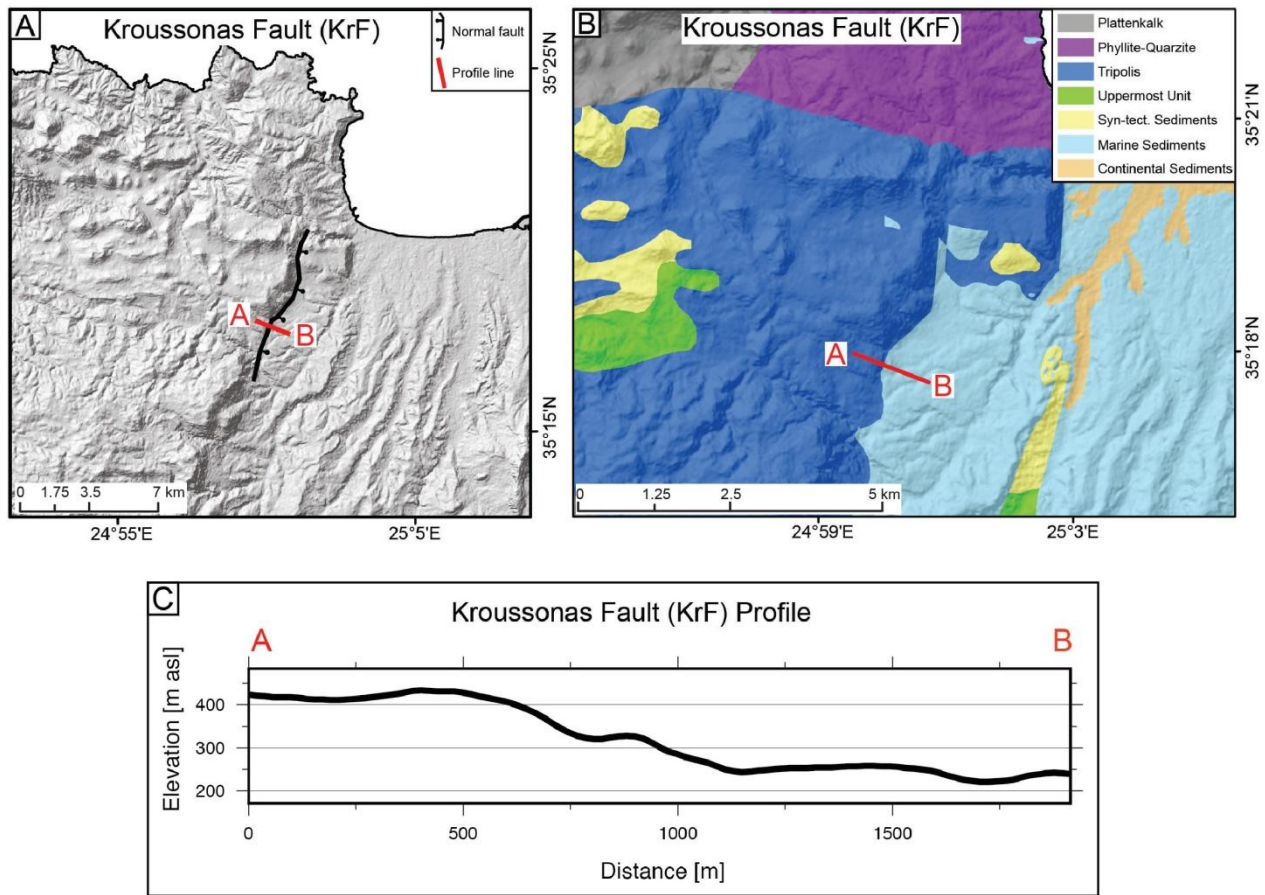


Figure 3.10: A) Topographic expression of the KrF and the location of the profile line A-B superimposed on the SPOT-DEM. B) Geological map of Crete (after Papanikolaou and Vassilakis, 2010) superimposed on the SPOT-DEM. C) Profile line across the KrF fault.

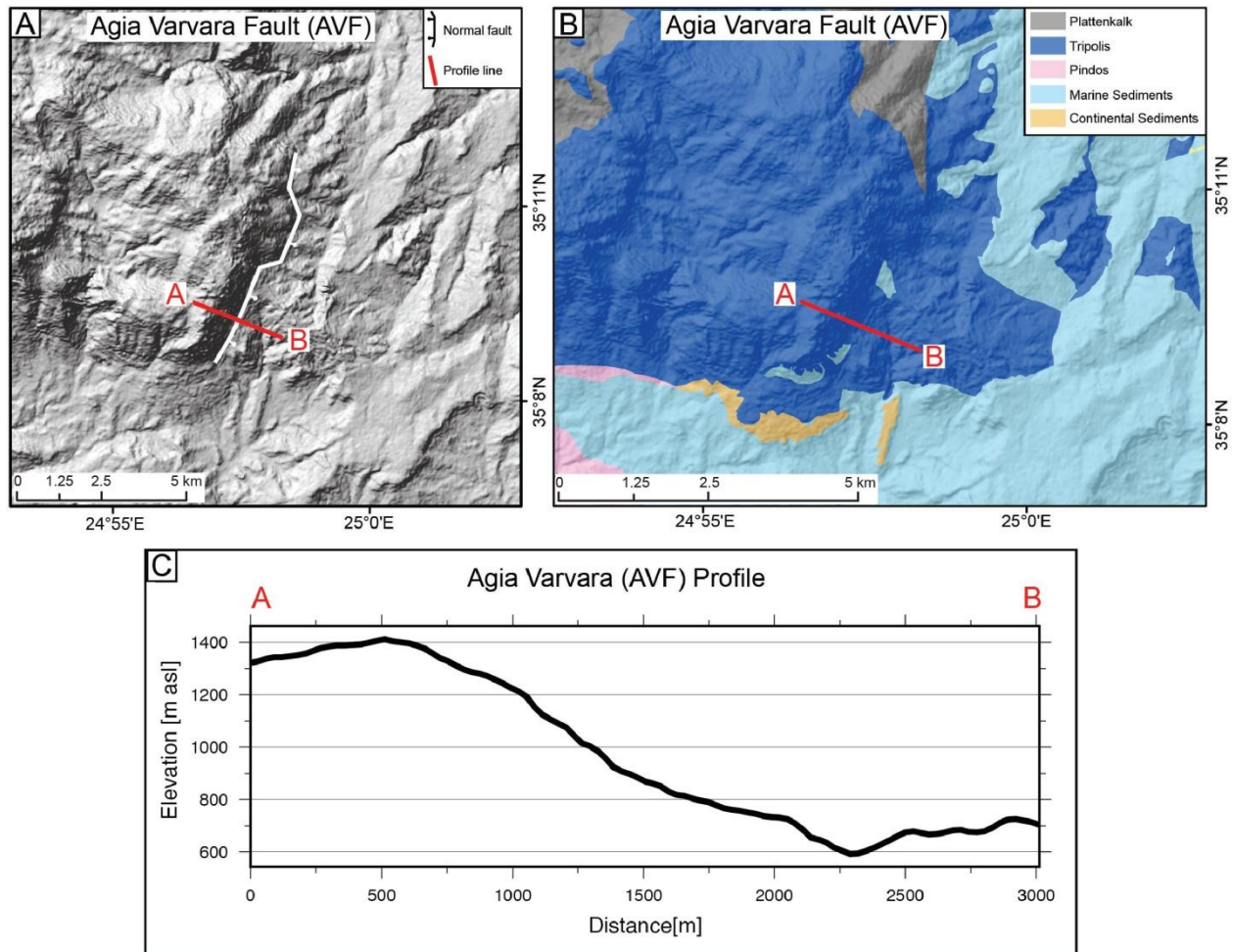


Figure 3.11: A) Topographic expression of the AvF and the location of the profile line A-B superimposed on the SPOT-DEM. B) Geological map of Crete (after Papanikolaou and Vassilakis, 2010) superimposed on the SPOT-DEM. C) Profile line across the AvF fault.

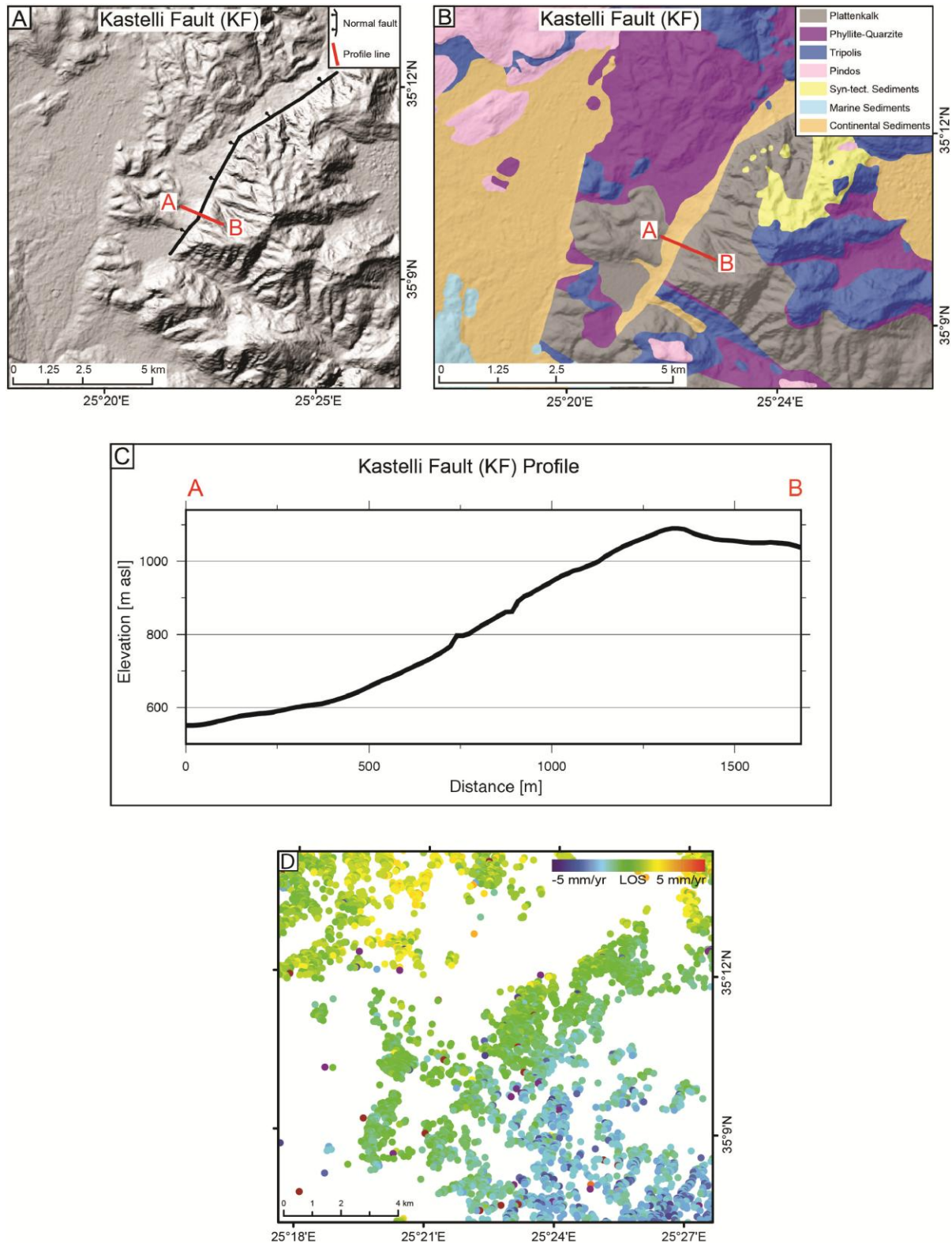


Figure 3.12: A) Topographic expression of the KF and the location of the profile line A-B superimposed on the SPOT-DEM. B) Geological map of Crete (after Papanikolaou and Vassilakis, 2010) superimposed on the SPOT-DEM. C) Profile line across the KF fault. D) PSI measurements.

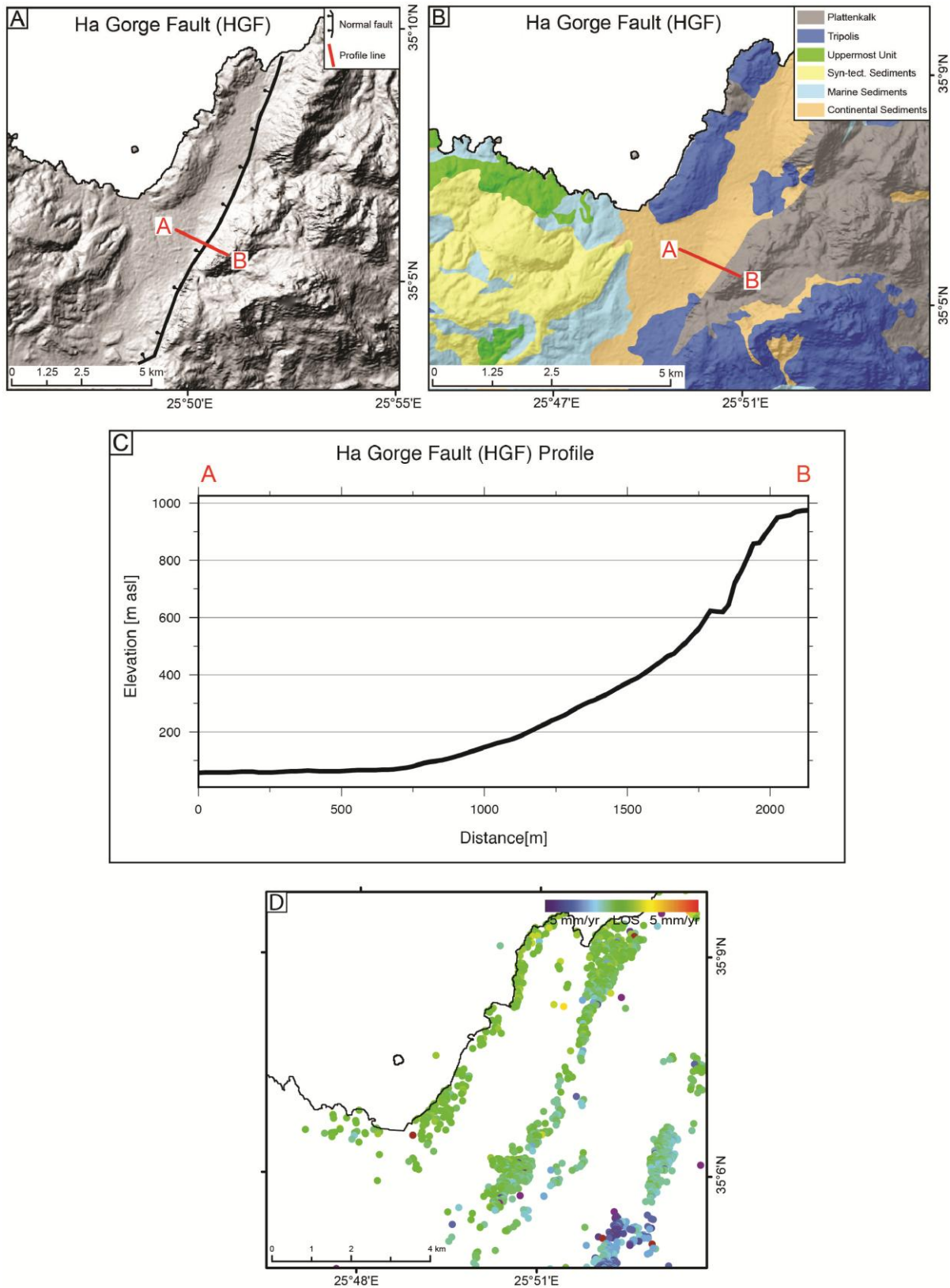


Figure 3.13: A) Topographic expression of the HGF and the location of the profile line A-B superimposed on the SPOT-DEM. B) Geological map of Crete (after Papanikolaou and Vassilakis, 2010) superimposed on the SPOT-DEM. C) Profile line across the HGF fault. D) PSI measurements.

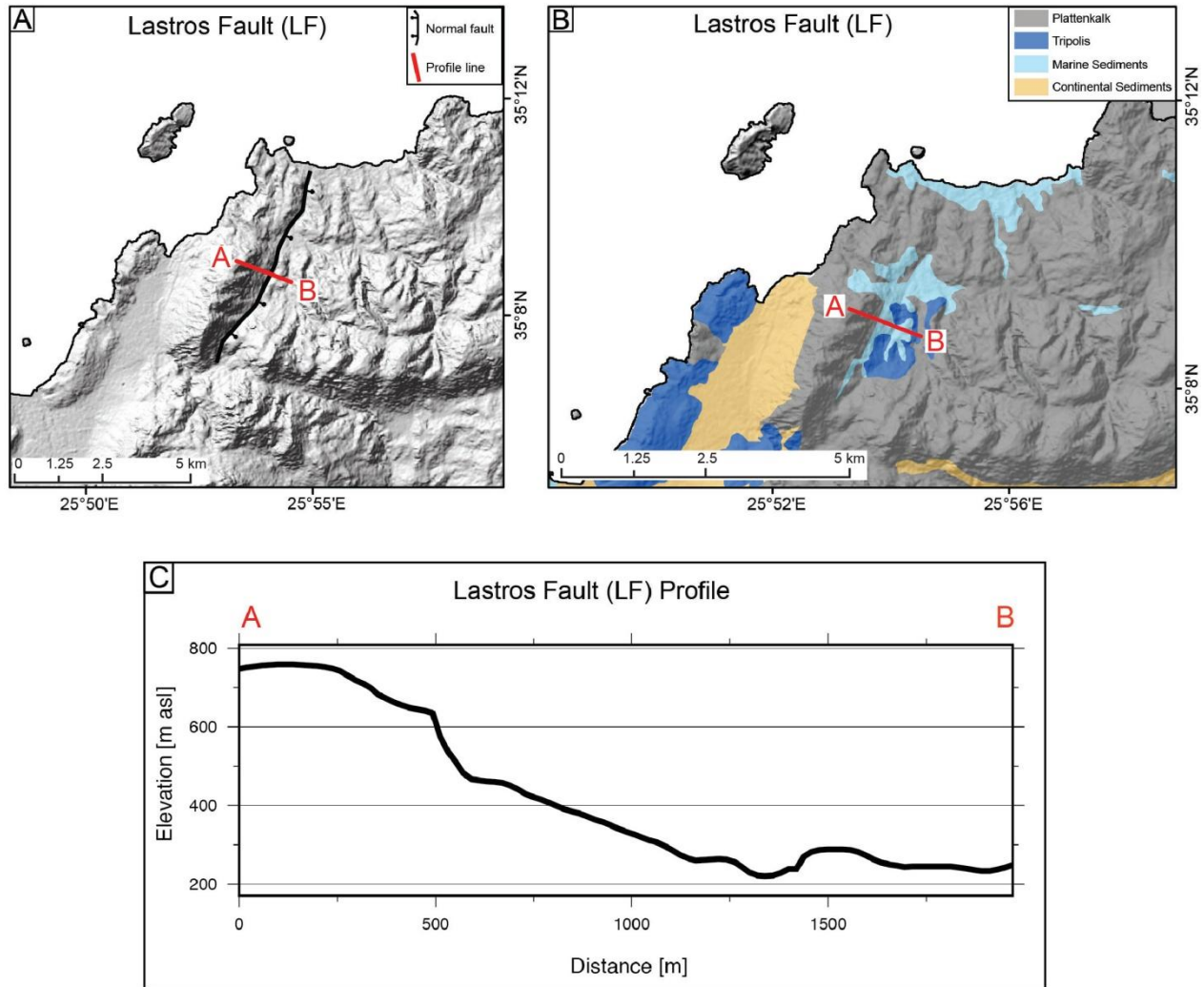


Figure 3.14: A) Topographic expression of the LF and the location of the profile line A-B superimposed on the SPOT-DEM. B) Geological map of Crete (after Papanikolaou and Vassilakis, 2010) superimposed on the SPOT-DEM. C) Profile line across the LF fault.

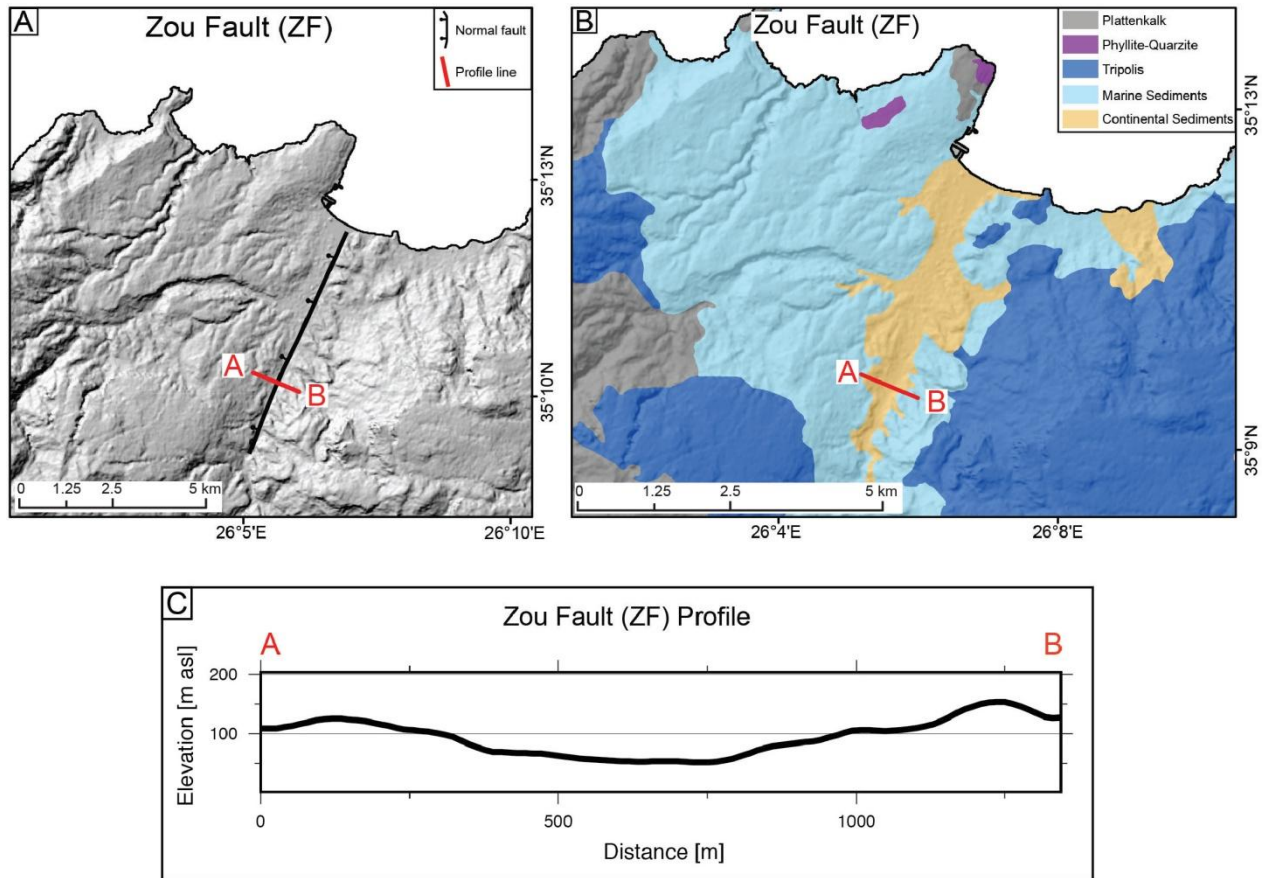


Figure 3.15: A) Topographic expression of the ZF and the location of the profile line A-B superimposed on the SPOT-DEM. B) Geological map of Crete (after Papanikolaou and Vassilakis, 2010) superimposed on the SPOT-DEM. C) Profile line across the ZF fault.

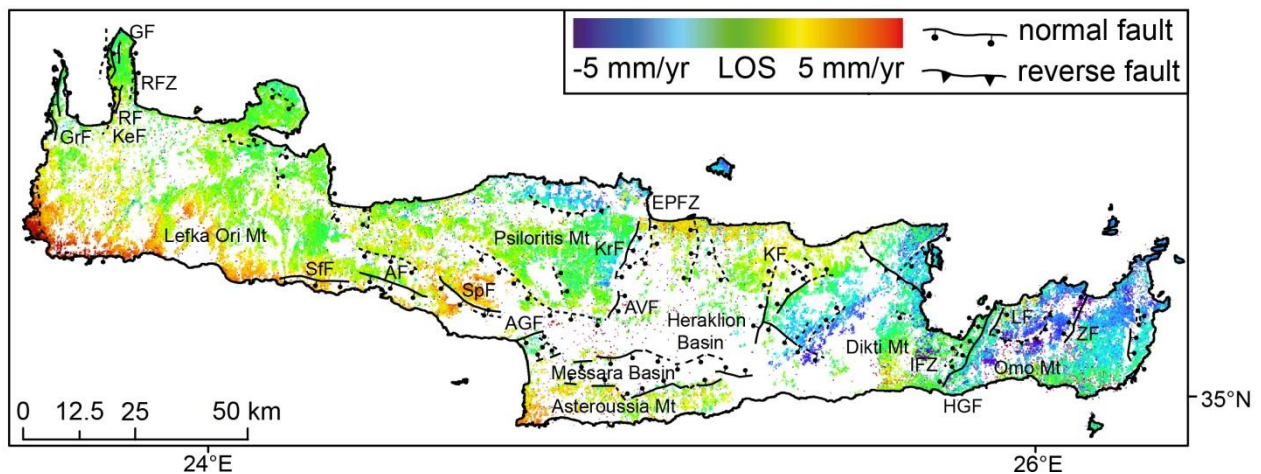


Figure 3.16: Fault map of Crete. Colored dots show 1992 to 2000 PSs velocities in LOS of 431.251 PSs in the GPS reference frame. Dashed lines are possible faults determined by geomorphic features in topography. GrF: Gramvousa Fault, RFZ: Rhodope Fault Zone, KeF: Kera Fault, RF: Rodope Fault, GF: Gionas Fault, SfF: Sfakia Fault, AF: Asomatos Fault, SpF: Spili Fault, AGF: Agia Galini Fault, EPFZ: Eastern Psiloritis Fault Zone, KrF: Kroussonas Fault, AVF: Agia Varvara Fault, KF: Kastelli Fault, IEZ: Ierapetra Fault Zone, HGF: Ha Gorge Fault, LF: Lastros Fault, ZF: Zou Fault.

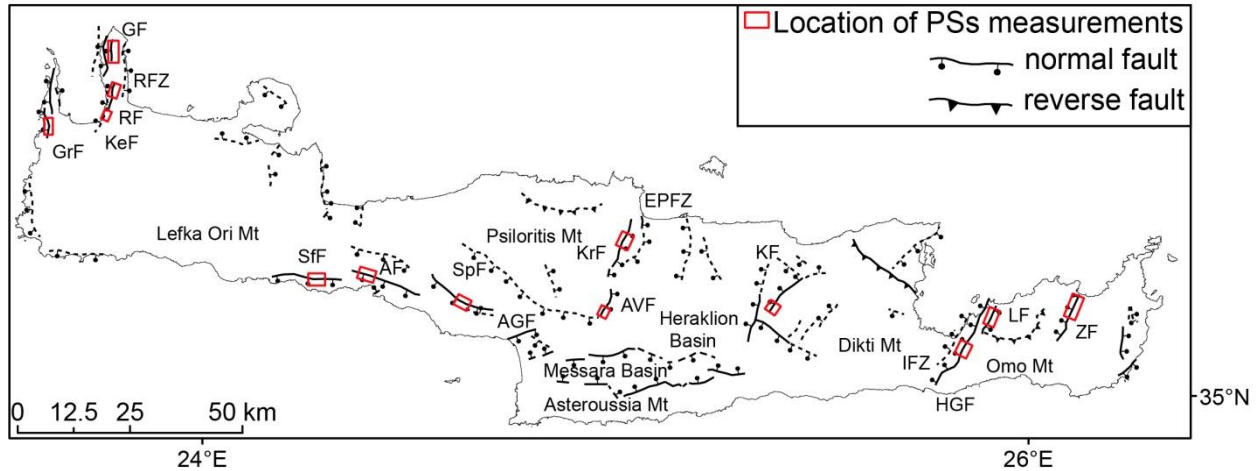


Figure 3.17: Fault map of Crete. Red rectangle show location of PSs measurements for analysis of deformation rates in LOS across the faults. Dashed lines are possible faults determined by geomorphic features in topography. For fault abbreviations please see Figure 3.16.

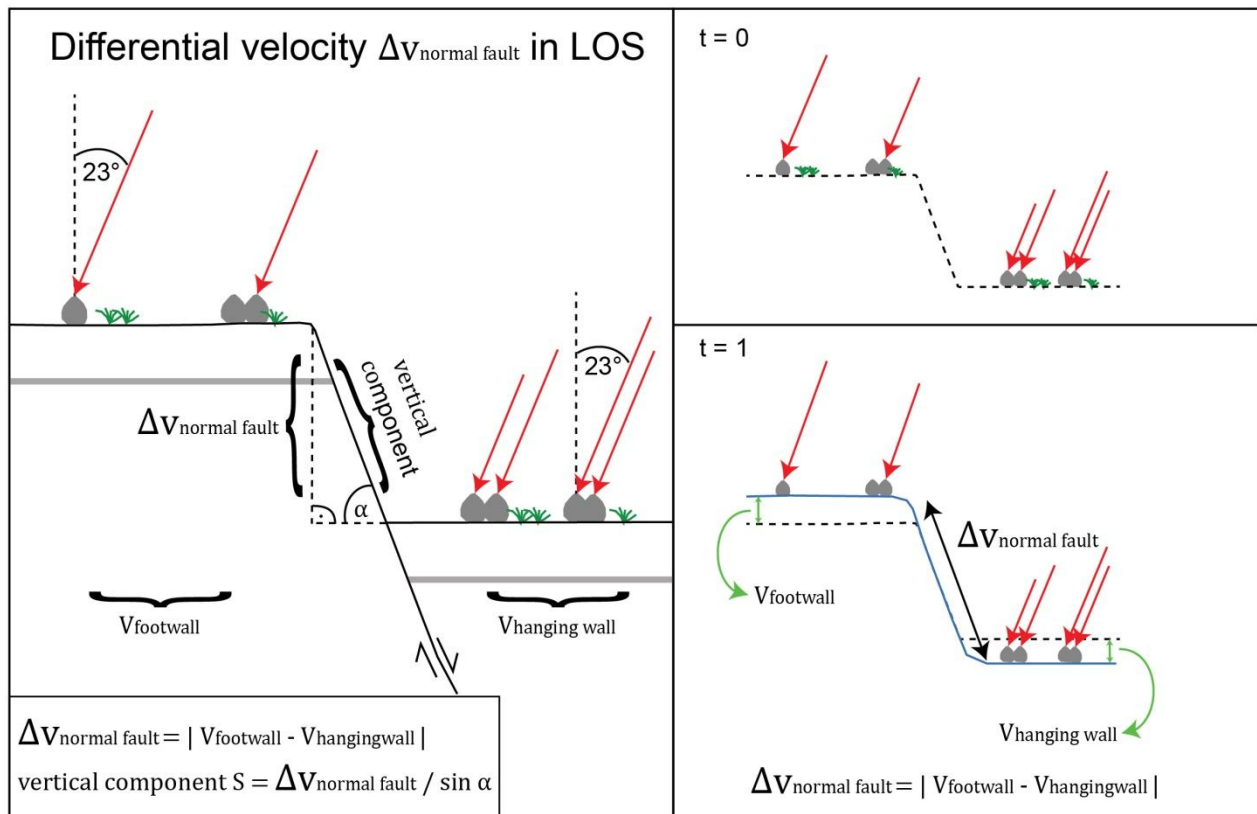


Figure 3.18: Schematic cross-section showing the relationship between differential velocity $\Delta v_{\text{normal fault}}$ in the LOS measured by PSI velocities of the footwall and the hanging wall. Illustration of the relationship between the dip-angle α and the dip slip component. Not drawn to scale. $t = 0$: is the start situation across the fault. $t = 1$: is the end situation of measurements, during which vertical motion occurred.

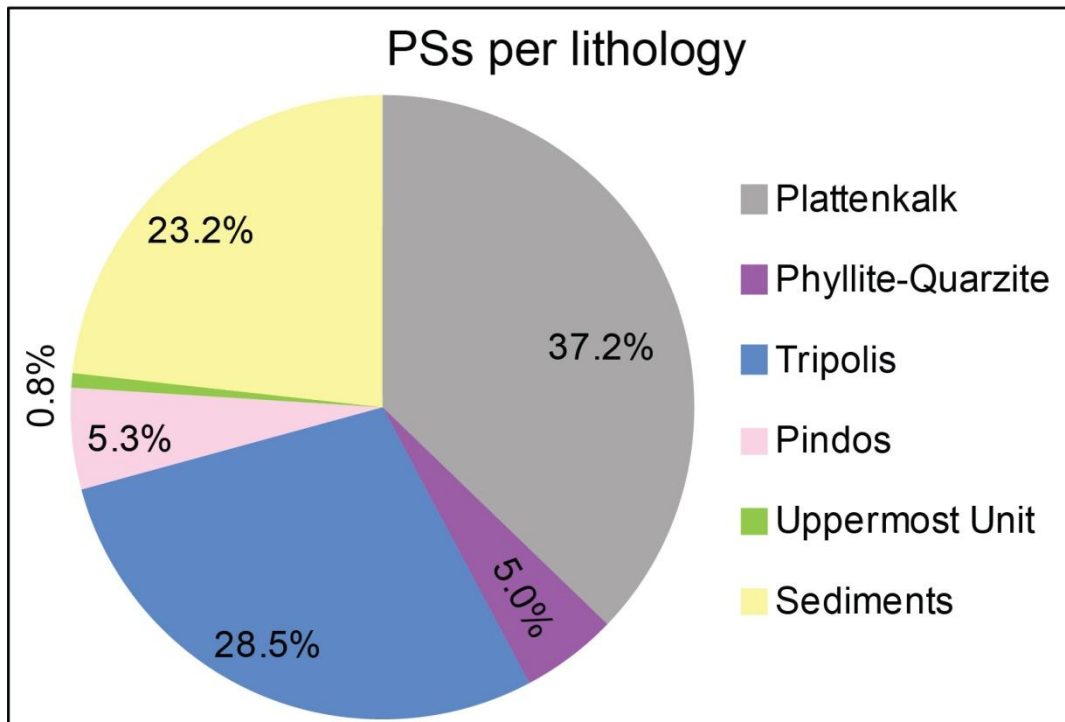


Figure 3.19: Percentage of PSs per lithological unit on Crete.

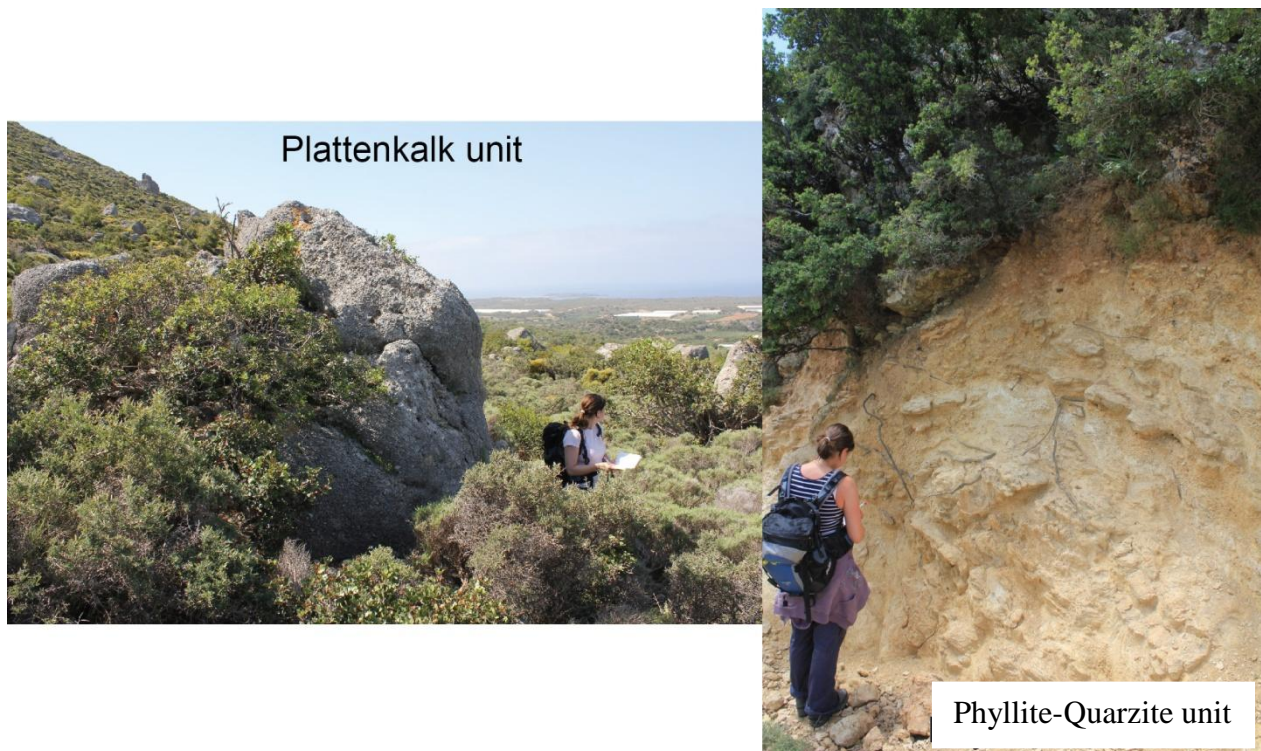


Figure 3.20: Fotos taken in the Plattenkalk and Phyllite-Quarzite unit on Crete during the field campaign in Mai 2012.

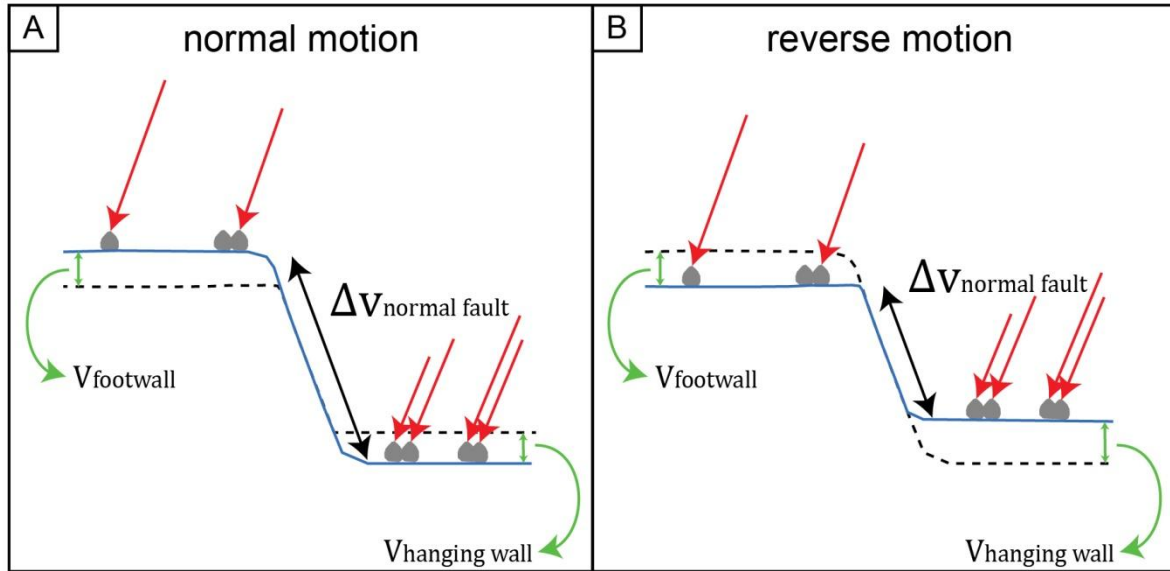


Figure 3.21: A) normal motion means that the footwall is uplifting and the hanging wall. B) reverse motion means that the footwall is subsiding and the hanging wall is uplifting.

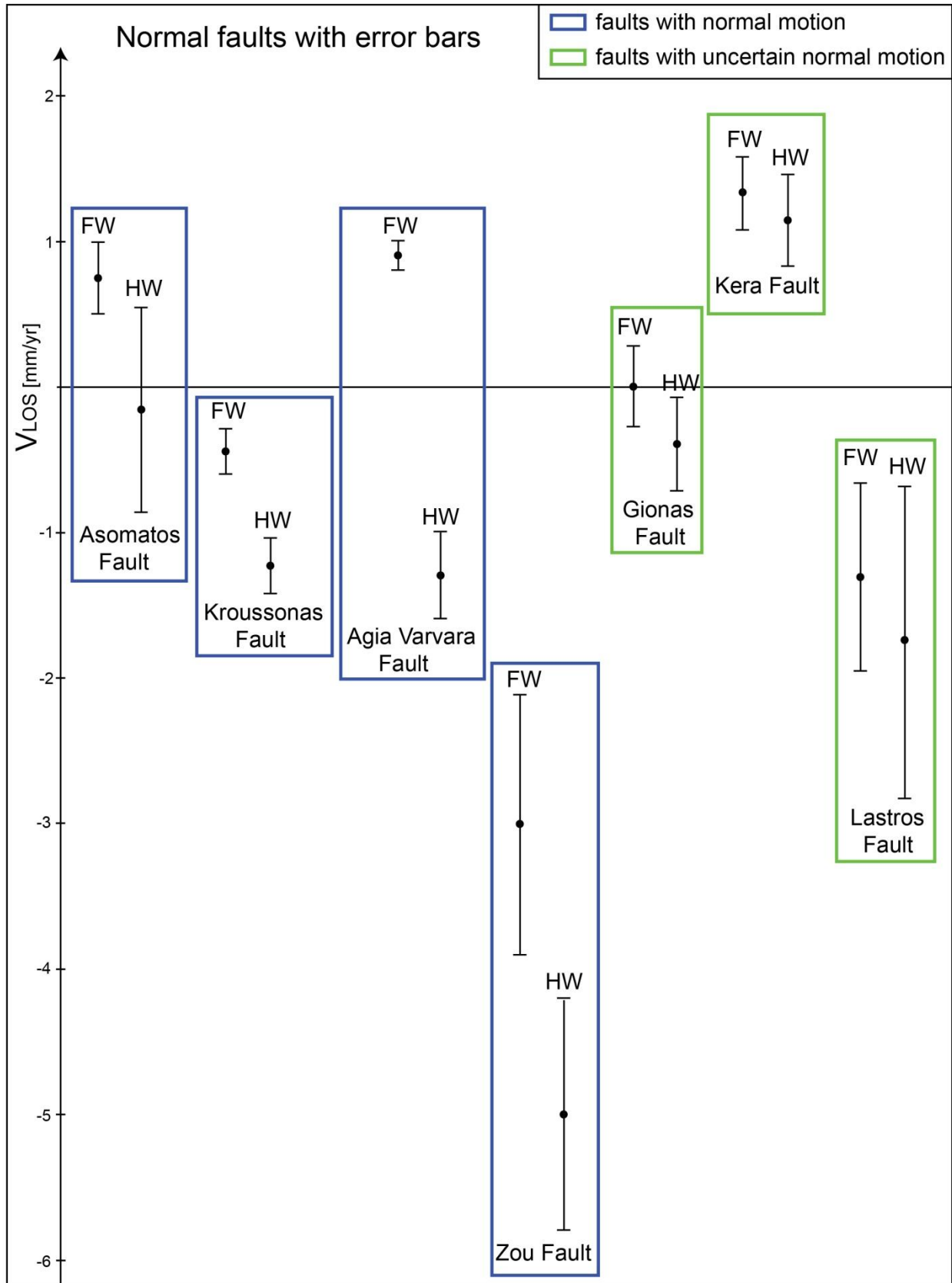


Figure 3.22: V_{LOS} motion across normal faults respectively for the footwall (FW) and the hanging wall (HW) with the corresponding error bars.

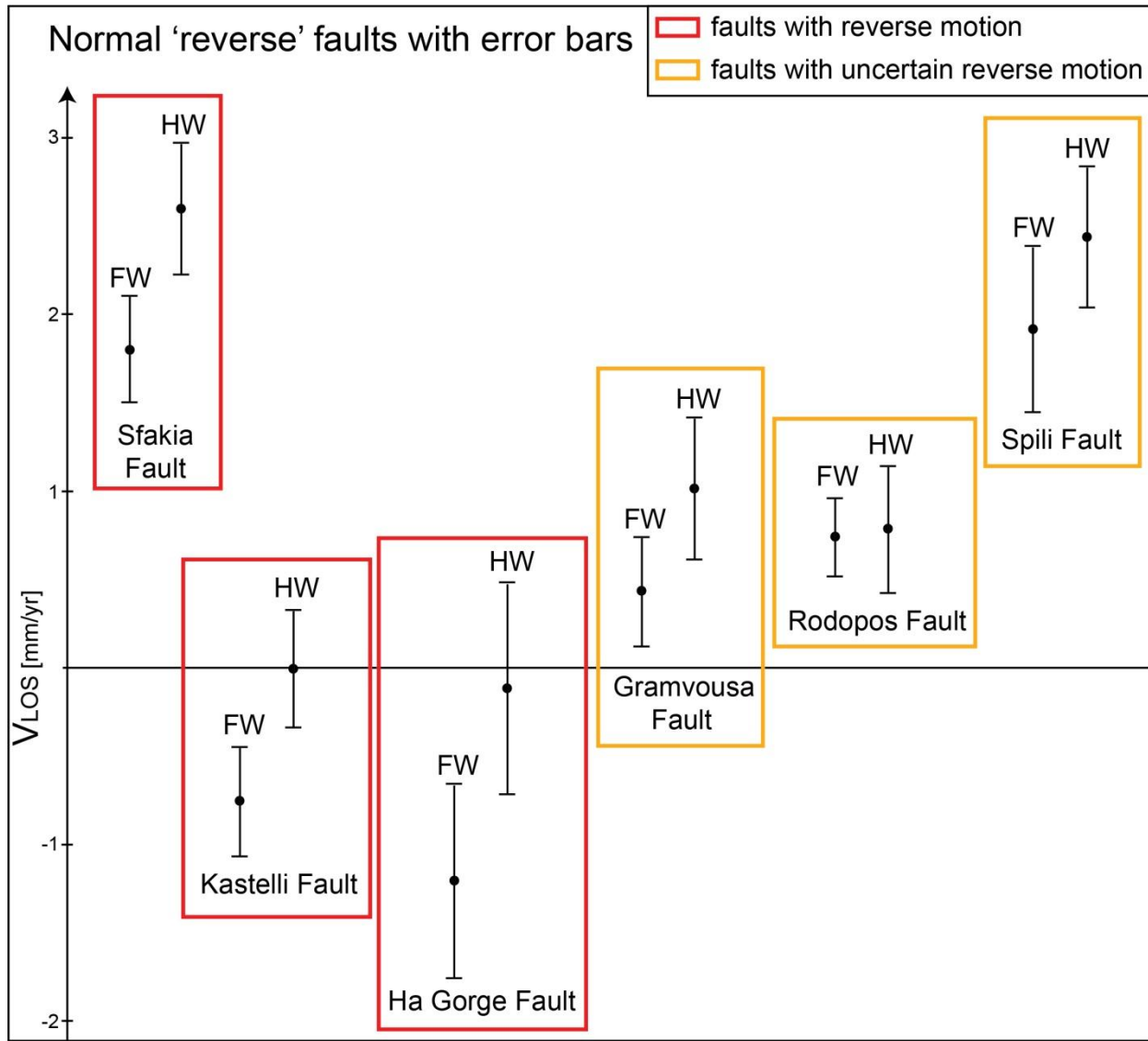


Figure 3.23: V_{LOS} motion across normal faults with reverse motion respectively for the footwall (FW) and the hanging wall (HW) with the corresponding error bars.

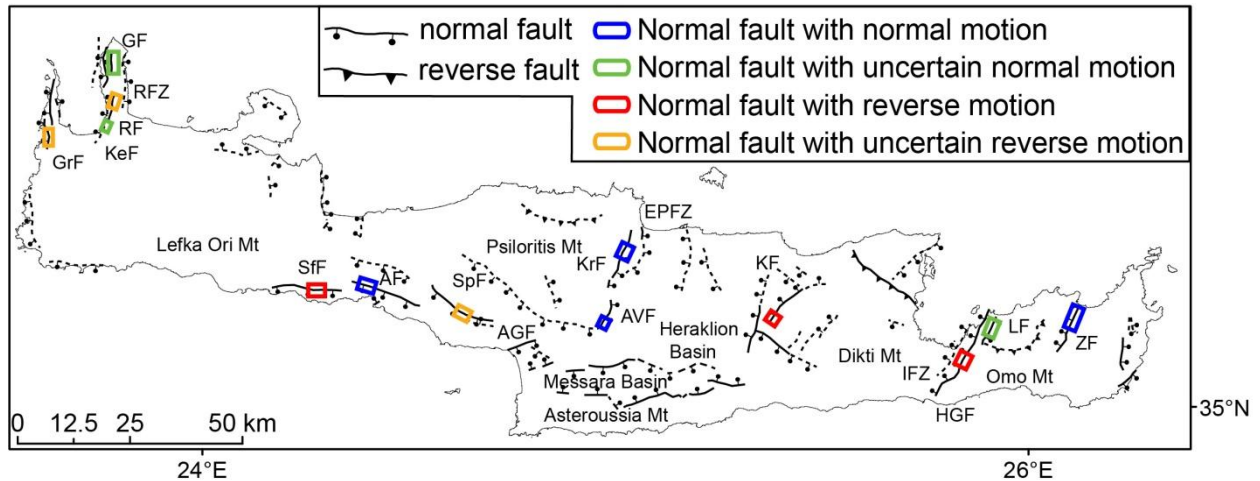


Figure 3.24: Distribution of normal faults with either normal motion or reverse motion along them. GrF: Gramvousa Fault, RFZ: Rhodope Fault Zone, KeF: Kera Fault, RF: Rodope Fault, GF: Gionas Fault, SfF: Sfakia Fault, AF: Asomatos Fault, SpF: Spili Fault, AGF: Agia Galini Fault, EPFZ: Eastern Psiloritis Fault Zone, KrF: Kroussonas Fault, AVF: Agia Varvara Fault, KF: Kastelli Fault, IEZ: Ierapetra Fault Zone, HGF: Ha Gorge Fault, LF: Lastros Fault, ZF: Zou Fault.

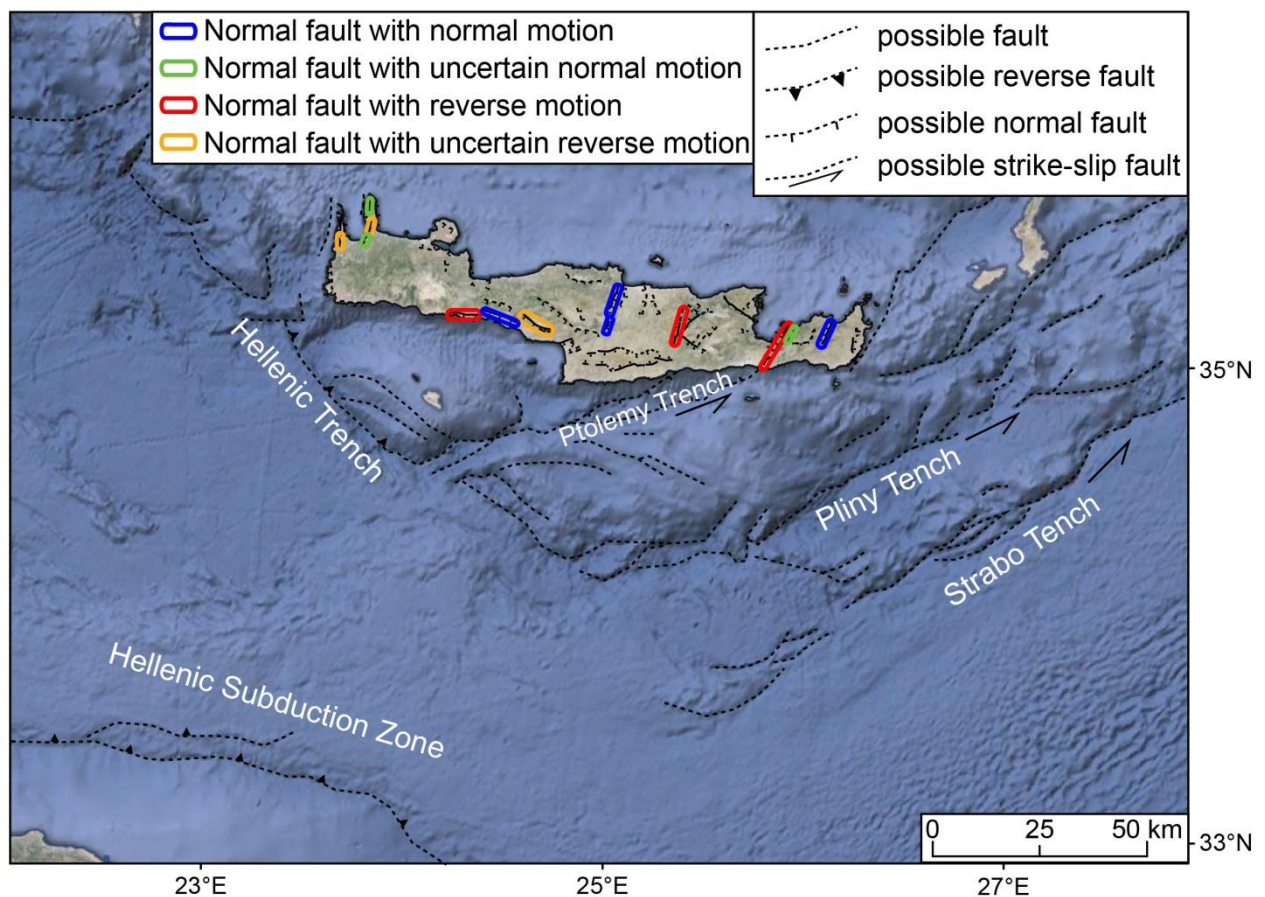


Figure 3.25: Distribution of normal faults with either normal motion or reverse motion superimposed on the bathymetry map of Google Earth.

Table 3.1: PS measurements for the footwall and hanging wall across normal faults on Crete, and the calculated dip-slip component S .

Fault	Number of PS measurements footwall	v_{FW}^{LOS} [mm/yr]	Number of PS measurements hanging wall	v_{HW}^{LOS} [mm/yr]	Δv^{LOS} [mm/yr]	α [°]*	S [mm/yr]
Asomatos (AF)	745	0.75 ± 0.49	152	-0.17 ± 1.43	0.92 ± 0.90	75S	0.95 ± 0.93
Kroussonas (KrF)	111	-0.42 ± 0.31	61	-1.23 ± 0.37	0.81 ± 0.48	70E	0.86 ± 0.51
Agia Varvara (AVF)	13	0.91 ± 0.23	5	-1.29 ± 0.61	2.2 ± 0.65	70E	2.34 ± 0.69
Zou (ZF)	82	-3.06 ± 1.80	128	-5.06 ± 1.62	2.0 ± 2.42	65W	2.21 ± 2.67
Gionas (GF)	470	-0.05 ± 0.56	259	-0.39 ± 0.64	0.34 ± 0.85	65W	0.38 ± 0.94
Kera (KeF)	49	1.34 ± 0.52	91	1.14 ± 0.63	0.2 ± 0.82	70W	0.21 ± 0.87
Lastros (LF)	109	-1.33 ± 1.30	74	-1.74 ± 2.16	0.41 ± 2.52	60E	0.47 ± 2.90
Sfakia (SfF)	408	1.79 ± 0.59	210	2.65 ± 0.75	0.86 ± 0.95	70S	0.92 ± 1.01
Kastelli (KF)	165	-0.76 ± 0.57	53	-0.04 ± 0.66	0.72 ± 0.87	70W	0.77 ± 0.93
Ha Gorge (HGF)	1233	-1.21 ± 1.13	56	-0.12 ± 1.23	1.09 ± 1.67	80W	1.10 ± 1.70
Gramvousa (GrF)	100	0.43 ± 0.62	123	1.03 ± 0.80	0.6 ± 1.01	70W	0.64 ± 1.07
Rodopos (RF)	187	0.73 ± 0.54	464	0.78 ± 0.71	0.05 ± 0.89	70W	0.05 ± 0.95
Spili (SpF)	607	1.93 ± 0.94	78	2.45 ± 0.82	0.52 ± 1.25	65S	0.57 ± 1.38

*Dip α along normal faults from Caputo et al. (2010)

Table 3.2: Geological and geodetic data of slip along normal faults in Crete.

Fault	Geological data ^a			Geodetic data ^b	
	α [°]	T_{max} [m]	S_{geol} [mm/yr]	$S_{geodetic}^{LOS}$ [mm/yr]	$S_{geodetic}^{vertical}$ [mm/yr]
Asomatos (AF)	75 S	8	0.6	0.95 ± 0.93	1.01 ± 0.98
Kroussonas (KrF)	70 E	12	1.0	0.86 ± 0.51	0.91 ± 0.54
Agia Varvara (AVF)	70 E	10	0.8	2.34 ± 0.69	2.48 ± 0.73
Zou (ZF)	65 W	8	0.7	2.21 ± 2.67	2.34 ± 2.83
Gionas (GF)	65 W	4	0.3	0.38 ± 0.94	0.40 ± 0.99
Kera (KeF)	70 W	5	0.4	0.21 ± 0.87	0.21 ± 0.92
Lastros (LF)	60 E	15	1.3	0.47 ± 2.90	0.49 ± 3.08
Sfakia (SfF)	70 S	12	1.0	0.92 ± 1.01	0.97 ± 1.07
Kastelli (KF)	70 W	6	0.5	0.77 ± 0.93	0.81 ± 0.98
Ha Gorge (HGF)	80 W	12	0.9	1.10 ± 1.70	1.16 ± 1.80
Gramvousa (GrF)	70 W	8	0.7	0.64 ± 1.07	0.68 ± 1.13
Rodopos (RF)	70 W	4	0.3	0.05 ± 0.95	0.05 ± 1.01
Spili (SpF)	65 S	10	0.8	0.57 ± 1.38	0.60 ± 1.46

^aGeological data taken from Caputo et al. (2010): α = Dip of fault; T_{max} : Maximum throw along fault scarp; S_{geol} : Average slip rate for the last 13 ka years.

^bGeodetic data based on my PSI analysis from 1992 - 2000: Deformation along fault plane, $S_{geodetic}^{LOS}$: slip-rate in LOS. $S_{geodetic}^{LOS} = \Delta v_{LOS} / \sin \alpha$. $S_{geodetic}^{vertical}$: true vertical slip-rate. Measured by $S_{geodetic}^{vertical} = S_{geodetic}^{LOS} * c$, with $c = 0.94$.

Table 3.3: Normal faults on Crete and their type of motion and lithology of footwall and hanging wall.

Fault name	Motion along fault - geodetic	Motion certain / uncertain	Footwall	Hanging wall
AF	normal	certain	Tripolis	Phyllite-Quartzite , Tripolis and Syntectonic sediments
KrF	normal	certain	Tripolis	Marine Sediments
AvF	normal	certain	Tripolis	Tripolis
ZF	normal	certain	Tripolis, Marine and Continental Sediments	Marine and Continental Sediments
GF	normal	uncertain	Tripolis	Tripolis
KeF	normal	uncertain	Phyllite-Quartzite and Tripolis	Phyllite-Quartzite and Tripolis
LF	normal	uncertain	Plattenkalk and Marine Sediments	Plattenkalk, Pindos and Marine Sediments
SfF	reverse	certain	Plattenkalk and Phyllite-Quartzite	Phyllite-Quartzite and Marine Sediments
KF	reverse	certain	Plattenkalk	Plattenkalk and Continental Sediments
HGF	reverse	certain	Continental Sediments	Continental Sediments
GrF	reverse	uncertain	Marine Sediments	Marine and Continental Sediments
RF	reverse	uncertain	Tripolis and Marine Sediments	Tripolis
SpF	reverse	uncertain	Pindos and Marine Sediments	Pindos and Marine Sediments

Chapter 4

MORPHOTECTONIC ANALYSIS AND IMPLICATIONS FOR THE INTERMEDIATE-TERM COASTAL UPLIFT PATTERN OF CRETE

4.1 Abstract

The island of Crete, Greece, is a forearc high located along the African - Eurasian plate boundary above the Hellenic subduction zone. Crete's subaerial exposure offers the opportunity to study deformation processes in a subduction forearc. Here, I investigate the pattern of vertical surface-deformation on the millennial time-scale using geomorphic markers. Morphotectonic markers, such as river channels and marine terraces, are utilized to derive information concerning rates and patterns of active deformation from topography.

I analysed ~ 300 river profiles extracted from a Digital Elevation Model (DEM), and determined concavity, steepness index and knickpoints distributions along these profiles. The resulting pattern is heterogeneous.

To analyse Pleistocene and Holocene paleo-shorelines, I compiled data from several publications conducted along the Cretan coastline. Age and elevation of paleo-shorelines were corrected for sea-level changes following the procedure by Rohling et al. (2014). I calculated a mean uplift rate for the Pleistocene paleo-shorelines of $\sim 1.03 \pm 0.01$ mm/yr. Data for Holocene shorelines show that the island is separated into a subsiding eastern part and an uplifting western part. The average subsidence rate for E Crete is ~ 0.57 mm/yr, and the average uplift rate for W-Crete is ~ 1.89 mm/yr.

My geomorphic analysis across Crete shows that the island is not uplifting as a rigid, homogenous block on the millennial time-scale. The island is separated into individual blocks with independent uplift histories. This may suggest that tectonic processes on Crete are not dominated by the Hellenic subduction zone, but rather by the interaction of the main plate interface of main upper crustal faults in the overriding plate and upper-crustal normal faults on Crete.

4.2 Introduction

Subduction zones are tectonically active plate-boundaries prone to strong destructive earthquakes. Accompanying coseismic and interseismic uplift or subsidence typically extends from the trench to the adjacent forarc regions. Subduction zone dynamics is complex due to interaction along the plate interface with those in the overriding plate (Plafker and Rubin, 1978). The vertical deformation pattern along subduction zones on different time-scales provides essential parameters to place constraints on fault geometry and kinematics. These tectonic processes lead to vertical deformation which can be preserved, hence recognized in the landscape. The landscape provides information about the millennial rates ($10^3 - 10^5$ yr) (Whipple and Tucker, 1999). Geomorphic markers, such as river channels and marine terraces, have been utilized to analyze vertical deformation rates and patterns (e.g., Whipple and Tucker, 1999; Lave and Avouac, 2000; Kirby and Whipple, 2001)

In non-glacial landscapes river channels shape the relief, and are the most geomorphologically sensitive indicators for uplift rates at millennial time-scales (Whipple, 2004;

Burbank and Anderson, 2012). Bedrock channels are found in actively uplifting regions, where rivers incise into bedrock (Whipple, 2004), such that longitudinal river-profiles provide information on the spatiotemporal variations for rock uplift-rates (Whipple and Tucker, 1999; Snyder et al., 2000; Kirby and Whipple, 2001; Whipple, 2004). Surface uplift causes steepening of the river profiles, which leads to the formation of knickpoints, which also depends on climatic and the lithology conditions in the study area (e.g., Schoenbohm et al., 2004; Whipple, 2004).

Along coastal regions, marine terraces are geomorphic markers recording former sea-level stands, tectonic uplift and tilting (Bloome et al., 1974; Chappell, 1974). Marine terraces with known age and elevation above present sea-level document coastal uplift and are a direct measure for the absolute vertical-motion locally (e.g., Bloome et al., 1974; Chappell, 1974). Currently used approaches to derive coastal uplift are based on the assumption that the uplift-rate of the landmass is constant. The sea-level changes instantaneously during coseismic events, whereas it fluctuates gradually over glacial cycles of thousands to hundred thousands of years (Burbank and Anderson, 2012).

In this chapter, I synthesize Crete's vertical uplift history by combining river-profile and paleo-shoreline analysis. I analyse the vertical surface-deformation pattern across Crete derived from river-profiles, and analyse the coastal uplift pattern based on Pleistocene and Holocene shorelines.

4.3 Morphotectonic Setting

The island is surrounded by major faults in the overriding plate, such as the Hellenic Trench, and the Ptolemy, Pliny and Strabo Trenches. The island is characterized by horst and graben structures separated by upper-crustal normal faults, resulting in mountainous relief with several mountains higher than 2000 m (Figure 4.1). The dominant morphological structures on the island are Lefka Ori Mountains (W-Crete) with a peak of ~ 2450 m, Psiloritis Mountain (Central Crete) with a peak of ~ 2450 m, and Dikti Mountains (E-Crete) with a peak height of ~2400 m. Furthermore, a great number of deep gorges and uplifted marine terraces can be identified along the coastline, which indicates past and ongoing uplift of Crete.

4.4 Present-Day Climate

The present-day climate on Crete is classified as Mediterranean climate (Köppen-Geiger climate classification) (Kottek et al., 2006). This climate is characterized by hot summers with little to no precipitation, which leads to a semi-arid climate with droughts in summer time and major precipitation in winter (Kottek et al., 2006). Data of the temperature and rainfall (Figure 4.2) for the time period of 1958 to 1997 show that climatic conditions are very homogenous across Crete (Figure 4.3) (Hellenic National Meteorological Service). Therefore, the climatic influence on erosion and sedimentation appears to be uniform across the region.

4.5 Millennial-Scale Uplift History of Crete

Previous studies investigated geomorphic markers across Crete.

Roberts et al. (2013) investigated river-longitudinal profiles on Crete for estimating the history of the vertical uplift-rates for the last 4 Ma. Their river analysis is based on ASTER GDEM data, with a resolution of 30 m, and a DEM accuracy of 7 to 14 m (<https://www.jspacesystems.or.jp/ersdac/GDEM/E/2.html>). The inverse modeling of given river profiles was used to estimate the uplift rate (Roberts and White, 2010): between 4 – 2 Ma Crete was uplifting 0.1 to 0.5 mm/yr, but accelerated to 1 to 1.2 mm/yr since 1 Ma (Roberts et al., 2013).

Several authors investigated Pleistocene along the coast of Crete (Figure 4.4 & Table 4.1). The first study was conducted by Anglier (1979), who recognized wave-cut notches and thin depositional platforms. The induced uplift rate ranges between 0.25 to 0.4 mm/yr.

Gaki-Papanassiou et al. (2009) reinvestigated the terraces mapped by Angelier (1979) at Ierapetra and utilized his age constrains. Two additional terraces were found, which are offset by the Ierapetra normal fault (P1) (Gaki-Papanassiou et al., 2009). The uplift rate was adjusted to 0.3 mm/yr, and the mean vertical displacement along the Ierapetra fault was calculated to 0.1 mm/yr.

Gallen et al. (2014) (P4, P6 – P18, and P20-P22) investigated paleo-shorelines along the southern coastline of the Asteroussia and Dikti Mountains. Sediments along marine terraces and alluvial fans were dated using the optically stimulated luminescence (OSL) method (Gallen et al., 2014). The average throw-rate for the South-Central Crete and the Lentas normal faults are 0.35 and 0.2 mm/yr, respectively (Gallen et al., 2014). The hanging wall of the South-Central Crete fault has an uplift rate between 0.1 and 0.4 mm/yr, along the coastline of the Asteroussia block the uplift rate is between 0.5 and 1 mm/yr, and along the coastline of the Lantas block the uplift rate is calculated between 0 and 0.8 mm/yr (Gallen et al., 2014).

Wegmann (2008) (P19, P23-P31, and P33-P38) dated Pleistocene depositional and marine terraces using OSL and radiocarbon dates. Wegmann (2008) calculated an average uplift rate of 1.5 mm/yr, with local rock uplift rates varies between 1.2 and 2.0 mm/yr for western Crete.

Strasser et al. (2011) (P24 & P25) used Palaeolithic artefacts and dated shell types to calculate an uplift rate ranging between 1.0 to 1.5 mm/yr for two locations (Preveli and Schinaria).

Tiberti et al. (2014) (P31/P32) found two Pleistocene marine terraces between Krios and Paleochora and assigned radiocarbon ages dating seasheels (Bivalve fragment and *Glycymeris* sp.). The average uplift rate is on the order of 2.5 to 2.7 mm/yr (Tiberti et al., 2014) for the Pleistocene and Holocene. For the time range 42 to 23 ka the vertical surface-deformation was characterized by subsidence with a rate of 2.6 to 3.2 mm/yr, followed by uplift (Tiberti et al., 2014). The uplift was between 23 to 5 ka on the order of ~7.7 mm/yr (Tiberti et al., 2014).

Several authors investigated Holocene uplift rates for eastern, southern and western Crete are based on archaeological Roman data and dating of marine organisms (Figure 4.5 & Table 4.2). Pavlopoulos et al. (1996) used dated geomorphological and archeological data and calculated an uplift rate between 0.3 – 0.6 mm/yr and a subsidence rate between 0.1 – 6.1 mm/yr.

Mourtzas (2012) investigated ancient fish tanks and fish traps of the Roman time. The eastern part of the island was submerged by an average tectonic rate of 0.65 mm/yr (Mourtzas, 2012).

Along the southern coastline further to the west Holocene shorelines are dated using radiocarbon dates of *Dendropoma petraeum*, *Neogoniolithon*, calcareous alga, *Serpulorbis* by Pirazzoli et al. (1996), and Price et al. (2002).

Shaw et al. (2010) dated using radiocarbon dates of coral and Bryozoans and calculated an uplift rate of ~ 2 mm/yr.

Tiberti et al. (2014) used radioacarbon dates for *Lithophaga* sp., *Spondylus* sp., and Vermetids, and calculated an uplift rate for the past 5 ka of an order of 3.0 – 3.3 mm/yr.

Along the eastern coastline, near Kato Zakros, Strobl et al. (2014) used surface exposure dating based on cosmogenic nuclides to determine the ages of fluvial sandstone clasts. The calculated uplift rate for eastern Crete is 0.4 – 0.6 mm/yr (Strobl et al., 2014).

4.6 Investigating Geomorphic Markers for Analysing the Surface Deformation Pattern and Uplift Rates

In this study I analyzed river profiles and synthesized published data to derive parameters to quantify the vertical surface deformation pattern and uplift rates on the millennial time-scales.

4.6.1 Longitudinal River Profiles

Erosion, E , of a river is expressed by the formulation of the stream-power (Whipple and Tucker, 1999),

$$E = KA^m S^n \quad (4.1)$$

where K is a dimensional coefficient of erosion, A stands for the upstream drainage area, S the local channel gradient, and m and n are positive constants that are functions of basin hydrology, channel geometry, and specific incision processes (Whipple and Tucker, 1999). The coefficient of erosion K integrates many variables controlling erosional efficiency, such as rock erodibility, sediment load, hydraulic geometry, climatic conditions, and return periods of effective discharges, e.g. storm events (Whipple, 2004; Burbank and Anderson, 2012). Therefore, the coefficient of erosion K is poorly constrained, and Stock and Montgomery (1999) suggest that K varies over several magnitudes among different study areas.

The equation for bedrock channel evolution (Whipple et al., 2000) provides information about the change in height with time based on the difference between the rock uplift rate and erosion along the longitudinal profile,

$$\frac{dz}{dt} = U - E \quad (4.2)$$

where dz/dt represents the change in elevation, U the uplift rate, and E the erosion.

Following Whipple et al. (2000) by combining equations (4.1) and (4.2) leads to

$$\frac{dz}{dt} = U - KA^m S^n \quad (4.3)$$

At steady-state conditions dz/dt equals to zero, inducing the slope to equilibrium, S_e

$$S_e = \left(\frac{U}{K}\right)^{\frac{1}{n}} A^{-\frac{m}{n}} \quad (4.4)$$

If U and K are constant, then the rate of change of the channel gradient is specified by the ratio m/n and the drainage area A . The exponent of the drainage area A is defined as the concavity index θ

$$\theta = \frac{m}{n} \quad (4.5)$$

The positive constants m and n depend on erosional processes, channel geometry, and basin hydrology (Whipple and Tucker, 1999). A channel with high concavity represents a channel with steep headwaters and gentle downstream slopes, whereas a channel with low to no concavity

represents a linear gradient (Duvall et al., 2004). The concavity index (θ) is independent of the rock uplift rate (U), as long as U is spatially uniform (Kirby et al., 2001).

Longitudinal profiles of rivers are described by Flint's law of the power-law relationship between the local slope, S , and the upstream area, A (Flint 1974; Hack 1973):

$$S = k_s A^{-\theta} \quad (4.6)$$

where k_s , is defined as steepness index

$$k_s = \left(\frac{U}{K}\right)^{\frac{1}{n}} \quad (4.7)$$

At steady-state conditions, where erosion rate and river incision are equal to rock uplift, the steepness index (k_s) correlates to the rock uplift rate (U), but also depends on climate and lithology (Snyder et al., 2000; Kirby et al., 2003).

Equation (4.6) holds for drainage areas above a critical threshold (A_{cr}), which is interpreted as the transition from divergent to convergent topography, respectively, from debris-flow-dominated to fluvial-dominated bedrock channels, A_{cr} as critical drainage area is defined as $10^5 - 10^6$ m² (Tarboton et al., 1989; Montgomery and Foufoula-Georgiou, 1993; Whipple and Tucker, 1999).

The steepness and concavity indices provide information of tectonically induced changes of the Earth's surface, such as varying uplift rates, while many rivers have only a single value for the steepness and concavity along their profiles, rivers with varying values of k_s and θ provide the opportunity to detect changes of the Earth's relief (Wobus et al., 2006; Kirby et al., 2001). Because values of k_s are not comparable between drainage areas varying in size, the steepness index is normalized (k_{sn}) to a reference value of channel reference concavity θ_{ref} (Snyder et al., 2000; Whipple, 2004).

If the river is not in an equilibrium state anylonger, due to factors such as base-level fall caused by increase in the uplift rate (coseismic), climatic change, eustatic change, or river capture, the channel begins to adjust its longitudinal profile (Schoenbohm et al., 2004; Whipple and Tucker, 1999). Therefore, the longitudinal river profile shows a discontinuity in its river concavity by steep or convex reaches, known as knickpoints (Penck, 1924; Seidl et al., 1994). Knickpoints separate segments of the river profile already adjusted to the new boundary conditions downstream, from segments still under influence of the old boundary conditions upstream. Knickpoints represent an increase in slope, leading to a stream power increase resulting in accelerated erosion and upstream migration of the knickpoints (e.g., Whipple and Tucker, 1999; Burbank and Anderson, 2001). The formation of knickpoints highly depends on the mechanical properties of the lithology (Whipple, 2004).

4.6.2 Marine Shorelines

Marine terraces of known age, such as abrasion platforms, are geomorphic markers recording former sea-level stands, tectonic uplift and tilting of coastal regions (e.g., Bloome et al., 1974; Chappell, 1974).

In general, eustatic sea-level changes are either caused by water-volume or ocean-basin volume changes (Pitman, 1978; Hallam, 1984; Miller et al., 2005; Rohling et al., 2014). Water-volume changes are dominated by the glacio-eustasy, which is the consequence of volume changes of the continental ice-sheets (Hallam, 1984). Glacio-eustasy produces sea-level changes with amplitude of up to 200 m and a rate of 20 m/ka (Miller et al., 2005). Other water volume changes caused by thermal expansion, groundwater and lake storage have an amplitude of ~ 5 to 10 m at a rate of 10 m/kyr (Miller et al., 2005).

Eustatic sea-level changes are also caused by ocean-basin changes of the shape, mainly due to tectonic eustasy, which is about three orders of magnitude slower than Pleistocene glacio-eustasy, but effective over millions of years (Hallam, 1984). Tectonic eustasy is the process of changing the water capacity of an ocean basin caused by variations in seafloor spreading (e.g., Pitman, 1978; Hallam, 1984; Miller et al., 2005). The amplitude of tectono-eustasy is on the order of 100 - 300 m, but with a rate of only 10 m/Ma (Miller et al., 2005). Additional minor processes influence the shape of ocean basins, which are sediment deposition and compaction, and dynamic topography due to mantle dynamics, but these processes operate on longer time-scales (Hallam, 1986; Stanley, 1995).

During the Pleistocene period the eustatic sea-level is mainly caused by glacio-eustasy (Hallam, 1984; Burbank and Anderson, 2001). The sea-level varies widely over glacial and interglacial cycles, over tens of thousands to one hundred thousand years, while the landmass is considered to rise steadily or instantaneously due to earthquakes (Burbank and Anderson, 2001).

Wave-cut abrasion platforms and notches along steep sea cliffs are formed due to erosion of the sea landwards during stationary sea-level with respect to the land (Figure 4.4) (Lajoie et al., 1986; Burbank and Anderson, 2001). A sea-notch approximates the location and elevation of the paleo-shoreline and is used as geomorphic marker (e.g., Lajoie et al., 1986). Therefore, emerged or submerged sequences of paleo-shorelines record uplift or subsidence along the coastal region (Lajoie et al., 1986; Burbank and Anderson, 2001).

Paleo-shorelines can form a staircase morphology, which may or may not have parallel sea-notches running above the modern coastline. Parallel notches indicate a constant uplift rate, whereas non parallel notches indicate a non constant uplift rate. These sequences are formed during separate highstand of interglacial stages, which are correlated to Marine Isotopic Stages (MIS) or the Oxygen Isotope Stage (OIS) (e.g., Bloome et al., 1974; Chappel, 1974) by dating marine organisms. The age of at least one terrace must be known, and all other successively higher terraces can be correlated to the preceding eustatic highstand (Merritts and Bull, 1989; Burbank and Anderson, 2001).

The average uplift rate (R) is determined by the vertical displacement (D) and the age (t) of the paleo-shoreline:

$$R = \frac{D}{t} = \frac{E_p - E_o}{t} \quad (4.8)$$

with $D = E_p - E_o$, the difference between the present elevation (E_p) and the elevation (E_o) of the correlative eustatic sea-level at time of formation (original elevation) (Lajoie, 1986; Merritts and Bull, 1989).

The tilt (T) is defined as the differential vertical displacement ($D_I - D_{II}$) and the horizontal distance (d) between the two observations (I and II):

$$T = \frac{(D_I - D_{II})}{d} = \tan \theta \dots\dots\dots (4.9)$$

with $\tan \theta$ as the tilt angle (θ) (Lajoie, 1986).

Holocene paleo-shorelines do not indicate eustatic sea-level changes, but only tectonic deformation (Lajoie et al., 1986), because global sea-level has become relatively stable since about 6000 before present (BP) (Fairbridge, 1961). Erosional Holocene paleo-shorelines are only preserved when coastal uplift exceeds 1 to 2 mm/yr (Lajoie et al., 1986). Therefore, Holocene paleo-shorelines need not be corrected for sea-level changes (Lambeck, 1995; Lambeck and Chappell, 2001). Holocene paleo-shorelines can be recognized by sea-notches along the Cretan coast. The necessary time for the formation of tidal notches in carbonate rocks ranges between 0.2 to 1 mm/yr for the Mediterranean region (Pirazzoli and Evelopidou, 2013). Laborel et al. (1999) considered a horizontal notch depth of 0.5 - 1 m, an activity time of sea-waves forming

the wave notch of 1500 ± 100 yr, and calculated a rate of $0.3 - 0.7$ mm/yr of erosion for sea notches in W-Crete.

Assuming that the average uplift rate (R) represents the vertical component of the slip rate along a fault, with known dip geometry, the slip rate can be determined along this fault by:

$$\text{slip rate} = \frac{R}{\text{Dip}} \quad (4.10)$$

The recurrence time of a certain earthquake with known magnitude and correspond slip of this event along the fault can be calculated by:

$$\text{recurrence time} = \frac{\text{slip of earthquake}}{\text{slip rate}} \quad (4.11)$$

4.7 Methods

In the first step I analyzed river longitudinal profiles concerning the concavity, the steepness index and knickpoints distribution across Crete. In the second step I analyzed published data concerning the Pleistocene and Holocene paleo-shorelines.

4.7.1 Vertical Deformation based on River Longitudinal Profiles

I used the procedure called *Stream Profiler* developed by *Snyder et al.* (2000), and Kirby et al. (2001), which was used for extracting drainage areas and longitudinal river-profiles from digital elevation models (DEM) (*Wobus et al.*, 2006; *Whipple et al.*, 2007). The extraction is done using the Geographical Information System (GIS) software ArcGIS and MATLAB (*Wobus et al.*, 2006; *Whipple et al.*, 2007). In this work I used a DEM generated from stereo pairs of satellite images of the Système Probatoire d'Observation de la Terre (SPOT) with a horizontal spatial resolution of 20 m and vertical accuracy of 15 ± 5 m.

A total number of 153 river channels are examined with their tributaries leading to a total number of 300 analyzed river profiles across the entire island of Crete. Steepness (k_s) and concavity (Θ) indices were calculated from least-squares regression of the logarithms of channel slope and area (*Whipple et al.*, 2007).

Due to the high correlation of the steepness index (k_s) concerning the concavity index (Θ), I calculated the normalized steepness index (k_{sn}), fitted to the slope and drainage area using a fixed reference concavity (Θ_{ref}) (*Whipple et al.*, 2007). The reference concavity is assigned the study area's mean value ($\Theta_{ref} = 0.45$) (*Whipple et al.*, 2007). The drainage area was set to 10^6 m² (1 km²). Further, the location of knickpoints along the river profiles was analysed.

The calculated normalized steepness-index k_{sn} is analyzed using the reference concavity ($\Theta_{ref} = 0.45$). Primarily the normalized steepness index is measured for the total length of the longitudinal river-profiles and afterwards for small individual separated segments along these river profiles.

I further analyzed the normalized steepness index for smaller segments of the river profiles. For this analysis *Stream Profiler* provides automated codes calculating the normalized steepness index k_{sn} for areas with critical values (*Whipple et al.*, 2007). The critical size of the area for this analysis was chosen as 10^6 m² (1 km²).

4.7.2 Vertical Deformation based on Paleo-Shorelines

For my study of Pleistocene and Holocene paleo-shorelines I compiled several publications of dated paleo-shorelines along the Cretan coastline. Data of dated Pleistocene paleo-shorelines were taken from publications by Gaki-Papanastassiou et al. (2009) for eastern Crete, Gallen et al. (2014), Strasser (2010) for south-central Crete, Wegmann (2008) and Tiberti et al. (2014) for western Crete. Dated Holocene data of paleo-shorelines and archeological data for whole Crete are based on publications by Mourtzas (2012), Pavlopoulos et al. (2011), Pirazzoli et al. (1996), Price et al. (2002), and Shaw et al. (2010).

4.7.2.1 Pleistocene Paleo-Shorelines

For the sea-level correction I took data from *Rohling et al.* (2014) for the sea-level curve derived from planktonic foraminiferal $\delta^{18}\text{O}$ records at the Red Sea (Bab-el-Mandab) reconstruction, with 1σ uncertainty of ~ 6 m, originated by data of Siddall et al. (2003) (Figure 4.11 & Table 4.2). Data from the Mediterranean sea have gaps in the record for times were Pleistocene terraces were dated on Crete (Rohling et al., 2014), These gaps are caused by sapropel intervals in combination with major surface freshwater dilution (Rohling et al., 2014). For this reason I did not use the sea-level curve based on Eastern Mediterranean planktonic foraminiferal $\delta^{18}\text{O}$ records.

The Red Sea sea-level curve was chosen due to its close location to the Eastern Mediterranean, and because both represent evaporative marginal seas (Siddall et al., 2003; Rohling et al., 2014). Evaporative marginal seas are characterized by small and narrow connections to the open ocean, therefore sea-level lowering reduces the sea water exchange (Siddall et al., 2003; Rohling et al., 2014). The reduced sea water exchange leads to an increase of the residence time of water within the evaporative marginal sea, and enhances the effect of evaporation (Siddall et al., 2003; Rohling et al., 2014). Evaporative marginal sea amplifies the signals of sea-level changes recorded in $\delta^{18}\text{O}$ values of foraminifera (Siddall et al., 2003; Rohling et al., 2014).

The correction was done by dated age and height constrains of the different authors, and corrected these to the sea-level curve of Rohling et al. (2014). For the correction I use the age of the terraces and assign the sea-level height at its formation (E0) graphically. I assumed a constant uplift rate. Then, I recalculated the average uplift rate by using equation (4.8).

4.7.2.2 Holocene Paleo-Shorelines

For the Holocene paleo-shorelines I took the age and height constraints of Pavlopoulos et al. (1996), Mourtzas (2012), Pirazzoli et al. (1996), Price et al. (2002), and Shaw et al. (2010) (Figure 4.14). I calculated for each location the average uplift or subsidence rate (Figure 4.14 & Figure 4.15) using equation (4.8) and considered E_0 to be equal to zero.

4.7.2.3 Pleistocene and Holocene Uplift Rates

For seven localities I was able to correlate data of Pleistocene and Holocene paleo-shorelines, because they are located at the same locality (Figure 4.16 & Table 4.5). I assumed constant uplift rate. Based on my analysis I calculated the average mean uplift rate, using equation 4.8. The slip rate is calculated using equation 4.10, and the recurrence times for the 365

A.D. and the 1303 earthquakes, respectively, is calculated by using equation 4.11. The 365 A.D. earthquake affected Aradena Gorge, Sougia, Kalamia, Moni Chryssoskalitissa, Cape Koutoulas, and Phalassarna (Figure 4.35), whereas the 1303 earthquake only affected Ierapetra.

I used the fault parameter by Shaw et al. (2008) for the 365 A.D. earthquake (Table 4.6), and fault parameters by Yolsal and Taymaz (2012) for the 1303 earthquake (Table 4.6).

4.8 Results

4.8.1. Concavity

The concavity index of the longitudinal profiles of Crete is determined by the total length of the river profiles (Figure 4.5). The concavity index varies from nearly zero ($\Theta \sim 0$) to values of higher concave profiles ($\Theta \sim 0.42$). Most profiles on Crete have concavities smaller than 0.1, well distributed over the island. Fewer river profiles have concavity indices in the range of 0.1 to 0.2; these profiles are located more frequently along the northern and the eastern coastline. Only nine river profiles have concavity values between 0.2 and 0.3. Three of these profiles are located along the SE coastline, and the remaining are located along the northern coastline of W-Crete. River profiles with concavity higher than 0.3 ($\Theta \sim 0.42$) are only found along the northern coastline of W-Crete, especially on the peninsulas.

4.8.2 Steepness Index

The normalized steepness index k_{sn} for the total length of the river profiles varies widely (Figure 4.6), ranging from k_{sn} values of 9 to 190. Most obvious is that the highest channel gradients ($k_{sn} > 120$) occur in topographically highest areas of Crete. Values for the normalized steepness index between $90 < k_{sn} < 120$ are located along river-profiles with highest gradients in mountainous regions. The Heraklion and the Messara basins are dominated by river profiles with smaller values of $k_{sn} < 60$. The coastal regions are dominated by rivers with k_{sn} smaller than 90, except the localities close to the mountainous regions on Crete.

The normalized steepness index k_{sn} for the total length of the river profiles shows that high steepness gradients correlate well with areas of highest topographical elevations, but are also located along the southern coastline of Central Crete where deep gorges are located (Figure 4.7). The Heraklion and Messara basins are dominated by steepness indices smaller than 30.

4.8.3 Knickpoints

On Crete I detected 385 knickpoints along the river profiles (Figure 4.8), which are evenly distributed. On Crete only 22% of all rivers have no knickpoints at all, whereas 78% of the river-profiles have one or even six knickpoints per stream. River profiles with knickpoints are ubiquitously distributed over Crete. Figure 4.9 shows some examples of river-profiles with one knickpoint along the western and the eastern coastline. Western profiles have more gentle slopes than eastern profiles. Eastern profiles are characterized by gentle topography above knickpoints and steeper topography below knickpoints. Stream profiles with four knickpoints (Figure 4.10) show that the river profiles along the northern coastline are similar in their gradients, whereas the river profiles along the eastern and southwestern coastline are characterized by steeper gradient of their river profiles.

4.8.4 Pleistocene Paleo-Shorelines

The individual recalculated Pleistocene uplift rates are shown in Figure 4.13. All Pleistocene shorelines indicate an uplift of the island, with varying uplift rates (Figure 4.13). The mean average Pleistocene uplift rate is 1.03 ± 0.01 mm/yr. For eastern Crete the uplift rate ranges from 0.01 to 2.8 mm/yr, whereas along the western coastline uplift rates range from 0.80 to 4.79 mm/yr.

4.8.5 Holocene Paleo-Shorelines

The calculated Holocene uplift rates are shown in Figure 4.14.

The subsidence rates of the eastern and the southeastern part of Crete (H1 – H16) are derived from Roman archaeological data by Pavlopoulos et al. (1996) and Mourtzas (2012).

Along the southern coastline further to the west Holocene shorelines are dated using radiocarbon dates of *Dendropoma petraeum*, *Neogoniolithon*, calcareous algae, *Serpulorbis* by Pirazzoli et al. (1996), and Price et al. (2002).

Shaw et al. (2010) used radiocarbon dates of coral and Bryozoans, and Tiberti et al. (2014) used radiocarbon dates for *Lithophaga* sp., *Spondylus* sp., and Vermetids.

For eastern Crete I calculated a mean average subsidence rate of -0.57 ± 0.18 mm/yr, and for western Crete I calculated a mean average uplift rate of 1.89 ± 0.11 mm/yr (Figure 4.14)

4.9 Analysis

The topography of the island correlates well with the geological units (Figure 4.17). The highest relief is associated with horst structures consisting of pre-Neogene units, whereas the grabens are filled with Neogene sediments covering the uppermost units of the basement (Hall et al., 1984; van Hinsbergen and Meulenkamp, 2006). Thus, I assume that the topography is strongly associated with the rock-uplift pattern on Crete.

4.9.1 Vertical Deformation based on River Longitudinal Profiles

As mentioned before, the analysis of river profiles shows that the concavity index varies between $0 < \theta < 0.42$, whereas most river-profiles have values less than 0.1 (Figure 4.5). I compared the concavity indices with the lithology (Figure 4.18) based on the map of geological units by Papanikolaou and Vassilakis (2008). From the analysis (Figure 4.19) it appears that the concavity index is not influenced by the geological units, as the highest percentage of concavity values is associated with rivers through sediments and not on basement rocks.

I further compared the concavity with the fault distribution across Crete (Figure 4.20), but there is no obvious correlation of the appearance of faults and the concavity index on Crete.

Based on the results concerning the steepness index k_{sn} on Crete for the total length (Figure 4.6) and small segments (Figure 4.7) along river profiles, I can correlate that the highest stream gradients coincide with the highest elevations, such as the Lefka Ori Mountains, the Psiloritis Mountains, and the Dikti Mountains. River-profiles with the lowest stream gradients coincide with the Messara and the Heraklion basins or plains along the northern coastline of Crete.

I compared the spatial distribution of k_{sn} values to the geological map by Papanikolaou and Vassilakis (2008) (Figure 4.21 & Figure 4.22). I found a high correlation of the Plattenkalk with the highest steepness gradient $k_{sn} < 120$ (Figure 4.23 E), which can be explained due to the resistance of Plattenkalk to erosion, also the topographically highest elevations occur in the Plattenkalk unit. The percentage of the steepness index for the Plattenkalk is decreasing with decreasing steepness index (Figure 4.23). The percentage of the Pindos unit is also increasing with an increasing steepness index. I further observed a correlation of the lowest steepness index $k_{sn} > 30$ with sediments. The percentage of sediments is decreasing with higher values of k_{sn} , and is least for $k_{sn} < 120$. For the Phyllite-Quartzite, the Tripolis, and the Uppermost Units I see no clear increase or decrease depending on k_{sn} (Figure 4.23). Despite these correlations, I see no clear influence of steepness index with geological unit boundaries (Figure 4.21 & Figure 4.22). Changes of the steepness index do not coincide in most cases with geological unit boundaries.

If I compare the steepness index for long river profiles and the existence of faults, I do not see any influence of the faults on the steepness index (Figure 4.24). If I compare the steepness index identified along small segments, I see two regions where faults influence the steepness index (Figure 4.25). Across the Sfakia fault (SfF) and the possible normal fault located S of the Psiloritis Mountains, there a lot of small segments with steepness indices $k_{sn} > 120$ can be found (Figure 4.25). These high steepness indices may indicate recent activities of these faults, and therefore the adjustments of the rivers across these faults to the new equilibrium.

I further analyzed the distribution of 385 knickpoints across Crete (Figure 4.26). The highest amount of knickpoints is located on western Crete, compared to Central and eastern Crete. I compared the spatial distribution of the knickpoints to the geological map by Papanikolaou and Vassilakis (2008) and analyzed the appearance of knickpoints due to geological unit boundaries (Figure 4.26). I counted a total of 30 knickpoints close to geological unit boundaries, whereas 355 knickpoints are located within a geological unit. I therefore can rule out an influence of knickpoints formation due to geological unit boundaries.

I also checked the knickpoints distribution along faults on Crete (Figure 4.28). Most knickpoints are found across the Sfakia fault (SfF), which coincides with rivers with highest steepness index. Along the remaining faults I cannot see any clear correlation between the distribution of knickpoints and the faults.

I checked the amount of knickpoints for the steepness index k_{sn} of small river segments. The distribution of knickpoints shows that most knickpoints are located along small rivers with steepness index of $k_{sn} > 120$ (Figure 4.29). The amount of knickpoints decreases with the values of k_{sn} , and the lowest amount of knickpoints is found along rivers with steepness values for $k_{sn} < 30$.

Wobus et al. (2006) suggest that elevation of knickpoints across an area helps to figure out if uplift is homogenous or heterogeneous. I analyzed the knickpoint-elevation distribution across Crete (Figure 4.30), and cannot see any correlation between certain elevations and the appearance of knickpoints. This may indicate that Crete is not homogeneously uplifting, but rather the uplift pattern is heterogeneously distributed across the island. Independent blocks have their distinct vertical history.

I further analysed the knickpoint distribution across the island from E to W (Figure 4.31 & Figure 4.32). I laid a grid of 10 x 10 km over Crete for quantifying the knickpoint distribution and color coded the tiles depending on the amount of knickpoints (Figure 4.31). For every column I summed up the knickpoints and plotted these, normalized from W to E (Figure 4.32). The highest number per raster is found in W-Crete, whereas Central and E-Crete have similar numbers of knickpoints.

4.9.2 Vertical Deformation based on Paleo-Shoreline Analysis

My data collection of paleo-shorelines, published by several authors, provides a unique data set for studying the deformation history of Crete from Pleistocene to Holocene.

4.9.2.1 Pleistocene Uplift Rates

All Pleistocene shorelines indicate an uplift of the island, with varying uplift rates (Figure 4.13). These data indicate that the eastern part of Crete is not as fast uplifting as the western part of the island. This is confirmed by the topography, which is higher in the W than in the E. I calculated a tilt of the island from E to W of $\tan \theta = 0.00000-0.00080$ for paleo-shorelines of MIS 5.5 and $\tan \theta = -0.00164-0.00045$ for paleo-shorelines of MIS 5.1.

In Figure 4.33 I only plotted dated Pleistocene terraces, and then connected these terraces concerning their MIS stages (Table 4.2). The oldest dated terraces, of MIS stage 5.5, are found at P1 and P8. Terraces of MIS 5.3/5.2 are located at the eastern coastline at P39, terraces of MIS 5.1 are found at locations P11 and P15. Terraces of MIS 3.4 and 3.3 are only located on the southern and western coastline. The youngest dated terraces, MIS 2, are found at P39. If I analyze the elevation distribution of the terraces (Figure 4.33), then terraces of MIS 5.5 rise from E to W. This cannot be explained by faults (Figure 4.34), because P1 is located on the footwall of a normal fault, and should therefore be at higher elevation than P8, if this normal fault would be responsible for the tilting. Terrace of MIS 5.3/5.2 are only dated along the eastern coastline (P39), therefore I cannot say anything about the vertical surface-displacement along this terrace. But these terraces of MIS 5.3/5.2 are found at higher elevations than the older terraces of MIS 5.5 at localities P1 and P8. This may imply that the eastern coastline was uplifted stronger than the southern coastline at P1 and P8. Between P39 and P1 I do not see any fault trace in the geomorphology (Figure 5.34). At P39 I also find the youngest dated terraces with MIS 2. The height of the terrace would indicate that the eastern coastline was strongly uplifted after MIS 2. The terrace of MIS 5.1 at P11 and P15 are located below the older terraces of MIS 5.5 and 5.3/5.2 (Figure 4.33). The terrace seems to be tilted downwards towards the W. I cannot see any clear fault structure in the geomorphology explaining this tilting (Figure 4.34). At location P19 two terraces of MIS 3.4 and 3.3 are found (Figure 4.33), but the younger terrace MIS 3.3 is located above the older terrace of MIS 3.4. As well as, at localities P24 and P25, the terrace of MIS 3.3 is found at a higher elevation than the terrace of MIS 3.4. The terrace of MIS 3.3 (P31 and P38) is found below the terrace of MIS 3.4 (P34), but at the location P33 the terrace of MIS 3.3 is higher than the terrace of MIS 3.4.

This seems to be very unrealistic, and most probably the dating was not correct or the material dated is not anymore at its original place. The oldest terraces are of MIS 5.5 and imply that the eastern part of Crete was tilting towards the east. After this the eastern coastline must have experienced strong vertical uplift, because terraces of MIS 5.3/5.2 are higher in elevation than terraces of MIS 5.5. Further to the W, terraces of MIS 5.1 also indicate that the eastern part was uplifting relatively to the western part in this small area. Along the southern coastline towards the W, I do not find any dated terraces older than MIS 3.4. This could imply that no older terraces are preserved along the coastline, or terraces are not obvious anymore due to erosion, or that the material of the coastline is not good enough for dating, or just no data were collected until now.

This pattern of elevated MIS stage terraces may imply that Crete is not behaving as one rigid block, because terraces of the same MIS stages should be located at the same elevation. Further, I cannot see a clear relation between the tilting of the terraces and the distribution of the

crustal faults on Crete. Therefore, I may conclude that the uplift history was a differentiated uplift of individual blocks along the western, southern and eastern coastline during the Pleistocene.

It seems unrealistic that W-Crete experienced less uplift than E-Crete, because the topography is much higher in the W than in the E. It seems more likely that the distribution of terraces is achieved by crustal-faults in the overriding plate offshore Crete, such as the Hellenic and the Ptolemy Trenches. Furthermore, investigations are needed along the whole coastline of Crete, and apply the same dating method for all terraces.

4.9.2.2 Holocene Uplift Rates

I collected published data for Holocene uplift rates based on sea-notches and archaeological data for whole Crete (Pavlopoulos et al, 2011; Mourtzas, 2012), and only for W-Crete (Pirazzoli et al., 1996; Price et al., 2002; Shaw et al., 2010). Based on these data eastern Crete experienced subsidence on the order of 1.11 to 0.29 mm/yr, whereas western Crete is uplifting on the order of 0.62 to 5.54 mm/yr (Figure 4.15). The most prominent paleo-shoreline along the western coast is the one uplifted up to 9 m by the coseismic event of 365 A.D. (Pirazzoli et al., 1996) (Figure 4.35).

Above this shoreline sea-notches of older shorelines are found and dated. Nearly all these profiles indicate that subsidence occurred before the earthquake of 365 A.D., especially at Moni Chryssaskalistas (Figure 4.36) where more than ten paleo-shorelines were identified indicating subsidence before 365 A.D. (Pirazzoli et al., 1996; Price et al., 2002). Except data of Shaw et al. (2010) identified five paleo-shorelines uplifting before the 365 A.D event. These discrepancies can be induced by contaminated paleo-shorelines with younger fossils, which were incorrectly dated by Pirazzoli et al. (1996) and Price et al. (2002). But also Shaw et al. (2010) found paleo-shorelines subsiding before the 365 A.D. earthquake at Agia Kiraki and Gramena.

4.9.2.3 Pleistocene and Holocene Paleo-Shorelines

At seven locations along the western and southern coastline of Crete I compiled data of Pleistocene and Holocene paleo-shorelines (Figure 4.16 & Table 4.5). I further analysed these data to identify the cause of the uplifted terraces. In the next three subchapters one locality, Moni Chryssoskalitissa (Figure 4.36), is given as an example.

I analysed all seven localities. Six localities (Ierapetra, Aradena Gorge, Sougia, Kalamia, Cape Koutoulas, and Phalasarna) and their analysis are found in the Appendix, Chapter 4.

4.9.2.3.1 Uplift-Rates only by Tectonics

First, I tested if the height distribution of Pleistocene and Holocene terraces at Moni Chryssoskalitissa can be inferred by tectonic coseismic uplift only (Figure 4.37). In Table 4.4 is listed the elevation of the terrace, their age, the present elevation and further calculated the uplift rate using equation (4.8) for each author (Table 4.5).

The mean average uplift rate R is 0.2 ± 0.28 mm/yr, and the slip rate on the Hellenic Trench is 0.4 ± 0.56 mm/yr. The average recurrence time for an earthquake similar to the 365 A.D. earthquake with 20 m slip and $M_w = 8.25$ is 50000 (+438.78/ -355.49) yr.

I further tested how large the magnitude of each earthquake had to be, to generate the elevation differences between each terrace (Table 4.9). The calculated coseismic displacement values between the different terraces caused only by coseismic uplift could be realistic at Moni

Chryssoskalitissa. I compared the displacement of terrace T2 to terrace T1 of 60 m, with the maximum displacements measured for recent large earthquakes. For the 2011 M_w 9.0 Tohoku-Oki (Japan) earthquake the maximum slip was calculated around 60 m (Simons et al., 2011). For the 2010 M_w 8.8 Maule (Chile) earthquake the maximum slip was calculated around 15 m (Vigny et al., 2011). The maximum slip of 15 m was modeled for the 2004 M_w 9.1 Sumatra-Andaman earthquake (Ammon et al., 2005). For the 1960 M_w 9.5 Chile earthquake the maximum slip is on the order of 17 m for a uniform slip planar model, and for a variable slip planar model, representing slip along asperities, the highest peak of slip reached a value of 41 m (Barrientos and Ward, 1990). I plotted the results of maximum displacement versus magnitude M_w (Wells and Coopersmith 1994), and infer that the displacement between the different terraces can be achieved by earthquake displacement at Moni Chryssoskalitissa (Figure 4.39).

The same could be reasoned for uplifted terraces at Kalamia (Appendix, II.1.4.1), and Cape Koutoulas (Appendix, II.1.5.1). At Aradena Gorge (Appendix, Figure II.1.2.1) a maximum slip of 900 m would be needed, for Sougia (Appendix, II.1.3.1) a maximum slip of 360 m, and for Phalasarna (Appendix, II.1.6.1), a maximum slip of 74 m would be needed. This seems a bit unrealistic because the corresponding magnitudes are extremely high: for Aradena Gorge $M_w = 9.35$, for Sougia $M_w = 9.09$, and for Phalasarna $M_w = 8.6$. Therefore, if these terraces were uplifted by such large earthquakes I should observe this along the other locations. But I do not have any evidence for such large earthquakes. Therefore, terrace formation must be controlled by additional factors.

4.9.2.3.2 Uplift-Rates only by Sea-Level Changes

Second, I tested if the height distribution of Pleistocene and Holocene terraces at Moni Chryssoskalitissa can be inferred by sea-level changes only. At Moni Chryssoskalitissa sea-level fall from individual terraces vary between 27 and 0.1 m (Figure 4.40 & Table 4.7). The corresponding sea-level change rates vary between 0.03 to 21.92 mm/yr (Table 4.7). Terrace formation caused only by sea-level changes seems very unrealistic, because terraces are formed during separate highstands of interglacial stages (Bloome et al., 1974; Chappel, 1974). At Moni Chryssoskalitissa, the highest terraces was formed during MIS 5.2, which corresponds to a sea-level height 20 m below today's sea-level (Figure 4.11). Therefore, this terrace would be drowned today if sea-level changes would be the only cause for the terrace formation.

Another reason because shoreline formation by only sea-level variations is unrealistic is that sea-level was relatively stable since 6000 B.P. Therefore, Holocene paleo-shorelines do not indicate eustatic sea-level changes but only tectonic deformation (Lajoe et al., 1986).

Further, if terrace deformation only depended on sea-level fluctuations, the amount and height difference between shorelines around Crete must be everywhere the same. This is not the case (see analysis of other locations in the Appendix: Ierapetra (Appendix, II.1.1.2), Aradena Gorge (Appendix, II.1.2.2), Sougia (Appendix, II.1.3.2), Kalamia (Appendix, II.1.4.2), Cape Koutoulas (Appendix, II.1.5.2), and for Phalasarna (Appendix, II.1.6.2). If I compare terraces of the same ages and the corresponding sea-level changes, I observe at Ierapetra (terraces T5 and T6) a sea-level change of 7.26 m, at Aradena Gorge (terraces T1 and T5) a sea-level change of 101.2 m, and at Sougia (terraces T1 and T3) a sea-level change of 133 m. Therefore, sea-level changes are not the main reason for the formation of the terraces around Crete.

4.9.2.1.3 Uplift-Rates based on Tectonic and Sea-Level corrected Analysis of Paleo-Shorelines

The terrace formation at Moni Chryssoskalitissa (Figure 4.42) is the combination of tectonic and sea-level changes. Therefore, I had to correct the terraces concerning their elevation by their time of formation using the sea-level curve of Rohling et al. (2014).

First, I assumed a constant uplift rate and calculated the uplift rate for each terrace (Figure 4.41 & Table 4.11). Second, I assigned the terraces to MIS highstands (Figure 4.42 & Table 4.13), resulting in a not constant uplift rate.

For a constant uplift rate, I calculated an average uplift rate (R) of 2.80 ± 0.24 mm/yr. The calculated slip rate on the Hellenic Trench is 5.6 ± 0.48 mm/yr, and the average recurrence time is 3571 (+322.65 / -272.52) yr. For a non uniform uplift rate the average uplift rate (R) is 2.83 ± 0.24 mm/yr, the slip rate is 5.7 ± 0.48 mm/yr, and the average recurrence time is 3508 (+322.65 / -272.52) yr. Results for both analysis are very similar.

All results of the remaining seven localities are listed in Table 4.17, corresponding analysis of these locations is listed in the Appendix, Chapter 4 (Aradena Gorge (Appendix, II.1.2.3), Sougia (Appendix, II.1.3.3), Kalamia (Appendix, II.1.4.3), Cape Koutoulas (Appendix, II.1.5.3), and for Phalasarina (Appendix, II.1.6.3),

4.10 Discussion

Absolute measurements of the uplift history of Crete cannot be distinguished from river profiles analysis. But these relative measurements provide relative measurements of the vertical surface-deformation. The analysis of the concavity index on Crete shows that values do not dependence of the index with the lithology or the distribution of upper crustal-faults. Brocklehurst and Whipple (2002) suggest that low values of concavity are associated with short and steep drainages mostly influenced by debris flow. This study on the concavity index does not support this hypothesis, because the highest values of concavity ($0.2 < \theta < 0.3$) are related to short river profiles along the northern coast on W-Crete and along the eastern coastline. Kirby and Whipple (2001) suggest that low values of concavity are linked to an increase in rock strength or an increase of the incision rate. This study showed no correlation between the lithology and the concavity index. Channels on Crete display not a wide range of concavity indices, varying only from $0 < \theta < 0.42$, and most values are less than $\theta < 0.1$. These low values of concavity indicate that river longitudinal-profiles are close to linear gradients, and therefore do not represent channels with steep headwaters and gentle downstream slopes (Whipple and Tucker, 1999; Duvall et al., 2004). I may therefore conclude that the low values of concavity are related to an increase in the incision rate, especially along the southern coastline of Crete.

As suggested by Whipple et al. (1999) in non-glacial landscapes, river channels control the relief structure of tectonically active regions. Surface uplift and tilting cause steepening of river profiles, but the steepness index also depends on climatic, base-level and lithological conditions of an area (Schoenbohm et al., 2004; Whipple, 2004). For Crete, factors influencing the steepness index such as climate or base-level variations can be ruled out, because climatic conditions are the same across the island and the Mediterranean is the base-level for Crete. Therefore, the steepness index can depend strongly on the lithology due to the resistance to erosion (Hack, 1957). I compared the spatial distribution of k_{sn} values to the lithological units on Crete and clearly see a correlation between the highest values of the steepness index with Plattenkalk, suggesting that the Plattenkalk is most resistant to erosion. Sediments are correlated

well with the lowest values of the steepness index, due to the low resistance of sediments to erosion.

I find a high number of knickpoints on Crete. Knickpoint formation occurs when the river is in a disequilibrium state anymore, caused by climatic change, eustatic change, river capture, lithology boundaries, or by active faulting and the corresponding change in uplift rate (coseismic) (Schoenbohm et al., 2004; Whipple and Tucker, 1999). I can eliminate climatic and eustatic changes as reason for the high amount of knickpoints on Crete. Furthermore, I can rule out river capture as driving force for the knickpoints formation due to the evenly knickpoint distribution across the island. The knickpoint-elevation distribution across Crete, suggest that the vertical deformation is not spatially homogeneous and temporal constant across Crete, but rather heterogeneously distributed for separated individual blocks with their individual vertical deformation history.

Absolute measurements of the uplift history of Crete cannot be distinguished from analysis of the paleo-shorelines. Therefore, I compiled published data of Pleistocene and Holocene paleo-shorelines. Pleistocene uplift rates show that Crete is not uplifted homogeneously but rather very heterogeneously (Figure 4.33).

Pleistocene uplift occurs along individual blocks, each with its individual history of vertical motion. I calculated a mean average Pleistocene uplift rate of 1.03 ± 0.01 mm/yr, whereas, eastern Crete has an uplift rate ranges from 0.1 to 2.8 mm/yr, and western coastline an uplift rate ranging from 0.80 to 4.79 mm/yr.

The influence of the choice of different sea-level curves is demonstrated by the mean uplift rates (Table 4.16) based on the Lambeck and Chappel (2001) and the Sosoian and Rosenthal (2009) curve versus the sea-level curve based on Rohling et al. (2014). The difference between the uplift rates is in the range from 0 to 0.31 mm/yr for my results.

Caputo (2007) compared twelve published sea-level curves concerning the similarities and the differences of the heights and ages of highstands of sea-level peaks during the last 450 ka. The differences between ages are of about 18 ka and the height differences are of about 35 m for the major interglacial peaks (MIS 5.5, 7.5, 9.3, and 11.3) (Caputo, 2007).

Lajoie (1986) plotted data of uplifted Pleistocene terraces throughout the world and found that most uplift rates are less than 2 mm/yr on the long-term (Figure 4.45). My investigated data are close to this global trend of Lajoie (1986).

Holocene paleo-shorelines show a clear pattern of vertical surface-deformation of W-Crete is uplifting and E-Crete is subsiding. Western Crete is uplifting on the order of 0.62 to 5.54 mm/yr, whereas eastern Crete subsides on the order of 1.11 to 0.29 mm/yr. The mean Holocene uplift rate is calculated on the order of 1.1 ± 0.1 mm/yr.

Pleistocene uplift rates and Holocene uplift rates are quite similar. The comparison of Pleistocene and Holocene uplift rates shows that uplift rates remained quite constant throughout the time. But eastern Crete experienced uplift in Pleistocene, whereas during Holocene this part of the island is subsiding. Western Crete experienced uplift throughout Pleistocene and Holocene, but the uplift rate nearly doubled at some locations from Pleistocene to Holocene, such as Moni Khrisoskalitisas. Furthermore, the tilt rate is not uniform from Pleistocene to Holocene, which further suggests that the uplift pattern of Crete during Pleistocene and Holocene times changed.

The tectonic uplift is caused by active faulting, most likely due to coseismic events during Quaternary.

4.11 Conclusions

Crete's topography is the result of tectonic processes and their spatiotemporal variations on various time-scales. The analysis of river profiles and paleo-shorelines on Crete, reveals a spatial pattern of differential surface-deformation. River profiles across the study area are characterized by low concavity for most streams, as well as high values for the normalized steepness index, and clearly defined knickpoints, which indicate transient responses in channel profiles for vertical surface deformation. The western and eastern parts of Crete have more knickpoints than the middle part of Crete, and the value of the steepness index is less obvious for changing conditions in the middle part, indicating less vertical surface motion. I do not observe any height/knickpoint correlation suggesting that surface-deformation is not uniform. The gradient of the river profiles along the northern coastline are more gentle than those along the southern and southeastern coastlines.

Analysis of paleo-shorelines shows that uplift rates of Crete are in the range of global values calculated by Lajoie (1986). I further calculated higher uplift rates for W than for E indicating stronger uplift in W than in E Crete which is also confirmed by higher topography in the W than in E-Crete. Along the northern coastline no Pleistocene shorelines are found because they probably do not exist or are covered by Holocene sediments, leading to a tilt towards the N. Analysis of Holocene terraces shows that eastern Crete is subsiding, whereas the western part of the island is uplifting, but tilt values for the Holocene shorelines are much smaller than for Pleistocene shorelines. Analysis of geomorphic features shows that the uplift of Crete is not uniform, and the island is tilting towards the N and the E. Tectonic uplift can be caused by coseismic events and/or aseismic creep along faults in the overriding plate, such as the Hellenic Trench. These upper-crustal faults control the coastal geomorphology.

References

- Ammon C.J., Ji C., Thio H.-K., Robinson D., Ni S., Hjorleifsdottir V., Kanamori H., Lay T., Das S., Helmberger D., Ichinose G., Polet J., Wald D. (2005): Rapture process of the 2004 Sumatra-Andaman earthquake. Vol. 308. No. 5725. Pages: 1133-1139. DOI: 10.1126/science.1112260.
- Angelier J. (1979): Neotectonique de l'arc Eggen. These d'etat. University de Paris VI, 405 pp.
- Angelier J., Lyberis N., LePichon X. (1982): The tectonic development of the Hellenic arc and the Sea of Crete – A synthesis. *Tectonophysics*. Vol. 86. Iss. 1-3. Pages: 159-196. DOI: 10.1016/0040-1951(82)90066-X.
- Armijo R., Lyon-Caen H., Papanastassiou D. (1992): East-west extension and Holocene normal-fault scarps in the Hellenic arc. *Geology*. Vol. 20. Pages: 491-494. DOI: 10.1130/0091-7619(1992)020<0491:EWEAHN>2.3.CO;2.
- Barrientos S.E., Ward S.N. (1990): The 1960 Chile earthquake: inversion for slip distribution from surface deformation. *Geophysical Journal International*. Vol. 103. Iss. 3. Pages: 589-598. DOI: 10.1111/j.1365-245X.1990.tb05673.x.
- Bloome A.L., Broecker W.S., Chappell J.M.A., Matthews R.K., Mesolello K.J. (1974): Quaternary Sea Level Fluctuations on a Tectonic Coast: New 230th/234u Dates from the Huon Peninsula, New Guinea. *Quaternary Research*. Vol. 4. Iss. 2. Pages: 185-205. DOI: 10.1016/0033-5894(74)90007-6.
- Bookhagen, B., Echtler, H.P., Melnick, D., Strecker, M.R., and Spencer, J.Q.G., 2006, Using uplifted Holocene beach berms for paleoseismic analysis on the Santa María Island, south-central Chile: *Geophysical Research Letters*, v. 33, p. L15302.
- Brocklehurst S.H. and Whipple K.W. (2002): Glacial erosion and relief production in the Eastern Sierra Nevada, California. *Geomorphology*. Vol. 42. Pages: 1-24. DOI: 10.1016/S0169-555X(01)00069-1.
- Burbank D.W. and Anderson R.S. (2001): *Tectonic Geomorphology*. Wiley-Blackwell. Chister. 288 pages.
- Burbank D.W. and Anderson R.S. (2012): *Tectonic Geomorphology* (2nd edition). Wiley-Blackwell. Chister. 464 pages.
- Caputo R., Catalano S., Monaco C., Romagnoli G., Tortorici G., Tortorici L. (2010) Active faulting on the island of Crete (Greece). *Geophysical Journal International*. Vol. 183. Iss. 1. Pages: 111-126. DOI: 10.1111/j.1365-246X.2010.04749.x.
- Chappel J. and Polach H.A. (1974): Holocene sea-level change and coral-reef growth at Huon Peninsula, Papua New Guinea. *Geological Society of America Bulletin*. Vol. 87. Iss. 2. Pages: 235-240. DOI: 10.1130/0016-7606(1976)87<235:HSCACG>2.0.CO;2
- Chamot-Rooke N., Rangin C., Le Pichon X. (2005): DOTMED – Deep Offshore Tectonics of the Mediterranean: A synthesis of deep marine data in Eastern Mediterranean, The Ionian basin and margins, the Calacria wedge and the Mediterranean ridge. *Société Géologique de France*. Paris. Pages: 64.
- Cloos M., Shreve R.L. (1988): Subduction-channel model of prism accretion, melange formation, sediment subduction, and subduction erosion at convergent plate margins. 1. Background and Description. *Pure and Applied Geophysics*. Vol. 128. Iss. 3-4. Pages: 455-500. DOI: 10.1007/BF00874548.

- Cloos M., Shreve R.L. (1988): Subduction-channel model of prism accretion, melange formation, sediment subduction, and subduction erosion at convergent plate margins. 2. Implications and Discussion. *Pure and Applied Geophysics*. Vol. 128. Iss. 3-4. Pages: 501-545. DOI: 10.1007/BF00874549.
- Crosby B.T. and Whipple K.W. (2006): Knickpoint initiation and distribution within fluvial networks: 236 waterfalls in the Waipaoa River, North Island, New Zealand. *Geomorphology*. Vol. 82. Iss. 1-2. DOI: 10.1016/j.geomorph.2005.08.023.
- Davies J.H. and von Blanckenburg F. (1995): Slab-breakoff – A model of lithosphere detachment and its test in the magmatism and deformation of collisional orogenes. *Earth and Planetary Science Letters*. Vol. 129. Iss. 1-4. Pages: 85-102. DOI: 10.1016/0012-821X(94)00237-S.
- Duvall A., Kirby E., Burbank D. (2004): Tectonic and lithological controls on bedrock channel profiles and processes in coastal California. *Journal of Geophysical Research*. Vol. 109. Iss. F3. DOI: 10.1029/2003JF000086.
- Fairbridge R.W. (1961): Eustatic changes in sea level. *Physics and Chemistry of the Earth*. Vol. 4. Pages: 99-185. DOI: 10.1016/0079-1946(61)90004-0.
- Fassoulas C., Kiliadis A., Mountrakis D. (1994): Postnappe stacking extension and exhumation of high-pressure/low-temperature rocks in the island of Crete, Greece. *Tectonics*. Vol. 13. Iss. 1. Pages: 127-138. DOI: 10.1029/93TC01955.
- Flint, J. J. (1974): Stream gradient as a function of order, magnitude, and discharge. *Water Resources Research*. Vol. 10. Iss. 5. Pages: 969–973. DOI: 10.1029/WR010i005p00969.
- Gaki-Papanastassiou K., Karymbalis E., Papanastassiou D., Maroukian H. (2009): Quaternary marine terraces as indicators of neotectonic activity of the Ierapetra normal fault SE Crete (Greece). *Geomorphology*. Vol. 104. Pages: 38-46. DOI: 10.1016/j.geomorph.2008.05.037.
- Gallen S.F., Wegmann K.W., Bohnenstiehl D.R., Pazzaglia F.J., Brandon M.T., Fassoulas C. (2014): Active simultaneous uplift and margin-normal extension in a forearc high, Crete, Greece. *Earth and Planetary Science Letters*. Vol. 398. Pages: 11-24. DOI: 10.1016/j.epsl.2014.04.038.
- Ganas, A., and Parsons T. (2009): 3-D model of Hellenic Arc deformation and origin of the Cretan uplift, *Journal of Geophysical Research*. Vol. 114. DOI: 10.1029/2008JB005599.
- Hack J.T. (1973): Stream-profile analysis and stream-gradient index. *US. Geol. Survey Jour. Research*. Vol. 1. No. 4. Pages: 421-429.
- Hall R., Audley-Charles M.G., and Cater D.J. (1984): The significance of Crete for the evolution of the Eastern Mediterranean. In Dixon J.E., and Robertson A.H.F. (eds): *The geological evolution of the Eastern Mediterranean: Geological Society of London Special Publication 17*. Pages: 449-516.
- Hallam A. (1984): Pre-Quaternary sea-level changes. *Annual Review of Earth and Planetary Sciences*. Vol. 12. Pages: 205-243. DOI: 10.1146/annurev.ea.12.050184.001225.
- Hinsbergen van D.J.J., and Meulenkamp J.E. (2006): Neogene supradetachment basin development on Crete (Greece) during exhumation of the South Aegean core complex. *Basin Research*. Vol 18. Pages: 103-124. DOI: 10.1111/j.1365-2117.2005.00282.x.
- Jolivet L., Goffé B., Monié P., Truffert-Luxey C., Patriat M., Bonneau M. (1996): Miocene detachment in Crete and exhumation P-T-t paths of high-pressure metamorphic rocks. *Tectonics*, Vol. 15, No. 6. Pages: 1129-1153. DOI: 10.1029/96TC01417.

- Jolivet L., Faccenna C., Goffé B., Burov E., and Agard P. (2003): Subduction tectonics and exhumation of high-pressure metamorphic rocks in the Mediterranean orogens. *American Journal of Science*. Vol. 303. Pages: 353-409. DOI: 10.2475/ajs.303.5.353.
- Kirby E. and Whipple K.X. (2001): Quantifying differential rock-uplift rates via stream profile analysis. *Geology*. Vol. 29. No. 5. Pages: 415-418. DOI: 10.1130/0091-7613(2001)029<0415:QDRURV>2.0.CO;2.
- Kirby E., Whipple K.X., Tang W., Chen Z. (2003): Distribution of active rock uplift along the eastern margin of the Tibetan Plateau: Inferences from bedrock channel longitudinal profiles. *Journal of Geophysical Research-Solid Earth*. Vol. 108. Iss. B4. DOI: 10.1029/2001JB000861.
- Kottek M., Grieser J., Beck C., Rudolf B., Rubel, F. (2006): World Map of the Köppen-Geiger climate classification updated. *Meteorologische Zeitschrift*. Vol. 15. Pages: 259-263. DOI: 10.1127/0941-2948/2006/0130.
- Lajoie K.R (1986): Coastal tectonics. In: *Active Tectonic*. National Academic Press. Washington DC. Pages: 95-124.
- Lambeck, K. and Chappell, J. (2001): Sea Level Change through the last Glacial Cycle. *Science*. Vol. 292. Pages: 679-686. DOI: 10.1126/science.1059549.
- Lambeck, K. and Purcell A. (2005): Sea-level change in the Mediterranean Sea since the LGM: model predictions for tectonically stable areas. *Quaternary Science Reviews*. Vol. 24. Pages: 1969-1988. DOI: 10.1016/j.quascirev.2004.06.025.
- Lavé J. and Avouac J.P. (2000): Active folding of fluvial terraces across the Siwalik Hills Himalaya of central Nepal. *Journal of Geophysical Research*. Vol. 105. Iss. B3. DOI: 10.1029/1999JB900292.
- Le Pichon X., Chamot-Rooke N., Lallemand S., Noomen R., Veis G. (1995): Geodetic determination of the kinematics of central Greece with respect to Europe: Implications for Eastern Mediterranean tectonics. *Journal of Geophysical Research*. Vol. 100. Iss. B7. Pages: 12675-12690. DOI: 10.1029/95JB00317.
- Masce, J., Huguen C., Benkhelil J., Chamot-Rooke N., Chaumillon E., Griboulard R., Kopf A., Lamarche G., Volkonskaia J., Woodside J., Zitter T. (1999): Images may show start of European-African plate collision. *Eos Trans. AGU*. 80(37). 421. DOI: 10.1029/99EO00308.
- McClusky S., Balassanian S., Barka A., Demir C., Ergintav S., Georgiev I., Gurkan O., Hamburger M., Hurst K., Kahle H., Kastens K., Kekelidze G., King R., Kotzev V., Lenk O., Mahmoud S., Mishin A., Nadariya M., Ouzounis A., Paradissis D., Peter Y., Prilepin M., Reilinger R., Sanli I., Seeger H., Tealeb A., Toksöz M. N., Veis G. (2000): Global Positioning System constraints on plate kinematics and dynamics in the Eastern Mediterranean and Caucasus. *Journal of Geophysical Research*. Vol. 105, No. B3. Pages: 5695-5719. DOI: 10.1029/1999JB900351.
- McKenzie D. (1972): Active Tectonics of the Mediterranean Region. *Geophysical Journal of the Royal Astronomical Society*. Vol. 30. Iss. 2. Pages: 109-185. DOI: 10.1111/j.1365-246X.1972.tb02351.x
- Meier T., Becker D., Endrun B., Rische M., Bohnhoff M., Stöckhert B., Harjes H. P. (2007): A model for the Hellenic subduction zone in the area of Crete based on seismological

- investigations. Geological Society. London. Special Publications 2007. Vol. 291. Pages 183-199. DOI: 10.1144/SP291.9.
- Melnick D., Bookhagen B., Echtler H., and Strecker M., (2006): Coastal deformation and great subduction earthquakes, Isla Santa María, Chile (37°S). Geological Society of America Bulletin: V. 118. Pages: 1463-1480. DOI: 10.1130/B25865.1.
- Merritts D. and Bull W.B. (1989): Interpreting Quaternary uplift rates at the Mendocino triple junction, northern California, from uplifted marine terraces. *Geology*. Vol. 17. Pages: 1020-1024. DOI: 10.1130/0091-7613(1989)017<1020:IQURAT>2.3CO;2.
- Meulenkamp J.P., Wortel M.J.R., Vanwamel W.A. (1988): On the Hellenic subduction zone and the geodynamic evolution of Crete since the late Middle Miocene. *Tectonophysics*. Vol. 146. Iss. 1-4. Pages: 203-215. DOI: 10.1016/0040-1951(88)90091-1.
- Miller K.G., Kominz M.A., Browning J.V., Wright J.D., Mountain G.S., Katz M.E., Sugarman P.J., Cramer B.S., Christie-Blick N., Pekar S.F. (2005): The Phanerozoic Record of Global Sea-Level Change. *Science*. Vol. 310. No. 5752. Pages: 1293-1298. DOI: 10.1126/science.1116412.
- Montgomery D.R. and Foufoula-Georgiou E. (1993): Channel network source representation using digital elevation models. *Water Resources Research*. Vol. 29. No. 12. Pages: 3925. DOI: 10.1029/93WR02463.
- Mourtzas N.D. (2012): Fish tanks of eastern Crete (Greece) as indicators of the Roman sea level. *Journal of Archaeological Science*. Vol. 39. Pages: 2392-2408. DOI: 10.1016/j.jas.2012.02.006.
- Papanikolaou D., Vassilakis E. (2010): Middle Miocene E-W Tectonic Horst Structure of Crete through Extensional Detachment Faults. *Tectonophysics*. Vol. 488, Iss. 1-4, 5. Pages: 233-247. DOI: 10.1088/1755-1307/2/1/012003.
- Pavlopoulos K., Kapsimalis V., Theodorakopoulou K., Panagiotopoulos I.P. (2011): Vertical displacement trends in the Aegean coastal zone (NE Mediterranean) during the Holocene assessed by geo-archaeological data. *The Holocene*. Vol. 22. No. 6. Pages: 717-728. DOI: 10.1177/0959683611423683.
- Penck W. (1924): *Die Morphologische Analyse: ein Kapitel der Physikalischen Geologie*. J. Engelhorns. Stuttgart. Pages: 200.
- Pirazzoli P.A., Laborel J., Stiros S.C. (1996): Earthquake clustering in the Eastern Mediterranean during historical times. *Journal of Geophysical Research*. Vol. 101. Iss. B3. Pages: 6083-6097. DOI: 10.1029/95JB00914.
- Pittman W.C. (1978): Relationship between eustacy and stratigraphic sequences of passive margins. *Geological Society of America Bulletin*. Vol. 89. Pages: 1389-1403. DOI: 10.1130/0016-7606(1978)89<1389:RBEASS>2.0.CO;2.
- Plafker G., Rubin M. (1978) Uplift history and earthquake recurrence as deduced from marine terraces on Middleton Island, Alaska. in *Proceedings of Conference VI. Methodology for identifying seismic gaps and soon-to-break gaps*: U.S. Geological Survey Open-File Report 78-943. Pages: 687-721.
- Price S., Higham T., Nixon L., Moody J. (2002): Relative sea-level changes in Crete: reassessment of radiocarbon dates from Sphakia and west Crete. *The Annual of the British School at Athens*. Vol. 97. Pages: 171-200. DOI: 10.1017/S0068245400017378.

- Rohling E.J., Foster G.L., Grant K.M., Marino G., Roberts A.P., Tamisiea M.E., Williams F. (2014): Sea-level and deep-sea-temperature variability over the past 5.3 million years. *Nature*. Vol. 508. Pages: 477-482. DOI: 10.1038/nature13230.
- Roberts G.G., White N. (2010): Estimating uplift rate histories from river profiles using African examples. *Journal of Geophysical Research*. Vol. 115. Iss. B2. DOI: 10.1029/2009JB006692.
- Roberts G.G., White N.J., Shaw B. (2013): An uplift history of Crete, Greece, from inverse modeling of longitudinal river profiles. *Geomorphology*. Vol. 198. Pages: 177-188. DOI: 10.1016/j.geomorph.2013.05.026.
- Schoenbohm L., Whipple, K., Burchfiel, B.C., Chen L. (2004): Geomorphic constraints on surface uplift, exhumation, and plateau growth in the Red River region, Yunnan Province, China. *Geological Society of America Bulletin*. Vol. 116. No. 7/8. Pages: 895-909. DOI: 10.1130/B25364.1.
- Seidl, M.A., Dietrich, W.E., Kirchner, J.W. (1994): Longitudinal profile development into bedrock: an analysis of Hawaiian channels. *Journal of Geology*. Vol. 102: Pages: 457-74.
- Shaw B., Ambraseys N.N., England P.C., Floyd M.A., Gorman G.J., Higham T.F.G., Jackson J. A., Nocquet J.-M., Pain C. C., Piggott M. D. (2008): Eastern Mediterranean tectonics and tsunami hazard inferred from the A.D. 365 earthquake. *Nature Geoscience*. Vol. 1. DOI: 10.1038/ngeo151.
- Shaw B., Jackson J.A., Higham T.F.G., England P.C. Thomas A.L. (2010): Radiometric dates of uplifted marine fauna in Greece: Implications for the interpretation of recent earthquake and tectonic histories using lithophilic dates. *Earth and Planetary Science Letters*. Vol. 297. Iss. 3-4. Pages: 395-404. DOI: 10.1016/j.epsl.2010.06.041.
- Shimazaki K., Nakata T. (1980): Time-predictable recurrence model for large earthquakes. *Geophysical Research Letters* Vol. 7. No. 4. Pages: 279-282. DOI: 10.1029/GL007i004p00279.
- Smith W.H.F. and Sandwell D.T. (1997): Global seafloor topography from satellite altimetry and ship depth soundings. *Science*. Vol. 277. No. 5224. Pages: 1957-1962. DOI: 10.1126/science.277.5334.1956.
- Snyder N.P., Whipple K.X., Tucker G.E., and Merritts D.J (2000): Landscape response to tectonic forcing: digital elevation model analysis of stream profiles in the Mendocino triple junction region, northern California. *Geological Society of America Bulletin*. Vol. 112. No. 8. Pages: 1250-1263. DOI: 10.1130/0016-7606(2000)112<1250:LRTTFD>2.0.CO;2.
- Siddal M., Rohling E.J., Almogi-Labin A., Hemleben C., Meischner D., Schmelzer I., Smeed D.A. (2003): Sea-level fluctuations during the last glacial cycle. *Nature*. Vol. 423. Pages: 853-858. DOI: 10.1038/nature01690.
- Simons M., Minson S.E., Sladen A., Ortega F., Jiang J., Owen S.E., Meng L., Ampuero J-P., Wei S., Chu R., Helmberger D.V., Kanamori H., Hetland E., Moore A.W., Webb F.H. (2011): The 2011 magnitude 9.0 Tohoku-Oki earthquake: Mosaicking the megathrust from seconds to centuries. *Science*. Vol. 332. No. 6036. Pages: 1421-1425. DOI: 10.1126/science.1206731.
- Stanley D.J. (1995): A global sea-level curve for the late Quaternary: the impossible dream? *Marine Geology*. Vol. 125. Iss. 1-2. Pages: 1-6. DOI: 10.1016/0025-3227(95)00057-6.

- Strasser T.F., Runnels C., Wegmann K., Panagopoulou E., McCoy F., Digregorio C., Karkanis P., Thompson N. (2011): Dating Palaeolithic sites in southwestern Crete, Greece. *Journal of Quaternary Science*. Vol. 26. Iss. 5. Pages: 553-560. DOI: 10.1002/jqs.1482.
- Strobl M., Hetzel R., Fassoulas C., Kubik P.W. (2014): A long-term rock uplift rate for eastern Crete and geodynamic implications for the Hellenic subduction zone. *Journal of Geodynamics*. Vol. 78. Pages: 21-31. DOI: 10.1016/j.jog.2014.04.002.
- Stock, J.D. and Montgomery, D. R. (1999): Geologic constraints on bedrock river incision using the stream power law. *Journal of Geophysical Research*. Vol. 104. Pages: 4983-4993. DOI: 10.1029/98JB02139.
- Tarboton D.G., Bras R.L., Rodriguez-Iturbe I. (1989): Scaling and elevation in river networks. *Water Resources Research*. Vol. 25. Iss. 9. Pages: 2037-2051. DOI: 10.1029/WR025i009p02037.
- Ten Veen J.H. and Kleinspehn K.L. (2003): Incipient continental collision and plate-boundary curvature: Late Pliocene-Holocene transtensional Hellenic forearc, Crete, Greece. *Journal of the Geological Society*. Vol. 160. Pages: 161-181 DOI: 10.1144/0016-764902-067.
- Thomson S.N., Stockhert B., Brix M.R. (1998): Thermochronology of the high-pressure metamorphic rocks of Crete, Greece: Implications for the speed of tectonic processes. *Geology*. Vol. 26. Iss. 9. Pages: 259-262. DOI: 10.1130/0091-7613(1998)026<0259:TOTHPM>2.3.CO;2.
- Tiberti M.M., Basili R., Vannoli P. (2014): Ups and downs in western Crete (Hellenic subduction zone). *Nature Scientific Reports* 4. DOI: 10.1038/srep05677.
- Van Hinsbergen D.J.J., Hafkenscheid E., Spakman W., Meulenkaamp J.E., Wortel R. (2005): Nappe stacking resulting from subduction of oceanic and continental lithosphere below Greece. *Geology*. Vol. 33. Iss. 4. Pages: 325-328. DOI: 10.1130/G20878.1.
- Vigny C., Socquet A., Peyrat S., Ruegg J.-C., Métois M., Madariaga R., Morvan S., Lancieri M., Lacassin R., Campos J., Carrizo D., Bejar-Pizarro M., Barrientos S., Armijo R., Aranda C., Valderas-Bermejo M.-C., Ortega I., Bondoux F., Baize S., Lyon-Caen H., Pavez A., Vilotte J.P., Bevis M., Brooks B., Smalley R., Parra H., Baez J.-C., Blanco M., Cimbaro S., Kendrick E. (2011): The 2010 Mw 8.8 Maule megathrust earthquake of Central Chile, monitored by GPS. *Science*. Vol. 332. No. 6036. Pages: 1417-1421. DOI: 10.1126/science.1204132.
- Waelbroeck C., Labeyrie L., Michel E., Duplessy J.C., McManus J.F., Lambeck K., Balbon E., Labracherie M. (2002): Sea-level and deep water temperature changes derived from benthic foraminifera isotopic records. *Quaternary Science Reviews*. Vol. 21. Pages: 295-305. DOI: 10.1016/S0277-3791(01)00101-9.
- Wegmann K.W. (2008): Tectonic Geomorphology above Mediterranean Subduction Zones. Northeastern Apennines of Italy and Crete, Greece. Lehigh University (Ph.D. thesis).
- Wobus C.W., Whipple K.X., Kirby E., Snyder N.P., Johnson J., Spyropolou K., Crosby B.T., Sheehan D. (2006): Tectonics from topography: Procedures, promise and pitfalls. In Willett S.D., Hovius N., Brandon M.T., and Fisher D. M., (Eds.) *Tectonics, Climate and Landscape Evolution: Geological Society of America Special Paper 398*. Penrose Conference Series. Pages: 55-74
- Whipple K.X. and Tucker G.E. (1999): Dynamics of the stream-power river incision model: Implications for height limits of mountain ranges, landscape response timescales, and research needs. *Journal of Geophysical Research*. Vol. 104. No. B8. Pages: 17.661. DOI: 10.1029/1999JB900120.

Whipple K.W., Snyder N.P., Dollenmayer K. (2000): Rates and processes of bedrock incision by the Upper Ukak River since the 1912 Novarupta ash flow in the Valley of Ten Thousand Smokes, Alaska. *Geology*. Vol. 28. No. 9. Pages: 835-838. DOI: 10.1130/0091-7613(2000)28<835:RAPOBI>2.0.CO;2.

Whipple K.X. (2004): Bedrock rivers and the geomorphology of active orogens. *Annual Review of Earth and Planetary Sciences*. Vol. 32. Pages: 151-185. DOI: 10.1146/annurev.earth.32.101802.120356.

Whipple K.X. Wobus C., Crosby B., Kirby E., Sheehan D. (2007): New tools for quantitative Geomorphology: Extraction and interpretation of stream profiles from digital topographic data. *Geological Society of America Annual Meeting Short Course*, 28. October 2007. http://geomorphtools.org/Tools/StPro/Tutorials/StPro_UserGuidees_Final.pdf

Yolsal-Cevikbilen S., Taymaz T. (2012): Earthquake source parameters along the Hellenic subduction zone and numerical simulations of historical tsunamis in the Eastern Mediterranean. *Tectonophysics*. Vol. 536-537. Pages: 61-100. DOI10.1016/j.tecto.2012.02.019.

ASTER Global Digital Elevation Model:
<https://www.jspacesystems.or.jp/ersdac/GDEM/E/2.html>

Geomorphtools.org: <http://geomorphtools.org/>

Hellenic National Meteorological Service: http://www.hnms.gr/hnms/english/index_html

Figures & Tables

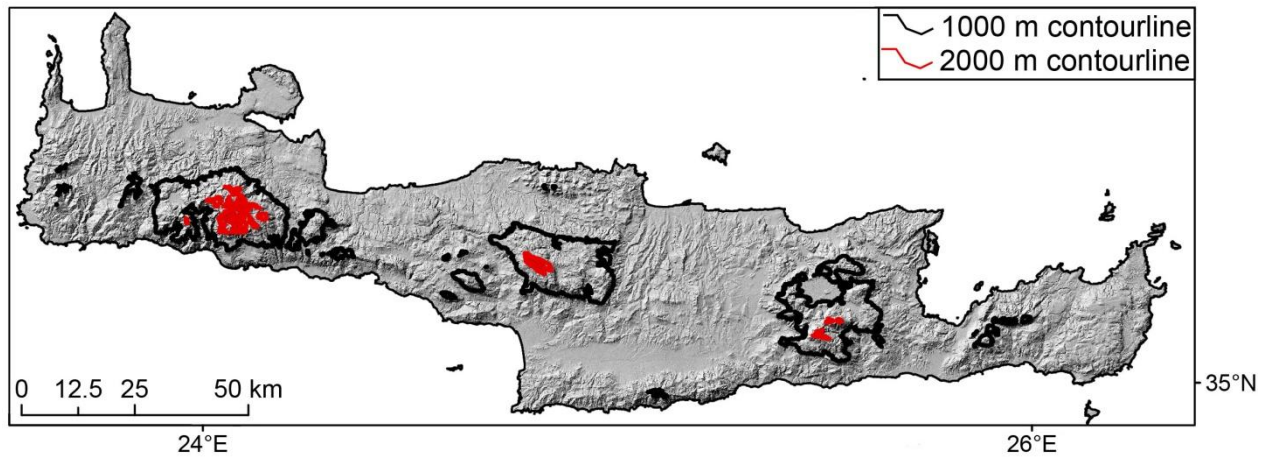


Figure 4.1: Geomorphic map with contour lines with 1000 m interval, derived on a Satellite Pour l’Observation de la Terre – Digital Elevation Model (SPOT-DEM) with a horizontal spatial resolution of 20 m and vertical accuracy of 15 ± 5 m.

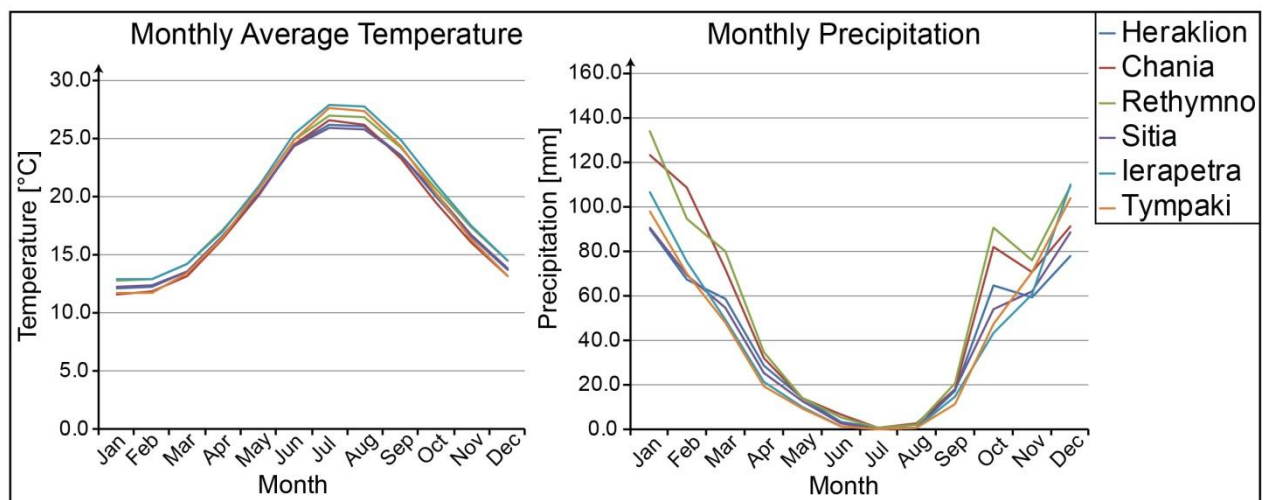


Figure 4.2: Average temperature in [°C] and average rainfall in [mm] based on Hellenic National Metrological Service data averaged for time period of 1955 to 1997 for stations in Heraklion (blue), Chania (red), Rethymno (green), Sitia (purple), Ierapetra (light blue), and Tympaki (orange).

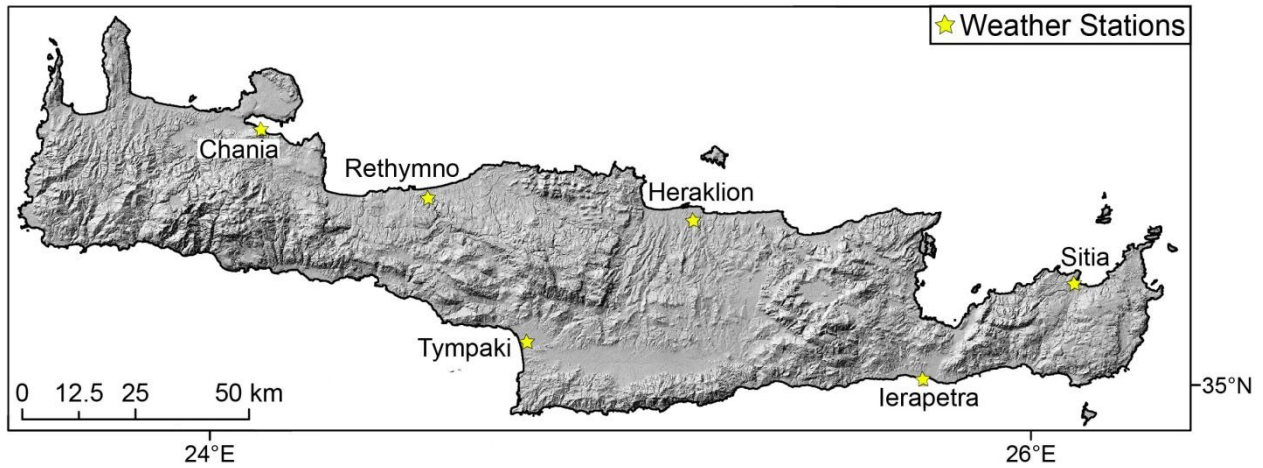


Figure 4.3: Locations of weather stations of the Hellenic National Metrological Service on Crete underlying the hill slope map generated from the SPOT-DEM.

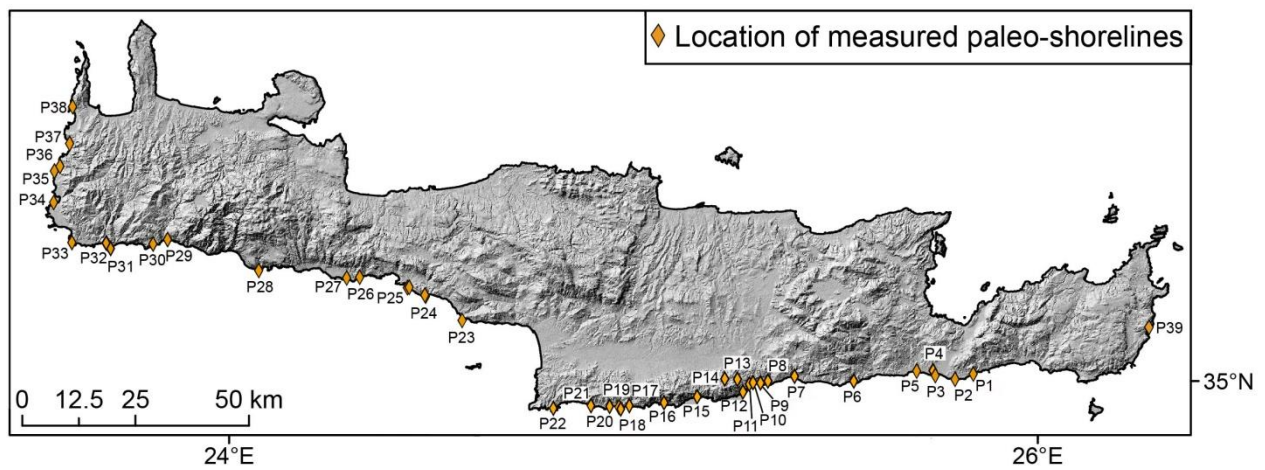


Figure 4.4: Location of Pleistocene paleo-shorelines. The hill slope map generated from the SPOT-DEM.

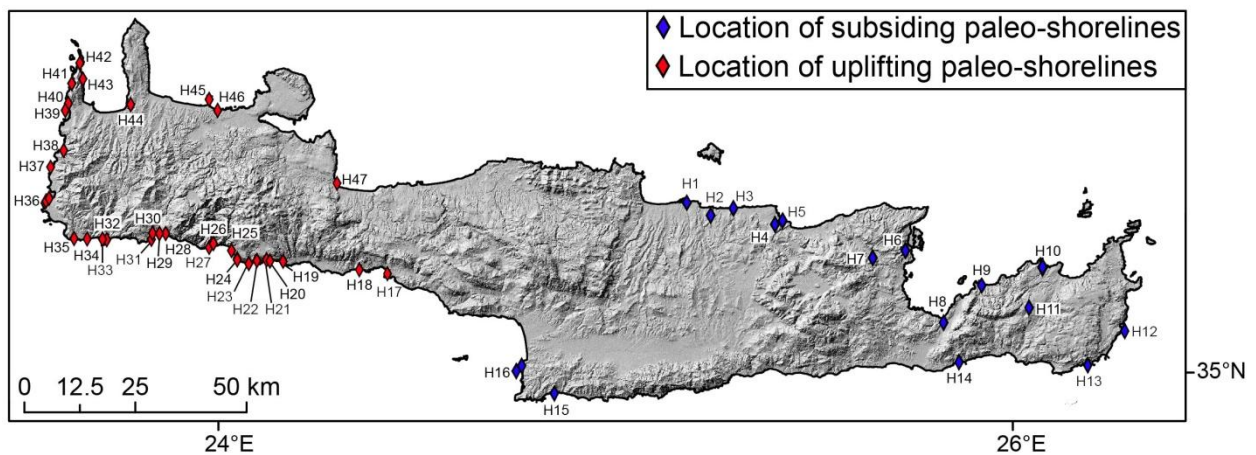


Figure 4.5: Location of Holocene paleo-shorelines. The hill slope map generated from the SPOT-DEM.

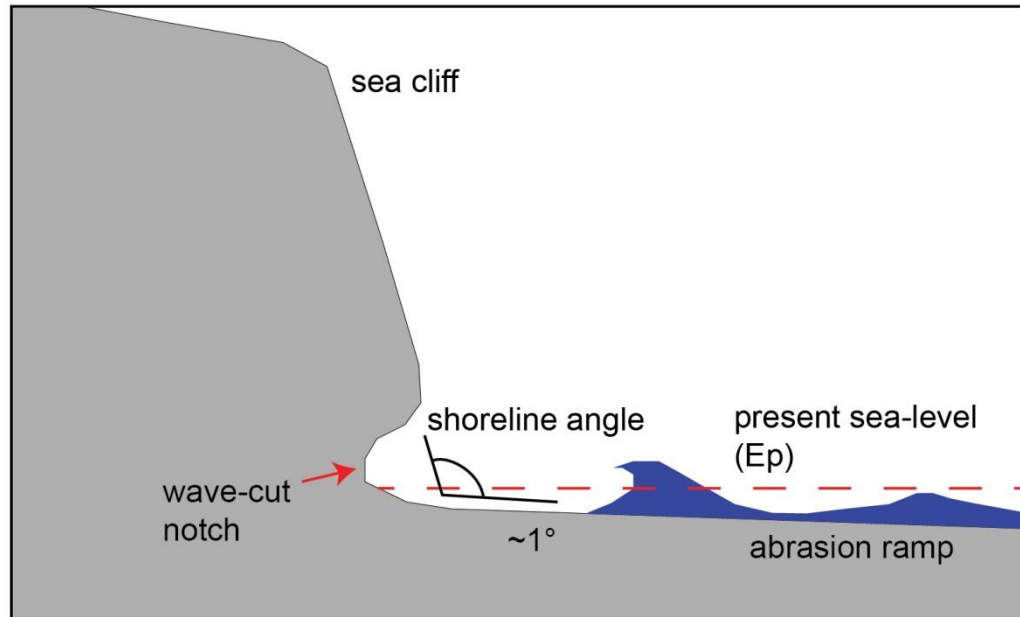


Figure 4.6: Schematic illustration of a wave-cut notch along an abrasion ramp modified after Burbank and Anderson (2015).

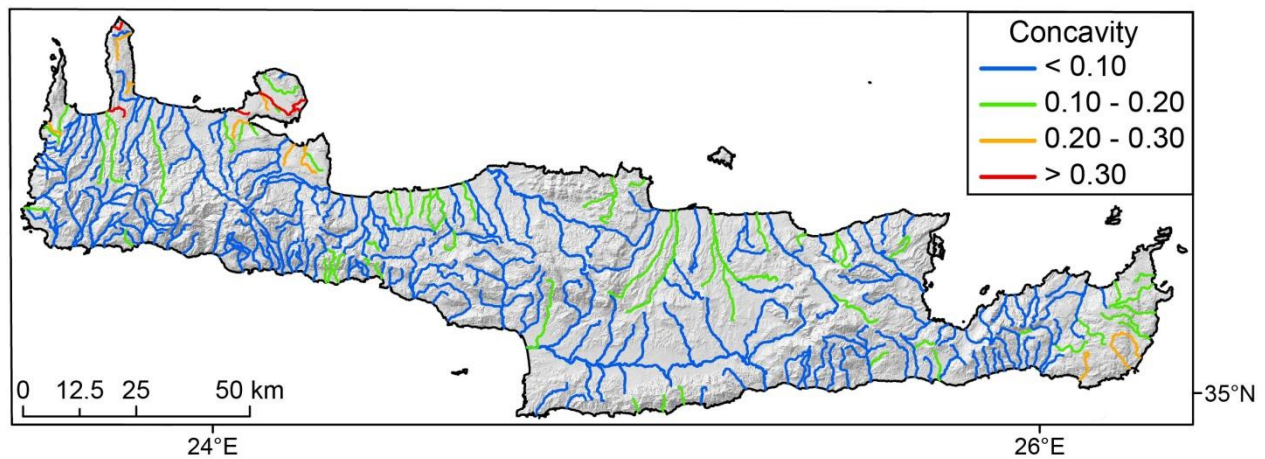


Figure 4.7: Map of concavity index Θ determined for Crete. Background is a shaded relief of Crete. The hill slope map generated from the SPOT-DEM.

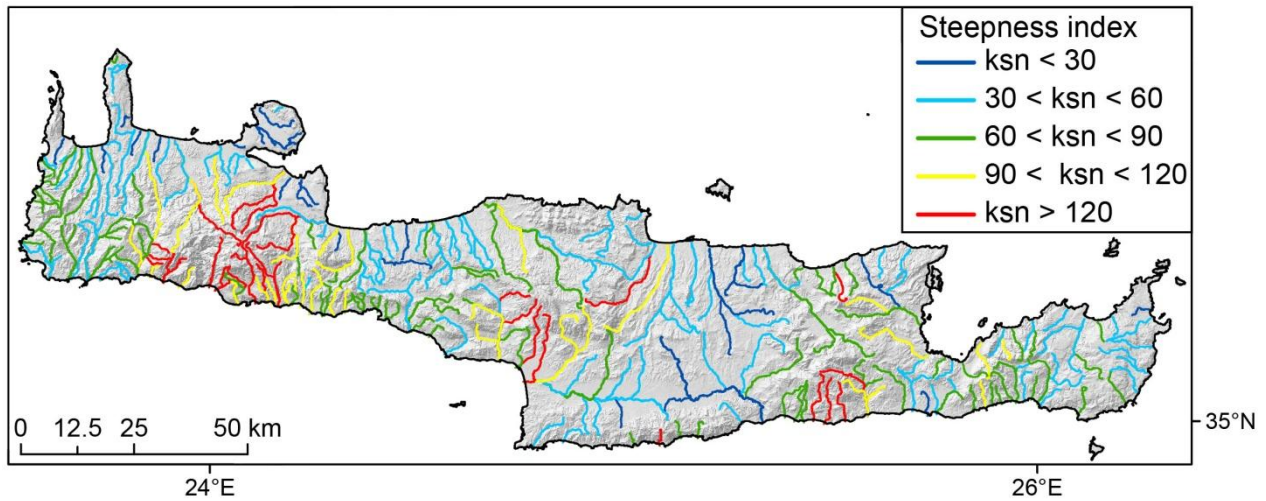


Figure 4.8: Map of normalized steepness index k_{sn} for Crete. Background is a shaded relief of Crete. The hill slope map generated from the SPOT-DEM.

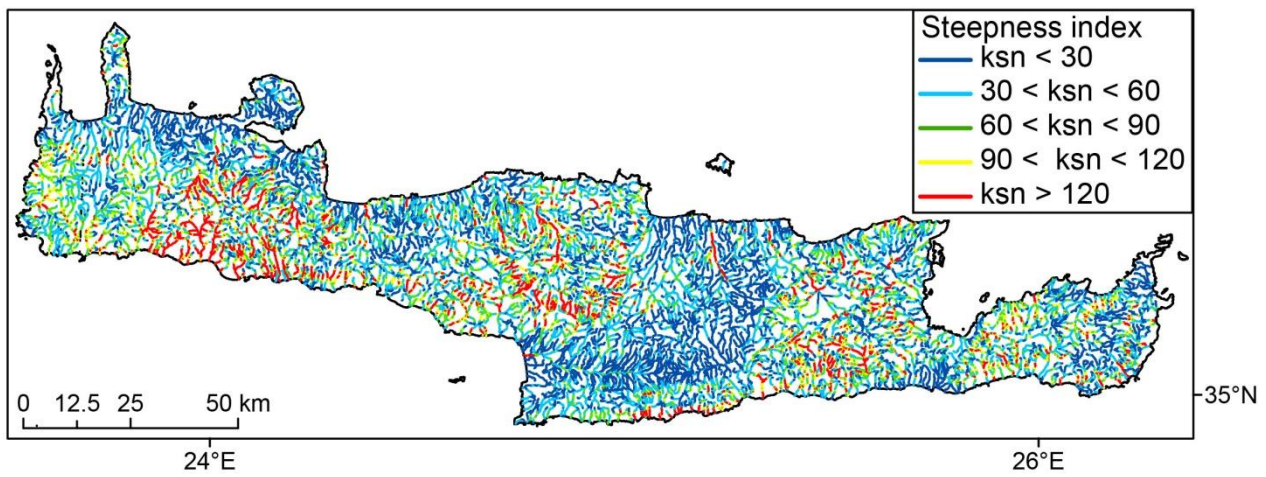


Figure 4.9: Map of normalized steepness index k_{sn} of small segments for Crete.

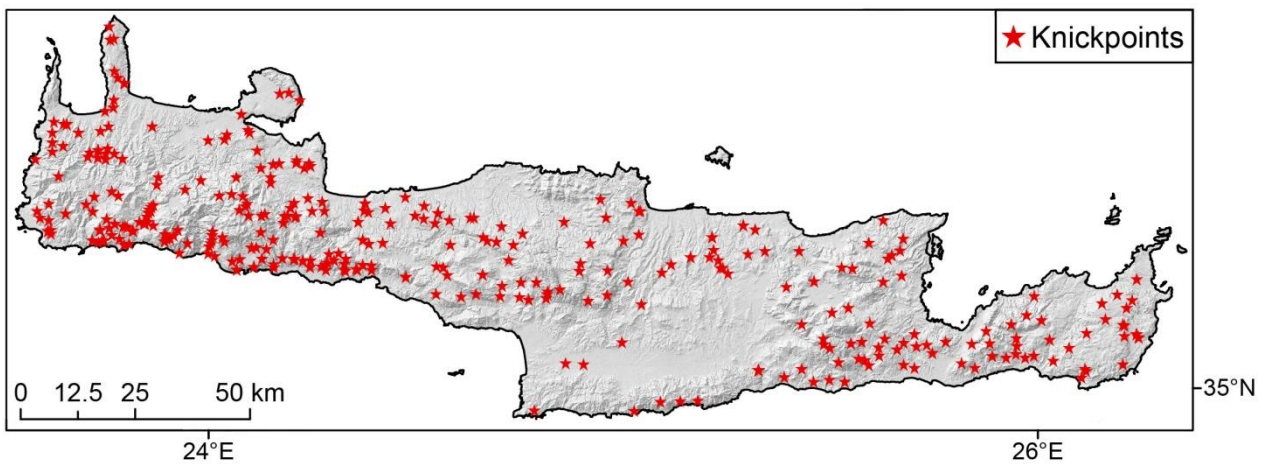


Figure 4.10: Map of knickpoint distribution and shaded relief of Crete. The hill slope map generated from the SPOT-DEM.

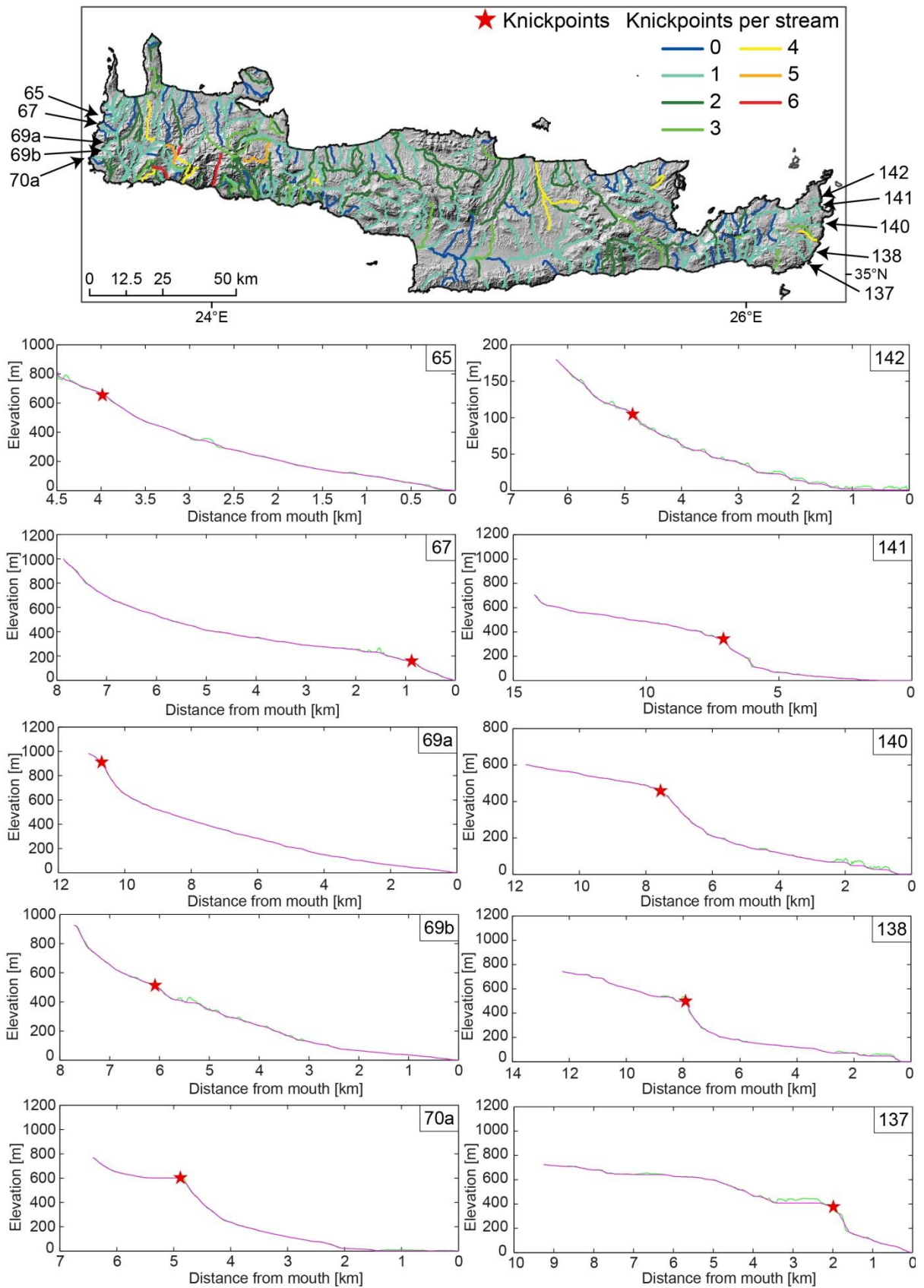


Figure 4.11: River profiles with one knickpoint. Background shaded relied from SPOT-DEM.

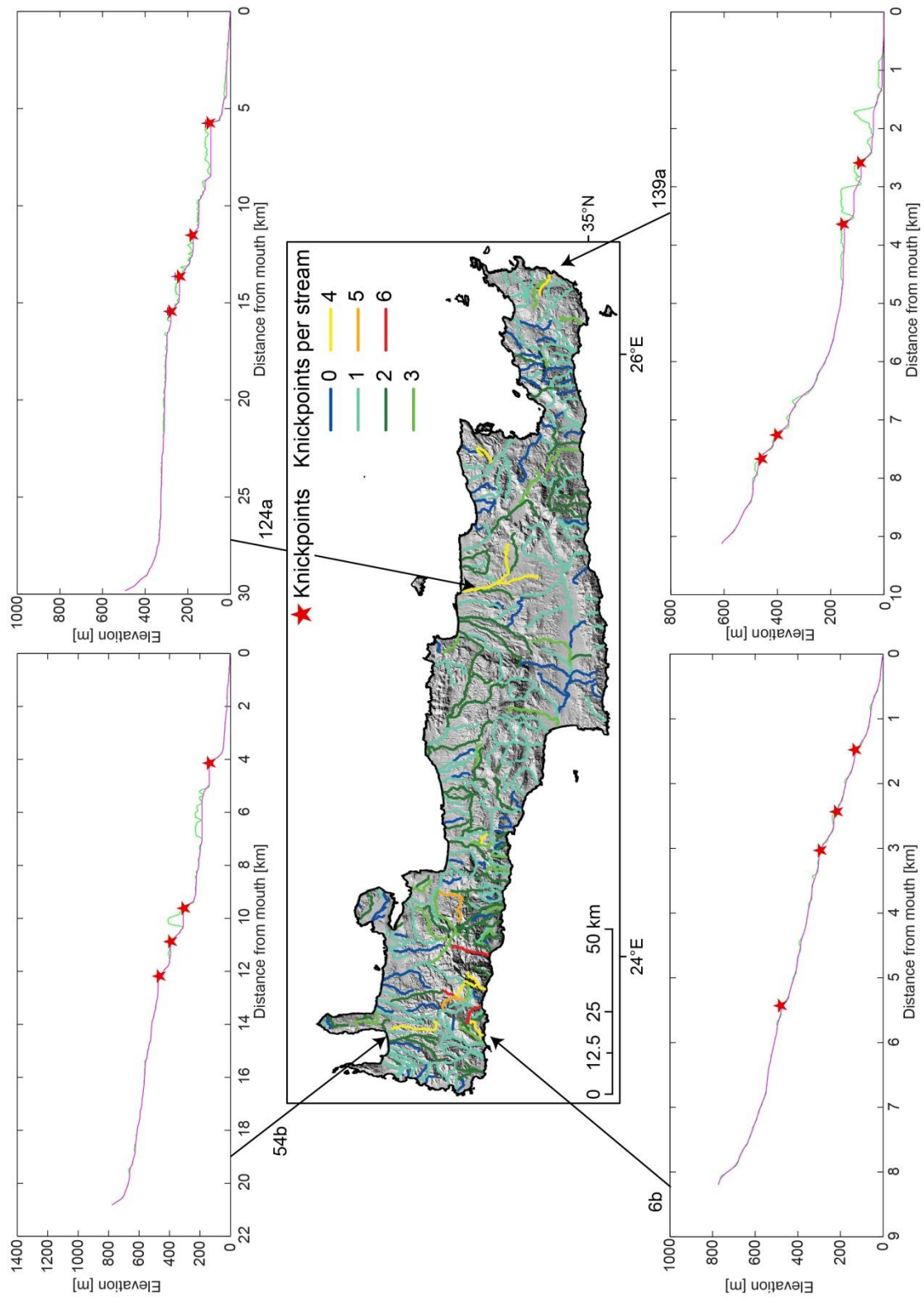


Figure 4.12: River profiles with four knickpoints. Background shaded relied from SPOT-DEM.

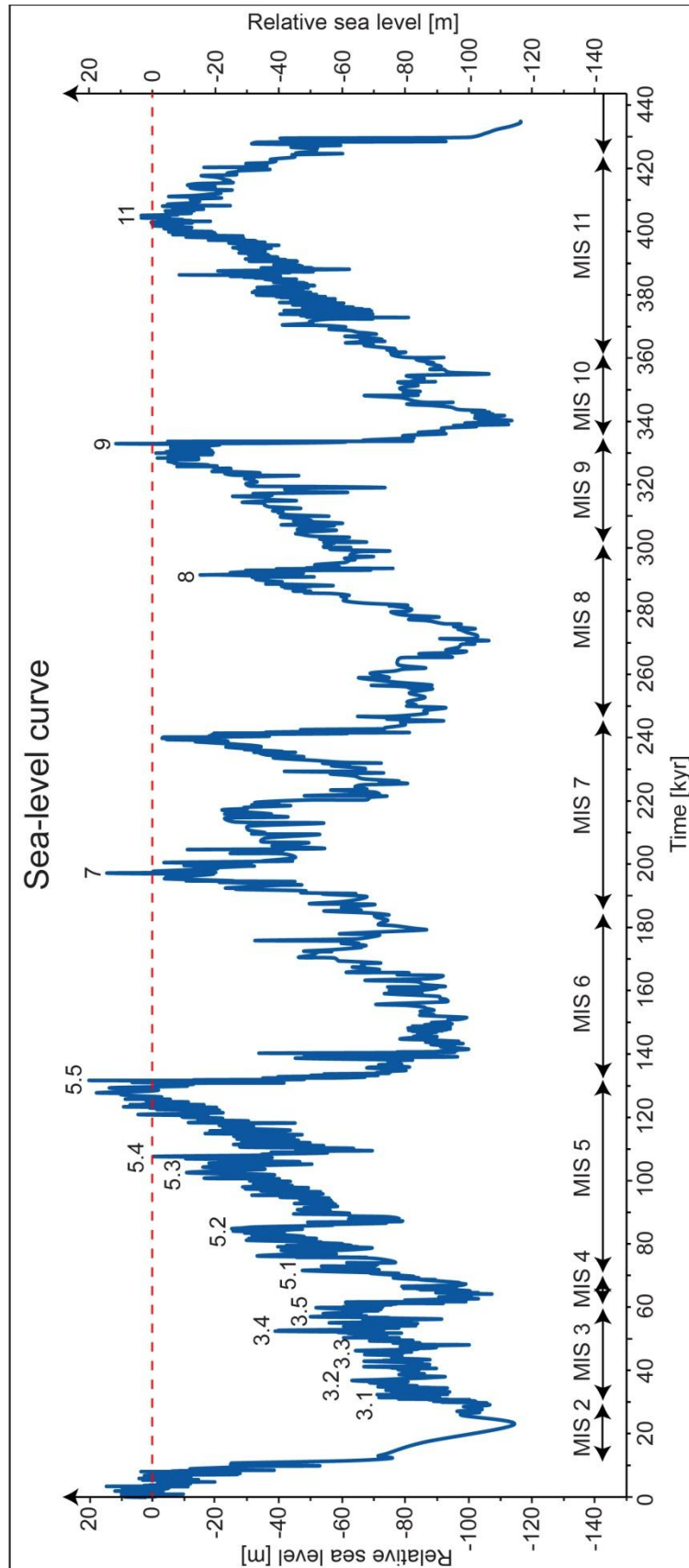


Figure 4.13: Sea-level curve for the past 440 kyr by Rohling et al. (2014).

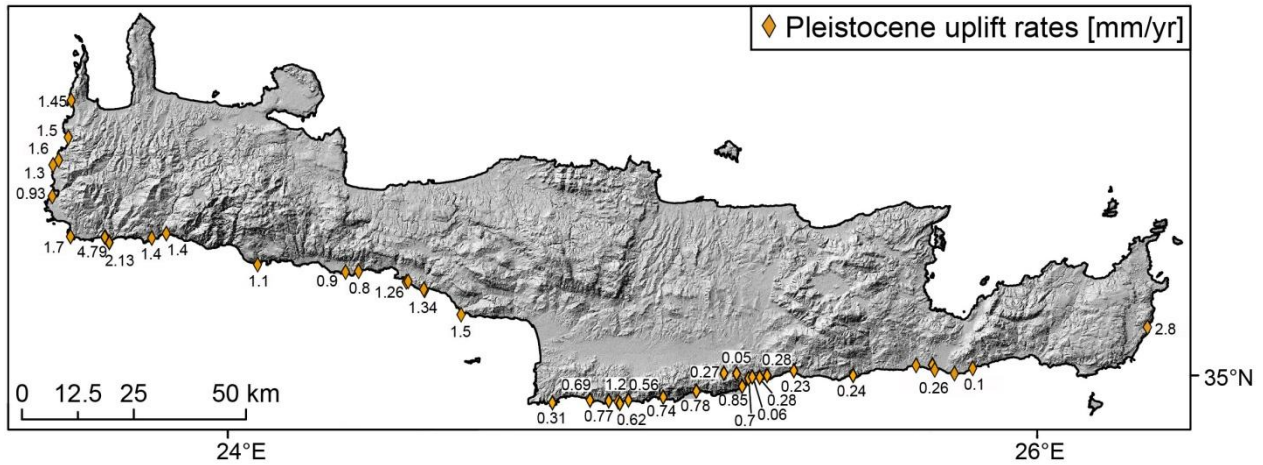


Figure 4.14: Pleistocene uplift rates in mm/yr. The hill slope map generated from the SPOT-DEM.

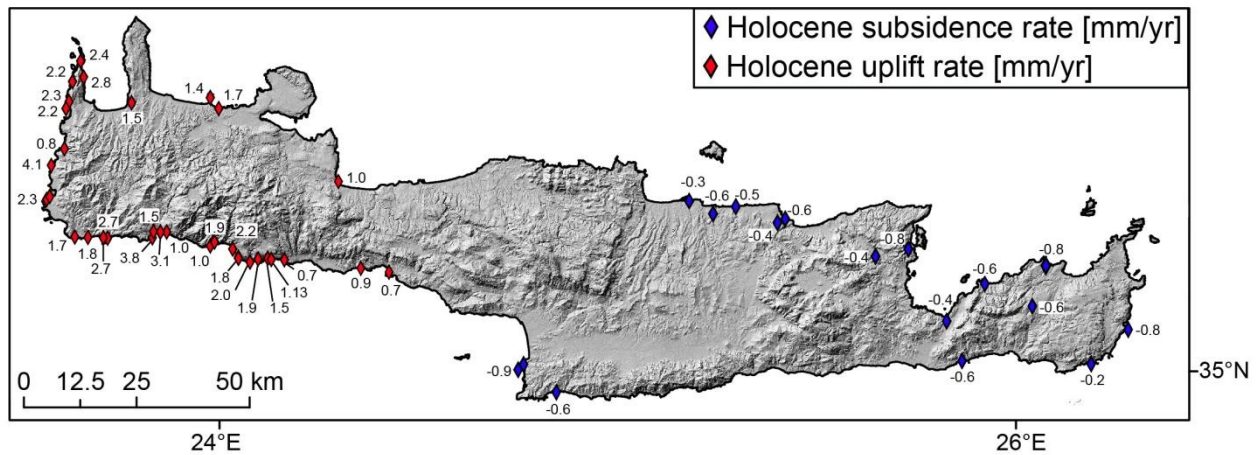


Figure 4.15: Holocene uplift rates in mm/yr. The hill slope map generated from the SPOT-DEM.

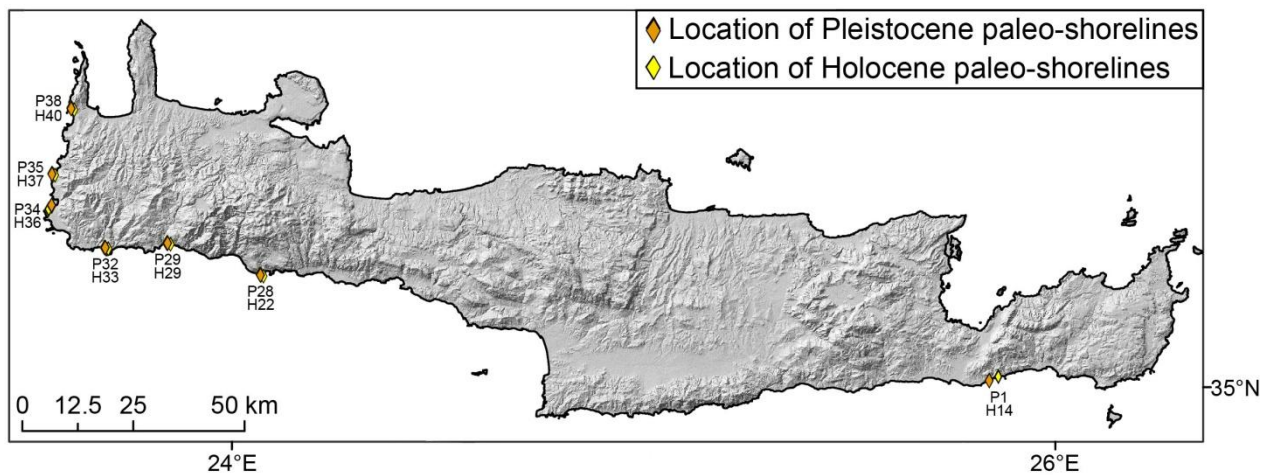


Figure 4.16: Location of Pleistocene and Holocene paleo-shorelines. The hill slope map generated from the SPOT-DEM.

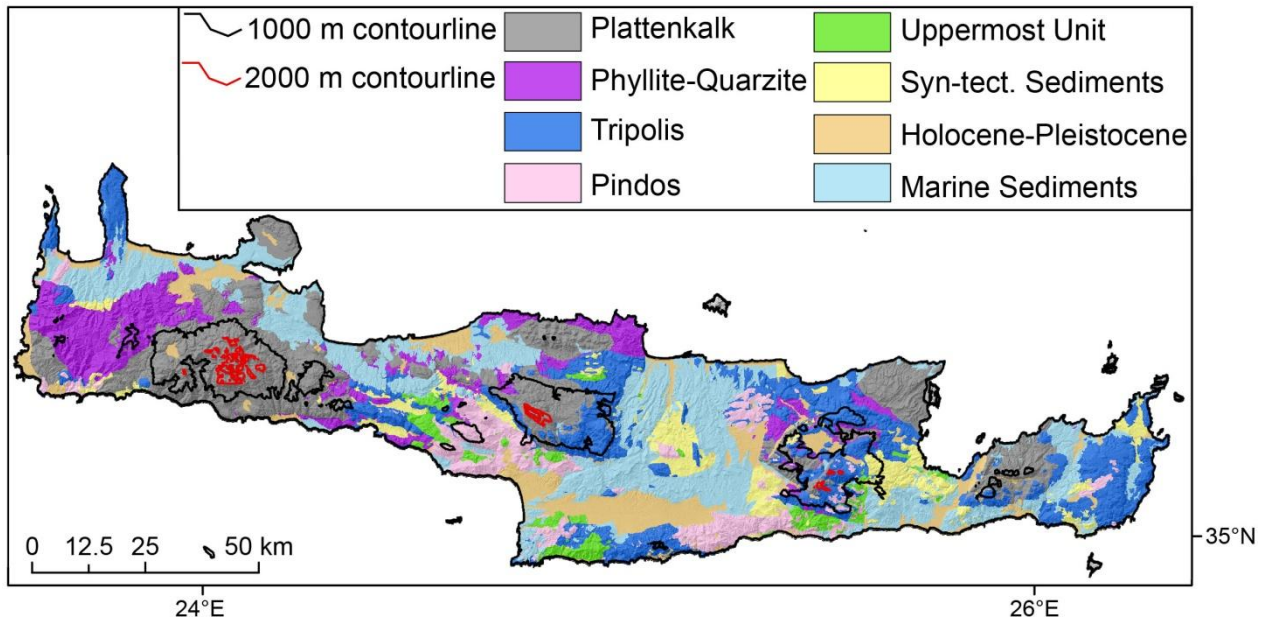


Figure 4.17: Geological map with contour lines every 1000 m interval. Background map of lithology by Papanikolaou and Vassilakis (2010) superimposed on SPOT-DEM.

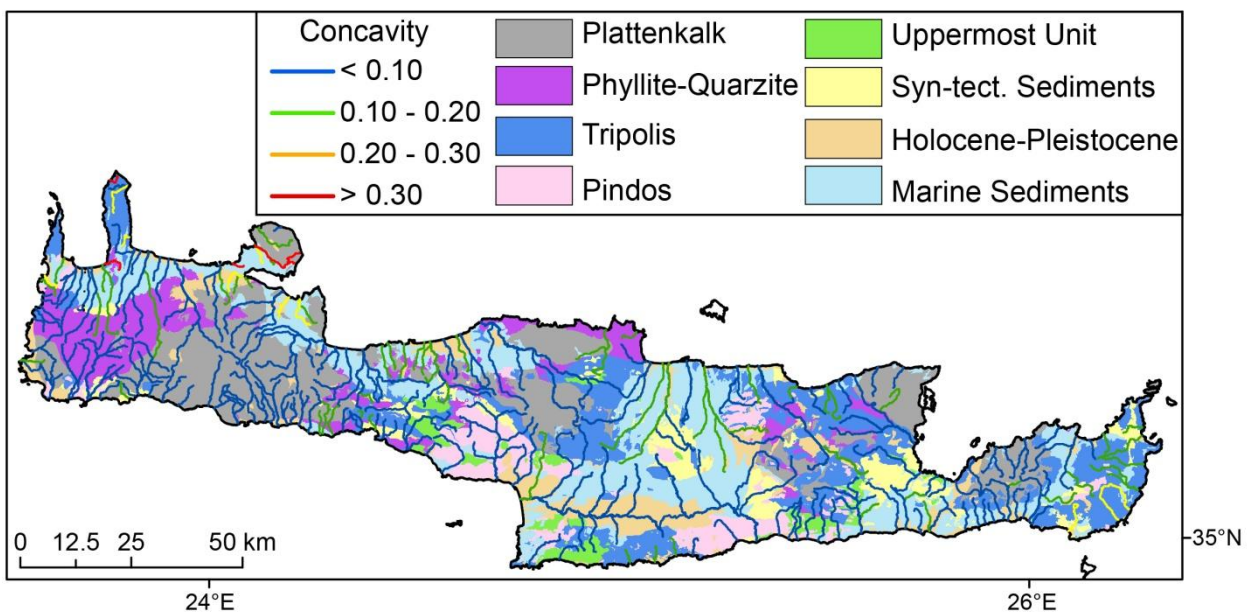


Figure 4.18: Map of concavity index Θ determined for Crete. Background is a map of lithology by Papanikolaou and Vassilakis (2010)

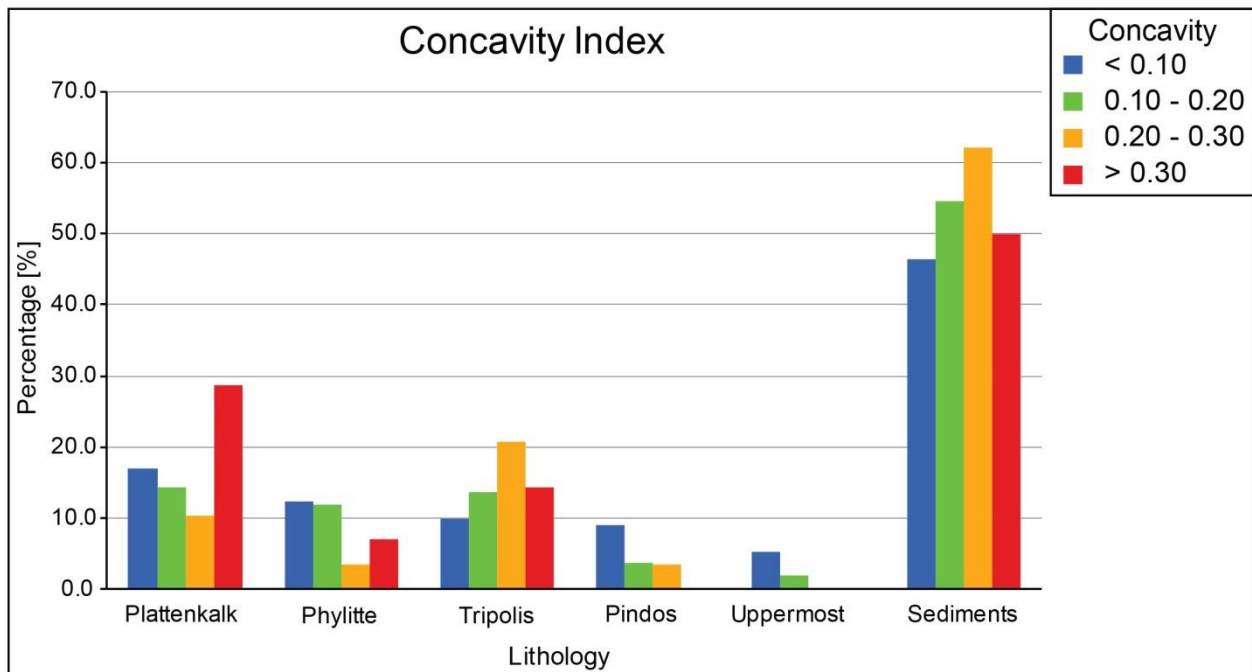


Figure 4.19: Concavity index versus geological units in percentage.

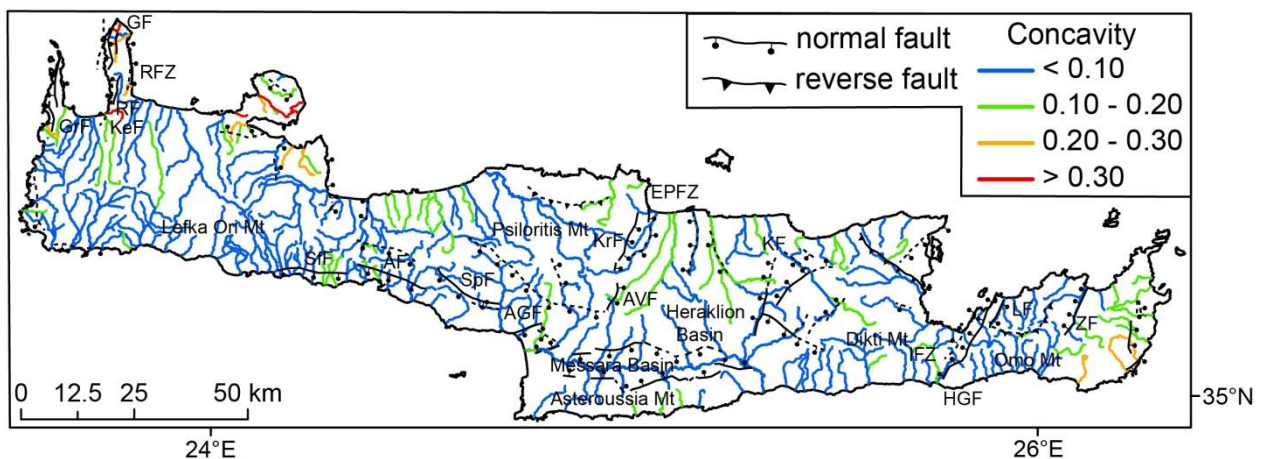


Figure 4.20: Map of concavity index Θ determined for Crete. Tectonic map showing faults on Crete and offshore underlying is the hill slope map generated from the SPOT-DEM. Dashed lines are possible faults determined by geomorphic features in topography. Fault traces are modified after Caputo et al. (2010). GrF: Gramvousa Fault, RFZ: Rhodope Fault Zone, KeF: Kera Fault, RF: Rodope Fault, GF: Gionas Fault, SfF: Sfakia Fault, AF: Asomatos Fault, SpF: Spili Fault, AGF: Agia Galini Fault, EPFZ: Eastern Psiloritis Fault Zone, KrF: Kroussonas Fault, AVF: Agia Varvara Fault, KF: Kastelli Fault, IEZ: Ierapetra Fault Zone, HGF: Ha Gorge Fault, LF: Lastros Fault, ZF: Zou Fault.

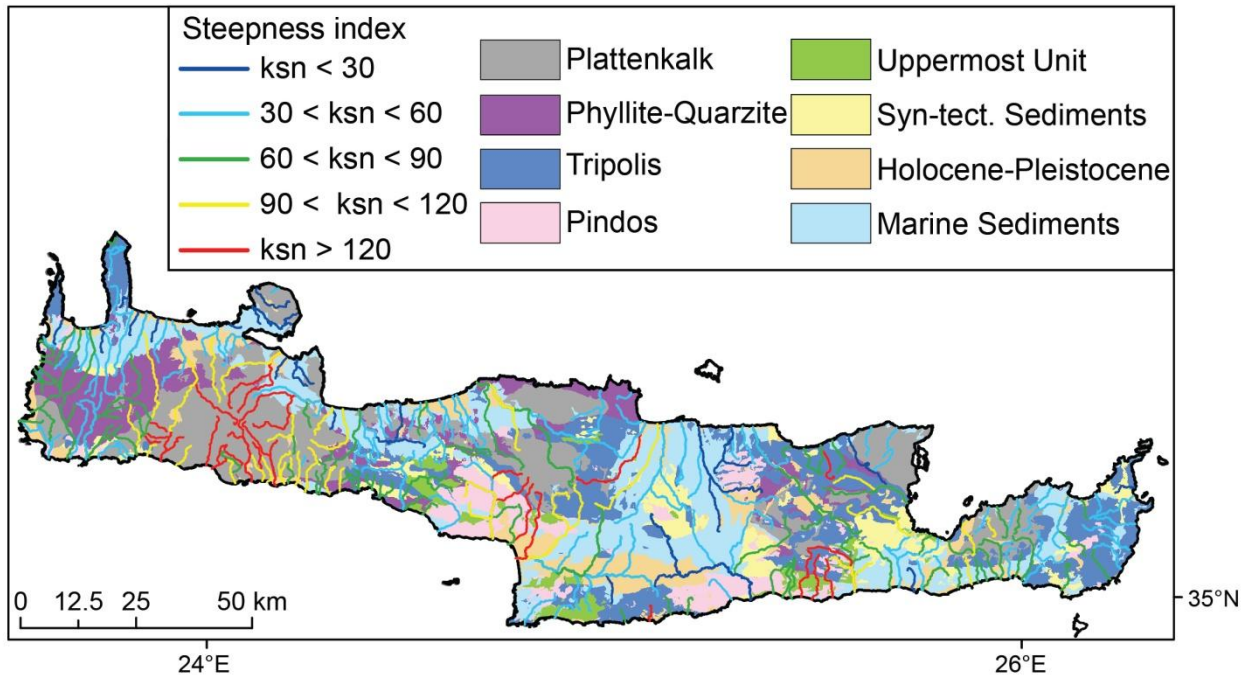


Figure 4.21: Map of normalized steepness index k_{sn} based on long profiles. Background is lithological map by Papanikolaou and Vassilakis (2010).

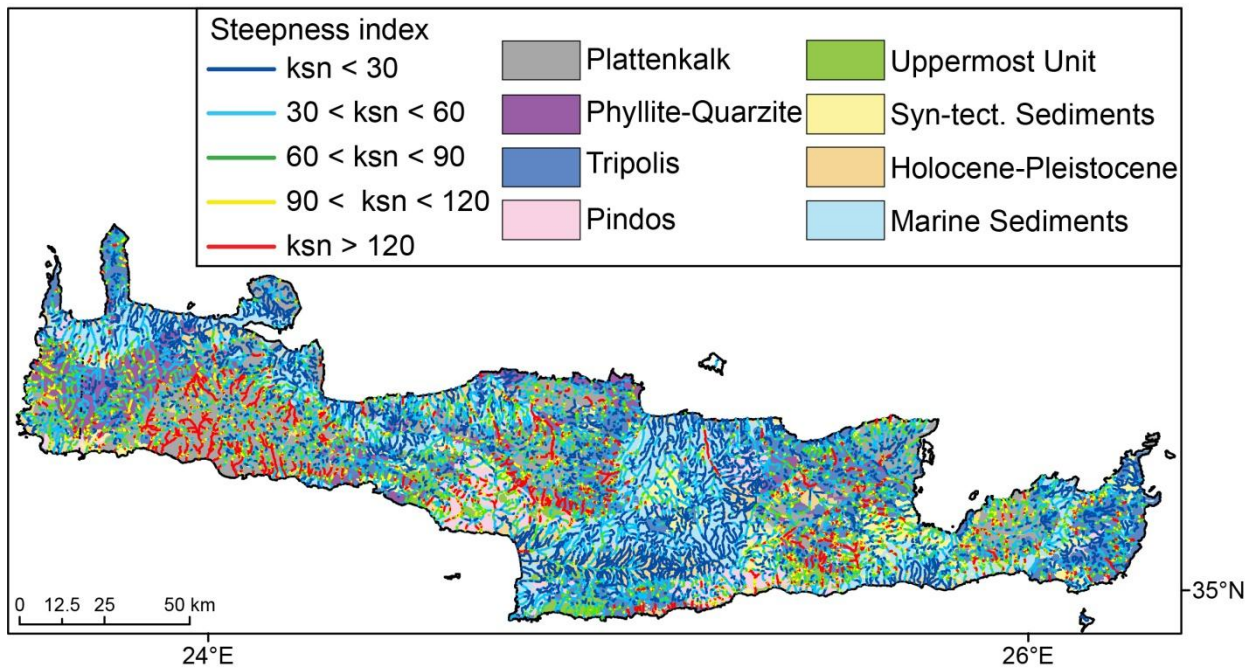


Figure 4.22: Map of normalized steepness index k_{sn} based on small segments of the profiles. Background is the lithological map by Papanikolaou and Vassilakis (2010).

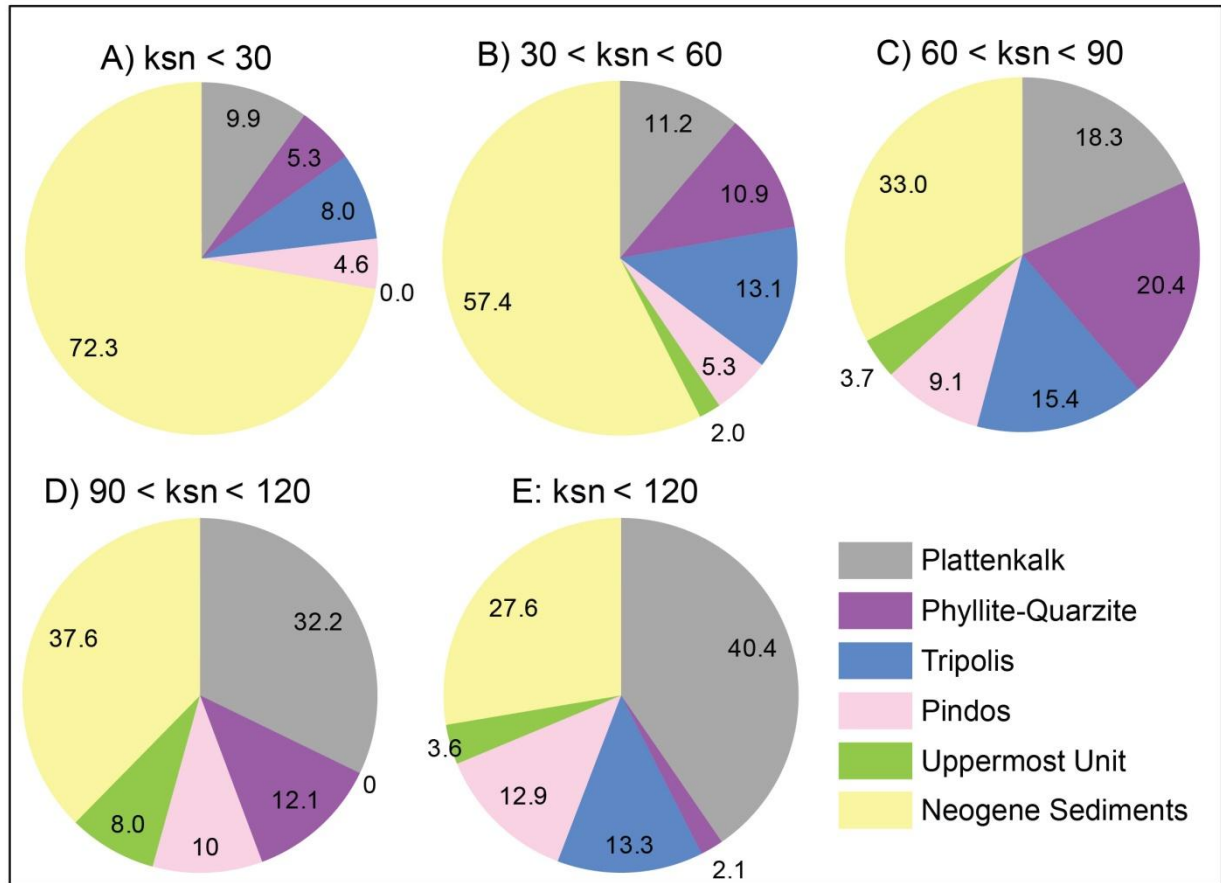


Figure 4.23: Percentage of k_{sn} values compared to the lithological units. A) k_{sn} value smaller than 30. B) k_{sn} value between 30 and 60. C) k_{sn} value between 60 and 90. D) k_{sn} value between 90 and 120. E) k_{sn} value higher than 120.

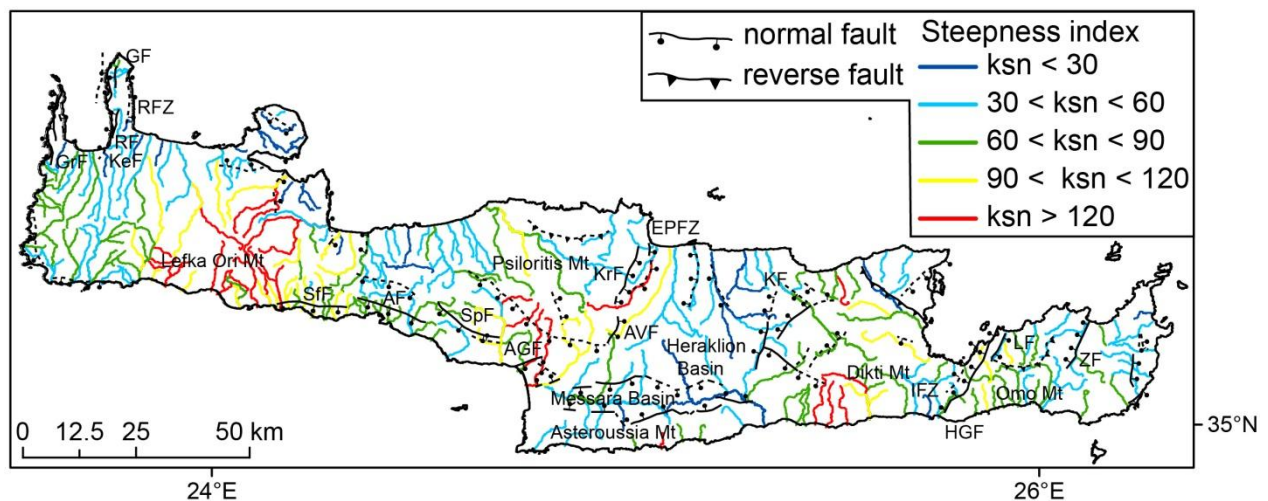


Figure 4.24: Map of normalized steepness index k_{sn} for Crete. Tectonic map showing faults on Crete and offshore underlying is the hill slope map generated from the SPOT-DEM. Dashed lines are possible faults determined by geomorphic features in topography. For fault abbreviations see Figure 4.20.

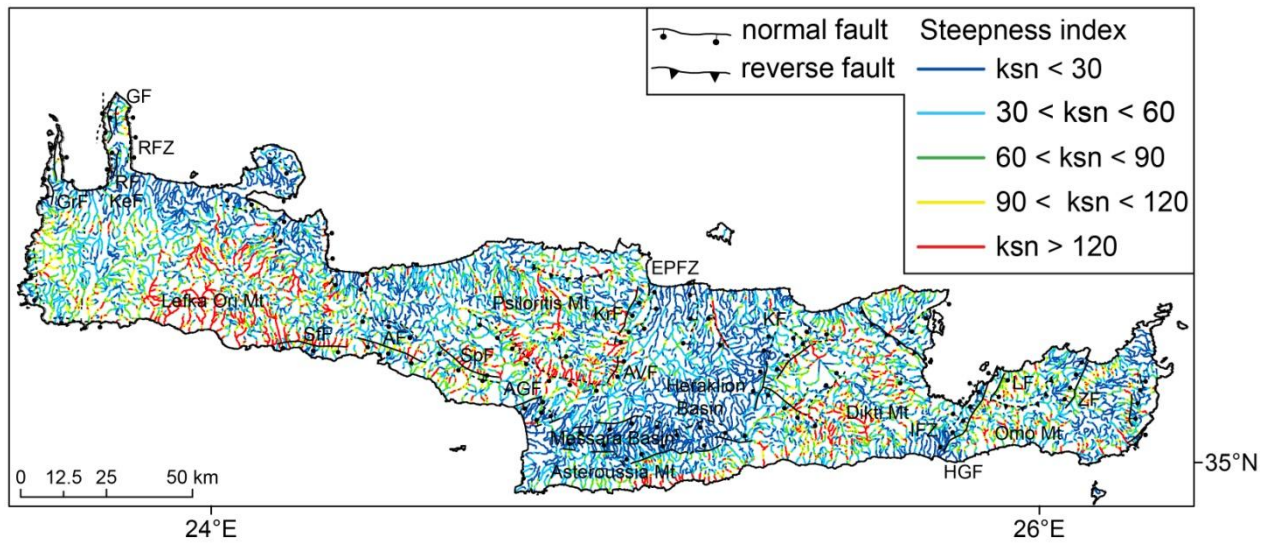


Figure 4.25: Map of normalized steepness index k_{sn} for Crete Background is a map of lithology by Papanikolaou and Vassilakis (2010). Tectonic map showing faults on Crete and offshore underlying is the hill slope map generated from the SPOT-DEM. Dashed lines are possible faults determined by geomorphic features in topography. For fault abbreviations see Figure 4.20.

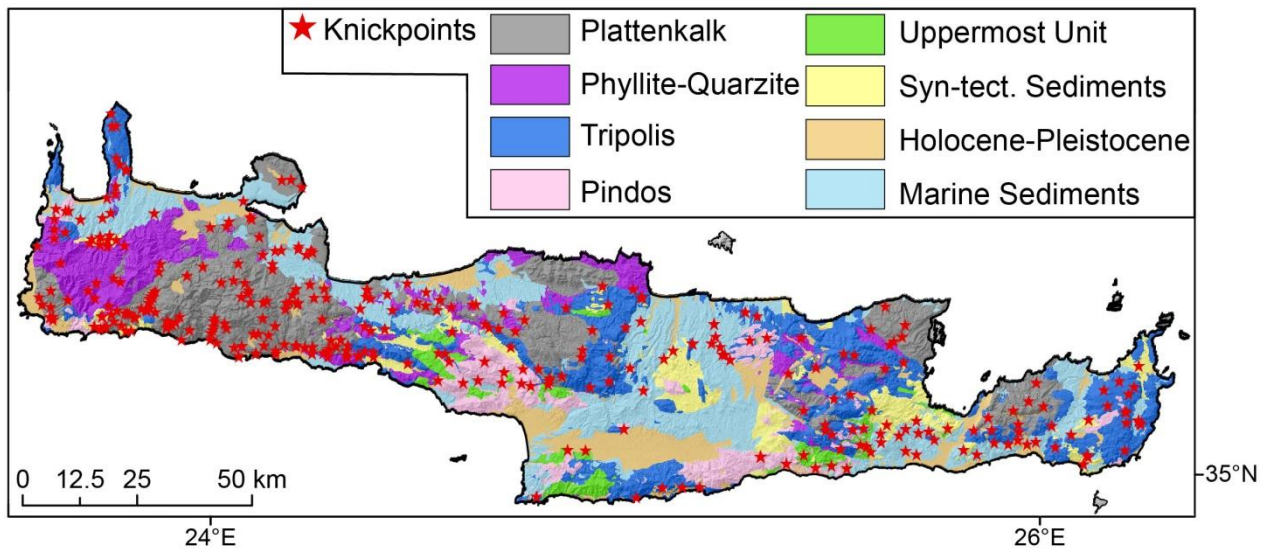


Figure 4.26: Knickpoints superimposed on the geological map (Papanikolaou and Vassilakis, 2010). Background is shaded relief generated from the SPOT-DEM.

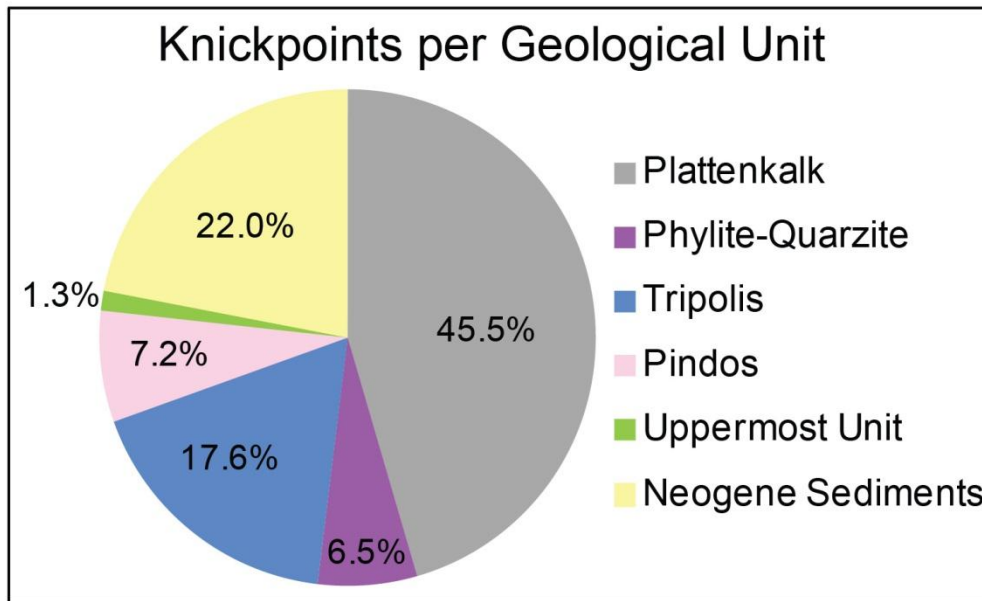


Figure 4.27: Percentage of knickpoints per lithological unit on Crete.

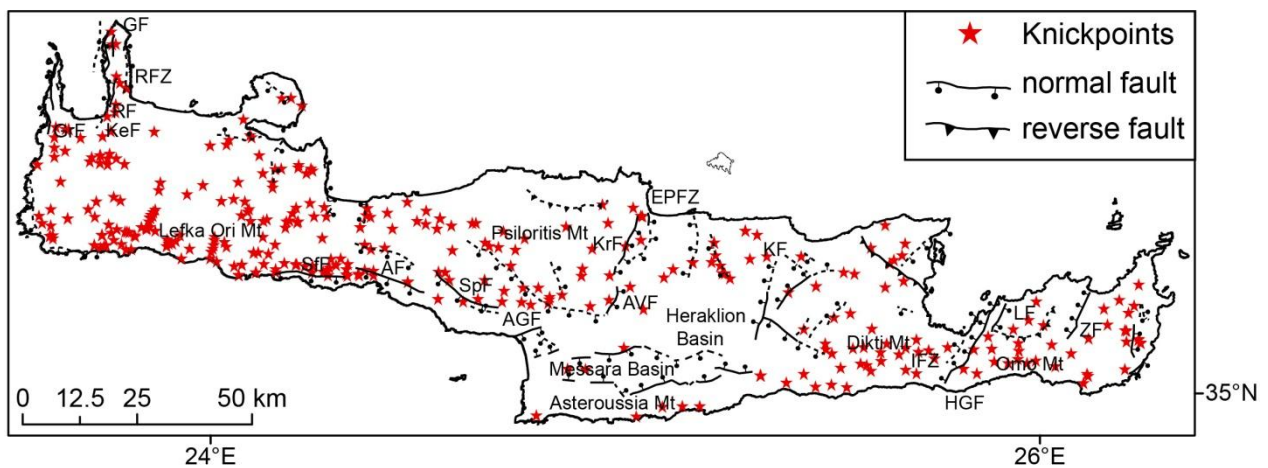


Figure 4.28: Map of knickpoints. Tectonic map showing faults on Crete and offshore underlying is the hill slope map generated from the SPOT-DEM. Dashed lines are possible faults determined by geomorphic features in topography. For fault abbreviations see Figure 4.20.

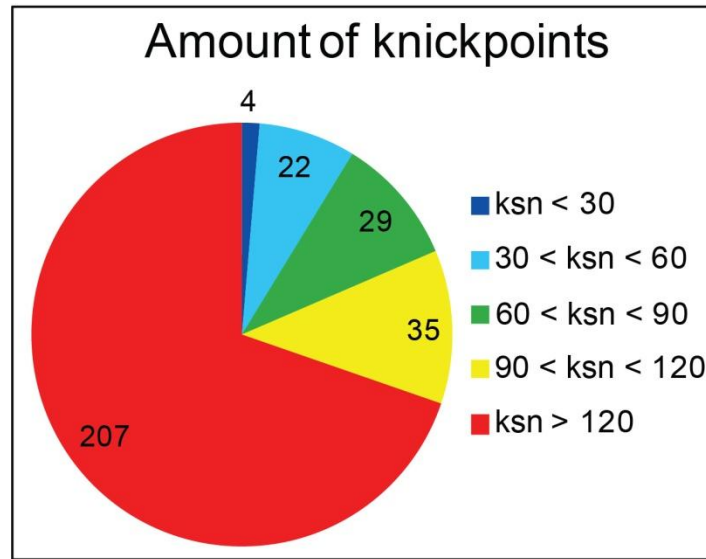


Figure 4.29: Distribution of knickpoints for small river segments.

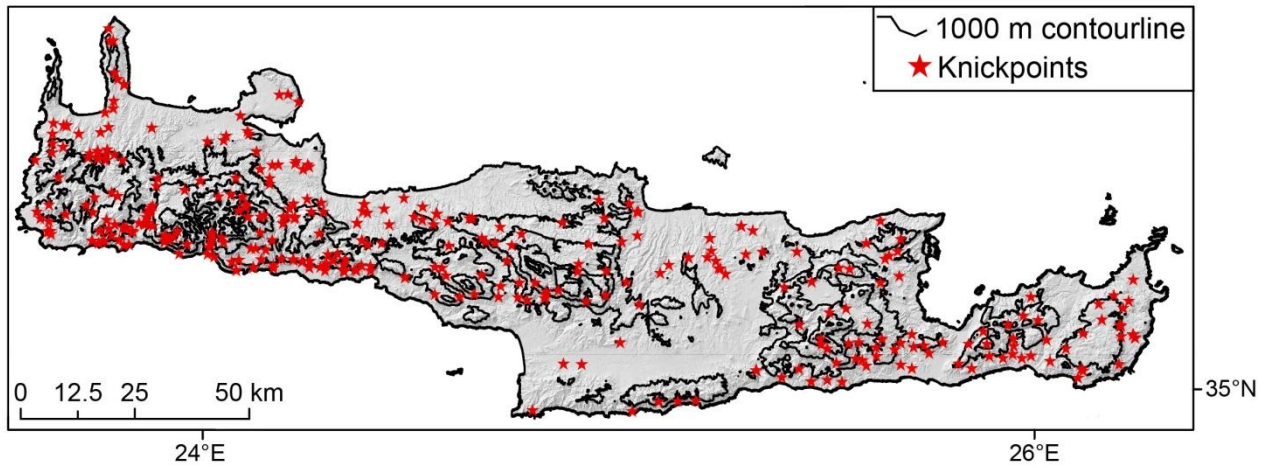


Figure 4.30: Map of knickpoints correlated to their elevation. Tectonic map showing faults on Crete and offshore underlying is the hill slope map generated from the SPOT-DEM.

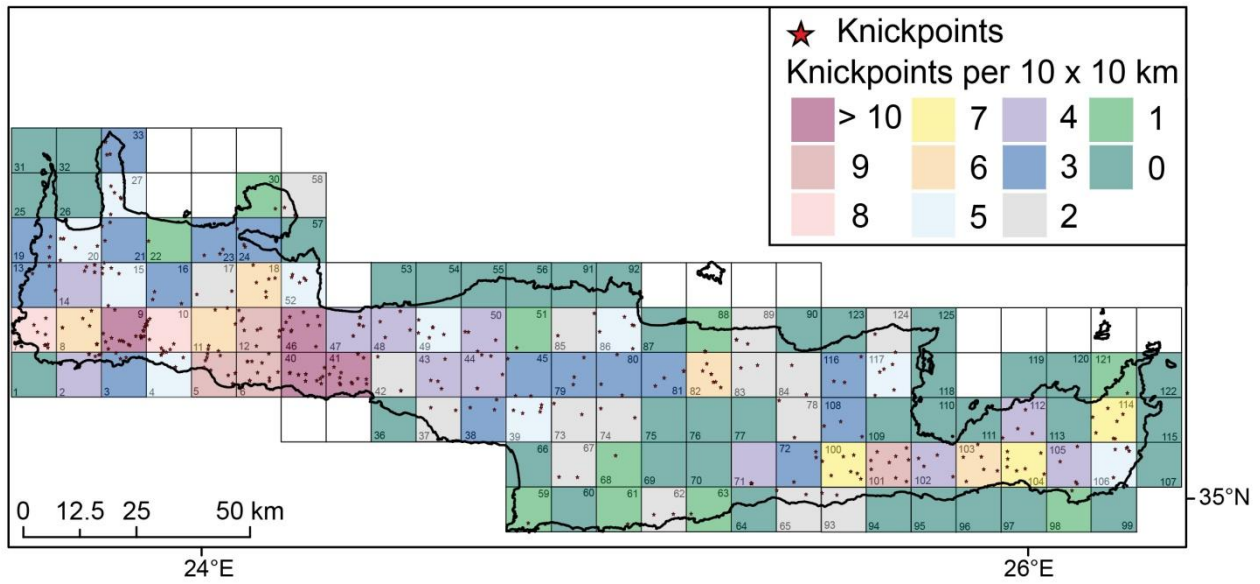


Figure 4.31: Knickpoint distribution for raster of 10 x 10 km across Crete. Color coded tiles represent number of knickpoints per 10 x 10 km tile.

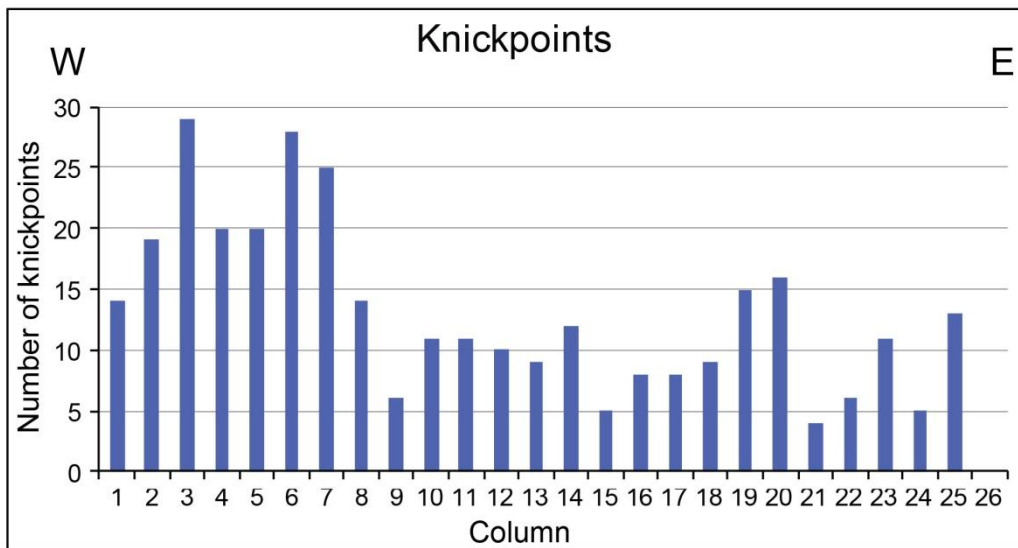


Figure 4.32: Number of knickpoint distribution from W to E based on Figure 4.31.

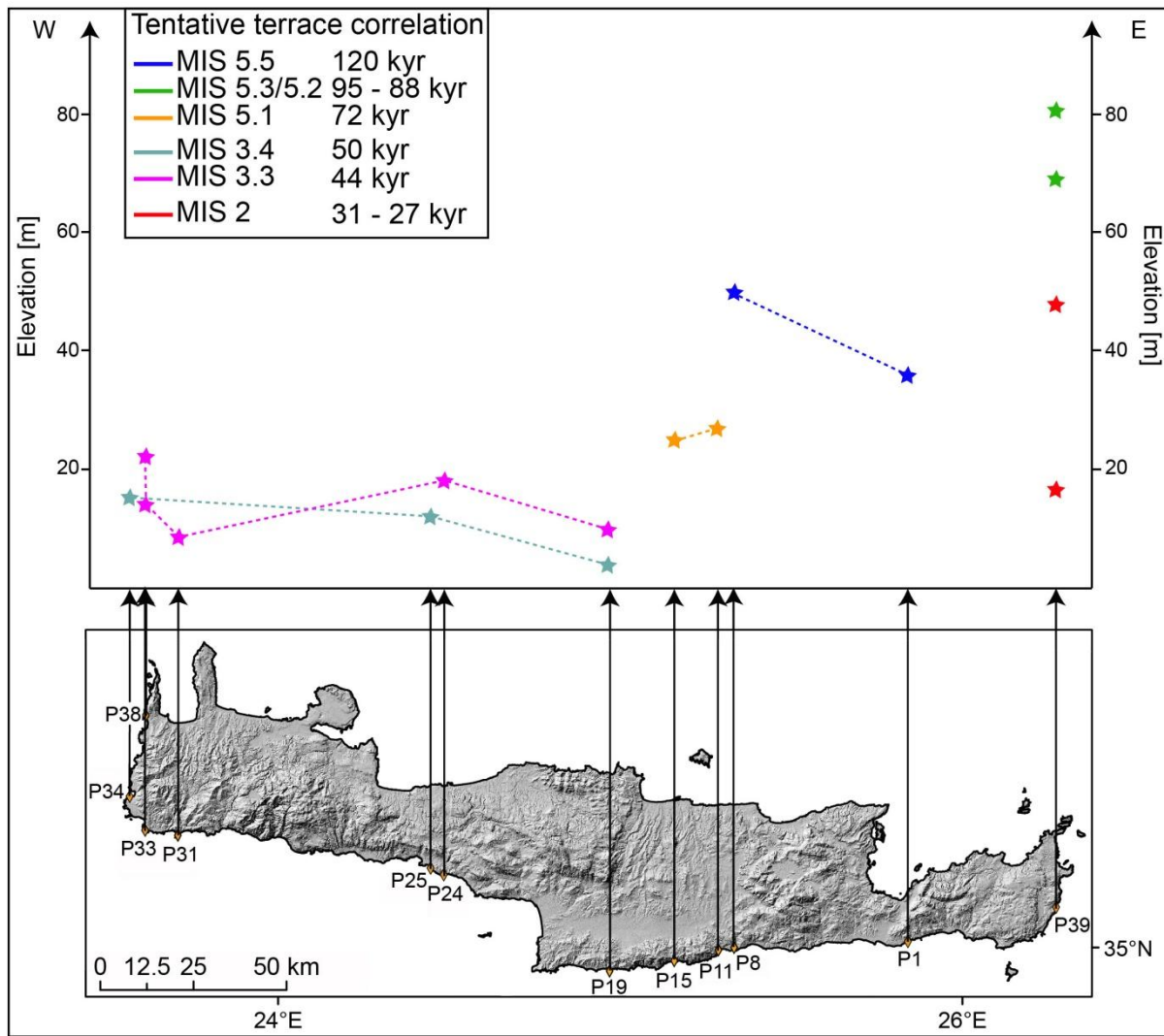


Figure 4.33: Tentative terrace correlation of dated terraces.

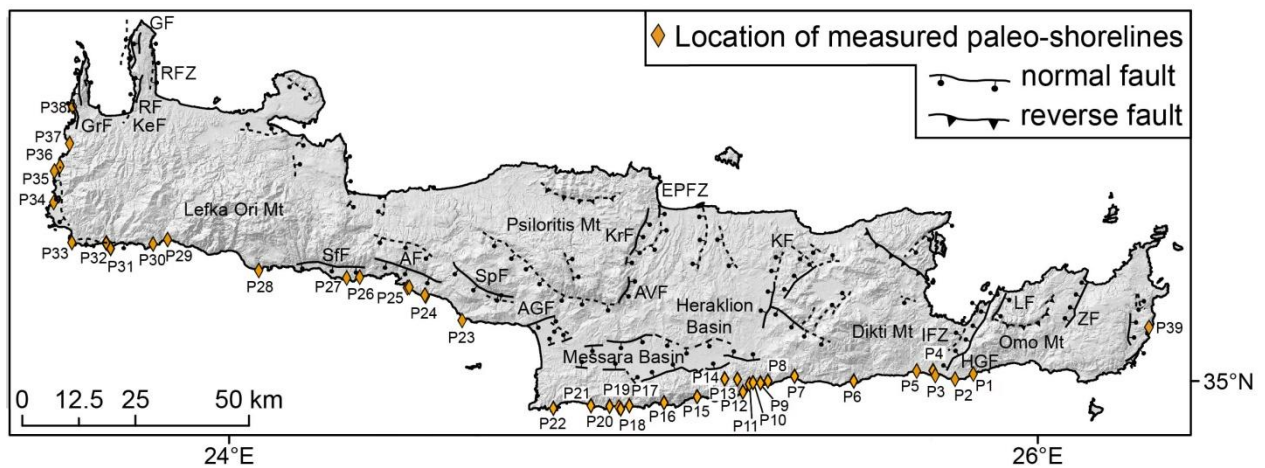


Figure 4.34: Tectonic map showing faults on Crete underlying is the hill slope map generated from the SPOT-DEM. Dashed lines are possible faults determined by geomorphic features in topography. For fault abbreviations see Figure 4.20.

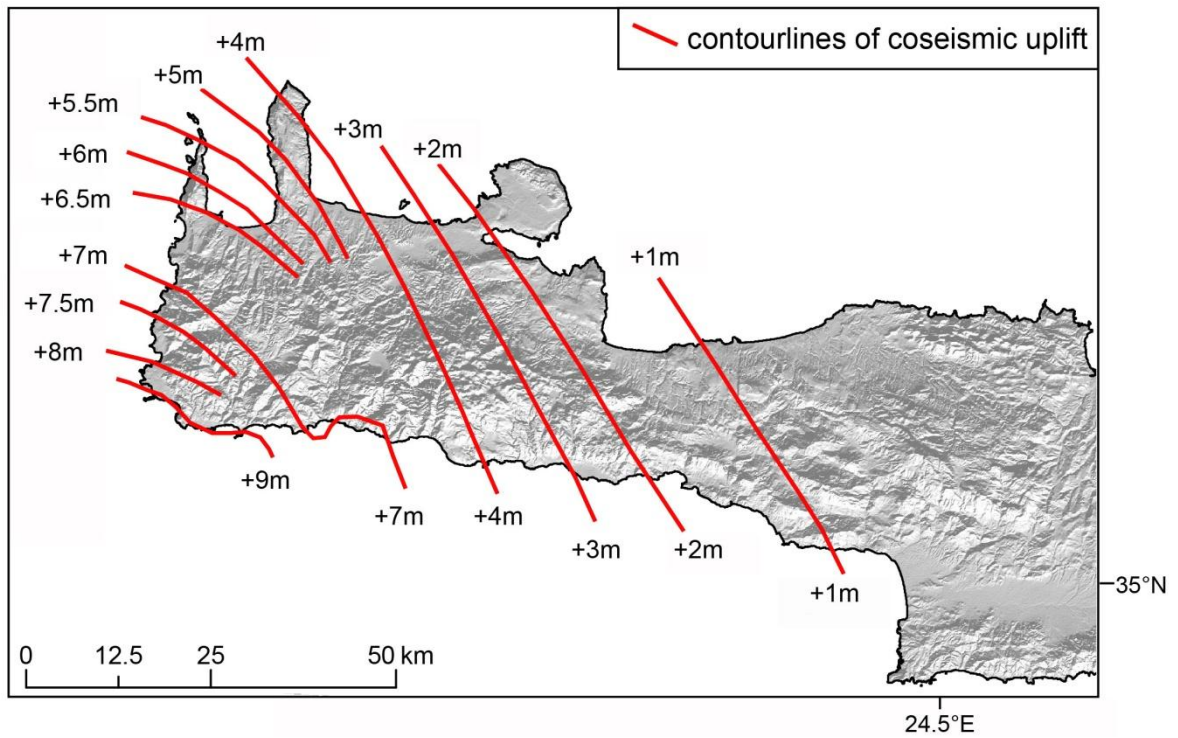


Figure 4.35: Coseismic uplift of the 365 A.D. earthquake. Uplift data based on Pirazzoli et al. (1996). Hill slope map generated from SPOT-DEM.

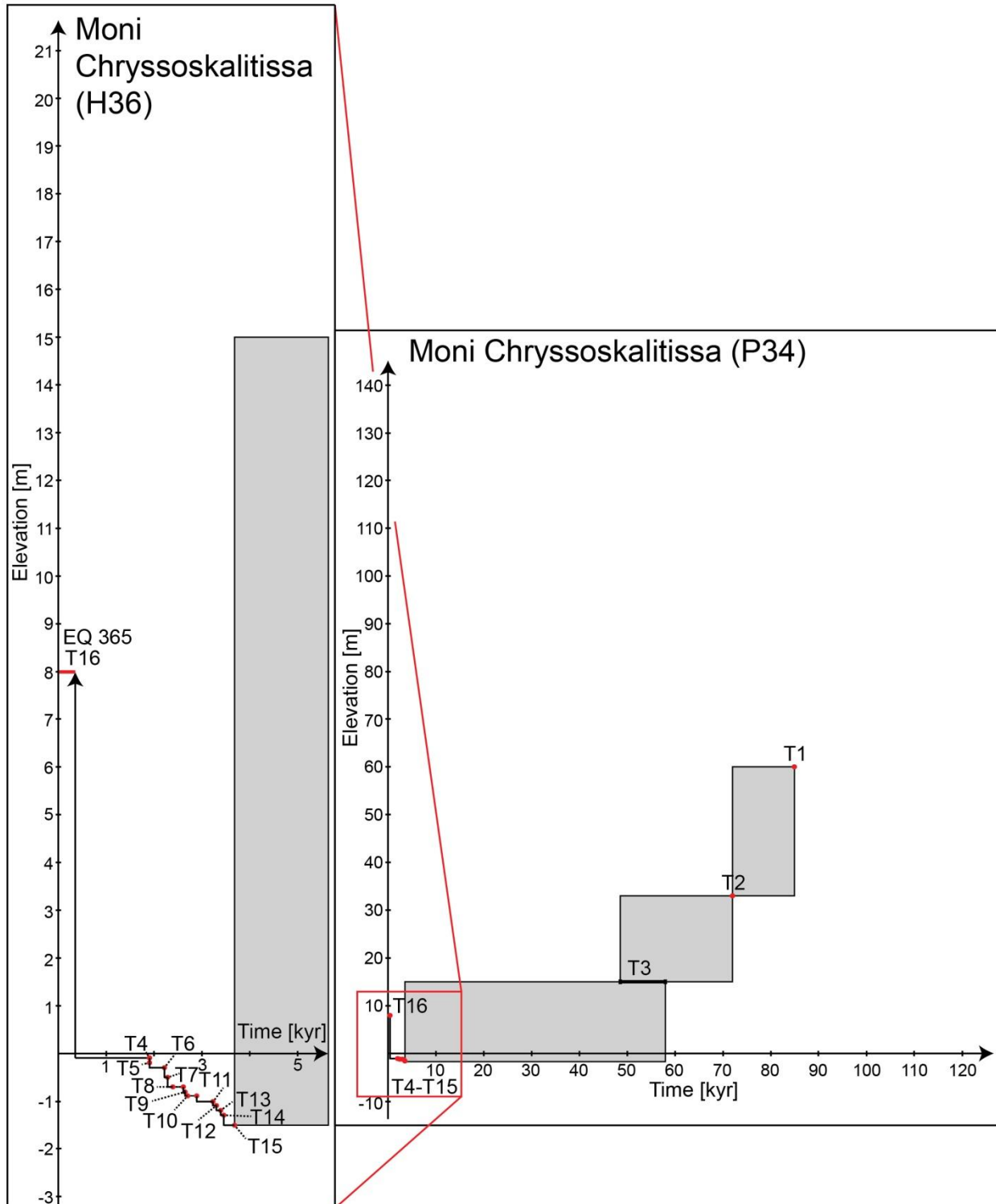


Figure 4.36: Elevation of Pleistocene and Holocene palae-shorelines plotted against time at Moni Chryssoskalitissa, modified after Pirazzoli et al. (1996), and Wegmann (2008).

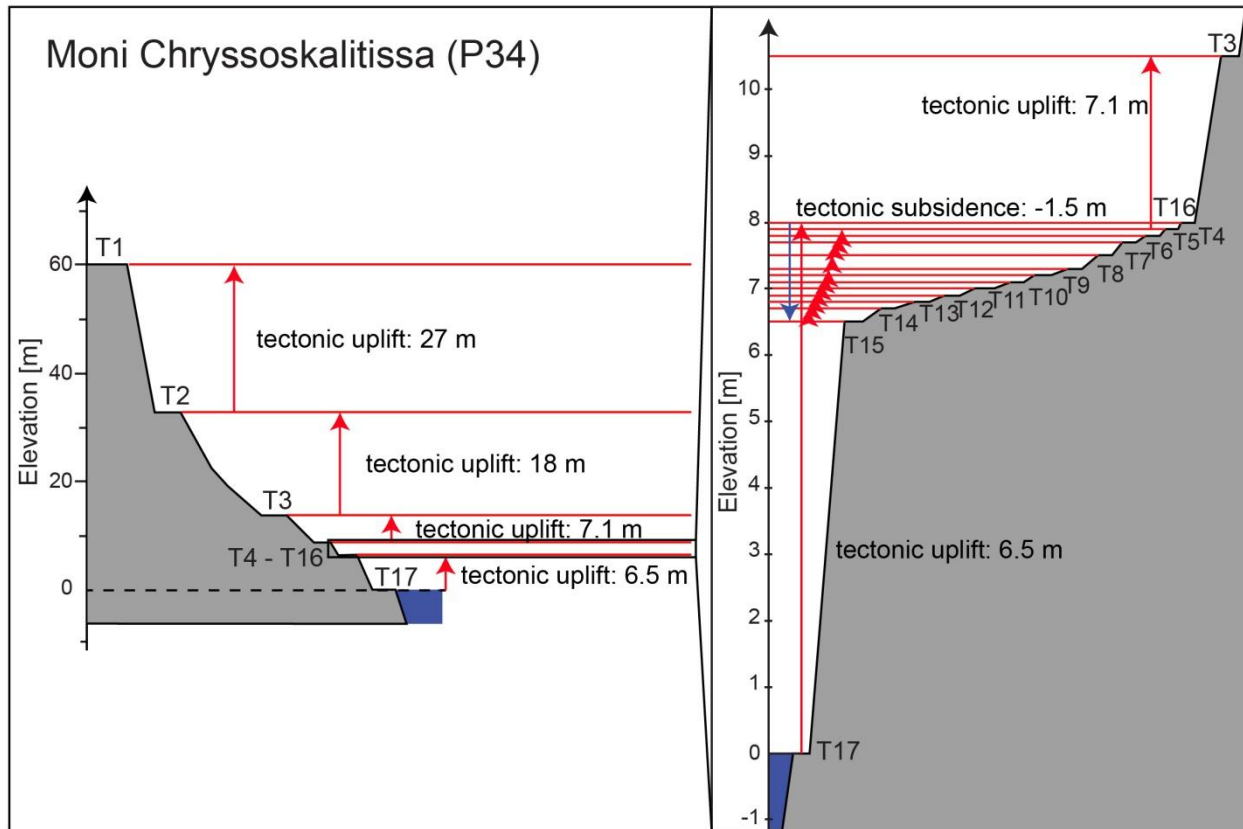


Figure 4.37: Elevation of terraces and the height difference needed for the tectonic uplift at Moni Chryssoskaliissa, modified after Pirazzoli et al. (1996), and Wegmann (2008).

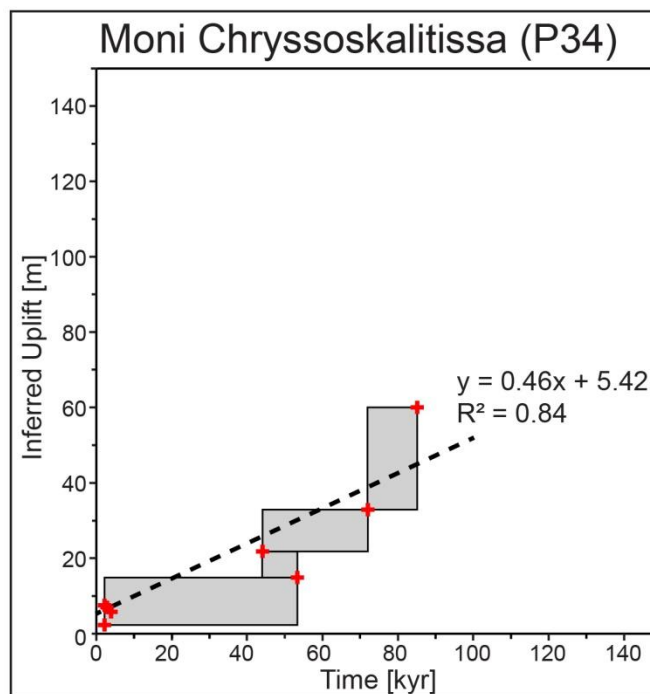


Figure 4.38: Inferred uplift diagram curve for tectonic uplift is determined by linear regression analysis at Moni Chryssoskalitissa.

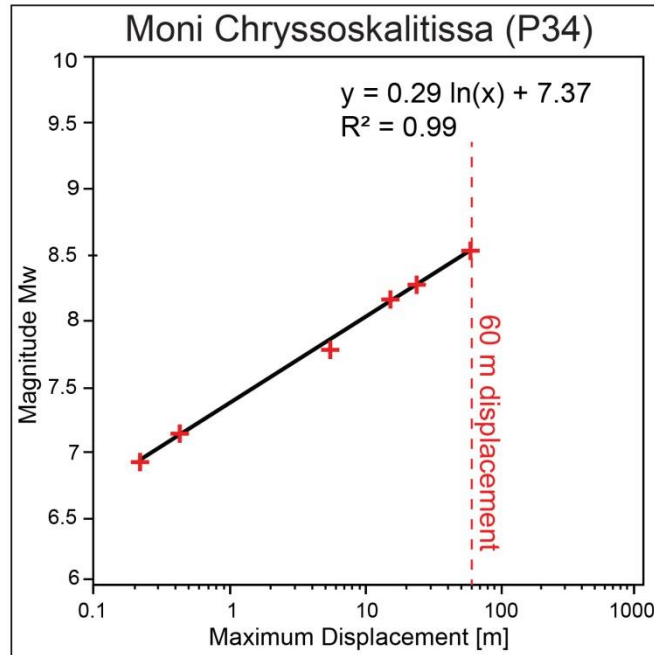


Figure 4.39: Regression of maximum displacement versus magnitude M_w modified after Wells and Coopersmith 1994. Maximum displacement 60 m ever measured for an earthquake is for the 2011 Mw 9.0 Tohoku-Oki (Japan) (Simons et al., 2011).

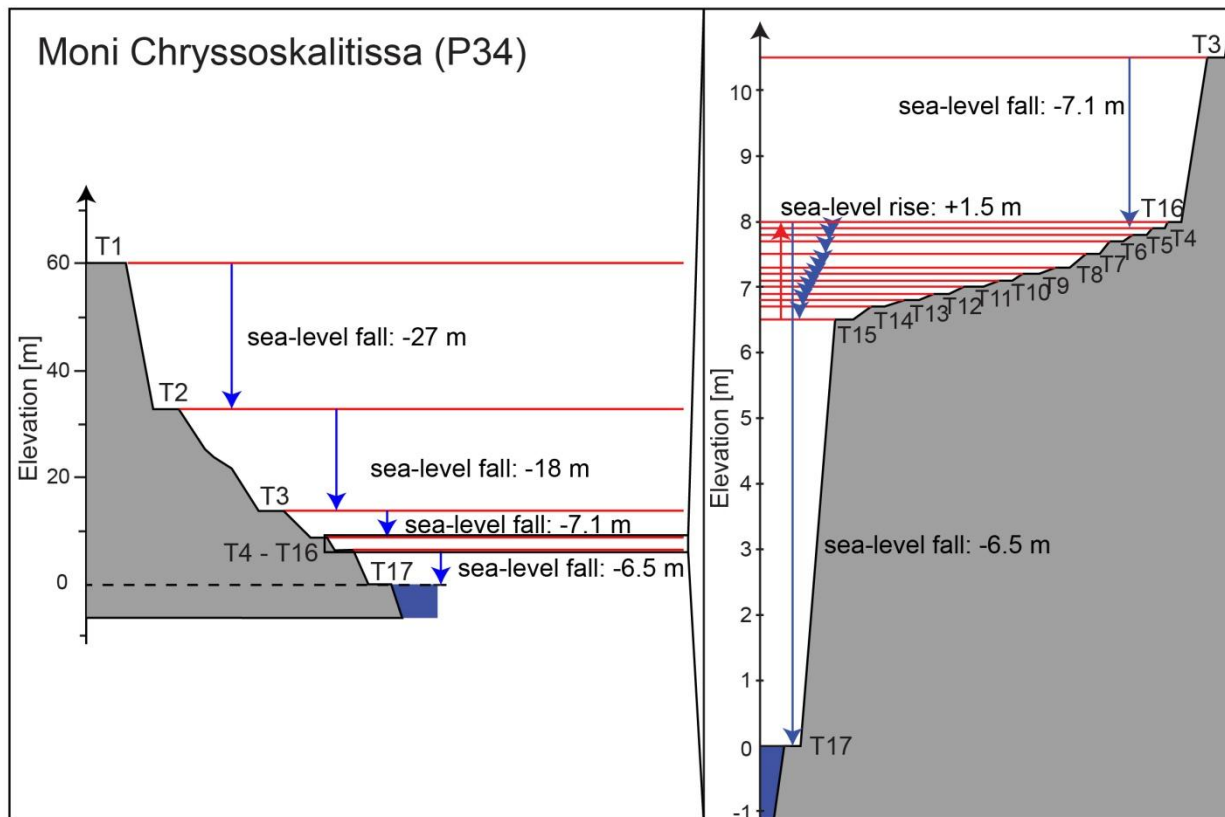


Figure 4.40: Elevation of terraces and the needed amount of sea-level fall at Moni Chryssoskalitissa, modified after Pirazzoli et al. (1996), and Wegmann (2008).

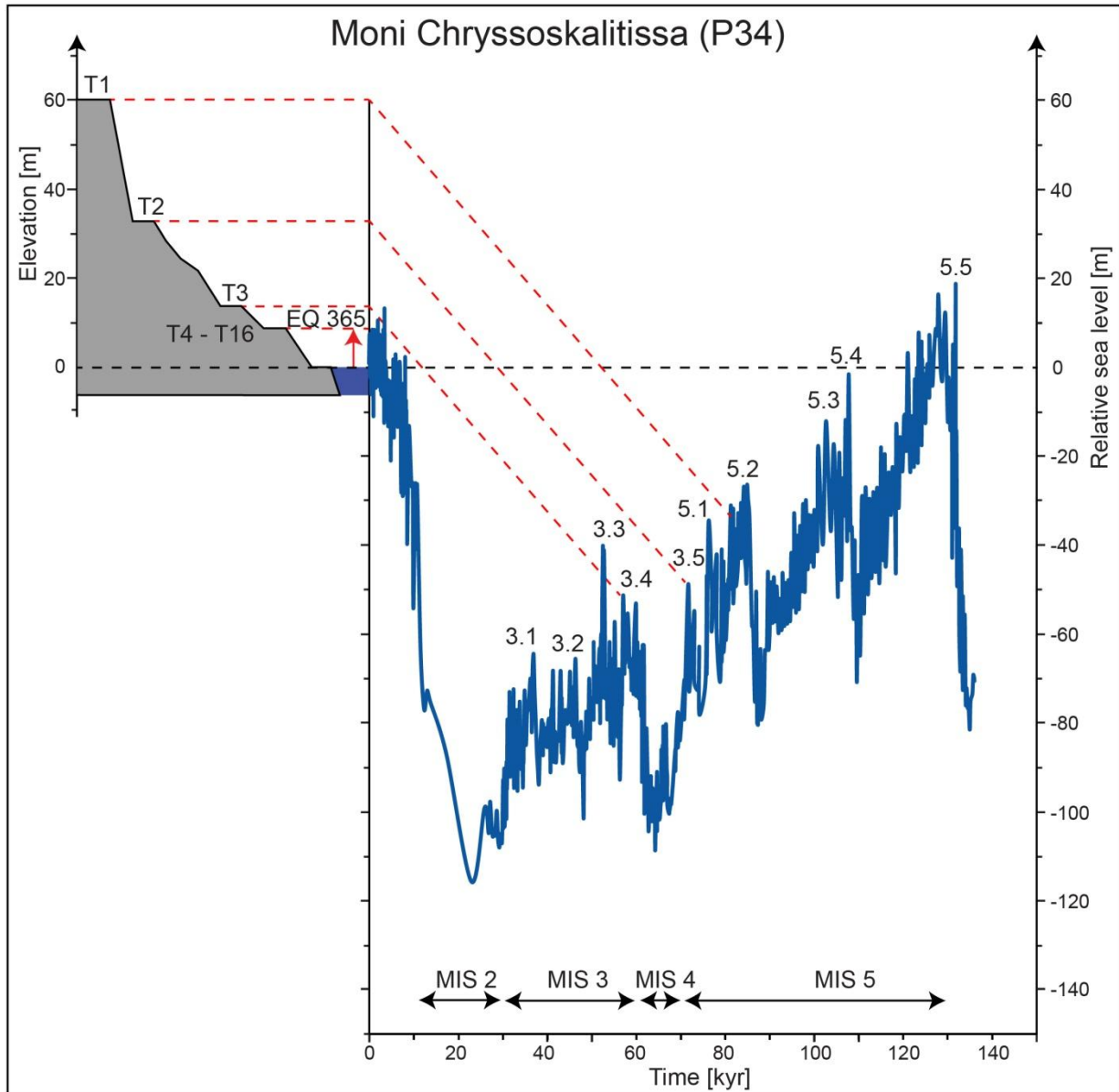


Figure 4.41: Correlation of terraces at Moni Chryssoskalitissa with constant uplift to the sea-level curve of Rohling et al. (2014).

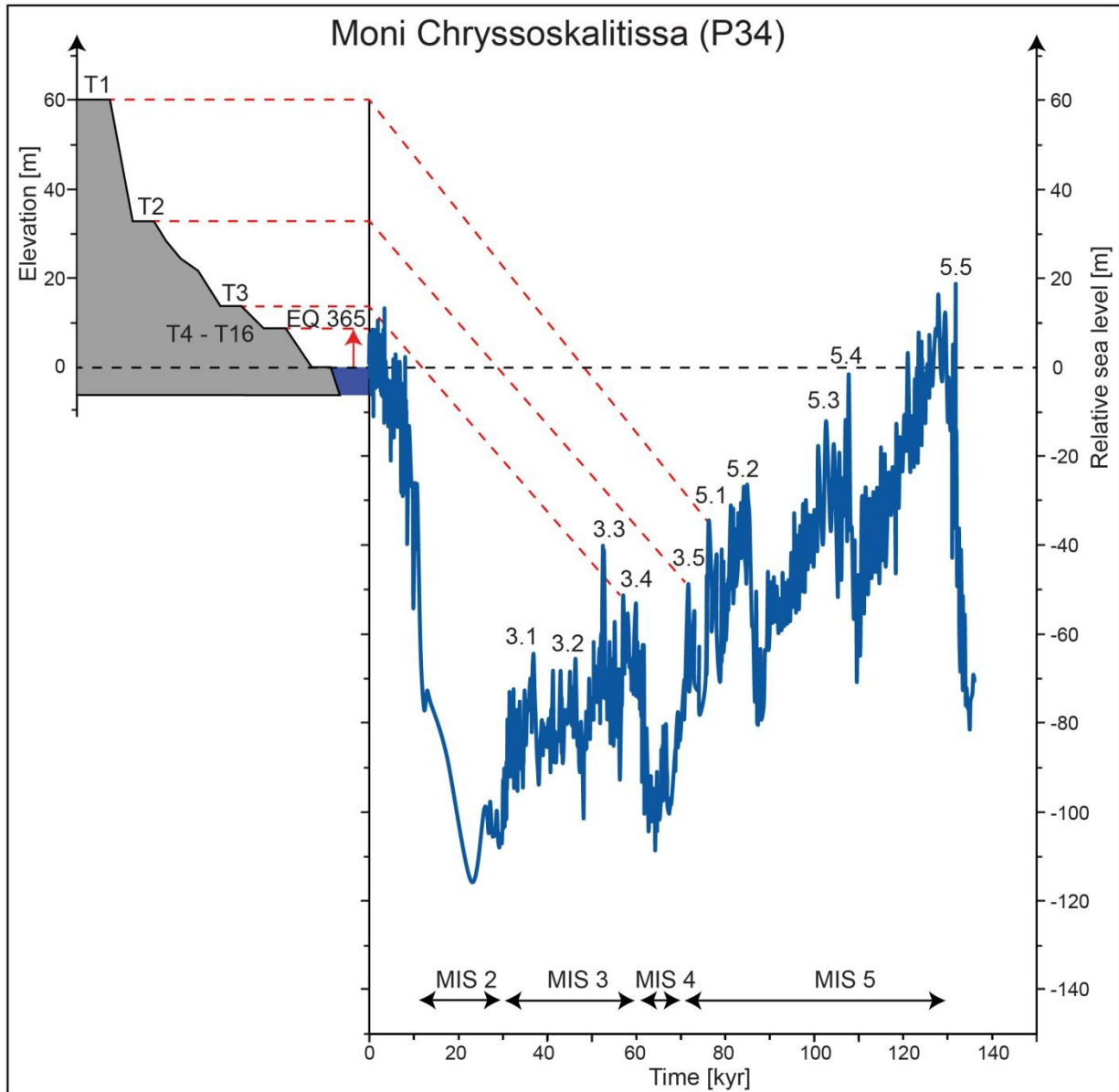


Figure 4.42: Correlation of terraces at Moni Chryssoskalitissa with not-constant uplift to the sea-level curve of Rohling et al. (2014).

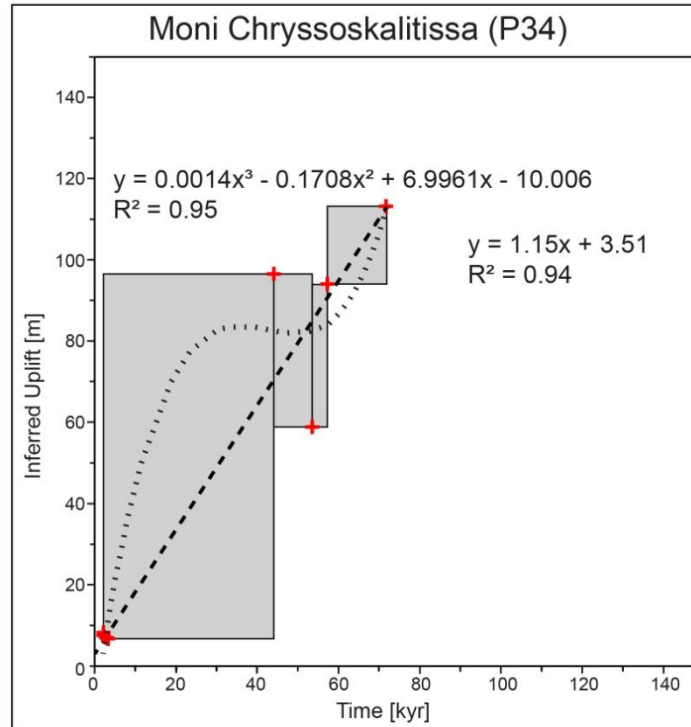


Figure 4.43: Inferred uplift diagram curve for sea-level correction is determined by linear regression analysis and the curve represents the polynomial fit.

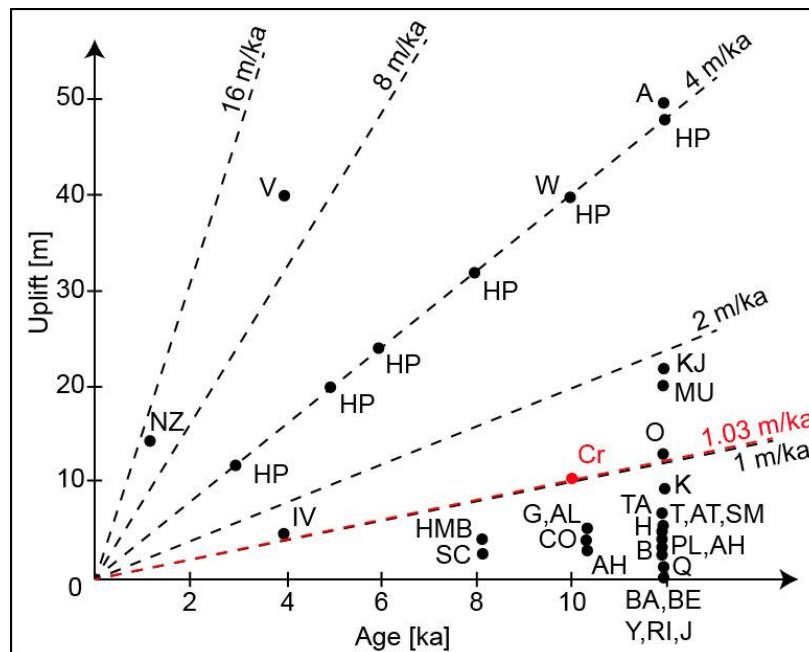


Figure 4.44: Pleistocene vertical coastal uplift rates. NZ: New Zealand, V: Ventura, A: Arauco, HP: Huon Peninsula, W: Wairarapa, KJ: Kikai Jima, MV: Muroto, O: Osado, K: Kosado, HMB: Half Moon Bay, SC: Santa Cruz, RI: Royalty Islands, TA: Taaanaki, T: Timor, AT: Atauro, H: Haiti, B: Barbados, AH: Arroyo Hondo, CO: Cojo, AL: Algeria, IV: Isla Vista, SM: Santa Monica, PL: Point Loma, J: Jamaica, BA: Bahamas, Y: Yucatan, BE: Bermuda, Q: Queensland, and Cr: Crete. All data taken from Lajoie (1986), except Cr: Crete.

Table 4.1: Locations of published Pleistocene paleo-shorlines and the corresponding author.

Author	Location
Gaki-Papanastassiou et al. (2009)	P1 – P4
Gallen et al. (2014)	P5 – P18
Wegmann (2008)	P19
Gallen et al. (2014)	P20 –P22
Wegmann (2008)	P23
Wegmann (2008)/Strasser (2011)	P24/P25
Wegmann (2008)	P26 – P30
Tiberti et al. (2014)	P31/P32
Wegmann (2008)	P33-P38
Strobl et al (2015)	P39

Table 4.2: Locations of published Holocene paleo-shorlines and the corresponding author.

Author	Location
Mourtzas (2012)	H1/H3/H5/H9/H12/H14-H16/H18/H22/H25/H27/H31/H36/H37/H41/H43/46/H47
Pavlopoulos et al. (1996)	H2/H4/H6-H8/H10/H11/H13/H16/H26/H36/H39/H40
Pirazolli et al. (1996)	H17/H20/H21/H26/H29/H36/H37/H39/H42/H45/H47
Price et al. (2002)	H17/H20/H21/H23/H24/H26/H29/H36/H37/H39/H42/H45
Shaw et al. (2010)	H19/H28/H30/H32/H34/H35/H36/H38/H39/H44
Tiberti et al. (2014)	H32/H33/H35
Strobl et al. (2014)	H12

Table 4.3: Marine isotopic stages (MIS), corresponding age and sea-level after Rohling et al. (2014).

MIS stage	Age [kyr]	Sea-level [m]
3.1	32	-82.65 ± 6
3.2	36.6	-80.69 ± 6
3.3	46	-74.65 ± 6
3.4	52.5	-55.75 ± 6
3.5	57	-60.90 ± 6
5.1	71.8	-53.26 ± 6
5.2	84.8	-47.07 ± 6
5.3	102.5	-24.66 ± 6
5.4	107.9	-19.50 ± 6
5.5	131.8	19.87 ± 6
7	197	-5.87 ± 6
8	292	-35.54 ± 6
9	330	-11.02 ± 6
11	404	-3.12 ± 6

Table 4.4: Locations of dated Pleistocene terraces, their corresponding MIS stage and the present elevation.

Location	MIS stage	Elevation (m)
P1 ^a	5.5	36
P8 ^b	5.5	50
P11 ^b	5.1	27
P15 ^b	5.1	25
P19 ^c	3.4	4
P19 ^c	3.3	10
P24 ^c	3.3	18
P25 ^c	3.4	12
P31 ^c	3.3	9
P33 ^c	3.3	22
P34 ^c	3.4	15
P38 ^c	3.3	14
P39 ^d	5.3/5.2	81
P39 ^d	5.3/5.2	69
P39 ^d	2	48
P39 ^d	2	17

^aGaki-Papanastassiou et al. (2009); ^bGallen et al. (2014); ^cWegmann (2008); ^dStrobl et al. (2014)

Table 4.5: Location and referring numbering of Pleistocene and Holocene shorelines at one locality.

Location Name	Location Nr in Figure 4.16	Author
Ierapetra	P1 / H14	Gaki-Papanastassiou et al. (2009) / Mourtzas (2012)
Araden Gorge	P28 / H22	Wegmann (2008) / Mourtzas (2012), and Pirazzoli et al. (1996)
Sougia/Pevkoi	P29 / H29	Wegmann (2008) / Pirazzoli et al. (1996), Price et al. (2002)
Kalamia	P32 / H33	Tiberti et al. (2014) / Pirazzoli et al. (1996)
Moni Chryssoskalitissa	P34 / H36	Wegmann (2008) / Pirazzoli et al. (1996)
Cape Koutoulas/ Peristerias	P 35 / H37	Wegmann (2008) / Pirazzoli et al. (1996)
Phalasarna	P38 / H40	Wegmann (2008) / Pirazzoli et al. (1996)

Table 4.6: Parameters for the 365 A.D. Mw 8.3 earthquake and the 1303 A.D. Mw7.9 earthquake.

Earthquake	Length [km]	Width [km]	Slip [m]	Dip [°]	Mw	Reference
Hellenic Trench 365 A.D.	100	45	20	30°	8,25	Shaw et al. (2008)
8 th August 1303 A.D.	100	30	8	45	7,87	Yolsal and Taymaz (2012)

Table 4.7: Terraces, their age, present elevation and calculated uplift rate. No sea-level.

Location	Terrace	Time (T) [kyr]	Displacement between terraces[m]	Uplift rate (R) ^m _[$\frac{m}{kyr}$]
Moni Chryssos- kalitissa (P34 & H36)	T1 ¹	85 ^a	27	0.31
	T2 ¹	72 ^a	18	0.25
	T3 ¹	48.60 – 58.12 ^a	0.1	0.002-0.001
	T4 ²	1.950 ± 0.08 ^b	0.1	0.05 ± 0.27
	T5 ²	1.950 ± 0.07 ^b	0.1	0.05 ± 0.29
		1.975 ± 0.07 ^b	0.1	0.05 ± 0.29
		1.965 ± 0.07 ^b	0.1	0.05 ± 0.29
	T6 ²	2.210 ± 0.08 ^b	0.2	0.09 ± 0.22
	T7 ²	2.270 ± 0.08 ^b	0.2	0.09 ± 0.20
	T8 ²	2.400 ± 0.07 ^b	0.1	0.04 ± 0.17
		2.625 ± 0.07 ^b	0.1	0.04 ± 0.19
	T9 ²	2.650 ± 0.07 ^b	0.1	0.04 ± 0.15
	T10 ²	2.680 ± 0.07 ^b	0.1	0.04 ± 0.14
		2.900 ± 0.07 ^b	0.1	0.03 ± 0.13
	T11 ²	3.230 ± 0.07 ^b	0.1	0.03 ± 0.14
	T12 ²	3.300 ± 0.08 ^b	0.1	0.03 ± 0.11
	T13 ²	3.400 ± 0.07 ^b	0.2	0.05 ± 0.10
	T14 ²	3.450 ± 0.07 ^b	1.5	0.44 ± 0.13
	T15 ²	3.690 ± 0.07 ^b	0.1	0.02 ± 0.09
	T4 ³	1.980 ± 0.082 ^c	0.1	0.05 ± 0.17
	T5 ³	1.995 ± 0.073 ^c	0.1	0.05 ± 0.14
		2.025 ± 0.073 ^c	0.1	0.05 ± 0.14
		1.985 ± 0.073 ^c	0.1	0.05 ± 0.15
	T6 ³	2.140 ± 0.082 ^c	0.2	0.09 ± 0.14
	T7 ³	2.300 ± 0.082 ^c	0.2	0.09 ± 0.12
	T8 ³	2.655 ± 0.073 ^c	0.2	0.04 ± 0.08
		2.680 ± 0.073 ^c	0.1	0.04 ± 0.07
	T9 ³	2.430 ± 0.073 ^c	0.1	0.04 ± 0.09
	T10 ³	1.995 ± 0.073 ^c	0.1	0.04 ± 0.13
		2.710 ± 0.073 ^c	0.1	0.03 ± 0.07
		2.930 ± 0.073 ^c	0.1	0.03 ± 0.06
	T11 ³	3.430 ± 0.073 ^c	0.2	0.05 ± 0.04
	T12 ³	3.430 ± 0.073 ^c	0.1	0.03 ± 0.04
	T13 ³	3.720 ± 0.073 ^c	0.1	0.03 ± 0.04
	T14 ³	2.025 ± 0.073 ^c	0.1	0.03 ± 0.12
	T15 ³	2.005 ± 0.073 ^c	0.1	0.05 ± 0.12
		3.760 ± 0.073 ^c	0.1	0.02 ± 0.04
		3.330 ± 0.073 ^c	0.1	0.03 ± 0.05
	T16 ³	3.260 ± 0.073 ^c	2.7	0.84 ± 0.04
	T4 ⁴	2.345 ± 0.027 ^d	0.3	0.13 ± 0.03
	T5 ⁴	2.129 ± 0.027 ^d	0.5	0.23 ± 0.02
	T6 ⁴	2.071 ± 0.027 ^d	0.4	0.2 ± 0.02

	T7⁴	2.019 ± 0.027^d	0.5	0.25 ± 0.02
		2.024 ± 0.026^d	0.5	0.25 ± 0.02
	T4⁵	1.595^e	0.1	0.06
	T5⁵	1.870^e	0.1	0.05
	T6⁵	2.250^e	0.1	0.04
	T7⁵	2.000^e	0.1	0.05
	T8⁵	2.280^e	0.2	0.09
	T9⁵	3.000^e	0.1	0.03
	T10⁵	3.050^e	0.1	0.03
	T11⁵	2.390^e	0.2	0.08
	T12⁵	3.300^e	0.1	0.03
	T13⁵	3.870^e	0.1	0.02
	T14⁵	2.830^e	0.1	0.03
	T4⁶	1.452 ± 0.077^f	1.0	0.7 ± 0.63
365 A.D. earthquake	T16²	0.365^b		

¹Wegmann (2008); ²Pirazzoli et al. (1996); ³Price et al. (2002); ⁴Shaw et al. (2010); ⁵Mourtzas (2012);

⁶Pavlopoulos et al. (2012)

^aAges taken from Wegmann (2008).

^bAges taken from Pirazzoli et al. (1996).

^cAges taken from Price et al. (2002).

^dAges taken from Shaw et al. (2010).

^eAges taken from Mourtzas (2012).

^fAges taken from Pavlopoulos et al. (2012).

^gPresent elevation taken from Wegmann (2008).

^hPresent elevation taken from Pirazzoli et al. (1996).

ⁱPresent elevation taken from Price et al. (2002).

^jPresent elevation taken from Shaw et al. (2010).

^kPresent elevation taken from Mourtzas (2012).

^lPresent elevation taken from Pavlopoulos et al. (2012).

^mUplift rate calculated using equation: tectonic change rate = (height change / age)

Table 4.8: Mean uplift rates (*R*) for each author listed in Table 4.4.

Author	Wegmann (2008)	Pirazzoli et al. (1996)	Price et al. (2002)	Shaw et al. (2010)	Mourtzas (2012)	Pavlopoulos et al. (2012)
Mean uplift rate [mm/yr]	0.14	0.07 ± 0.18	0.08 ± 0.09	0.2 ± 0.22	0.04	0.7 ± 0.63

Table 4.9: Displacement between terraces, the corresponding slip, M_0 and M_w .

Terraces	Terrace elevation [m]	Terrace elevation [m]	Displacement between terraces [m]	Corresponding slip along the Hellenic Trench [m] ^a	M_0^b [dyne/cm]	M_w^c
T17 – T16	T17 = 9	T16 = 6.5	2.5	5.56	7.51*10 ²⁷	7.8
T16 – T15	T16 = 6.5	T15 = 6.7	0.2	0.44	5.9*10 ²⁶	7.15
T15 – T14	T15 = 6.7	T14 = 6.8	0.1	0.22	2.97*10 ²⁶	6.94
T14 – T13	T14 = 6.8	T13 = 6.9	0.1	0.22	2.97*10 ²⁶	6.94
T13 – T12	T13 = 6.9	T12 = 7.0	0.1	0.22	2.97*10 ²⁶	6.94
T12 – T11	T12 = 7.0	T11 = 7.1	0.1	0.22	2.97*10 ²⁶	6.94
T11 – T10	T11 = 7.1	T10 = 7.2	0.1	0.22	2.97*10 ²⁶	6.94

T10 – T9	T10 = 7.2	T9 = 7.3	0.1	0.22	2.97*10 ²⁶	6.94
T9 – T8	T9 = 7.3	T8 = 7.5	0.2	0.44	5.9*10 ²⁶	7.15
T8 - T7	T8 = 7.5	T7 = 7.7	0.2	0.44	5.9*10 ²⁶	7.15
T7 – T6	T7 = 7.7	T6 = 7.8	0.1	0.22	2.97*10 ²⁶	6.94
T6 – T5	T6 = 7.8	T5 = 7.9	0.1	0.22	2.97*10 ²⁶	6.94
T5 –T4	T5 = 7.9	T4 = 15	7.1	15.78	2.13*10 ²⁸	8.18
T4 – T3	T4 = 15	T3 = 22	7.0	15.56	2.10*10 ²⁸	8.17
T3 – T2	T3 = 22	T2 = 33	11.0	24.44	3.31*10 ²⁸	8.29
T2 – T1	T2 = 33	T1 = 60	27.0	60.00	8.10*10 ²⁸	8.55

^aCorresponding slip along is measured based on the slip of 20 m which equals a vertical displacement of 9 m

^bSeismic Moment: $M_0 = \mu AD$

^cMoment Magnitude: $M_w = \frac{2}{3} \log M_0 - 10.7$

Table 4.10: Terraces, their age and calculated age, present elevation and sea-level change rate. No tectonics.

Location	Terrace	Time (T) [kyr]	Elevation present E_p [m]	Sea-level change to lower terrace [m] ^e	Sea-level change rate ^f [$\frac{m}{kyr}$]
Moni Chryssos-kalitissa (P34 & H36)	T1 ¹	85 ^a	60 ^c	-27	0.32
	T2 ¹	72 ^a	33 ^c	-18	0.25
	T3 ¹	48.60 – 58.12 ^a	15 ^c	-7.1	0.14 - 0.12
	T4 ²	1.950 ± 0.08 ^b	7.900 ± 0.2 ^d	-0.1	0.05
	T5 ²	1.950 ± 0.07 ^b	7.800 ± 0.3 ^d	-0.1	0.05
		1.975 ± 0.07 ^b	7.800 ± 0.3 ^d	-0.1	0.05
		1.965 ± 0.07 ^b	7.800 ± 0.3 ^d	-0.1	0.05
	T6 ²	2.210 ± 0.08 ^b	7.700 ± 0.2 ^d	-0.1	0.045
	T7 ²	2.270 ± 0.08 ^b	7.500 ± 0.2 ^d	-0.2	0.08
	T8 ²	2.400 ± 0.07 ^b	7.300 ± 0.2 ^d	-0.1	0.04
		2.625 ± 0.07 ^b	7.300 ± 0.3 ^d	-0.1	0.038
	T9 ²	2.650 ± 0.07 ^b	7.200 ± 0.2 ^d	-0.1	0.038
	T10 ²	2.680 ± 0.07 ^b	7.100 ± 0.2 ^d	-0.1	0.038
		2.900 ± 0.07 ^b	7.100 ± 0.2 ^d	-0.1	0.03
	T11 ²	3.230 ± 0.07 ^b	7.000 ± 0.3 ^d	-0.1	0.03
	T12 ²	3.300 ± 0.08 ^b	6.900 ± 0.2 ^d	-0.1	0.03
T13 ²	3.400 ± 0.07 ^b	6.800 ± 0.2 ^d	-0.1	0.029	
T14 ²	3.450 ± 0.07 ^b	6.700 ± 0.3 ^d	-0.2	0.05	
T15 ²	3.690 ± 0.07 ^b	6.500 ± 0.2 ^d	+1.5	0.4	
365 A.D. earthquake	T16 ²	0.365 ^b	8 ^d	-8	21.92
Today shoreline	T17	0	0		

¹Wegmann (2008); ²Pirazzoli et al. (1996); ³Price et al. (2002); ⁴Shaw et al. (2010); ⁵Mourtzas (2012);

⁶Pavlopoulos et al. (2012)

^aAges taken from Wegmann (2008).

^bAges taken from Pirazzoli et al. (1996).

^cPresent elevation taken from Wegmann (2008).

^dPresent elevation taken from Pirazzoli et al. (1996).

^eSea-level fall → -

^fSea-level change rate calculated using equation: $sea\text{-level change rate} = (height\ change / age)$

Table 4.11: Constant uplift rate at Moni-Chryssoskalitissa terrace numbers, elevation heights, and uplift rates (Rohling et al., 2014).

Location	Terrace	Time (T) [kyr]	Elevation present E_p [m]	Elevation original E_o [m]	$E_p - E_o$ [m]	Uplift rate $(R)^n$ [$\frac{m}{kyr}$]	Dated material
Moni Chryssoskalitissa (P34 & H36)	T1 ¹	81	60±1 ^g	-33±6 ^m	93 ±6.08	1.14±0.08	
	T2 ¹	57	33±1 ^g	-60.9±6 ^m	93.9 ±6.08	1.65±0.11	
	T3 ¹	48.60 – 58.12 ^a	15±1 ^g	-69.56±6 ^m	70.8 ±6.08	1.22±0.10 to 1.45±0.13	*1
	T4 ²	1.950 ± 0.08 ^b	7.900 ± 0.2 ^h	0	7.900 ± 0.2 ^h	4.1 ± 0.27	*5
	T5 ²	1.950 ± 0.07 ^b	7.800 ± 0.3 ^h	0	7.800 ± 0.3 ^h	3.9 ± 0.29	*3
		1.975 ± 0.07 ^b	7.800 ± 0.3 ^h	0	7.800 ± 0.3 ^h	3.9 ± 0.29	*3
		1.965 ± 0.07 ^b	7.800 ± 0.3 ^h	0	7.800 ± 0.3 ^h	4.0 ± 0.29	*3
	T6 ²	2.210 ± 0.08 ^b	7.700 ± 0.2 ^h	0	7.700 ± 0.2	3.5 ± 0.22	*3
	T7 ²	2.270 ± 0.08 ^b	7.500 ± 0.2 ^h	0	7.500 ± 0.2	3.3 ± 0.20	*3
	T8 ²	2.400 ± 0.07 ^b	7.300 ± 0.2 ^h	0	7.300 ± 0.2	3.0 ± 0.17	*3
		2.625 ± 0.07 ^b	7.300 ± 0.3 ^h	0	7.300 ± 0.3	2.8 ± 0.19	*3
	T9 ²	2.650 ± 0.07 ^b	7.200 ± 0.2 ^h	0	7.200 ± 0.2	2.7 ± 0.15	*3
	T10 ²	2.680 ± 0.07 ^b	7.100 ± 0.2 ^h	0	7.100 ± 0.2	2.6 ± 0.14	*3
		2.900 ± 0.07 ^b	7.100 ± 0.2 ^h	0	7.100 ± 0.2	2.4 ± 0.13	*3
	T11 ²	3.230 ± 0.07 ^b	7.000 ± 0.3 ^h	0	7.000 ± 0.3	2.2 ± 0.14	*4
T12 ²	3.300 ± 0.08 ^b	6.900 ± 0.2 ^h	0	6.900 ± 0.2	2.1 ± 0.11	*3	
T13 ²	3.400 ± 0.07 ^b	6.800 ± 0.2 ^h	0	6.800 ± 0.2	2.0 ± 0.10	*3	
T14 ²	3.450 ± 0.07 ^b	6.700 ± 0.3 ^h	0	6.700 ± 0.3	1.9 ± 0.13	*3	
T15 ²	3.690 ± 0.07 ^b	6.500 ± 0.2 ^h	0	6.500 ± 0.2	1.8 ± 0.09	*3	
T4 ³	1.980 ±	7.9 ⁱ	0	7.9	4.0 ± 0.17	*5	

		0.082^c					
	T5³	1.995 ± 0.073^c	7.8ⁱ	0	7.8	3.9 ± 0.14	*6
		2.025 ± 0.073^c	7.8ⁱ	0	7.8	3.9 ± 0.14	*6
		1.985 ± 0.073^c	7.8ⁱ	0	7.8	3.9 ± 0.15	*7
	T6³	2.140 ± 0.082^c	7.7ⁱ	0	7.7	3.6 ± 0.14	*7
	T7³	2.300 ± 0.082^c	7.5ⁱ	0	7.5	3.3 ± 0.12	*7
	T8³	2.655 ± 0.073^c	7.3ⁱ	0	7.3	2.7 ± 0.08	*8
		2.680 ± 0.073^c	7.3ⁱ	0	7.3	2.7 ± 0.07	*7
	T9³	2.430 ± 0.073^c	7.2ⁱ	0	7.2	3.0 ± 0.09	*7
	T10³	1.995 ± 0.073^c	7.1ⁱ	0	7.1	3.6 ± 0.13	*9
		2.710 ± 0.073^c	7.1ⁱ	0	7.1	2.6 ± 0.07	*7
		2.930 ± 0.073^c	7.1ⁱ	0	7.1	2.4 ± 0.06	*7
	T11³	3.430 ± 0.073^c	7.0ⁱ	0	7.0	2.0 ± 0.04	*7
	T12³	3.430 ± 0.073^c	6.8ⁱ	0	6.8	2.0 ± 0.04	*7
	T13³	3.720 ± 0.073^c	6.7ⁱ	0	6.7	1.8 ± 0.04	*7
	T14³	2025 ± 0.073^c	6.6ⁱ	0	6.6	3.3 ± 0.12	*9
	T15³	2005 ± 0.073^c	6.5ⁱ	0	6.5	3.2 ± 0.12	*6
		3.760 ± 0.073^c	6.5ⁱ	0	6.5	1.7 ± 0.04	*7
		3.330 ± 0.073^c	6.5ⁱ	0	6.5	2.0 ± 0.05	*7
	T16³	3.260 ± 0.073^c	5.6ⁱ	0	5.6	1.7 ± 0.04	*7
	T4⁴	2.345 ± 0.027^d	6.0^j	0	6.0	2.6 ± 0.03	*10
	T5⁴	2.129 ± 0.027^d	3.3^j	0	3.3	1.6 ± 0.02	*11
	T6⁴	2.071 ± 0.027^d	3.0^j	0	3.0	1.4 ± 0.02	*11
	T7⁴	2.019 ± 0.027^d	2.5^j	0	2.5	1.2 ± 0.02	*11
		2.024 ± 0.026^d	2.5^j	0	2.5	1.2 ± 0.02	*11
	T4⁵	1595^e	7.9^k	0	7.9	5.0	*12
	T5⁵	1870^e	7.5^k	0	7.5	4.0	*12

	T6⁵	2250^e	7.3^k	0	7.3	3.2	*12
	T7⁵	2000^e	7.2^k	0	7.2	3.6	*12
	T8⁵	2280^e	7.1^k	0	7.1	3.1	*12
	T9⁵	3000^e	7.0^k	0	7.0	2.3	*12
	T10⁵	3050^e	6.8^k	0	6.8	2.2	*12
	T11⁵	2390^e	6.7^k	0	6.7	2.0	*12
	T12⁵	3300^e	6.5^k	0	6.5	2.0	*12
	T13⁵	3870^e	6.3^k	0	6.3	1.6	*12
	T14⁵	2830^e	5.6^k	0	5.6	2.0	*12
	T4⁶	1.452 ± 0.077^f	7.900 ± 0.5^l	0	7.9	5.4 ± 0.63	*13
365 A.D. earthquake	T16²	0.365^b	8^h	0	8	21.92	

Bold terraces are dated terraces.

¹Wegmann (2008); ²Pirazzoli et al. (1996); ³Price et al. (2002); ⁴Shaw et al. (2010); ⁵Mourtzas (2012);

⁶Pavlopoulos et al. (2012)

^aAges taken from Wegmann (2008).

^bAges taken from Pirazzoli et al. (1996).

^cAges taken from Price et al. (2002).

^dAges taken from Shaw et al. (2010).

^eAges taken from Mourtzas (2012).

^fAges taken from Pavlopoulos et al. (2012).

^gPresent elevation taken from Wegmann (2008).

^hPresent elevation taken from Pirazzoli et al. (1996).

ⁱPresent elevation taken from Price et al. (2002).

^jPresent elevation taken from Shaw et al. (2010).

^kPresent elevation taken from Mourtzas (2012).

^lPresent elevation taken from Pavlopoulos et al. (2012).

^mSea-level correction done after Rohling et al. (2014).

ⁿUplift rate calculated using equation: $R = (Ep - E0) / T$

*1: Correlation is uncertain, because no inner shoreline angle is preserved, it is a terrace island. Wegmann (2008)

*2: Radiocarbon date ¹⁴C of *Bivalve* by Wegmann (2008).

*3: Radiocarbon date ¹⁴C of *Dendropoma (Novastoa) petraeum* and *calcareous alga* by Pirazzoli et al. (1996). Calculated using a reservoir effect of 320 ± 25 years for the Mediterranean.

*4: Radiocarbon date ¹⁴C of *Dendropoma (Novastoa) petraeum* by Pirazzoli et al. (1996). Calculated using a reservoir effect of 320 ± 25 years for the Mediterranean.

*5: Radiocarbon date ¹⁴C of *Neogoniolithon* and *Dendropoma* by Price et al. (2002). Corrected the original radiocarbon dates (BP) by adding 430 ¹⁴C years to each.

*6: Radiocarbon date ¹⁴C of *Dendropoma* by Price et al. (2002). Corrected the original radiocarbon dates (BP) by adding 430 ¹⁴C years to each.

*7: Radiocarbon date ¹⁴C of *Dendropoma* and *calcareous alga* by Price et al. (2002). Corrected the original radiocarbon dates (BP) by adding 430 ¹⁴C years to each.

*8: Radiocarbon date ¹⁴C of *Dendropoma* and *Melobesies* by Price et al. (2002). Corrected the original radiocarbon dates (BP) by adding 430 ¹⁴C years to each.

*9: Radiocarbon date ¹⁴C of *Serpulorbis* by Price et al. (2002). Corrected the original radiocarbon dates (BP) by adding 430 ¹⁴C years to each.

*10: Radiocarbon date ¹⁴C of *Coral* by Shaw et al. (2010). Corrected the original radiocarbon dates (BP) by 400 ¹⁴C years.

*11: Radiocarbon date ¹⁴C of *Bryozoans* by Shaw et al. (2010). Corrected the original radiocarbon dates (BP) by 400 ¹⁴C years.

*12: Mourtzas (2012).

*13: Radiocarbon date ^{14}C of *notches*, *Neogoniolithon*, and *Dendropoma* by Pavlopoulos et al. (2011).

Table 4.12: Mean uplift rates (R) for each author listed in Table 4.8.

Author	Wegmann (2008)	Pirazzoli et al. (1996)	Price et al. (2002)	Shaw et al. (2010)	Mourtzas (2012)	Pavlopoulos et al. (2012)
Mean uplift rate [m/kyr]	1.36±0.11	2.88 ± 0.18	2.87 ± 0.09	1.6 ± 0.22	2.8	5.4 ± 0.63

Table 4.13: Not constant uplift rate at Moni-Chryssoskalitissa terrace numbers, elevation heights, and uplift rates (Rohling et al., 2014).

Location	Terrace	Time (T) [kyr]	Elevation present E_p [m]	Elevation original E_o [m]	$E_p - E_o$ [m]	Uplift rate (R) ⁿ [$\frac{m}{kyr}$]	Dated material
Moni Chryssoskalitissa (P34 & H36)	T1 ¹	71.8	60±1 ^g	-53.3±6 ^m	113.3 ±6.08	1.58±0.08	
	T2 ¹	57	33±1 ^g	-60.9±6 ^m	93.9 ±6.08	1.65±0.11	
	T3 ¹	48.60 – 58.12 ^a	15±1 ^g	-69.56±6 ^m	70.8 ±6.08	1.22±0.10 to 1.45±0.13	*1
	T4 ²	1.950 ± 0.08 ^b	7.900 ± 0.2 ^h	0	7.900 ± 0.2 ^h	4.1 ± 0.27	*5
	T5 ²	1.950 ± 0.07 ^b	7.800 ± 0.3 ^h	0	7.800 ± 0.3 ^h	3.9 ± 0.29	*3
		1.975 ± 0.07 ^b	7.800 ± 0.3 ^h	0	7.800 ± 0.3 ^h	3.9 ± 0.29	*3
		1.965 ± 0.07 ^b	7.800 ± 0.3 ^h	0	7.800 ± 0.3 ^h	4.0 ± 0.29	*3
	T6 ²	2.210 ± 0.08 ^b	7.700 ± 0.2 ^h	0	7.700 ± 0.2	3.5 ± 0.22	*3
	T7 ²	2.270 ± 0.08 ^b	7.500 ± 0.2 ^h	0	7.500 ± 0.2	3.3 ± 0.20	*3
	T8 ²	2.400 ± 0.07 ^b	7.300 ± 0.2 ^h	0	7.300 ± 0.2	3.0 ± 0.17	*3
		2.625 ± 0.07 ^b	7.300 ± 0.3 ^h	0	7.300 ± 0.3	2.8 ± 0.19	*3
	T9 ²	2.650 ± 0.07 ^b	7.200 ± 0.2 ^h	0	7.200 ± 0.2	2.7 ± 0.15	*3
	T10 ²	2.680 ± 0.07 ^b	7.100 ± 0.2 ^h	0	7.100 ± 0.2	2.6 ± 0.14	*3
	2.900 ± 0.07 ^b	7.100 ± 0.2 ^h	0	7.100 ± 0.2	2.4 ± 0.13	*3	
T11 ²	3.230 ± 0.07 ^b	7.000 ± 0.3 ^h	0	7.000 ± 0.3	2.2 ± 0.14	*4	
T12 ²	3.300 ± 0.08 ^b	6.900 ± 0.2 ^h	0	6.900 ± 0.2	2.1 ± 0.11	*3	
T13 ²	3.400 ±	6.800 ±	0	6.800 ±	2.0 ± 0.10	*3	

		0.07^b	0.2^h		0.2		
	T14²	3.450 ± 0.07^b	6.700 ± 0.3^h	0	6.700 ± 0.3	1.9 ± 0.13	*3
	T15²	3.690 ± 0.07^b	6.500 ± 0.2^h	0	6.500 ± 0.2	1.8 ± 0.09	*3
	T4³	1.980 ± 0.082^c	7.9ⁱ	0	7.9	4.0 ± 0.17	*5
	T5³	1.995 ± 0.073^c	7.8ⁱ	0	7.8	3.9 ± 0.14	*6
		2.025 ± 0.073^c	7.8ⁱ	0	7.8	3.9 ± 0.14	*6
		1.985 ± 0.073^c	7.8ⁱ	0	7.8	3.9 ± 0.15	*7
	T6³	2.140 ± 0.082^c	7.7ⁱ	0	7.7	3.6 ± 0.14	*7
	T7³	2.300 ± 0.082^c	7.5ⁱ	0	7.5	3.3 ± 0.12	*7
	T8³	2.655 ± 0.073^c	7.3ⁱ	0	7.3	2.7 ± 0.08	*8
		2.680 ± 0.073^c	7.3ⁱ	0	7.3	2.7 ± 0.07	*7
	T9³	2.430 ± 0.073^c	7.2ⁱ	0	7.2	3.0 ± 0.09	*7
	T10³	1.995 ± 0.073^c	7.1ⁱ	0	7.1	3.6 ± 0.13	*9
		2.710 ± 0.073^c	7.1ⁱ	0	7.1	2.6 ± 0.07	*7
		2.930 ± 0.073^c	7.1ⁱ	0	7.1	2.4 ± 0.06	*7
	T11³	3.430 ± 0.073^c	7.0ⁱ	0	7.0	2.0 ± 0.04	*7
	T12³	3.430 ± 0.073^c	6.8ⁱ	0	6.8	2.0 ± 0.04	*7
	T13³	3.720 ± 0.073^c	6.7ⁱ	0	6.7	1.8 ± 0.04	*7
	T14³	2025 ± 0.073^c	6.6ⁱ	0	6.6	3.3 ± 0.12	*9
	T15³	2005 ± 0.073^c	6.5ⁱ	0	6.5	3.2 ± 0.12	*6
		3.760 ± 0.073^c	6.5ⁱ	0	6.5	1.7 ± 0.04	*7
		3.330 ± 0.073^c	6.5ⁱ	0	6.5	2.0 ± 0.05	*7
	T16³	3.260 ± 0.073^c	5.6ⁱ	0	5.6	1.7 ± 0.04	*7
	T4⁴	2.345 ± 0.027^d	6.0^j	0	6.0	2.6 ± 0.03	*10
	T5⁴	2.129 ± 0.027^d	3.3^j	0	3.3	1.6 ± 0.02	*11
	T6⁴	2.071 ± 0.027^d	3.0^j	0	3.0	1.4 ± 0.02	*11

	T7⁴	2.019 ± 0.027^d	2.5^j	0	2.5	1.2 ± 0.02	*11
		2.024 ± 0.026^d	2.5^j	0	2.5	1.2 ± 0.02	*11
	T4⁵	1595^e	7.9^k	0	7.9	5.0	*12
	T5⁵	1870^e	7.5^k	0	7.5	4.0	*12
	T6⁵	2250^e	7.3^k	0	7.3	3.2	*12
	T7⁵	2000^e	7.2^k	0	7.2	3.6	*12
	T8⁵	2280^e	7.1^k	0	7.1	3.1	*12
	T9⁵	3000^e	7.0^k	0	7.0	2.3	*12
	T10⁵	3050^e	6.8^k	0	6.8	2.2	*12
	T11⁵	2390^e	6.7^k	0	6.7	2.0	*12
	T12⁵	3300^e	6.5^k	0	6.5	2.0	*12
	T13⁵	3870^e	6.3^k	0	6.3	1.6	*12
	T14⁵	2830^e	5.6^k	0	5.6	2.0	*12
	T4⁶	1.452 ± 0.077^f	7.900 ± 0.5^l	0	7.9	5.4 ± 0.63	*13
365 A.D. earthquake	T16²	0.365^b	8^h	0	8	21.92	

Bold terraces are dated terraces.

¹Wegmann (2008); ²Pirazzoli et al. (1996); ³Price et al. (2002); ⁴Shaw et al. (2010); ⁵Mourtzas (2012);

⁶Pavlopoulos et al. (2012)

^aAges taken from Wegmann (2008).

^bAges taken from Pirazzoli et al. (1996).

^cAges taken from Price et al. (2002).

^dAges taken from Shaw et al. (2010).

^eAges taken from Mourtzas (2012).

^fAges taken from Pavlopoulos et al. (2012).

^gPresent elevation taken from Wegmann (2008).

^hPresent elevation taken from Pirazzoli et al. (1996).

ⁱPresent elevation taken from Price et al. (2002).

^jPresent elevation taken from Shaw et al. (2010).

^kPresent elevation taken from Mourtzas (2012).

^lPresent elevation taken from Pavlopoulos et al. (2012).

^mSea-level correction done after Rohling et al. (2014).

ⁿUplift rate calculated using equation: $R = (Ep - E0) / T$

*1: Correlation is uncertain, because no inner shoreline angle is preserved, it is a terrace island. Wegmann (2008)

*2: Radiocarbon date ¹⁴C of *Bivalve* by Wegmann (2008).

*3: Radiocarbon date ¹⁴C of *Dendropoma (Novastoa) petraeum* and *calcareous alga* by Pirazzoli et al. (1996). Calculated using a reservoir effect of 320 ± 25 years for the Mediterranean.

*4: Radiocarbon date ¹⁴C of *Dendropoma (Novastoa) petraeum* by Pirazzoli et al. (1996). Calculated using a reservoir effect of 320 ± 25 years for the Mediterranean.

*5: Radiocarbon date ¹⁴C of *Neogoniolithon* and *Dendropoma* by Price et al. (2002). Corrected the original radiocarbon dates (BP) by adding 430 ¹⁴C years to each.

*6: Radiocarbon date ¹⁴C of *Dendropoma* by Price et al. (2002). Corrected the original radiocarbon dates (BP) by adding 430 ¹⁴C years to each.

*7: Radiocarbon date ¹⁴C of *Dendropoma* and *calcareous alga* by Price et al. (2002). Corrected the original radiocarbon dates (BP) by adding 430 ¹⁴C years to each.

*8: Radiocarbon date ¹⁴C of *Dendropoma* and *Melobesiees* by Price et al. (2002). Corrected the original radiocarbon dates (BP) by adding 430 ¹⁴C years to each.

*9: Radiocarbon date ^{14}C of *Serpulorbis* by Price et al. (2002). Corrected the original radiocarbon dates (BP) by adding 430 ^{14}C years to each.

*10: Radiocarbon date ^{14}C of *Coral* by Shaw et al. (2010). Corrected the original radiocarbon dates (BP) by 400 ^{14}C years.

*11: Radiocarbon date ^{14}C of *Bryozoans* by Shaw et al. (2010). Corrected the original radiocarbon dates (BP) by 400 ^{14}C years.

*12: Mourtzas (2012).

*13: Radiocarbon date ^{14}C of *notches, Neogoniolithon, and Dendropoma* by Pavlopoulos et al. (2011).

Table 4.14: Mean uplift rates (R) for each author listed in Table 4.8.

Author	Wegmann (2008)	Pirazzoli et al. (1996)	Price et al. (2002)	Shaw et al. (2010)	Mourtzas (2012)	Pavlopoulos et al. (2012)
Mean uplift rate [m/kyr]	1.47±0.11	2.88 ± 0.18	2.87 ± 0.09	1.6 ± 0.22	2.8	5.4 ± 0.63

Table 4.15: Average uplift rate, slip rate, recurrence time for the 21st July 365 A.D. earthquake.

Earthquake 21 st July 365 A.D.	Mw	Time interval [kyr]	Average uplift rate [mm/yr]	Slip rate [mm/yr]	Recurrence time [yr]
Moni Chryssoskalitissa Tectonic only	8.25 ¹	85 ² until today	2.67	5.34	3745.32
Moni Chryssoskalitissa Constant/Not Constant ³	8.25 ¹	72 ² until today	2.23 ± 0.25	4.7 ± 0.50	4255.50

¹ Shaw et al. (2008); ²Wegmann (2008); ³Rohling et al. (2014)

Table 4.16: Average uplift rate, slip rate, recurrence time for 21st July 365 earthquake, and total slip for highest and oldest terrace. All values are sea-level corrected after Rohling et al. (2014).

Earthquake 21 st July 365 A.D.	Mw	Time interval [kyr]	Average uplift rate [mm/yr]	Slip rate [mm/yr]	Recurrence time [yr]
Aradena Gorge ^{1,4,5} Constant	8.25	107 ² until today	1.37±0.08	2.74±0.16	7299.27
Sougia ^{1,2,3,4} Constant	8.25	107 ² until today	2.26±0.16	4.52±0.32	4424.78
Kalamia ⁷ Constant	8.25	39.19 ² until today	4.24±0.21	8.48±0.42	2358.49
Moni ^{1,2,3,4,5,6} Chryssoskalitissas: Constant/Not Constant	8.25	72 until today	2.23 ± 0.25	4.7 ± 0.50	4255.5
Cape Koutoulas ^{1,2,3,4} Constant	8.25	50 until today	3.27±0.16	6.54±0.32	3058.10
Phalasarna ^{1,6} Constant	8.25	72 until today	1.93±0.17	3.86±0.32	5181.35

¹Wegmann (2008); ²Pirazzoli et al. (1996); ³Price et al. (2002); ⁴Shaw et al. (2010); ⁵Mourtzas (2012); ⁶Pavlopoulos et al. (2012); ⁷Tiberti et al. (2014)

Table 4.17: Influence on uplift rates based on the choice of the sea-level curve.

Location	Mean uplift rate [mm/yr] ^a	Mean uplift rate [mm/yr] ^b	Difference between uplift rates [mm/yr]
Ierapetra (constant)	0.21	0.27 ± 0.04	0.06
Ierapetra (not constant)	0.09	0.17±0.03	0.08
Aradena Gorge	1.24	1.37 ± 0.08	0.13
Sougia	2.21 ± 0.23	2.26 ± 0.16	0.05
Kalamia	4.24	4.24 ± 0.21	0
Moni Chryssoslalitissa (constant)	2.74 ± 0.28	2.85 ± 0.24	0.11
Moni Chryssoslalitissa (not constant)	2.76 ± 0.28	2.86 ± 0.25	0.10
Cape Koutoulas	3.23 ± 0.19	3.27 ± 0.16	0.04
Phalasarna	1.62 ± 0.38	1.93 ± 0.17	0.31

^aBased on sea-level curves by Lambeck and Chappell (2001), and for Ierapetra the additional sea-level curve by Sosoian and Rosenthal (2009).

^bBased on sea-level curve by Rohling et al. (2014).

Chapter 5

SYNTHESIS OF NEOGENE GEOLOGICAL STRUCTURES AND SEDIMENTOLOGICAL DATA ACROSS CRETE AND IMPLICATIONS FOR THE LONG-TERM VERTICAL SURFACE-DEFORMATION PATTERN OF CRETE

5.1 Abstract

The objective of this work was to examine the vertical deformation and uplift history of Crete on the Ma time-scale. Sedimentary basins represent a geological archive of the timing of tectonic processes. I calculated uplift rates derived from Neogene sedimentary rocks by their depositional depth, age, and present outcrop elevation. Results show a heterogeneously pattern of vertical uplift motion on the Ma time-scale. This indicates that tectonic processes on Crete were not only dominated by the Hellenic subduction zone, but also by the activity of upper-crustal normal faults.

5.2 Introduction

Determination of long-term vertical surface-deformation is helpful to assess vertical surface motion of continental crust above subduction lithosphere.

Analysis of the depositional depth and age constrains of Neogene sedimentary rocks on Crete provide information about vertical surface-deformation on the Ma time-scale (Meulenkamp et al., 1988; Hinsbergen et al., 2006; Zachariasse et al., 2008).

Further the analysis of sedimentation can be used for estimating the activation of fault systems, and therefore provide information about the regional and local stress field in this area.

In this chapter, I aim to calculate the uplift rates of sedimentary rocks on the Ma time-scale. For the calculation data of the depositional depth and age constrains of Neogene sedimentary rocks van Hinsbergen and Meulenkamp (2006) were used. I estimated the height of the outcrop at present-time, and calculated the corresponding uplift rates. I was able to estimate the uplift rates for the coast of Crete starting in Middle Miocene (~12 Ma) until late Pliocene (3 Ma).

5.3 Neogene Structures and Sediments

Crete is characterized by a horst and graben structure, where horsts are of pre-Neogene age and grabens are filled with Neogene and recent sediments (Figure 5.1 & Figure 5.2) (Hall et al., 1984; van Hinsbergen and Meulenkamp, 2006). Neogene sediments range from Middle Miocene to Holocene (van Hinsbergen and Meulenkamp, 2006; Papanikolaou and Vassilakis., 2010). The syn-tectonic sediments are lacustrine-continental sediments from Middle Miocene (17 to 12 Ma), the marine sediments are from Late Miocene to Early Pleistocene (12 to 2 Ma), and the continental sediments are deposited since the Holocene (2 Ma) (Papanikolaou and Vassilakis., 2010).

In Middle to early Late Miocene time, the Aegean crust was affected by slab rollback by of the subducting plate (van Hinsbergen and Meulenkamp, 2006; Seidel et al., 2007). This led to exhumation of metamorphic core complexes on Crete along the Cretan detachment (van Hinsbergen and Meulenkamp, 2006).

The oldest sediments in these E-W trending basins/half-grabens consists of, which were derived from the non-metamorphic hanging wall of the Cretan detachment during Middle Miocene (Figure 5.3), the footwall was not yet exposed to erosion (van Hinsbergen and Meulenkamp, 2006; Seidel et al., 2007).

In Middle to Late Miocene time (Serravallian - Tortonian boundary), the hanging wall of the Cretan detachment was extended, which resulted in deposition of large olistoliths in central and eastern Crete (van Hinsbergen and Meulenkamp, 2006). Simultaneously, the active detachment shifted northward in western Crete, leading into the break-up of the hanging wall into extensional klippen (van Hinsbergen and Meulenkamp, 2006). Due to the flexural response caused by the removal of the hanging wall, W-Crete experienced uplift (van Hinsbergen and Meulenkamp, 2006). Therefore, clasts from the high pressure - low temperature (HP-LT) metamorphic tectonic lower unit are found in Tortonian sediments (Seidel et al., 2007). At the end of the Serravallian (Figure 5.4) to the Early Tortonian, the Aegean landmass fragmented and Crete lost its connection to the European mainland, which is based on reports of mammal faunas (Drogger and Meulenkamp, 1973; van Hinsbergen and Meulenkamp, 2006). In the Early Tortonian (Figure 5.5) (ca. 11 Ma), 100-130°-trending normal faults controlled asymmetric half-grabens that reflected continued N-S extension associated with a southward trench retreat (tenVenn and Kleinspehn, 2003). About 1 Ma later, a Tortonian (Figure 5.6) fault system trending 020° fragmented the existing half-grabens into orthogonal horst and graben structures with both arc-parallel and arc-normal fault systems (tenVenn and Kleinspehn, 2003). Van Hinsbergen and Meulenkamp (2006) propose that due to the northward shift of the detachment fault the stress regime on Crete changed from formerly N-S to E-W, due to the curvature of the Aegean arc. At the Tortonian-Messinian boundary (Figure 5.7), strong uplift along 100° fault zones developed roughly E-W striking topographical highs (e.g. Central Iraklion Ridge) and adjacent deep-marine basins (tenVenn and Kleinspehn, 2003). At the beginning of the Messinian (Figure 5.8), depositional conditions were relatively uniform in the Neogene basins (van Hinsbergen and Meulenkamp, 2006; Zachariasse et al., 2008). Starting in late Early Pliocene (Figure 5.9) (4.4 Ma) shallow-marine sequences along the N and S coasts of Crete suggest an overall emergence and northward tilting of the island (tenVenn and Kleinspehn, 2003), due to the possible collision of Crete with the African promontory (ten Veen and Kleinspehn, 2003; van Hinsbergen and Meulenkamp, 2006). In late Pliocene (~2-4 Ma) (Figure 5.10) the stress conditions on Crete changed from N-S to E-W extension due to onset of the collision of Aegean with the northern margin of Africa based on fault analysis (Angelier, 1979; Armijo et al., 1992). This change in the extensional regime led to two generations of normal faults. The first generation of normal faults trends E-W and was generated during the N-S extension (Angelier, 1979; Armijo et al., 1992). The second generation of N-S trending normal faults was generated by the E-W extension (Angelier, 1979; Armijo et al., 1992).

Meulenkamp (1979) subdivided the Neogene sediments into six groups.

The Prina Group forms the base of the Neogene sediments, and consists of limestone breccias and breccio-conglomerates (van Hinsbergen and Meulenkamp, 2006). It was deposited in a non-marine brackish or shallow marine environment (Fassoulas, 2001) during Serravallian-Tortonian (van Hinsbergen and Meulenkamp, 2006). The Tefelion Group comprises poorly consolidated marine and fluvio-lacustrine conglomerate, sand, silt and clay (van Hinsbergen and Meulenkamp, 2006). During Tortonian the Tefelion Group was deposited in fresh-water, brackish

and marine environment (Fassoulas, 2001; van Hinsbergen and Meulenkamp, 2006). The Vrysses Group consists of marine bioclastic or reefal limestones or alternating laminated and homogenous marls, in some areas containing evaporates intercalations (van Hinsbergen and Meulenkamp, 2006). The Vrysses Group represents marine sediments of late Tortonian to Messinian (Fassoulas, 2001; van Hinsbergen and Meulenkamp, 2006). The Hellenikon Group comprises red, terrestrial conglomerates and lacustrine, fluvial and lagoonal sands and clays with thin evaporates locally (van Hinsbergen and Meulenkamp, 2006). This Group was deposited during the Messinian salinity crisis (Meulenkamp, 1979). The Finikia Group consists of open marine marls and diatomites deposited during early Pliocene (Fassoulas, 2001; van Hinsbergen and Meulenkamp, 2006). The Aghia Galini Group comprises reddish, terrestrial conglomerates and fluvio-deltaic sands and clays deposited during the Upper Plio-Pleistocene (Fassoulas, 2001; van Hinsbergen and Meulenkamp, 2006).

5.4 Methods

I calculated uplift rates using the estimates of the depositional depth and age of Neogene sediments (Table: Appendix - Chapter 5) of van Hinsbergen and Meulenkamp (2006). Today's height of the outcrop was estimated by topographic mapping.

The depositional depth of sediments is derived from van Hinsbergen and Meulenkamp (2006). The depositional depth was estimated by the general relationship between the depth and the percentage of planktonic foraminifera (%P) to the total (planktonic and benthic) foraminiferal population (van Hinsbergen et al., 2005 (b)). Benthic foraminifera are most frequent on the outer shelf and the continental edge, whereas the planktonic foraminifera are nearly absent in shallow water and increase with water depth (van Hinsbergen et al., 2005 (b); van der Zwaan et al., 1990). Therefore, the planktonic percentage (%P) is related to the water depth and increases with distance to the shore and reaches nearly 100% in lower bathyal and abyssal regions (van Hinsbergen et al., 2005 (b)). But %P is also related to the oxygen level of bottom waters, which can vary under the influence of astronomically induced climate variations on the order of 100 and 400 kyr (van Hinsbergen et al., 2005 (b)). This is reflected by benthic foraminiferal species indicating oxygen stress, and therefore, the values are corrected for the percentage of stress markers with respect to the total benthic foraminiferal population (van Hinsbergen et al., 2005 (b); van der Zwaan et al., 1990). Further corrections were done for redeposition and downslope transport, recognizable by the mixed associations from shallower and deeper parts, and by sampling the fractions of rock fragments (van Hinsbergen and Meulenkamp, 2006). All results are listed in Table 3.2.

I used the location (Figure 5.11) of the Neogene stratigraphic outcrops by georeferencing the map of van Hinsbergen and Meulenkamp (2006) (Figure 2 in their paper) in the Geographical Information System (GIS) software ArcGIS. I estimated the mean elevation-variation of the outcrops using the contour lines derived by the DEM. I calculate the total height by adding my estimates of the mean elevation to the depth. The age range is given by van Hinsbergen and Meulenkamp (2006). The uplift rate (R) is calculated by:

$$R = \frac{\text{total height [km]}}{\text{Age [Ma]}} \quad (5.1)$$

All values for the outcrops (Figure 5.11) are listed in Table: Appendix - Chapter 5.

There are several uncertainties in my uplift rate estimation.

The method for estimating the paleo-depth of sediments is accurate for water depths between 50 and 1100 m (van Hinsbergen and Meulenkamp, 2006), with error bars of the 95% confidence

limit at about 50 m at shallow depths, and increasing to 100 - 150 m at about 1100 m (van Hinsbergen et al., 2005; van der Zwaan et al., 1990). I correlated these age ranges to time ranges in Ma years listed in Table 5.1.

Further, today's height of the outcrops depends strongly on the resolution of the DEM, which has a horizontal-resolution of 20 m and vertical-resolution of 15 ± 5 m.

5.5 Results

Calculation results for the uplift rates based on Neogene sediments, from Middle Miocene to late Pliocene, are listed in Table: Appendix - Chapter 5.

Further, I calculated coastal uplift rates for the NW-, and SW-Crete, for N-Central Crete, and for NE-, and SE-Crete listed in table 5.2. For S-Central Crete no data are available.

Since Middle Miocene until Tortonian NW-Crete (Figure 5.12 & Figure 5.13) was above sea-level. Starting in Late Tortonian/Early Messinian until Early Pliocene NW-Crete was below sea-level, and was uplifting in Late Pleistocene. SW-Crete (Figure 5.12 & Figure 5.13) was above sea-level in Middle Miocene, and subsided in Late Serravalian below sea-level. Since Early Tortonian, this region was above sea-level. N-Central Crete was from Middle Miocene until Late Tortonian/Early Messinian above sea-level, experienced subsidence from Messinian until Late Pliocene (Figure 5.12 & Figure 5.13). S-Central Crete was above sea-level from Middle Miocene until Late Serravalian (Figure 5.12 & Figure 5.13). In Early Tortonian this region was below sea-level, and uplifted above the sea-level since Tortonian until the Late Tortonian/Early Messinian. In the Messinian this part of the coastline was below sea-level until the Early Pliocene. In Late Pliocene this regions was above the sea-level. Since Middle Miocene until Tortonian the NE-coastline was above sea-level, and from Late Trotonian/Early Messinian until Early Pliocene this region was below sea-level. In late Pliocene the region experienced uplift above the sea-level (Figure 5.12 & Figure 5.13). SE-Crete was above sea-level from Middle Miocene until Late Serravalian (Figure 5.12 & Figure 5.13). Since Early Tortonian until the Early Pliocene this region was below sea-level. In Late Pliocene this region was located above sea-level.

5.6 Discussion

I used Neogene sediments for analyzing the vertical surface-motion of Crete for the last 16 to 2.58 Ma years. The uplift history of Crete starting in Middle Miocene shows that different parts of the island were below sea-level or above sea-level at different times (Figure 5.12 and Table 5.2).

The different uplift rates (Table 5.2) show that the strongest uplift occurred in eastern Crete, followed by the northwestern Crete. I further calculate the mean uplift rate from 16 Ma until 2.58 Ma using all uplift rates of the individual outcrops, with $R = 0.13 \pm 0.03$ km/Ma. These values seem to be very slow, compared to the PSI measurements of up to 5 mm/yr of uplift or subsidence (Chapter 2). Calculations based on Neogene sediments are not very precise, because of the large error range in the mean height of the outcrop today, of up to ± 260 m (Appendix, Chapter 5, Table II.33). There are no GPS coordinates available for the outcrops (Van Hinsbergen, personal communication). Further, the age constrains have a precision on the Ma-scale (Appendix, Chapter 5, Table II.33).

The analysis of Neogene sedimentary rocks showed that the depositional history was heterogeneous over this time range, based on the different appearances in timing and places of the Neogene sedimentary rocks. This differential pattern of the appearances of Neogene sediments can be caused by differential surface-deformation or by different erosion patterns over time

Analysis of different uplift-rates for the geological time-scale may imply that the long-term vertical surface-motion of Crete is related to regional tectonics. The slab roll back of the subducting African lithospheric plate (Royden et al., 1993) led to N-S extension of the Aegean microplate, and the exhumation of metamorphic core-complexes along an E-W detachment fault on Crete (van Hinsbergen and Meulenkamp, 2006). The stress field changed from N-S extension to E-W extension probably due to the incipient continent-continent collision of the African continental lithosphere with the Aegean continental lithosphere in Pliocene (Armijo et al., 1992, ten Veen et al., 2003). Due to the regional tectonic pattern the local tectonic setting of Crete was affected and experienced segmentation in its characteristic horst and graben structure (Armijo et al., 1992). These led to local deposition of sediments, along the bounding normal faults of the horst and graben structures.

The heterogeneous uplift pattern on Crete may imply that the vertical deformation on Crete is not fully related to the Hellenic subduction zone interface, but is also controlled by upper-normal faults. If the Hellenic subduction zone would be the controlling tectonic process I would expect a more homogeneous vertical surface motion across the whole island.

5.7 Conclusions

This chapter presents the vertical deformation rate history on Crete for the last 16 to 2.58 Ma years. The mean uplift rate is based on depositional depth and age constraints of Neogene sediments by van Hinsbergen and Meulenkamp (2006). I calculated a mean uplift rate of $R = 0.127 \pm 0.026$ km/Ma. The eastern part shows larger uplift than the rest of the island.

The overall pattern of vertical surface-deformation on the geological time-scale is not uniform, but rather heterogeneously distributed. This may imply that the vertical surface-deformation is not controlled by one major tectonic process, but by a combination of tectonic processes along the Hellenic subduction zone, and upper-crustal normal faults. Due to the slab rollback of the Hellenic subduction zone and the starting incipient continent-continent collision, the island of Crete is segmented into its characteristic horst and graben structure. Sedimentary basins record these processes regional and local processes.

References

- Angelier J. (1978): Tectonic Evolution of the Hellenic Arc since the Late Miocene. *Tectonophysics*. Vol. 49. Pages: 23-36. DOI: 10.1016/0040-1951(78)90096-3.
- Angelier J. (1979): Neotectonique de l'arc Eggen. These d'etat. University de Paris VI, 405 pp.
- Armijo R., Lyon-Caen H., Papanastassiou D. (1992): East-west extension and Holocene normal-fault scarps in the Hellenic arc. *Geology*. Vol. 20. Pages: 491-494. DOI: 10.1130/0091-7619(1992)020<0491:EWEAHN>2.3.CO;2.
- Bohnhoff M., Makris J., Papanikolaou D., and Stavrakakis G. (2001): Crustal investigation of the Hellenic subduction zone using wide aperture seismic data. *Tectonophysics*. Vol. 343. Pages: 239-262. DOI: 10.1016/S0040-1951(01)00264-5.
- Bohnhoff M., Harjes H.-P., Meier T. (2005): Deformation and stress regimes in the Hellenic subduction zone from focal Mechanisms. *Journal of Seismology*. Vol. 9. Pages: 341-366. DOI: 10.1007/s10950-005-8720-5.
- Bonneau M. (1984): Correlation of the Hellenic Nappes in the south-east Aegean and their tectonic reconstruction. In Dixon J.E. and Robertson A.H.F (eds): *The geological evolution of the Eastern Mediterranean: Geological Society of London Special Publication 17*. Pages: 517-527.
- Chamot-Rooke N., Rangin C., Le Pichon X. (2005): DOTMED – Deep Offshore Tectonics of the Mediterranean: A synthesis of deep marine data in Eastern Mediterranean, The Ionian basin and margins, the Calacria wedge and the Mediterranean ridge. *Société Géologique de France*. Paris. Pages: 64.
- Creutzburg N., and Seidel E. (1975): Zum Stand der Geologie des Präneogens auf Kreta. *Neues Jahrbuch für Geologie und Paläontologie. Abhandlungen*. 141. Pages: 259-285.
- Dewey, J.F. and Sengor, A.M.C., 1979. Aegean and surrounding regions: complex multiplate and continuum tectonics in a convergent zone. *Geol. Soc. Amer. Bull.* Vol. 90. No. 1. Pages: 84-92. DOI: 10.1130/0016-7606(1979)90<84:AASRCM>2.0.CO;2.
- Drooger C.W., Meulenkamp J.E. (1973): Stratigraphic contributions to geodynamics in the Mediterranean area: Crete as a case history. *Bull. Geol. Soc. Greece*. Vol. 10. Pages: 193-200.
- Endrun B., Meier T., Bischoff M., and Harjes H.-P. (2004): Lithospheric structure in the area of Crete constrained by receiver functions and dispersion analysis of Rayleigh phase velocities. *Geophysical Journal International*. Vol. 158. Pages 592-608. DOI: 10.1111/j.1365-246X.2004.02332.x.
- Fassoulas C., Kiliass A., Mountrakis D. (1994): Postnappe stacking extension and exhumation of high-pressure/low-temperature rocks in the island of Crete, Greece. *Tectonics*. Vol. 13. Iss. 1. Pages: 127-138. DOI: 10.1029/93TC01955.
- Fassoulas C. (2001): The tectonic development of a Neogene basin at the leading edge of the active European margin: the Heraklion basin, Crete, Greece. *J. Geodyn*, Vol. 31. Pages: 49-70. DOI: 10.1016/S0264-3707(00)00017-X.
- Hafkenschied E., Wortel M.J.R., and Spakman W. (2006): Subduction history of the Tethyan region derived from seismic tomography and tectonic reconstructions. *Journal of Geophysical Research*. Vol. 111. B08401. DOI: 10.1029/2005JB003791.

- Hall R., Audley-Charles M.G., and Cater D.J. (1984): The significance of Crete for the evolution of the Eastern Mediterranean. In Dixon J.E., and Robertson A.H.F. (eds): The geological evolution of the Eastern Mediterranean: Geological Society of London Special Publication 17. Pages: 449-516.
- Hinsbergen van D.J.J, Hafkenscheid E., Spakman W., Meulenkamp J.E. and Wortel R. (2005a): Nappe stacking resulting from subduction of oceanic and continental lithosphere below Greece. *Geology*. Vol. 33. Pages: 325-328. DOI: 10.1130/G20878.1.
- Hinsbergen van D.J.J, Kouwenhoven T.J., van der Zwaan G.J.: (2005 (b)): Paleobathymetry in the backstripping procedure: Correction for oxygenation effects on depth estimates. *Palaeogeography, Palaeoclimatology, Palaeoecology*. Vol. 221. Iss. 3-4. Pages: 245-265. DOI: 10.1016/j.palaeo.2005.02.013.
- Hinsbergen van D.J.J., and Meulenkamp J.E. (2006): Neogene supradetachment basin development on Crete (Greece) during exhumation of the South Aegean core complex. *Basin Research*. Vol 18. Pages: 103-124. DOI: 10.1111/j.1365-2117.2005.00282.x.
- Jacobshagen, V.H. (1986): *Geologie von Griechenland*. Beiträge zur regionalen Geologie der Erde 19, Berlin.
- Jolivet L., Goffé B., Monié P., Truffert-Luxey C., Patriat M., Bonneau M. (1996): Miocene detachment in Crete and exhumation P-T-t paths of high-pressure metamorphic rocks. *Tectonics*. Vol. 15. No. 6. Pages: 1129-1153. DOI: 10.1029/96TC01417.
- Jolivet L., Faccenna C., Goffé B. Burov E., and Agard P. (2003): Subduction tectonics and exhumation of high-pressure metamorphic rocks in the Mediterranean orogens. *American Journal of Science*. Vol. 303. Pages: 353-409. DOI: 10.2475/ajs.303.5.353.
- Kopf A., Mascle J., and Klaeschen D. (2003): The Mediterranean Ridge: A mass balance across the fastest growing accretionary complex on Earth. *Journal of Geophysical Research*. Vol. 108. No. B8. DOI: 10.1029/2001JB000473.
- Le Pichon X., Angelier J. (1979): The Hellenic Arc and Trench System: A Key to the Neotectonic Evolution of the Eastern Mediterranean Area. *Tectonophysics*. Vol. 60. Pages: 1-42. DOI: 10.1016/0040-1951(79)90131-8.
- Le Pichon X., Chamot-Rooke N., Lallemand S., Noomen R., Veis G. (1995): Geodetic determination of the kinematics of central Greece with respect to Europe: Implications for Eastern Mediterranean tectonics. *Journal of Geophysical Research*. Vol. 100. Iss. B7. Pages: 12675-12690. DOI: 10.1029/95JB00317.
- Lyon-Caen H., Armijo R., Drakopoulos J., Baskoutass J., Delibassis N., Gaulon R., Kouskouna V., Latoussakis J., Markopoulos K., Papadimitriou P., Papanastassiou D., Pedotti G. (1988): The 1986 Kalamata (South-Peloponnesus) Earthquake - Detailed study of a normal-fault, evidences for East-West extension in the Hellenic Arc. *Journal of Geophysical Research*. Vol. 93. Pages: 14967-15000. DOI: 10.1029/JB093iB12p14967.
- Mascle, J., Huguen C., Benkhelil J., Chamot-Rooke N., Chaumillon E., Griboulard R., Kopf A., Lamarche G., Volkonskaia J., Woodside J., Zitter T. (1999): Images may show start of European-African plate collision. *Eos Trans. AGU*. 80(37). 421. DOI: 10.1029/99EO00308.

- McKenzie D. (1972): Active Tectonics of the Mediterranean Region. *Geophysical Journal of the Royal Astronomical Society*. Vol. 30. Iss. 2. Pages: 109-185. DOI: 10.1111/j.1365-246X.1972.tb02351.x.
- Meier T., Rische M., Endrun B., Vafidis A., and Harjes H.-P. (2004): Seismicity of the Hellenic subduction zone in the area of western and central Crete observed by temporary local seismic networks. *Tectonophysics*. Vol. 383. Pages: 149-169. DOI: 10.1016/j.tecto.2004.02.004.
- Meier T., Becker D., Endrun B., Rische M., Bohnhoff M., Stöckhert B., and Harjes H.-P. (2007): A model for the Hellenic subduction zone in the area of Crete based on seismological investigations. *Geological Society, London, Special Publications*. Vol. 291. Pages: 183-199. DOI: 10.1144/SP291.9.
- Meulenkamp J.E. (1979): Filed guide to the Neogene of Crete. *Publ. Dep. Geol. Pal. Univ. Athens*. 32. 32.
- Meulenkamp J.E., Wortel M.J.R., Wamel van W.A., Spakman W., and Hoogerduyn Strating E. (1988): On the Hellenic subduction zone and the geodynamic evolution of Crete since the late Middle Miocene. *Tectonophysics*. Vol. 146. Iss. 1-4. Pages: 203-215. DOI: 10.1016/0040-1951(88)90091-1.
- Papanikolaou D., Vassilakis E. (2010): Middle Miocene E-W Tectonic Horst Structure of Crete through Extensional Detachment Faults. *Tectonophysics*. Vol. 488, Iss. 1-4, 5. Pages: 233-247. DOI: 10.1088/1755-1307/2/1/012003.
- Papazachos, B.C., Comninakis, P.E., Karakaisis, G.F., Karakostas, B.G., Papaioannou, Ch.A., Papazachos, C.B., Scordilis E.M. (2000): A catalogue of earthquakes in Greece and surrounding area for the period 550BC-1999. *Publ. Geophys. Lab., Univ. of Thessaloniki*. 1. 333pp.
- Ricou L.E., Burg J.P., Godfriaux I., Ivanov Z. (1998): Rhodope and Vardar: the metamorphic and the olistostromic paired belts related to the Cretaceous subduction under Europe. *Geodynamic Acta*. Vol. 11. Pages: 285-309. DOI: 10.1016/S0985-3111(99)80018-7.
- Royden L.H. (1993): The Tectonic Expression Slab Pull At Continental Convergent Boundaries. *Tectonics*. Vol. 12. No. 2. Pages: 303-325. DOI: 10.1029/92TC02248.
- Seidel E., Okrusch M., Kreuzer H., Raschka H., and Harre W. (1981): Eo-alpine metamorphism in the uppermost unit of the Cretan nappe system. *Petrology and geochronology. Part 2. Synopsis of high-temperature metamorphic and associated ophiolites: Contributions to Mineralogy and Petrology*. Vol. 76. Pages: 351-361.
- Seidel M., Seidel E., Stöckhert B. (2007): Tectono-sedimentary evolution of lower to middle Miocene halfgraben basins related to an extensional detachment fault (western Crete, Greece). *Terra Nova*. Vol. 19. Iss: 1. Pages: 39-47. DOI: 10.1111/j.1365-3121.2006.00707.x.
- Shaw B., Ambraseys N.N., England P.C., Floyd M.A., Gorman G.J., Higham T.F.G., Jackson J. A., Nocquet J.-M., Pain C. C., Piggott M. D. (2008): Eastern Mediterranean tectonics and tsunami hazard inferred from the A.D. 365 earthquake. *Nature Geoscience*. Vol. 1. DOI: 10.1038/ngeo151.
- Smith W.H.F. and Sandwell D.T. (1997): Global seafloor topography from satellite altimetry and ship depth soundings. *Science*. Vol. 277. No. 5224. Pages: 1957-1962. DOI: 10.1126/science.277.5334.1956.

Stöckhert B., Wachmann M., Küster M. and Bimmermann S. (1999): Low effective viscosity during high pressure metamorphism due to dissolution precipitation creep: The record of HP-LT metamorphic carbonates and siliciclastic rocks from Crete. *Tectonophysics*. Vol. 303. Pages: 299-319. DOI: 10.1016/S0040-1951(98)00262-5.

Ten Veen J.H. and Kleinspehn K.L. (2003): Incipient continental collision and plate-boundary curvature: Late Pliocene-Holocene transtensional Hellenic forearc, Crete, Greece. *Journal of the Geological Society*. Vol. 160. Pages: 161-181 DOI: 10.1144/0016-764902-067.

Thomson S.N., Stöckhert B., and Brix M.R. (1998): Thermochronology of the high-pressure metamorphic rocks of Crete, Greece: Implications for the speed of tectonic processes. *Geology*. Vol. 26. No. 3. Pages: 259-262. DOI: 10.1130/0091-7613(1998)026<0259:TOTHPM>2.3.CO;2.

Van der Zwaan G.J., Jorissen F.J., and De Stigter H.C. (1990): The depth dependency of planktonic/benthonic foraminiferal ratios: constraints and applications. *Marine Geology*. Vol. 95. Pages: 1-16. DOI: 10.1016/0026-3227(90)90016-D.

Wortel M.J.R., and Spakman W. (2000): Subduction and Slab Detachment in the Mediterranean-Carpathian Region. *Science*. Vol. 290. No. 2498. Pages: 1910-1917. DOI: 10.1126/science.290.5498.1910.

Zachariasse W.J., Hinsbergen van D.J.J., and Fortuin A.R. (2008): Mass wasting and uplift on Crete and Karpathos during the early Pliocene related to initiation of south Aegean left-lateral, strike-slip tectonics. *GSA Bulletin*. Vol. 120. No. 7/8. Pages: 976-993. DOI: 10.1130/B26175.1.

Figures & Tables

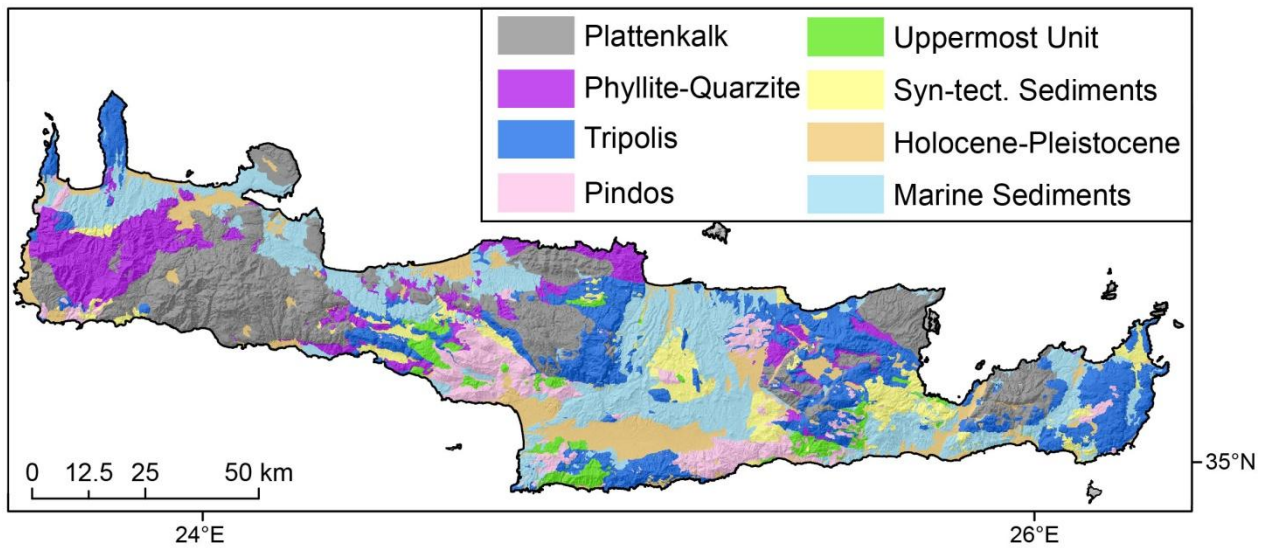


Figure 5.1: Geological map of Crete (after Papanikolaou and Vassilakis, 2010) superimposed on the Digital Elevation Model (DEM) derived from SPOT images with a 20 m resolution.

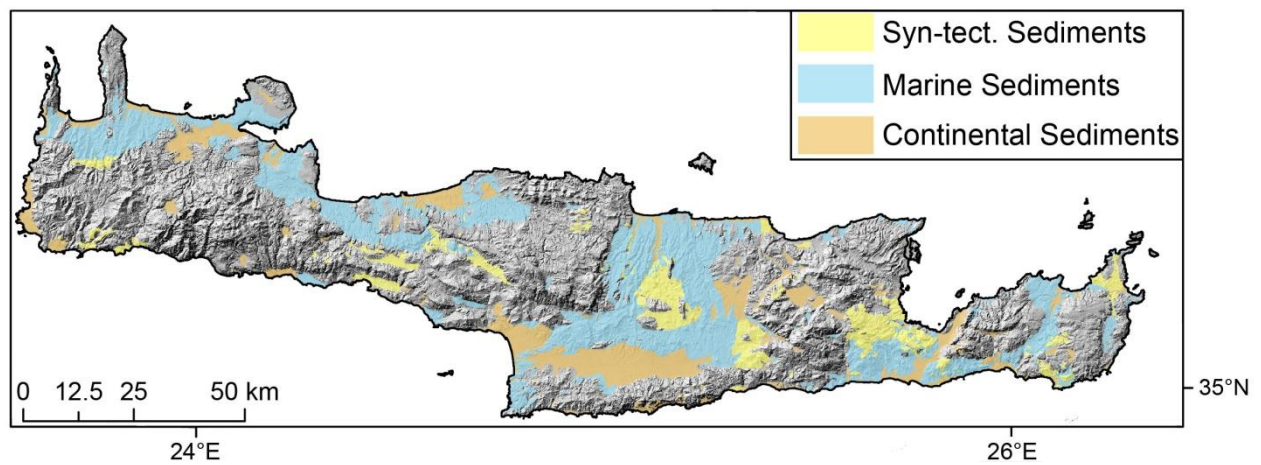


Figure 5.2: Distribution of Neogene sediments on Crete (after Papanikolaou and Vassilakis, 2010) superimposed on the DEM.

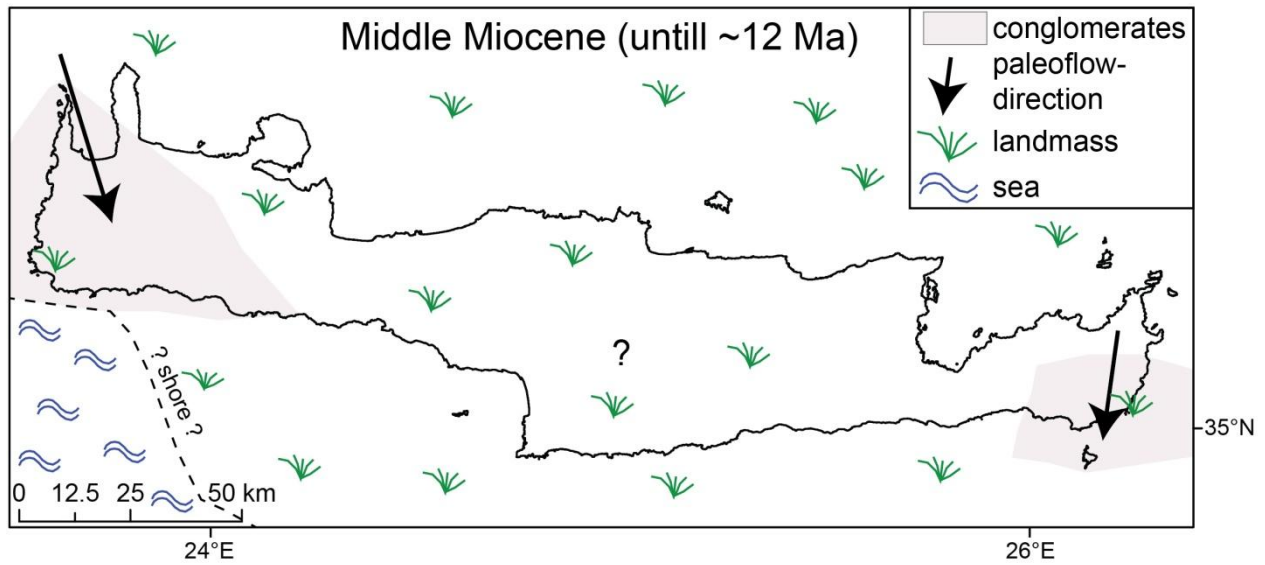


Figure 5.3: Depositional environment of the Middle Miocene of lacustrine-continental sediments modified after van Hinsbergen et al. (2006).

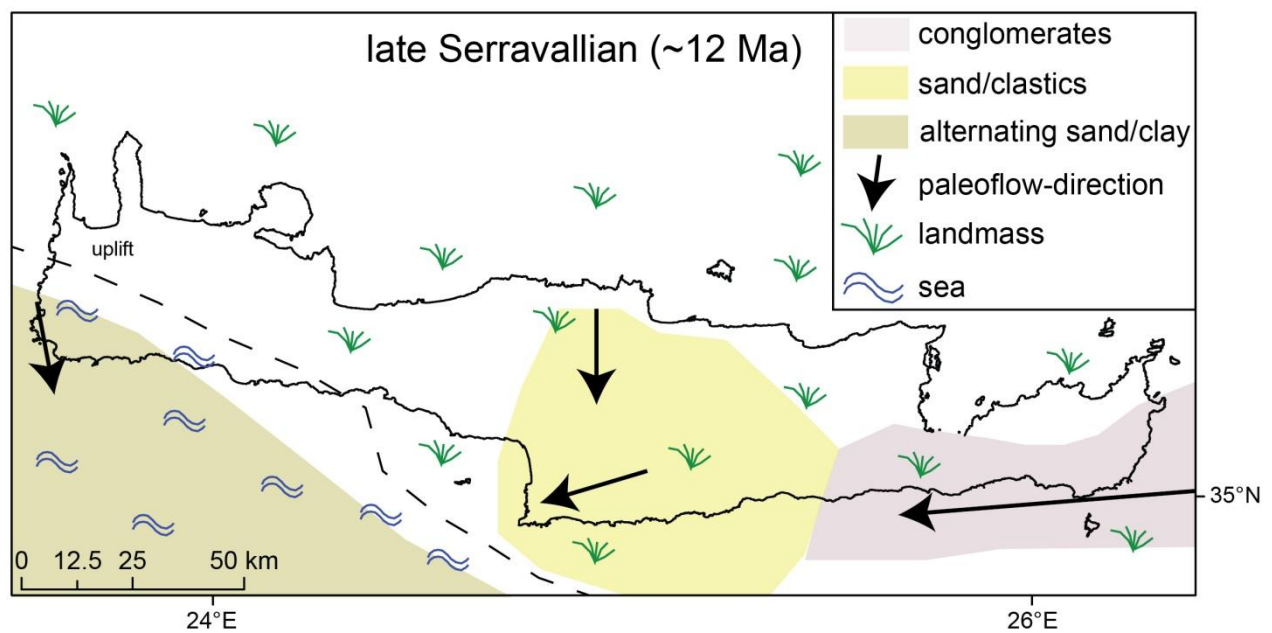


Figure 5.4: Depositional environment of late Serravallian modified after van Hinsbergen et al. (2006).

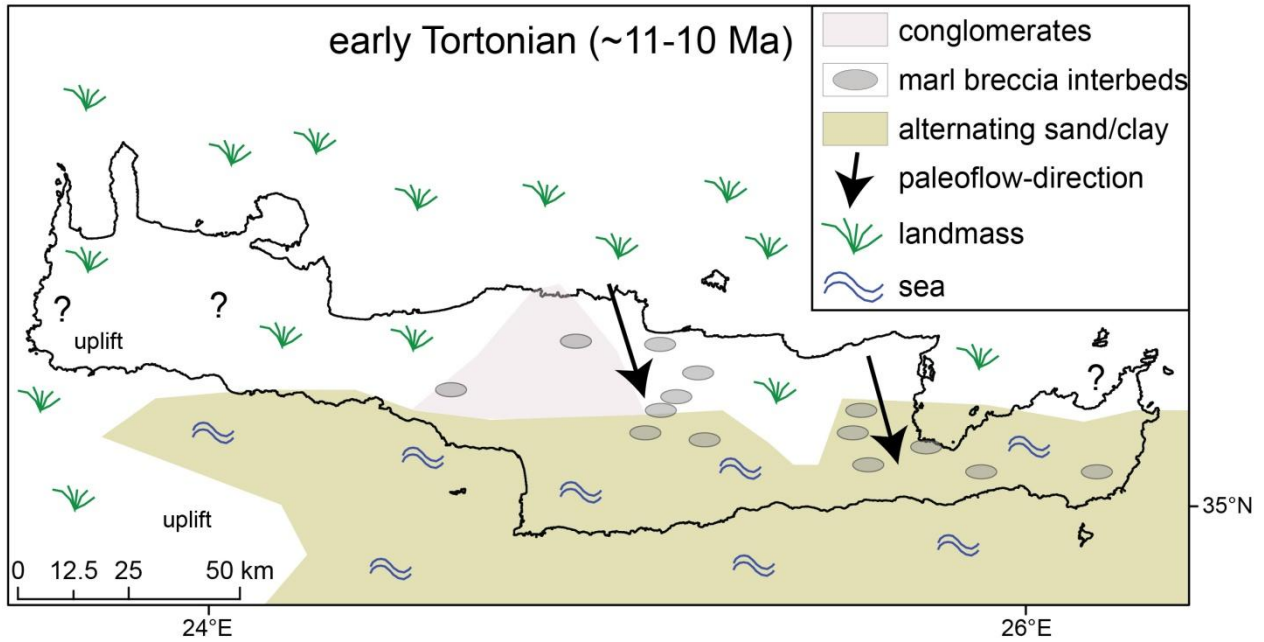


Figure 5.5: Depositional environment of early Tortonian modified after van Hinsbergen et al. (2006).

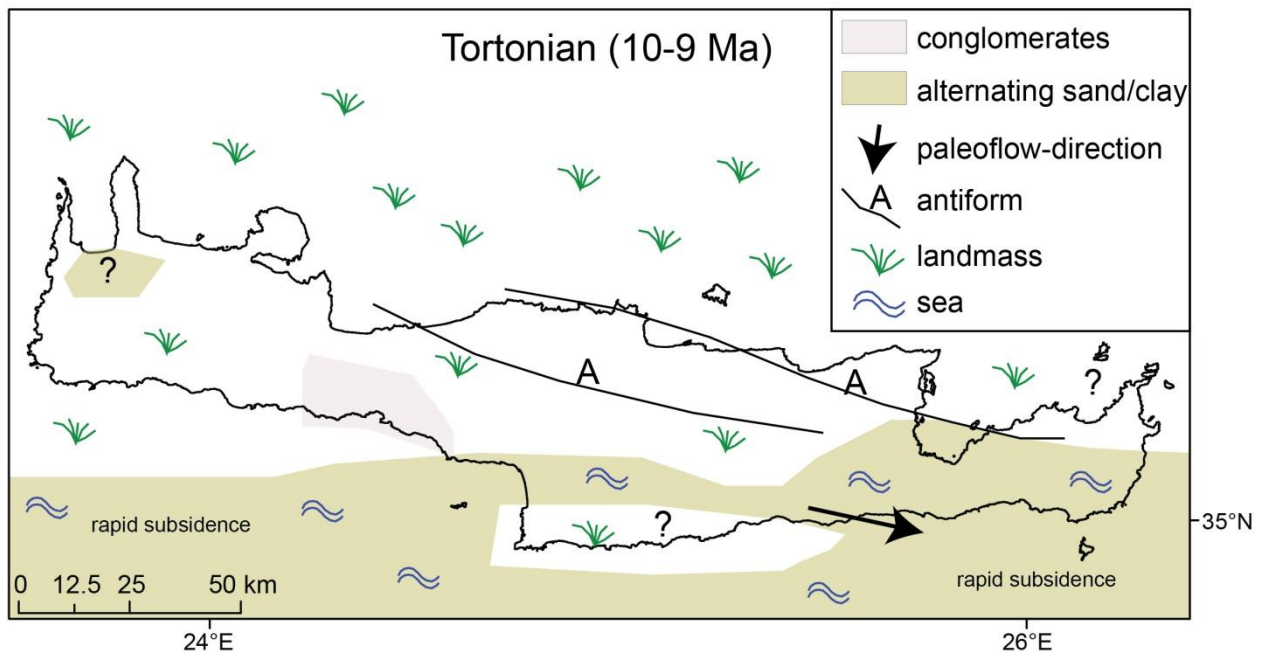


Figure 5.6: Depositional environment of Tortonian modified after van Hinsbergen et al. (2006).

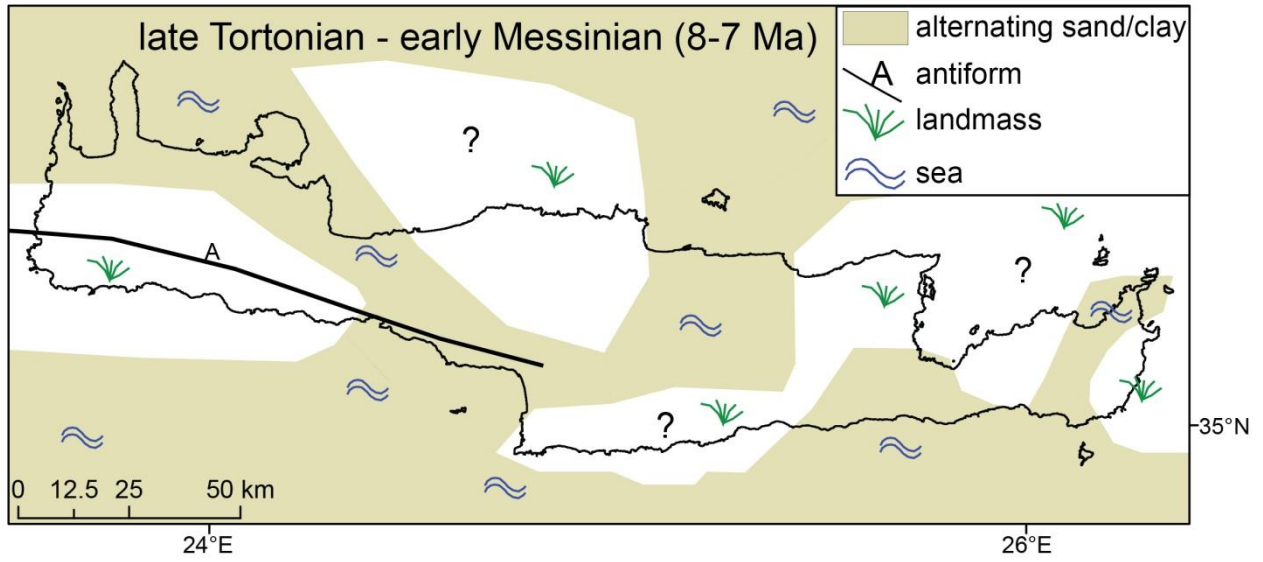


Figure 5.7: Depositional environment of late Tortonian – early Messinian modified after van Hinsbergen et al. (2006).

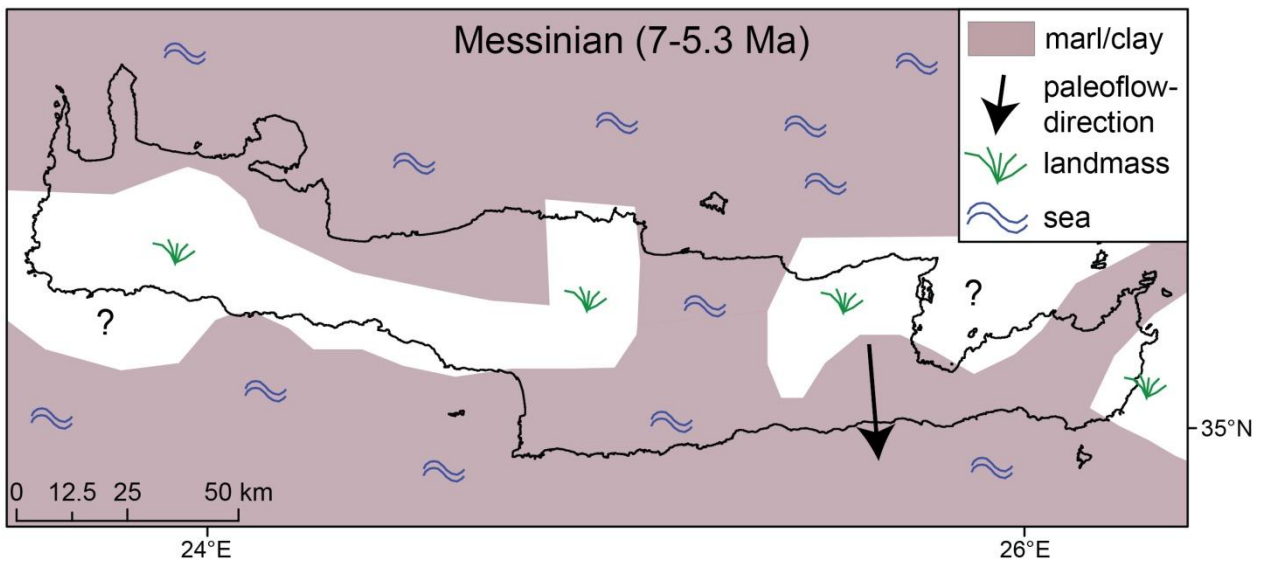


Figure 5.8: Depositional environment the Messinian modified after van Hinsbergen et al. (2006).

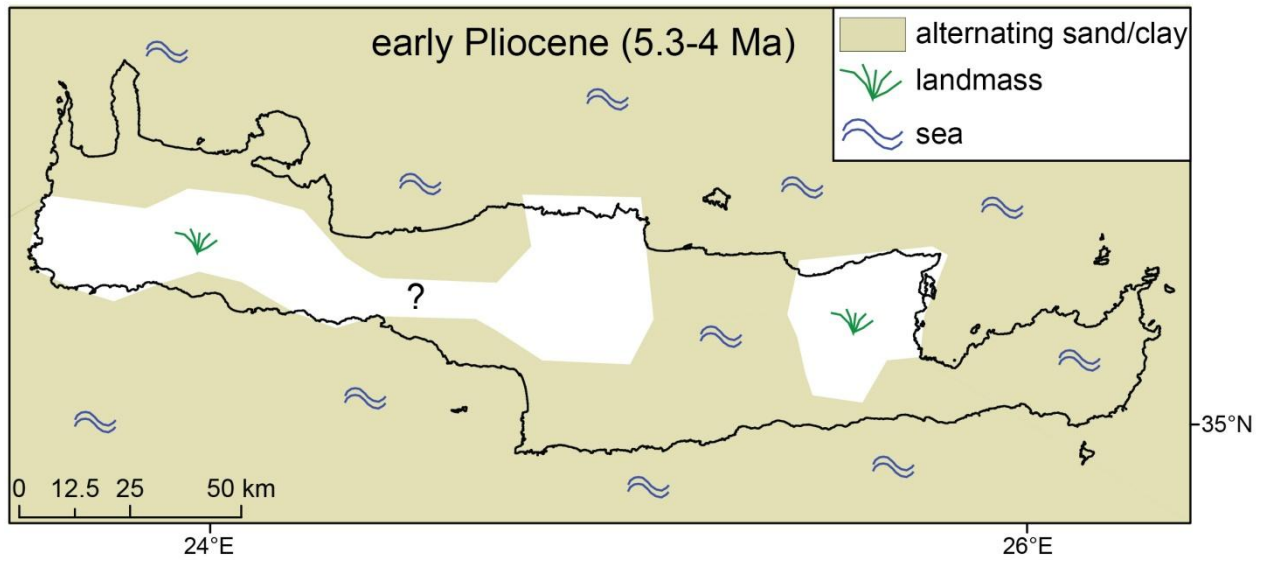


Figure 5.9: Depositional environment in early Pliocene modified after van Hinsbergen et al. (2006).

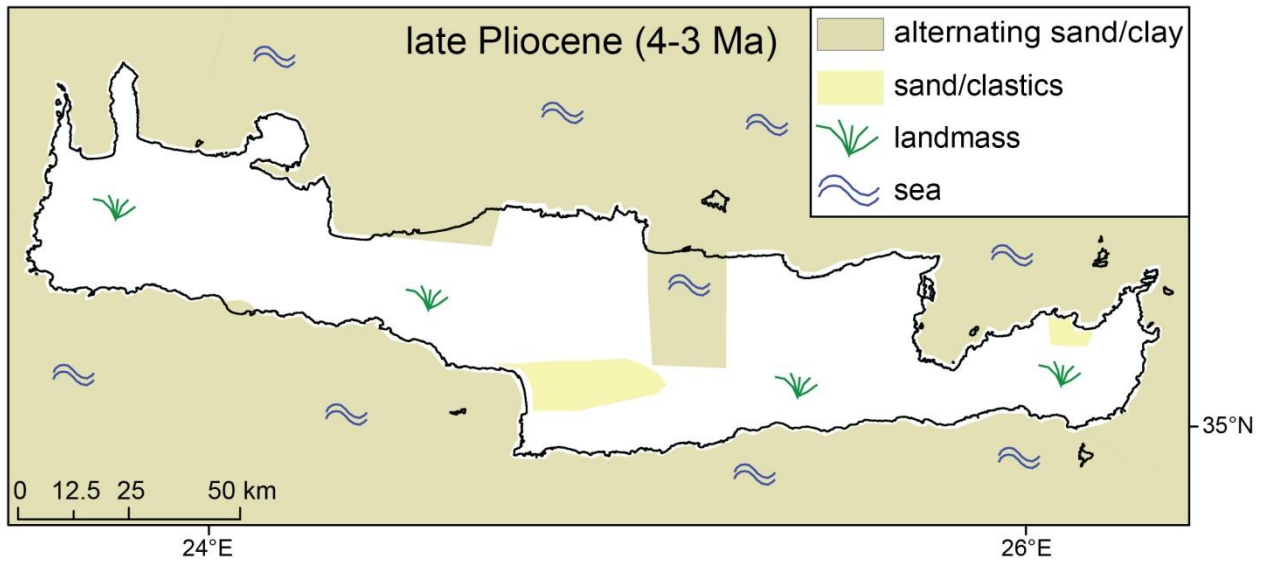


Figure 5.10: Depositional environment in late Pliocene modified after van Hinsbergen et al. (2006).

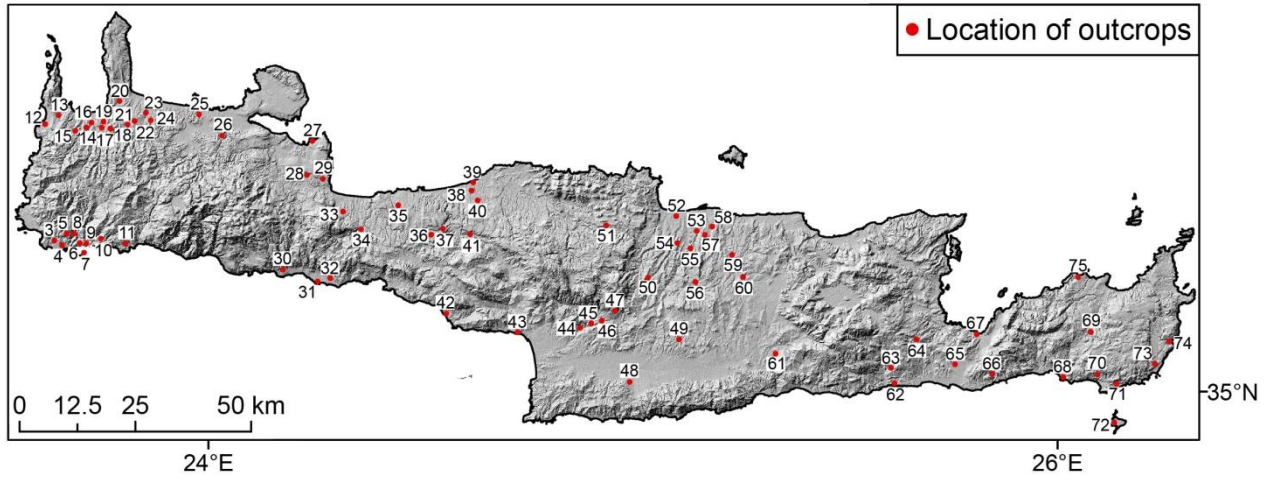


Figure 5.11: Location of sections for analysis the paleo-bathymetry after van Hinsbergen and Meulenkamp (2006) superimposed on the DEM.

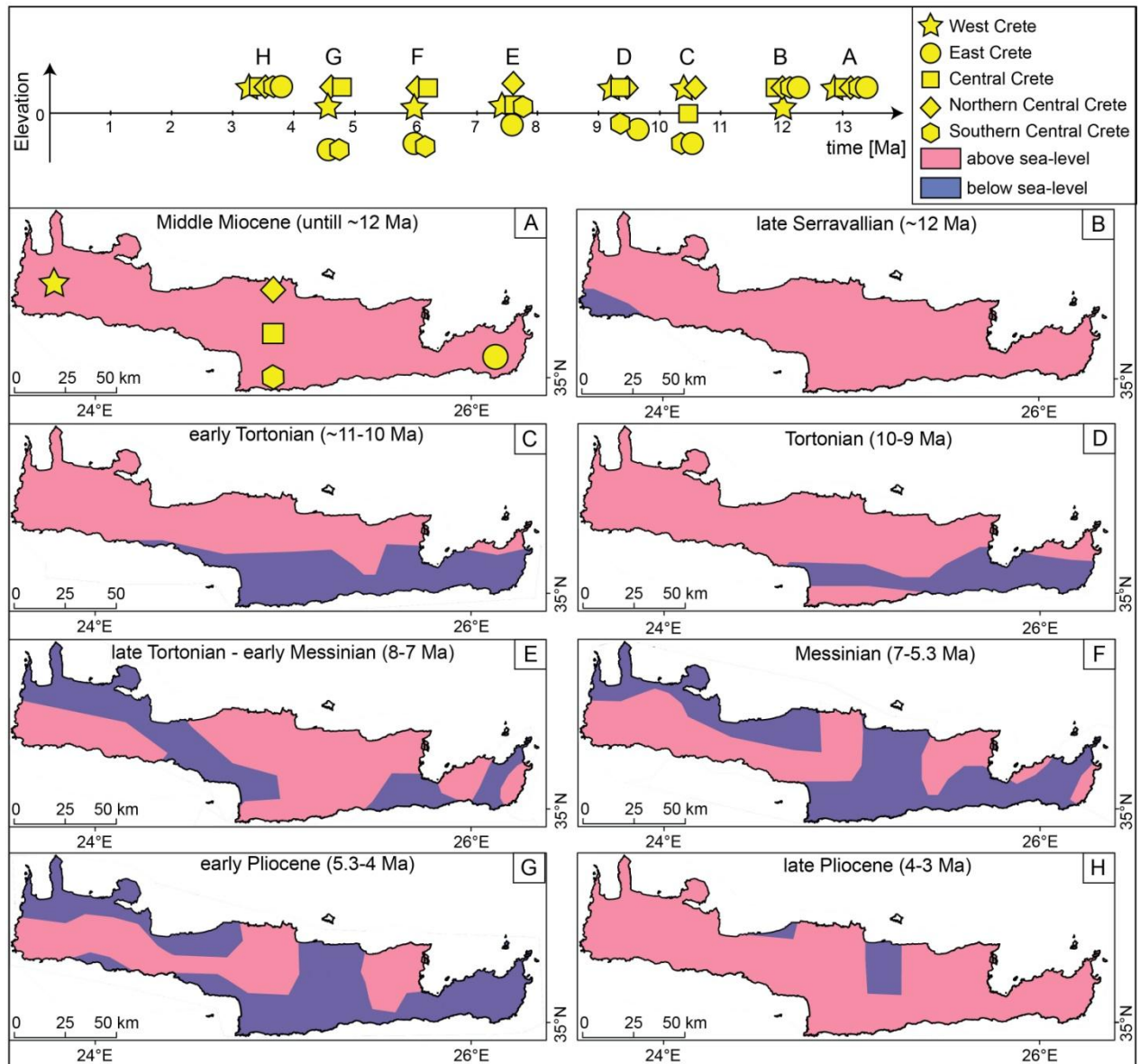


Figure 5.12: Schematic diagram of West, East, Central, North-Central and South-Central Crete above or below sea-level modified after van Hinsbergen and Meulenkamp (2006).

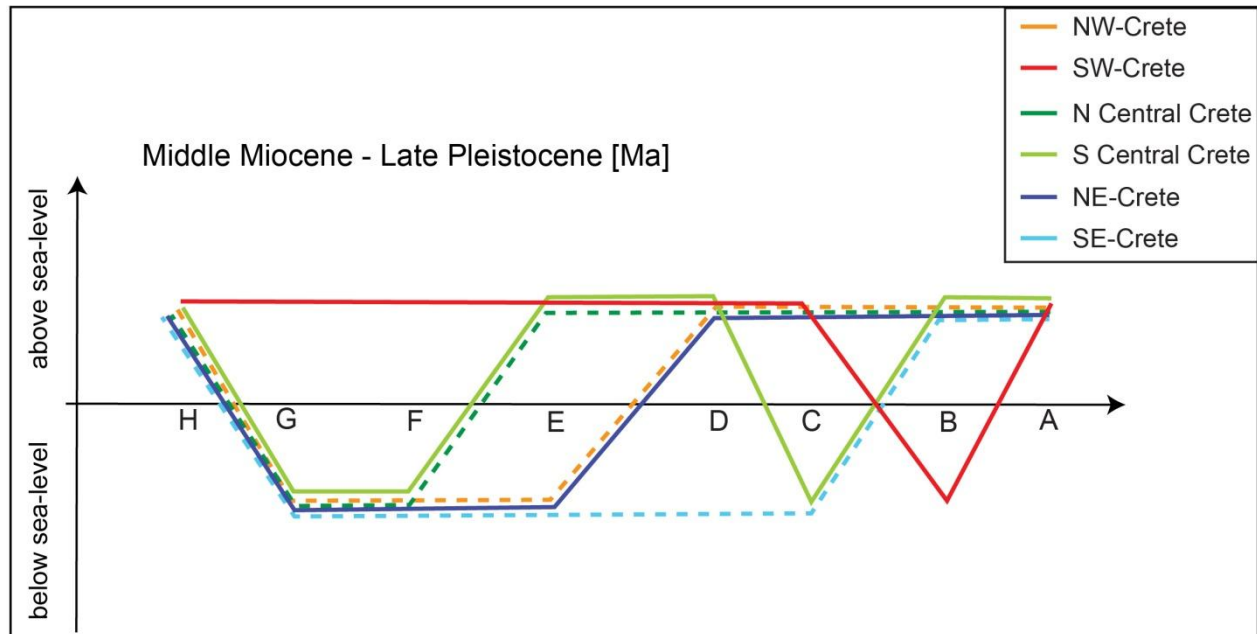


Figure 5.13: Vertical deformation since Middle Miocene until Late Pleistocene. For time intervals labeled with letters please refer to Figure 5.12.

Table 5.1: Age ranges of van Hinsbergen and Meulenkaamp (2006) correlated to ages [Ma].

Age range ^a	Age [Ma]
U. Langhian / l. Serravallian	16 to 12
U. Serravallian / L. Tortonian	12 to 8
U. Middle Miocene	12
U. Serravallian	12
Tortonian	10 to 9
U. Tortonian / l. Messinian	8 to 5,3
U. Tortonian	8
Messinian	7 to 5,3
L. Messinian	5,3
Pliocene	5,3 to 2,58
L. Pliocene	4 to 3
U. Pliocene	4 to 3
lowermost Pliocene	3 to 2,58

^aAge range based on Table 1 by van Hinsbergen and Meulenkaamp (2006)

Table 5.2: Calculated uplift rates for coastal regions.

		Uplift rate [km/Ma]
W-Crete	N	0.11 ± 0.03
	S	0.04 ± 0.01
Central Crete	N	0.08 ± 0.03
	S	?
E-Crete	N	0.18 ± 0.04
	S	0.28 ± 0.03

Chapter 6

PATTERN OF VERTICAL SURFACE DEFORMATION OF CRETE BASED ON A SYNTHESIS OF GEODETIC, GEOMORPHOLOGICAL, AND GEOLOGICAL DATA, AND IMPLICATIONS FOR CRUSTAL DEFORMATION MECHANISMS

6.1 Abstract

Deciphering the tectonic significance of complex deformation patterns is particularly challenging in the case of the island of Crete, due to its special location above the Hellenic subduction zone, where the actively deforming tectonic provinces of the forearc region and Aegean sea meet. The relatively well-understood geology of the island offers the opportunity to place the regional-scale PSI surface deformation pattern (Chapter 2) in its longer term context. In this study, I synthesized the vertical surface-deformation pattern on three different time-scales, the decadal- (Chapter 2), the millennial- (Chapters 3 and 4), long-term- (Chapter 5) time-scale, to evaluate the history of the vertical surface-deformation pattern across Crete. The resulting compilation shows that the island is not behaving as a coherent block on any temporal scale, but rather like a patchwork of individual crustal- and upper crustal-scale blocks. The pattern of independent vertical surface-deformation history is complex: while some blocks experience uplift on the order of 2 (millennial scale) to 5 (decadal scale) mm/yr, some adjacent blocks subsided on the order of 2 (millennial scale) to 5 (decadal scale) mm/yr. This study also shows that along subduction zones, not only the main plate interface of the subduction zone is responsible for the vertical surface-deformation pattern, but major faults in the overriding plate are equally, if not more, active. Any of these faults are capable of producing large earthquakes, and will need to be considered in seismic hazard assessment and mitigation studies. Long-term constraints on the active deformation pattern provided by geological measurements are an important data source, in particular in the absence of effective kinematic and mechanical faulting models.

6.1 Introduction

The comparison of vertical surface-deformation patterns on different geological time-scales is important to understand contemporary and past subsurface tectonic processes. In complex plate boundary settings, such as subduction zones affected by rollback, earthquakes occur both along the main plate interface and also along major faults in the overriding plate (Plafker, 1978). These superimposed tectonic processes lead to active vertical deformation in the forearc region on a range of scales. Past vertical deformation is preserved in the geological record, and may be recognized in the landscape, which allows longterm geological measurements of these processes.

Geodetic measurements, such as tide-gauge data, GPS or PSI, detect best the current vertical surface-deformation (e.g., Bürgmann and Thatcher, 2013). These measurements are used to test models of the earthquake cycle (Figure 6.1), which describe the vertical deformation during the interseismic period and the coseismic event. Large coseismic events, for example, require the accumulation and sudden release of large amounts of elastically stored energy, which builds up when the plate interface is locked. This locking leads to elastic bending and in turn to

transient vertical surface-displacement of both, the subducting and the overriding plate during the interseismic period (Figure 6.1 A). Quantification of transient vertical deformation signals of this and other tectonic processes, therefore, provide important constraints on the elastic rebound model (Reid 1910). During the coseismic event, the vertical displacement pattern is reversed - former areas of subsidence experience coseismic uplift and vice versa (Figure 6.1 B). Therefore, the determination of this transient vertical-deformation behaviour provides important constraints on subsurface processes such as strain accumulation along the subduction zone interface or along faults in the overriding plate during the interseismic period.

Testing the elastic rebound model along subduction zones is challenging, because most subduction zones lack data on vertical surface-deformation patterns on different time-scales. The recent M_w 9.0 Tohoku-Oki earthquake (Simons et al., 2011) along the NE Japan coastline showed for the first time that the conceptual models of the earthquake cycle and the recurrence time of earthquakes may not be valid. The NE Japan coastline experienced subsidence during the interseismic period AND the coseismic event. Furthermore, the possibility of such a large earthquake along this coastline was not realized, because long-term vertical deformation data were not considered.

This thesis provides an analysis of the vertical surface deformation pattern for the island of Crete on three different time-scales. Crete represents a forearc high due its position between the trench and the volcanic arc (Figure 1.6). For the decadal time-scale, geodetic PSI measurements (Chapter 2 and 3) reflect only a small time fraction of the vertical surface-deformation history during the earthquake cycle. The vertical surface-deformation on the millennial-, and long-term time-scale is preserved in the landscape (Chapters 3 to 5). Data on these time-scales provide more, yet incomplete, information of the vertical surface-deformation history along a subduction zone where different fault systems are superimposed. Analysis of geomorphic markers, such as river profiles and paleo-shorelines provide information on the vertical surface-deformation pattern on the ka time-scale (Chapter 4). Estimates on geological markers such as depositional depth and ages of Neogene sediments provide information on vertical surface-deformation on the Ma time-scale (Chapter 5).

An important question concerns the steadiness of deformation on longer time scales, beyond these of earthquake cycles, as a frame in which to place the results of short-term studies. For example, the distinction of whether a signal is steady or transient depends on it's context on a range of neighboring scales; this chapter is a humble first attempt at providing this frame.

6.2 Synthesis of Vertical Deformation Rates across different Time-Scales

Here, I evaluate the surface-deformation pattern for the island of Crete on the decadal-, the millennial-, and the million-year time-scale.

For the decadal time-scale, I projected the results of the PSI analysis of Chapter 3 to construct a schematic vertical deformation map of the Cretan coastline (Figure 6.2). For the millennial time-scale, I used Holocene (Figure 6.3) and Pleistocene (Figure 6.4) vertical uplift rates derived in Chapter 4. For the long-term vertical deformation motion, I used data of Neogene sedimentary rocks previously published by van Hinsbergen et al. (2006). I then converted their results to uplift rates (Chapter 5) (Figure 6.5).

6.3 Results

From the Middle Miocene to the Tortonian, NW-Crete (Figure 6.5 & Figure 6.6, van Hinsbergen et al. 2006) was exposed above sea level, followed by a Late Tortonian/Early Messinian marine transgression, and renewed uplift in the Late Pleistocene. Therefore, Pleistocene paleo-shorelines along this coastal region are absent (Figure 6.7). In the Holocene, this region experienced tectonically controlled uplift despite postglacial sea-level rise. Interestingly, PSI measurements indicate no vertical motion along this coastal region today (Figure 6.2.).

SW-Crete (Figure 6.6) was above sea-level in the Middle Miocene, and subsided in the Late Serravalian below the sea-level. Since the Early Tortonian, this region was above sea-level, throughout the Pleistocene until today (Figure 6.6 & Figure 6.7). Paleo-shorelines indicate continuous uplift since the Pleistocene and throughout the Holocene, and PSI measurements show an increase in uplift.

N-Central Crete was exposed above sea-level from the Middle Miocene until the Late Tortonian/Early Messinian, but experienced subsidence from Messinian until Late Pliocene time (Figure 6.6). Pleistocene paleo-shoreline data along this coastal region are missing (Figure 6.7). Holocene paleo-shorelines indicate subsidence, whereas recent PSI measurements show uplift along this coastal region.

S-Central Crete was exposed above sea-level from the Middle Miocene until the Late Serravalian (Figure 6.6). In Early Tortonian time, this region was below sea-level, and uplifted above the sea-level from the Tortonian until the Late Tortonian/Early Messinian. In the Messinian, this part of the coastline was below sea-level until the Early Pliocene. In Late Pliocene this region was exposed above the sea-level. Pleistocene paleo-shorelines (Figure 6.7) indicate uplift, which changed to subsidence during the Holocene. PSI measurements also indicate rapid uplift of the S-Central Cretan coast.

Since Middle Miocene until Tortonian time, the NE-coastline was exposed above sea-level, and from Late Tortonian/Early Messinian until Early Pliocene time, this region was below sea-level. In the late Pliocene, the region experienced uplift above the sea-level (Figure 6.6). Data of Pleistocene paleo-shorelines in this region are missing (Figure 6.7). Data of Holocene paleo-shorelines indicate subsidence in Holocene, and an increase in subsidence today based on PSI measurements.

SE-Crete was exposed above sea-level from Middle Miocene until Late Serravalian time (Figure 6.6). Since the Early Tortonian until the Early Pliocene, this region was below sea-level. In the Late Pliocene, this region was located above sea-level. Pleistocene paleo-shorelines data are missing along this coastal region (Figure 6.7). Holocene paleo-shorelines indicate subsidence, whereas PSI measurements indicate no vertical motion along this coastal region today.

6.4 Discussion

Results of the synthesis and comparison of the pattern of vertical surface deformation along the Cretan coastline from Middle Miocene until today (Figure 6.6 & Figure 6.7) imply that deformation is not constant over time and space. The SW coastal region of the island experienced uplift since the Tortonian until today, whereas the northwestern part in Crete showed uplift from Middle Miocene until Tortonian time, followed by subsidence below sea-level from the Late Tortonian/Early Messinian, and uplift from the Early Pliocene to the Holocene, followed by no

vertical surface deformation today. Data along the S-central Cretan coastline show a very alternating history of vertical motion, characterized by ups and downs, and recent strong uplift.

The comparison of the vertical deformation history along the coast showed a very heterogeneous spatiotemporal distribution. This indicates that Crete is not behaving as a single rigid block, because then the vertical deformation pattern along the coast should be more coherent on the different time-scales. The differential vertical motion indicates the segmentation of the island into individual smaller blocks, experiencing distinct vertical deformation history.

Vertical surface deformation on the long-term scale represents processes active on the regional and local scale (Table 6.1). The horst and graben structure on Crete is the result of extension of the Aegean microplate caused by slab rollback of the subducting African lithosphere, and incipient continent-continent collision.

The millennial time-scale represents an average of tectonic processes (Table 6.1). It shows the result of the average tectonic displacement of a number of earthquake cycles along the Hellenic subduction zone and upper-crustal faults.

Geodetic measurements detect only a small fraction of the earthquake cycle (Table 6.1). The geodetic detected signal of vertical deformation is most likely induced by the faults in the overriding plate, and may represent transient motion.

All three data sets are limited to analytical imprecision, such as general limitations of the PSI method (Chapter 2), dating of paleo-shorelines (Chapter 4), and erosion of Neogene sedimentary rocks (Chapter 5). This may explain the discrepancies between uplift rates on the three different time-scales (Table 6.3 & Table 6.2).

Discrepancies between the short-term and the long-term vertical measurements (Table 6.3) were measured likewise along the coastline of northeastern Japan (Ikeda, 2012). Here, the short-term signal of ~ 5 mm/yr of subsidence measured by GPS data (1997-2001) (Suwa et al., 2005) is interpreted as interseismic coupling along the subduction zone interface. The long-term signal of 0.1 – 0.5 mm/yr of uplift, based on studies of paleo-shorelines, is attributed to isostatic uplift caused by crustal thickening and enhanced by magmatic underplating (Ikeda, 2012). The 2011 M_w 9.0 Tohoku-Oki earthquake (Simons et al., 2011) offshore of the coast of northeastern Japan was not expected due to the lack of long-term data and the interpretation of this plate boundary to be weakly coupled (Matsuzawa et al., 2012), due to the old age of the subducting plate, the high seismic activity of small- to moderated earthquakes in this region, and GPS measurements (Matsuzawa et al., 2012). The earthquake induced coseismic subsidence of up to ~ 1 m along the NE coastline (Ikeda, 2012; Kamiyama et al., 2012). Earlier GPS, and monthly-tide gauge-data showed subsidence of 5 mm/yr based on GPS data from 1997-2001 (Suwa et al., 2005), and up to 5 to 10 mm/yr of subsidence based on tide gauge data from 1951-1981 (Kato, 1983). So, vertical surface deformation during interseismic period and the coseismic event has the same tendency of motion, and is not opposite as expected from the deformation pattern during the earthquake cycle. Along the SW coastline of Crete the 365 A.D. earthquake induced an uplift of 9 m coseismically (Pirazzoli et al., 1996), and our PSI measurements in the region of highest coseismic uplift coincides with the highest PSI uplift rates of 5 mm/yr in this region. Therefore, the vertical surface-deformation is the same for the interseismic period and the coseismic event.

Observations based the earthquake cycle prior the 2011 M_w 9.0 Tohoku-Oki earthquake, and the observations of this analysis may lead to a rethinking of the conceptual earthquake cycle model. Until today, only along few subduction zones it is possible to compare geodetic data and longer-term data, as for most subduction zones these measurements are missing. Dense GPS station networks are expensive and only available along the Cascadian and Japan subduction zones. PSI measurements, in combination with geological data, are therefore a powerful tool for the detection of the vertical surface-deformation pattern along subduction zones. More vertical

geodetic-data in context with their geological setting are needed to quantify if the conceptual model of vertical motion during the earthquake cycle is reliable.

6.4 Conclusions

Comparison of the vertical surface deformation pattern along the Cretan coastline on three different time-scales showed that the spatio-temporal distribution is very heterogeneous. This indicates that Crete is not behaving as one rigid block, but rather segmented into small individual blocks with their own vertical surface motion history. Furthermore, this study showed that the coseismic and interseismic surface pattern along the SW coastline of Crete is not in accordance to the conceptual model of vertical surface-deformation during the earthquake cycle. Such deformation behavior was also found along the NE coast of Japan (Ikeda, 2012). For testing the reliability of the conceptual model of vertical surface-deformation during the earthquake cycle more measurements along subduction zones are needed. The quantification of the deformation over the geodetic time-scale alone is not sufficient to understand the earthquake potential along a subduction zone or upper-crustal fault systems. The application of this type of multi-spatio-temporal deformation study, including PSI measurements in their geological context, is therefore highly recommended for assessing the earthquake potential and seismic hazards along subduction zones.

References

- Angelier J., Lyberis N., LePichon X. (1982): The tectonic development of the Hellenic arc and the Sea of Crete – A synthesis. *Tectonophysics*. Vol. 86. Iss. 1-3. Pages: 159-196. DOI: 10.1016/0040-1951(82)90066-X.
- Armijo, R., Lyon-Caen, H. Papanastassiou, D. (1992): East-west extension and Holocene normal fault scarps in the Hellenic arc. *Geology*. Vol. 20. Pages: 491-494. DOI: 10.1130/0091-7613(1992)020<0491:EWEAHN>2.3.CO;2.
- Becker D., Meier T., Bohnhoff M., Harjes H.P. (2010): Seismicity at the convergent plate boundary offshore Crete, Greece, observed by an amphibian network. *Journal of Seismology*. Vol. 14: Pages: 369-392. DOI: 10.1007/s10950-009-9170-2.
- Bohnhoff M., Makris J., Papanikolaou D., and Stavrakakis G. (2001): Crustal investigation of the Hellenic subduction zone using wide aperture seismic data. *Tectonophysics*. Vol. 343. Pages: 239-262. DOI: 10.1016/S0040-1951(01)00264-5.
- Bohnhoff M., Harjes H.-P., Meier T. (2005): Deformation and stress regimes in the Hellenic subduction zone from focal Mechanisms. *Journal of Seismology*. Vol. 9. Pages: 341-366. DOI: 10.1007/s10950-005-8720-5.
- Bürgmann R., Thatcher W. (2013): Space geodesy: A revolution in crustal deformation measurements of tectonic processes. *GSA Special Papers 2013*. Vol. 500. Pages: 397-430. DOI: 10.1130/2013.2500(12).
- Endrun B., Meier T., Bischoff M., and Harjes H.-P. (2004): Lithospheric structure in the area of Crete constrained by receiver functions and dispersion analysis of Rayleigh phase velocities. *Geophysical Journal International*. Vol. 158. Pages 592-608. DOI: 10.1111/j.1365-246X.2004.02332.x.
- Gallen S.F., Wegmann K.W., Bohnenstiehl D.R., Pazzaglia F.J., Brandon M.T., Fassoulas C. (2014): Active simultaneous uplift and margin-normal extension in a forearc high, Crete, Greece. *Earth and Planetary Science Letters*. Vol. 398. Pages: 11-24. DOI: 10.1016/j.epsl.2014.04.038.
- Ganas, A., and Parsons T. (2009): 3-D model of Hellenic Arc deformation and origin of the Cretan uplift, *Journal of Geophysical Research*. Vol. 114. DOI: 10.1029/2008JB005599.
- Goldfinger C., Ikeda Y., Yeats R.S., Ren J. (2013): Superquakes and Supercycles. *Seismological Research Letters*. Vol. 84. No. 1. Pages: 24-32. DOI: 10.1785/0220110135.
- Hyndman R.D., Wang K., (1993): Thermal constraints on the zone of major thrust earthquake failure: The Cascadia Subduction Zone. *Journal of Geophysical Research*. Vol. 98. Iss. B2. Pages: 2039-2060. DOI: 10.1029/92JB02279.
- Ikeda Y. (2012): Long-term strain buildup in the northeast Japan arc-trench system and its implications for the gigantic subduction earthquake of March 11, 2011. *Proceedings of the International Symposium on Engineering Lessons Learned from the 2011 Great East Japan Earthquake*, March 1-4. 2012. Tokyo. Japan.
- Le Pichon X., Angelier J. (1981): The Aegean Sea. *Philosophical Transactions of the Royal Society of London*. Vol. 300. No. 1454. Pages: 357-372. DOI: 10.1098/rsta.1981.0069.
- Meier T., Rische M., Endrun B., Vafidis A., and Harjes H.-P. (2004): Seismicity of the Hellenic subduction zone in the area of western and central Crete observed by temporary local seismic networks. *Tectonophysics*. Vol. 383. Pages: 149-169. DOI: 10.1016/j.tecto.2004.02.004.

- Meier T., Becker D., Endrun B., Rische M., Bohnhoff M., Stöckhert B., Harjes H.P. (2007): A model for the Hellenic subduction zone in the area of Crete based on seismological investigations. Geological Society. London. Special Publications. Vol. 291. Pages: 183-199. DOI: 10.1144/SP291.9.
- Plafker G., Rubin M. (1978) Uplift history and earthquake recurrence as deduced from marine terraces on Middleton Island, Alaska. in Proceedings of Conference VI. Methodology for identifying seismic gaps and soon-to-break gaps: U.S. Geological Survey Open-File Report 78-943. Pages: 687-721.
- Platt J.P. (1986): Dynamics of orogenic wedges and the uplift of high-pressure metamorphic rocks. The Geological Society of America Bulletin. Vol. 97. No. 9. Pages: 1037-1053. DOI: 10.1130/0016-7606(1986)97<1037:DOOWAT>2.0CO;2.
- Reilinger R., McClusky S., Paradissis D., Ergintav S., Vernant P. (2010): Geodetic constraints on the tectonic evolution of the Aegean region and strain accumulation along the Hellenic subduction zone. Tectonophysics. Vol. 488. Pages: 22-30. DOI: 10.1016/j.tecto.2009.05.027.
- Roberts G.G., White N.J., Shaw B. (2013): An uplift history of Crete, Greece, from inverse modeling of longitudinal river profiles. Geomorphology. Vol. 198. Pages: 177-188. DOI: 10.1016/j.geomorph.2013.05.026.
- Savage J.C., Lisowski M. (1991): Strain measurements and the Potential for a Great Subduction Earthquake Off the Coast of Washington. Science. Vol. 252. No. 5002. Pages: 101-103. DOI: 10.1126/science.252.5002.101.
- Shaw B., Jackson J. (2010): Earthquake mechanisms and active tectonics of the Hellenic subduction zone. Geophysical Journal International. Vol. 181. Pages: 966-984. DOI: 10.1111/j.1365-246X.2010.04551.x.
- Shimazaki K., Nakata T. (1980): Time-predictable recurrence model for large earthquakes. Geophysical Research Letters. Vol. 7. No. 4. Pages: 279-282. DOI: 10.1029/GL007i004p00279.
- Strobl M., Hetzel R., Fassoulas C., Kubik P.W. (2014): A long-term rock uplift rate for eastern Crete and geodynamic implications for the Hellenic subduction zone. Journal of Geodynamics. Vol. 78. Pages: 21-31. DOI: 10.1016/j.jog.2014.04.002.
- Taymaz T., Jackson J., Westaway R. (1990): Earthquake mechanisms in the Hellenic Trench near Crete. Geophysical Journal International. Vol. 102. Pages: 695-731. DOI: 10.1111/j.1365-246X.1990.tb04590.x.
- Tiberti M.M., Basili R., Vannoli P. (2014): Ups and downs in western Crete (Hellenic subduction zone). Nature Scientific Reports 4. DOI: 10.1038/srep05677.
- Vernant P., Reilinger R., McClusky S. (2014): Geodetic evidence for low coupling on the Hellenic subduction plate interface. Earth and Planetary Science Letters. Vol. 385. Pages: 122-129. DOI: 10.1016/j.epsö.2013.10.018.
- Wallace R.E. (1987): Grouping and migration of surface faulting and variations in slip rates on faults in the Great Basin Province. Bulletin of the Seismological Society of America. Vol. 77. No. 3. Pages: 868-876.

Figures & Tables

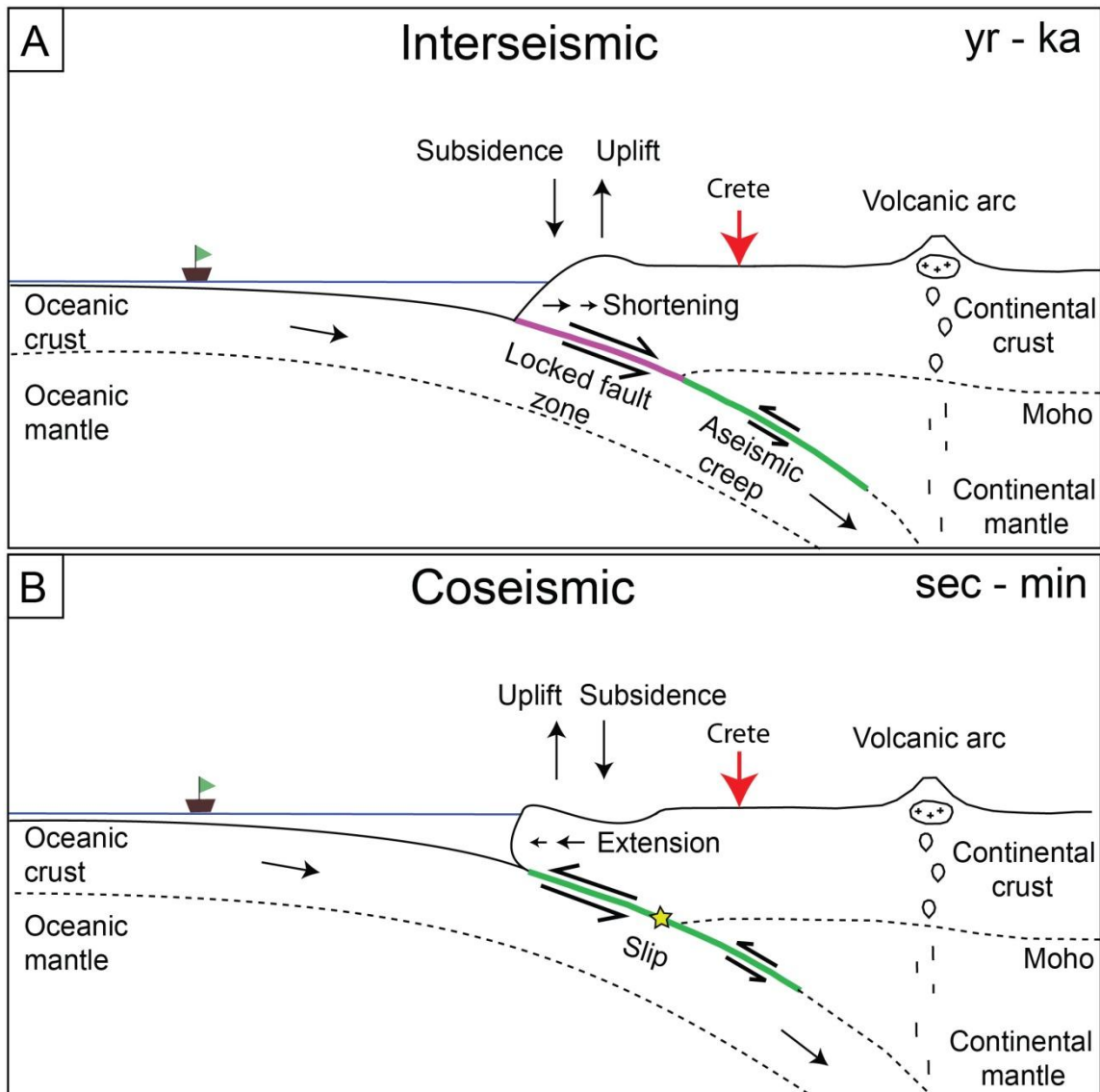


Figure 6.1: Vertical surface-deformation after Savage et al. (1991) and Hyndman and Wang (1993). A) The interseismic period lasting from years to thousand's of years. B) The coseismic moment lasting sec's to min's.

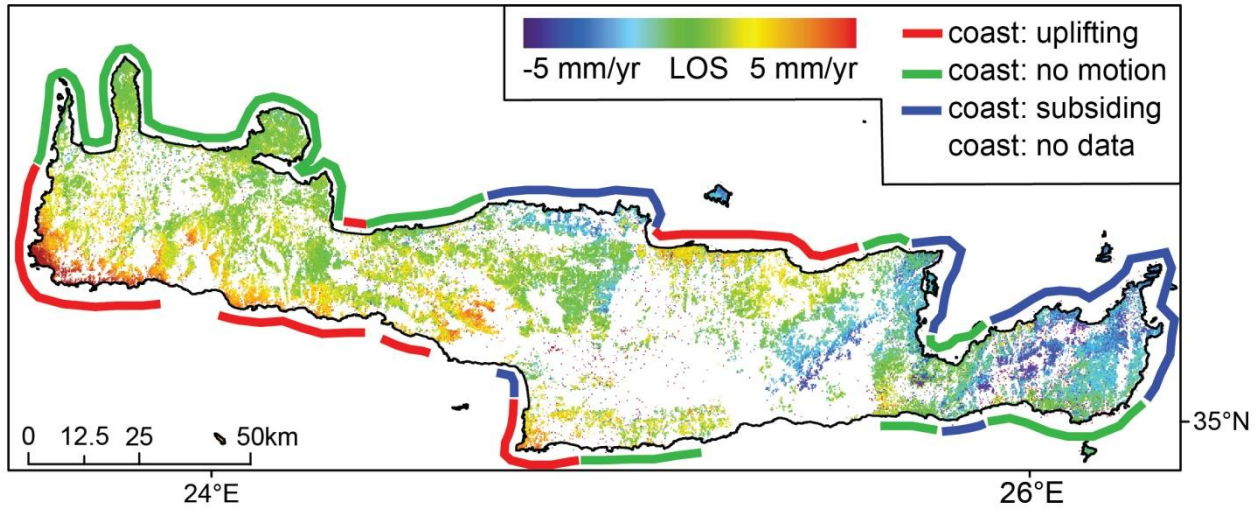


Figure 6.2: Recent coastal vertical deformation pattern.

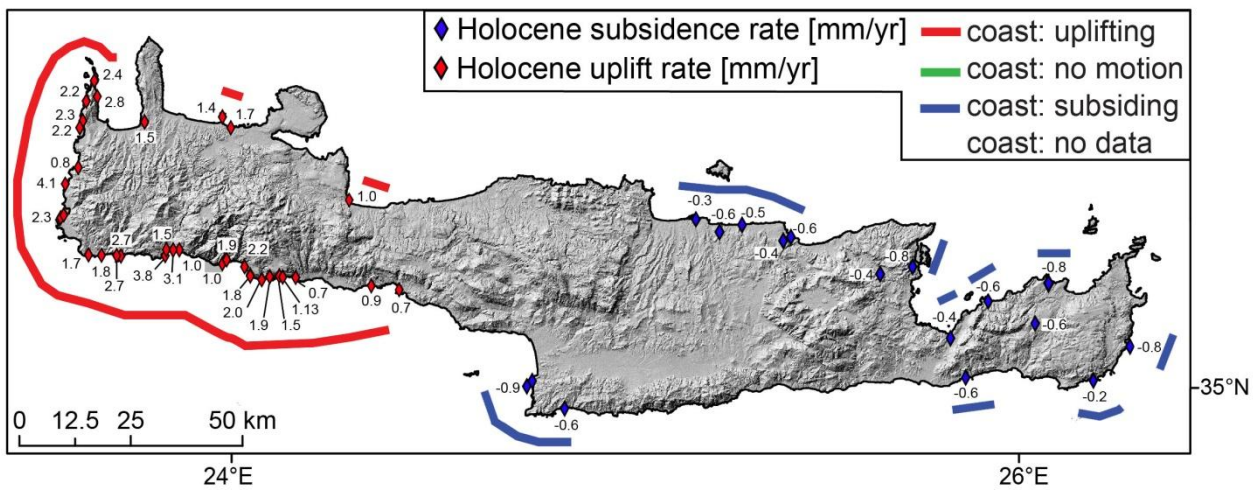


Figure 6.3: Holocene coastal vertical deformation pattern.

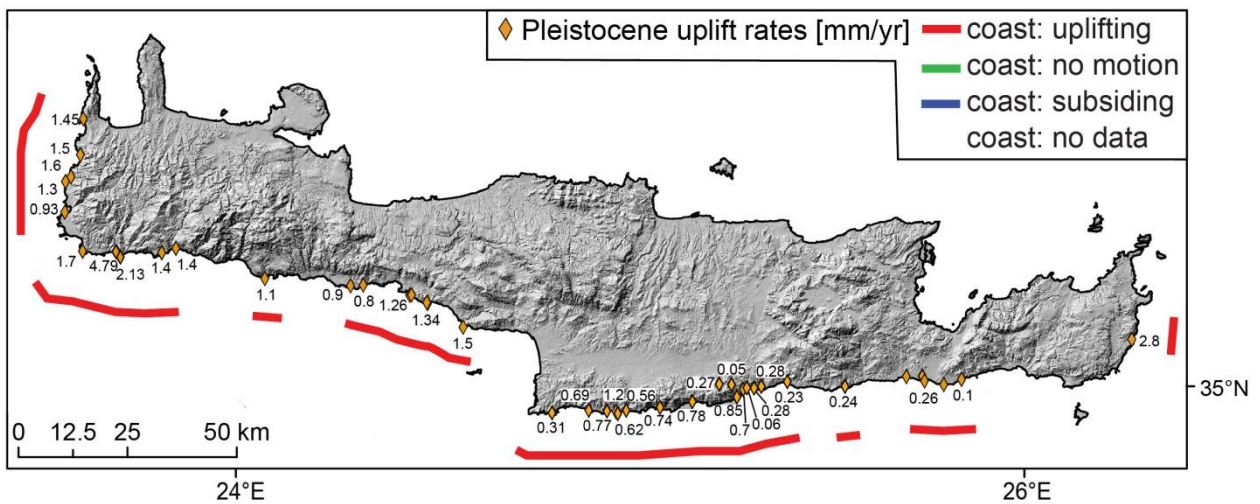


Figure 6.4: Pleistocene coastal vertical deformation pattern.

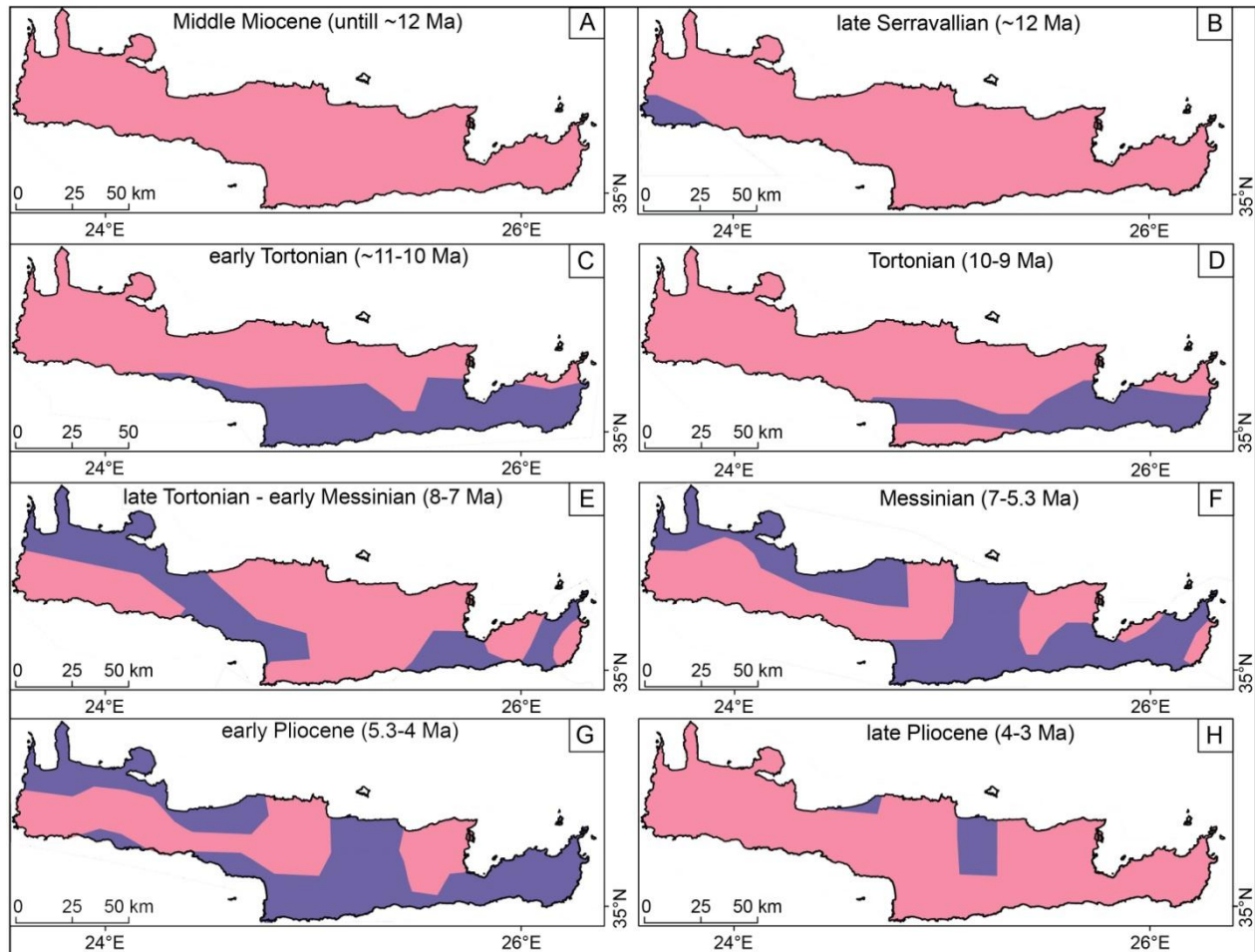


Figure 6.5: Schematic diagram of Crete above or below sea-level modified after van Hinsbergen and Meulenkamp (2006).

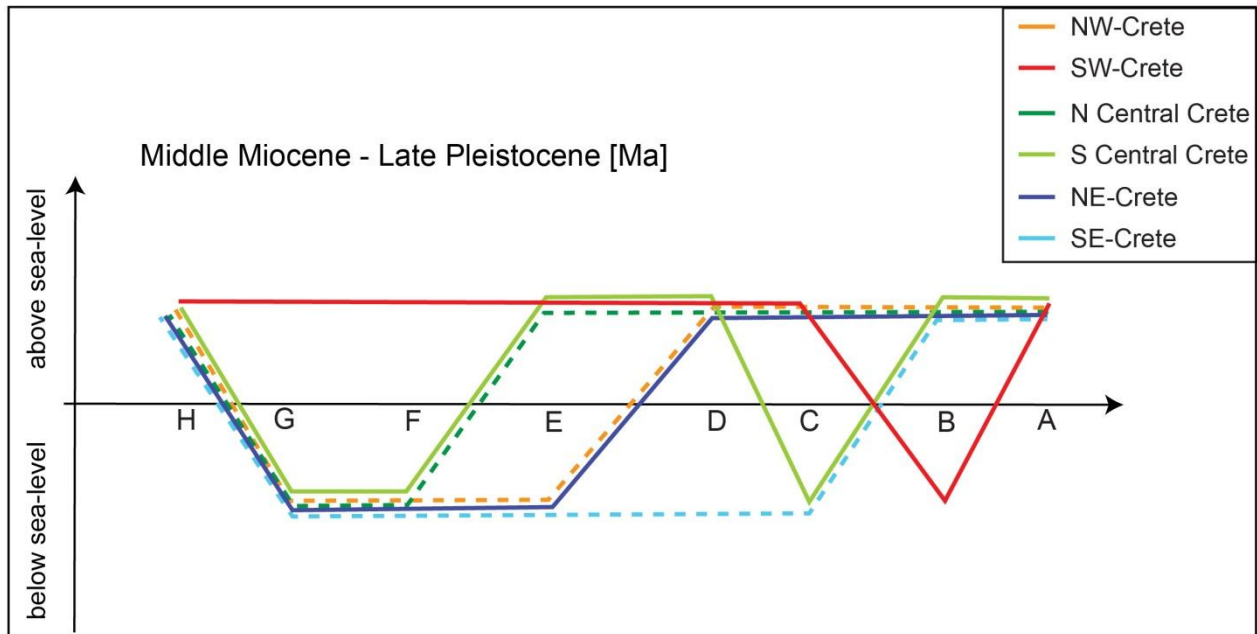


Figure 6.6: Vertical deformation since Middle Miocene until Late Pleistocene. For time intervals labeled with letters please refer to Figure 6.5.

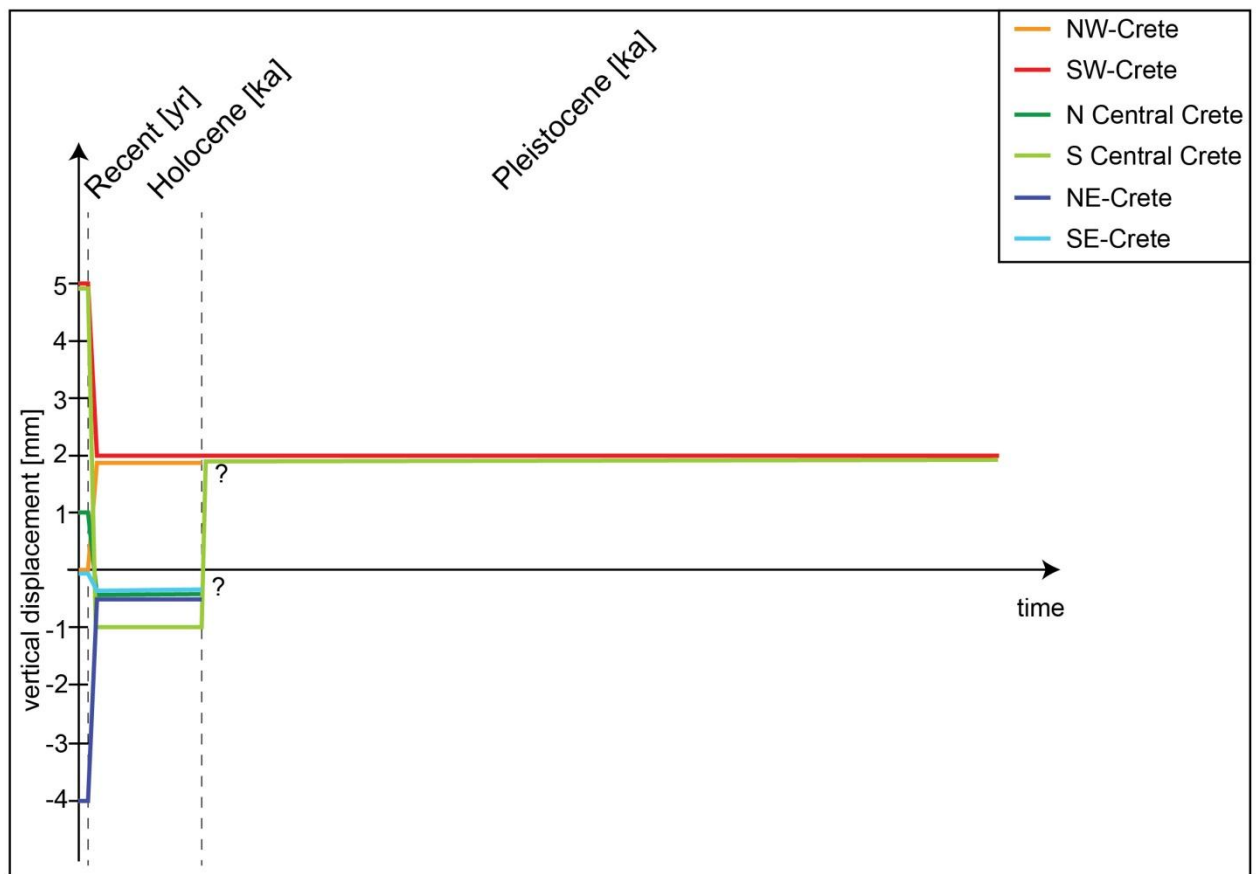


Figure 6.7: Comparison of vertical deformation on the Pleistocene-, Holocene-, and recent time-scale.

Table 6.1: Vertical surface-deformation above a subduction zone, Crete.

Method	Time interval	What is measured? (Typical Units)	Significance of measurements for Crete located above a subduction zone
Geologic	10^6 to 10^7 years	vertical displacement rate [km/Myr]	Average tectonic displacement on the regional spatial scale: - Formation of the Hellenic subduction zone - Average tectonic fault displacement above a subduction zone - Average tectonic fault displacement of faults in the overriding plate
Geomorphic	10^3 to 10^5 years	vertical displacement (m) and age of geomorphic marker (ka) [m/ka]	Average tectonic displacement rates of a number of seismic cycles, concerning: - The Hellenic Subduction zone - The Hellenic Trench - Faults on Crete
Geodetic	up to years	surface-deformation → velocity in the line of sight [mm/yr]	Measurements during the earthquake cycle: - Interseismic vertical surface-deformation → strain accumulation - Coseismic vertical displacement - Postseismic vertical surface deformation

Table 6.2: Calculated uplift rates for coastal regions.

		Uplift rate [km/Ma]
W-Crete	N	0.11 ± 0.03
	S	0.04 ± 0.01
Central Crete	N	0.08 ± 0.03
	S	?
E-Crete	N	0.18 ± 0.04
	S	0.28 ± 0.03

Table 6.3: Vertical uplift-rates on the decadal-, and the millennial time-scale on Crete.

		Recent [mm/yr]	Holocene [mm/yr]	Pleistocene [mm/yr]
W-Crete	N	0	~2	?
	S	5	~2	~2
Central Crete	N	1	-0.3	?
	S	5	-0.8	~0.5
E-Crete	N	-5	-0.6	?
	S	0	-0.4	?

Table 6.4: Above (+) or below (-) sea level. Please consider Figure 6.6 for time intervals.

		H	G	F	E	D	C	B	A
W-Crete	N	+	-	-	-	+	+	+	+
	S	+	+	+	+	+	+	-	+
Central Crete	N	-	-	-	+	+	+	+	+
	S	+	-	-	+	+	-	+	+
E-Crete	N	+	-	-	-	+	+	+	+
	S	+	-	-	-	-	-	+	+

Table 6.5: Vertical uplift-rates on the decadal-, millennial-, and long-term time-scale for NE Japan.

Geodetic measurements		Geomorphic measurements
~ 5 mm/yr ¹	~ 10 mm/yr ²	~ 0.1 – 0.5 mm/yr ³

¹: GPS measurements from 1997-2001 by Suwa et al. (2006)

²: Monthly tidal-gauge measurements from 1951-1981 by Kato (1983).

³: Quaternary marine terraces by Ikeda (2012).

II. APPENDIX

Chapter 3

Table II.1: Slip rates based on geological and geodetic data for the normal faults on Crete.

Fault	Geological data ^a		Geodetic data ^b	
	Slip rate [m/ka]	Slip rate * 13 kyr	Slip rate [mm/yr]	Slip rate * 8 kyr
Sfakia (SfF)	1.0	13	0.97 ± 1.07	7.76 ± 8.56
Asomatos (AF)	0.6	7.8	1.01 ± 0.98	8.08 ± 7.84
Spili (SpF)	0.8	10.4	0.60 ± 1.46	4.8 ± 11.68
Gramvousa (GrF)	0.7	9.1	0.68 ± 1.13	5.44 ± 9.04
Gionas (GF)	0.3	3.9	0.40 ± 0.99	3.2 ± 7.92
Rodopos (RF)	0.3	3.9	0.05 ± 1.01	0.4 ± 8.08
Kera (KeF)	0.4	5.2	0.21 ± 0.92	1.68 ± 7.36
Kroussonas (KrF)	1.0	13	0.91 ± 0.54	7.28 ± 4.32
Agia Varvara (AVF)	0.8	10.4	2.48 ± 0.73	19.84 ± 5.84
Kastelli (KF)	0.5	6.5	0.81 ± 0.98	6.48 ± 7.84
Ha Gorge (HGF)	0.9	11.7	1.16 ± 1.80	9.28 ± 14.4
Lastros (LF)	1.3	16.9	0.49 ± 3.08	3.92 ± 24.64
Zou (ZF)	0.7	9.1	2.34 ± 2.83	18.72 ± 22.64

^aGeological data taken from Caputo et al. (2010).

^bGeodetic data based on my PSI analysis

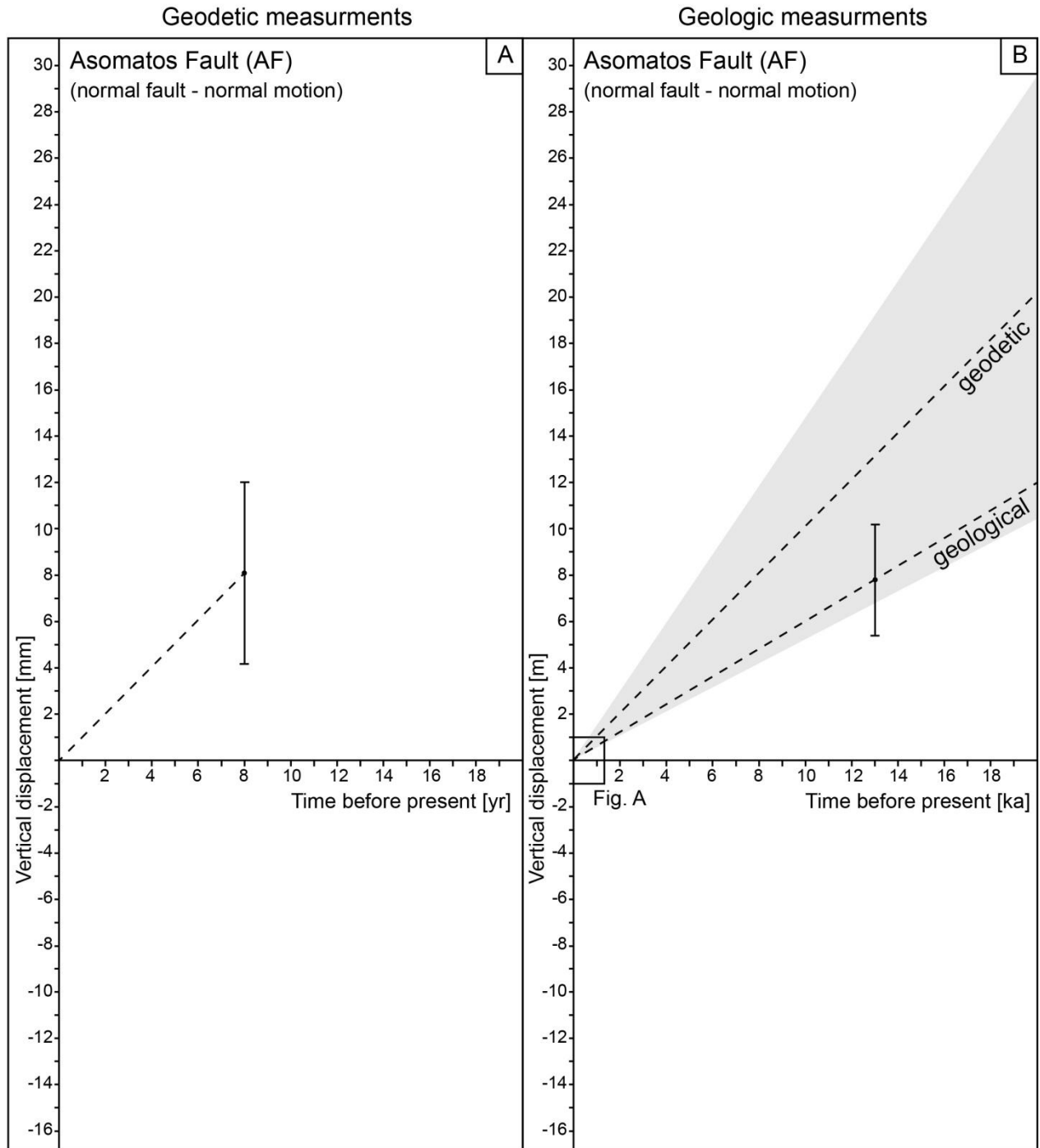


Figure II.1: A) Shows the vertical displacement in mm/yr measured by PSI along the Asomatos fault. B) Shows the geodetic measurements versus the geologic slip-rate in ka/m derived from Caputo et al. (2010). The grey shade shows the error range of PSI measurements adjusted to the geological time.

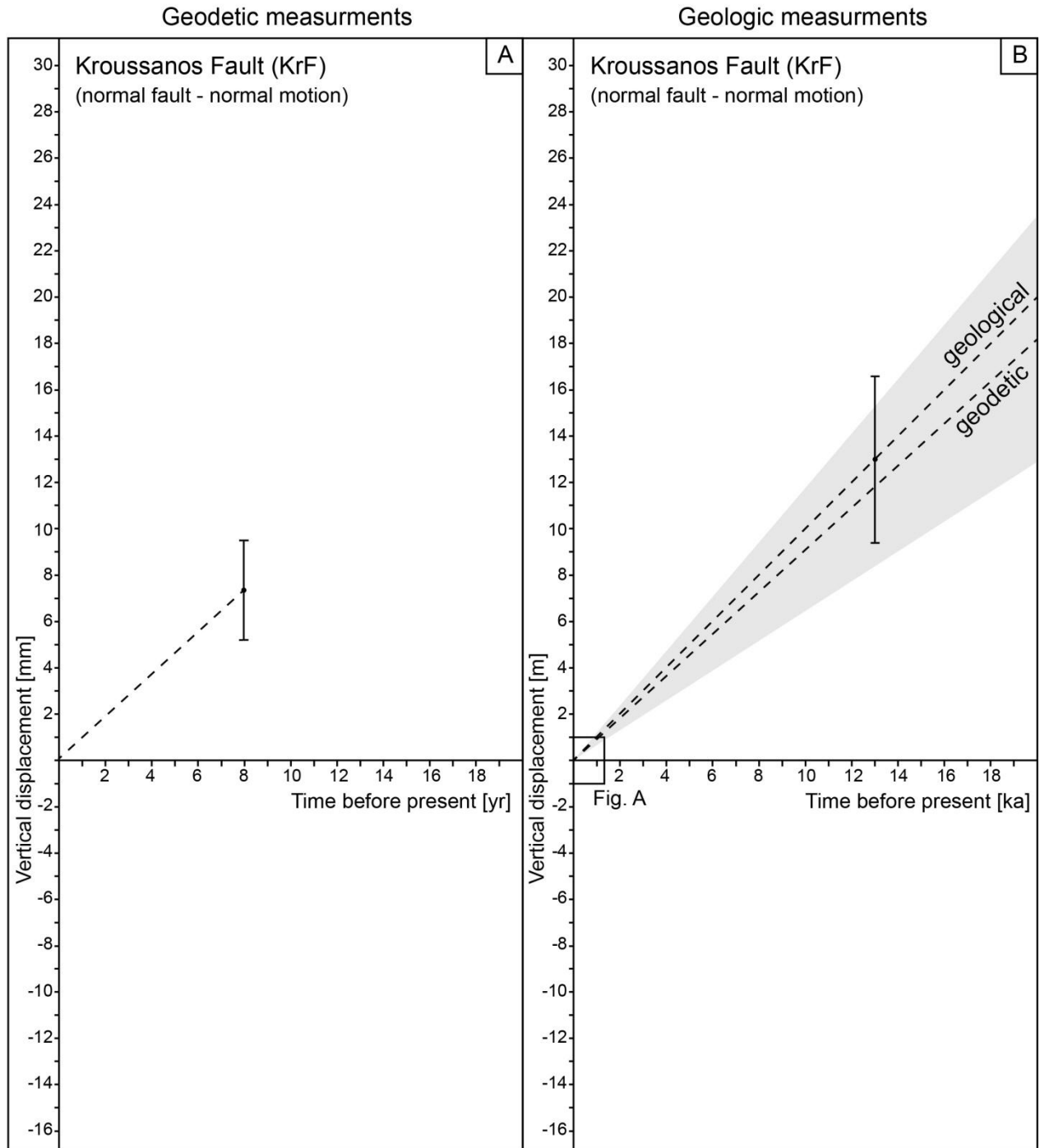


Figure II.2: A) Shows the vertical displacement in mm/yr measured by PSI along the Kroussanos fault. B) Shows the geodetic measurements versus the geologic slip-rate in ka/m derived from Caputo et al. (2010). The grey shade shows the error range of PSI measurements adjusted to the geological time.

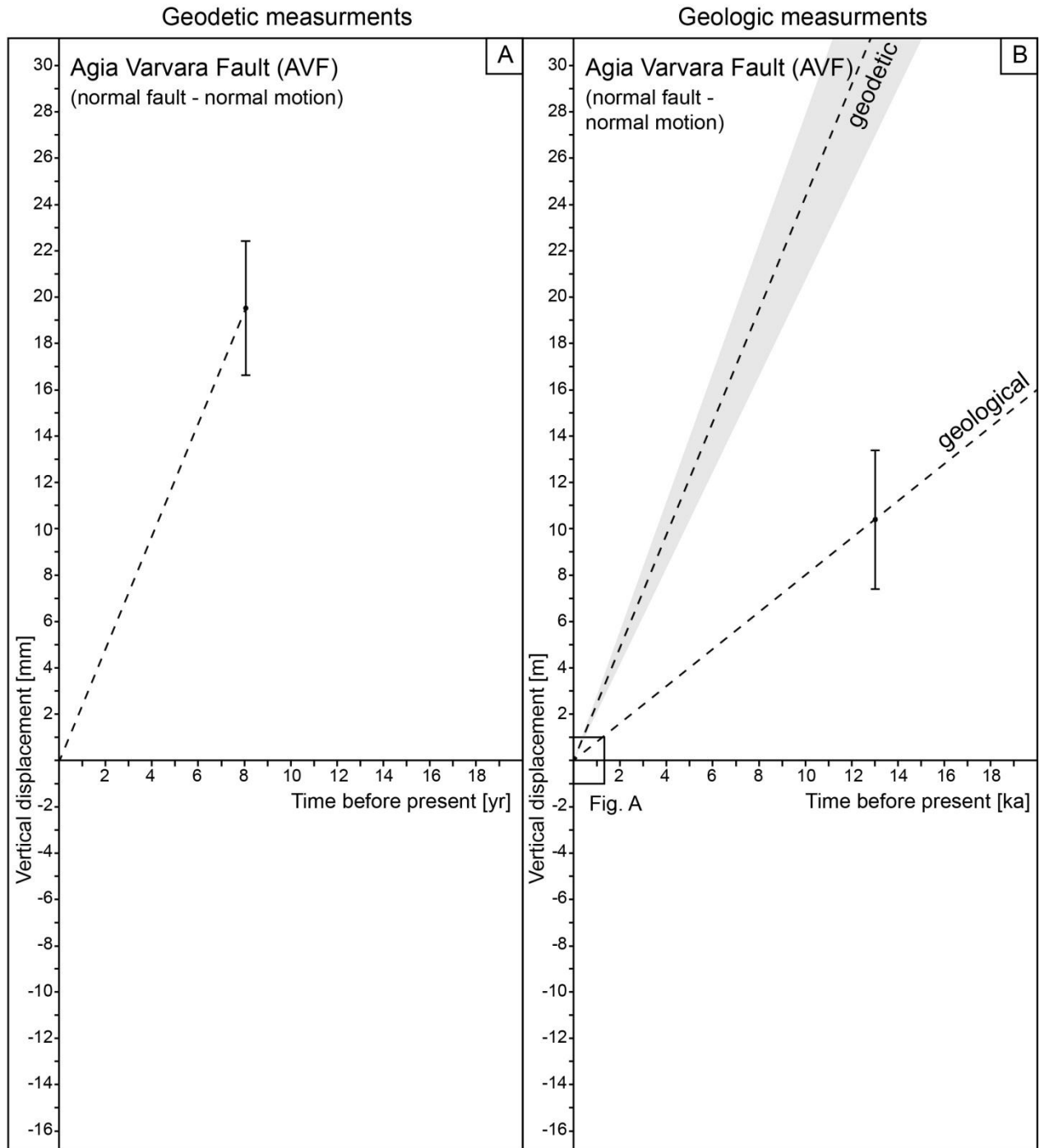


Figure II.3: a) Shows the vertical displacement in mm/yr measured by PSI along the Agia Varvara fault. B) Shows the geodetic measurements versus the geologic slip-rate in ka/m derived from Caputo et al. (2010). The grey shade shows the error range of PSI measurements adjusted to the geological time.

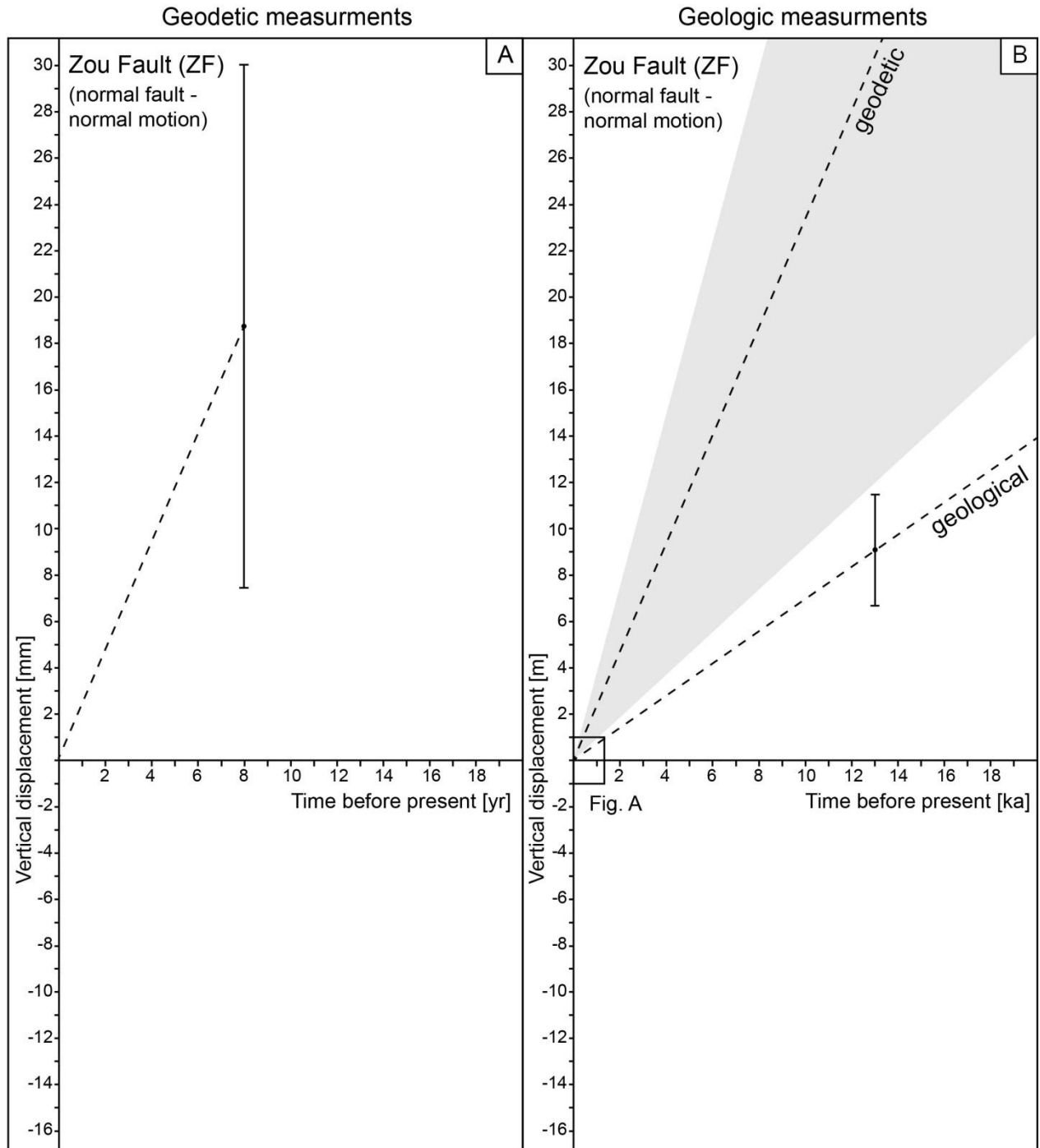


Figure II.4: A) Shows the vertical displacement in mm/yr measured by PSI along the Zou fault. B) Shows the geodetic measurements versus the geologic slip-rate in ka/m derived from Caputo et al. (2010). The grey shade shows the error range of PSI measurements adjusted to the geological time.

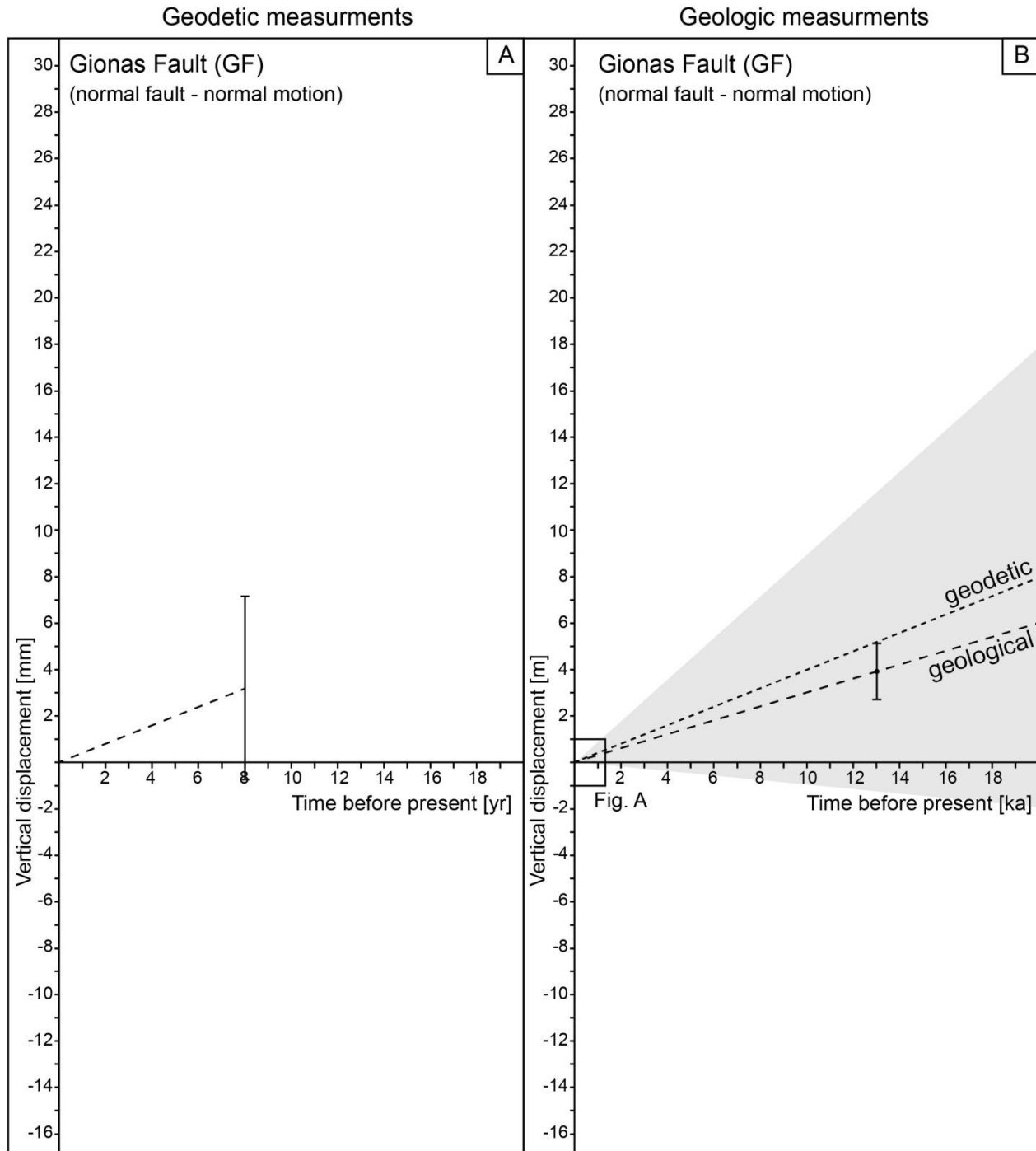


Figure II.5: A) Shows the vertical displacement in mm/yr measured by PSI along the Gionas fault. B) Shows the geodetic measurements versus the geologic slip-rate in ka/m derived from Caputo et al. (2010). The grey shade shows the error range of PSI measurements adjusted to the geological time.

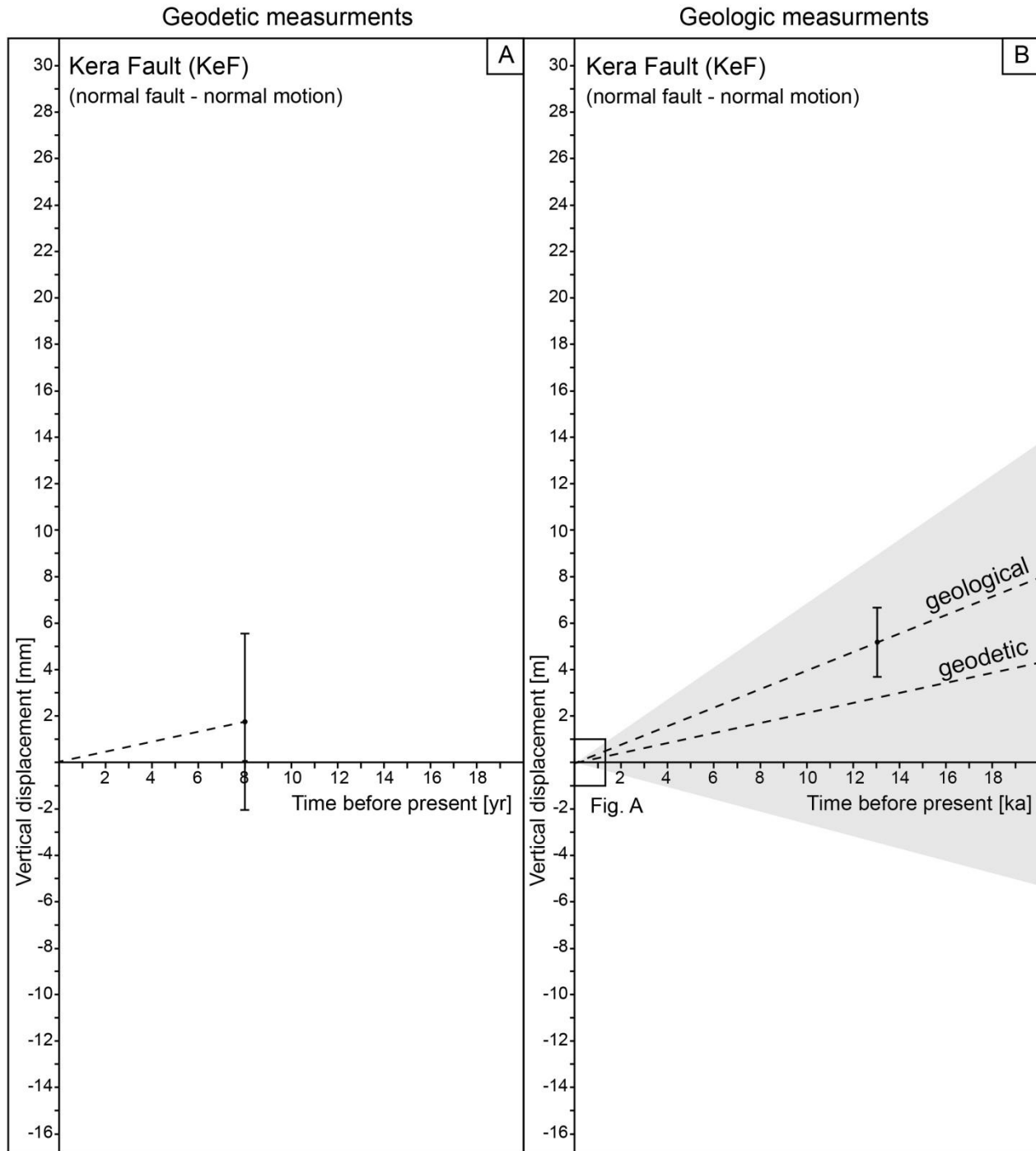


Figure II.6: A) Shows the vertical displacement in mm/yr measured by PSI along the Kera fault. B) Shows the geodetic measurements versus the geologic slip-rate in ka/m derived from Caputo et al. (2010). The grey shade shows the error range of PSI measurements adjusted to the geological time.

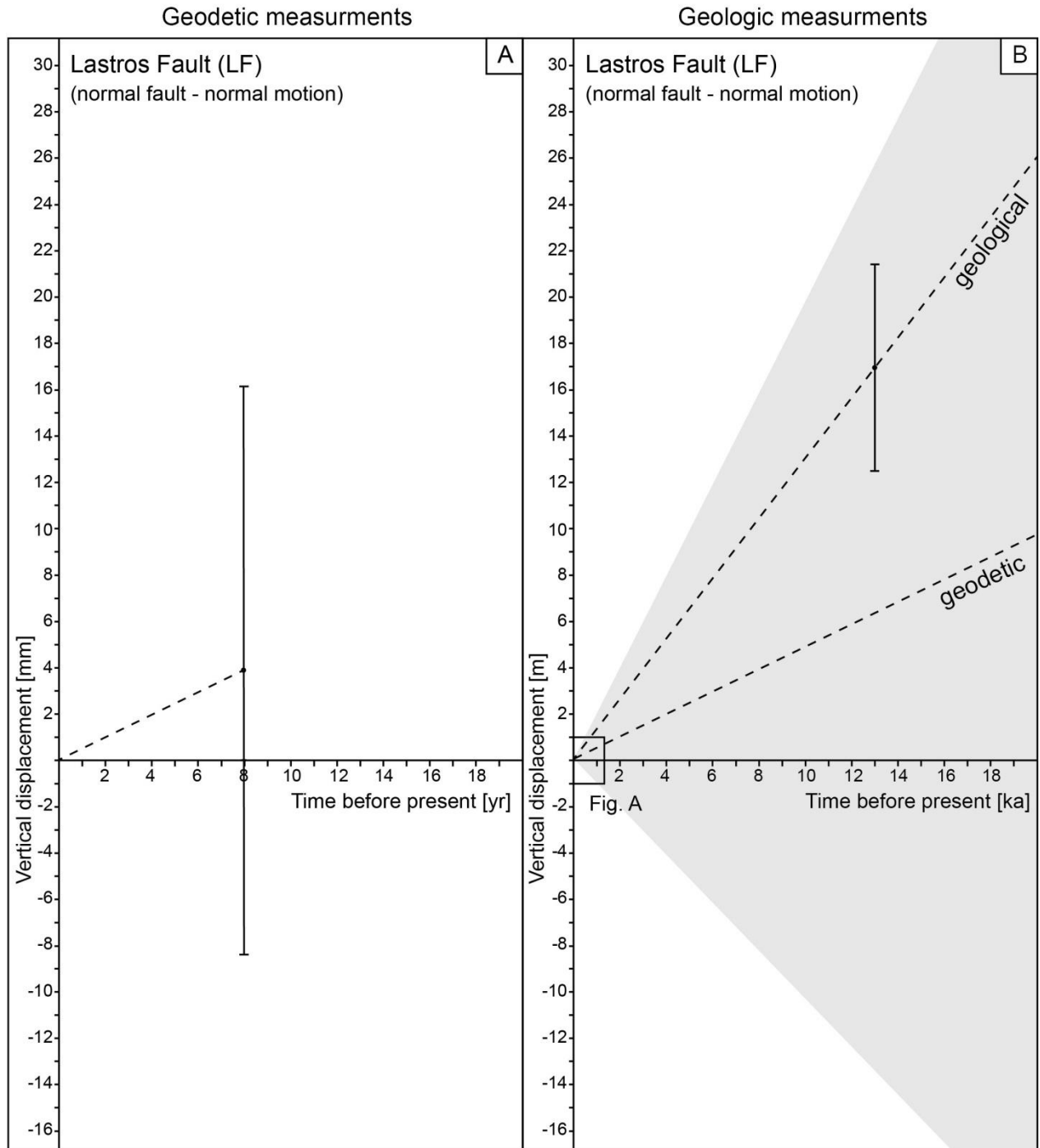


Figure II.7: A) Shows the vertical displacement in mm/yr measured by PSI along the Lastros fault. B) Shows the geodetic measurements versus the geologic slip-rate in ka/m derived from Caputo et al. (2010). The grey shade shows the error range of PSI measurements adjusted to the geological time.

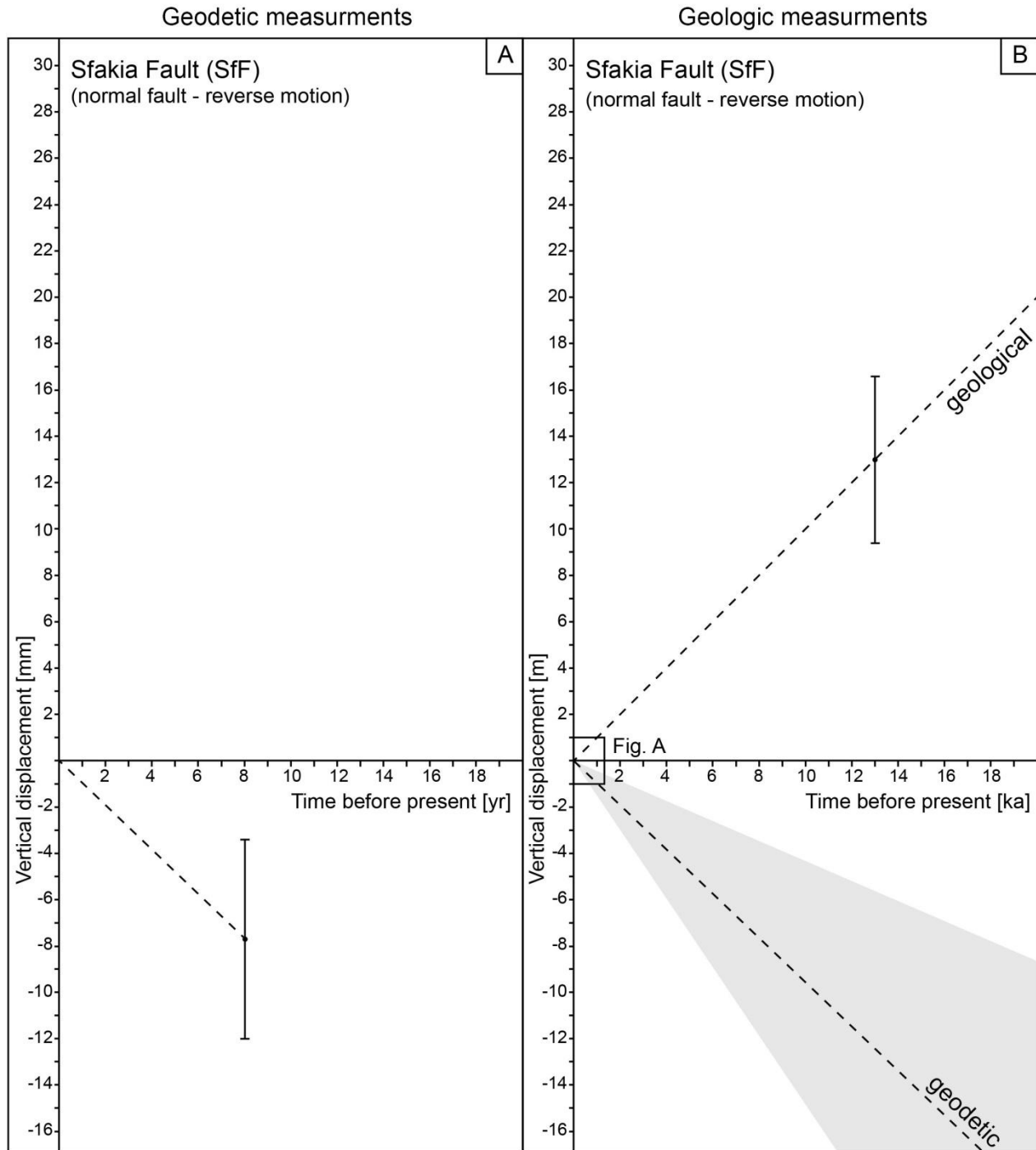


Figure II.8: A) Shows the vertical displacement in mm/yr measured by PSI along the Sfakia fault. B) Shows the geodetic measurements versus the geologic slip-rate in ka/m derived from Caputo et al. (2010). The grey shade shows the error range of PSI measurements adjusted to the geological time.

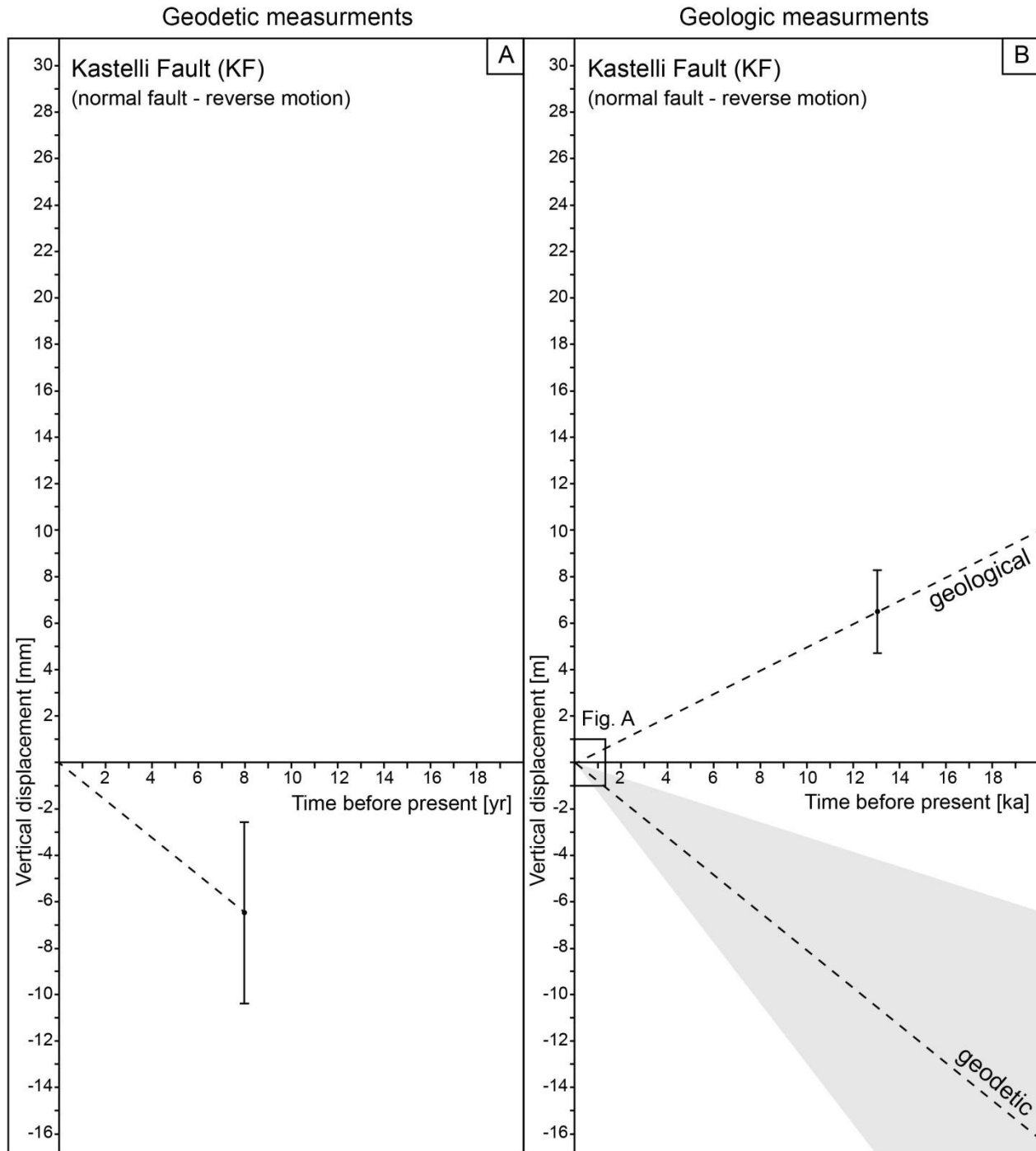


Figure II.9: A) Shows the vertical displacement in mm/yr measured by PSI along the Kastelli fault. B) Shows the geodetic measurements versus the geologic slip-rate in ka/m derived from Caputo et al. (2010). The grey shade shows the error range of PSI measurements adjusted to the geological time.

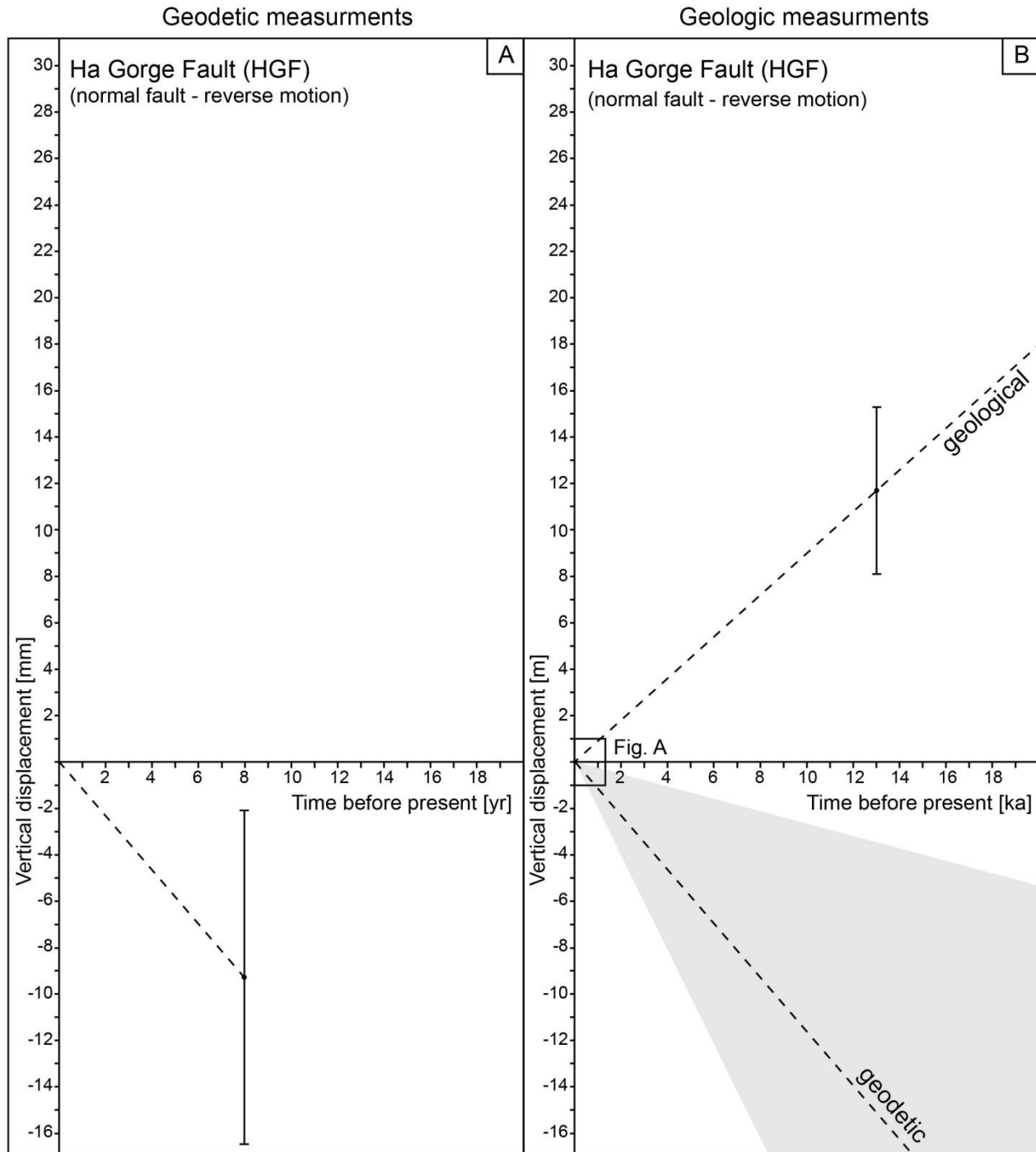


Figure II.10: A) Shows the vertical displacement in mm/yr measured by PSI along the Ha Gorge fault. B) Shows the geodetic measurements versus the geologic slip-rate in ka/m derived from Caputo et al. (2010). The grey shade shows the error range of PSI measurements adjusted to the geological time.

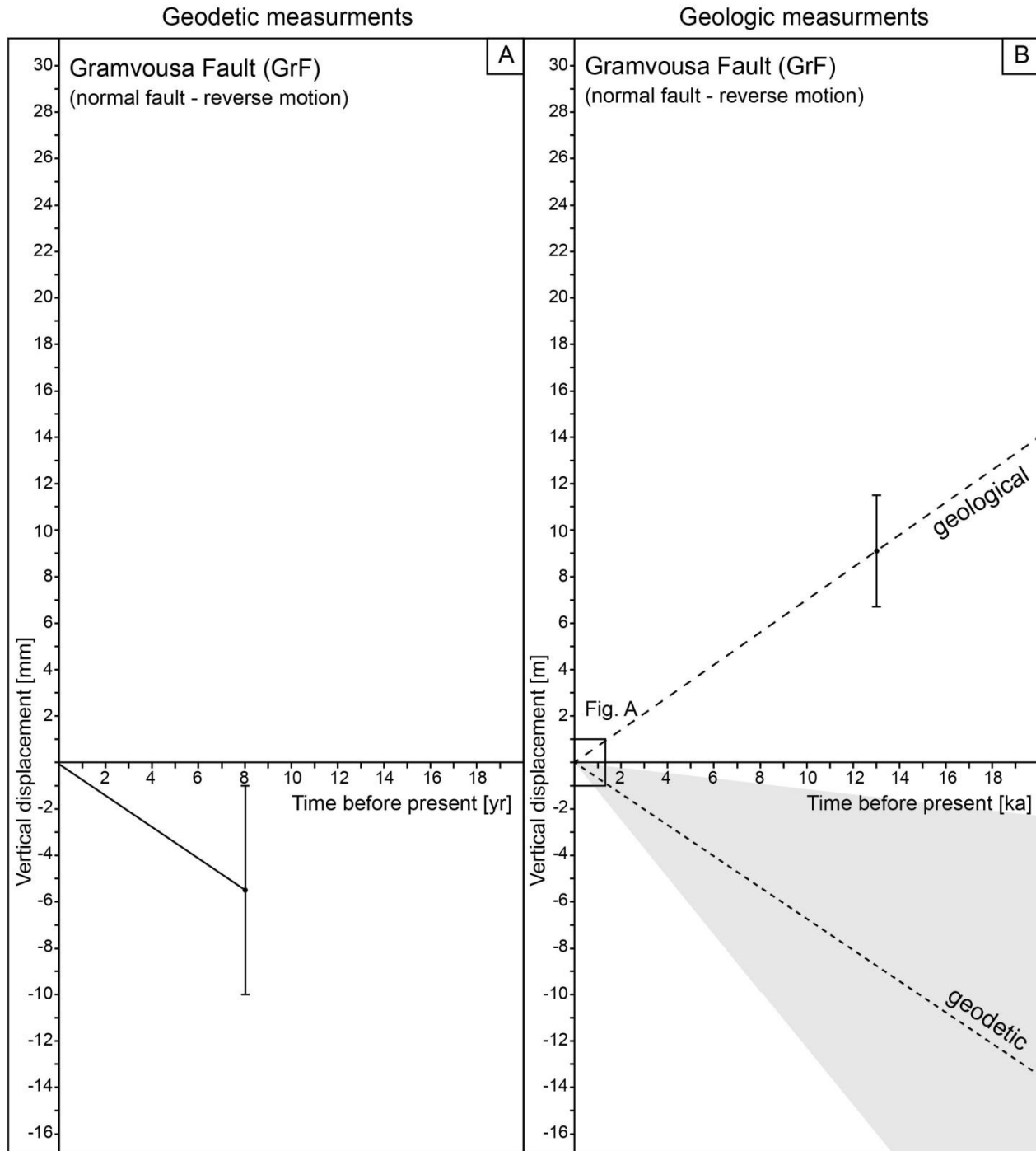


Figure II.11: A) Shows the vertical displacement in mm/yr measured by PSI along the Gramvousa fault. B) Shows the geodetic measurements versus the geologic slip-rate in ka/m derived from Caputo et al. (2010). The grey shade shows the error range of PSI measurements adjusted to the geological time.

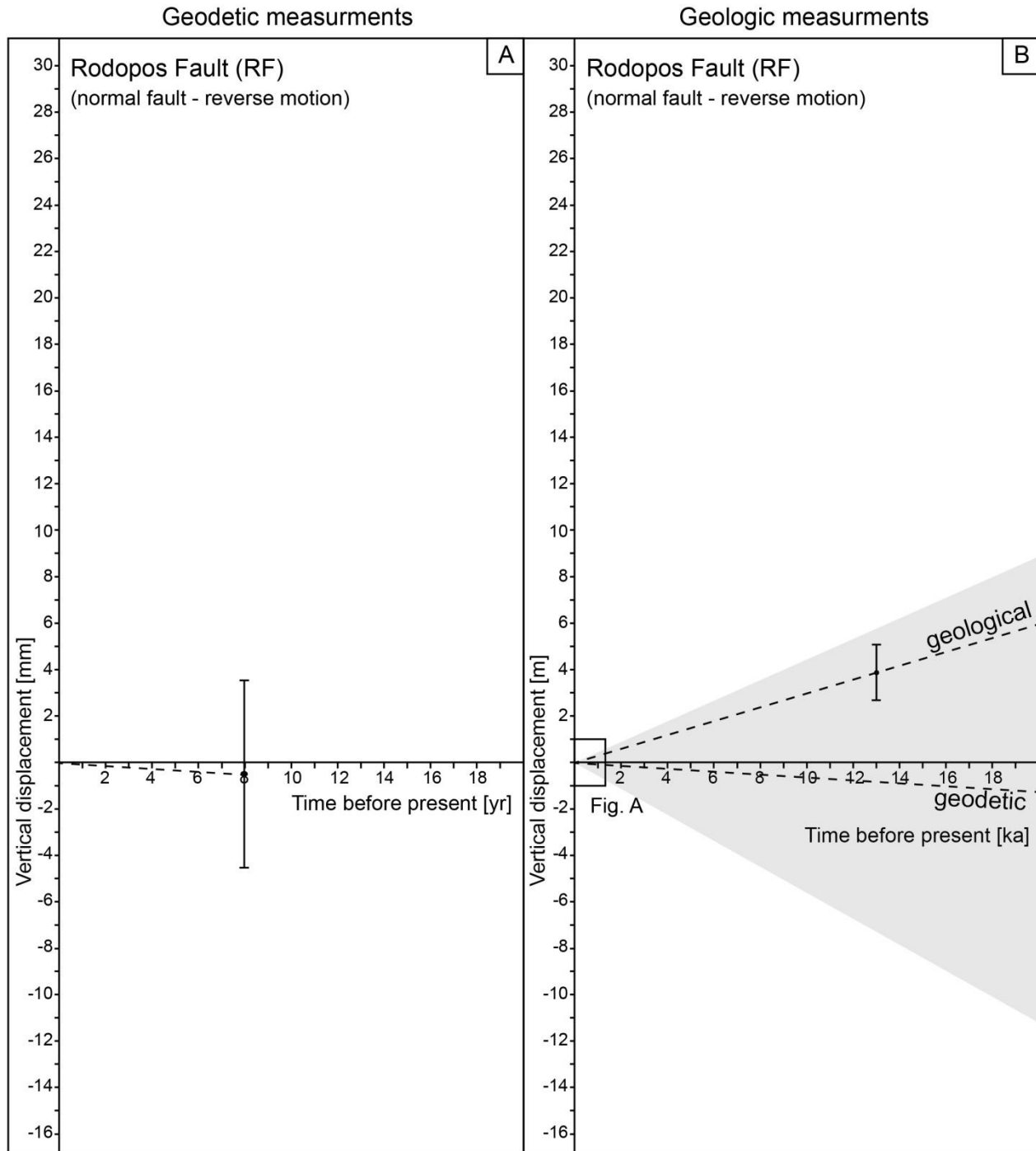


Figure II.12: A) Shows the vertical displacement in mm/yr measured by PSI along the Rodopos fault. B) Shows the geodetic measurements versus the geologic slip-rate in ka/m derived from Caputo et al. (2010). The grey shade shows the error range of PSI measurements adjusted to the geological time.

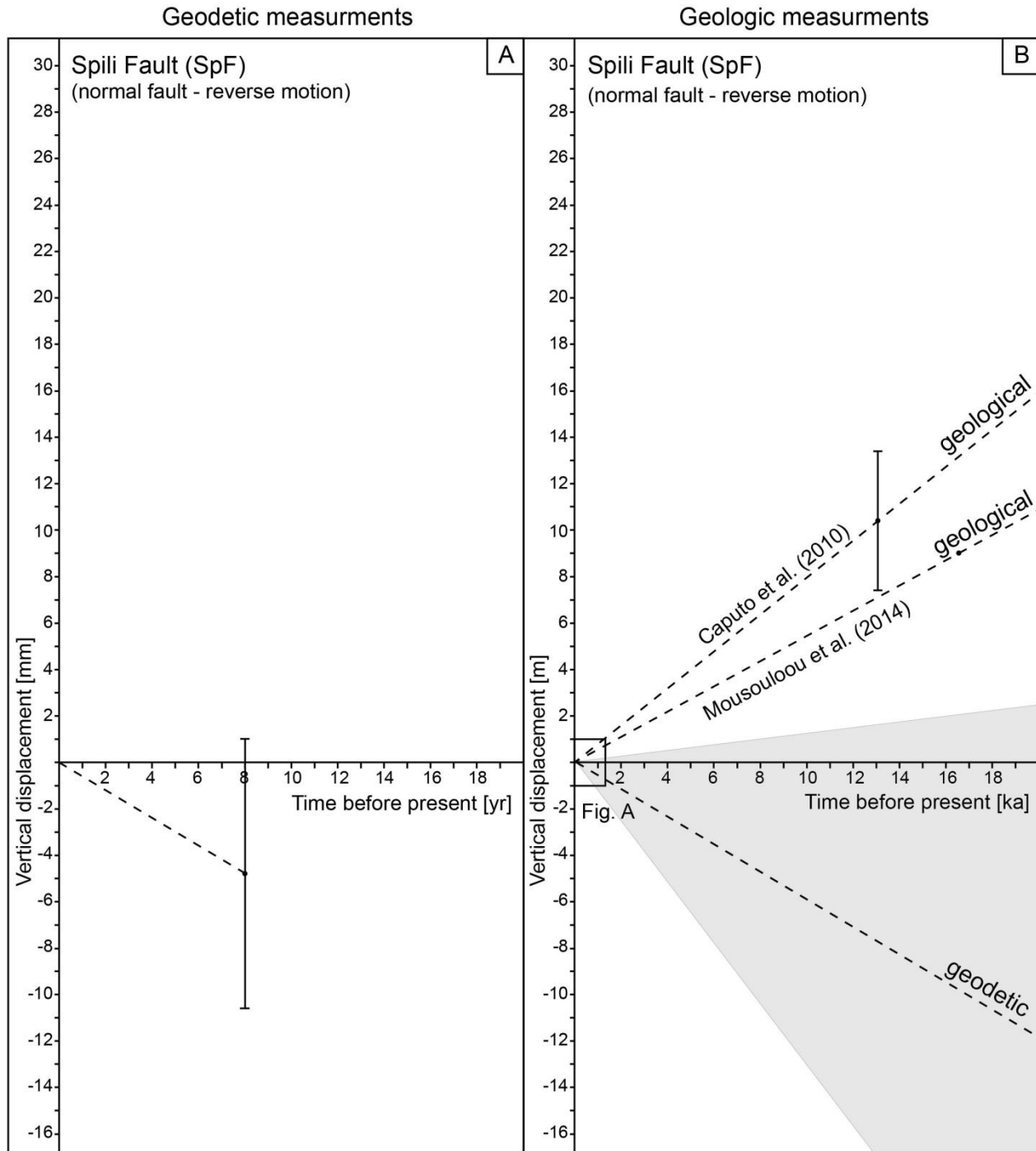


Figure II.13: A) Shows the vertical displacement in mm/yr measured by PSI along the Spili fault. B) Shows the geodetic measurements versus the geologic slip-rate in ka/m derived from Caputo et al. (2010). The grey shade shows the error range of PSI measurements adjusted to the geological time.

Chapter 4

II.1 Pleistocene and Holocene uplift rates based on paleo-shorelines

II.1.1 Ierapetra

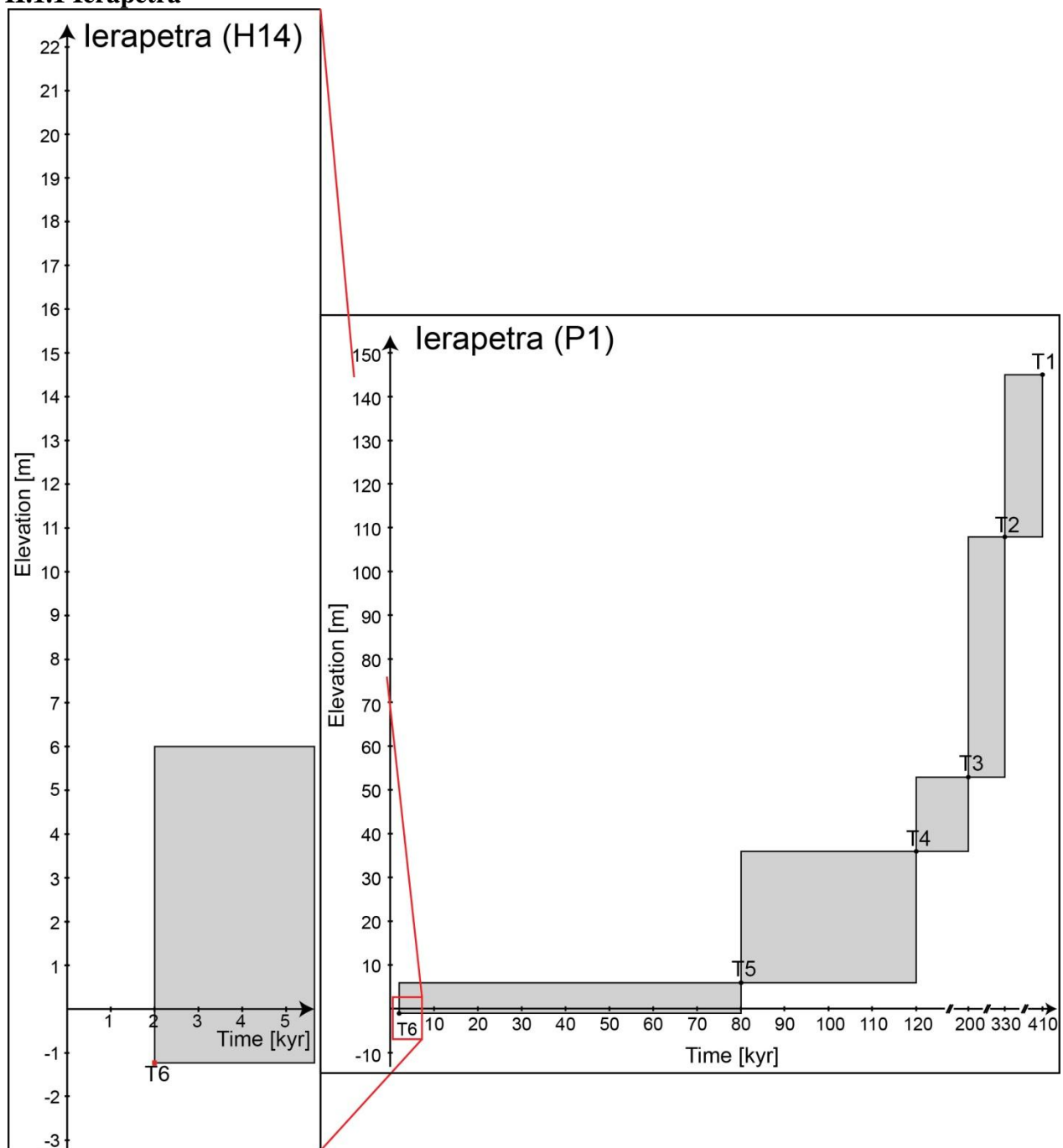


Figure II.14: Elevation of Pleistocene and Holocene palae-shorelines plotted against time, modified after Gaki-Papanastassiou et al. (2009) and Mourtzas (2012).

II.1.1.1 Uplift rates only by tectonics

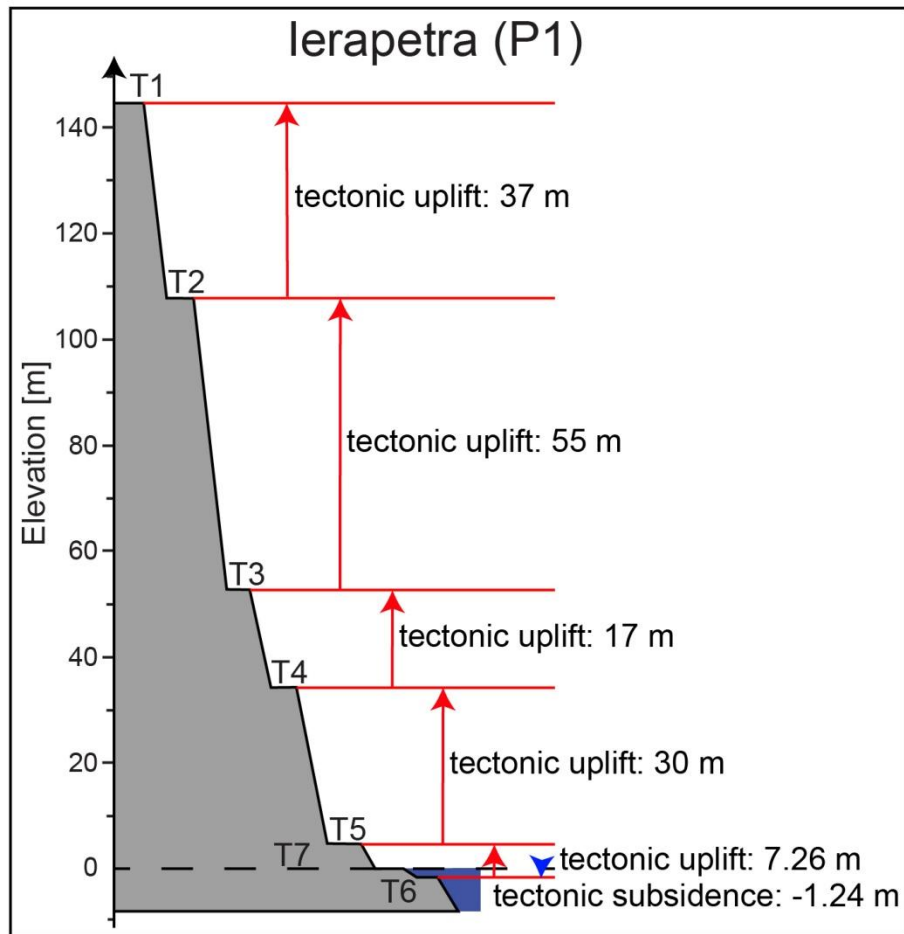


Figure II.15: Elevation of terraces and the height difference needed for the tectonic uplift, modified after Gaki-Papanastassiou et al. (2009) and Mourtzas (2012).

Table II.2: Terraces, their age, present elevation and calculated uplift rate. No sea-level.

Location	Terrace	Time (T) [kyr]	Elevation present E_p [m]	Uplift rate (R) ^e [$\frac{m}{kyr}$]
Ierapetra	T1 ¹	404	145 ^c	0.36
	T2 ¹	327	108 ^c	0.33
	T3 ¹	197	53 ^c	0.27
	T4 ¹	120 ^a	36 ^c	0.3
	T5 ¹	107	6 ^c	0.06
	T6 ²	2 ^b	-1.24 ^d	-0.62

¹Gaki-Papanastassiou et al. (2009); ²Mourtzas (2012)

^aAges taken from my calculations and sea-level curve of Rohling et al. (2014).

^bAges taken from Mourtzas (2012).

^cPresent elevation taken from Gaki-Papanastassiou et al. (2009).

^dPresent elevation taken from Mourtzas (2012).

^eUplift rate calculated using equation: $R = (E_p - E_0) / T$

Table II.3: Average uplift rate, slip rate, and recurrence time.

Average uplift rate (R) [mm/yr]	Slip rate [mm/yr]	Recurrence time [yr]
0.12	0.17	47058.8

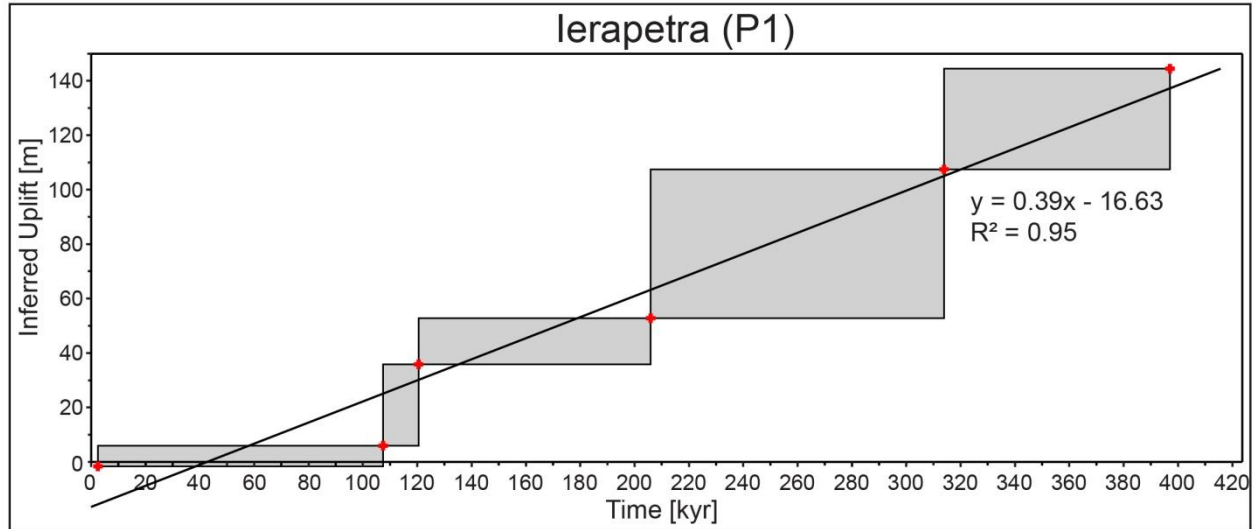


Figure II.16: Inferred uplift diagram curve for tectonic uplift is determined by linear regression analysis.

II.1.1.2 Uplift rates only by sea-level

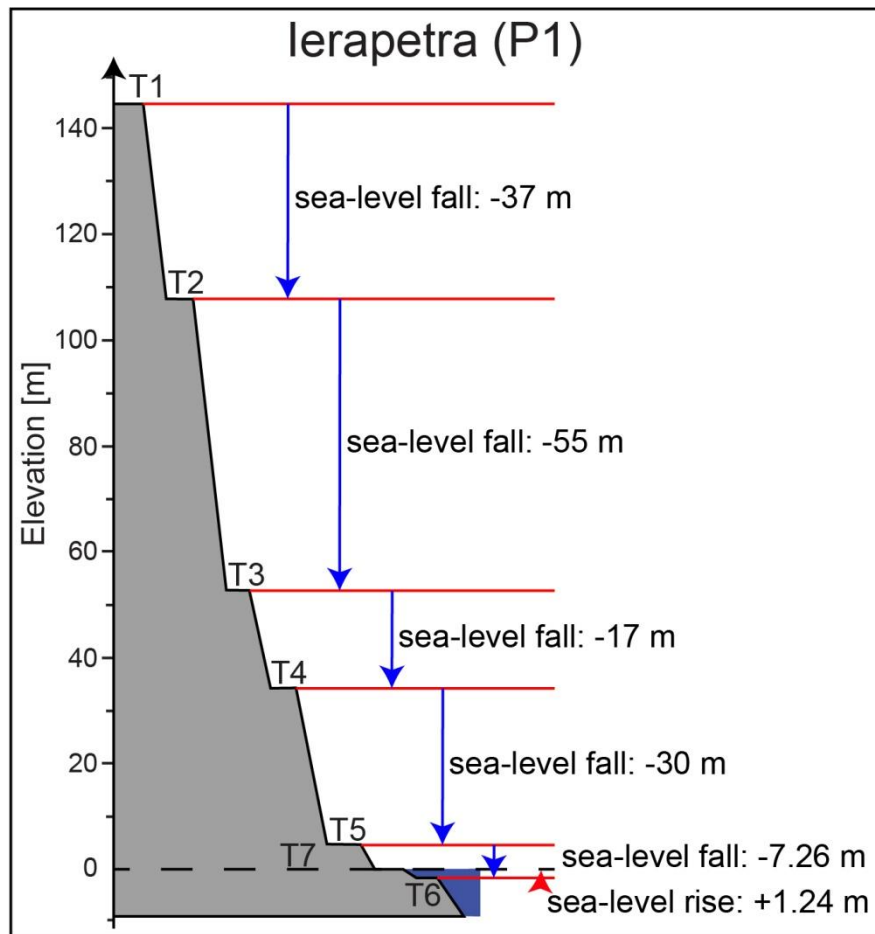


Figure II.17: Elevation of terraces and the needed amount of sea-level fall, modified after Gaki-Papanastassiou et al. (2009) and Mourtzas (2012).

Table II.4: Terraces, their age and calculated age, present elevation and sea-level change rate. No tectonics.

Location	Terrace	Time (T) [kyr]	Elevation present E_p [m]	Sea-level change to lower terrace [m]	Sea-level change rate ^h [$\frac{m}{kyr}$]
Ierapetra	T1 ¹	404 ^a	145 ^d	-37 ^f	0.09
	T2 ¹	327 ^a	108 ^d	-55 ^f	0.17
	T3 ¹	197 ^a	53 ^d	-17 ^f	0.08
	T4¹	120^b	36^d	-30^f	0.25
	T5 ¹	107 ^a	6 ^d	-7.26 ^f	0.07
	T6²	2^c	-1.24^e	+1.24 ^g	0.62
Today shoreline	T7	0	0		

¹Gaki-Papanastassiou et al. (2009); ²Mourtzas (2012)

^aAges taken from my calculations and sea-level curve of Rohling et al. (2014).

^bAges taken from Gaki-Papanastassiou et al. (2009).

^cAges taken from Mourtzas (2012).

^dPresent elevation taken from Gaki-Papanastassiou et al. (2009).

^ePresent elevation taken from Mourtzas (2012).

^fSea-level fall \rightarrow -

^gSea-level rise \rightarrow +

^hSea-level change rate calculated using equation: sea-level change rate = (height change / age)

II.1.1.3 Constant uplift rates by tectonics and sea-level change

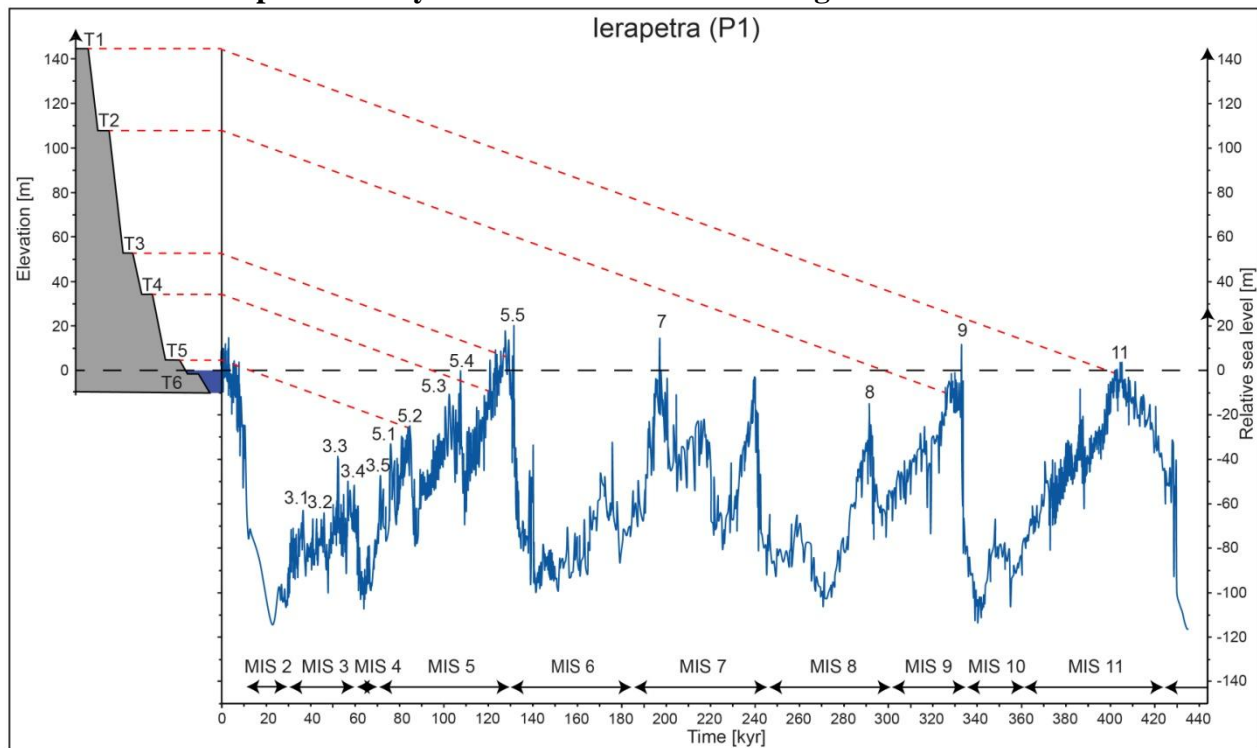


Figure II.18: Correlation of terraces at Ierapetra with the sea-level curve of Rohling et al. (2014), modified after Gaki-Papanastassiou et al. (2009) and Mourtzas (2012).

Table II.5: Ierapetra (P1) terrace numbers, elevation heights, and uplift rates (Rohling et al., 2014).

Location	Terrace	Time (T) [kyr]	Elevation present E_p [m]	Elevation original E_0 [m]	$E_p - E_0$ [m]	Uplift rate (R) ^f [$\frac{m}{kyr}$]	Dated material
Ierapetra	T1 ¹	401	145 ^c	-1±6 ^c	146±6	0.36±0.01	
	T2 ¹	326	108 ^c	-10±6 ^c	118±6	0.36±0.02	
	T3 ¹	128	53 ^c	7±6 ^c	46±6	0.36±0.03	
	T4 ¹	120 ^a	36 ^c	-12.10±6 ^c	48.10±6	0.40±0.05	*
	T5 ¹	83	6 ^c	-26±6 ^c	32±6	0.38±0.06	
	T6 ²	2 ^b	-1.24 ^d	0	-1.24	-0.62	**

Bold terraces are dated terraces.

¹Gaki-Papanastassiou et al. (2009); ²Mourtzas (2012)

^aAges taken from Gaki-Papanastassiou et al. (2009).

^bAges taken from Mourtzas (2012).

^cPresent elevation taken from Gaki-Papanastassiou et al. (2009).

^dPresent elevation taken from Mourtzas (2012).

^eSea-level correction done after Rohling et al. (2014).

^fUplift rate calculated using equation: $R = (E_p - E_0) / T$

*Radiometric dates and associated errors taken from Angelier (1979):

- Radiometric method $^{231}\text{Pa}/^{235}\text{U}$ dated fauna Pectenidae and Callista Chione at altitude 10 m with an age of 109_{-12}^{+22} ka and $130_{-65}^{+\infty}$, respectively

- Radiometric method $^{230}\text{Th}/^{235}\text{U}$ dated fauna Pectenidae at altitude 10 m with an age of 131_{-7}^{+9} and 103_{-6}^{+6} ka and $130_{-65}^{+\infty}$, and Callista Chione at altitude 10 m with an age of 90_{-3}^{+5} ka

**Mourtzas (2012)

Table II.6: Average uplift rate, slip rate, and recurrence time.

Average uplift rate (R) [mm/yr]	Slip rate [mm/yr]	Recurrence time [yr]
41 ± 0.03	0.83 ± 0.04 mm/yr	9368 (+6666.67 / -4761.9)

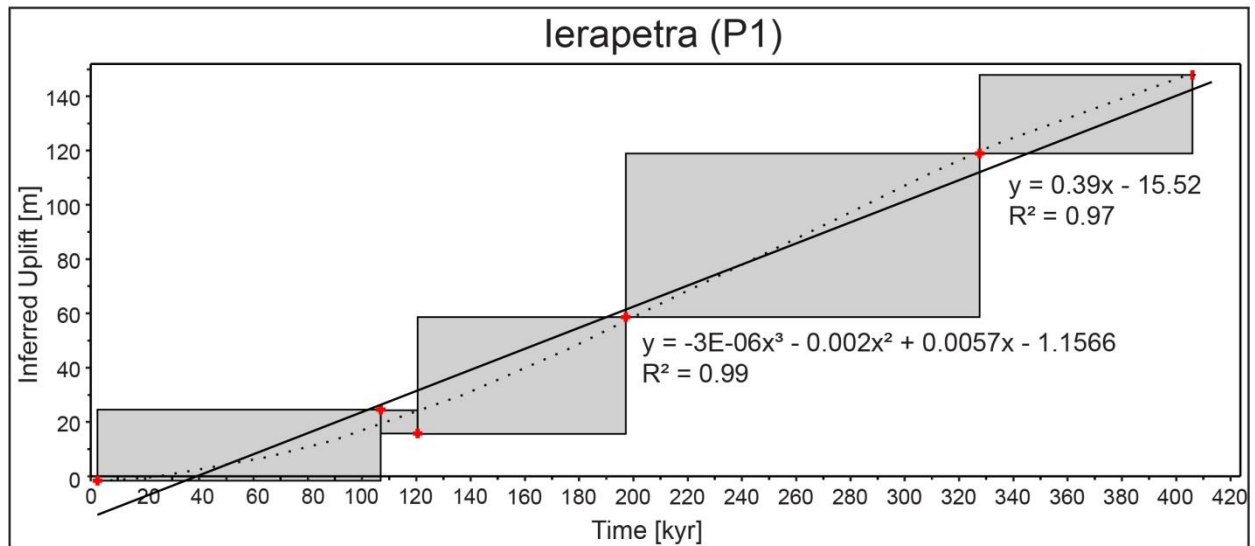


Figure II.19: Inferred uplift diagram curve for sea-level correction is determined by linear regression analysis.

II.1.2 Aradena Gorge

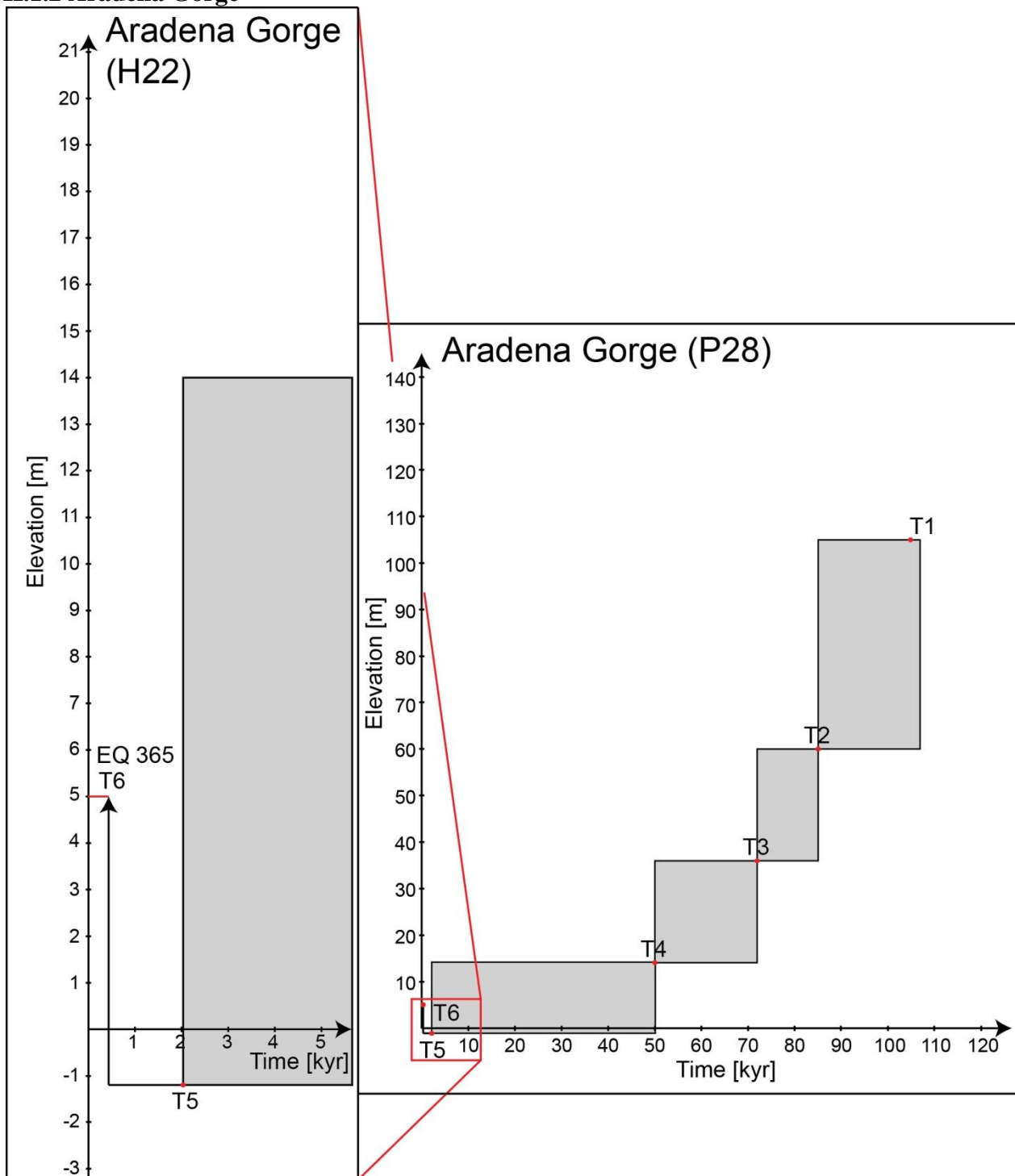


Figure II.20: Elevation of Pleistocene and Holocene palaeo-shorelines plotted against time, modified after Wegmann (2008), Mourtzas (2012), and Pirazzoli et al. (1996). Elevation uncertainties for Pleistocene terraces are ± 1 m (Wegmann, 2008).

II.1.2.1 Uplift rates only by tectonics

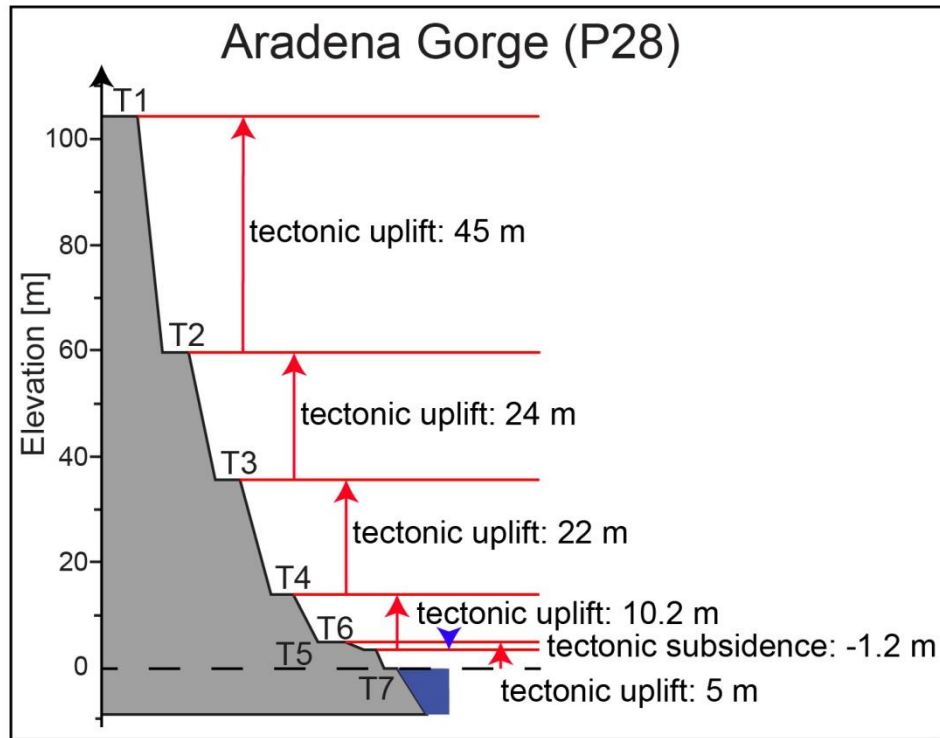


Figure II.21: Elevation of terraces and the height difference needed for the tectonic uplift, modified after Wegmann (2008), Mourtzas (2012), and Pirazzoli et al. (1996).

Table II.7: Terraces, their age, present elevation and calculated uplift rate. No sea-level.

Location	Terrace	Time (T) [kyr]	Elevation present E_p [m]	Uplift rate (R) ^g [$\frac{m}{kyr}$]
Aradena Gorge (P28 & H22)	T1 ¹	107 ^a	105 ^d	0.98
	T2 ¹	85 ^a	60 ^d	0.71
	T3 ¹	72 ^a	36 ^d	0.50
	T4 ¹	50 ^a	14 ^d	-0.28
	T5²	2,05^b	3,8^e	1.85
365 A.D. earthquake	T6³	0.365^c	5^f	13.69

¹Wegmann (2008); ²Mourtzas (2012); ³Pirazzoli et al. (1996)

^aAges taken from Wegmann (2008).

^bAges taken from Mourtzas (2012).

^cAges taken from Pirazzoli et al. (1996).

^dPresent elevation taken from Wegmann (2008).

^ePresent elevation taken from Mourtzas (2012).

^fPresent elevation taken from Pirazzoli et al. (1996).

^gSea-level change rate calculated using equation: sea-level change rate = (height change / age)

Table II.8: Average uplift rate, slip rate, and recurrence time.

Average uplift rate (R) [mm/yr]	Slip rate [mm/yr]	Recurrence time [yr]
0.75	1.5	13333.33

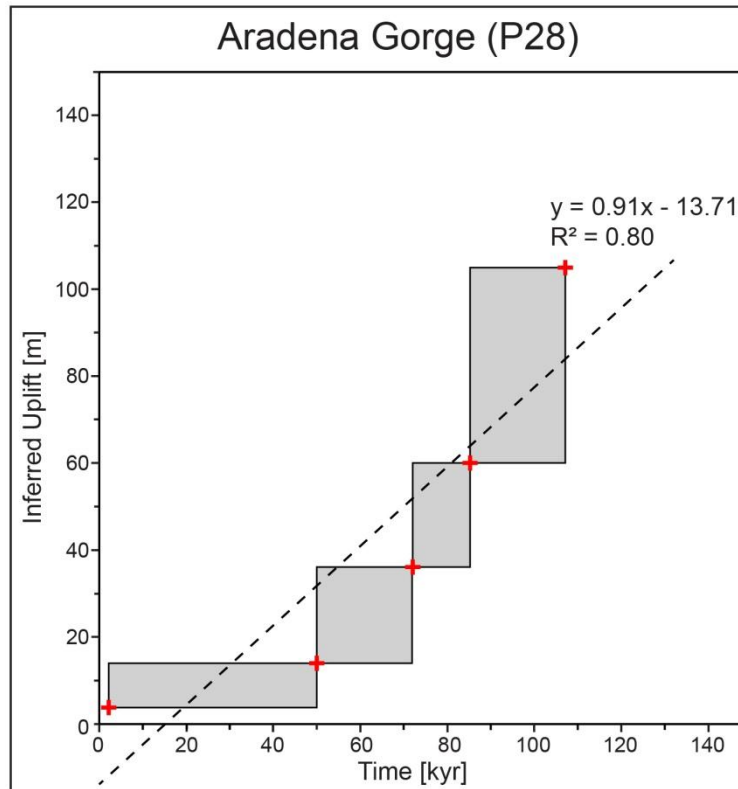


Figure II.22: Inferred uplift diagram curve for tectonic uplift is determined by linear regression analysis.

Table II.9: Displacement between terraces, the corresponding slip, M_0 and M_w .

Terraces	Terrace elevation [m]	Terrace elevation [m]	Displacement between terraces [m]	Corresponding slip along the Hellenic trench [m] ^a	M_0^b [dyne/cm]	M_w^c
T6 – T5	T6 = 5	T5 = 3.8	~1.0	20	$2.7 \cdot 10^{28}$	8.25
T5 – T4	T5 = 3.8	T4 = 14	~10.0	200	$2.7 \cdot 10^{29}$	8.29
T4 – T3	T4 = 14	T3 = 36	22	440	$5.9 \cdot 10^{29}$	9.14
T3 – T2	T3 = 36	T2 = 60	24	480	$6.48 \cdot 10^{29}$	9.17
T2 – T1	T2 = 60	T1 = 105	45	900	$1.21 \cdot 10^{30}$	9.35

^aCorresponding slip along is measured based on the slip of 20 m which equals a vertical displacement of 9 m

^bSeismic Moment: $M_0 = \mu AD$

^cMoment Magnitude: $M_w = \frac{2}{3} \log M_0 - 10.7$

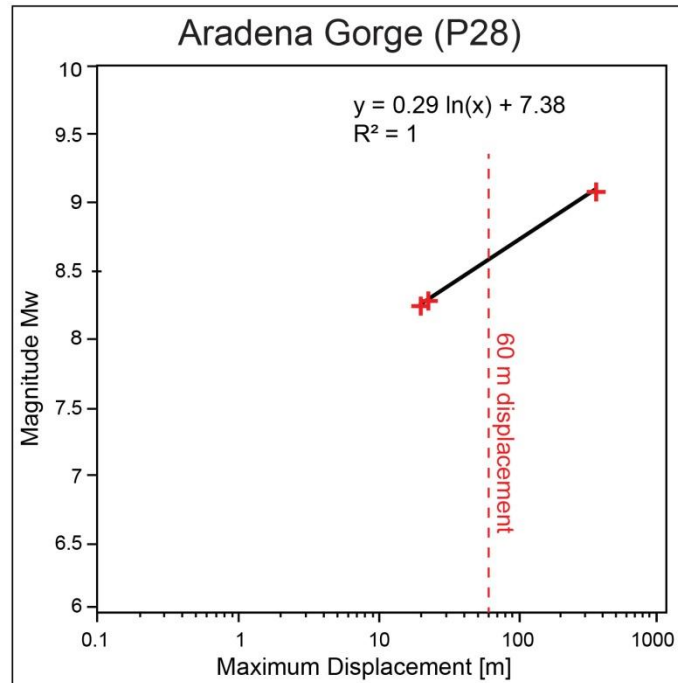


Figure II.23: Regression of maximum displacement versus magnitude Mw. Maximum displacement 60 m ever measured for an earthquake is for the 2011 Mw 9.0 Tohoku-Oki (Japan).

For the 2011 Mw 9.0 Tohoku-Oki (Japan) earthquake the maximum slip is modeled with displacement of around 60 m (Simons et al., 2011). For the 2010 Mw 8.8 Maule (Chile) earthquake the maximum slip reached around 15 m (Vigny et al., 2011). The maximum slip of 15 m was modeled for the 2004 Mw 9.1 Sumatra-Andaman earthquake (Ammon et al., 2005). For the 1960 Mw 9.5 Chile earthquake the maximum slip is on the order of 17 m for a uniform slip planar model, and for a variable slip planar model, representing slip along asperities, the highest peak of slip reached a value of 41 m (Barrientos and Ward, 1990).

II.1.2.2 Uplift rates only by sea-level changes

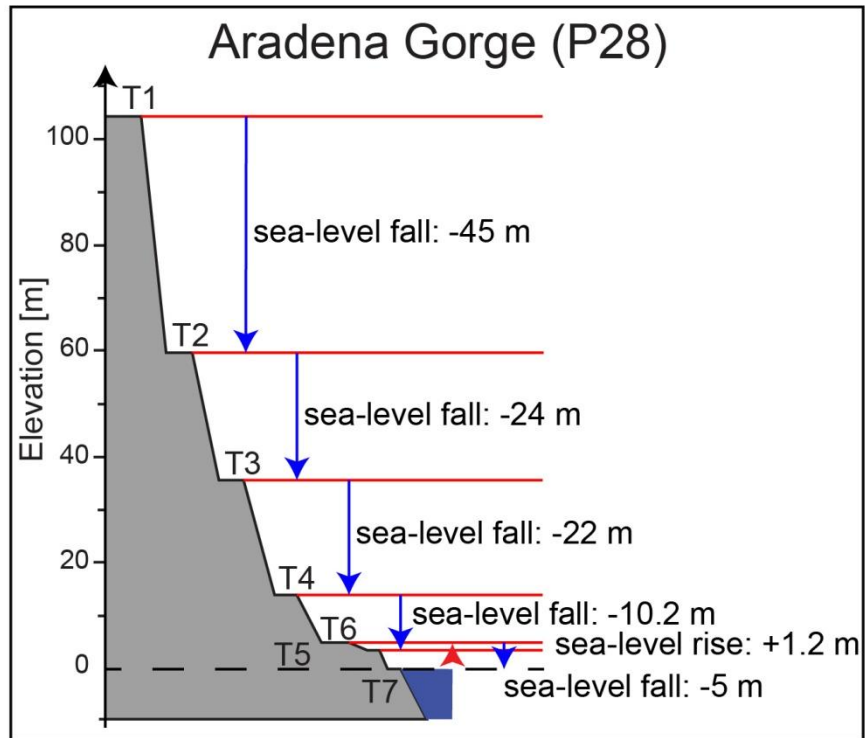


Figure II.24: Elevation of terraces and the needed amount of sea-level fall, modified after Wegmann (2008), Mourtzas (2012), and Pirazzoli et al. (1996).

Table II.10: Terraces, their age and calculated age, present elevation and sea-level change rate. No tectonics.

Location	Terrace	Time (<i>T</i>) [<i>kyr</i>]	Elevation present <i>E_p</i> [m]	Sea-level change to lower terrace [m]	Sea-level change rate ⁱ [$\frac{m}{kyr}$]
Aradena Gorge (P28 & H22)	T1 ¹	107.9 ^a	105 ^d	-45 ^g	0.42
	T2 ¹	84.8 ^a	60 ^d	-24 ^g	0.28
	T3 ¹	71.8 ^a	36 ^d	-22 ^g	0.31
	T4 ¹	52.5 ^a	14 ^d	-10.2 ^g	0.19
	T5²	2.05^b	3.8^e	+1.2^h	0.58
365 A.D. earthquake	T6³	0.365^c	5^f	-5^g	-13.69
Today shoreline	T7	0	0		

¹Wegmann (2008); ²Mourtzas (2012); ³Pirazzoli et al. (1996)

^aAges taken from Wegmann (2008). MIS stages taken and ages corrected after Rohling et al. (2014).

^bAges taken from Mourtzas (2012).

^cAges taken from Pirazzoli et al. (1996).

^dPresent elevation taken from Wegmann (2008).

^ePresent elevation taken from Mourtzas (2012).

^fPresent elevation taken from Pirazzoli et al. (1996).

^gSea-level fall → -

^hSea-level rise → +

ⁱSea-level change rate calculated using equation: sea-level change rate = (height change / age)

II.1.2.3 Uplift rates by tectonics and sea-level change

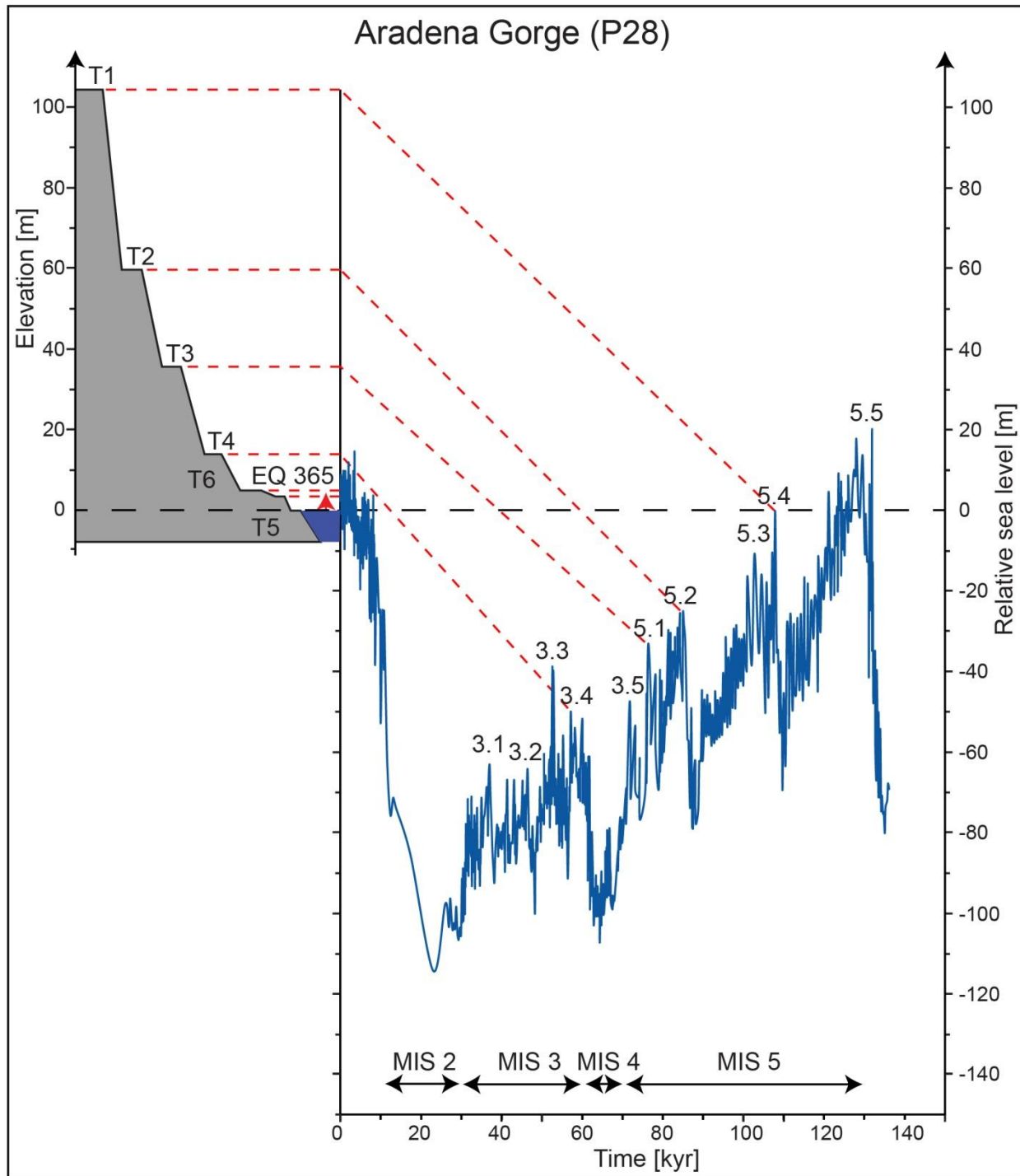


Figure II.25: Correlation of terraces at Aradena Gorge with the sea-level curve of Rohling et al. (2014), modified after Wegmann (2008), Mourtzas (2012), and Pirazzoli et al. (1996).

Table II.11: Terrace numbers, elevation heights, and uplift rates. Sea-level corrected and tectonics (Rohling et al., 2014).

Location	Terrace	Time (T) [kyr]	Elevation present E_p [m]	Elevation original E_0 [m]	$E_p - E_0$ [m]	Uplift rate (R) ^h [$\frac{m}{kyr}$]	Dated material
Aradena Gorge (P28 & H22)	T1 ¹	107.9 ^a	105±1 ^d	-19.50±6 ^g	124.5±6.08	1.15±0.06	*
	T2 ¹	84.8 ^a	60±1 ^d	-47.1±6 ^g	107.1±6.08	1.26±0.07	*
	T3 ¹	71.8 ^a	36±1 ^d	-53.3±6 ^g	89.3±6.08	1.24±0.08	*
	T4 ¹	52.5 ^a	14±1 ^d	-55.8±6 ^g	69.8±6.08	1.33±0.12	**
	T5²	2.05^b	3.8^e	0	3.8	1.85	***
365 A.D. earthquake	T6³	0.365^c	5^f	0	5	13.69	

Bold terraces are dated terraces.

¹Wegmann (2008); ²Mourtzas (2012); Pirazzoli et al. (1996)

^aAges taken from Wegmann (2008). MIS stages taken and ages corrected after Rohling et al. (2014).

^bAges taken from Mourtzas (2012).

^cAges taken from Pirazzoli et al. (1996).

^dPresent elevation taken from Wegmann (2008).

^ePresent elevation taken from Mourtzas (2012).

^fPresent elevation taken from Pirazzoli et al. (1996).

^gSea-level correction done after Rohling et al. (2014).

^hUplift rate calculated using equation: $R = (E_p - E_0) / T$

*Facies relationship for lateral correlation of spatially separated locations are taken from Wegmann (2008): Facies D - Corresponds to clastic pebble-to cobble beach associated with wave-cut erosion notch.

** Facies relationship for lateral correlation of spatially separated locations are taken from Wegmann (2008): Facies A - Corresponds to Algal bioherms and patch reefs along sediment-poor coastline

***Mourtzas (2012)

Table II.12: Average uplift rate, slip rate, and recurrence time.

Average uplift rate (R) [mm/yr]	Slip rate [mm/yr]	Recurrence time [yr]
1.37 ± 0.08	2.74 ± 0.16	7299.27 (+452.67 / -402.72)

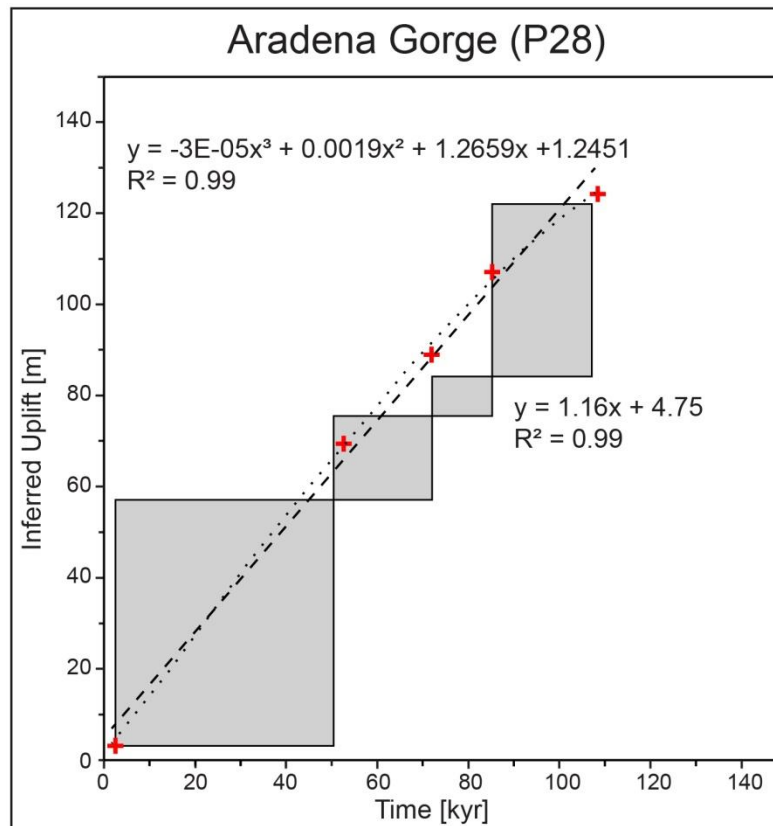


Figure II.26: Inferred uplift diagram curve for tectonic uplift is determined by linear regression analysis.

Table II.13: Average uplift rate, slip rate, recurrence time for the 21st July 365 A.D. earthquake, and total slip for highest and oldest terrace at Aradena Gorge.

Earthquake 21 st July 365 A.D.	Mw	Time interval [kyr]	Average uplift rate [mm/yr]	Slip rate [mm/yr]	Recurrence time [yr]	Total slip for highest and oldest terrace [m]
Aradena Gorge Tectonic only	8.25 ¹	10 ⁷ until today	0.75	1.5	13333.33	160.5
Aradena Gorge Sea-level corrected ³	8.25 ¹	10 ⁷ until today	1.37±0.08	2.74±0.16	7299.27	295.65

¹ Shaw et al. (2008); ² Wegmann (2008); ³ Rohling et al. (2014)

II.1.3 Sougia

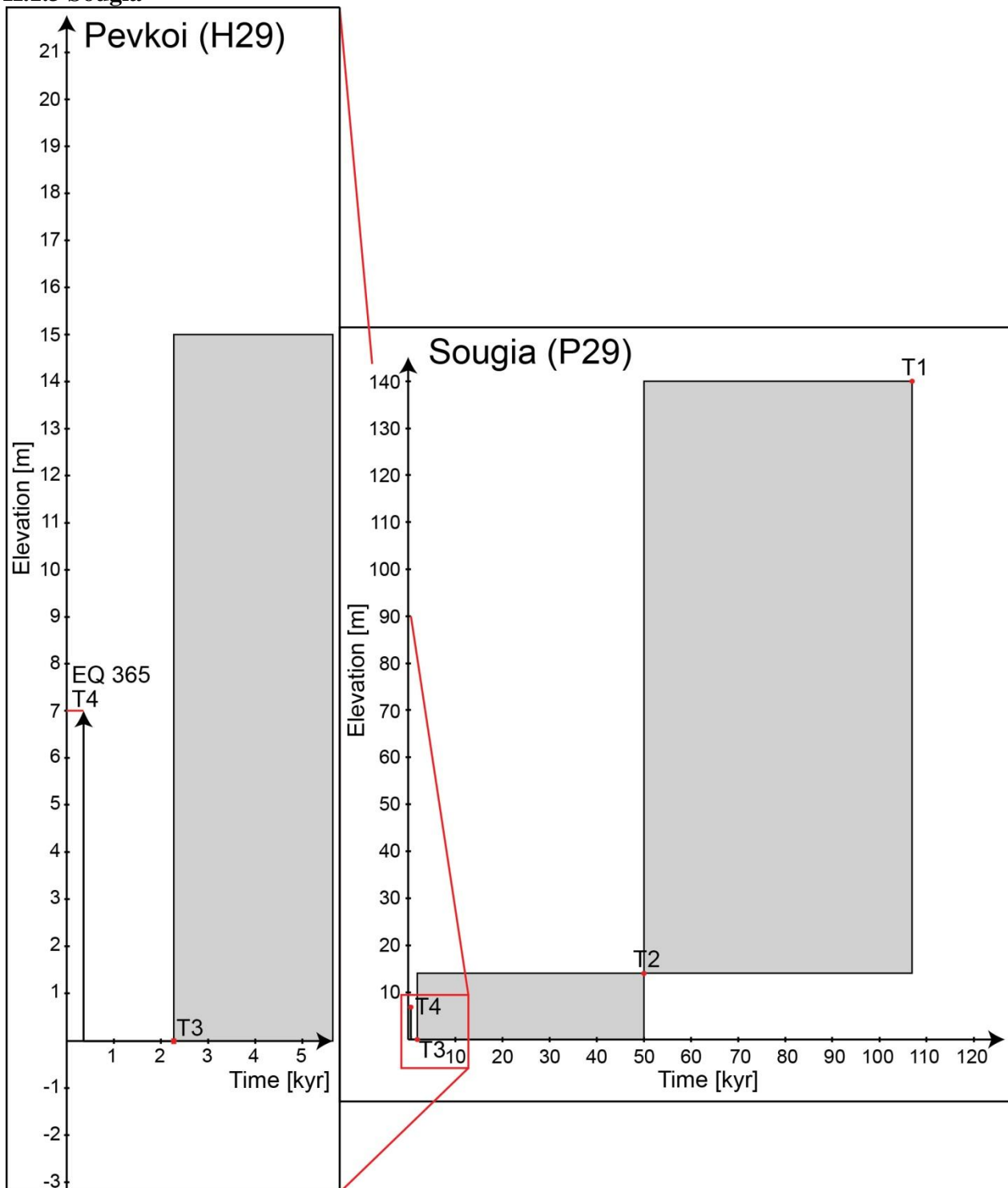


Figure II.27: Elevation of Pleistocene and Holocene palaeo-shorelines plotted against time, modified after Wegmann (2008), Pirazzoli et al. (1996), and Price et al. (2002). Elevation uncertainties for Pleistocene terraces are ± 1 m (Wegmann, 2008).

II.1.3.1 Uplift rates only by tectonics

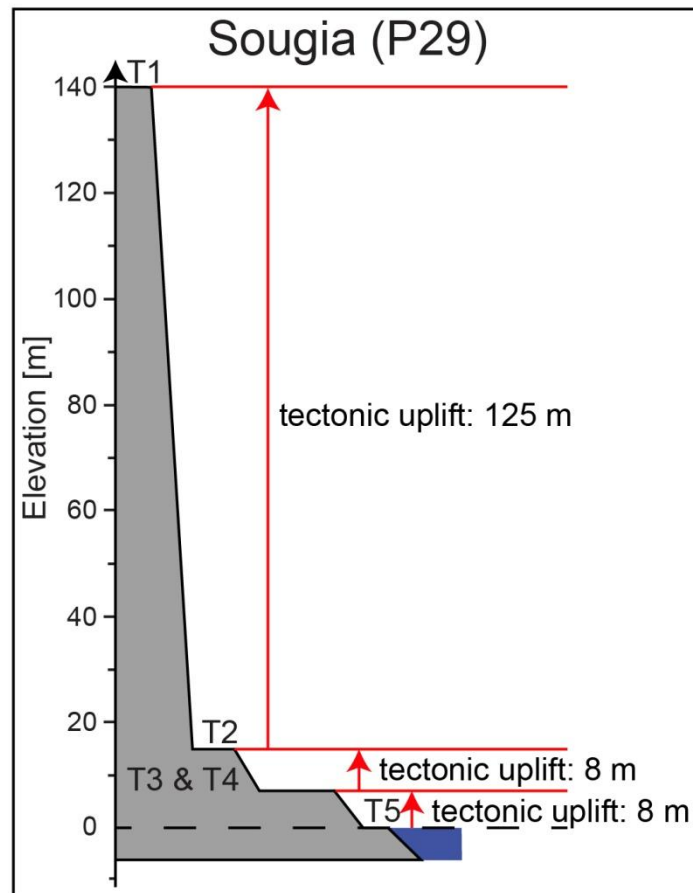


Figure II.28: Elevation of terraces and the height difference needed for the tectonic uplift, modified after Wegmann (2008), Pirazzoli et al. (1996), and Price et al. (2002).

Table II.14: Terraces, their age, present elevation and calculated uplift rate. No sea-level.

Location	Terrace	Time (T) [kyr]	Elevation present E_p [m]	Uplift rate (R) ^h [$\frac{m}{kyr}$]
Sougia (P29 & H29)	T1 ¹	107 ^a	140 ^e	1.31
	T2 ¹	50 ^a	15 ^e	0.30
Pevkoi	T3 ²	2.250 ± 0.07 ^b	7 ^f	3.1 ± 0.23
	T3 ³	2.280 ± 0.073 ^c	7 ^g	3.1 ± 0.23
365 A.D. earthquake	T4 ²	0.365 ^b	7 ^f	19.18

¹Wegmann (2008); ²Pirazzoli et al. (1996); ³Price et al. (2002).

^aAges taken from Wegmann (2008).

^bAges taken from Pirazzoli et al. (1996).

^cAges taken from Price et al. (2002).

^ePresent elevation taken from Wegmann (2008).

^fPresent elevation taken from Pirazzoli et al. (1996).

^gPresent elevation taken from Price et al. (2002).

^hUplift rate calculated using equation: $R = (E_p - E_0) / T$

Table II.15: Average uplift rate, slip rate, and recurrence time.

Average uplift rate (R) [mm/yr]	Slip rate [mm/yr]	Recurrence time [yr]
1.95 ± 0.23	3.9 ± 0.46	5128.21 (+685.74 / -541.05)

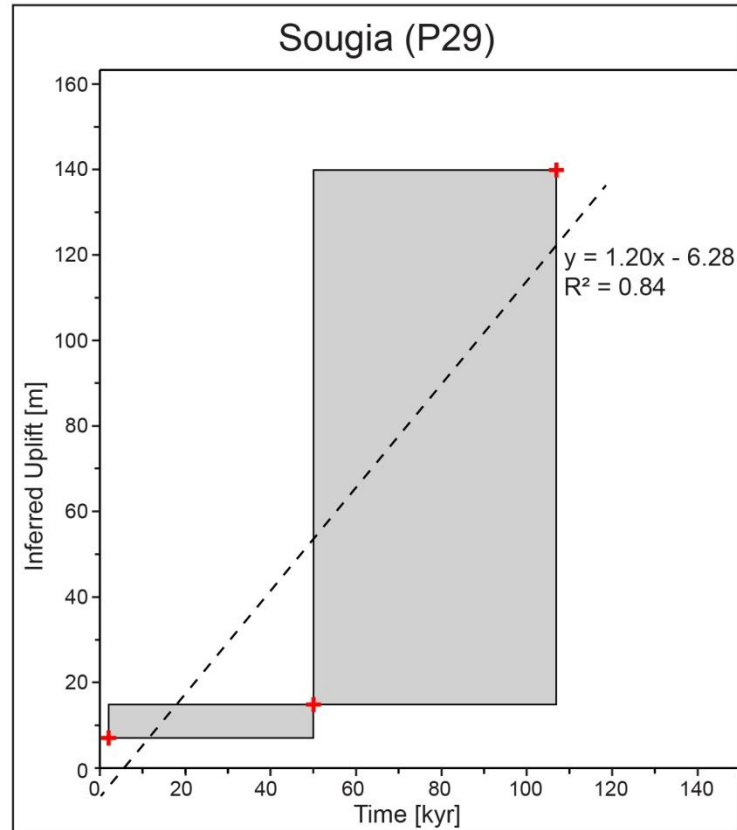


Figure II.29: Inferred uplift diagram curve for tectonic uplift is determined by linear regression analysis.

Table II.16: Displacement between terraces, the corresponding slip, M_0 and M_w .

Terraces	Terrace elevation [m]	Terrace elevation [m]	Displacement between terraces [m]	Corresponding slip along the Hellenic trench [m] ^a	M_0 ^b [dyne/cm]	M_w ^c
T4 – T3	T4 = 7	T3 = 7	0	0	0	0
T3 – T2	T3 = 7	T2 = 15	8	22.86	$3.09 \cdot 10^{28}$	8.29
T2 – T1	T2 = 15	T1 = 140	125	357.12	$4.82 \cdot 10^{29}$	9.09

^aCorresponding slip along is measured based on the slip of 20 m which equals a vertical displacement of 9 m

^bSeismic Moment: $M_0 = \mu AD$

^cMoment Magnitude: $M_w = \frac{2}{3} \log M_0 - 10.7$

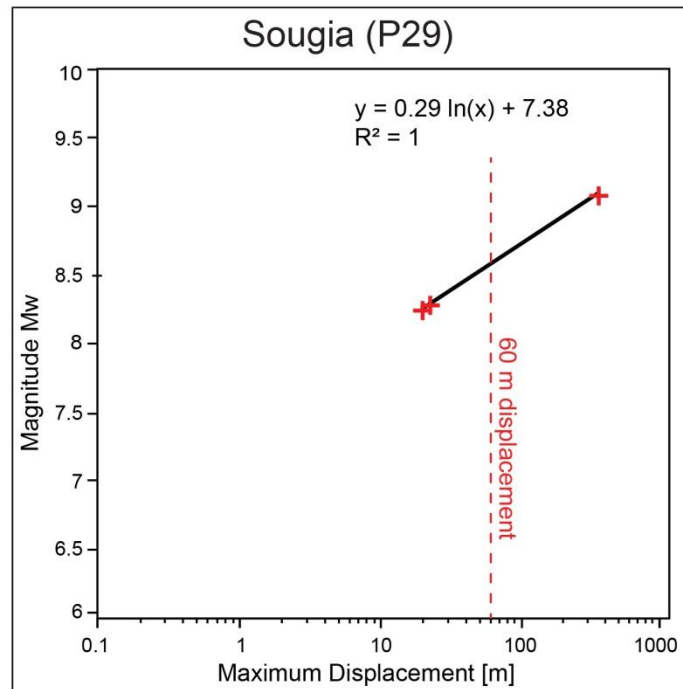


Figure II.30: Regression of maximum displacement versus magnitude Mw. Maximum displacement 60 m ever measured for an earthquake is for the 2011 Mw 9.0 Tohoku-Oki (Japan).

II.1.3.2 Uplift rates only by sea-level changes

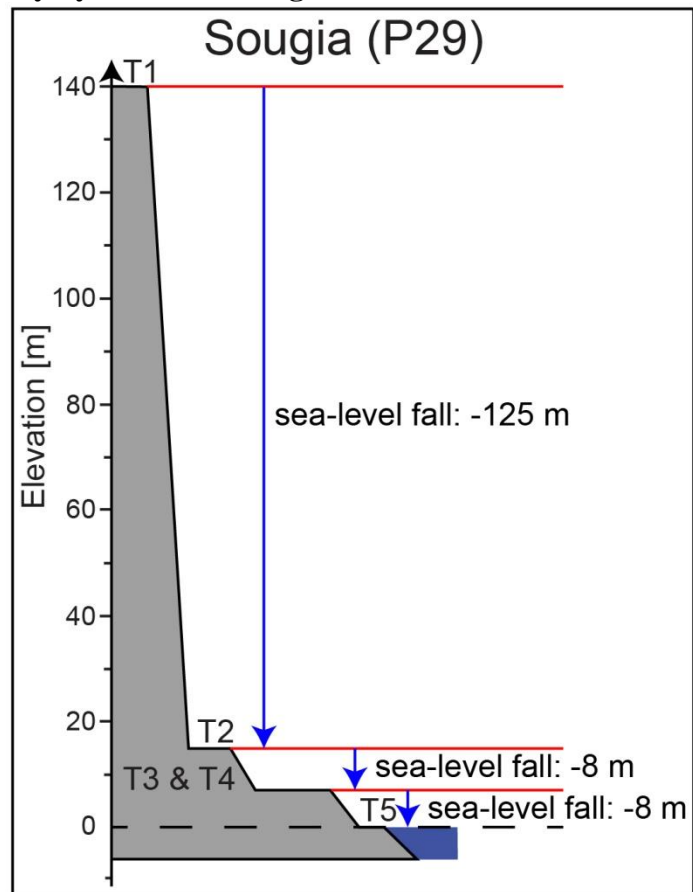


Figure II.31: Elevation of terraces and the needed amount of sea-level fall, modified after Wegmann (2008), Pirazzoli et al. (1996), and Price et al. (2002).

Table II.17: Terraces, their age and calculated age, present elevation and sea-level change rate. No tectonics.

Location	Terrace	Time (T) [kyr]	Elevation present E_p [m]	Sea-level change to lower terrace [m]	Sea-level change rate ^h [$\frac{m}{kyr}$]
Sougia (P29 & H29)	T1 ¹	107.9 ^a	140 ^d	-125 ^g	1.16
	T2 ¹	52.9 ^a	15 ^d	-8 ^g	0.15
Pevkoi	T3 ²	2.250 ± 0.07 ^b	7 ^e	0	0
	T3 ³	2.280 ± 0.073 ^c	7 ^f	0	0
365 A.D. earthquake	T4 ²	0.365 ^b	7 ^e	-7 ^g	19.18
Today shoreline	T5	0	0		

¹Wegmann (2008); ²Pirazzoli et al. (1996); ³Price et al. (2002).

^aAges taken from Wegmann (2008). MIS ages taken and then converted to ages with Rohling et al. (2014)

^bAges taken from Pirazzoli et al. (1996).

^cAges taken from Price et al. (2002).

^dPresent elevation taken from Wegmann (2008).

^ePresent elevation taken from Pirazzoli et al. (1996).

^fPresent elevation taken from Price et al. (2002).

^gSea-level fall → -

^hSea-level change rate calculated using equation: sea-level change rate = (height change / age)

II.1.3.3 Uplift rates by tectonic and sea-level changes

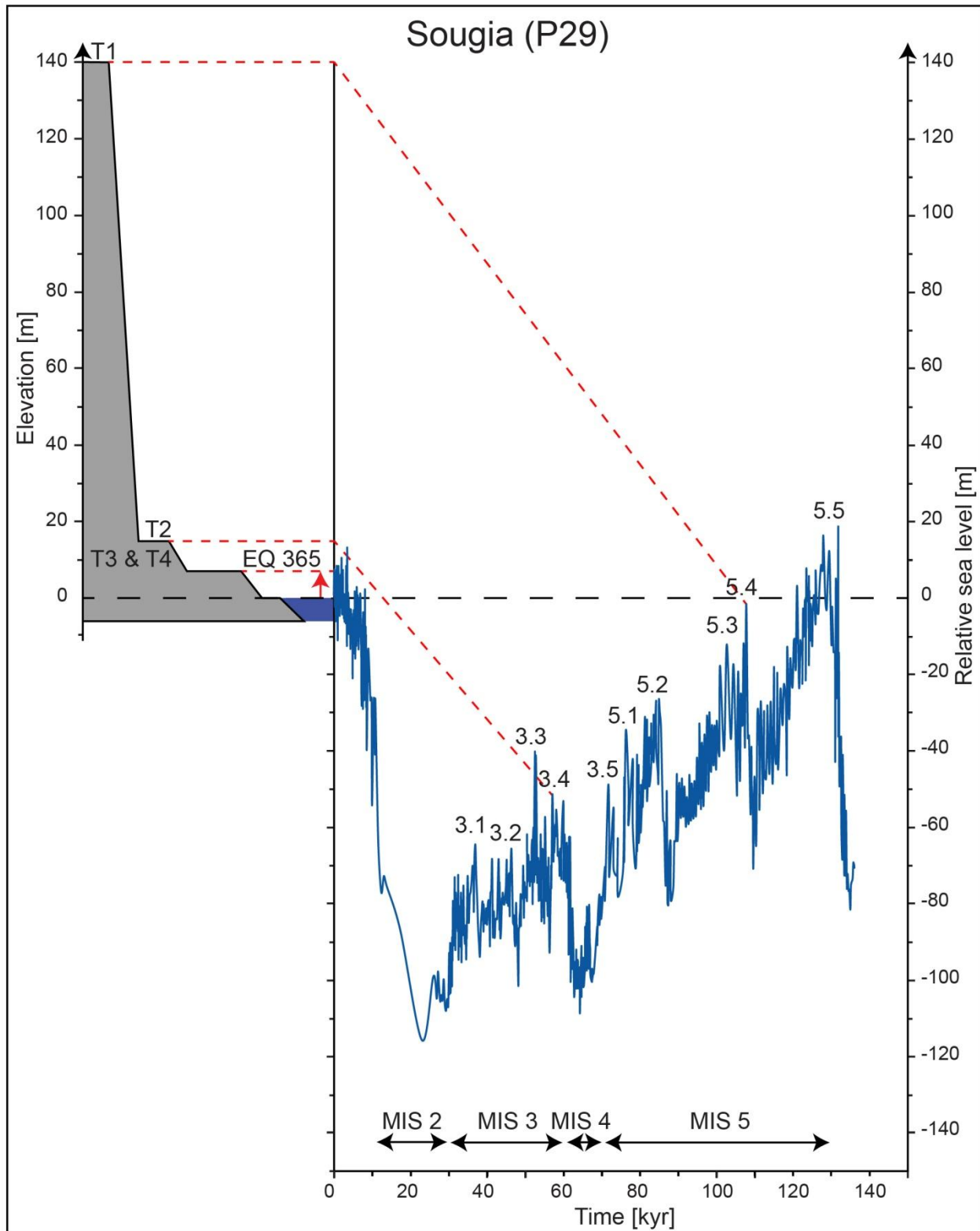


Figure II.32: Correlation of terraces at Sougia with the sea-level curve of Rohling et al. (2014), modified after Wegmann (2008), Pirazzoli et al. (1996), and Price et al. (2002).

Table II.18: Sougia terrace numbers, elevation heights, and uplift rates (Rohling et al., 2014).

Location	Terrace	Time (T) [kyr]	Elevation present E_p [m]	Elevation original E_0 [m]	$E_p - E_0$ [m]	Uplift rate (R) ⁱ [$\frac{m}{kyr}$]	Dated material
Sougia (P29 & H29)	T1 ¹	107.9 ^a	140±1 ^c	-19.50±6 ^h	159±6.08	1.48±0.06	*
	T2 ¹	52.9 ^a	15±1 ^c	-55.8±6 ^h	70.8±6.08	1.35±0.12	*
Pevkoi	T3 ²	2.250 ± 0.07^b	7^f	0	7 ± 0.3	3.1 ± 0.23	**
	T3 ³	2.280 ± 0.073^c	7^g	0	7 ± 0.3	3.1 ± 0.23	***
365 A.D. earthquake	T4 ²	0.365^b	7^f	0	7	19.18	

Bold terraces are dated terraces.

¹Wegmann (2008); ²Pirazzoli et al. (1996); ³Price et al. (2002).

^aAges taken from Wegmann (2008). MIS ages taken and then converted to ages with Rohling et al. (2014)

^bAges taken from Pirazzoli et al. (1996).

^cAges taken from Price et al. (2002).

^ePresent elevation taken from Wegmann (2008).

^fPresent elevation taken from Pirazzoli et al. (1996).

^gPresent elevation taken from Price et al. (2002).

^hSea-level correction done after Rohling et al. (2014).

ⁱUplift rate calculated using equation: $R = (E_p - E_0) / T$

*Facies relationship for lateral correlation of spatially separated locations are taken from Wegmann (2008): Facies D - Corresponds to clastic pebble-to cobble beach associated with wave-cut erosion notch.

**Radiocarbon date ¹⁴C of Dendropoma (Novastoa) petraeum by Pirazzoli et al (1996). Calculated using a reservoir effect of 320 ± 25 years for the Mediterranean.

*** Radiocarbon date ¹⁴C of Dendropoma by Price et al (2002). Corrected the original radiocarbon dates (BP) by adding 430 ¹⁴C years to each.

Table II.19: Average uplift rate, slip rate, and recurrence time.

Average uplift rate (R) [mm/yr]	Slip rate [mm/yr]	Recurrence time [yr]
2.26 ± 0.16	4.52 ± 0.32	4424.78 (+337.12 / -292.55)

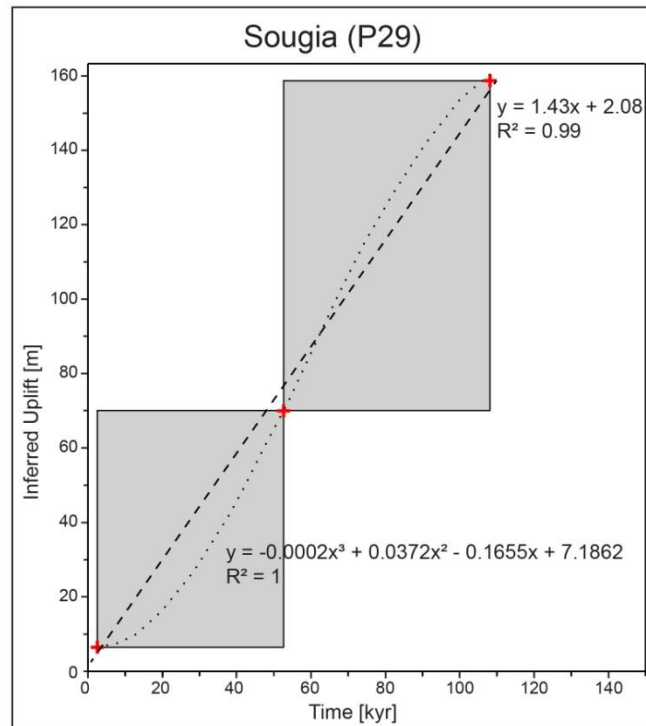


Figure II.33: Inferred uplift diagram curve for sea-level correction is determined by linear regression analysis.

Table II.20: Average uplift rate, slip rate, recurrence time for the 21st July 365 A.D. earthquake, and total slip for highest and oldest terrace at Sougia.

Earthquake 21 st July 365 A.D.	Mw	Time interval [kyr]	Average uplift rate [mm/yr]	Slip rate [mm/yr]	Recurrence time [yr]	Total slip for highest and oldest terrace [m]
Sougia Tectonic only	8.25 ¹	107 ² until today	1.95	3.9	5128.21	417.3
Sougia Constant Sea-level corrected ³	8.25 ¹	107 ² until today	2.26±0.16	4.52±0.32	4424.78	487.71

¹ Shaw et al. (2008); ²Wegmann (2008); ³Rohling et al. (2014)

II.1.4 Kalamia

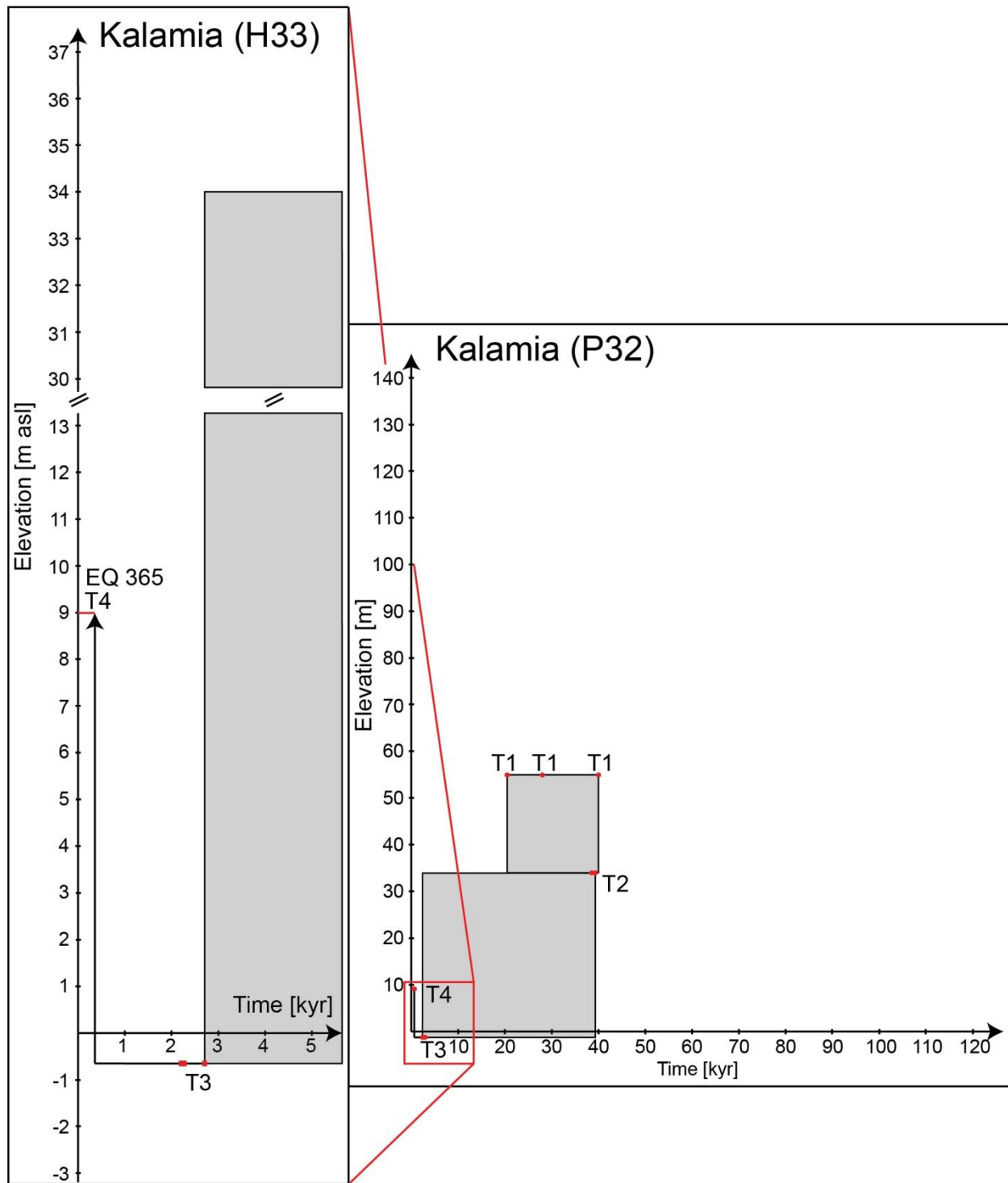


Figure II.34: Elevation of Pleistocene and Holocene palaeo-shorelines plotted against time, modified after Tibert et al. (2014), and Pirazzoli et al. (1996).

II.1.4.1 Uplift rates only by tectonics

Table II.21: Terraces, their age, present elevation and calculated uplift rate. No sea-level.

Location	Terrace	Time (T) [kyr]	Elevation present E_p [m]	Uplift rate (R) ^e [$\frac{m}{kyr}$]
Kalamia (P32 & H33)	T1 ¹	26.93 ± 0.0002^a	55 ^c	2.04
		19.48 ± 0.00009^a	55 ^c	2.82
		39.19 ± 0.0004^a	55 ^c	1.40
	T2 ¹	37.53 ± 0.33^a	34 ^c	0.91
		38.25 ± 0.38^a	34 ^c	0.89
	T3 ¹	2.710 ± 0.00004^a	8.34 ^c	3.08
		2.260 ± 0.00004^a	8.34 ^c	3.69
		2.190 ± 0.00004^a	8.34 ^c	3.80
	365 A.D. earthquake	T4 ²	0.365 ^b	9 ^d

¹Tiberti et al. (2014); ²Pirazzoli et al. (1996)

^aAges taken from Tiberti et al. (2014).

^bAges taken from Pirazzoli et al. (1996).

^cPresent elevation taken from Tiberti et al. (2014).

^dPresent elevation taken from Pirazzoli et al. (1996).

^eUplift rate calculated using equation: $R = (E_p - E_0) / T$

Table II.22: Average uplift rate, slip rate, and recurrence time.

Average uplift rate (R) [mm/yr]	Slip rate [mm/yr]	Recurrence time [yr]
2.33	4.66	4291.8

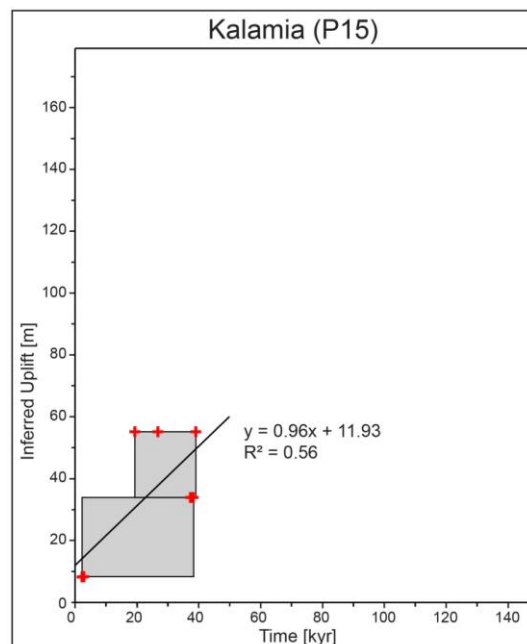


Figure II.35: Inferred uplift diagram curve for tectonic uplift is determined by linear regression analysis.

Table II.23: Displacement between terraces, the corresponding slip, M_0 and M_w .

Terraces	Terrace elevation [m]	Terrace elevation [m]	Displacement between terraces [m]	Corresponding slip along the Hellenic trench [m] ^a	M_0^b [dyne/cm]	M_w^c
T4 – T3	T4 = 9	T3 = 8.34	0.66	1.47	$1.98 \cdot 10^{27}$	7.5
T3 – T2	T3 = 8.34	T2 = 34	25.66	57.02	$7.7 \cdot 10^{28}$	8.56
T2 – T1	T2 = 34	T1 = 55	21	46.67	$6.3 \cdot 10^{28}$	8.47

^aCorresponding slip along is measured based on the slip of 20 m which equals a vertical displacement of 9 m

^bSeismic Moment: $M_0 = \mu AD$

^cMoment Magnitude: $M_w = \frac{2}{3} \log M_0 - 10.7$

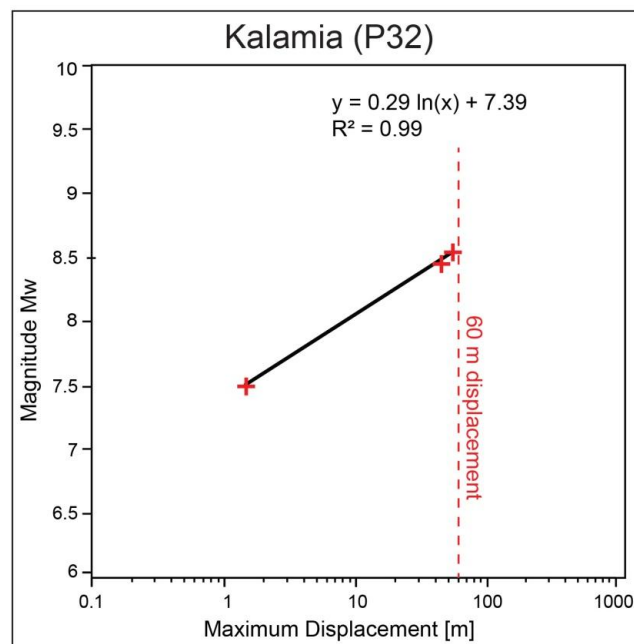


Figure II.36: Regression of maximum displacement versus magnitude M_w . Maximum displacement 60 m ever measured for an earthquake is for the 2011 M_w 9.0 Tohoku-Oki (Japan)

II.1.4.2 Uplift rates only by sea-level changes

Table II.24: Terraces, their age and calculated age, present elevation and sea-level change rate. No tectonics.

Location	Terrace	Time (<i>T</i>) [<i>kyr</i>]	Elevation present <i>E_p</i> [m]	Sea-level change to lower terrace [m]	Sea-level change rate ^g [$\frac{m}{kyr}$]
Kalamia (P32 & H33)	T1 ¹	26.93 ± 0.0002 ^a	55 ^c	-21 ^e	0.78
		19.48 ± 0.00009 ^a	55 ^c	-21 ^e	1.08
		39.19 ± 0.0004 ^a	55 ^c	-21 ^e	0.54
	T2 ¹	37.53 ± 0.33 ^a	34 ^c	-25.66 ^e	0.68
		38.25 ± 0.38 ^a	34 ^c	-25.66 ^e	0.67
	T3 ¹	2.710 ± 0.00004 ^a	8.34 ^c	+0.66 ^f	0.24
		2.260 ± 0.00004 ^a	8.34 ^c	+0.66 ^f	0.29
		2.190 ± 0.00004 ^a	8.34 ^c	+0.66 ^f	0.30
	365 A.D. earthquake	T4 ²	0.365 ^b	9 ^d	-9 ^e
Today shoreline	T5	0	0		

All terraces are dated terraces.

¹Tiberti et al. (2014); ²Pirazzoli et al. (1996)

^aAges taken from Tiberti et al. (2014).

^bAges taken from Pirazzoli et al. (1996).

^cPresent elevation taken from Tiberti et al. (2014).

^dPresent elevation taken from Pirazzoli et al. (1996).

^eSea-level fall → -

^fSea-level rise → +

^gSea-level change rate calculated using equation: sea-level change rate = (height change / age)

II.1.4.3 Uplift rates by tectonic and sea-level changes

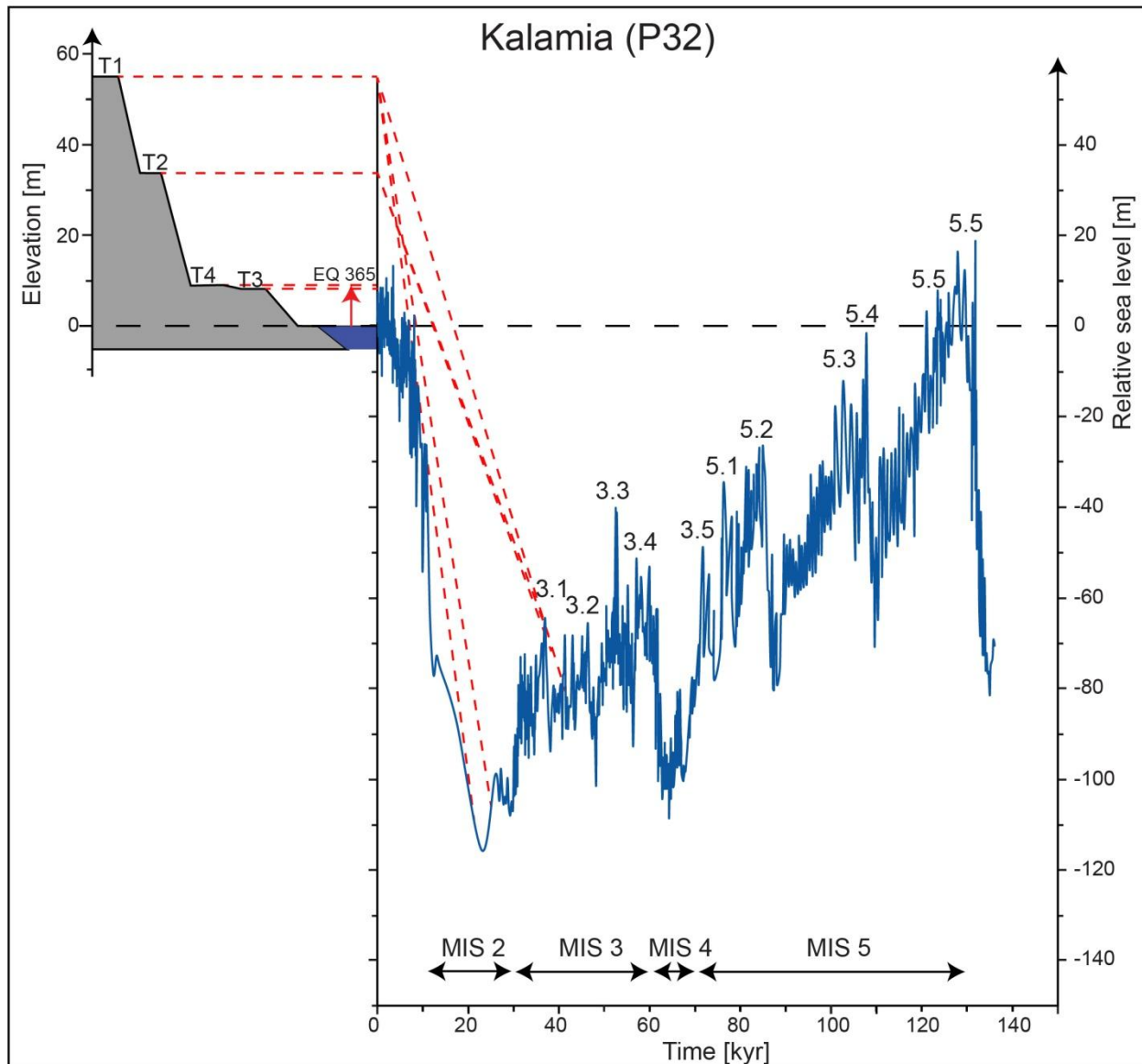


Figure II.37: Correlation of terraces at Kalamia with the sea-level curve of Rohling et al. (2014), modified after Pirazzoli et al. (1996); Tiberti et al. (2014); and Wegmann (2008).

Table II.25: Kalamia terrace numbers, elevation heights, and uplift rates (Rohling et al., 2014).

Location	Terrace	Time (T) [kyr]	Elevation present E_p [m]	Elevation original E_0 [m]	$E_p - E_0$ [m]	Uplift rate (R) ^f [$\frac{m}{kyr}$]	Dated material
Kalamia (P32 & H33)	T1 ¹	26.93 ± 0.0002 ^a	55 ^c	-103.38±6 ^e	158.38±6	5.88±0.22	*
		19.48 ± 0.00009 ^a	55 ^c	-96 ^e	174.4	7.75±0.31	*
		39.19 ± 0.0004 ^a	55 ^c	-78.76±6 ^e	133.76±6	3.41±0.15	*
	T2 ¹	37.53 ± 0.33 ^a	34 ^c	-77.55±6 ^e	111.55±6	2.97±0.19	*
		38.25 ± 0.38 ^a	34 ^c	-92.34 ± 6 ^e	126.34±6	3.30±0.19	**
	T3 ¹	2.710 ± 0.00004 ^a	8.34 ^c	0	8.34	3.08	***
		2.260± 0.00004 ^a	8.34 ^c	0	8.34	3.69	****
		2.190± 0.00004 ^a	8.34 ^c	0	8.34	3.80	*****
365 A.D. earthquake	T4 ²	0.365 ^b	9 ^d	0	9	24.66	

All terraces are dated terraces.

¹Tiberti et al. (2014); ²Pirazzoli et al. (1996)

^aAges taken from Tiberti et al. (2014).

^bAges taken from Pirazzoli et al. (1996).

^cPresent elevation taken from Tiberti et al. (2014).

^dPresent elevation taken from Pirazzoli et al. (1996).

^eSea-level correction done after Rohling et al. (2014).

^fUplift rate calculated using equation: $R = (E_p - E_0) / T$

*Radiocarbon date ¹⁴C of a shell (Bivalve fragment) by Tiberti et al. (2014).

**Radiocarbon date ¹⁴C of a shell (Glycymeris sp.) by Tiberti et al. (2014).

***Radiocarbon date ¹⁴C of a shell (Lithophaga sp.) by Tiberti et al. (2014).

****Radiocarbon date ¹⁴C of a shell (Spondylus sp.) by Tiberti et al. (2014).

*****Radiocarbon date ¹⁴C of a shell (Vermetids) by Tiberti et al. (2014).

Table II.26: Average uplift rate, slip rate, and recurrence time.

Average uplift rate (R) [mm/yr]	Slip rate [mm/yr]	Recurrence time [yr]
4.24 ± 0.21	8.48 ± 0.42	2358.49 (+122.9 / -111.3)

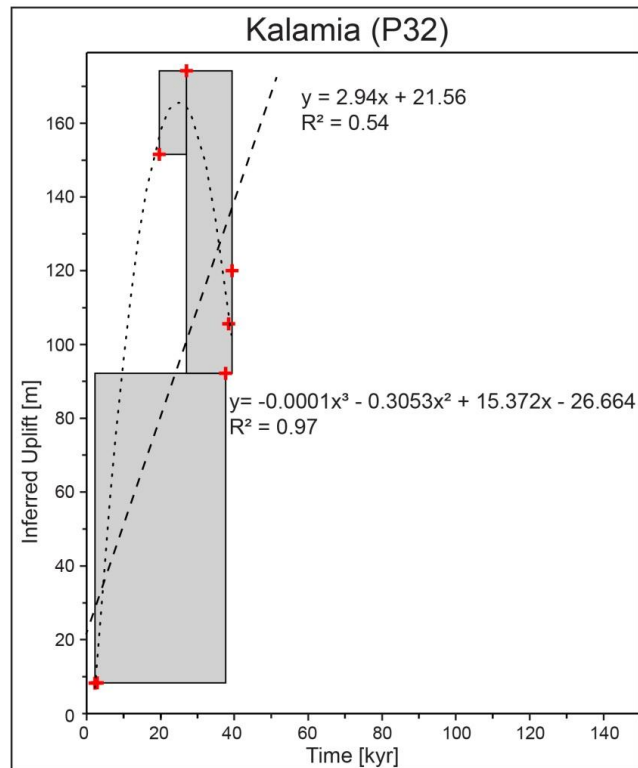


Figure II.38: Inferred uplift diagram curve for sea-level correction is determined by linear regression analysis.

Table II.27: Average uplift rate, slip rate, recurrence time for the 21st July 365 A.D. earthquake, and total slip for highest and oldest terrace at Kalamia.

Earthquake 21 st July 365 A.D.	Mw	Time interval [kyr]	Average uplift rate [mm/yr]	Slip rate [mm/yr]	Recurrence time [yr]	Total slip for highest and oldest terrace [m]
Kalamia Tectonic only	8.25 ¹	39.19 ² until today	2.33	4.66	4291.8	182.6
Kalamia Constant Sea-level corrected ³	8.25 ¹	39.19 ² until today	4.24±0.21	8.48±0.42	2358.49	332.33

¹Shaw et al. (2008); ²Tiberti et al. (2014), ³Rohling et al. (2014)

II.1.5 Cape Koutouls

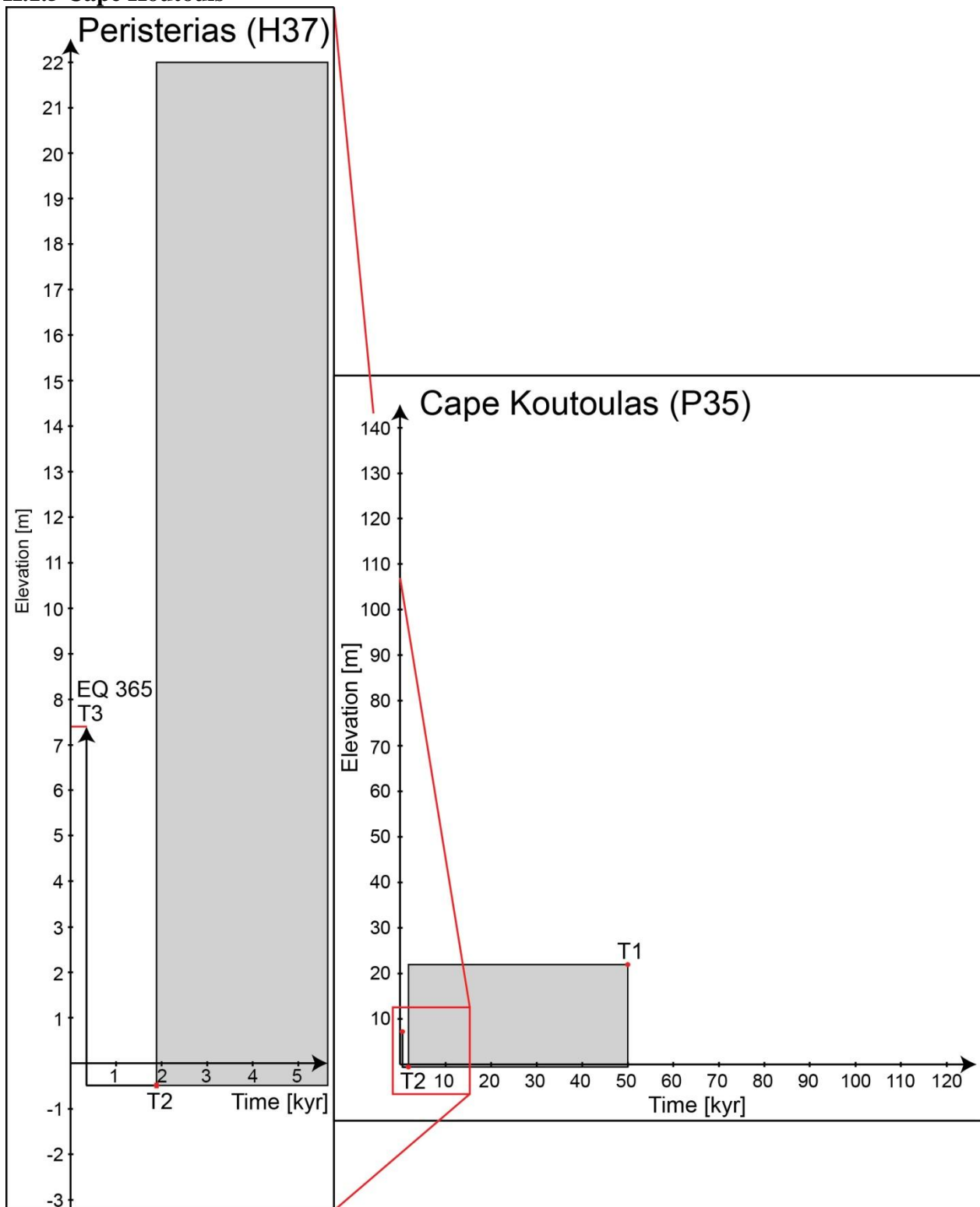


Figure II.39: Elevation of Pleistocene and Holocene palae-shorelines plotted against time, modified after Wegmann (2008), and Pirazzoli et al. (1996).

II.1.5.1 Uplift rates only by tectonics

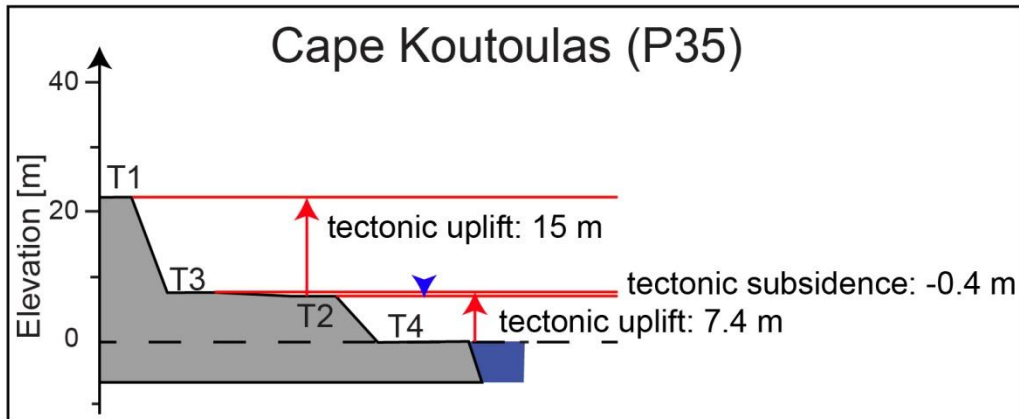


Figure II.40: Elevation of terraces and the height difference needed for the tectonic uplift, , modified after Wegmann (2008), and Pirazzoli et al. (1996).

Table II.28: Terraces, their age, present elevation and calculated uplift rate. No sea-level.

Location	Terrace	Time (T) [kyr]	Elevation present E_p [m]	Uplift rate (R) ⁱ [$\frac{m}{kyr}$]
Cape Koutoulas (P18 & H37)	T1 ¹	50 ^a	22 ^e	0.44
	T2 ²	1.890 ± 0.07 ^b	7.0 ± 0.2 ^f	3.7 ± 0.24
	T2 ³	2.010 ± 0.073 ^c	7 ^g	3.5 ± 0.073
	T2 ⁴	1580 ^d	7 ^h	4.4
365 A.D. earthquake	T3 ²	0.365 ^b	7.4 ^f	20.27

¹Wegmann (2008); ²Pirazzoli et al. (1996); ³Price et al. (2002); ⁴Mourtzas (2012).

^aAges taken from Wegmann (2008).

^bAges taken from Pirazzoli et al. (1996).

^cAges taken from Price et al. (2002).

^dAges taken from Mourtzas (2012).

^ePresent elevation taken from Wegmann (2008).

^fPresent elevation taken from Pirazzoli et al. (1996).

^gPresent elevation taken from Price et al. (2002).

^hPresent elevation taken from Mourtzas (2012).

ⁱUplift rate calculated using equation: $R = (E_p - E_0) / T$

Table II.29: Average uplift rate, slip rate, and recurrence time.

Average uplift rate (R) [mm/yr]	Slip rate [mm/yr]	Recurrence time [yr]
3.01 ± 0.15	6.02 ± 0.3	3322.3 (+174.2 / -157.7)

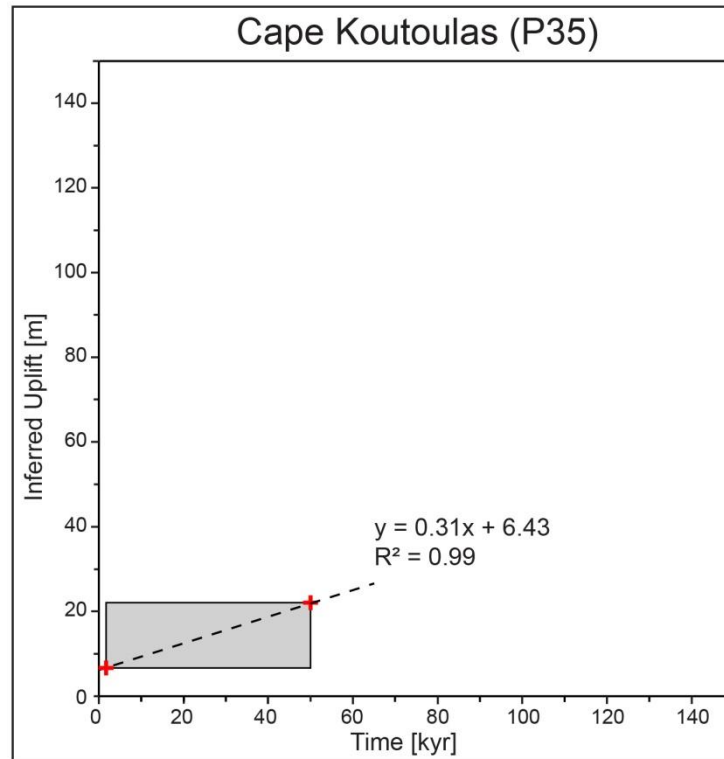


Figure II.41: Inferred uplift diagram curve for tectonic uplift is determined by linear regression analysis.

Table II.30: Displacement between terraces, the corresponding slip, M_0 and M_w .

Terraces	Terrace elevation [m]	Terrace elevation [m]	Displacement between terraces [m]	Corresponding slip along the Hellenic trench [m] ^a	M_0^b [dyne/cm]	M_w^c
T3 – T2	T3 = 7.4	T2 = 7	0.4	1.14	$1.54 \cdot 10^{27}$	7.42
T2 – T1	T2 = 7.0	T1 = 22	15	42.86	$5.7 \cdot 10^{28}$	8.45

^aCorresponding slip along is measured based on the slip of 20 m which equals a vertical displacement of 9 m

^bSeismic Moment: $M_0 = \mu AD$

^cMoment Magnitude: $M_w = \frac{2}{3} \log M_0 - 10.7$

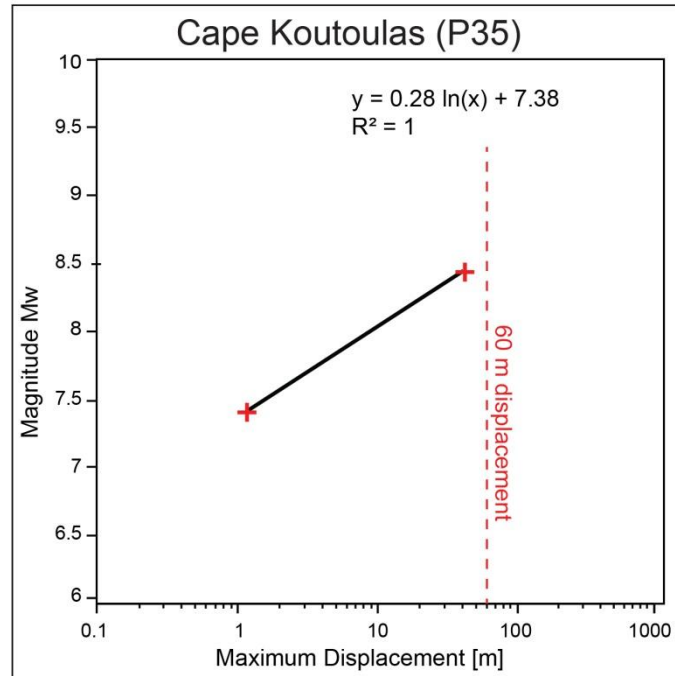


Figure II.42: Regression of maximum displacement versus magnitude Mw. Maximum displacement 60 m ever measured for an earthquake is for the 2011 Mw 9.0 Tohoku-Oki (Japan)

II.1.5.2 Uplift rates only by sea-level changes

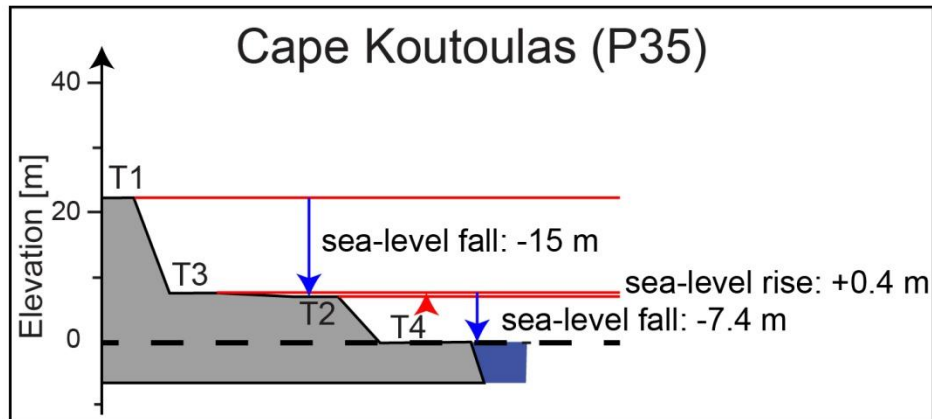


Figure II.43: Elevation of terraces and the needed amount of sea-level fall, modified after Wegmann (2008), and Pirazzoli et al. (1996).

Table II.31: Terraces, their age and calculated age, present elevation and sea-level change rate. No tectonics.

Location	Terrace	Time (T) [kyr]	Elevation present E_p [m]	Sea-level change to lower terrace [m]	Sea-level change rate ^k $\left[\frac{m}{kyr}\right]$
Cape Koutoulas (P18 & H37)	T1 ¹	52.5 ^a	22 ^e	-15 ⁱ	0.28
	T2 ²	1.890 ± 0.07 ^b	7.0 ± 0.2 ^f	+0.4 ¹	0.21
	T2 ³	2.010 ± 0.073 ^c	7 ^g	+0.4 ¹	0.19
	T2 ⁴	1.580 ^d	7 ^h	+0.4 ¹	0.23
365 A.D. earthquake	T3 ²	0.365 ^b	7.4 ^f	-7.4 ^j	-20.27
Today shoreline	T4	0	0		

¹Wegmann (2008); ²Pirazzoli et al. (1996); ³Price et al. (2002); ⁴Mourtzas (2012).

^aAges taken from Wegmann (2008). MIS ages taken and then converted to ages with Rohling et al. (2014)

^bAges taken from Pirazzoli et al. (1996).

^cAges taken from Price et al. (2002).

^dAges taken from Mourtzas (2012).

^ePresent elevation taken from Wegmann (2008).

^fPresent elevation taken from Pirazzoli et al. (1996).

^gPresent elevation taken from Price et al. (2002).

^hPresent elevation taken from Mourtzas (2012).

ⁱSea-level fall → -

^jSea-level fall → +

^kSea-level change rate calculated using equation: sea-level change rate = (height change / age)

II.1.5.3 Uplift rates by tectonic and sea-level changes

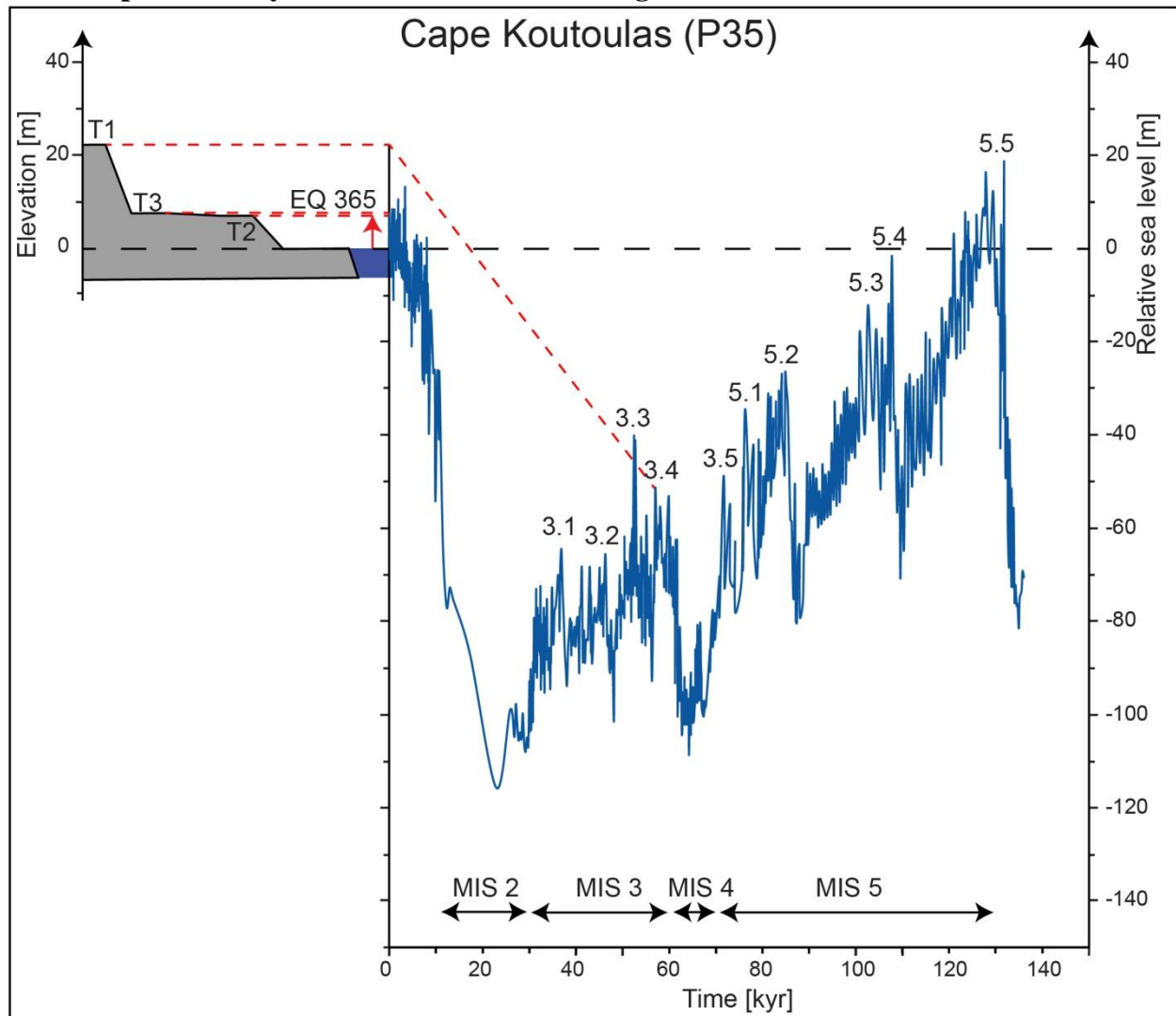


Figure II.44: Correlation of terraces at Cape Koutoulas with the sea-level curve of Rohling et al. (2014), modified after Wegmann (2008), and Pirazzoli et al. (1996).

Table II.32: Cape Koutoulas terrace numbers, elevation heights, and uplift rates (Rohling et al., 2014).

Location	Terrace	Time (T) [kyr]	Elevation present E_p [m]	Elevation original E_0 [m]	$E_p - E_0$ [m]	Uplift rate (R) ^j [$\frac{m}{kyr}$]	Dated material
Cape Koutoulas (P35 & H37)	T1 ¹	52.5 ^a	22±1 ^e	-55.8±6 ⁱ	77.8 ± 6.08	1.48±0.12	*
	T2²	1.890 ± 0.07^b	7.0 ± 0.2^f	0	7.0 ± 0.2	3.7 ± 0.24	**
	T3³	2.010 ± 0.073^c	7^g	0	7	3.5 ± 0.13	***
	T2⁴	1580^d	7^h	0	7	4.4	****
365 A.D. earthquake	T3²	0.365^b	7.4^f	0	7.4	20.27	

Bold terraces are dated terraces.

¹Wegmann (2008); ²Pirazzoli et al. (1996); ³Price et al. (2002); ⁴Mourtzas (2012).

^aAges taken from Wegmann (2008).

^bAges taken from Pirazzoli et al. (1996).

^cAges taken from Price et al. (2002).

^dAges taken from Mourtzas (2012).

^ePresent elevation taken from Wegmann (2008).

^fPresent elevation taken from Pirazzoli et al. (1996).

^gPresent elevation taken from Price et al. (2002).

^hPresent elevation taken from Mourtzas (2012).

ⁱSea-level correction done after Rohling et al. (2014).

^jUplift rate calculated using equation: $R = (E_p - E_0) / T$

*Facies relationship for lateral correlation of spatially separated locations are taken from Wegmann (2008): Facies A - Corresponds to Algal bioherms and patch reefs.

**Radiocarbon date ¹⁴C of *Dendropoma* (*Novastoa*) *petraeum* by Pirazzoli et al. (1996). Calculated using a reservoir effect of 320 ± 25 years for the Mediterranean.

***Radiocarbon date ¹⁴C of *Dendropoma* by Price et al. (2002). Corrected the original radiocarbon dates (BP) by adding 430 ¹⁴C years to each.

****Mourtzas (2012).

Table II.33: Average uplift rate, slip rate, and recurrence time.

Average uplift rate (R) [mm/yr]	Slip rate [mm/yr]	Recurrence time [yr]
3.27 ± 0.16	6.54 ± 0.32	3058.10 (+157.33 / -142.65)

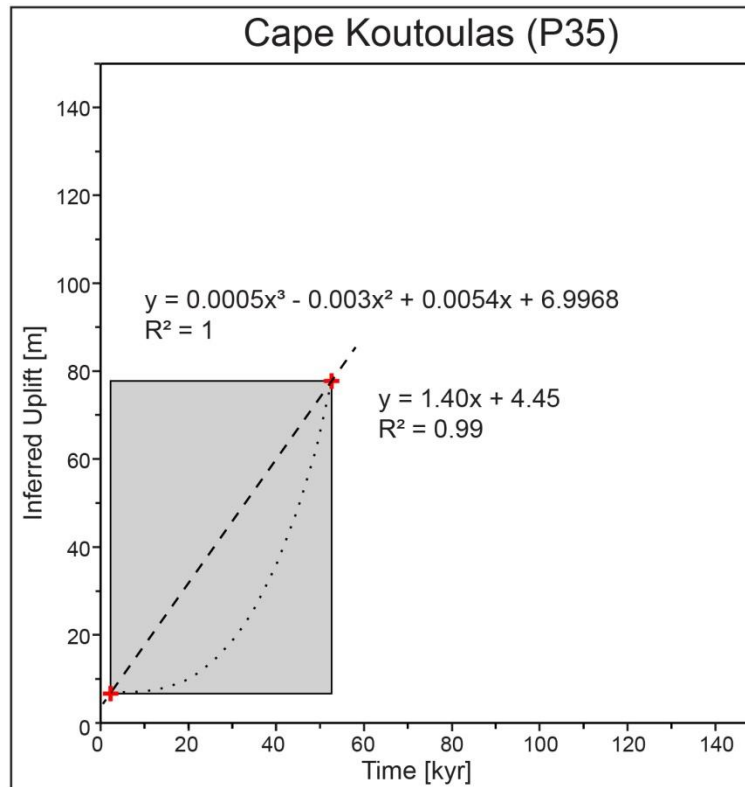


Figure II.45: Inferred uplift diagram curve for sea-level correction is determined by linear regression analysis.

Table II.34: Average uplift rate, slip rate, recurrence time for the 21st July 365 A.D. earthquake, and total slip for highest and oldest terrace at Cape Koutoulas.

Earthquake 21 st July 365 A.D.	Mw	Time interval [kyr]	Average uplift rate [mm/yr]	Slip rate [mm/yr]	Recurrence time [yr]	Total slip for highest and oldest terrace [m]
Cape Koutoulas Tectonic only	8.25 ¹	50 ² until today	3.01	6.02	3322.3	301
Cape Koutoulas Constant Sea-level corrected ³	8.25 ¹	50 ² until today	3.27±0.16	6.54±0.32	3058.10	343.35

¹ Shaw et al. (2008); ²Wegmann (2008); ³Rohling et al. (2014)

II.1.6 Phalasarna

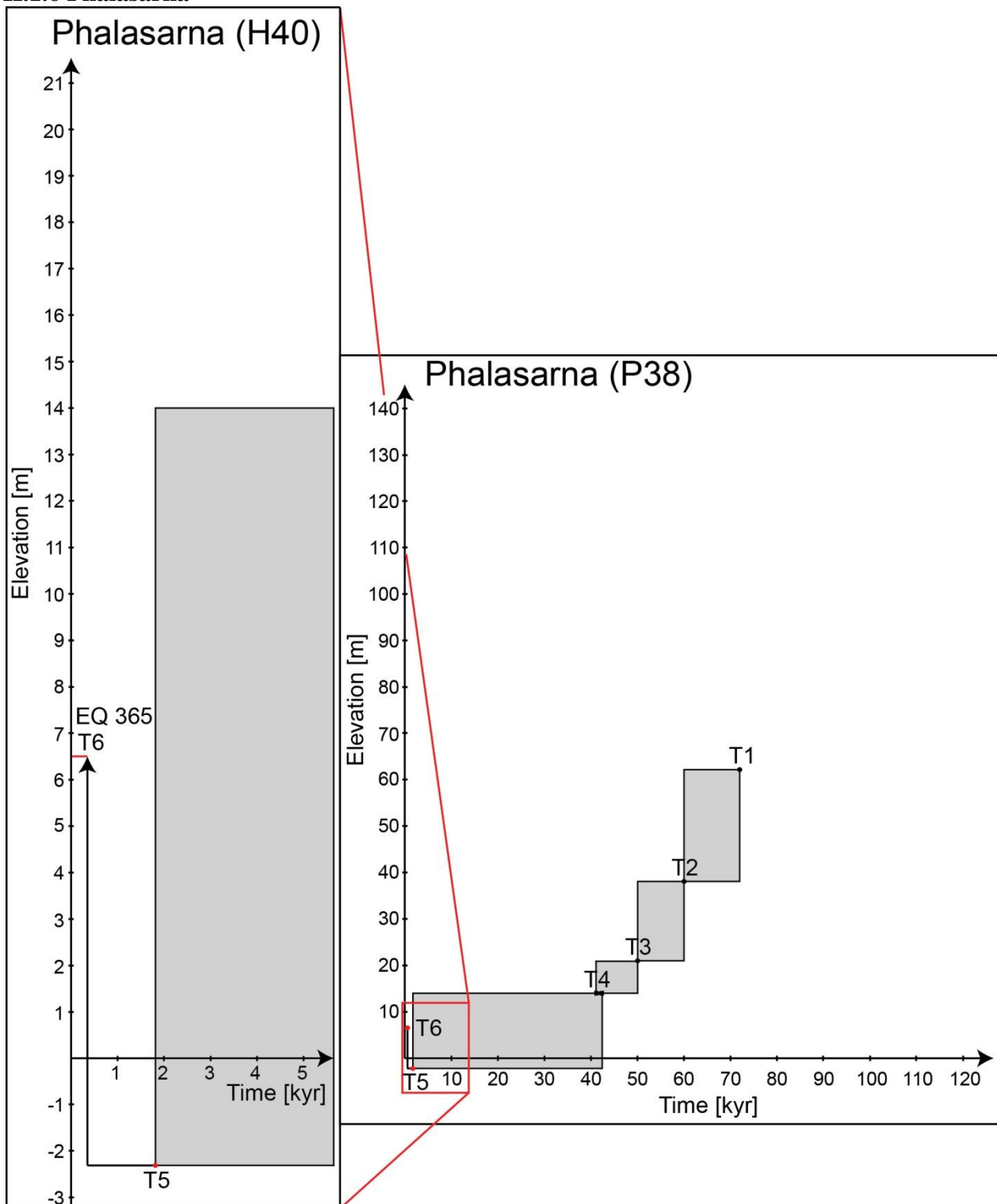


Figure II.46: Elevation of Pleistocene and Holocene palae-shorelines plotted against time, modified after Wegmann (2008), and Pirazzoli et al. (1996).

II.1.6.1 Uplift rates only by tectonics

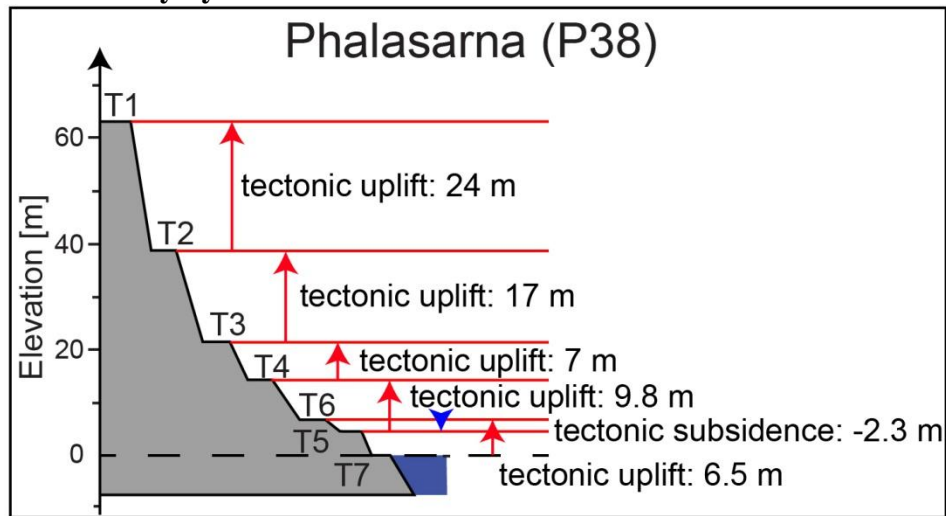


Figure II.47: Elevation of terraces and the height difference needed for the tectonic uplift, modified after Pirazzoli et al. (1996), Wegmann (2008), and Price et al. (2002).

Table II.35: Terraces, their age, present elevation and calculated uplift rate. No sea-level.

Location	Terrace	Time (T) [kyr]	Elevation present E_p [m]	Uplift rate (R) ^g [$\frac{m}{kyr}$]
Phalasarna (P38 & H40)	T1 ¹	72 ^a	62 ^c	0.86
	T2 ¹	60 ^a	38 ^c	0.63
	T3 ¹	50 ^a	21 ^c	0.42
	T4 ¹	41.28 – 42.53 ^a	14 ^d	0.33
	T5 ²	1.798 ± 0.077 ^b	4.2 ± 0.5 ^e	2.33 ± 0.38
365 A.D. earthquake	T6 ³	0.365 ^c	6.5 ^f	17.81

¹Wegmann (2008); ²Pavlopoulos et al. (2011); ³Pirazzoli et al. (1996)

^aAges taken from Wegmann (2008).

^bAges taken from Pavlopoulos et al. (2011).

^cAges taken from Pirazzoli et al. (1996).

^dPresent elevation taken from Wegmann (2008).

^ePresent elevation taken from Pavlopoulos et al. (2011).

^fPresent elevation taken from Pirazzoli et al. (1996).

^gUplift rate calculated using equation: $R = (E_p - E_0) / T$

Table II.36: Average uplift rate, slip rate, and recurrence time.

Average uplift rate (R) [mm/yr]	Slip rate [mm/yr]	Recurrence time [yr]
0.91 ± 0.38	1.82 ± 0.72	10989.01(+7192.8 / -3114.9)

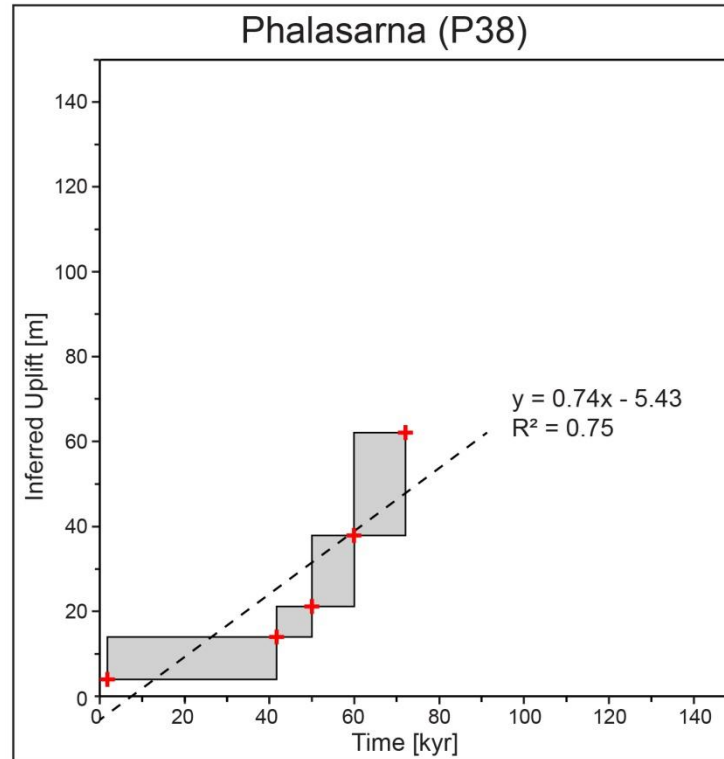


Figure II.48: Inferred uplift diagram curve for tectonic uplift is determined by linear regression analysis.

Table II.37: Displacement between terraces, the corresponding slip, M_0 and M_w .

Terraces	Terrace elevation [m]	Terrace elevation [m]	Displacement between terraces [m]	Corresponding slip along the Hellenic trench [m] ^a	M_0^b [dyne/cm]	M_w^c
T6 – T5	T6 = 6.5	T5 = 4.2	2.3	7.07	$9.54 \cdot 10^{27}$	7.95
T5 – T4	T5 = 4.2	T4 = 14	9.8	42.86	$1.3 \cdot 10^{28}$	8.02
T4 – T3	T4 = 14	T3 = 21	7	21.54	$2.9 \cdot 10^{28}$	8.26
T3 – T2	T3 = 21	T2 = 38	17	52.31	$7.1 \cdot 10^{28}$	8.5
T2 – T1	T2 = 38	T1 = 62	24	73.85	$9.9 \cdot 10^{28}$	8.6

^aCorresponding slip along is measured based on the slip of 20 m which equals a vertical displacement of 9 m

^bSeismic Moment: $M_0 = \mu AD$

^cMoment Magnitude: $M_w = \frac{2}{3} \log M_0 - 10.7$

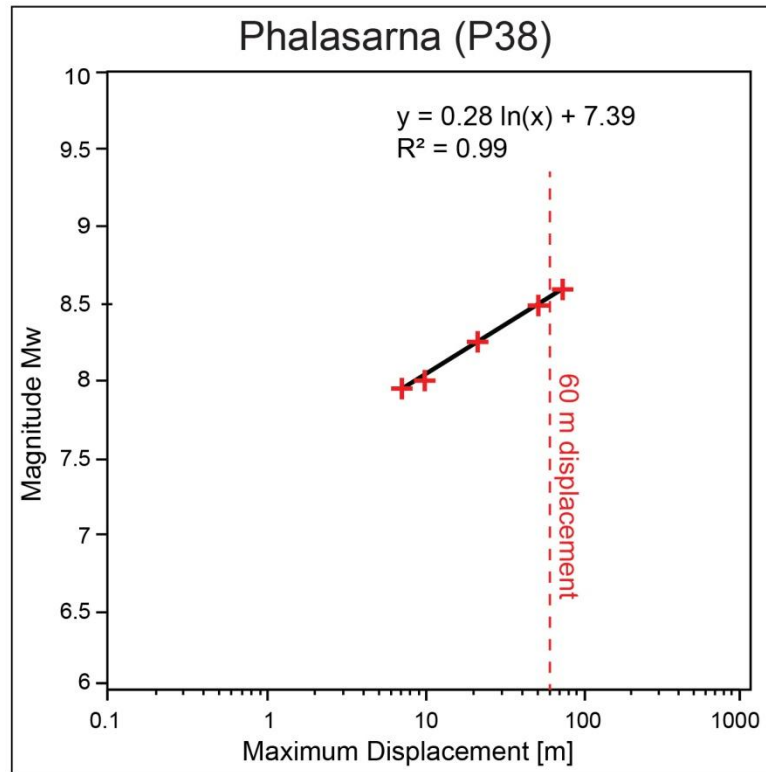


Figure II.49: Regression of maximum displacement versus magnitude Mw. Maximum displacement 60 m ever measured for an earthquake is for the 2011 Mw 9.0 Tohoku-Oki (Japan).

II.1.6.2 Uplift rates only by sea-level changes

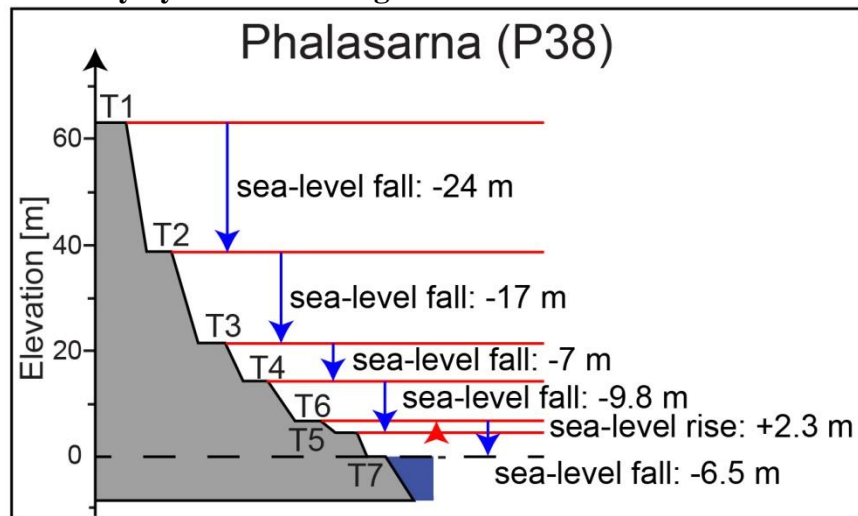


Figure II.50: Elevation of terraces and the needed amount of sea-level fall, modified after Pirazzoli et al. (1996), Wegmann (2008), and Price et al. (2002).

Table II.38: Terraces, their age and calculated age, present elevation and sea-level change rate. No tectonics.

Location	Terrace	Time (T) [kyr]	Elevation present E_p [m]	Sea-level change to lower terrace [m]	Sea-level change rate ^j [$\frac{m}{kyr}$]
Phalasarua (P38 & H40)	T1 ¹	71.8 ^a	62 ^e	-24 ^h	0.33
	T2 ¹	57 ^a	38 ^e	-17 ^h	0.30
	T3 ¹	52.5 ^a	21 ^e	-7 ^h	0.13
	T4 ¹	41.28 – 42.53 ^b	14 ^e	-9.8 ^h	0.23
	T5 ²	1.798 ± 0.077 ^c	4.2 ± 0.5 ^f	+2.3 ⁱ	1.28
365 A.D. earthquake	T6 ³	0.365 ^d	6.5 ^g	-6.5 ^h	-17.81
Today shoreline	T7	0	0		

¹Wegmann (2008); ²Pavlopoulos et al. (2011); ³Pirazzoli et al. (1996)

^aAges taken from Wegmann (2008). MIS stages taken and corrected the age after Rohling et al. (2014).

^bAges taken from Wegmann (2008).

^cAges taken from Pavlopoulos et al. (2011).

^dAges taken from Pirazzoli et al. (1996).

^ePresent elevation taken from Wegmann (2008).

^fPresent elevation taken from Pavlopoulos et al. (2011).

^gPresent elevation taken from Pirazzoli et al. (1996).

^hSea-level fall → -

ⁱSea-level rise → +

^jSea-level change rate calculated using equation: sea-level change rate = (height change / age)

II.1.6.3 Uplift rates by tectonic and sea-level changes

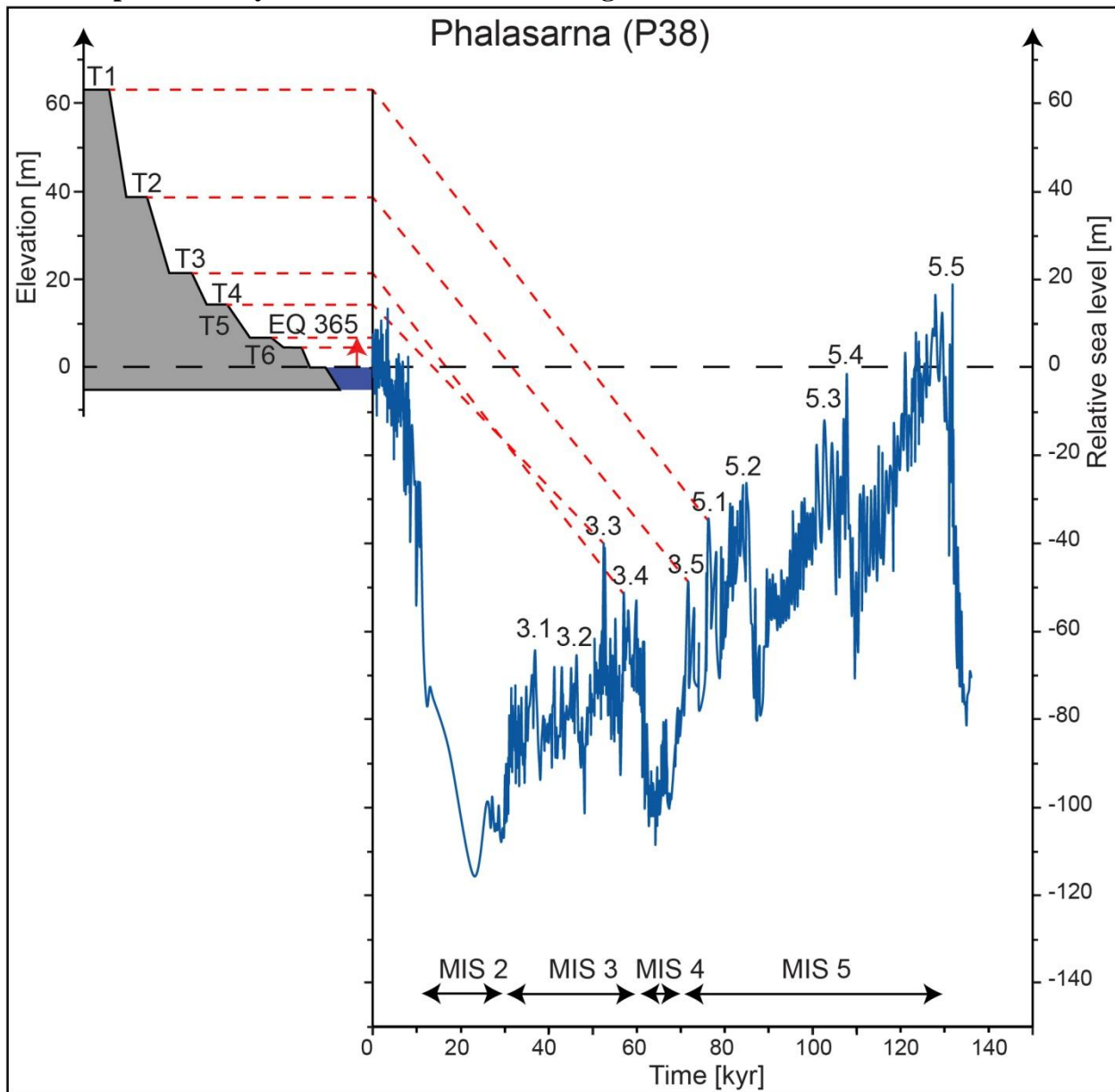


Figure II.51: Correlation of terraces at Phalasarna with the sea-level curve of Rohling et al. (2014), modified after Pirazzoli et al. (1996), Wegmann (2008), and Price et al. (2002).

Table II.39: Phalasarna terrace numbers, elevation heights, and uplift rates (Rohling et al., 2014).

Location	Terrace	Time (T) [kyr]	Elevation present E_p [m]	Elevation original E_0 [m]	$E_p - E_0$ [m]	Uplift rate (R) ^h [$\frac{m}{kyr}$]	Dated material
Phalasarna (P38 & H40)	T1 ¹	71.8 ^a	62±1 ^d	-53.3±6 ^g	115.3 ± 6.08	1.61±0.08	
	T2 ¹	57 ^a	38±1 ^d	-60.9±6 ^g	98.9 ± 6.08	1.74±0.11	
	T3 ¹	52.5 ^a	21±1 ^d	-55.8±6 ^g	76.8 ± 6.08	1.46±0.12	
	T4 ¹	41.28 – 42.53 ^a	14±1 ^d	-80.38±6 ^g	94.38 ± 6.08	2.27±0.15 to 2.22±0.15	*
	T5 ²	1.798 ± 0.077 ^b	4.2 ± 0.5 ^e	0	4.2 ± 0.5	2.3 ± 0.38	**
	365 A.D. earthquake	T6 ³	0.365 ^c	6.5 ^f	0	6.5	17.81

Bold terraces are dated terraces.

¹Wegmann (2008); ²Pavlopoulos et al. (2011); ³Pirazzoli et al. (1996)

^aAges taken from Wegmann (2008). MIS stages taken and corrected the age after Rohling et al. (2014).

^bAges taken from Pavlopoulos et al. (2011).

^cAges taken from Pirazzoli et al. (1996).

^dPresent elevation taken from Wegmann (2008).

^ePresent elevation taken from Pavlopoulos et al. (2011).

^fPresent elevation taken from Pirazzoli et al. (1996).

^gSea-level correction done after Rohling et al. (2014).

^hUplift rate calculated using equation: $R = (E_p - E_0) / T$

*Radiocarbon date ¹⁴C of bioerosion notch with fringing trottoir-style reef by Wegmann (2008).

**Radiocarbon date ¹⁴C of notches, Neogoniolithon by Pavlopoulos et al. (2011).

Table II.40: Average uplift rate, slip rate, and recurrence time.

Average uplift rate (R) [mm/yr]	Slip rate [mm/yr]	Recurrence time [yr]
1.93 ± 0.17	3.86 ± 0.34	5181.35 (+500.47 / -419.45)

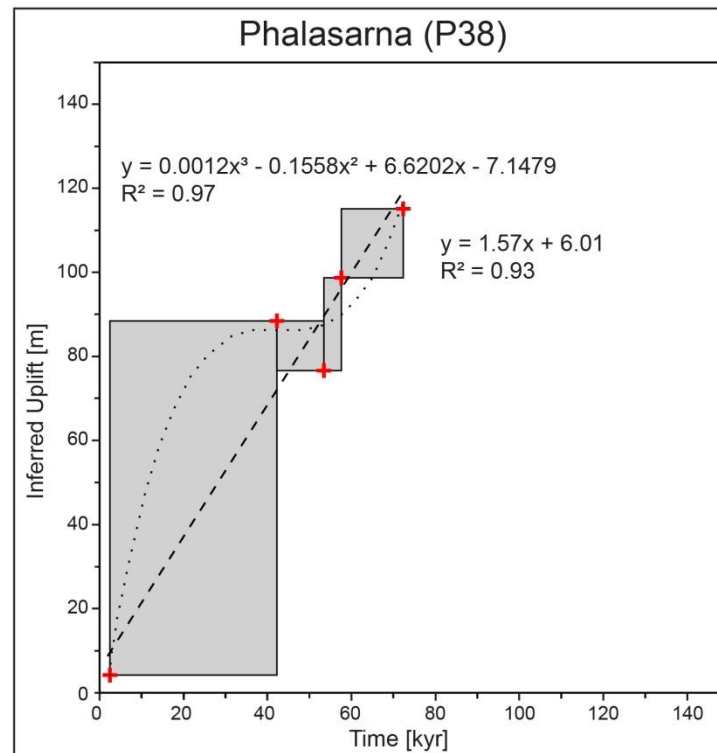


Figure II.52: Inferred uplift diagram curve for sea-level correction is determined by linear regression analysis.

Table II.41: Average uplift rate, slip rate, recurrence time for 21st July 365 earthquake, and total slip for highest and oldest terrace. For tectonic only, sea-level only, and sea-level corrected.

Earthquake 21 st July 365 A.D.	Mw	Time interval [kyr]	Average uplift rate [mm/yr]	Slip rate [mm/yr]	Recurrence time [yr]	Total slip for highest and oldest terrace [m]
Aradena Gorge Tectonic only	8.25 ¹	10 ⁷ ² until today	0.75	1.5	13333.33	160.5
Aradena Gorge Sea-level corrected ³	8.25 ¹	10 ⁷ ² until today	1.37±0.08	2.74±0.16	7299.27	295.65
Sougia Tectonic only	8.25 ¹	10 ⁷ ² until today	1.95	3.9	5128.21	417.3
Sougia Constant Sea-level corrected ³	8.25 ¹	10 ⁷ ² until today	2.26±0.16	4.52±0.32	4424.78	487.71
Kalamia Tectonic only	8.25 ¹	39.19 ² until today	2.33	4.66	4291.8	182.6
Kalamia Constant Sea-level corrected ³	8.25 ¹	39.19 ² until today	4.24±0.21	8.48±0.42	2358.49	332.33
Moni	8.25 ¹	85 ²	2.67	5.34	3745.32	453.9

Chryssoskalitissa Tectonic only		until today				
Moni Chryssoskalitissa Constant ³	8.25 ¹	85 ² until today	2.85 ± 0.24	5.7 ± 0.48	3508.77	484.5
Moni Chryssoskalitissa Not Constant ³	8.25 ¹	72 ² until today	2.86 ± 0.25	5.72 ± 0.50	3496.50	410.69
Cape Koutoulas Tectonic only	8.25 ¹	50 ² until today	3.01	6.02	3322.3	301
Cape Koutoulas Constant Sea-level corrected ³	8.25 ¹	50 ² until today	3.27±0.16	6.54±0.32	3058.10	343.35
Phalasarna Tectonic only	8.25 ¹	72 ² until today	0.91	1.82	10989.01	131.04
Phalasarna Constant Sea-level corrected ³	8.25 ¹	72 ² until today	1.93±0.17	3.86±0.32	5181.35	272.15

¹ Shaw et al. (2008); ²Wegmann (2008); ³Rohling et al. (2014)

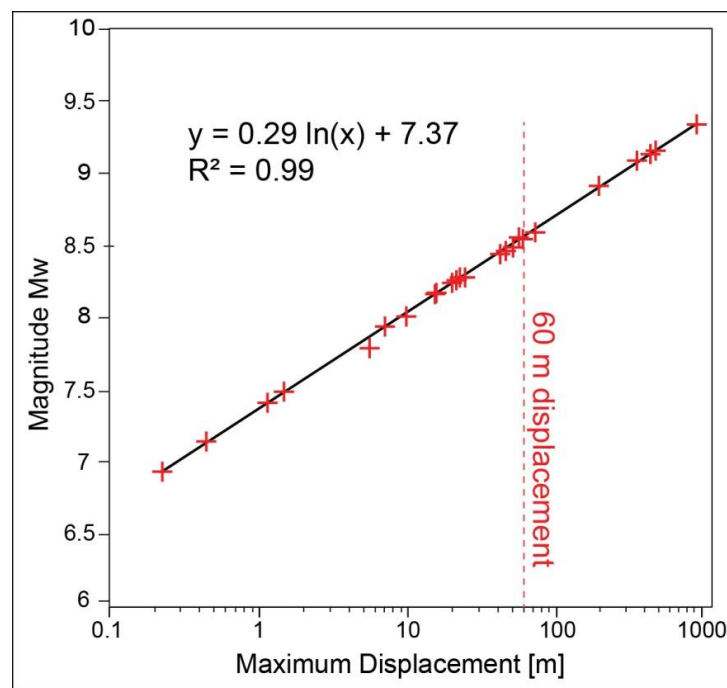


Figure II.53: Regression of maximum displacement versus magnitude M_w . Maximum displacement 60 m ever measured for an earthquake is for the 2011 M_w 9.0 Tohoku-Oki (Japan).

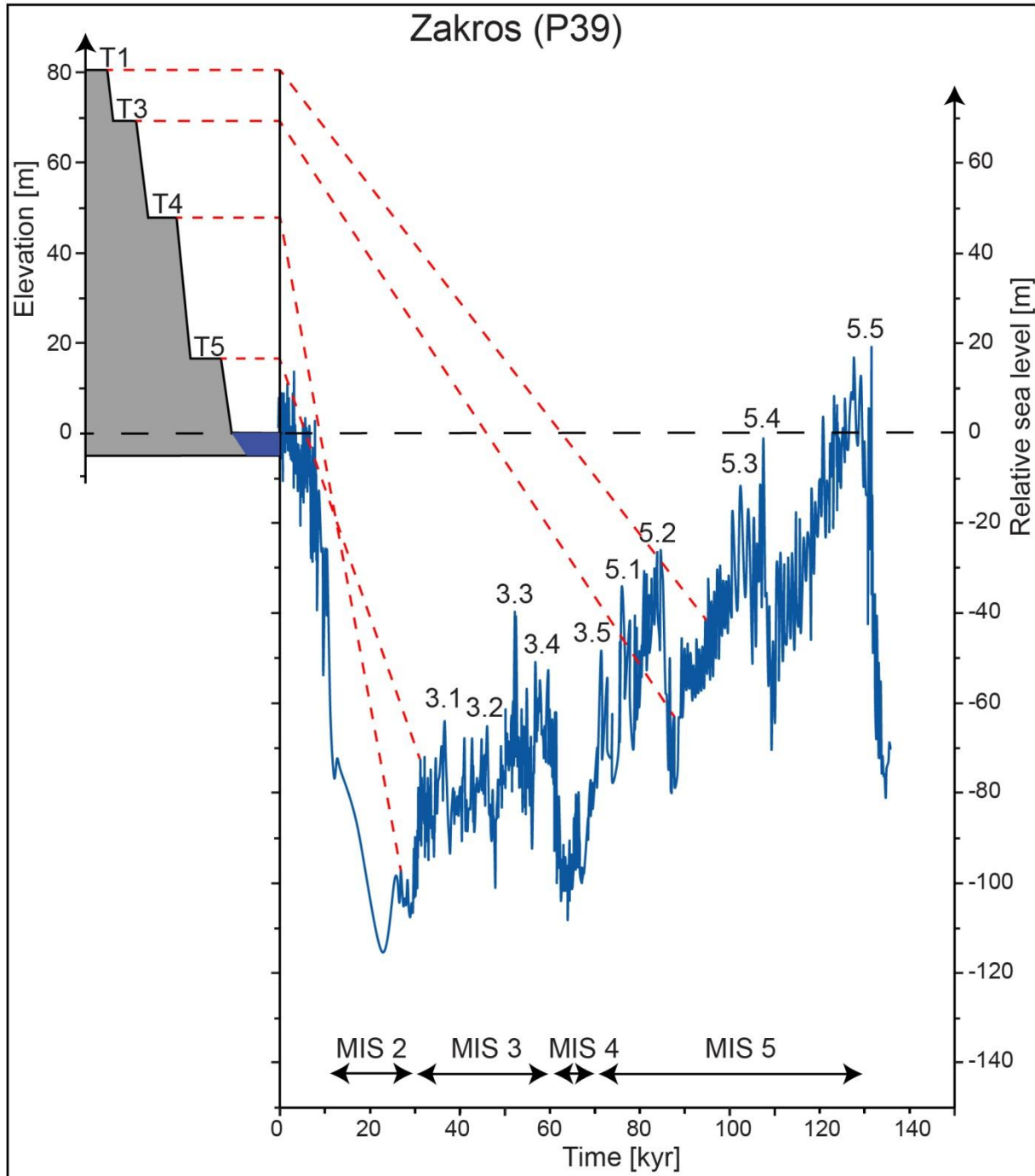


Figure II.54: Correlation of terraces at Zakros with the sea-level curve of Rohling et al. (2014), modified after Strobl et al. (2014).

Table II.42: Zakros terrace numbers, elevation heights, and uplift rates (Strobl et al., 2014; Rohling et al., 2014).

Location	Terrace	Time (T) [kyr]	Elevation present E_p [m]	Elevation original E_0 [m]	$E_p - E_0$ [m]	Uplift rate (R) ¹ [$\frac{m}{kyr}$]	Dated material
Zakros (P39)	T1	95±21	81	-42	123	1.3	
	T2	88±22	69	-63	132	1.5	
	T3	27±19	48	-97	145	5.4	
	T4	31±19	17	-72	89	2.9	*

¹Uplift rate calculated using equation: $R = (E_p - E_0) / T$

*Radiocarbon date ¹⁴C of bioerosion notch with fringing trottoir-style reef by Wegmann (2008).

**Radiocarbon date ¹⁴C of notches, Neogoniolithon by Pavlopoulos et al. (2011).

Chapter 5

Table II.43: Uplift rates from 16 Ma until 2.58 Ma derived from van Hinsbergen and Meulenkamp (2006).

Number ^a	Mean elevation [m]	Depth ^a [m]	standard deviation ^a [m]	Total height [km]	Age range ^a	Age range ^a [Ma]	Uplift rate ^b [km/Ma]
3	130±30	36		0.166±0.030	U. Serravallian	12	0.014±0.003
4	50±10	935	131	0.985±0.131	U. Serravallian	12	0.082±0.011
5	370±110	36		0.406±0.110	U. Serravallian	12	0.034±0.009
6	260±80	775	207	1.035±0.222	U. Serravallian	12	0.086±0.018
7	10±10	804	136	0.814±0.136	U. Serravallian	12	0.068±0.011
8	210±130	249	168	0.459±0.212	U. Serravallian	12	0.038±0.018
9	150±110	136	14	0.286±0.111	U. Langhian/ l. Serr.	16 to 12	0.018±0.007 to 0.024±0.009
10	360±140	93	35	0.453±0.144	U. Serravallian	12	0.038±0.012
11	280±100	36		0.316±0.100	U. Langhian/ l. Serr.	16 to 12	0.020±0.006 to 0.026±0.008
12	30±10	532	158	0.562±0.158	L. Messinian	5.3	0.106±0.030
12	30±10	496	269	0.526±0.269	L. Pliocene	4 to 3	0.132±0.067 to 0.175±0.090
13	110±30	335	69	0.445±0.075	L. Pliocene	4 to 3	0.111±0.019 to 0.175±0.025
14	150±70	719	92	0.869±0.116		7.1 to 7.4	0.117±0.016 to 0.122±0.016
15	180±60			0.180±0.060			
16	40±20	463	300	0.503±0.301	Messinian	7 to 5.3	0.072±0.043 to 0.095±0.057
17	210±50	743	109	0.953±0.120	U. Tortonian/ l. Messinian	8 to 5.3	0.119±0.015 to 0.18±0.023
18	260±120	624	176	0.884±0.213	U. Tortonian/ l. Messinian	8 to 5.3	0.111±0.027 to 0.167±0.040
19	90±30	1039	85	1.129±0.090	L. Pliocene	4 to 3	0.282±0.023 to 0.376±0.030
20	130±10	636	125	0.766±0.125	U. Tortonian/ l. Messinian	8 to 5.3	0.096±0.016 to 0.145±0.024
21	150±30	609	93	0.759±0.098	U. Tortonian/ l. Messinian	8 to 5.3	0.095±0.012 to 0.143±0.018
22	200±40	605	177	0.805±0.181	U. Tortonian/ l. Messinian	8 to 5.3	0.101±0.023 to 0.152±0.034
23	120±40	831	144	0.951±0.149	L. Pliocene	4 to 3	0.238±0.037 to 0.317±0.050

24	80±40	593	198	0.673 ± 0.20 2	Pliocene	5.3 to 2.58	0.127 ± 0.038 to 0.261 ± 0.078
25	70±30	372	131	0.442 ± 0.13 4	U. Tortonian/ l.Messinian	8 to 5.3	0.055 ± 0.017 to 0.083 ± 0.025
26	280±60	183	66	0.463 ± 0.08 9	U. Tortonian/ l.Messinian	8 to 5.3	0.058 ± 0.011 to 0.087 ± 0.017
27	60±20	784	159	0.844 ± 0.16 0	L. Pliocene	4 to 3	0.211 ± 0.040 to 0.281 ± 0.053
28	140±40	265	98	0.405 ± 0.10 6	Messinian	7 to 5.3	0.058 ± 0.015 to 0.076 ± 0.020
29	210±70			0.210 ± 0.07 0	U. Tortonian/ l.Messinian	8 to 5.3	0.026 ± 0.009 to 0.040 ± 0.013
30	260±120	809	133	1.069 ± 0.17 9	L. Pliocene	4 to 3	0.267 ± 0.045 to 0.356 ± 0.060
31	10±10	549	171	0.559 ± 0.17 1	U. Pliocene	4 to 3	0.140 ± 0.043 to 0.186 ± 0.057
32	90±50	59		0.149 ± 0.05 0	Tortonian	10 to 9	0.015 ± 0.005 to 0.017 ± 0.006
33	130±50	760	91	0.890 ± 0.10 4	Pliocene	5.3 to 2.58	0.168 ± 0.020 to 0.345 ± 0.040
34	220±80	482	167	0.702 ± 0.18 5	Pliocene	5.3 to 2.58	0.132 ± 0.035 to 0.272 ± 0.072
35	250±30	87	8	0.337 ± 0.03 1	U. Tortonian/ l.Messinian	8 to 5.3	0.042 ± 0.004 to 0.064 ± 0.006
35	250±30	902	115	1.152 ± 0.11 9	L. Pliocene	4 to 3	0.288 ± 0.030 to 0.384 ± 0.040
36	490±50	117	42	0.607 ± 0.06 5	U. Tortonian	8	0.076 ± 0.008
37	490±70			0.490 ± 0.07 0	U. Tortonian	8	0.061 ± 0.009
38	70±30	360	80	0.430 ± 0.08 5	Pliocene	5.3 to 2.58	0.081 ± 0.016 to 0.167 ± 0.033
39	20±20	355	221	0.375 ± 0.22 2	Pliocene	5.3 to 2.58	0.071 ± 0.042 to 0.145 ± 0.086
40	170±30	362	67	0.532 ± 0.07 3	Pliocene	5.3 to 2.58	0.100 ± 0.014 to 0.206 ± 0.028
40	170±30	535	284	0.705 ± 0.28 6	Pliocene	5.3 to 2.58	0.133 ± 0.054 to 0.273 ± 0.111
41	350±130			0.350 ± 0.13 0	U. Tortonian	8	0.044 ± 0.016
42	80±60	44	13	0.124 ± 0.06 1	U. Middle Miocene	12	0.010 ± 0.005
43	110±110	83	26	0.193 ± 0.11 3		4.52	0.043 ± 0.025
44	200±60			0.200 ± 0.06 0	L. Pliocene	4 to 3	0.050 ± 0.015 to 0.067 ± 0.020
45	340±80	774	217	1.114 ± 0.23 1	Messinian	7 to 5.3	0.159 ± 0.033 to 0.210 ± 0.044
46	350±50			0.350 ± 0.05 0		7.05 to 7.95	0.044 ± 0.006 to 0.050 ± 0.007
47	1040±26	82	25	1.122 ± 0.26	U. Tortonian	8	0.140 ± 0.033

	0			1			
47	1040±26 0	87	47	1.127±0.26 4	U. Tortonian	8	0.141±0.033
48	220±20	967	77	1.187±0.08 0	L. Pliocene	4 to 3	0.297±0.020 to 0.396±0.027
49	450±70			0.450±0.07 0	U. Pliocene	4 to 3	0.113±0.018 to 0.150±0.023
50	380±120	300		0.680±0.12 0	Messinian	7 to 5.3	0.097±0.017 to 0.128±0.023
51	660±60			0.660±0.06 0			
52	30±10	158	98	0.188±0.09 9	U. Pliocene	4 to 3	0.047±0.025 to 0.063±0.033
53	110±50	574	206	0.684±0.21 2	Pliocene	5.3 to 2.58	0.129±0.040 to 0.265±0.082
54	170±50			0.170±0.05 0		3.2 to 4.2	0.040±0.012 to 0.053±0.016
55	110±30			0.110±0.03 0		3.1 to 4.7	0.023±0.006 to 0.035±0.010
56	260±60	100		0.360±0.06 0	U. Middle Miocene	12	0.030±0.005
56	260±60	200		0.460±0.06 0	U. Middle Miocene	12	0.038±0.005
57	160±40			0.160±0.04 0		3.7 to 5.3	0.030±0.008 to 0.043±0.011
58	100±40	531	168	0.631±0.17 3	Pliocene	5.3 to 2.58	0.119±0.033 to 0.245±0.067
59	230±70			0.230±0.07 0		3.3 to 4.0 Ma	0.058±0.018 to 0.070±0.021
60	330±30	87		0.417±0.03 0	U. Pliocene	4 to 3	0.104±0.008 to 0.139±0.010
61	320±40	60	13	0.380±0.04 2	U. Middle Miocene	12	0.032±0.004
62	70±50	848	285	0.918±0.28 9	L. Pliocene	4 to 3	0.230±0.072 to 0.309±0.096
62	70±50	389	70	0.459±0.08 6	Pliocene	5.3 to 2.58	0.087±0.016 to 0.178±0.033
63	270±90	644	165	0.914±0.18 8	U. Serravallian/ L.Tortonian	12 to 8	0.076±0.016 to 0.114±0.023
64	630±90	694	128	1.324±0.15 6	U. Middle Miocene	12	0.110±0.013
65	110±30	819	120	0.929±0.12 4	Tortonian	10 to 9	0.093±0.012 to 0.103±0.014
66	220±160	932	170	1.152±0.23 3	Tortonian	10 to 9	0.115±0.023 to 0.128±0.026
67	50±50	666	145	0.716±0.15 3	L. Pliocene	4 to 3	0.179±0.038 to 0.239±0.051
68	20±20	745	283	0.765±0.28 4	L. Pliocene	4 to 3	0.191±0.071 to 0.255±0.095
69	260±60	699	284	0.959±0.29	Messinian	7 to 5.3	0.137±0.041 to

				0			0.181±0.055
70	340±160	536	161	0.876±0.22 7	Tortonian	10 to 9	0.088±0.023 to 0.097±0.025
71	170±70	1067	130	1.237±0.14 8	lowermost Pliocene	3 to 2.58	0.412±0.049 to 0.479±0.057
73	160±40	1169	35	1.329±0.05 3	lowermost Pliocene	3 to 2.58	0.443±0.018 to 0.515±0.021
74	60±60	1056	37	1.116±0.07 0	lowermost Pliocene	3 to 2.58	0.372±0.023 to 0.433±0.027
74	60±60	823	116	0.883±0.13 1	lowermost Pliocene	3 to 2.58	0.294±0.044 to 0.342±0.0051

^a: van Hinsbergen and Meulenkamp, 2006

^b: Uplift rate calculated by $R = \text{height}/\text{age}$

CURRICULUM VITAE

08/2013 – 08/2015

Research assistant at the IMF (Remote Sensing Technology institute) of the DLR, Oberpfaffenhofen

Education

09/2008 – 03/2013

Research Assistant in Geology, Department of Earth and Environmental Sciences, LMU Munich

04/2011 – 07/2012

Graduate Student Fellow in the THESIS graduate school of the Bavarian Elite Network Program (University of Munich, Germany).

Since 09/2008

PhD student in Geology, Department of Earth and Environmental Sciences, LMU Munich.

Advisors: Prof. Anke Friedrich (LMU Munich), Prof. Michael Eineder (Technical University Munich, Faculty of Civil, Geo and Environmental Engineering)

02/2007 – 09/2008

Research Assistant in Geology, Department of Earth and Environmental Sciences, LMU Munich

1999 – 2005

‘Diploma’ (MSc equivalent) in Physical Geography, Department of Earth and Environmental Sciences, LMU Munich, Main subjects: Geophysics and Remote Sensing
Diploma thesis: "*Visualization of Synthetic Earthquake Scenarios with a PHP - based interactive Database*". Data of simulated earthquake scenarios of historical earthquakes were visualized for an interactive web page programmed with PHP (Hypertext Preprocessor). Thesis Advisor: Prof. Heiner Igel.

Abstracts

Oral Presentation

Rieger S, Adam N, Friedrich AM (2012): Quantification of crustal deformation based on analysis of Persistent Scatterer Interferometry of W-Crete. EGU2012-9635, presented at 2012 EGU Meeting, Vienna, Austria, 23-27 April.

Rieger S, Adam N, Friedrich AM (2012): Quantifying vertical surface motion on different time-scales, example of Crete, Greece, presented at 14th Symposium on Tectonics, Structural Geology and Geology of Crystalline Rocks, Kiel, Germany, 28-30 March.

Rieger S, Adam N, Friedrich AM (2011): Vertical displacement above a subduction zone (SW Crete): Spatial Coincidence of Co- and Interseismic Surface Uplift – From Historic Data and Persistent Scatterer Interferometry Analysis, presented at 2011 Fragile Earth Meeting. International Meeting, Munich, Germany, 4-7 Sept.

Poster Presentation

Rieger S, Adam N, Friedrich AM (2011): Detection of vertical surface motion using Persistent Scatterer Interferometry of W-Crete, presented at 4th Workshop on Remote Sensing and Geology, EARSel, Mykonos, Greece, 21-24 May.

Rieger S, Adam N, Friedrich AM (2011): Observation of vertical motion above a subduction zone using Persistent Scatterer Interferometry Wide Area Product, SW Crete, Abstract: G23A-0835, presented at 2011 Fall Meeting, AGU, San Francisco, Calif., 5-9 Dec.

Selected Work experience and Internships

06/2005 – 11/2006

Employee at the GAF AG (Company for Applied Remote Sensing), Munich
Involved in monitoring for agricultural subsidy payment of the European Union and in wide-area mapping based on IKONOS satellite images

09/2003

Internship in India at the P.G.S.S (Purvanchal Gramin Seva Samiti) a catholic foreign aid project in Gorakhpur (Uttar Pradesh): Social aid for women, education of children and environmental projects.

08/2003

Internship at the Department of Physics of the Earth at the GFZ Potsdam (German Research Center for Geosciences)
Personal assistant of Prof. Peter Bormann for preparing lectures for seismology using the "IASPEI Manual of Seismological Observatory Practice"

05/2003 – 06/2003

Internship at the DFD (German Remote Sensing Data Center) of the DLR, Oberpfaffenhofen. Involved in the project "Landsat 7 Scientific Data Pool" for geocoding Landsat 7 images, and the project "CORINE Land Cover 2000 (CLC 2000)" statistical comparison of results of CLC 2000 with ministerial data of Germany

11/2002 – 02/2003

Student assistant at the DFD, DLR, Oberpfaffenhofen
Correction of satellite orbit (roll, pitch, and yaw) using "Terrascan" software